Transactions of the ASME

TRANSACTIONS OF THE AMERICAN SOCIETY OF MECHANICAL ENGINEERS

VOLUME 79 — JULY 1957 — NUMBER 5

Transactions

of The American Society of Mechanical Engineers

Published on the tenth of every month, except March, June, September, and December

Published monthly by The American Society of Mechanical Engineers. Publication office at 20th and Northampton Streets, Easton, Pa. The editorial department is located at the headquarters of the Society, 29 West Thirty-Ninth Street, New York 18, N. Y. Cable address, "Mechaneer," New York. Price $1.50 a copy, $12.00 annually for Transactions and the *Journal of Applied Mechanics* to members, $1.00 a copy, $6.00 annually. Add $1.50 for postage to all countries outside the United States, Canada, and Pan American Union. Changes of address must be received at Society headquarters seven weeks before they are to be effective on the mailing list. Please send old as well as new address. . . . By-Laws: The Society shall not be responsible for statements or opinions advanced in papers or . . . printed in its publications (B13, Par. 4). . . . Entered as second-class matter March 2, 1928, at the Post Office at Easton, Pa., under the Act of August 24, 1912. . . .

The Application of a New Structural Index to Compare Titanium Alloys With Other Materials in Airframe Structures

By L. R. JACKSON[1] and S. A. GORDON,[2] COLUMBUS, OHIO

The evaluation of structural materials for airframes is based on the strength/density ratio or, more precisely, the ultimate strength/density ratio, the compressive yield strength/density ratio, and the structural indexes for plates and columns. The structural indexes developed for plate elements have, in the past, been based on the formula

$$S_s = \frac{1}{K^{1/3}}\left[\frac{12(1-\mu^2)}{\pi^2}\right]^{1/3}\frac{F_{bu}^{1/3}}{E_r^{1/3}}$$

The application of this relationship to complex sections depends on the weighted average of the various plate elements that constitute the section and on the proper selection of their end fixities. Past experience indicates that this method is often unreliable and does not predict the failing load of the section, since the formula predicts only the stress at which the first buckle occurs in each respective element. A new method of predicting the failing load of a section in compression was suggested in 1954 by R. A. Needham. His method has been used to develop a new structural index for the evaluation of the strength/density ratio of materials in compression. In this report, this new structural index

$$S_s = \frac{2.56\,F_{ce}^{2.18}}{(\eta F_{cy} E)^{0.59}}$$

is compared with the results of compression tests on aluminum sections at room temperature, and similar tests on titanium-alloy angles and channels at room and elevated temperatures. The aluminum test data are from Needham's report; the titanium-alloy test data were supplied by Convair (San Diego) and Boeing (Seattle). Excellent agreement is obtained in all cases. It is believed that the new structural index will provide a reliable method of evaluating the elevated-temperature performance of materials such as titanium, in comparison with other materials, when only the compressive stress-strain curves are available at each temperature.

Introduction

IN the process of introducing any new alloy in the airframe industry, it is necessary to go through a period in which the know-how acquired over years of experience with "familiar" materials is translated in terms of the new alloys being considered. The translation is never complete until the behavior of actual structural components made from the new alloy is understood as fully as is that of components made from conventional alloys.

At early stages in the introduction of a new alloy there is always a period during which there is neither enough of the "new" alloy available to make all of the structural components that eventually must be tested in order to integrate the material into the background of previous experience, nor is there sufficient time to make the tests as rapidly as is desired.

During this period, before a background of actual experience is available, it is necessary to try to bridge the gap by attempting to predict the behavior of possible structural components from the simple test-coupon data on the new alloy.

In the integration of titanium alloys into the family of construction materials for airframes, an additional problem is present in that it is anticipated that titanium alloys will be of great usefulness in airframes built to withstand higher temperatures. For this use there is no background of experience, so it is necessary not only to find ways of predicting the performance of titanium alloys in structures that will operate in environments within the range of previous experience, but also to predict the performance of structures that will operate in environments on which there is no background of experience for any material.

Recently, data obtained by Convair (San Diego) and Boeing (Seattle) on some simple structural elements made from titanium alloys have become available.

In this paper it is shown that these data may not only be used to weld the behavior of components made from titanium alloys to the background of experience on conventional materials, but also to take the first steps toward the prediction of behavior that might be expected at high temperatures.

Criteria for Comparing Behavior of Titanium Alloys With Conventional Materials

Many of the criteria by which the behavior of structural components are evaluated are difficult to apply because there is no general agreement among airframe designers on either the definition of the criterion or how it can be measured. Thus many possible comparisons are clouded by controversies that really are concerned with procedures and have nothing to do with the actual comparison of materials.

There are a few important types of criteria, however, which do not suffer from these difficulties and which can be used to bring the relations between the behavior of titanium alloys (or any other new material for that matter) into sharp focus against the background of experience on conventional materials.

In this paper the two basic criteria of this type that are discussed are the ultimate tensile strength and the crippling (not buckling) strength of columns. The distinction between "buckling" and "crippling" will be treated in more detail later.

The Ultimate Tensile Strength. The ultimate tensile strength belongs in the category of foundation criteria for the comparison of materials, primarily for two reasons: (*a*) Because there are very few pitfalls involved in measuring ultimate tensile strength as a

---

[1] Co-ordination Director, Battelle Memorial Institute.

[2] Consultant, Battelle Memorial Institute.

Contributed by the Aviation Division and presented at the Aviation Division Conference, Los Angeles, Calif., March 14–16, 1956, of The American Society of Mechanical Engineers.

Note: Statements and opinions advanced in papers are to be understood as individual expressions of their authors and not those of the Society. Manuscript received at ASME Headquarters, January 18, 1956. Paper No. 56—AV-10.

material property, and (*b*) because one of the basic design principles codified into most specifications for air worthiness is that maximum design tensile yield stresses should not exceed

$$\frac{\text{Ultimate tensile strength}}{1.5}$$

With the exception of exceedingly pure metals (which are not of interest in airframe design anyway), no metallic material has yet been found in which the factor 1.5 does not insure that applied stresses will not produce permanent deformation at room temperatures.

Thus, in integrating titanium alloys into the family of construction materials, once it is established that the factor 1.5 is adequate, then titanium alloys can be compared with other materials by putting all materials on the basis of

$$\frac{\text{Ultimate tensile strength}}{\text{Density}} = \frac{F_{tu}}{d}$$

Fig. 1 compares some titanium alloys with more conventional materials on this basis.

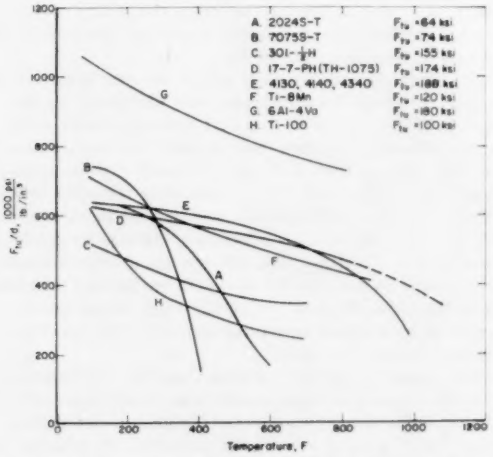

FIG. 1 STRENGTH-WEIGHT COMPARISON ON THE BASIS OF ULTIMATE TENSILE STRENGTH/DENSITY

It was mentioned that there are very few pitfalls in measuring the ultimate tensile strength of a ductile alloy. There are some, however, and the nature of these should be understood in order to avoid possible confusion.

Most of these difficulties enter when measurements are made at elevated temperatures. However, one may be present at any temperature and arises from the following considerations:

The measurement of ultimate tensile strength involves only having some means of measuring the load being applied to a test specimen. The usual course of events in the test is for the load to rise gradually, during the plastic extension of the test piece, to a broad maximum and then to fall off. The ultimate tensile strength is then defined as this maximum load divided by the original area of the test piece regardless of how much the area may have decreased during the plastic flow.

In so far as the material itself is concerned, the physical significance of the test can be described as follows: When a ductile metal is plastically deformed, it becomes stronger or "work-hardened." At the same time this work-hardening process is going on, the test piece is becoming smaller in diameter so that the actual stress on the test area is increasing faster than the load. In the normal course of events, whenever the increase in strength from work hardening is no longer great enough to compensate for the reduction in area, the maximum load is reached, and on further strain the load will decrease.

When the metal being tested does not have sufficient ductility, it may fracture before its work-hardening capacity (in the sense just described) has been exhausted. Fracture also produces a decrease in load so that in cases of this type a "false" ultimate tensile strength is reported.

It often happens that in order to obtain other desired strength properties, it is impossible to provide enough ductility to realize all of the work-hardening capacity of an alloy. Nevertheless, it is the responsibility of the materials engineer to know whether the ultimate tensile strengths he reports are true "ultimate strengths" or whether they represent premature fracture. The distinction between the two modes of behavior does not affect the usefulness of ultimate tensile strength as a design criterion. It does provide the materials engineer with a clue he may possibly use in improving the alloy, in that he may find metallurgical means of realizing more of the potential strength of the alloy. Even if he cannot do so, however, the ultimate tensile strength he reports is still a valid design criterion.

At elevated temperatures the difficulties that arise in measuring ultimate tensile strength arise from the fact that work hardening no longer has the simple significance it has at room temperature; and ultimate tensile strengths not only do not have a simple interpretation but become multivalued, depending not only on the testing speed, but also on the environment and test procedures.

In Fig. 1, difficulties of this type at elevated temperatures have been evaded by comparing all materials at roughly the same testing speed and for exposure to temperature for roughly the same length of time (approximately 30 min). These procedures make the comparison in Fig. 1 reasonably valid; however, the designer should bear in mind that long exposure of some alloys to the temperatures covered by Fig. 1 will not only result in lower ultimate strength at temperature but also may produce lower room-temperature strength (or room-temperature ductility). This remark applies particularly to the aluminum alloys above 250 F and, possibly, to titanium alloys above 800 F.

One of the reasons that F_{tu}/d is an important design criterion is that up to 40 per cent of an airframe may be designed in tension. While the comparisons in Fig. 1 indicate the same titanium alloys have potential regions of superiority of all temperatures, it should be pointed out that the comparisons in Fig. 1 are only the first step toward determining where the tensile behavior of titanium alloys places them in the family of airframe materials. Before their position can be set with complete confidence, data on the strength of joints in titanium alloys must be compared with those for the conventional materials. This comparison is not attempted in this paper.

Crippling Strength of Columns. Since from 60 to 90 per cent of an airframe is designed for compression, the crippling stress in compression is an exceedingly important design criterion.

In order to compare the behavior of titanium alloys with respect to other materials in structures on the basis of buckling or crippling, two steps are involved:

1 A method of analysis must be developed that will predict the behavior of conventional construction materials when built into structures from a knowledge of material properties that can be measured on simple test coupons.

2 Having a method that applies to materials on which there is a background of experience, it is then necessary to determine whether titanium alloys fit into the same pattern.

As will be developed later in this paper, both of these steps have been accomplished for stiffeners, which include not only the most

important type of compression components in present aircraft, but which will become increasingly important in new designs. Experimental data now exist which indicate that within rather close limits the relative behavior of titanium alloys with respect to other materials can be predicted.

Before presenting the method by which this agreement has been obtained, it is worth while to clarify concepts that will be used.

When a stiffener or a stiffened panel is subjected to a compression load (but not affected by column length), buckling will start in a free edge. The exact load at which buckling starts is difficult both to define and to measure, and depends on the sensitivity of the measuring device. As load is increased, however, the initial buckle will pass through one of the corners in a stiffener.

As the testing on the stiffener proceeds, a point is finally reached at which the load it can carry reaches a maximum value and then begins to drop off as the stiffener collapses.

This behavior bears a superficial resemblance to what happens in a tensile test and provides a way of defining the crippling load, P_{cc}. In the remainder of this paper P_{cc} will be defined in this manner.

To demonstrate how the crippling strength of stiffened-sheet components can be related to basic material properties, it is desirable to discuss briefly the background of the problem. Early in the history of aircraft design, it was recognized that the total length of a stiffened panel l, becomes greater than about three times its width b. The buckle pattern that forms is effectively independent of the length but depends strongly on the width b. From this point it seemed natural for investigators to attempt to find ways of predicting the relation between the load and width of a stiffened panel as a means of comparing the relative efficiency of several materials.

Considerations of this type led to the concept of a "structural index" in the form

$$S_s \cong \frac{P_c}{b^2} \quad \ldots\ldots\ldots\ldots\ldots\ldots\ldots\ldots [1]$$

The concept of an index in this form seems to have occurred to a number of investigators independently and almost simultaneously. It does not seem worth while to attempt to determine the first appearance of such a concept. However, a well-written account of the development of this type of index related to elastic buckling of stiffeners is given by Heimerl and Barrett.[3]

In this technical note[3] the structural index is given by the relation

$$S_s \cong \frac{P_{bu}}{b^2} = \frac{1}{K^{1/2}} \left[\frac{12(1-\mu^2)}{\pi^2}\right]^{1/2} \frac{F_{bu}^{3/2}}{E_r^{1/2}} \quad \ldots\ldots\ldots [2]$$

In Equation [2], it will be noted that all of the terms on the right-hand side of the equation (with the exception of K) are either independent variables such as the buckling stress F_{bu} or are constants of the material, such as E_r, the elastic modulus (or reduced modulus near the yield strength) and Poisson's ratio μ. The constant K is a sort of geometric factor that takes into account the shape of the stiffener.

The definition of structural index given in Equation [2] is associated with buckling, and the establishment of the validity of this index is tied to the difficulty of defining and measuring P_{bu} or F_{bu}.

Through the years many investigators have recognized this difficulty and have proposed various ways of working with crippling loads and stresses rather than the more ambiguous buckling criteria. In a recent paper Needham[4] discusses the history of this problem and makes an important suggestion that allows prediction of the performance of a wide variety of structural shapes. Essentially, Needham suggests that any possible shape of stiffener that can be bent from sheet can be considered to be a series of angles, and that the characteristic width b of each angle is defined by the relation

$$b' = \frac{a_1 + b_1}{2} \quad \ldots\ldots\ldots\ldots\ldots\ldots [3]$$

Fig. 2 shows the method Needham uses for measuring the values of $a_1 + b_1$. These values are measured from the center line of the sheet in each leg.

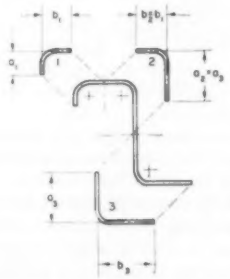

FIG. 2 SUBDIVISION OF SECTION FOR CRIPPLING ANALYSIS

Using this method of defining width, Needham shows that the crippling strength of very complex shapes can be predicted by the equation

$$F_{cc} = C_e \sqrt{(F_{cy}E)} \left(\frac{t}{b}\right)^{3/4} \quad \ldots\ldots\ldots\ldots [4]$$

where F_{cc} is the crippling stress in each angle element, C_e is a constant depending on whether the angle has a free edge or not, b is defined by Equation [3], t is the sheet thickness, F_{cy} is the compression yield strength of the material (0.2 per cent offset), and E is the elastic modulus of the material.

The crippling load of each angle is then given by the equation

$$P_{cc(x)} = F_{cc(x)}A_{(x)} \quad \ldots\ldots\ldots\ldots\ldots [5]$$

where $F_{cc(x)}$ is the crippling stress in angle x. The area of each angle section is associated with b by the relation

$$A_x = \left[\frac{b'}{t} - 0.214\,\frac{R}{t}\right] 2t^2 \quad \ldots\ldots\ldots\ldots [6]$$

where R is the bend radius of the angle.

The total crippling stress then is given by Needham from the equation

$$F_{cc} = \frac{\Sigma(\text{crippling loads of angles})}{\Sigma(\text{area of angles})} \quad \ldots\ldots\ldots [7]$$

On examination of the data presented by Needham and by adapting a device used by Gallaher,[5] a further simplification appears to be possible. That is to define the average characteristic length associated with each angle by the equation

[3] "Efficiency Evaluation of Ti at Elevated and Normal Temperatures," by G. J. Heimerl and P. F. Barrett, NACA TN 2269, January, 1951.

[4] "The Ultimate Strength of Aluminum-Alloy Formed Structural Shapes in Compression," by R. A. Needham, *Journal of the Aeronautical Sciences*, vol. 21, April, 1954, pp. 217–229.

[5] "Plate Compressive Strength of FS-1h Magnesium Alloy Sheet and a Maximum Strength Formula for Magnesium Alloy and Aluminum Alloy Formed Sections," by G. L. Gallaher, NACA TN 1714, October, 1948.

$$b' = \frac{A}{2Nt} \quad [8]$$

where A is the total area of the section (obtained by weight and length measurements), N is the total number of angles it contains, and t is the thickness of the sheet from which the stiffener was made.

It is found that all data in Table VI of Needham's paper[4] as well as those in the references he cites (where such references give data on areas), including the data in Gallaher's paper[5] on Z-sections made from FS-1h, 17S-T, and 24S-T, fall along a common curve. The deviation of any point representing any shape or material from this curve is no greater than the reproducibility between duplicate tests. As will be shown later, data on titanium-alloy shapes also fit the curve.

The curve has the general form

$$F_{cc} = k_1 \sqrt{(F_{cy}E)} \left(\frac{t}{b'}\right)^n \quad [9]$$

where it must be remembered that b' is defined by Equation [8].

The best fit for all data is obtained by making $n = 0.847$ and $k_1 = 0.45$. It will be noted that Equation [9] is the same as Needham's relation, Equation [4], except for the different method of defining b' and a change in the values n and k.

Equation [9] can be used to define a structural index of the same form as defined by Equation [1] and it can be shown that

$$S_s \cong \frac{P_{cc}}{b'^2} = \frac{F_{cc}\dfrac{n+1}{n}}{(\eta F_{cy}E)^{1/2n}k_1^{1/n}} \quad [10]$$

where b' is defined by Equation [8]; $\eta = E_r/E$ where E_r is a "reduced modulus" that differs from the value 1 only when F_{cc} approaches F_{cy}.

Inserting the constants found by the best fit for the curve expressed by Equation [9], the definition of structural index becomes

$$S_s \cong \frac{P_{cc}}{b'^2} = \frac{2.56\ F_{cc}^{2.18}}{(\eta F_{cy}E)^{0.59}} \quad [11]$$

Before showing how the structural index defined by Equation [11] can be used to reduce data on a wide variety of shapes and materials to a common basis, several features of the equation should be discussed:

1 The crippling stress F_{cc} is defined as the crippling load P_{cc} (the maximum load it will bear) divided by the total area A of the section. Thus it should be realized that F_{cc} is an average. The actual stress distribution between the corners of angles and the centers of "captive" flanges or those with "free" edges is quite complex. However (as will be shown by the use of Equation [11]) the average crippling stress F_{cc} seems to be predictable within as great a precision as it can be measured on duplicate test stiffeners.

2 Equation [11] really provides two definitions of structural index. The first

$$S_s \cong \frac{P_{cc}}{b'^2}$$

is determined by a crippling test on a short column. The second

$$S_s = \frac{2.56\ F_{cc}^{2.18}}{(\eta F_{cy}E)^{0.59}}$$

is obtained entirely from the stress-strain curve of the material.

3 In the second definition, Se always contains the group $(\eta F_{cy}E)$. The significance of this grouping is that an increase or decrease in F_{cy} has exactly the same effect as the same percentage increase or decrease in elastic modulus E for all values of F_{cc}, even where they are far below the yield strength. The reason for this, apparently, is that where crippling occurs, even though the average stress F_{cc} may seem to be quite low, when the corners of the angles in the section collapse, the actual stress in the corners is probably at the yield strength.

4 The definition of structural index in terms of the stress-strain curve can be used to study the relative behavior of materials without the necessity of deciding on specific shapes. However, where it is desired to obtain "design" curves, the structural index can be simply related to the familiar design parameters in the following manner

$$S_s \cong \frac{P_{cc}}{b'^2} \cong \frac{F_{cc}t}{b'} = F_{cc}\frac{2Nt^2}{A} \quad [12]$$

where, as in Equation [8], A is the total area of the stiffener under consideration and N is the total number of angles it contains.

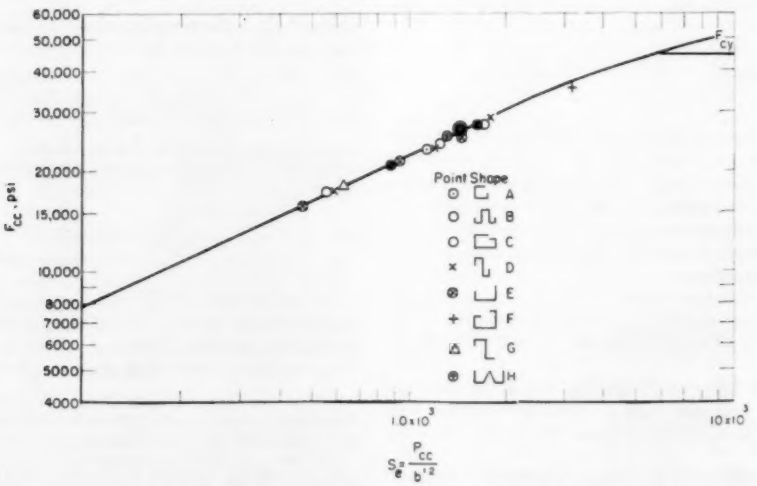

FIG. 3 STRUCTURAL-INDEX CURVE FOR 2024-T3 ALCLAD
(F_{cy} = 45,000-psi room temperature. For comparison with data in Table 6 of Needham.[4])

Use of Structural Index to Predict Performance of Stiffeners of Various Shapes and From Various Materials

A structural-index curve was constructed for 24S-T Alclad at a yield strength of $F_{cy} = 45{,}000$ psi using a compression stress-strain curve for this material and Equation [11]. The value of η used for this curve was $\eta = E \sec/E$.

The structural indexes of all stiffeners tested by Needham and quoted in his Table VI were computed by means of Equation [12].

The nature of the agreement obtained is shown in Fig. 3. The points on Fig. 3 do not contain all of the values in Needham's table because there was so much overlap; however, representative points are shown for every type of section.

Test data for stiffeners made from RC-130A, RC-70, MST-3A1-5Cr, RC-130B, RC-55, C-110M, and C-130AM titanium alloys were made available through the courtesy of Convair (San Diego) and Boeing (Seattle). Some of the stiffeners were angles and some were channels. Some were bent from sheet, some were machined from bars or were extruded. In some cases tests were made at elevated temperatures. In all cases compression stress-strain curves were available on the same material tested under the same condition (temperature) as the stiffener was tested.

Table 1 summarizes the pertinent test information from the data obtained by Convair (San Diego), and Tables 2 and 3 summarize the data from Boeing (Seattle).

Using the stress-strain data on the various alloys, structural-index curves were constructed for each alloy and condition. At the time this was done it was not known whether η should be defined by E_{sec}/E or by $\sqrt{(E_{tan}\, E)}/E$ or by some other definition.

Accordingly, both of these values as well as several other possibilities were computed for each stress on each curve. In order to reduce the labor of these computations this was done with a CPC digital-type computer.

Fig. 4 shows the results on RC-130A, MST-3A1-5Cr and RC-130B channels obtained by Convair. The yield strengths and compression stress-strain curves on the different test pieces varied slightly. The structural-index curve shown in Fig. 4 was for $F_{cy} = 140{,}000$. The change in shape in going from $E_r = E_{sec}$ to $E_r = \sqrt{(E_{tan}\, E)}$ is shown, as is also the "cutoff" at F_{cy}. All points for which the structural index has a practical meaning fall either on the E_{sec} curve or near F_{cy}. Considering the slight variation in stress-strain curves and the fact that both sharp and rounded channels are represented, the agreement with prediction is good.

TABLE 1 SPECIMEN DATA AND TEST RESULTS ON CHANNELS FORMED FROM TITANIUM-ALLOY SHEET OR MACHINED FROM BAR STOCK (CONVAIR, SAN DIEGO)

Specimen	F_{cy}, ksi	$Ex10^6$, psi	H, in.	W, in.	L, in.	t, in.	$A^{(a)}$, in^2.	$F_{cc}{}^{(b)}$, ksi	$\frac{F_{cc}}{\sqrt{F_{cy}E}}$	$\frac{A^{(c)}}{2Nt^2}$	$\frac{F_{cc}2Nt^{2(d)}}{A}$
						RC-130A[e]					
16A	146	18.68	0.563	1.406	5	0.107	0.2100	141	0.085	4.6	30.8
10	112	16.9	0.625	1.375	5	0.091	0.1921	117	0.086	5.64	20.8
15	124	17.02	0.625	1.406	5.25	0.087	0.1885	125.8	0.086	6.30	19.8
9	120	16.89	0.625	1.313	5.25	0.063	0.1552	110.2	0.078	9.85	11.2
11	137	17.68	0.625	1.375	5.375	0.056	0.1310	88.5	0.057	10.4	8.5
12	138.9	17.34	0.625	1.313	5.375	0.045	0.1040	72.0	0.046	13.0	5.5
14	138.6	16.49	0.625	1.344	5.375	0.032	0.0769	52.8	0.035	19.2	2.75
						RC-70[e]					
6	78.9	15.78	0.563	1.188	4.50	0.125	0.2129	93.5	0.084	3.38	27.5
5	78.9	15.78	0.813	1.438	5.50	0.125	0.3172	96.1	0.086	5.00	19.2
4	78.9	15.78	1.063	2.125	8.50	0.126	0.4530	87.8	0.078	3.42	25.6
3	82.1	16.13	0.656	1.344	5.25	0.061	0.1509	76.3	0.066	10.2	7.49
1	85.2	15.78	0.656	1.219	5.25	0.048	0.1170	62.9	0.054	12.7	4.95
8	77.0	15.48	0.625	1.219	5.50	0.040	0.0958	51.9	0.048	13.4	3.87
2	64.4	16.59	0.625	1.281	5.50	0.032	0.0798	39.8	0.039	23.9	1.67
						MST-3A1-5Cr[f]					
9	142.5	15.99	0.819	2.177	8.75	0.071	0.248	73.5	0.049	12.4	9.95
11	142.5	15.99	0.816	2.219	8.75	0.063	0.220	66.3	0.044	14.1	4.70
13	142.5	16.72	0.814	2.221	8.75	0.051	0.179	56.6	0.038	17.2	3.30
15	135.0	16.72	0.503	1.502	6.00	0.187	0.361	126.3	0.084	2.52	50.0
27	135.0	16.72	0.817	2.190	8.75	0.190	0.609	136.9	0.091	4.22	32.4
29	135.0	16.72	0.817	2.189	8.75	0.160	0.524	133.8	0.089	5.24	25.5
						RC-130B[f]					
31	135.0	17.63	0.816	2.190	8.75	0.131	0.429	133	0.089	6.40	20.8
19	138.5	16.20	0.817	2.181	8.75	0.075	0.260	84.6	0.056	11.7	7.2
21	138.5	16.20	0.823	2.177	8.75	0.064	0.224	75.6	0.050	13.7	5.5
23	141.5	17.63	0.811	2.215	6.00	0.053	0.182	60.5	0.040	16.2	3.7
25	138.5	16.20	0.503	1.502	8.75	0.189	0.359	128.1	0.085	2.50	51.0
33	141.5	17.63	0.817	2.190	8.75	0.190	0.604	134.8	0.085	4.2	32.1
35	141.5	17.63	0.818	2.188	8.75	0.159	0.529	135.3	0.086	5.3	25.6
37	141.5	17.63	0.816	2.188	5.25	0.128	0.427	135.2	0.086	6.7	20.2
						RC-55[e]					
52	56.1	16.26	0.656	1.313	5.25	0.063	0.154	66	0.069	9.65	6.84
53	61.0	14.96	0.656	1.313	5.25	0.053	0.123	60.5	0.063	11.0	5.50
55	59.5	15.15	0.625	1.25	5.00	0.045	0.098	51.5	0.054	12.2	4.22
56	61.5	16.0	0.625	1.25	5.00	0.032	0.071	41.5	0.043	17.8	2.33
51A	57.8	17.25	0.59	1.34	5.53	0.119	0.23	69.4	0.069	4.12	16.8
52A	57.8	17.25	0.81	1.42	4.43	0.119	0.25	71.7	0.072	4.45	16.0
53A	57.8	17.25	1.08	2.12	8.42	0.119	0.445	68.1	0.068	7.95	8.55

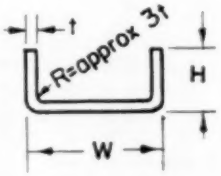

(a) Area from length and weight.
(b) $\frac{P_{cc}}{A}$ P_{cc} = ultimate load, lb.
(c) $\frac{A}{2Nt^2} = \frac{b'}{t}$.
(d) $\frac{F_{cc}2Nt^2}{A} = \frac{P_{cc}}{b'^2}$
(e) Bent from sheet.
(f) Machined from bar stock with sharp corners and sharp inside radii.

TABLE 2 SPECIMEN DATA AND TEST RESULTS ON ANGLES FORMED FROM SHEET C-110M TITANIUM OR EXTRUDED FROM C-130AM TITANIUM AND TESTED AT VARIOUS TEMPERATURES AT BOEING

Specimen[a]	Test Temp, F	F_{cy}, kpsi	E, x10^6, psi	Nominal Dimensions, in. Leg A	t	Leg B	t	Nominal Length, L, in.	Average Area, A, in.^{2}[b]	F_{cc} Average,[b] kpsi	$\frac{F_{cc}}{\sqrt{F_{cy}E}}$[c]	$\frac{A}{2Nt^2}$[c]	$\frac{F_{cc}2Nt^2}{A}$[c]
GL28R 1, 2, 3	Room	130	16.5	0.333	0.034	0.318	0.034	1.49	0.019	102.2	0.069	8.25	12.4
4, 5, 6	300	90	14.9		0.034		0.034	1.49	0.0193	81.4	0.070	8.39	9.7
7, 8, 9	500	65	14.3		0.034		0.034	1.49	0.0194	64.3	0.067	8.42	7.65
10, 11, 12	800	53	12.3		0.034		0.034	1.49	0.0192	56.8	0.069	8.35	6.80
GL20R 13, 14, 15	Room	130	16.5	0.650	0.034	0.645	0.034	3.42	0.0413	54.1	0.037	18.0	3.0
16, 17, 18	300	90	14.9		0.034		0.034	3.42	0.0410	43.4	0.037	17.5	2.48
19, 20, 21	500	65	14.3		0.034		0.034	3.42	0.041	35.1	0.037	17.1	2.05
22, 23, 24	800	55	12.3		0.034		0.034	3.42	0.042	30.8	0.037	17.2	1.79
GL20R 25, 26, 27	Room	130	16.5	0.970	0.034	0.966	0.034	5.20	0.0624	38.8	0.027	27.1	1.43
28, 29, 30	300	90	14.9		0.034		0.034	5.20	0.062	32.3	0.028	26.5	1.21
31, 32, 33	500	65	14.3		0.034		0.034	5.20	0.0625	27.2	0.028	26.2	1.04
34, 35, 36	800	55	12.2		0.034		0.034	5.20	0.0610	22.6	0.028	27.0	0.84
GL30R 1, 2, 3	Room	134	16.5	0.760	0.053	0.767	0.053	3.80	0.0749	64.5	0.043	12.5	5.17
GL31R 1, 2, 3	300	116	15		0.053		0.053	3.80	0.073	54.9	0.041	13.1	4.18
GL30R 4, 5, 6	500	77	14.3		0.053	0.742	0.053	3.80	0.0748	44.3	0.042	13.1	3.38
GL31R 4, 5, 6	800	76	11.9		0.053	0.750	0.053	3.80	0.074	40.5	0.048	13.7	2.96
GL30R 7, 8, 9	Room	134	16.5	1.96	0.055	1.98	0.055	11.0	0.2094	31.3	0.021	34.5	0.905
GL31R 7, 8, 9	300	116	15		0.055		0.055	11.0	0.209	27.2	0.020	36.2	0.750
GL30R 10, 11, 12	500	77	14.3		0.055		0.055	11.0	0.209	24.2	0.023	34.2	0.707
GL31R 10, 11, 12	800	76	11.9		0.055		0.055	11.0	0.205	21.0	0.022	35.4	0.594
Extruded Angles Made From C-130AM (Boeing)													
GL103A1	Room	155.1	18.0	1.29	0.154	1.295	0.154	5.55	0.3798	147.7	0.089	7.95	18.6
GL103A2	Room	155.1	18.0	1.30	0.118	1.304	0.118	5.58	0.2990	107.0	0.064	10.7	10.0
GL103A3	Room	155.1	18.0	1.30	0.113	1.304	0.114	5.58	0.2977	103.8	0.062	11.3	9.2
GL103A4	Room	155.1	18.0	1.10	0.0816	1.103	0.082	4.51	0.1750	86.8	0.052	13.1	6.6
GL103A5	Room	155.1	18.0	1.10	0.0898	1.103	0.838	4.51	0.1898	96.4	0.057	12.6	7.65

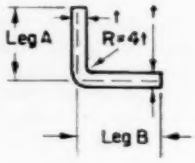

(a) Average of three specimens.
(b) All specimens formed at room temperature and stress relieved at 1050 F for 30 minutes. Furnace cooled to 900 F then air cooled.
(c) See notes to Table 1.

TABLE 3 SPECIMEN DATA AND TEST RESULTS ON CHANNELS FORMED FROM SHEET C-110M TITANIUM ALLOY AND TESTED AT VARIOUS TEMPERATURES AT BOEING

Specimen	Test Temp, F	F_{cy}, kpsi	Ex10^6, psi	Nominal Dimensions,[a] in. Leg A	Leg B	Leg C	t	Nominal Length, L, in.	Average Area, A, in.^{2}	F_{cc}, kpsi	$\frac{F_{cc}}{\sqrt{F_{cy}E}}$[b]	$\frac{A}{2Nt^2}$[b]	$\frac{F_{cc}2Nt^2}{A}$[b]
GL2R 1, 2, 3	Room	130	16.5	0.33	0.675	0.33	0.034	3.00	0.0393	121.5	0.083	8.48	14.3
4, 5, 6	300	90	14.9	0.33	0.675	0.33	0.034	3.00	0.0398	96.3	0.083	8.60	11.2
7, 8, 9	500	65	14.3	0.33	0.675	0.33	0.034	3.00	0.0391	80.3	0.084	8.45	9.50
10, 11, 12	800	55	12.3	0.33	0.675	0.33	0.034	3.00	0.0398	68.9	0.084	8.6	8.0
GL2R 13, 14, 15	Room	130	16.5	0.65	1.300	0.65	0.034	5.75	0.0830	64.6	0.044	17.3	3.73
16, 17, 18	300	90	14.9	0.65	1.300	0.65	0.034	5.75	0.0872	48.8	0.042	17.6	2.77
19, 20, 21	500	65	14.3	0.65	1.300	0.65	0.034	5.75	0.0800	39.4	0.041	17.5	2.25
22, 23, 24	800	55	12.3	0.65	1.300	0.65	0.034	5.75	0.0828	31.4	0.038	17.3	1.81
GL2R 25, 26, 27	Room	130	16.5	0.97	1.94	0.97	0.034	8.675	0.1232	46.8	0.032	26.3	1.78
28, 29, 30	300	90	14.9	0.97	1.94	0.97	0.034	8.675	0.1255	37.3	0.032	27.4	1.36
31, 32, 33	500	65	14.3	0.97	1.94	0.97	0.034	8.675	0.1248	29.3	0.031	26.4	1.11
34, 35, 36	800	55	12.2	0.97	1.94	0.97	0.034	8.675	0.1245	24.5	0.031	27.1	0.905
30R 1, 2, 3	Room	134	16.5	0.75	1.52	0.75	0.055	6.40	0.152	79.1	0.053	12.7	6.24
31R 1, 2, 3	300	116	15.0	0.75	1.52	0.75	0.055	6.40	0.1443	64.5	0.049	13.3	4.84
30R 4, 5, 6	500	77	14.3	0.75	1.52	0.75	0.055	6.40	0.1523	55.0	0.0575	12.7	4.33
31R 4, 5, 6	800	76	11.9	0.75	1.52	0.75	0.055	6.40	0.1455	48.6	0.051	13.5	3.60
30R 7, 8, 9	Room	134	16.5	1.98	3.96	1.97	0.055	17.9	0.1403	36.4	0.0245	35.8	1.02
31R 7, 8, 9	300	116	15.0	1.98	3.96	1.97	0.055	17.9	0.398	30.2	0.0277	35.6	0.842
30R 10, 11, 12	500	77	14.3	1.98	3.96	1.97	0.055	17.9	0.391	25.5	0.0244	34.8	0.734
31R 10, 11, 12	800	76	11.9	1.98	3.96	1.97	0.055	17.9	0.405	21.6	0.0227	36.0	0.600

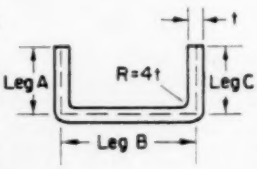

(a) Average of three specimens.
(b) All specimens formed at room temperature and stress relieved at 1050 F for 30 minutes. Furnace cooled to 900 F then air cooled.

Fig. 5 shows the data on channels made from RC-70; again the curve for $E_r = E_{sec}$ provides reasonable agreement.

Fig. 6 shows the data on channels made from RC-55. Here there are three points that lie above the curve. However, this might not be unexpected. The RC-55 material is relatively soft and easily work-hardened, and the channel sections were short and relatively thick. It would take less than 1 per cent cold work to raise the compression yield strength of the RC-55 alloy to 70,000 psi, which would account for the three high points. It is possible that if compression stress-strain tests had been made on the material after testing as a channel, it would have been found that the three points actually belonged in the positions shown. In any case, they represented enough deformation to make channels of such high structural index in RC-55 impractical. Fig. 7 shows results of room-temperature tests on both channels and angles made by Boeing (note that a single curve agrees with both).

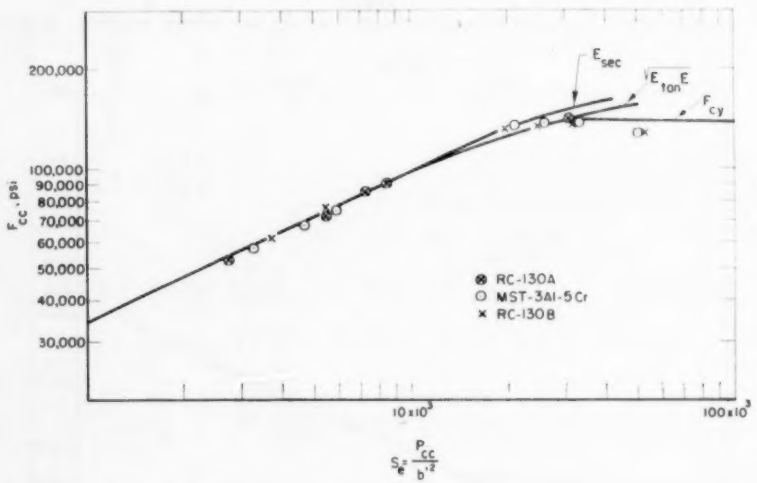

FIG. 4 TITANIUM ALLOY CHANNELS (CONVAIR)

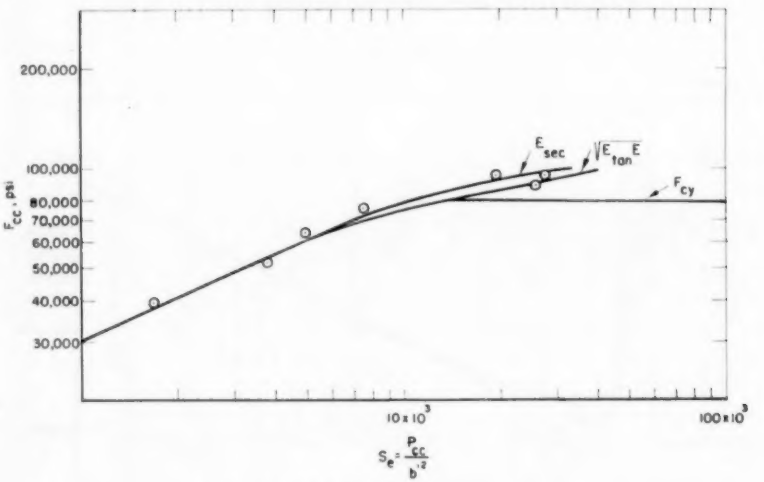

FIG. 5 RC-70 CHANNELS (CONVAIR)

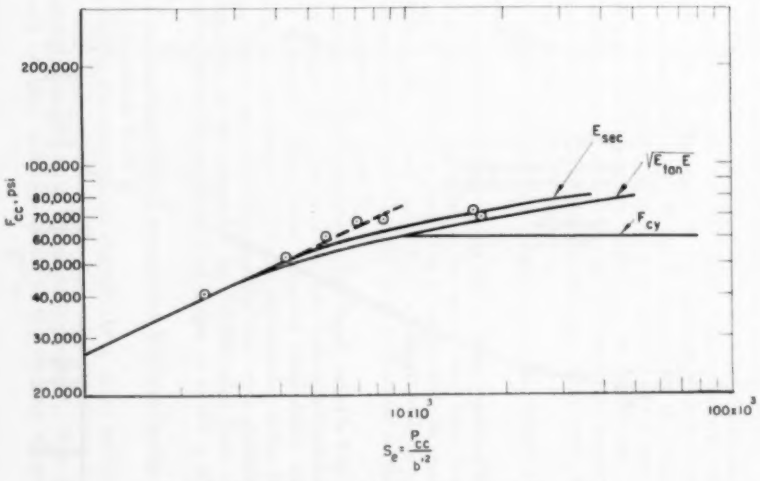

FIG. 6 RC-55 TITANIUM ALLOY CHANNELS (CONVAIR)

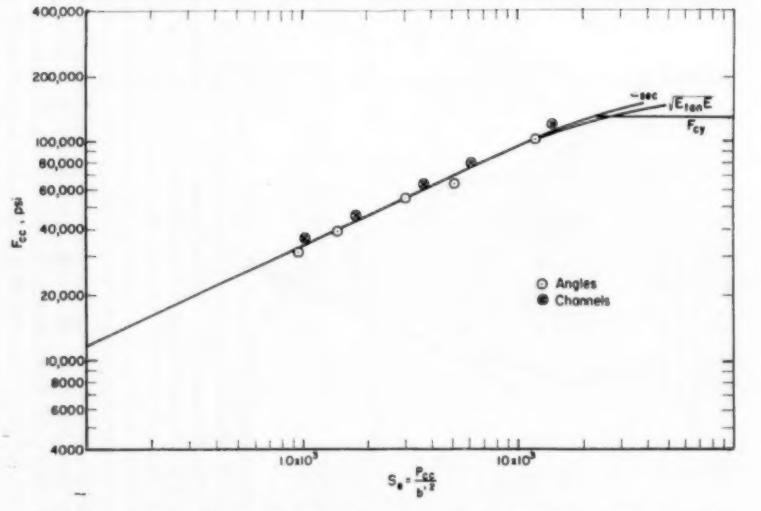

FIG. 7 ROOM-TEMPERATURE TESTS BY BOEING (SEATTLE); TITANIUM ALLOY C-110M

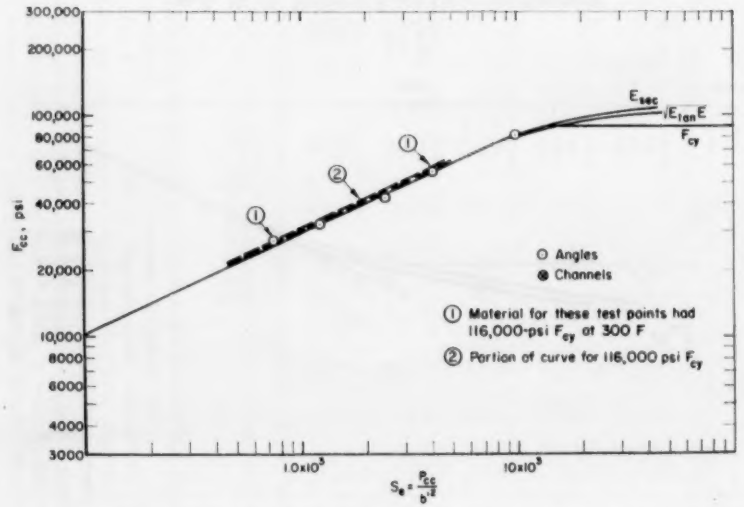

FIG. 8 TITANIUM ANGLES AND CHANNELS (BOEING) TESTED AT 300 F; TITANIUM ALLOY C-110M

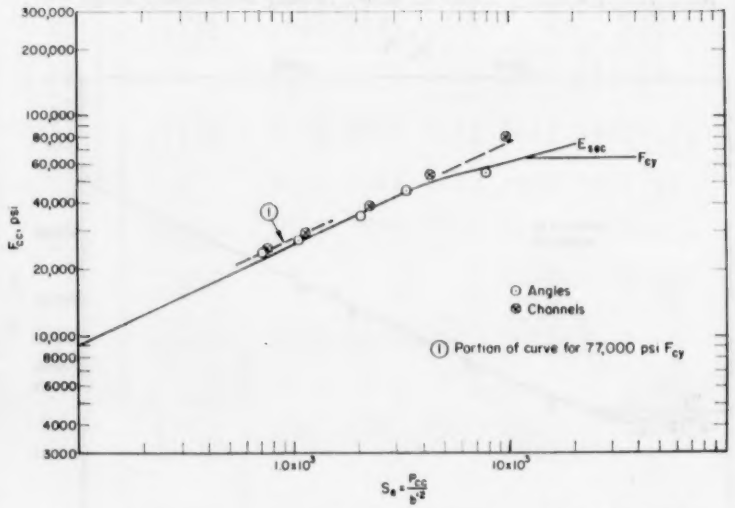

FIG. 9 TITANIUM ANGLES AND CHANNELS (BOEING) TESTED AT 500 F; TITANIUM ALLOY C-110M

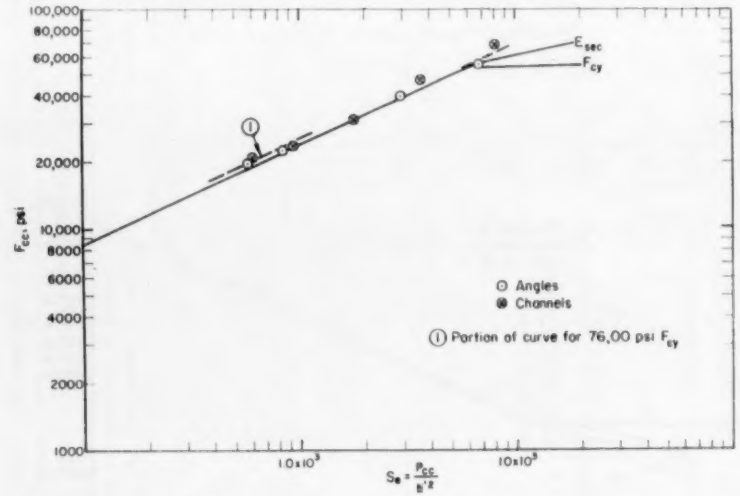

FIG. 10 TITANIUM ANGLES AND CHANNELS (BOEING) TESTED AT 800 F; TITANIUM ALLOY C-110M

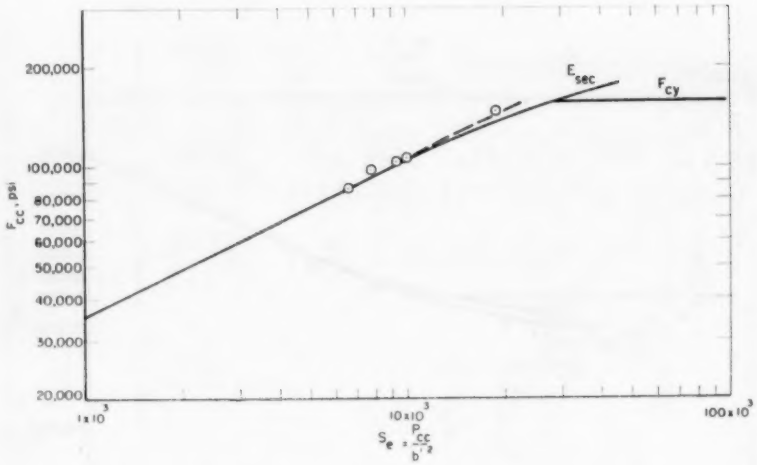

FIG. 11 C-130AM TITANIUM ALLOY EXTRUDED ANGLES (BOEING)

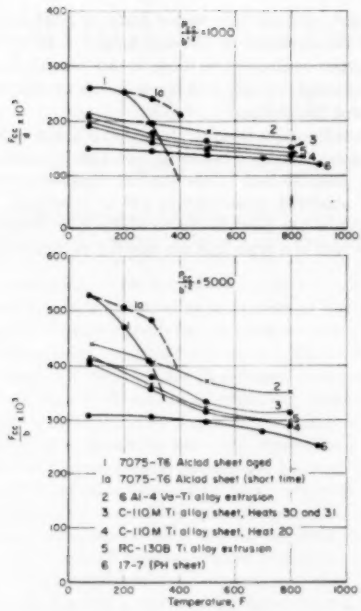

FIG. 12 STRENGTH-DENSITY RATIO OF SEVERAL MATERIALS AT TWO STRUCTURAL INDEXES

TABLE 4 MEASURED CONSTANTS OF ALLOYS USED FOR CONSTRUCTION OF STRUCTURAL-INDEX CURVES

Material	Source of Data	Temp, F	F_{cy} x10^3, psi	E x10^6, psi	$\left(\frac{F_{cc}}{d}\right)_{max}$ x10^3
RC-130B	Battelle	80	140	16.5	825
		300	98	14.9	575
		500	70	14.3	412
		800	60	12.0	353
7075-T6 short time	ANC5	80	75	10.5	750
		200	70	10.3	700
		300	60	10.0	600
		400	45	9.3	450
7075-T6 aged	ANC5	80	75	10.5	750
		200	60	10.3	600
		300	23.2	10.0	230
		400	14.3	9.3	140
17-7PH	Producers Data	80	180	29.0	640
		300	177	26.6	630
		500	170	24.5	605
		700	152	22.3	540
		900	112	20.0	400
6Al-4V-Ti Alloy (Boeing)	Extrusion	80	169	17.0	1000
		300	134	16.0	790
		500	110	14.2	645
		800	96	13.2	564
C-110M (Boeing)	Ht20R	80	130	16.5	765
	Ht20R	300	90	14.9	530
	Ht20R	500	65	14.3	382
	Ht20R	800	53	12.3	312
C-110M (Boeing)	30R	80	134	16.5	780
	31R	300	116	15.0	682
	30R	500	77	14.3	453
	31R	800	76	11.9	446

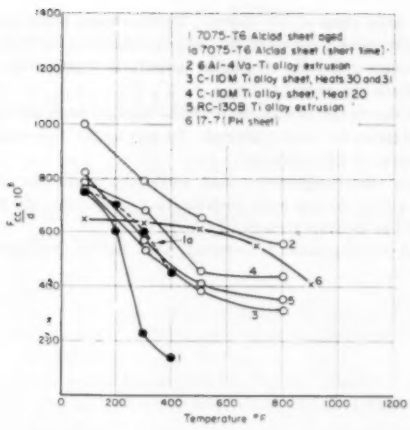

FIG. 13 COMPARISON OF MATERIALS AT MAXIMUM PRACTICAL VALUE OF STRUCTURAL INDEX

Fig. 8 shows test results on both channels and angles tested at 300 F. Here two heats of material with somewhat different high-temperature properties were involved. The complete curve for the lower-strength material is shown in full, while a portion of the curve for the higher-strength material is shown as a dash line. The difference between the curves is no greater than the scatter in the points. The same device was used for displaying the tests at 500 and 800 F, shown respectively, in Figs. 9 and 10. In both these latter curves there was one high point at a high structural index—again it may be possible that work hardening is involved.

It is to be noted that at the temperatures at which this deviation from the curve seems marked, both the strength level and the shape of the stress-strain curve are not far from that for RC-55 at room temperature (see Fig. 6). While deformation and work hardening may be the reason for the apparent deviation, there may be another possibility. At higher temperatures the shape of the stress-strain curve is much more sensitive to rate of loading than it is at room temperature, particularly for stresses near F_{cy}, so that if the loading rates in the stiffener tests were somewhat different from the compression stress-strain tests, some discrepancy in results could be expected.

Fig. 11 shows test results on extruded angles made from C-130-AM alloy.

In view of the excellent agreement between crippling strength of stiffeners and structural-index curves constructed from stress-strain data, it now seems possible to use such curves to explore the relative efficiencies of materials on a strength/weight basis by the use of structural-index curves. Such comparisons are made on two bases in Figs. 12 and 13.

It will be noted that points are shown on all curves in Figs. 12 and 13 because all points were obtained from structural-index curves constructed from actual measured compression yield, modulus, and stress-strain data (with the exception of the data on the 17-7PH on which only tension data were available). Furthermore, the test points for the C-110M alloy have been further validated by actual tests on shapes as shown in Figs. 7–10.

The pertinent basic data on the materials illustrated in Figs. 12 and 13 are given in Table 4.

In Fig. 12, the materials are compared at a rather low and a fairly high structural index. The high value was chosen to be within the practical range of all materials compared. Note that on both of these comparisons all of the titanium alloys il-

lustrated have areas of usefulness. Furthermore, if material having the properties illustrated by the particular heat of 6 Al-4V-Ti alloy becomes generally available, a definite superiority is indicated at both structural indexes.

Fig. 13 shows the comparison at the highest practical value of structural index for each material. In this figure, the comparison is the same as for F_{cy}/density.

Note on this comparison that while the currently available titanium alloys do not have outstanding properties, the 6 Al-4V alloy still has definite superiority.

It must be emphasized, however, that before this superiority can be realized, at least two major hurdles must be overcome. First, it will be necessary to develop means of producing alloys having properties equivalent to those in this heat in sheet form as well as in extruded shapes, and these sheets or shapes must be capable of some fabrication.

The next hurdle arises from the fact that it is not easy to design or build airframe components having such high structural indexes. It is entirely possible that to use the full capability of materials, some sort of sandwich construction will be involved. So far no practical method has been found to make large shapes of sandwich construction of a type that can operate at high temperatures.

Optimum Stresses of Structural Elements at Elevated Temperatures[1]

By ARTHUR SCHNITT,[2] M. A. BRULL,[3] AND H. S. WOLKO,[4] BUFFALO, N. Y.

A method is developed by which optimum-stress curves for a given material at any temperature may be calculated from the room-temperature optimum-stress curves for a different material. The only data required to perform this transformation are stress-strain curves of both materials. As examples, optimum-stress envelopes are obtained for wide columns and multiweb beams over a wide range of temperatures. Relations are developed between the properties of optimized elements of different materials so that the detailed dimensions of any element may be calculated by considering a properly selected equivalent aluminum element. An approximate procedure is developed for the determination of maximum life when creep is significant. The method is then extended so as to permit comparison of unprotected structures with insulated and cooled structures, on the basis of minimum weight-strength and as a function of temperature and exposure time. Thus these developments lead to a systematic procedure by which the optimum structural arrangement and material may be selected for a given loading and known thermal environment.

Nomenclature

The following nomenclature is used in the paper:

b = width of skin panel
c = structural chord
c_s = specific heat of structural material
E = Young's modulus
E_t = tangent modulus
E_s = secant modulus
h = structural depth
H = heat of vaporization of coolant
k_3 = shape factor for wide-column buckling
k_i = thermal conductivity of insulation
K = buckling coefficient for single-skin panel
L_e = effective column length
M = bending moment
q = loading per unit of chord length
S = parameter defined in Equation [26]
t_s = structural-skin thickness
t_w = structural-web thickness
$\bar{t}$ = average structural thickness for a wide column
T_0 = equilibrium or adiabatic wall temperature
T_i = initial temperature of structure
T_α = operating temperature specified for a given insulated structure
$T_R = \dfrac{T_0 - T_i}{T_0 - T_\alpha}$
w_p = weight per unit wetted-skin area of protective system
w_1 = weight per unit wetted-skin area of insulation supporting structure
w_2 = weight per unit wetted-skin area of coolant
w_3 = weight per unit wetted-skin area of pumping and valving equipment
y = distance from neutral axis
η = plasticity coefficient
θ_F = duration of flight
θ = time of exposure to elevated temperature
ν = Poisson's ratio
ρ_s = weight density of structural material
ρ_i = weight density of insulation
σ = stress
Σ = solidity of multiweb beam
φ = heat flux

Introduction

The principal objective of the aircraft structural designer is to produce a structure which will have minimum weight for a given strength. In order to facilitate the attainment of this goal, a considerable amount of experimental and theoretical research has been carried out over a period of years to obtain optimum design information. In particular, extensive experimental programs have been undertaken by the National Advisory Committee for Aeronautics (NACA) (1, 2, 3, 4)[5] to determine optimum stresses in typical elements such as aluminum-alloy wide columns and multiweb beams. In addition, analytical methods applicable to a variety of configurations have been developed by Shanley (5, 6), Gerard (7), Micks (8), and many others. This wealth of available information facilitates the selection of material and structural configuration for a given aircraft for room-temperature operation. It has been shown (5, 7) that for room-temperature operations the choice of structural configuration can be made purely on the basis of loading and size. For elevated-temperature operation, however, the additional factors of operating temperature and time of loading at temperature are introduced. It is clear that in general aircraft structures will not be subjected to the simplified condition of constant temperature and short or long-time loading. Recent results of materials research indicate, however, that it may be possible in certain instances to account for the true load-temperature-time history of an aircraft by the use of properly defined equivalent constant-temperature and constant-load conditions. In order to simplify the analysis, it is therefore assumed in the remainder of the paper that constant-load and constant-temperature conditions constitute a valid approximation in structural design.

Even with this important simplification, the prospect of elevated-temperature operation introduces great complexity in the optimum design problem. Where, in the past, aluminum and

[1] The developments presented in this paper were obtained during the course of work sponsored by the Wright Air Development Center. Permission to publish this material is gratefully acknowledged.

[2] Chief Structures Engineer, Bell Aircraft Corporation.

[3] Head, Analytical Methods Group, Structures Section, Bell Aircraft Corporation. Assoc. Mem. ASME.

[4] Structures Engineer, Bell Aircraft Corporation.

Contributed by the Aviation Division and presented at the Aviation Division Conference, Los Angeles, Calif., March 14–16, 1956, of The American Society of Mechanical Engineers.

Note: Statements and opinions advanced in papers are to be understood as individual expressions of their authors and not those of the Society. Manuscript received at ASME Headquarters, January 18, 1956. Paper No. 56—AV-11.

[5] Numbers in parentheses refer to the Bibliography at the end of the paper.

magnesium alloys were the only materials seriously considered for primary structures, it is now necessary to consider a large number of other materials over a wide range of temperatures and to include the effects of material creep.

Certain investigators have chosen to compare materials for elevated-temperature operation on the basis of the yield stress-to-density ratio. While this procedure is more adequate for elements in simple tension, it is obviously inadequate for compression structures since it is well known (8) that, even for optimum compressive elements, the allowable stress may be far below the yield stress.

Recently other investigators (3, 4) have refined this approach by considering parameters which include column and plate buckling. Although this type of comparison represents an improvement over the yield strength-density criterion, it still does not account for all the factors which should be considered; namely, (*a*) type of structure (wide column, multiweb, etc.), (*b*) loading, (*c*) size and geometry, (*d*) operating temperature, (*e*) time of loading at temperature. A stress-density ratio is clearly an appropriate parameter by means of which materials may be compared since, for constant loading, a maximum value of this quantity corresponds to minimum weight-strength; but, in order to account for all the factors listed, the stress value used in this ratio should be the maximum attainable (i.e., optimum) working stress in a given type of structure. Thus we are led to the logical conclusion that a fair comparison between materials can be made only by considering optimized structures made of different materials but designed for the same ultimate load and identical environmental conditions. The information needed to make such comparisons is then a knowledge of the variation of optimum stress with loading and temperature, for typical materials and structural arrangements. Clearly, the experimental determination of such optimum-stress curves would require a formidable amount of research, so that it would be desirable to develop a method which would make it possible to transform optimum-stress curves for a given material at room temperature into the corresponding optimum-stress curve for another material at a different temperature. With this procedure, the experimental results already available for aluminum structures at room temperature (1, 2) could be extended to other materials at different temperature.

Younger (9) has recently proposed a graphical method of transformation for wide-column optimum-stress curves. Although this attempt represents a most important step in the right direction, the authors feel that some of the assumptions implied in this method invalidate the results. A different procedure, based on less restrictive assumptions is developed herein. Relations are derived between the sizes and proportions of optimum elements of different materials so that the detailed geometry of any element may be determined from the characteristics of a suitably chosen aluminum-alloy element designed for room-temperature operation.

Finally, the structural design of high-speed vehicles requires investigating the possibility of using insulation or cooling to protect the structure. The decision to use such protective devices must be made on a weight-strength basis and the development of a suitable efficiency parameter for protected structures is presented.

Transformation Laws for Optimum-Stress Curves

Zahorski (14) has proposed that a criterion for optimizing any compression structure is to require that all modes of failure occur simultaneously. This requirement implies that all elements of the structure will buckle at the same stress and insures that the structure will have no reserve strength when the design load is reached. Although this criterion will be used throughout the present paper, it is not always valid and we should therefore examine its limitations. In the analysis of stiffened panels and multiweb beams, it is usually assumed that the skin-stringer or skin-web junction act as simple supports; this means that the possibility of failure by forced crippling is neglected. This type of failure may occur when the webs or stringers are formed channels, so that the attachments between the compression cover and the webs or stringers are eccentric with respect to the stringer or web; in such cases the stringer or web acts as an elastic, rather than rigid support, and the simple-support assumption is violated. It follows that the stringer or web will be less effective as a stiffening member and that the attainable stresses will be somewhat lower than as predicted by the simple-support assumption. These observations have been confirmed by theoretical and experimental investigations carried out by Bijlaard and Johnston (13, 15) and at the NACA (2).

Since the optimum curves developed in this paper are based on Zahorski's criterion, they apply to structures in which the forced crippling-failure mode is not present; integral construction, which is currently in wide use, satisfies this requirement. It is most likely that the transformation laws which will be developed will not be greatly affected by the presence of the forced crippling mode so that, by using an experimentally determined curve as a starting point, these transformation laws may be applied to nonintegral construction.

By making use of the condition that the buckling stresses of all elements are equal, in general we will be able to obtain a number of relations between the various structural dimensions which will therefore be known in terms of a single reference dimension. It is then possible to obtain an equation relating stress and associated quantities (such as plasticity coefficient, tangent modulus, etc.) to the loading index; this type of expression is written in the general form

$$f(\sigma) = F(q) \qquad [1]$$

Since a relation such as Equation [1] does not involve the dimensions of the structure, it must be satisfied by all optimized structures of the type considered, regardless of material. This property of optimum structures allows the transformation of optimum-stress curves for a given material into corresponding curves for another material. This type of transformation will be illustrated for wide columns and multiweb beams.

Wide Columns. The term wide column is meant to denote skin-stiffener combinations. The optimum design of such members has been considered by Shanley (6) and Micks (8), the latter having proved that minimum weight-strength is indeed attained when the buckling stress for each element of the panel is equal to the buckling stress of the wide column. Shanley (6) has shown that the buckling stress for wide columns is given by

$$\sigma = \pi^{2/3} E_t^{1/3} k_3^{2/3} (q/L_0)^{2/3} \qquad [2]$$

where k_3 is a shape factor defined as the ratio of the radius of gyration of the cross section to its equivalent average thickness. Micks (8) has further shown that for optimized wide columns, the shape factor k_3 may be expressed as a function of the quantity t_s/b only, where t_s is the skin thickness and b is the width of a skin panel. If we now make use of this fact, together with the requirement that all elements of the panel buckle simultaneously, we will be able to obtain a universal relation such as Equation [1]; thus the buckling stress of a single-skin panel is given by

$$\sigma_1 = K\eta E \left(\frac{t_s}{b}\right)^2 \qquad [3]$$

where η = plasticity coefficient. Since $\sigma = \sigma_1$ for an optimum structure, we may write Equation [3] as

$$\left(\frac{t_s}{b}\right)^2 = \frac{1}{K}\left(\frac{\sigma}{\eta E}\right) \quad [4]$$

and Equation [4] shows that $(t_s/b)^2$ is a function of $\sigma/\eta E$ only. Since k_3 depends on $(t_s/b)^2$ only, the implication of Equation [4] is that the shape factor k_3 of Equation [2] is a function of $\sigma/\eta E$ only and therefore depends only on stress. Now, we may write Equation [2] in the form

$$\frac{\sigma^{3/2}}{E_t^{1/2}k_3} = \pi\left(\frac{q}{L_e}\right) \quad [5]$$

and since k_3 depends only on $\sigma/\eta E$, the left-hand side of Equation [5] is dependent only on material properties while the right-hand side is completely determined by loading. Thus Equation [5] implies that, for a given structural index q/L_e, the optimum stress for wide columns of any material must be such that the quantity $\sigma^{3/2}/(E_t^{1/2}k_3)$ has the same value for all materials. It is then clear that Equation [5] is a universal relation similar to Equation [1]. By using the expression for k_3 developed by Micka (8), it would be possible to obtain from Equation [5] an analytical expression applicable to wide columns of any material. It is more convenient, however, to use Equation [5] as a means of transforming existing experimental optimum-stress curves rather than to obtain new analytical curves. We then proceed as follows:

(*a*) Given an optimum-stress curve for some particular material we compute k_3 from

$$k_3 = \frac{\sigma^{3/2}}{\pi E_t^{1/2}(q/L_e)} \quad [6]$$

(*b*) For the same values of stress as used in Equation [6] we calculate the quantity $\sigma/\eta E$. Values of η as a function of stress for plates are available in the literature (10, 11).

(*c*) With the values determined for k_3 and $\sigma/\eta E$ we may now plot a curve of k_3 versus $\sigma/\eta E$ which is applicable to any material.

(*d*) To obtain an optimum-stress curve for material B, we now start from the stress-strain curve of material B and calculate values of $\sigma/\eta E$ corresponding to the chosen values of stress.

(*e*) With these values of $\sigma/\eta E$, the corresponding values of k_3 are read from the universal curve plotted under (*c*) and finally the loading index q/L_e corresponding to each selected value of stress is obtained from

$$\frac{q}{L_e} = \frac{\sigma^{3/2}}{\pi E_t^{1/2}k_3} \quad [7]$$

With this procedure, it is then possible to obtain wide-column optimum-stress curves for any material at any temperature as long as the stress-strain curve for the material is known so that values of the tangent and secant moduli and the plasticity coefficient may be determined.

The method of transformation just developed is used to obtain optimum-stress curves for a number of materials at different temperatures. The materials considered are: 2024 T-4 aluminum alloy, 7075 T-6 aluminum alloy, FS1-H24 magnesium alloy, RC C-110M titanium alloy, 17-7 PH stainless steel, Inconel X nickel-base alloy. With the individual optimum-stress curves obtained in this manner it is then possible to obtain optimum-stress envelopes which permit a rapid choice of material for a given loading and temperature. Such envelopes are presented in Fig. 1.

Multiweb Beams. The development of a transformation law for the optimum-stress curves of multiweb beams follows closely from the work of Gerard (12) on optimum proportions for such structures. In his paper Gerard optimizes the multiweb beam by assuming that the web-to-skin junctions are simple supports and by requiring that the skin buckle in compression and the webs in

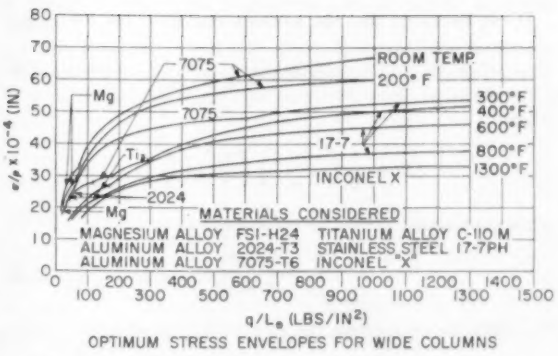

OPTIMUM STRESS ENVELOPES FOR WIDE COLUMNS

FIG. 1 OPTIMUM-STRESS ENVELOPES FOR WIDE COLUMNS

bending at the same stress. It is cautioned that this assumption may result in optimistic buckling stresses when the webs are formed channels and the mode of failure is by forced crippling of the webs. With these assumptions, the buckling stress for the compression cover is given by

$$\sigma_c = \frac{4\pi^2\eta E}{12(1-\nu^2)}\left(\frac{t_s}{b}\right)^2 \quad [8]$$

while the web buckling stress is given by

$$\sigma_w = \frac{25\pi^2\eta_w E}{12(1-\nu^2)}\left(\frac{t_w}{h}\right)^2 \quad [9]$$

where η_w = plasticity coefficient for webs

If we assume that $\eta = \eta_w$, equating σ_c and σ_w gives

$$\frac{t_w}{t_s} = \frac{2}{5}\left(\frac{h}{b}\right) \quad [10]$$

Following Gerard, the optimum number of cells is found by writing an expression for the solidity of the beam Σ, differentiating this expression with respect to the number of cells n, and setting the result equal to zero. Thus the solidity is found to be

$$\Sigma = \left[\frac{12(1-\nu^2)q}{4\pi^2\eta E c}\right]\left[n^{-3/4}\left(\frac{c}{h}\right) + \frac{2}{5}(n+1)n^{1/4}\left(\frac{h}{c}\right)\right] \quad [11]$$

where

$q = \sigma_c t_s$ = loading in compression cover
n = number of cells

Differentiating Equation [11] with respect to n and equating the result to zero yields, for the optimum number of cells, the equation

$$n^2 + \frac{1}{4}n - \frac{5}{4}\left(\frac{c}{h}\right)^2 = 0$$

from which the optimum number of cells is found to be the integer closest to the quantity

$$n_0 = -\frac{1}{8} + \left(\frac{5}{4}\right)^{1/2}\left(\frac{c}{h}\right) \quad [12]$$

It follows that the optimum ratio of cell width to beam depth is

$$\left(\frac{b}{h}\right)_o = \left(\frac{4}{5}\right)^{1/2}\left[1 + \frac{1}{8n_0}\right] \approx 1 \quad [13]$$

It can be shown that the moment carried by the covers is

$$M_c = \frac{M}{1+R} \quad [14]$$

where

$$R = \frac{1}{6}\left(\frac{n+1}{n}\right)\left(\frac{t_w}{t_c}\right)\left(\frac{h}{b}\right)$$

while the moment carried by the webs is

$$M_w = \frac{RM}{1+R} \quad [15]$$

For optimum proportions, the value of R is found to be

$$R_0 = \frac{1}{960}\left(\frac{h}{c}\right)^2 + \frac{1}{8\sqrt{5}}\left(\frac{h}{c}\right) + \frac{1}{12} \approx \frac{1}{12} \quad [16]$$

from which it is seen that in an optimum multiweb the covers will carry approximately 92 per cent of the applied moment. It should be noted that in the foregoing expressions the nonlinearity of stress distribution due to plastic bending has been neglected. This would have relatively little effect in a multiweb beam because the flat compression cover carries most of the moment.

The stress in the compression cover is given by

$$\sigma_c = \frac{M}{(1+R)\left(\frac{t_c}{b}\right)h^2c}$$

For a beam of optimum proportions, $R = R_0 = {}^1/_{12}$ and this expression may be written

$$\sigma_c\left(\frac{t_c}{b}\right) = \frac{M}{(1+R_0)h^2c}$$

Substituting for t_c/b from Equation [8], rearranging, and setting R_0 equal to ${}^1/_{12}$ gives

$$\sigma_c\left(\frac{\sigma_c}{\eta E}\right)^{1/2} = \frac{2\pi}{13}\sqrt{\frac{12}{1-\mu^2}}\left(\frac{M}{h^2c}\right) \quad [17]$$

Equation [17] is a relation involving only the structural index on the right-hand side (Poisson's ratio is taken as a constant for all materials) and a function of stress on the left-hand side. It is therefore a universal relation of the type of Equation [1] and it must be satisfied by all optimized multiweb beams. Equation [17] may then be used to determine particular optimum-stress curves for any material if a stress-strain curve is known so that $\sigma(\sigma/\eta E)^{1/2}$ may be determined as a function of σ. We also may make use of Equation [17] to transform multiweb optimum-stress curves from one material to another. The use of an experimental curve as the starting point should help to minimize any errors due to the neglect of plastic bending or forced crippling. Optimum-stress envelopes for various materials are presented in Fig. 2. These curves were obtained by using Equation [17] as an analytical universal relation because the only experimental data available (2) were carried out for a low range of structural loading index which, unfortunately, lies below the values for which multiweb beams have high efficiencies.

Geometry and Size Considerations

In some cases we may be interested in comparing structures which have the same proportions or the same size or both. By the term size as used here is meant the same reference thickness, which implies that the cross-sectional areas are the same although the proportions are different. For wide columns, the reference thickness is the average thickness of the cross section $\bar{t}$, while for multiweb beams the reference thickness is taken to be the compression-cover thickness. For wide columns the stress is uniform and the average thickness $\bar{t}$ is given by

$$\bar{t} = \frac{q}{\sigma} \quad [18]$$

and, for multiweb beams, the compression-cover thickness is obtained from

$$t_c = \frac{q}{\sigma_c} = \frac{M_c}{hc\sigma_c} \quad [19]$$

It is clear from Equations [18] and [19] that radial lines on the optimum-stress curves are lines of constant size (for a constant column length L_0 or beam thickness h). It should be understood clearly, however, that these lines represent only constant cross-sectional area and not necessarily constant geometry (i.e., proportions).

It is also possible to determine conditions that two structures must satisfy in order to have the same geometry. It has been shown previously that for both wide columns and multiweb beams, the proportions are determined by the quantity t_c/b. From Equations [4] and [8] it is clear that for both types of structures constant t_c/b corresponds to a constant value of $\sigma/\eta E$; it is then apparent that constant geometry implies constant value of $\sigma/\eta E$. These properties may be used to show that two identical panels (of similar size and geometry) but made of different materials are not in general both optimum panels. This procedure is indicated schematically in Fig. 3 where curves 1 and 2 are the optimum-stress curves for 75ST and 24ST, respectively, while curves 3 and 4 are curves of σ versus $\eta E/\sigma$ for 75ST and 24ST, respectively.

We pick a point A on 24ST optimum curve and draw a radial line through this point; the radial line therefore represents all panels having the same average thickness as that of point A. The value of $\eta E/\sigma$ for this panel is determined by point B on curve 4. Therefore panels having the same geometry as the panel of point A must have values of $\eta E/\sigma$ lying on a vertical line through point B. The stress corresponding to a 75ST panel having the same geometry as panel A is therefore determined by point C or on curve 3. Then, proceeding at constant stress, we determine point D which represents a panel having the same size and geometry as panel A. It is seen that point D does not lie on the optimum-

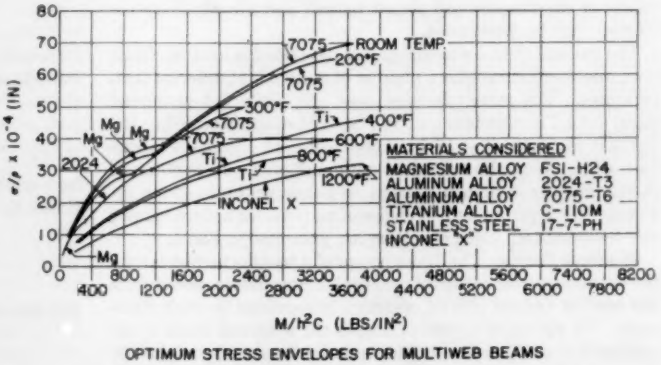

Fig. 2 Optimum-Stress Envelopes for Multiweb Beams

stress curve for 75ST. It should be noted that, in Fig. 3, point E represents an optimum 75ST panel which has the same geometry as panel A but a different size (i.e., different average thickness) while point F represents an optimum 75ST panel having the same size as panel A but a different geometry.

A family of such curves is shown in Fig. 4 for 24ST multiweb beams.

Since, in general, the structural arrangement and material are chosen on the basis of the short-time and ultimate loading conditions, the problem of determining the expected life is reduced to

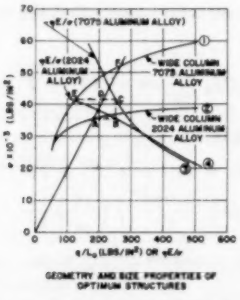

FIG. 3 GEOMETRY AND SIZE PROPERTIES OF OPTIMUM STRUCTURES

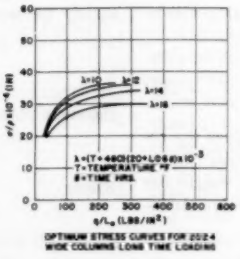

FIG. 4 OPTIMUM-STRESS CURVES FOR 2024 WIDE COLUMNS (LONG-TIME LOADING)

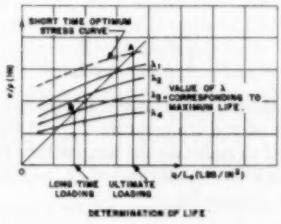

FIG. 5 DETERMINATION OF LIFE

It is now clear that if points D, E, and F were merged together, they would correspond to a 75ST optimum panel having identical size and geometry to our original 24ST panel. It is easily seen that this condition cannot be satisfied in general unless the curves of σ versus $\eta E/\sigma$ (i.e., stress-strain curves) for both materials are identical; this is obviously a trivial situation. If we recall that the method of transformation proposed by Younger (9) is almost identical with the procedure followed in going from point A to point D, the foregoing remarks will help to shed some light on the reasons for the rather severe restrictions inherent in Younger's transformation procedure.

Another and most important implication of these properties of optimum curves is that we are now able to determine the detail dimensions of any optimum panel in a very simple way. This is accomplished by making use of the fact that panels related as are panels A and E of Fig. 3 have identical proportions while their dimensions are in the ratio of $(q/\sigma)_A$ to $(q/\sigma)_E$.

LIFE-STRENGTH CONSIDERATIONS

In many cases, high-speed vehicles will be subjected to extended exposure to load at elevated temperatures; in such cases we must consider the effect of creep and associated phenomena on the life of the airframe. As explained previously, it is reasonable to assume that the true conditions of load-time-temperature history may be replaced by some equivalent constant-temperature conditions. It is likely that the choice of structural material and configuration for a given vehicle will be made at first on the basis of short-time exposure to ultimate loading at a constant temperature, so that we must now provide a means by which to check a given design for creep buckling by considering its allowable life under some specified condition of long-time exposure to a lower than ultimate loading.

Since the methods developed in the foregoing provide a means of determining optimum-stress curves for any material, we may use these methods to develop optimum-stress curves accounting for creep by using the isochronous stress-strain curves as a basis for performing the transformations. In this manner we obtain for a given material a family of optimum-stress curves where the parameter, instead of being temperature, is now the Larson-Miller constant λ, defined as

$$\lambda = (T + 460)(20 + \log_{10} \theta)(10^{-3}) \quad [20]$$

that of determining the maximum allowable value of λ for a structure of given size and geometry. This procedure is illustrated schematically in Fig. 5, point A representing the panel chosen on the basis of the short-time ultimate loading conditions; in view of the properties proved in the foregoing for optimum design curves, a radial line through point A is then the locus of all panels having same cross-sectional areas as panel A. We now determine the intersection of the radial line with a vertical line corresponding to the given long-time loading conditions, as point B. Point B then represents a panel which has the same cross-sectional area as panel A although its proportions are in general different. If we now assume that the life of the panel depends only on the cross-sectional area, the maximum allowable value of λ is determined from point B which lies on the optimum-stress curve for $\lambda = \lambda_4$.

The assumption that the life of the panel is not affected by geometry makes this procedure approximate so that only an estimate of the life of the structure is obtained. The method does have the advantage of being extremely simple so that rapid preliminary design estimates are possible.

METHOD OF COMPARISON BETWEEN PROTECTED AND UNPROTECTED STRUCTURES

In many cases of interest, the use of protective equipment such as insulation and cooling may result in a more efficient structure since in general it will allow the use of a less heat-resistant but lighter material. Since, by proper choice of protective equipment such materials could be made to operate near room temperature, their high strength-to-density ratios could be used to advantage. It is apparent, however, that a fair comparison between protected and unprotected structures can be made only if we define a structural-efficiency parameter which accounts for the added weight of the protective equipment. We therefore define the following quantities:

$(\sigma/\rho)_s$ = effective structural efficiency for a protected structure

t_s = effective structural thickness defined so that total structural weight per unit area (including protective equipment) is $\rho_s t_s$

ρ_s = weight density of structural material

$(\sigma/\rho)_a$ = structural efficiency for material at temperature T_a

T_α = maximum structural temperature which protective equipment is designed to maintain

For any structure, the stress-density ratio is related to the edge loading by the equation

$$\frac{\sigma}{\rho} = \frac{q}{\rho t} \quad [21]$$

so that, for a structure designed to operate at the temperature T_α, we have

$$\left(\frac{\sigma}{\rho}\right)_\alpha = \frac{q}{\rho_s t_\alpha} \quad [22]$$

where t_α is the thickness of material necessary to produce the required strength at the temperature T_α. If the structure is insulated or cooled to maintain the temperature T_α, the weight per unit wetted area is now $\rho_s t_s$ instead of $\rho_s t_\alpha$ and the effective stress-to-density ratio is given by

$$\left(\frac{\sigma}{\rho}\right)_s = \frac{q}{\rho_s t_s} = \frac{q}{\rho_s t_\alpha}\left(\frac{t_\alpha}{t_s}\right)$$

Making use of Equation [22] in the last expression gives

$$\left(\frac{\sigma}{\rho}\right)_s = \left(\frac{\sigma}{\rho}\right)_\alpha \left(\frac{t_\alpha}{t_s}\right) \quad [23]$$

It is obvious from Equation [23] that the factor t_α/t_s represents the reduction of structural efficiency due to the weight of the protective equipment.

The total weight of the structure, including the protective equipment is

$$\rho_s t_s = \rho_s t_\alpha + w_p \quad [24]$$

where w_p is the weight per unit wetted area of the insulation or cooling system. From Equation [24] we may write

$$\frac{t_\alpha}{t_s} = 1 + S w_p \quad [25]$$

where

$$S = \frac{1}{\rho_s t_\alpha} = \left[\frac{q}{(\sigma/\rho)_\alpha}\right]^{-1} \quad [26]$$

Finally, substituting Equation [25] in Equation [23] gives

$$\left(\frac{\sigma}{\rho}\right)_s = \left(\frac{\sigma}{\rho}\right)_\alpha \frac{1}{1 + S w_p} \quad [27]$$

We can see from Equation [27] that in order to determine the effective structural efficiency it is necessary to develop expressions for w_p appropriate to different types of cooling and insulation systems.

It should be noted that the weight of protective equipment required to maintain the structure temperature below a given value T_α depends on the structural thickness t_α since the heat capacity of the structure will determine the rate of its temperature rise.

Expressions for w_p will now be developed for two protection systems which are considered to show promise for aircraft applications. These systems are (*a*) insulation system, and (*b*) insulation-cooling system. If, with the use of these systems the heat capacity of the insulation is neglected as small compared to that of the structure, the heat flux into the primary structure may be expressed as

$$\varphi = \frac{k_i}{t_i}(T_0 - T) \quad [28]$$

For simplicity, the equilibrium temperature T_0 will hereafter be assumed constant with time. We now consider the particular systems listed previously.

Insulation System. In this system the insulation is used to delay the temperature rise in the structural skin so that the transient heat flow must be considered. With the assumptions discussed previously, the heat-balance requirement for an element of the primary structure shows that the temperature must satisfy the equation

$$\rho_s C_s t_\alpha \frac{dT}{d\theta} = \frac{k_i}{t_i}(T_0 - T) \quad [29]$$

the solution of which is

$$T(\theta) = T_0[1 - e^{-\epsilon\theta}] + T_i e^{-\epsilon\theta}$$

where

$$\epsilon = \frac{k_i}{\rho_s c_s t_\alpha t_i}$$

If the duration of one flight is θ_F and the maximum allowable temperature in the primary structure is T_α, the expression becomes

$$T_\alpha = T_0[1 - e^{-\epsilon\theta_F}] + T_i e^{-\epsilon\theta_F}$$

which may be put in the form

$$\epsilon\theta_F = \ln T_R$$

where

$$T_R = \frac{T_0 - T_i}{T_0 - T_\alpha}$$

Substituting for ϵ in this last expression, we obtain an equation which may be solved for the thickness of insulation t_i required to maintain the structural temperature below T_α. The result is

$$t_i = \frac{S k_i \theta_F}{C_s \ln T_R} \quad [30]$$

The weight per unit wetted area of the system is

$$w_p = w_1 + \rho_i t_i$$

where w_1 is the weight per unit wetted area of the supporting structure for the insulation and is assumed constant.

Substituting for t_i in this last expression yields

$$w_p = w_1 + \frac{\rho_i k_i}{c_s} \frac{S\theta_F}{\ln T_R} \quad [31]$$

Hence, for an insulated structure, the effective structural efficiency is obtained from Equation [23] with t_α/t_s calculated from Equations [25] and [31] as

$$\frac{t_\alpha}{t_s} = \frac{1}{1 + S\left[w_1 + \frac{\rho_i k_i}{c_s}\frac{S\theta_F}{\ln T_R}\right]} \quad [32]$$

Insulation and Cooling System. In this system the heat flux to the structure is absorbed by a coolant which is in contact with the supporting structure. Since the coolant is used to absorb the heat input continuously, we consider only the steady-state heat-balance equation, written as

$$\frac{k_i}{t_i}(T_0 - T)\theta = H w_2 \quad [33]$$

where H is the heat of vaporization of the coolant and w_2 is the

weight of coolant required per unit wetted area. The total weight of the system is then given by

$$w_p = w_1 + w_2 + w_3 + \rho_i t_i$$

where w_3 is the weight per unit wetted area of the pumping and valving equipment; this quantity is usually small compared to the other weight increments and will hereafter be neglected. Substituting for w_2 from Equation [33], we obtain

$$w_p = w_1 + \rho_i t_i + \frac{k_i}{t_i}\left(\frac{T_0 - T_a}{H}\right)\theta_F \quad \ldots\ldots [34]$$

The weight of the system is now minimized by differentiating w_p with respect to t_i and setting the result equal to zero. The optimum value of t_i is found to be

$$t_i = \left[\left(\frac{k_i}{\rho_i}\right)\left(\frac{T_0 - T_a}{H}\right)\theta_F\right]^{1/2} \quad \ldots\ldots [35]$$

Substituting Equation [35] in Equation [34] gives the weight of the optimized system as

$$w_p = w_1 + 2\sqrt{\left(\frac{\rho_i k_i (T_0 - T_a)\theta_F}{H}\right)} \quad \ldots\ldots [36]$$

It is interesting to note that the optimum is achieved when the weights of the insulation and the coolant are equal. From Equations [25] and [36], we find t_a/t_s for an insulated and cooled structure as

$$\frac{t_a}{t_s} = \frac{1}{1 + S\left[w_1 + 2\sqrt{\left(\frac{\rho_i k_i (T_0 - T_a)\theta_F}{H}\right)}\right]} \quad \ldots [37]$$

It is of interest to determine the value of the parameter S for which the weight of the insulation system will be equal to that of the insulation and cooling system. From Equations [31] and [37], we obtain

$$S^* = 2c_s\sqrt{\left(\frac{T_0 - T_a}{H\rho_i k_i\,\theta_F}\right)}\ln T_R \quad \ldots\ldots [38]$$

where S^* is the critical value of S for which the two systems have equal weight. We note that for $S < S^*$ the system with insulation only is the lightest while for $S > S^*$ the system with both insulation and cooling should be used.

By using Equations [32], [37], and [38] we may now compare protected and unprotected structures on the basis of minimum weight-strength. The procedure to be used is as follows:

(*a*) Given the loading index, and external temperature, we may use the optimum-stress envelopes to determine the most efficient material and the corresponding value of σ/ρ for the best unprotected structure.

(*b*) For protected structures, the most efficient arrangement is found to be a primary structure of aluminum or magnesium alloy maintained at a temperature of not more than 300 F. Thus for the given loading we may determine $(\sigma/\rho)_a$ and $S = q/(\sigma/\rho)_a$.

(*c*) We now compute S^* from Equation [38]; if $S < S^*$, the system with insulation only is used and $(\sigma/\rho)_s$ is calculated from Equations [25] and [32]. The insulation thickness is then obtained from Equation [30]; if $S > S^*$, the insulated and cooled system is adopted and $(\sigma/\rho)_s$ and t_i are then calculated from Equations [25], [37], and [35].

(*d*) The value of $(\sigma/\rho)_s$ for the protected structure should be compared to the value of σ/ρ obtained in step (*a*) for the best unprotected structure. This will determine whether or not a protective device is advantageous for the case considered.

It should be pointed out that the foregoing method makes no attempt to account for the reduction of structural depth h due to the insulation. This reduction in structural depth will cause an increase in the loading index so that in fact the unprotected structure should be compared to a protected structure subjected to higher loading. It would be possible to account for this change in the loading by a process of successive approximation by simply repeating the foregoing procedure for a new structural depth reduced by the proper insulation thickness. This more refined procedure is not felt to be necessary, however, because the effect of thermal stresses has been neglected. Thermal stresses in general will be fairly severe for the unprotected structure, while the protected structure will experience little or no thermal stresses. Thus it is probable that the increase in effective loading due to thermal stresses in the unprotected structure will be of the same order as that due to reduction of structural depth for the insulated or cooled structure. It seems logical, therefore, to compare the protected and unprotected structures at constant loading index.

Calculations carried out for suitable insulation materials have shown that it is not advantageous to insulate (or cool) any material other than the lighter alloys such as aluminum and magnesium. This results from the fact that these materials have larger specific heats than the more heat-resistant alloys, so that a given insulation thickness would allow a smaller temperature rise in an aluminum or magnesium structure than in an equivalent titanium or steel structure.

As a final point in the discussion of protected structures, it should be pointed out that since insulants are of low density, their use is limited in practice only by the maximum permissible insulation thickness which is in turn limited by the maximum allowable decrease in structural depth. When the required insulation thickness exceeds this practical limit, it is necessary to reduce it by cooling the structure even though the insulation-cooling arrangement is not the optimum. Calculations have shown that the weight penalty due to such deviations is small.

Conclusions

It has been shown that optimum-stress curves for wide columns and multiweb beams of any material at any temperature may be obtained from the corresponding optimum-stress curves for any other material at room temperature. Since a great deal of experimental information is available for optimized aluminum structures at room temperature, these transformations extend the applicability of this information to all materials and temperatures.

It also has been shown that there exists a relation between the geometry and size of optimized structures made of different materials so that the detailed configuration of any element can be obtained from a geometrically equivalent element made of aluminum alloy. Thus the entire design of optimized elements for any material and temperature can be accomplished with design data which are already available, and an estimate of the life limitation due to creep buckling can be made.

In addition, methods have been developed by which to compare insulated and cooled structures with unprotected structures on the basis of minimum weight-strength. As an example Fig. 6 presents a curve illustrating the variation of weight penalty resulting from elevated-temperature operation with Mach number for a particular optimized structure subjected to a given loading and exposure time. This curve illustrates the advantages which may be gained by the use of insulation and cooling.

The methods presented herein should prove useful in narrowing down the scope of preliminary structural design investigations, since they provide rapid systematic means of selecting material, structural arrangement, and detail geometry.

Finally, it should be clear that while the methods developed

here apply to wide columns and multiweb beams, similar methods could be developed for other types of optimum structures.

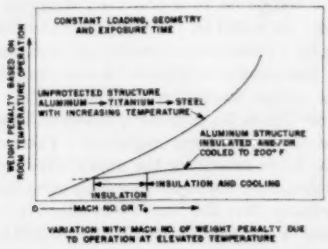

FIG. 6 VARIATION WITH MACH NUMBER OF WEIGHT PENALTY DUE TO OPERATION AT ELEVATED TEMPERATURE

BIBLIOGRAPHY

1 "Design Charts for Flat Compression Panels Having Longitudinal Extruded Y-Section Stiffeners and Comparison With Panels Having Formed Z-Section Stiffeners," by N. F. Dow and W. A. Hickman, NACA TN 1389, 1947.

2 "Experimental Investigation of the Pure Bending Strength of 75ST6 Aluminum Alloy Multiweb Beams With Formed Channel Webs," by R. A. Pride and M. S. Anderson, NACA TN 3082, 1954.

3 "Structural Efficiencies of Various Aluminum, Titanium and Steel Alloys at Elevated Temperatures," by G. J. Heimerl and P. J. Hughes, NACA TN 2975, 1953.

4 "A Structural Efficiency Evaluation of Titanium at Normal and Elevated Temperatures," by G. J. Heimerl and P. F. Barret, NACA TN 2269, 1951.

5 "Weight-Strength Analysis of Aircraft Structures," by F. R. Shanley, McGraw-Hill Book Company, Inc., New York, N. Y., first edition, 1952.

6 "Principles of Structural Design for Minimum Weight," by F. R. Shanley, *Journal of the Aeronautical Sciences*, vol. 16, March, 1949, p. 133.

7 "Minimum Weight Analysis of Compression Structures," by G. Gerard, to be published.

8 "A Method of Estimating the Compressive Strength of Optimum Sheet-Stiffener Panels for Arbitrary Material Properties, Skin Thickness and Stiffener Shape," by W. R. Micks, *Journal of the Aeronautical Sciences*, vol. 20, October, 1953, p. 705.

9 "The Development of Optimum Design Envelope Curves of Sheet-Stiffener Compression Panels Having Hat, Z- or Y-Section Stiffeners for Various Materials and Temperature Environments," by D. G. Younger, Proceedings of the First Midwestern Conference on Solid Mechanics, University of Illinois, Urbana, Ill., 1953, p. 5.

10 "Theory and Test on the Plastic Stability of Plates and Shells," by P. P. Bijlaard, *Journal of the Aeronautical Sciences*, vol. 16, September, 1949, p. 529.

11 "Plasticity Coefficients for the Plastic Buckling of Plates and Shells," by A. Krivetsky, *Journal of the Aeronautical Sciences*, vol. 22, June, 1955, p. 432.

12 "Optimum Number of Webs Required for a Multicell Box Under Bending," by G. Gerard, *Journal of the Aeronautical Sciences*, vol. 15, January, 1948, p. 53.

13 "Compressive Buckling of Plates Due to Forced Crippling of the Stiffeners," by P. P. Bijlaard and G. S. Johnston, Institute of the Aeronautical Sciences, Sherman M. Fairchild Publication Fund, Paper No. FF-8, 1953.

14 "Effects of Material Distribution on Strength of Panels," by A. Zahorski, *Journal of the Aeronautical Sciences*, vol. 11, July, 1944, p. 247.

15 "Attainable Compressive Stresses of Stringer Panels Having Bent-Up Z-Section Stiffeners," by G. S. Johnston, Bell Aircraft Corporation, Report No. 02-984-017, June, 1954.

Thermostructural Efficiencies of Compression Elements and Materials

By GEORGE GERARD,[1] NEW YORK, N. Y.

Minimum-weight equations for failure of solid and wide columns, plates and plate assemblies (crippling), and optimum stringer panels are presented in terms of suitable structural loading and material-efficiency parameters. From these equations the comparative structural efficiency of plates and stringer panels was investigated. Similarly, the comparative efficiency of various materials was studied for elevated-temperature, stringer-panel applications. By analytically determining the optimum spacing of ribs or webs in stringer panel-rib or multiweb construction, respectively, a composite structure of minimum weight is obtained. For such structures the structural-loading and material-efficiency parameters are generally different from those obtained for the individual elements. Typical results are presented for composite structures and some general considerations are presented for selection of materials for thermal-flight aircraft.

Nomenclature

The following nomenclature is used in the paper:

A = area
b = plate width
c = end-fixity coefficient
C = number of corners
E = modulus of elasticity
E = generalized plastic modulus
E_s = secant modulus
E_t = tangent modulus
f = shape factor
h = over-all height
k = buckling coefficient
k_c = centroidal-height coefficient
L = length
M = bending moment
N = loading per inch
P = load
S = supporting-structure ratio
t = thickness
V = volume
w = structural chord
W = weight
X_i = generalized dimension
α = panel-efficiency coefficient
β = plate coefficient, also rib coefficient
β_c = crippling coefficient
η = plasticity factor for plates
ν = Poisson's ratio
ρ = radius of gyration
Σ = solidity
σ = stress
σ_a = applied stress
σ_{cr} = buckling stress
σ_{cy} = compressive yield strength
σ_f = failing stress
τ = plasticity factor for wide columns
$\bar{\tau}$ = plasticity factor for stringer panels
φ = density

Subscripts

o = optimum value
r = rib
$\sim$ = effective value

Introduction

To determine the efficiencies of various compression elements and materials in normal and elevated-temperature applications, a considerable array of structural-efficiency criteria has been proposed. These range from a simple criterion such as density-compressive yield-strength ratio, to criteria based upon failure of columns and plates and include those for composite-stringer panel-rib, or multiweb constructions.

Since buckling considerations govern the design of a major proportion of the airframe (it has been variously estimated that from 60 to 95 per cent of the structure is critical in compression), the importance of proper efficiency criteria should not be underestimated. Solutions to the problems of suitable structural arrangements and materials for thermal-flight aircraft of minimum weight can thus be greatly aided by the selection of proper structural and material-efficiency criteria.

It is the objective of this investigation to delineate the minimum-weight considerations involved in comparative structural-efficiency studies as contrasted with comparative material-efficiency studies. The former aids the selection of proper structural arrangements for minimum weight whereas the latter indicates the proper material which leads to minimum weight for a selected structure.

The analysis considers structural and material efficiencies of the basic elements, i.e., solid and wide columns, and failure of plates and plate assemblies (crippling). All of these elements are combined in a stringer panel, and for one of optimum design, efficiency criteria can be obtained readily. In all the foregoing cases it is assumed that the over-all length of columns and stringer panels, and the width for plates are prescribed.

In the design of an airframe, certain dimensions such as the wing span and chord are generally fixed by nonstructural considerations. However, as the structure is divided into components, the rib or web spacing, and consequently the stringer-panel length or plate width, often can be set by structural con-

[1] Assistant Director, Research Division, College of Engineering, New York University. Mem. ASME.

Contributed by the Aviation Division and presented at the Aviation Division Conference, Los Angeles, Calif., March 14–16, 1956, of The American Society of Mechanical Engineers.

Note: Statements and opinions advanced in papers are to be understood as individual expressions of their authors and not those of the Society. Manuscript received at ASME Headquarters, January 18, 1956. Paper No. 56—AV-12.

siderations. These spacings can be selected so as to achieve minimum weight for the composite structure and are therefore considered as open dimensions.

In considering the minimum-weight analysis of composite structures such as stringer panel-rib construction or multiweb construction, it is possible to determine analytically the optimum spacing of the supporting structure (ribs or webs). Thus the open dimensions are determined analytically under the condition that the weight of the composite structure be a minimum. In such cases, structural and material-efficiency criteria are obtained for optimum composite structures different from those obtained for the basic elements.

The results presented herein are built up successively from basic compression elements to the optimum composite structure. In this manner it is possible to choose suitable efficiency criteria at the particular level of optimization desired.

Basic Elements

General Analysis. The basic relationships and assumptions required for the minimum-weight analysis or design of a compression element subject to buckling are as follows:

(*a*) A relationship for the failure stress $\bar{\sigma}_f$ of the element. In cases where the element may be subject to several buckling modes, it is an axiom of optimum design that the several modes occur simultaneously, thereby establishing relationships for the open dimensions.

(*b*) The relation between the load P or loading N and the applied stress

$$\sigma_a = P/A = N/bt \quad [1]$$

The load terms may contain appropriate factors of safety.

(*c*) The margin of safety is zero. Thus

$$\bar{\sigma}_f - \sigma_a = 0 \quad [2]$$

(*d*) The weight is given simply by

$$W = \varphi AL = \varphi tbL \quad [3]$$

The essential difference among the various compression elements lies in the relationship for the failing stress. Both the failing stress and resultant weight equations are summarized later for basic elements in which the leading dimensions are prescribed.

Solid Columns. For columns of solid cross section as discussed in reference (1),[2] bending instability is the possible buckling mode and, therefore, buckling and failure are essentially coincident

$$\sigma_f = \sigma_{cr} = c\pi^2 E_t/(L/\rho)^2 \quad [4]$$

The optimum stress in terms of the applied load

$$\sigma_a = (\pi^2 cfE_t P/L^2)^{1/3} \quad [5]$$

where $f = \rho^2/A$ represents the shape of the cross section. The weight equation for this case

$$\frac{W}{L^3} = \frac{\varphi}{(\pi^2 cf)^{1/2}} \left(\frac{P}{E_t L^2}\right)^{1/2} \quad [6]$$

Wide Columns. The buckling of wide columns is essentially coincident with failure. Thus, as given in reference (1)

$$\sigma_f = \sigma_{cr} = \frac{c\pi^2 \tau E}{12(1-\nu^2)} \left(\frac{t}{L}\right)^2 \quad [7]$$

where

$$\tau = E_s/4E + 3E_t/4E$$

The optimum stress in terms of the applied loading

$$\sigma_a = \left[\frac{\pi^2 c\tau E}{12(1-\nu^2)}\right]^{1/3} \left(\frac{N}{L}\right)^{2/3} \quad [8]$$

The weight equation

$$\frac{W}{bL^2} = \varphi \left[\frac{12(1-\nu^2)}{\pi^2 c}\right]^{1/3} \left(\frac{N}{\tau EL}\right)^{1/3} \quad [9]$$

Plates. It is well known that for plates, the failure stress can exceed substantially the buckling stress when the latter occurs elastically. From test data at room and elevated temperatures, the following relationships have been established

$$\bar{\sigma}_f = \beta\, \sigma_{cr}^{1/3}\, \sigma_{cy}^{2/3} \quad \text{for} \quad \bar{\sigma}_f/\sigma_{cy} \leq 3/4 \quad [10]$$

$$\bar{\sigma}_f = \frac{\pi^2 k E_s}{12(1-\nu^2)} \left(\frac{t}{b}\right)^2 \quad \text{for} \quad \bar{\sigma}_f/\sigma_{cy} > 3/4 \quad [11]$$

In reference (2) the following weight equations are given based on Equations [10] and [11]

$$\frac{W}{Lb^2} = \varphi \left[\frac{12(1-\nu^2)}{\pi^2 k\beta^4}\right]^{1/3} \left(\frac{N}{Eb}\right)^{2/3} \times \left(\frac{E}{\sigma_{cy}}\right)^{1/3} \quad \text{for} \quad \bar{\sigma}_f/\sigma_{cy} \leq 3/4 \quad [12]$$

$$\frac{W}{Lb^2} = \varphi \left[\frac{12(1-\nu^2)}{\pi^2 k}\right]^{1/3} \left(\frac{N}{E_s b}\right)^{1/3} \quad \text{for} \quad \bar{\sigma}_f/\sigma_{cy} > 3/4 \quad [13]$$

Plate Assembly. The crippling strength of a plate assembly such as a formed section or monolithic panel with formed stringers ($L'/\rho = 20$) is given by the following semi-empirical relation in reference (3)

$$\frac{\bar{\sigma}_f}{\sigma_{cy}} = \beta_c \left[\frac{Ct^2}{A} \left(\frac{E}{\sigma_{cy}}\right)^{1/3}\right]^{0.85} \quad [14]$$

where C is the number of corners in the cross section. The coefficient β_c has a value of 1.30 for sections with three or more corners (lipped Z, channel, or hat sections, for example). The weight equation for this case is

$$\frac{W}{Lt^2} = \frac{\varphi}{\beta_c^{5.67} C^{3.67}} \left(\frac{P}{Et^2}\right)^{3.67} \left(\frac{E}{\sigma_{cy}}\right)^{2.33} \quad [15]$$

Optimum Stringer Panel. For a stringer panel of optimum design, the various possible buckling modes occur simultaneously as discussed in references (4) and (5). For such panels, the failing stress is given by

$$\bar{\sigma}_f = \alpha c^{1/4} (N\bar{\tau}E/L)^{1/2} \quad [16]$$

The coefficient α is the panel efficiency factor. Results of both extensive experimental and theoretical studies summarized in reference (6) indicate that $\alpha = 1$ approximately for Z and hat stiffened panels and $\alpha = 1.15$ for Y stiffened panels. The plasticity reduction factor was found to be

$$\bar{\tau} = (E_s/E)\,(E_t/E_s)^{1/2} \quad [17]$$

The weight equation for the optimum panel

$$\frac{W}{bL^2} = \frac{\varphi}{\alpha c^{1/4}} \left(\frac{N}{\bar{\tau}EL}\right)^{1/2} \quad [18]$$

Comparative Efficiencies

Structural Efficiencies. The various weight relations given

[2] Numbers in parentheses refer to the Bibliography at the end of the paper.

by Equations [6], [9], [12], [13], [15], and [18] all contain structural coefficient terms which are constant for structures of the same geometry. In addition, structural-loading parameters of the form N/X_1 or P/X_2^2 appear as well as terms representative of the structural material such as φ/E^n and σ_{cy}/E.

To investigate the comparative structural efficiencies of various elements such as wide columns, plates, and stringer panels it is desirable for the moment to suppress the influence of the physical properties of the materials. This can be accomplished by plotting the parameter $W/\varphi bL^2$ as a function of $N/\bar{E}L$ as shown in Fig. 1. In this manner it is possible to compare compression elements of the same material for various structural-loading parameters to determine the regions in which each type may have efficient structural applications.

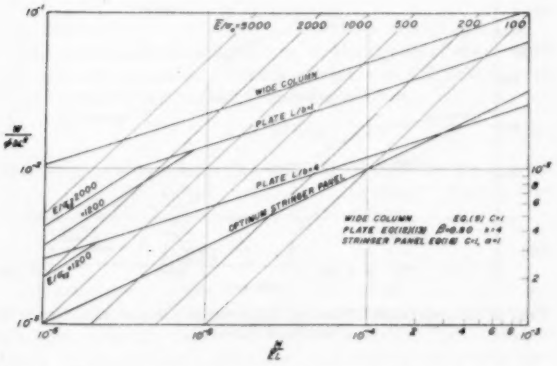

FIG. 1 COMPARATIVE STRUCTURAL-EFFICIENCY CHART FOR BASIC COMPRESSION ELEMENTS

From Fig. 1 it is evident that the stringer panel has a wide range of application. At high values of $N/\bar{E}L$, however, plate elements of sufficiently large L/b can be more efficient than the stringer panel. Since wide columns are essentially plates of small L/b, it is not unexpected that they should have the lowest efficiency of those considered.

In Fig. 1 the 45-deg lines represent constant values of $\bar{E}/\sigma_o$. This follows directly from

$$\frac{W/\varphi\, bL^2}{N/\bar{E}L} = \frac{1/L}{\sigma_o/\bar{E}L} = \frac{\bar{E}}{\sigma_o} \qquad [19]$$

Thus it is evident that for a prescribed value of $N/\bar{E}L$, the stringer panel achieves superior efficiency by virtue of higher value of $\sigma_o/\bar{E}$ than other elements in a certain range of $N/\bar{E}L$ values.

However, it is not evident from Fig. 1 in what ranges composite stringer panel-rib construction is more efficient than multiweb construction and the converse. This requires a knowledge of the rib spacing L and web spacing b which can be determined analytically so as to achieve minimum weight for the composite structure. Before considering the composite structure, however, it is pertinent to return to consideration of material efficiency to complete the picture for the basic compression elements.

Material Efficiencies. In conducting comparative material-efficiency studies, a considerable simplification can be effected by use of idealized stress-strain curves such as shown in Fig. 2. This simplification is achieved at the expense of little, if any, error in results. By use of the idealized representation, stress-strain characteristics for a particular material of density φ are characterized only by values of E and σ_{cy} at a given temperature

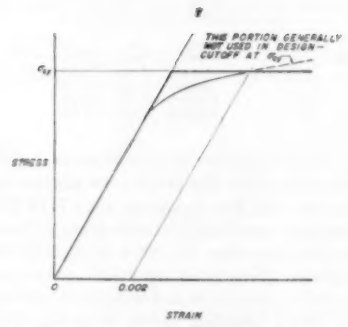

FIG. 2 IDEALIZED STRESS-STRAIN CURVE USED FOR MATERIAL-EFFICIENCY STUDY

T. This has the obvious advantage that E and σ_{cy} values are generally given as a function of temperature, whereas the pertinent stress-strain data are often not available. In addition, the stress-strain data beyond σ_{cy} are generally not used in design and therefore the use of a cutoff at σ_{cy} is in accord with design procedures.

For a particular compression element such as a stringer panel, a material-efficiency investigation at a particular temperature can be conducted. This is readily accomplished by choosing W/bL^2 and N/L as the variables in plotting the weight relation, Equation [18], for various materials. Thus, for the stringer panel constructed of a material with the idealized stress-strain characteristics

$$\frac{W}{bL^2} = \frac{1}{\alpha c^{1/4}} \frac{\varphi}{E^{1/4}} \left(\frac{N}{L}\right)^{1/4} \quad \text{for} \quad \sigma_o < \sigma_{cy} \qquad [20]$$

$$\frac{W}{bL^2} = \frac{\varphi}{\sigma_{cy}} \frac{N}{L} \quad \text{for} \quad \sigma_o = \sigma_{cy} \qquad [21]$$

It can be observed from Equation [20] that the physical properties of the material influence the weight according to $\varphi/E^{1/4}$ in this case whereas for $\sigma_o = \sigma_{cy}$ the material efficiency depends upon φ/σ_{cy}.

To illustrate the use of the material-efficiency chart, Fig. 3 has been prepared for stringer panels of various materials at room temperature. The physical properties used in this evaluation are representative room-temperature values. In each case the best sheet material in its class was selected on the basis of the highest available compressive yield strength.

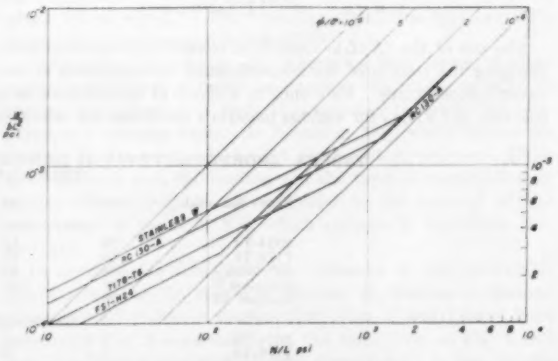

FIG. 3 COMPARATIVE MATERIAL-EFFICIENCY CHART FOR OPTIMUM STRINGER PANELS AT ROOM TEMPERATURE

TABLE 1 PHYSICAL PROPERTIES OF ENGINEERING ALLOYS AT ROOM TEMPERATURE

Sheet material	E, psi	σ_{cy}, psi	φ, pci	$\varphi/E^{1/2}$, pci/(psi)$^{1/2}$	φ/σ_{cy}, pci/psi
FS1-H24.....	6.5×10^6	28000	0.064	2.51×10^{-4}	2.28×10^{-4}
7178-T6.....	10.5	80000	0.101	3.12	1.26
RC-130A.....	16.2	140000	0.17	4.22	1.21
Stainless W...	30.2	220000	0.28	5.09	1.27

From Fig. 3 it is apparent that of those materials considered the magnesium alloy FS1-H24 is the most efficient up to N/L = 190 psi. Beyond this, the aluminum alloy 7178-T6 is the most efficient in stringer-panel applications although beyond N/L = 1200 psi the titanium alloy RC-130A is slightly more efficient. Actually, however, there is no significant difference among the aluminum and titanium alloys and stainless W steel in this region by virtue of almost identical values of φ/σ_{cy}. Note that the 45-deg lines represent constant values of φ/σ_c.

Fig. 3 is typical of the type of results obtained in material-efficiency studies. Consequently, it is convenient to elucidate certain basic rules which are of considerable utility in elevated-temperature investigations. It is quite obvious from the results for RC-130A as compared to stainless W that if

$$\left.\begin{aligned} &(\varphi/E^n)_1 > (\varphi/E^n)_2 \\ \text{and} \\ &(\varphi/\sigma_{cy})_1 > (\varphi/\sigma_{cy})_2 \end{aligned}\right\} \quad \ldots\ldots\ldots\ldots [22]$$

then material 1 is always more efficient than material 2.

Because of the fact that the lower-density materials have lower E and particularly lower σ_{cy} values, a typical situation illustrated by the FS1-H24 and 7178-T6 materials in Fig. 3 is often obtained. Here

$$\left.\begin{aligned} &(\varphi/E^n)_1 < (\varphi/E^n)_2 \\ \text{however} \\ &(\varphi/\sigma_{cy})_1 > (\varphi/\sigma_{cy})_2 \end{aligned}\right\} \quad \ldots\ldots\ldots\ldots [23]$$

In this case an intersection occurs for the two materials and a transition from material 1 to material 2 is indicated in the interests of efficiency. For the stringer panel, for example, the value of $(N/L)_{tr}$ at the transition can be obtained by equating Equation [21] for material 1 and Equation [20] for material 2. For the idealized stress-strain relation

$$\left(\frac{\varphi}{\sigma_{cy}}\right)_1 \frac{N}{L} = \frac{1}{\alpha c^{1/4}} \left(\frac{\varphi}{E^{1/2}}\right)_2 \left(\frac{N}{L}\right)^{1/2} \quad \ldots\ldots\ldots [24]$$

Thus

$$\left(\frac{N}{L}\right)_{tr} = \frac{1}{\alpha^2 c^{1/2}} \left[\frac{(\varphi/E^{1/2})_2}{(\varphi/\sigma_{cy})_1}\right]^2 \quad \ldots\ldots\ldots [25]$$

The use of the $(N/L)_{tr}$ term is of considerable value in summarizing the results of material-efficiency investigations at elevated temperatures. Reference to a chart of temperature as a function of $(N/L)_{tr}$ for various materials facilitates the selection of the most efficient material for prescribed loading and temperature conditions.

Such a chart can be constructed from a series of charts such as Fig. 3 for various temperatures. Values of $(N/L)_{tr}$ can also be established directly by use of Equations [22] and [23]. For the short-time elevated-temperature physical properties listed in Table 2, Fig. 4 has been constructed for optimum stringer panels. It can be observed that the aluminum alloys have no range of efficient application beyond approximately 650 F and that the titanium alloy RC-130A has no range of efficiency beyond 1000 F, approximately.

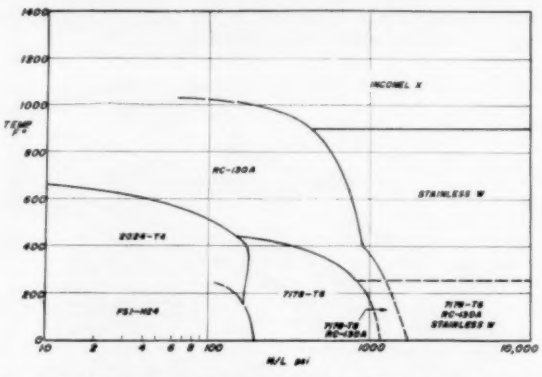

FIG. 4 MATERIAL-EFFICIENCY TRANSITION CHART FOR OPTIMUM STRINGER PANELS

It is to be noted that if actual stress-strain curves are used in place of the idealized ones, the procedure is the same although somewhat more complicated since it is necessary to introduce the proper values of $\bar{E}$ into Equation [18]. For the basic compression elements; solid and wide columns, and plates and plate assemblies, charts such as Fig. 4 can be constructed using the foregoing procedures.

COMPOSITE COMPRESSION STRUCTURES

A higher level of optimization can be achieved by considering the rib spacing or plate width as an open dimension. In this manner minimum-weight designs can be obtained for the composite compression structures involved in stringer panel-rib and multiweb construction. Instead of specifying the rib spacing L or plate width b at the start as done in the previous sections, these spacings are now considered as open dimensions subject to optimization.

The subject of minimum-weight analysis of composite structures has been treated at length (6). It is the purpose here to summarize some of the pertinent results for stringer panel-rib and multiweb construction in order to round out the comparative efficiency study.

TABLE 2 SHORT-TIME PHYSICAL PROPERTIES OF ENGINEERING ALLOYS AT ELEVATED TEMPERATURES (7, 8)

Sheet material	400 F	600 F	800 F	1000 F	1200 F
	Compressive yield strength, ksi				
2024-T4.....	38	14			
7178-T6.....	43	10			
RC-130A.....	100	88	75	40	
Stainless W.....	196	180	132	55	47
Inconel X.....	108		106		102
	Elastic modulus, $\times 10^6$ psi				
2024-T4.....	9.3	7.8			
7178-T6.....	8.3	6.6			
RC-130A.....	15	13	11.5	10	
Stainless W.....	29	28	25	20	13
Inconel X.....	31		30		26

The results of reference (6) can be summarized in terms of the parameters given in the following. The volume of structural material of a composite structure is

$$V = (1 + S)\, \bar{t}\, Lw \quad [26]$$

where S is the ratio of the weighted effective thickness of the supporting structure relative to the effective cover thickness $\bar{t}$. The solidity is defined as

$$\Sigma = \frac{V}{Lwh} = (1 + S)\, \bar{t}/h \quad [27]$$

Note that the solidity is analogous to the parameter $W/\varphi X_c^2$ obtained for the basic compression elements. Therefore the weight of a composite structure is

$$W = \varphi\, \Sigma Lwh \quad [28]$$

The applied axial loading acting on the covers of the wing or tail surface is prescribed by the bending moment M, the over-all height of the structural box h, and the width w

$$N = M/k_c hw \quad [29]$$

The coefficient k_c relates the centroidal height to the over-all height h for the various types of construction. Finally, the applied stress is equal to the allowable stress

$$N = \bar{\sigma}\, \bar{t} \quad [30]$$

Stringer Panel-Rib Construction. To evaluate the solidity according to Equation [27], it is necessary to determine analytically the supporting structure ratio S and the effective thickness ratio $(\bar{t}/h)_o$ of the optimum structure. For stringer panel-rib construction the optimum relationships were established in reference (6) as follows

$$S = 1/4$$

$$\left(\frac{\bar{t}}{h}\right)_o = \left(\frac{4\beta\varphi_r}{\alpha^4 c\varphi}\right)^{1/3} \left(\frac{h}{\rho_r}\right) \left(\frac{w}{h}\right)^2 \frac{\bar{\sigma}^{3/2}}{\bar{\tau} E E_r^{1/2}} \quad [31]$$

The various terms in Equation [31] have the following definitions and values as used in the analysis

$c = 1$	for pin-ended stringer panel
$\varphi = 1.15$	for optimum Y-stringer panel
$\beta = 4/\pi^4$	for effectively rigid pin-ended ribs
$h/\rho_r = 2$	for ideal full-depth ribs with concentrated flanges
$h/w =$	structural-thickness ratio

It is further assumed that the stringer panel and ribs are constructed of the same material. Thus

$$\varphi_r = \varphi$$

$$E_r = E$$

Under these conditions the optimum rib spacing for minimum weight of the composite structure is found to be

$$\left(\frac{L}{h}\right)_o = 0.994 \left(\frac{w}{h}\right)^{2/3} \left(\frac{N\bar{\tau}}{Eh}\right)^{1/3} \quad [32]$$

The sole function of the ribs as used here is to just stabilize the compression cover against general instability. Equation [32] is plotted in Fig. 5 for various structural-thickness ratios.

By use of Equation [30] and the foregoing assumptions, Equation [31] reduces to

$$\left(\frac{\bar{t}}{h}\right)_o = 0.823 \left(\frac{w}{h}\right)^{0.8} \frac{1}{\bar{\tau}^{0.4}} \left(\frac{N}{hE}\right)^{0.6} \quad [33]$$

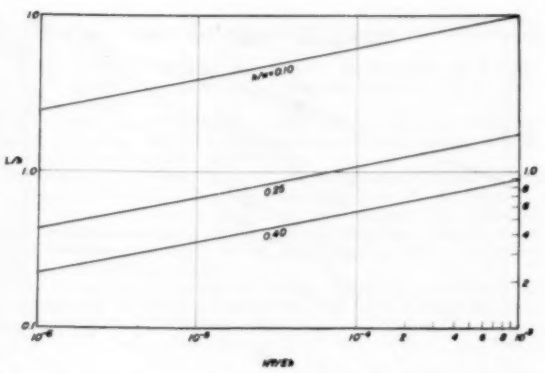

FIG. 5 OPTIMUM RIB SPACING FOR RIBS WITH HINGED ENDS

By use of Equation [27], $S = 1/4$ and Equation [33] the weight equation is obtained

$$\frac{W}{\varphi Lwh} = \Sigma = 1.03 \left(\frac{w}{h}\right)^{0.8} \frac{1}{\bar{\tau}^{0.4}} \left(\frac{N}{hE}\right)^{0.6} \quad [34]$$

In comparing Equation [34] for the composite construction with Equation [18] for the stringer panel alone, it can be observed that the two types depend somewhat differently upon the physical properties of the materials. The stringer-panel weight is proportional to $\varphi/(\bar{\tau}E)^{1/2}$ whereas for the stringer panel-rib construction the weight is proportional to $\varphi/\bar{\tau}^{0.4}\, E^{0.6}$.

Multiweb Construction. With the assumptions that the cover and hinged web are of the same material and buckle simultaneously, the following results were established for multiweb construction in reference (6)

$$S = 1/2$$

$$\left(\frac{t}{h}\right)_o = \left(\frac{12(1 - \nu^2)}{5\pi^2} \frac{\sigma}{\eta E}\right)^{1/2} \quad [35]$$

The optimum web spacing b is given by

$$(h/b)_o = (5/4)^{1/2} \quad [36]$$

The weight equation

$$\frac{W}{\varphi Lwh} = \Sigma = 0.905\, (N/\eta Eh)^{1/2} \quad [37]$$

In this case the cover of the multiweb depends upon the physical properties of the materials in the same manner as plates which fail at $\bar{\sigma}_f/\sigma_{cy} > 3/4$. Both in Equations [13] and [37], the weight is proportional to $\varphi/(\eta E)^{1/2}$.

Comparative Efficiencies. In comparing two forms of composite construction in order to establish the ranges of efficient structural application of each, it is essential that they be compared on a common basis. In Equation [29], which defines the loading N, the centroidal-height coefficient k_c appears. Since k_c varies both with the loading and the type of construction, it is desirable to compare the structures on the basis of M/h^2w rather than in terms of N/h which appears in Equations [34] and [37].

To demonstrate the significant influence of the centroidal-height effects on the ranges of efficient application of stringer panel-rib and multiweb construction, Figs. 6 and 7 have been prepared. Fig. 6 is essentially of the same form as Fig. 1 and does not contain centroidal-height corrections. It can be observed that as the structural-thickness ratio h/w decreases, the

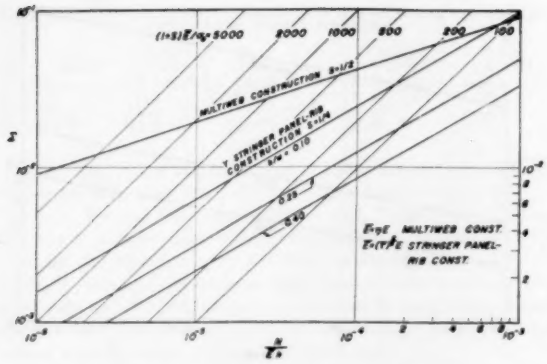

FIG. 6 COMPARATIVE STRUCTURAL-EFFICIENCY CHART FOR COMPOSITE COMPRESSION STRUCTURES

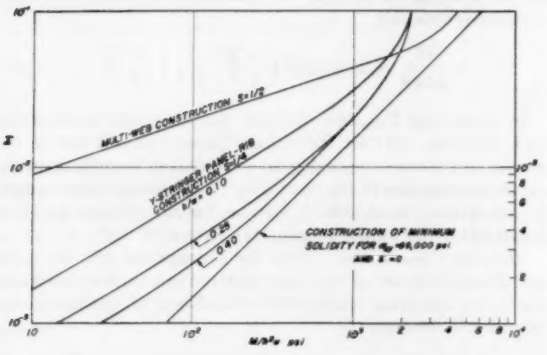

FIG. 7 COMPARATIVE EFFICIENCY OF COMPOSITE CONSTRUCTION OF 7075-T6 ALUMINUM ALLOY INCLUDING CENTROIDAL-HEIGHT EFFECTS

solidity of stringer panel-rib construction approaches that of multiweb construction at larger values of $N/\bar{E}h$.

By contrast, the abscissa of Fig. 7 is the parameter M/h^2w instead of N/h and thus the centroidal-height effects are reflected directly in the curves for the two forms of construction. Further, the results pertain to the aluminum alloy 7075-T6 at room temperature with σ_{cy} = 69,000 psi. Actual rather than idealized stress-strain data have been used in preparing Fig. 7.

Of particular significance here is the fact that stringer panel-rib construction has an upper limit of efficient application of M/h^2w = 2000 psi, approximately. By comparison with Fig. 6 which did not indicate an upper limit, it can be observed that this limit is primarily due to centroidal-height effects of the 7075-T6 stringer panels.

To conduct material-efficiency studies, charts such as Fig. 4 can be prepared for the composite forms of construction. Since each type of construction is being evaluated individually from the material-efficiency standpoint, it is generally not necessary to include centroidal effects in such investigations.

EFFICIENT MATERIAL AND CONFIGURATION SELECTION

With the considerable array of material and structural-efficiency criteria available one may legitimately inquire as to how the results are to be applied in design, and what are some of the other considerations which have not been included in the analysis.

In the preliminary design stages where first approximations may be sufficient, efficiency charts for the composite structure can be of considerable aid in selecting materials and structural arrangements of minimum weight. As the structural design progresses beyond the preliminary stages, there is more difficulty in designing the over-all structure purely from optimum considerations and therefore the results of efficiency studies for the individual compression elements become of greater importance.

Within certain limitations, minimum-weight studies appear to offer a rational approach to the selection of structural arrangements and materials in the design of aircraft. Because of the assumptions made in the analysis and the neglect of many considerations involved in the design of a wing such as fuel storage, for example, the results of minimum-weight analyses can only be considered as first approximations. These results must be modified by other structural requirements such as those of torsional rigidity, and by practical considerations such as minimum skin gages in the refinement of the approximation.

Thermal-Flight Considerations. With the advent of thermal flight, those concerned with the design of the airframe have been faced with three basic problems in the quest for structural efficiency; namely, structural arrangement, material selection, and insulation and cooling techniques. These problems are all interrelated so that it is not possible with our current state of knowledge to arrive at general minimum-weight design principles which automatically could specify structural configuration, structural material, insulation material, and cooling techniques for various flight paths. In fact, the fairly large number of material-efficiency criteria which have appeared in the literature can be confusing to those concerned with the problem of material selection until protection techniques have been explored sufficiently.

In all cases, however, it is necessary in the design of a wing to consider the spanwise weight variation of the compression, shear, and tension structures whether protected or not. As an illustrative example, Fig. 8 indicates the spanwise weight variation of the composite compression structure of a wing of two different materials at some elevated temperature. The weight variation is not necessarily that of the optimum structure but can include torsional as well as bending requirements, secondary-load considerations for the primary structure, the weight of the secondary structure, and insulation and cooling-equipment weight.

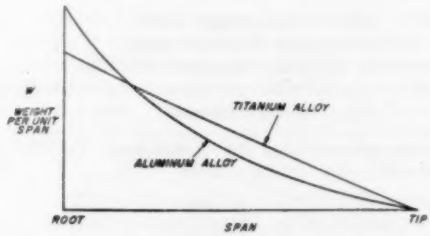

FIG. 8 SCHEMATIC SPANWISE-WEIGHT VARIATION OF TWO MATERIALS AT ELEVATED TEMPERATURE

For the example shown, because of the high loading intensity in the root region, titanium alloy is considerably more efficient than aluminum alloy. However in the outboard regions, the reverse is true since the load intensity has decreased. Thus, as a consequence of the fact that the comparative efficiency of structural arrangements and materials may vary spanwise for the compression structure as well as for the shear and tension structures, it is necessary to consider the total wing weight in selecting the most efficient material and arrangement.

In addition, the use of aluminum alloy generally leads to greater rigidity than titanium alloy since larger skin gages are

used to satisfy the load requirements for aluminum alloy. Furthermore, it has been found that, in the relatively lightly loaded secondary structures, the material of lower density is the most efficient. Such considerations indicate that serious attention must be given to insulation and cooling techniques before abandoning the use of the lower-density alloys in piloted aircraft.

BIBLIOGRAPHY

1 "Weight-Strength Analysis of Aircraft Structures," by F. R. Shanley, McGraw-Hill Book Company, Inc., New York, N. Y., 1952.

2 "Buckling Efficiencies of Plate Materials at Elevated Temperatures," by G. Gerard, *Journal of the Aeronautical Sciences*, vol. 22, March, 1955, pp. 194–196.

3 "Generalized Crippling Analysis of Formed Sections," by G. Gerard, *Journal of the Aeronautical Sciences*, vol. 23, January, 1956, pp. 88–90.

4 "Effects of Material Distribution on Strength of Panels," by A. Zahorski, *Journal of the Aeronautical Sciences*, vol. 11, July, 1944, pp. 247–253.

5 "The Design of Compression Structures for Minimum Weight," by D. J. Farrar, *Journal of the Royal Aeronautical Society*, vol. 53, November, 1949, pp. 1041–1052.

6 "Minimum Weight Analysis of Compression Structures," by G. Gerard, New York University Press, New York, N. Y., 1956.

7 "Elevated Temperature Compressive Stress-Strain Data for 24S-T3 Aluminum Alloy Sheet and Comparisons With Extruded 75S-T6 Aluminum Alloy," by W. M. Roberts and G. J. Heimerl, NACA TN 1837, March, 1949.

8 "Structural Efficiencies of Various Aluminum, Titanium, and Steel Alloys at Elevated Temperatures," by G. J. Heimerl and P. J. Hughes, NACA TN 2975, July, 1953.

Weight-Efficiency Analysis of Thin-Wing Construction

By R. A. ANDERSON,[1] LANGLEY FIELD, VA.

Information on the weight efficiency of multiweb thin-wing construction is reviewed and presented in a form suitable for preliminary design purposes. The effects of corrugated-web systems and steel-sandwich cover skins on weight efficiency are analyzed, and simple criteria are given for estimating the effect on weight of changes in the material properties of the structure.

Introduction

A number of studies have been made in the past of the weight efficiency of structures for thin wings. See, for example, references (1 and 2).[2] In general these studies have led to diagrams which define the minimum weight of various structural configurations for a range of bending moments. More recently, this same type of analysis has been extended to give the weight of the optimum structure when both over-all stiffness and strength requirements must be met (3). Essentially, this has meant considering the skin thickness as a primary design variable and therefore defining the optimum structure for a range of bending moments for various values of the wing depth-to-skin thickness ratio. This is necessary inasmuch as the optimum structural arrangement for a given wing is as likely to be a function of the desired skin thickness as of the loading intensity.

The information necessary for the latter type of analysis is reviewed in the present paper and comparisons given of the weight efficiency of various forms of multiweb wing construction. Both corrugated-web systems and steel-sandwich skins are analyzed. Simple criteria are given for estimating the effect on weight of a change in the material properties of the structure.

Nomenclature

The following nomenclature is used in the paper:

A_c = area of compression structure per chordwise inch
b = spacing of web supports
E = Young's modulus of elasticity
E_s = secant modulus of elasticity
f = effective offset of rivet line from plane of web
h = thickness of a sandwich plate
H = over-all depth of beam
M_c = bending moment per chordwise inch
P_c = compressive loading per chordwise inch
t = thickness of solid plate (sum of face thicknesses in sandwich plate)
t_w = thickness of channel web
$\bar{t}$ = equivalent flat-plate thickness of sandwich plate on a weight basis
$\bar{t}_w$ = equivalent flat-plate thickness of corrugated web on a weight basis
$\bar{\sigma}_f$ = average compressive stress in a plate at failure
σ_{cy} = compressive yield stress for a material (taken as 0.2 per cent offset yield stress in this presentation)
ρ = density of a solid material
ρ_e = effective density of sandwich core material

Cover Skin Compressive Efficiency

For many thin wings the desired structure is of the multiweb type in which the major portion of the material can be allocated to the cover skin where its contribution to local as well as over-all stiffness is the greatest. Structural weight in this case depends to a great extent upon the efficiency of plate elements of the cover skin in transmitting edge compressive loading. The first part of this paper, therefore, summarizes information on the compressive strength and weight of cover skins for support conditions encountered in multiweb construction. Both solid cover skins of various materials and steel-sandwich cover skins are treated.

Solid Cover Skin. A weight-efficiency study of multiweb construction is based upon the strength analysis of a structural element such as that shown in Fig. 1. Attention is directed to that

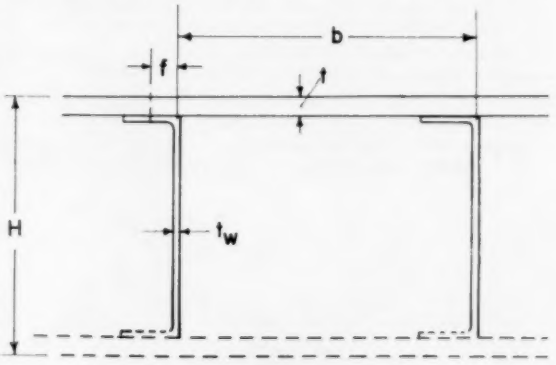

Fig. 1 Cross Section of Multiweb-Wing Structure

portion designed by compressive loading; that is, the compression skin and supporting webs. The allowable stress in the compression skin is determined by the width-thickness ratio of the skin between web lines, and by the support stiffness offered the skin by the web construction. The design details for the webs have been the object of much research (3, 4, 5), and tests show that flexibility of the web-skin attachment is the primary cause for reduction in allowable stresses from those achievable with webs which are integral with the skin. Even with the simple channel-web design illustrated in Fig. 1, however, near integral beam behavior is obtainable with proper rivet pitch, diameter, and offset from the web plane. Combinations of these three quantities define an effective rivet offset f. Values of f required for near integral behavior are defined in reference (5).

Average skin stresses at failure that have been achieved in adequately riveted multiweb beams of 7075-T6 aluminum alloy are

---

[1] Langley Aeronautical Laboratory, National Advisory Committee for Aeronautics.

[2] Numbers in parentheses refer to the Bibliography at the end of the paper.

Contributed by the Aviation Division and presented at the Aviation Division Conference, Los Angeles, Calif., March 14–16, 1956, of The American Society of Mechanical Engineers.

Note: Statements and opinions advanced in papers are to be understood as individual expressions of their authors and not those of the Society. Manuscript received at ASME Headquarters, January 18, 1956. Paper No. 56—AV-13.

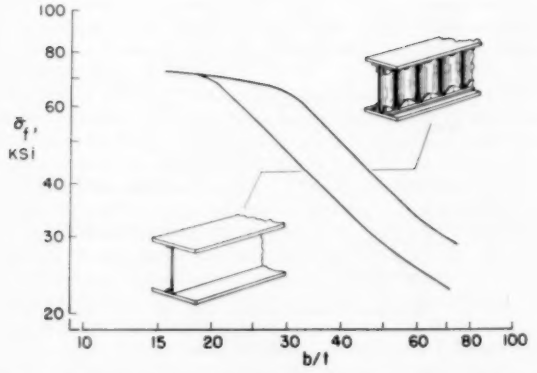

FIG. 2 COVER-SKIN STRESSES ACHIEVED IN TESTS OF MULTIWEB CONSTRUCTION OF 7075-T6 ALUMINUM ALLOY

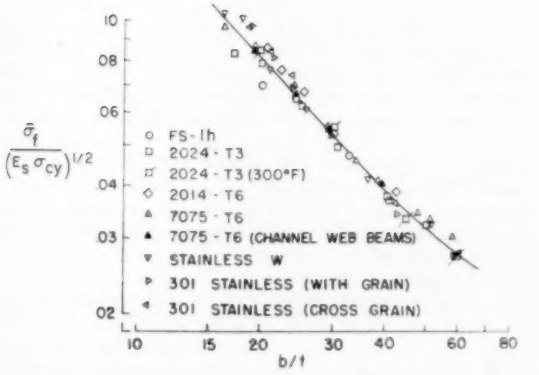

FIG. 3 CORRELATIONS OF COMPRESSIVE STRENGTH OF PLATES AMONG MATERIALS OF DIFFERENT PROPERTIES

given in Fig. 2. The lower curve gives the stresses in beams with channel webs which offer a stiff deflectional restraint to the skin but a negligible rotational restraint. These stresses were found to be relatively independent of web thickness so long as the web thickness is greater than that required to prevent crushing failure of the beam. The upper curve gives the stresses obtained in beams with a corrugated-web system. In the latter construction a high degree of rotational restraint of the skin is obtained with some loss in structural simplicity. However, the corrugated-web construction aids in reducing stresses arising from differential thermal expansion under rapid heating conditions and is at the same time very efficient in carrying shear. The area of the attachment angles is minimized by scalloping the leg which attaches to the crests of the vertically corrugated web.

In order that materials other than 7075-T6 may be included in an efficiency analysis a relationship must be established between failure stresses and material properties. One such relationship is shown in Fig. 3. The plotted points correspond to the maximum compressive stresses achieved in plates of various b/t and material properties when tested in edge compression in a V-groove edge fixture and when tested as covers of beams with channel webs. Correlation of these stresses with material properties is obtained by dividing failure stress by a quantity $(E_s\sigma_{cy})^{1/2}$. This quantity is analogous in purpose to the buckling modulus used to correlate buckling stresses and therefore has been called a plate-strength modulus (6). The value of the secant modulus E_s is obtained from the compressive stress-strain curve for the material at the failure stress of the plate.

A significant conclusion drawn from Fig. 3 is that the failure stresses of plates in a V-groove edge-supported compression test are in close agreement with the stresses achieved by the cover skins of 7075-T6 aluminum-alloy beams having channel webs. Similar agreement can be expected for channel web-beam tests of plates of other materials. Except in the plastic-stress region such stresses are appreciably higher than the simply supported buckling stresses for plates.

Allowable stress data such as those previously presented can be used to calculate the weight of cover skin required to transmit an edge compression loading P_i at a given web-support spacing b. The curves of Fig. 4 giving this weight have been drawn for a number of materials and support conditions. The value of $t\rho/b$ is a measure of the weight of a plate required for various values of the plate structural index P_i/b.

A comparison of the weight of aluminum-alloy cover skins supported by corrugated webs and by channel webs is provided by two of the curves in Fig. 4. The reduction in cover-skin weight

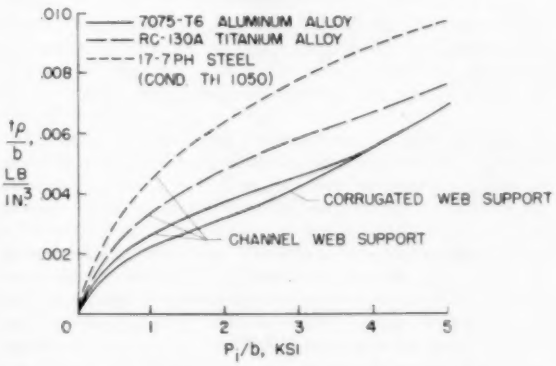

FIG. 4 WEIGHT EFFICIENCY OF PLATES OF VARIOUS MATERIALS UNDER EDGE COMPRESSIVE LOADING

for the corrugated web-supported plates is due to rotational restraint provided by this web system. The reduction is the greatest in the low-index range where the average stress in the plates at failure is in the elastic range of the material and diminishes at the larger index values where failure stresses approach the material yield stress.

A comparison of the weight of solid plates having the equivalent of channel-web support and made of 7075-T6 aluminum alloy, RC-130A titanium alloy, and 17-7 PH (cond. TH 1050) stainless steel is also given in Fig. 4. The properties assigned to these materials in calculating the curves are given in Table 1. Where plate-failure stresses are in the elastic range of the materials (low and intermediate structural-index range) the weight required is found to be approximately inversely proportional to the factor $(E\sigma_{cy})^{1/2}/\rho$ evaluated for each material. In this range, 7075-T6

TABLE 1 MATERIAL PROPERTIES USED IN CALCULATIONS

Material	ρ, lb/in.^{3}	σ_{cy}, ksi	E, ksi	$\frac{(E\sigma_{cy})^{1/2}}{\rho}$, (in.^{4}/lb)$^{1/2}$	$\frac{\sigma_{cy}}{\rho}$, in.
7075-T6 aluminum alloy	0.1	70	10500	9250	700000
RC-130A titanium alloy 70 F	0.17	140	16500	7250	824000
RC-130A titanium alloy 600 F	0.17	85	13000	6040	500000
17-7 PH steel (Cond. TH 1050), 70 F	0.28	180	30000	5440	644000
17-7 PH steel (Cond. TH 1050), 600 F	0.28	150	27500	5090	536000

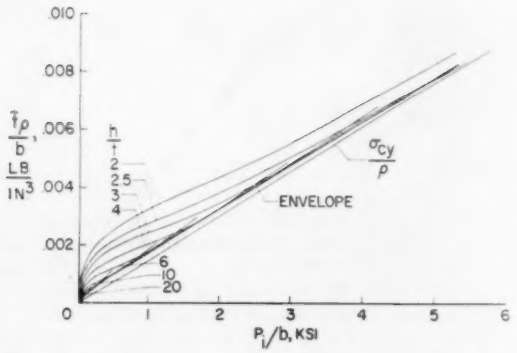

FIG. 5 WEIGHT EFFICIENCY OF 17-7 PH STEEL-SANDWICH PLATES OF VARIOUS PROPORTIONS UNDER EDGE COMPRESSIVE LOADING

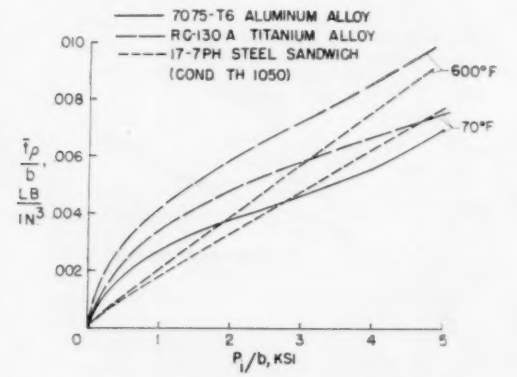

FIG. 6 COMPARISON OF WEIGHT EFFICIENCY OF STEEL-SANDWICH PLATES AND SOLID PLATES OF VARIOUS MATERIALS AT ROOM AND ELEVATED TEMPERATURES

aluminum alloy is the most efficient material. At very high values of the index, RC-130A titanium alloy, which has the highest value of σ_{cy}/ρ, will be the most efficient.

Despite a high modulus and yield stress, plates of stainless steel are seen to be not competitive on a compression-efficiency basis with plates of the lower-density materials. By fabrication into a sandwich, however, the density disadvantage of steel can be overcome as is shown in the next section.

Steel-Sandwich Cover Skin. The plate compressive efficiency of steel in the form of sandwich plates is presented in Fig. 5 (from reference 7). Each of the curves in this figure represents a different sandwich proportion as shown by the ratio of over-all sandwich thickness h to total face-sheet thickness t. The sandwich plates are assumed to have face sheets of 17-7 PH stainless steel which are either brazed or welded to a steel honeycomb core having a density of 9.7 pcf. The calculations were made assuming that the simple-support buckling load is the failure load and that the buckling stress does not exceed the yield stress. The failing stress along any curve therefore varies from zero at the origin to a value equal to the material compressive yield stress.

Material plasticity and the shearing stiffness of the steel honeycomb-core material are accounted for in computing the buckling load for the plates as explained in reference (7). Results are presented for only one core density inasmuch as the calculations of reference (7) indicate that a core lighter than that assumed in preparing Fig. 5 can lead to only small increases in over-all plate compressive efficiency. This results from the increasing effect of core shear flexibility on buckling.

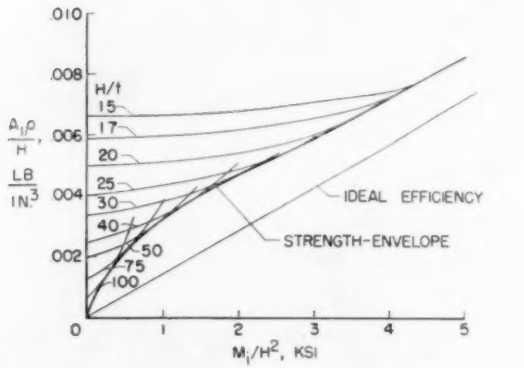

FIG. 7 WEIGHT EFFICIENCY DIAGRAM FOR 7075-T6 ALUMINUM-ALLOY MULTIWEB BEAMS OF CHANNEL-WEB CONSTRUCTION

The lower envelope curve in Fig. 5 defines the optimum proportions of the sandwich. It is significant that over a large range of structural-index values the most efficient sandwiches are obtained with small values of h/t; that is, sandwiches that have a high percentage of face-plate material. The weight of such sandwiches differs by only a small amount from the weight of the sandwich of ideal efficiency given by the line labeled σ_{cy}/ρ. This line gives the minimum possible weight assuming that the yield stress is the maximum stress that can be developed in the faces and that the core is of zero weight.

A comparison of the envelope curve of optimum steel-sandwich proportions with the weight-efficiency curves for solid plates of aluminum and titanium is given in Fig. 6. The comparison is made for temperatures of 70 and 600 F. The figure shows that at 70 F a plate compressive efficiency is obtained with steel sandwich which compares favorably with solid plates of the lower-density materials.

At 600 F, steel-sandwich plates are shown to have a large weight advantage over solid plates of titanium. Over a substantial range of the structural index they are more efficient than solid plates of aluminum alloy at 70 F. The weight change between optimum steel-sandwich plates at 70 and 600 F is very close to the change in the ratio ρ/σ_{cy} for the face plate material.

EFFICIENCY OF MULTIWEB-BEAM CONSTRUCTION

The minimum-weight proportions of web structure required to achieve the cover-skin efficiency previously presented have been investigated in a number of multiweb-beam tests. In particular, the behavior of beams with channel webs has been rather thoroughly investigated (3, 8) and a limited number of tests have been made on beams with corrugated webs. Because of extensive experimental verification, the weight efficiency of 7075-T6 aluminum-alloy beams with channel webs will be used in the presentation that follows as a standard for comparison of the efficiency of other methods and materials of construction. Beams made of solid plates are treated first and the probable efficiency of beams of stainless-steel sandwich construction is reserved for a separate section.

Beams Made of Solid Plates

The weight efficiency of beams of 7075-T6 aluminum alloy having channel webs is presented in Fig. 7 (from reference 3). In this diagram a parameter $A_1\rho/H$ which is a measure of the weight of both the compression skin and its supporting webs per unit of chord is plotted as a function of the structural index for a beam

under a bending moment M_i/H^2. The weight variation is given for a number of values of the beam depth-to-skin thickness ratio H/t. Small values of this ratio correspond to the thinnest wings and/or the thickest skins.

A feature of Fig. 7 is that the compression-structure weight required to meet a given strength requirement can be determined when the skin thickness is fixed by some other design condition such as torsional stiffness. For any H/t curve, the value of the ordinate at M_i/H^2 equal to zero is $t\rho/H$, a measure of the weight of the compression skin alone. The increase in weight along the curve is that arising from the weight of webs required to stabilize the skin for the higher compressive-loading intensities. At the right-hand end of each curve, where allowable stresses approach the yield stress of the material, web weight increases rapidly for small changes in loading intensity.

When skin thickness is an arbitrary variable in the design, the minimum-weight structure lies on the familiar strength-envelope curve. This curve approaches an ideal efficiency curve (no webs, allowable stress equal to compressive yield stress) at very high values of the structural index.

Over most of the diagram it is evident that a weight increase is incurred if a desired skin thickness is greater than that which is optimum for strength. The curves also show that structures designed for values of M_i/H^2 and H/t which lie to the right of the intersection of an H/t curve with the strength envelope not only weigh more but are less stiff than the most efficient structure.

The strength envelope for 7075-T6 aluminum-alloy channel-web

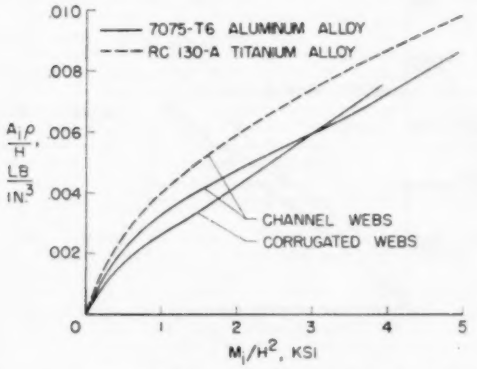

FIG. 8 EFFECT OF A CHANGE IN MATERIAL AND OF A CHANGE IN WEB DESIGN ON WEIGHT OF MULTIWEB CONSTRUCTION

construction is used in Fig. 8 as the basis for evaluating the effects on weight of a change in the method of construction and of a change in material. In one case channel webs are replaced by corrugated webs and in the other case channel webs are retained and the material of construction is changed to RC-130A titanium alloy.

The corrugated web-beam envelope shown in Fig. 8 is based on a conservative analysis of the existing test data and indicates that the weight efficiency of this construction is substantially better than that for channel-web construction over a large range of the structural index. This is a reflection of the increased allowable skin stresses shown in Fig. 2. There is reason to believe that additional tests will reveal the more optimum web proportions and attachment design that will lower the weight of this construction at the higher values of structural index.

A characteristic of corrugated-web construction not revealed by a presentation of the strength envelope alone is that a skin thinner than that associated with channel-web design is obtained at comparable values of the structural index. Therefore, in circumstances where a minimum skin thickness greater than the optimum is required for stiffness or other reasons, some of the apparent weight advantage of the corrugated-web design cannot be realized. On the other hand, if buckling from thermal stresses would dictate a channel-web spacing that is less than optimum, the use of corrugated webs at a larger spacing may be advantageous.

The strength-envelope curve in Fig. 8 for channel-web beams of RC-130A titanium alloy is based on the strength analysis found applicable to beams of high-strength aluminum alloy (3). The titanium-alloy compression structure is found to vary from a maximum of 125 per cent of the weight of the aluminum-alloy structure at a low index value to a minimum of about 85 per cent at index values greater than 10. These percentage weight changes are approximately proportional to the changes that occur, respectively, in the compressive-efficiency parameters

$$(E\sigma_{cy})^{1/4}/\rho \text{ and } \sigma_{cy}/\rho$$

for cover skins of these two materials. It is evident from this comparison that the weight efficiency of multiweb construction is heavily dependent upon the plate compressive efficiency of the cover-skin material and therefore that the efficiency parameters for the cover skins can be used to predict the maximum effects on beam weight of a change to any other material (or of an elevated temperature).

Beams of Steel-Sandwich Construction. At present little experience exists with multiweb construction employing steel-sandwich material and it is therefore necessary to base an efficiency analysis on a number of assumptions. The most important of these is the weight of sandwich plate required for various loading intensities. The curves presented in Fig. 5 giving this weight variation are believed to be representative of current production capabilities and are used in the analysis. The detailed assumptions regarding a conservatively designed web system capable of providing at least simple support to the sandwich plate are given in the derivation of the weight-efficiency equations in the Appendix.

In contrast to beams with solid skins, the core weight of sandwich plates must be considered along with the web members as stabilization material. It follows therefore that the lightest structure for a given loading intensity and wing depth-to-skin thickness ratio will have the optimum distribution of stabilization material between sandwich core and full-depth webs.

To illustrate the variation in total weight that can occur with arbitrary distributions of stabilization material, Fig. 9 has been

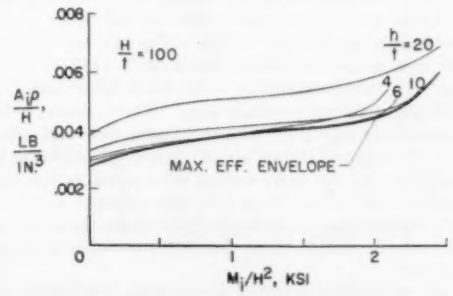

FIG. 9 EFFECT OF DIFFERENCES IN SANDWICH-CORE HEIGHT ON WEIGHT OF SANDWICH MULTIWEB CONSTRUCTION

prepared. In this figure the beam depth, the face-plate thickness, and the core density are held constant. Each curve therefore represents a sandwich plate with a different core height. Along a

given curve, the variation in weight is due to the changes in web spacing required for a variation in the beam bending strength.

The lower envelope to these curves defines the optimum method of stabilizing the face-plate material for various values of loading intensity. Along the envelope the sandwich height to face-plate thickness ratio h/t varies from unity (at M_i/H^2 equal to zero) to a maximum of 10. The maximum value of h/t decreases for values of H/t smaller than that used in this example.

A family of envelope curves for various values of wing depth-to-skin thickness ratio is presented in Fig. 10. These curves are equivalent to, and may be compared with, those in Fig. 7 for channel-web beams having solid-plate cover skins of aluminum alloy. Despite the much lower plate-compression efficiency of steel (Fig. 4), an efficient use of stabilization material to increase the moment of inertia of the skin itself (as in a sandwich) as well as to reduce the unsupported width of the skin panels leads to weight curves which have about the same slope as those for beams of aluminum alloy. When steel is stabilized in this manner, a strength envelope is obtained for steel beams which compares favorably at room temperature with the best conventional aluminum-alloy construction even though the yield-to-density ratio of the sandwich face-plate material is considerably less than that of 7075-T6 aluminum alloy. This comparison is shown in Fig. 11. In this figure the calculated envelope curve for the steel-sandwich construction is shown dashed to differentiate it from the solid curves that have been verified by test data.

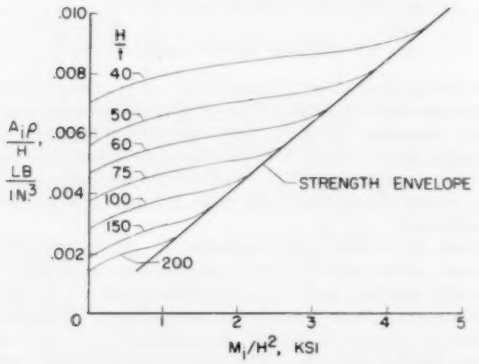

FIG. 10 WEIGHT EFFICIENCY DIAGRAM FOR STAINLESS-STEEL-SANDWICH MULTIWEB CONSTRUCTION
(17-7 PH Cond. TH 1050 steel.)

The family of parallel dotted lines in Fig. 11 gives the weight of another type of sandwich-beam construction which is of current interest. In this construction a full-depth honeycomb core is used between steel outer-surface skins. The minimum weight of such beams was calculated with the assumption that full-depth cores of the densities shown are all capable of producing an allowable stress for the outer-surface skins equal to the material compressive yield stress. Even with this optimistic assumption it is clearly evident that an extremely light full-depth core is required to compete on a weight basis with other methods of cover-skin stabilization.

To give an indication of the actual weights corresponding to the curves in Fig. 11, the weight of compression material per square foot of wing surface at a structural index value of 2 ksi and a wing depth of 6 in. is given in Table 2.

To the weights in Table 2 must be added the weight of the tension skin, any necessary ribs, and any additional web material that might be necessary for shear.

TABLE 2 COMPRESSION STRUCTURE WEIGHT

		Lb/ft²
Full-depth honeycomb beam	0-pcf core	2.7
	2-pcf core	3.7
	4-pcf core	4.7
	6-pcf core	5.7
Aluminum-alloy beams	Corrugated webs	3.7
	Channel webs	4.1
Steel-sandwich beam		3.7

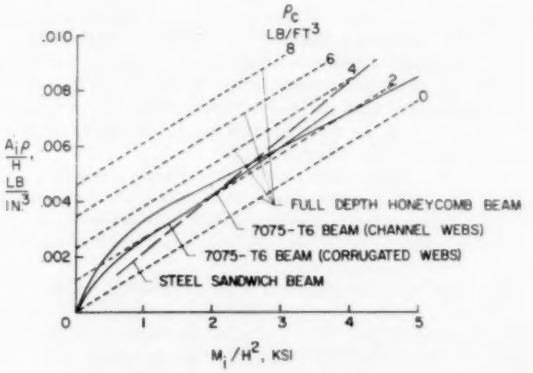

FIG. 11 WEIGHT COMPARISON OF STEEL-SANDWICH AND ALUMINUM ALLOY MULTIWEB CONSTRUCTION

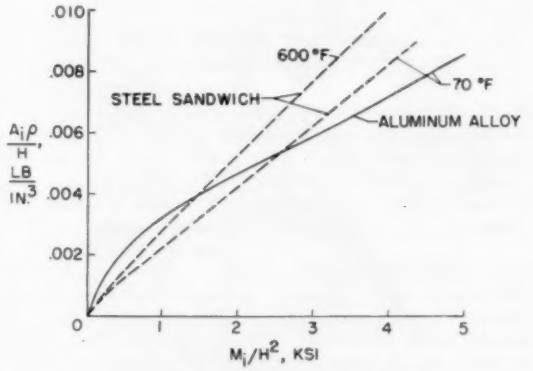

FIG. 12 EFFECT OF ELEVATED TEMPERATURE ON WEIGHT OF MULTIWEB CONSTRUCTION

In Fig. 12 a comparison is made of room-temperature weight-efficiency curves with the calculated envelope curve for steel-sandwich construction operating at 600 F. The weight change of the steel-sandwich structure is very nearly proportional to the change in the ratio ρ/σ_{cy} for the material with temperature. Over the lower end of the index range the indicated weight at 600 F of those parts of the structure designed by compression loading is comparable to solid-plate aluminum-alloy beams at room temperatures. At the higher values of the structural index, however, the weight required is more closely related to the yield stress-density ratio for materials, and substantial increases in weight are indicated as temperature is increased. The development of temperature-resistant sandwich-plate materials with yield stresses higher than those assumed in the present calculations could alleviate this situation somewhat.

CONCLUDING REMARKS

Some of the factors that determine the weight of multiweb thin-wing construction have been reviewed with the intention of

directing attention toward developments that will lead to further improvements in weight efficiency. One of these is the use of a corrugated-web system which can provide not only a stiff deflectional support to the cover skins but also a high degree of rotational fixity to the skin panels. An associated problem is the provision of simple attachment members which are light in weight and capable of utilizing the web stiffness to support the cover skins.

For structures requiring temperature-resistant materials, the use of sandwich-plate construction will greatly reduce the buckling instability problems inherent with the high density of these materials. The total sandwich thickness need not be greater than 10 times the total face-plate thickness for this to be accomplished efficiently. The calculations presented for stainless-steel sandwich of current manufacturing capability indicate that even at room temperature multiweb-wing construction of such material is competitive in weight with conventional aluminum-alloy structure. Because sandwich construction permits efficient utilization of the strength of presently available temperature-resistant materials, further improvement in weight efficiency largely depends upon any improvement that can be made in the yield strength-to-density ratio of such materials.

BIBLIOGRAPHY

1 "Comparative Efficiency in Bending of Structural Elements of Various Designs and Solidities," by G. Gerard, New York University Report to Office of Naval Research, April, 1952.

2 "Factors Affecting the Design of Thin Wings," by W. J. Conway, Society of Automotive Engineers Preprint No. 357, October, 1954.

3 "Ultimate Strength and Optimum Proportions of Multiweb Wing Structures," by B. W. Rosen, NACA TN 3633.

4 "Some Information on the Strength of Thick-Skin Wings With Multiweb and Multipost Stabilization," by R. A. Anderson, R. A. Pride, and A. E. Johnson, Jr., NACA RM L53F16, August, 1953.

5 "An Analysis of the Stability and Ultimate Compressive Strength of Short Sheet-Stringer Panels With Special Reference to the Influence of Riveted Connection Between Sheet and Stringer," J. W. Semonian and J. P. Peterson, NACA TN 3431.

6 "Correlation of Crippling Strength of Plate Structures With Material Properties," by R. A. Anderson and M. S. Anderson, NACA TN 3600.

7 "The Efficiency of Stainless Steel Cellular-Core Sandwich Plates in Compression," by J. W. Semonian and A. E. Johnson, Jr., prospective NACA Technical Note.

8 "Experimental Investigation of the Pure Bending Strength of 75S-T6 Aluminum Alloy Multiweb Beams With Formed Channel Webs," by R. A. Pride and M. S. Anderson, NACA TN 3082.

Appendix

Calculated Weight Efficiency of a Steel-Sandwich Beam

The bending moment per chordwise inch carried by a multiweb beam having two sandwich cover skins and vertically corrugated webs may be written

$$M_i = P_i(H - h) + \frac{P_a}{b}(H - 2h) \quad [1]$$

where P_a is the compressive load carried by the attachment and reinforcement area at a web-cover skin joint, and the other symbols are as defined in the nomenclature. The assumption is made that the centroid of the attachment area lies at the inner face of the sandwich cover skin. The area of compression structure per chordwise inch is

$$A_i = \bar{t} + \frac{A_a}{b} + \frac{t_W}{b}(H - 2h) \quad [2]$$

where A_a is the attachment area on the compression side of the beam, and t_W is the equivalent flat-sheet thickness of a corrugated web.

Equations [1] and [2] may be rewritten

$$\frac{M_i}{H^2} = \frac{P_i}{b}\frac{b}{H}\left(1 - \frac{h}{t}\frac{t}{H}\right) + \frac{P_a}{bH}\left(1 - 2\frac{h}{t}\frac{t}{H}\right) \quad [3]$$

$$\frac{A_i}{H} = \frac{\bar{t}}{H} + \frac{A_a}{bH} + \frac{t_W}{\bar{t}}\frac{\bar{t}}{b}\left(1 - 2\frac{h}{t}\frac{t}{H}\right) \quad [4]$$

The value of $\bar{t}/H$ can be given as

$$\frac{\bar{t}}{H} = \frac{t}{H} + \frac{\rho_a}{\rho}\left(\frac{h - t}{H}\right) = \frac{t}{H}\left[1 + \frac{\rho_c}{\rho}\left(\frac{h}{t} - 1\right)\right] \quad [5]$$

and the value of b/H as

$$\frac{b}{H} = \frac{b}{\bar{t}}\frac{\bar{t}}{H} = \frac{b}{\bar{t}}\frac{t}{H}\left[1 + \frac{\rho_c}{\rho}\left(\frac{h}{t} - 1\right)\right] \quad [6]$$

An assumption for the attachment and reinforcement area at a web joint in a sandwich panel that appears conservative is that this area is equal to the square of the thickness of the sandwich panel. Therefore

$$\frac{A_a}{bH} = \frac{h^2}{bH} = \frac{h}{\bar{t}}\frac{\bar{t}}{b}\frac{h}{t}\frac{t}{H} = \frac{\frac{\bar{t}}{b}\left(\frac{h}{t}\right)^2\frac{t}{H}}{1 + \frac{\rho_c}{\rho}\left(\frac{h}{t} - 1\right)} \quad [7]$$

Similarly, available test data on beams with corrugated webs indicate that the following expression for web thickness should be conservative

$$\frac{t_W}{\bar{t}} = \frac{1}{2} \quad [8]$$

The load carried by the attachment area at failure is determined by the failing stress for the sandwich panel. Therefore P_a/bH may be written

$$\frac{P_a}{bH} = \frac{\sigma_f A_a}{bH} = \frac{P_i}{t}\frac{A_a}{bH} = \frac{P_i}{b}\frac{t}{H}\left(\frac{h}{t}\right)^2 \quad [9]$$

Substitution of Equations [5] to [9] into Equations [3] and [4] yields

$$\frac{M_i}{H^2} = \frac{P_i}{b}\frac{t}{H}\frac{b}{t}\left(1 - \frac{h}{t}\frac{t}{H}\right)\left[1 + \frac{\rho_a}{\rho}\left(\frac{h}{t} - 1\right)\right] + \frac{P_i}{b}\frac{t}{H}\left(\frac{h}{t}\right)^2\left(1 - 2\frac{h}{t}\frac{t}{H}\right) \quad [10]$$

$$\frac{A_i}{H} = \frac{t}{H}\left[1 + \frac{\rho_c}{\rho}\left(\frac{h}{t} - 1\right)\right] + \frac{\frac{\bar{t}}{b}\frac{t}{H}\left(\frac{h}{t}\right)^2}{1 + \frac{\rho_c}{\rho}\left(\frac{h}{t} - 1\right)} + \frac{1}{2}\frac{\bar{t}}{b}\left(1 - 2\frac{h}{t}\frac{t}{H}\right) \quad [11]$$

Equations [10] and [11] have been solved simultaneously using the curves of P_i/b versus $\bar{t}/b$ for the sandwich panels given in Fig. 5. The results are presented in Figs. 9 and 10.

Design Criteria for Heated Aircraft Structures

By ROBERT GOLDIN,[1] BUFFALO, N. Y.

Engineering considerations which constitute structural criteria are briefly reviewed, and the use of "safety factor" in the "working-stress" approach is compared with its use in the "limit-load" design concept. It is recalled that in current aircraft-design practice, primary "limit conditions" are arbitrarily formulated on the basis of not combining two or more maximum severity conditions. Aerodynamic heating superimposes: (*a*) Maximum temperature, (*b*) temperature gradients, and (*c*) creep life as additional parameters which severely influence design. The design-criteria problem is to define realistic combinations of these with each of the previous key parameters used in aircraft design. The possible design combinations are vastly increased, and it is contended that only a criteria framework and basic philosophy can be generally applicable to all heated aircraft. Proposals relative to safety factors, creation of limit load-and-temperature condition combinations, and how to introduce creep life are presented, together with illustrative examples of criteria for two types of aircraft.

Introduction

As THE demands upon the structural engineer to provide airframes capable of sustaining aerodynamic heating increase, the urgency of establishing basic criteria assumptions has become paramount. Perhaps not since the very beginnings of the formulation of airplane structural criteria has the task been so formidable and solutions so obscure. By defining the problems and mustering present knowledge and past experience, the solution of these problems may be approached if not fully realized.

We will first examine the question: What are "structural criteria," and also the present procedures used in establishing structural integrity. Most of the time the engineer turns to specifications and codes, and uses them with little or no thought of how they were evolved and what philosophies they represent. Now that we must revise or add to them drastically, it is appropriate to take some time to reflect on what we have been doing before advancing farther.

We will then review the influence of thermal aspects upon structural criteria and categorize the new parameters which must be established. Because of the vast variety of aircraft and performance missions possible, it is the author's firm belief that specification tables of design load factors, speeds, gross weights, and associated specific design conditions are not practicable to define "hot" design conditions completely. In lieu of such specific criteria, rules for formulating basic design values for any heated aircraft are proposed. The issues affecting safety factor are examined and a proposal is advanced for use in heated-structure design.

Our objective, therefore, is to assemble a practical structural design philosophy. We believe that a criteria framework is the fundamental thing we can provide to help solve the heated aircraft-criteria problem, and that future specifications should be concerned with this to supplement the specific numbers and detailed conditions applicable to "normal temperature" aircraft. With such a framework the designer can proceed, and with the aid of his customer establish realistic particular strength-level numbers applicable to a new aircraft design.

What Are Structural Criteria?

When we think of structural criteria it is necessary for us to consider: Safety factors, limit operating conditions, aircraft life, design material allowables (or working stresses), stress analysis, qualification tests (laboratory and flight), and inspection tests (see Fig. 1). Taken all together these items are the things we consider prior to establishing "strength level" for a particular application. Variation in the magnitude or scope of any of these can affect materially the strength level that might be considered adequate for a job; or conversely, doubt about one of the foregoing elements will stimulate addition of conservatism to one of the others. So, for example, comprehensive structural testing permits de-emphasis of stress analysis; reduction of analytical or test investigations stimulates use of increased safety factor; or, if conservative limit loads are used, less conservative stress analysis is permissible. In selecting criteria for a given task, the engineer's objective is to achieve a desired degree of safety and at the same time keep the ratio of performance versus over-all costs as high as possible.

It is therefore impossible when speaking of structural criteria—or any of its elements— to consider one part exclusive of the whole. If, however, a general criteria framework such as MIL-S-5700 (1)[2] is defined and accepted, and a new load parameter appears (like Mach number did some years back), the new item can be interjected without appreciable re-evaluation of the whole. But this is not true for aerodynamic heating, for it has drastic and interrelated effect on: (*a*) Limit-condition combinations; (*b*) aircraft life; (*c*) reliability of stress analysis; (*d*) material allowables; and (*e*) capability to qualification test realistically. It therefore is necessary at this point to re-evaluate the entire criteria framework.

There are two fundamental approaches to the general problem of formulating structural criteria, both of which use safety factors. We can name them by their key features as follows: (*a*) The working-stress design concept (used in mechanical and civil engineering); and (*b*) the limit-load design concept (used in aeronautical engineering). In order better to understand structural criteria and how safety factors are variously used, a brief review of the two methods follows.

Working-Stress Approach. This type of strength criteria usually emphasizes endurance (essentially unlimited life) and conservatism. Safety factors are used to assure adequate coverage of all conceivable transient loads, fabrication uncertainties, and even misuse of the final product. The strength allowables are based primarily upon endurance-limit strength of materials.

[1] Head, Criteria and Loads Group, Bell Aircraft Corporation.

Contributed by the Aviation Division and presented at the Aviation Division Conference, Los Angeles, Calif., March 14–16, 1956, of The American Society of Mechanical Engineers.

Note: Statements and opinions advanced in papers are to be understood as individual expressions of their authors and not those of the Society. Manuscript received at ASME Headquarters, January 18, 1956. Paper No. 56—AV-14.

[2] Numbers in parentheses refer to the Bibliography at the end of the paper.

A classic paper which delineates this criteria approach was prepared by Soderberg in 1929 (2). In it he defines the relationship of working stresses and safety or "ignorance" factors required to assure adequate strength.

Limit-Load Approach. In this type of criteria a great deal of credence is placed upon relatively exact knowledge of maximum static and dynamic loading conditions to be experienced, material allowables for both yield and ultimate, and degree of uniformity of fabrication practices. The importance of safety factor is far less in this approach than in the working-stress system. This method is used universally in aircraft design, where weight is of paramount importance and fatigue life has been a somewhat secondary consideration. A large family of maximum (or limit) operating-condition combinations is selected and structural elements are designed for yield at precisely these limit loads, or failure at an arbitrary 1.5 times limit loads.[1] Every effort is exerted to rationalize and calculate precisely the limit loads, and likewise the material allowables are closely determined by inspection and test to obtain "guaranteed" values. Stress analysis is performed carefully and static and dynamic laboratory tests are performed to corroborate the analyses. Furthermore, the limit operating conditions are usually simulated in closely controlled flight and ground tests to verify loads analysis as well as stress analysis. The arbitrary 1.5 ultimate factor of safety serves to some extent both as a safety or ignorance factor; it also helps make often-repeated loads fall below the endurance limit of the materials. In modern high-performance aircraft, the occurrence of small amounts of yield can sometimes cause catastrophic failure; furthermore, with improved rational analysis and test for structural fatigue, it has been seriously questioned that the 1.5 ultimate factor of safety serves a useful purpose even relative to fatigue. This, as well as associated items in the limit-load design approach, is thoroughly covered in Mangurian's paper on this subject (3).

It cannot be overemphasized that the selection of design operating conditions by either method is, to an appreciable extent, quite arbitrary and based only upon general experience and opinion. Even after a maneuver load factor is selected "on the basis of past needs" for design of an airplane, our criteria invariably assumes: (*a*) Maximum design gusts do not occur at the same time as maximum maneuvers; (*b*) maximum unsymmetrical loads do not occur with maximum maneuvers; (*c*) maximum design-gust velocity does not occur at maximum dive speed; (*d*) maximum landing sinking speed does not occur at overload-landing gross weights; and many others. The possibility that some or nearly all of these occur in combination nonetheless exists, but an uncalculated risk is taken in view of the very low probabilities involved. There is a tacit understanding among criteria engineers which amounts to a corollary:

Sustained operating conditions may have superimposed upon them maximum-expected severity conditions, but two or more distinct types of maximum severity conditions are not considered to be combined except in unusual design situations where such occurrences are reasonably probable.

Also, in aircraft systems wherein malfunctions of various types are known to occur, we often design for essentially normal operation to occur after such a malfunction occurs. But here again, in the interests of achieving less penalty to performance, the following is accepted practice:

In general, design for satisfactory operation after a double malfunction occurs is not required; however, in major systems or components, design features to prevent catastrophic failure as a result of double malfunctions are desirable.

Fortunately for us at this time, the precedents and assumptions which have proved satisfactory in actual airplane operations are summarized, tabulated, and delineated in specifications such as MIL-S-5700 (1), MIL-A-8629 (4), and CAR-04 (5) for conventional aircraft. Deviations from these, for variations which are desirable in particular designs, are the subject of considerable criteria discussions between interested parties—but these deviations still are usually embodied in the basic framework of the afore-mentioned specifications.

Influence of Thermal Aspects on Structural Criteria

Most of the criteria presently used in design of present normal-temperature (up to 250 F) aircraft is quite applicable in design of aircraft subjected to aerodynamic heating. There must be superimposed upon these the assumptions and ground rules for introducing the new parameters associated with the heating. The material allowable, stress analysis, and hardware-design problems are defined in other studies, such as that performed at Bell Aircraft and published as WADC TR-55-305 (6), and will not be repeated here. However, the nature and severity of these problems do affect the design criteria, and therefore these, along with the other significant characteristics of flight involving elevated temperatures, are now reviewed briefly from a criteria standpoint.

In the flight plans for any particular aircraft, the severity of the thermal condition is primarily defined by maximum temperature experienced, time-rate-of-change of temperature of structures, and time duration at temperature. If the maximum temperature does not exceed about 150 to 250 F, most structural materials can be treated as if there were no thermal condition in so far as material allowables are concerned; furthermore, if the rate of heating is gradual, no major thermal-stress problem exists. On the other hand, if the maximum temperature and/or the thermal gradient becomes excessive, we must consider the design of such heated structures in a different light from a normal temperature structure. Also, while repeated loads at room temperature are of somewhat secondary concern, both repeated and steady loads at elevated temperatures directly affect usable life because of the aggravated aspects of creep. Careful examination of each of the many characteristics affected by elevated temperatures indicates that the criteria required prior to attempting their analysis are those needed to define the three items just described.

As soon as it is evident that the new parameters of temperature, thermal gradient, and time duration at temperature enter into the design picture, a reorientation of thinking immediately takes place. Heretofore in preliminary design, structural weight was kept to a minimum by obtaining a realistic balance between (*a*) maneuvering requirements, (*b*) limit speeds, and (*c*) maneuver-condition combinations. We must now add (*d*) maximum temperatures, (*e*) maximum temperature gradients and (*f*) creep life (see Fig. 2). Whereas before we could consider the effects on weight of variations of the three elements simply by standard stress calculations (P/A, Mc/I, etc.), now the additional three elements require calculations for load and thermal stress, heat flow, insulation and/or cooling, and estimation of the effects of creep. The new elements may require design of systems for cooling to be balanced against structural and insulation weight. In extending the criteria to embrace the elevated-temperature operations the following items now must be defined:

(*a*) *Load and Temperature Combinations.* To obtain efficient design, it is usually too costly in weight to assume arbitrarily that maximum loads and temperatures occur simultaneously.

[1] Design for yield strength at limit load is specified by the U. S. Air Force and the CAA, with design for ultimate strength at 1.5 times limit. The U. S. Navy specifies design for yield at 1.15 times limit and the same value, 1.5 times limit, for design for ultimate strength. In all cases both the yield and the ultimate must be investigated, and the critical one is used to design each structural element.

Accordingly, a desirable balance between design maneuver, gust, and elevated-temperature conditions must be achieved based on flight-plan or operating restriction.

(*b*) *Thermal Gradient and Load Combinations.* Since stresses arising from thermal gradients are of the same order of severity as stresses from load conditions, the load combinations used during transient temperature conditions should be evaluated in the same manner as is discussed in item (*a*).

(*c*) *Time at Elevated Temperature and Loads.* Design life of a heated aircraft structure appears to be a governing design parameter. Accordingly, the definition of time duration of temperature-and-load combinations and number of repetitions required is an essential part of the basic structural criteria.

A fundamental consideration affecting criteria, but not related directly to the purely technical aspects of the aerodynamic heating problem, is the pilot's knowledge of the instantaneous thermal-strength condition during flight. We use accelerometers, airspeed and Mach meters, and fuel-quantity gages to assist the pilot in maintaining operations within the design limits. Conversely, the criteria engineer utilizes these instruments as the cornerstones upon which to base definition of design conditions. When this is done, deficiencies in strength level can be translated directly into operating restrictions of load factor, speed, and/or gross weight. Definition of heated-structure design criteria in terms of some instrument which the pilot can observe during flight would likewise make design parameters better understood and easily usable in setting forth operating instructions.

With the addition of the thermal parameters into the structural design job, large quantities of physical-characteristic and material allowable data must be determined and assembled into a giant-sized extension of ANC-5 (7). New methods of analysis need to be developed immediately. Methods of substantiating structural airworthiness in laboratory and flight tests likewise must be explored, and new precedents in quality-control procedures must be evolved. While all these items enter into the establishment of strength level, this paper is concerned only with the

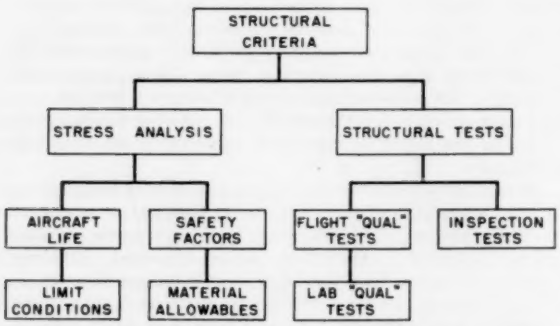

FIG. 1 ELEMENTS COMPRISING STRUCTURAL CRITERIA

basic design criteria; i.e., the relationship of limit-condition combinations, aircraft life, safety factors, and material allowables (see Fig. 1).

ELEVATED-TEMPERATURE DESIGN CRITERIA

(*a*) *General.* In the preceding discussions the nature of structural criteria and the influences of superposition of thermal parameters upon "normal" temperature criteria have been reviewed. We will now discuss the specific items which must be defined during the initial phase of design of heated aircraft structure, and provide some examples. These design criteria are (*a*) safety

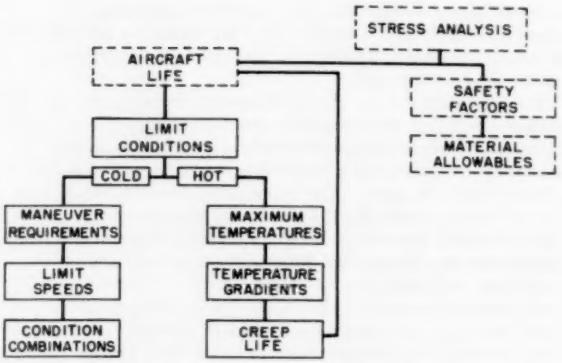

FIG. 2 DESIGN-CONDITION PARAMETERS

factors; and (*b*) the values and relationship of the design-condition parameters shown in Fig. 2. It may be possible to establish safety factors which are generally applicable to all heated aircraft, but unfortunately, too great a variety of condition-combination possibilities exist relative to item (*b*) to hope to establish specific criteria for all types. Eventually, however, our structural-design specifications should provide a framework and general rules for formulating criteria for two broad classes of aircraft; namely (*a*) those aircraft with a broad operating regime similar to present-day aircraft; and (*b*) vehicles with a closely restricted preprogrammed trajectory, in which the pilot (if one is aboard) has virtually no control during the critical regions of flight operations.

(*b*) *Factor-of-Safety Considerations.* As indicated previously, the limit-load concept is the most rational method of proceeding with a structural design where weight is a vital parameter. With the vast increase in design-condition combinations associated with heated aircraft structures, this fact becomes further emphasized. Unless careful rational analysis is made of each of the key elements of the thermal environment, the weight cost to achieve safe structures could easily become prohibitive, and even the proper placing of such weight to achieve a higher strength level would be uncertain. This is true to such an extent that even the use of our well-established—but arbitrary—ultimate factor of safety of 1.5 is questionable both in how to apply it, and in achieving an appreciable increase in safety. It is therefore considered logical to design heated aircraft exclusively for satisfactory operation at limit thermal-and-load combination conditions established with essentially the same degree of conservatism used presently in formulating limit-load conditions. On the other hand, thermal characteristics display large changes with small variations of conditions, and therefore it is particularly necessary to use conservatism in thermal calculations, associated assumptions, and in material allowables at elevated temperatures. So numerous are the possible variations in the assumptions (because of the very nature of the physical properties involved), that the use of any one arbitrary factor of safety becomes essentially meaningless and might only serve to reduce the care exercised in conservatively choosing basic physical characteristics.

In this connection it should be remembered that over and above the ultimate factor of safety a number of other factors are in current use for design of conventional aircraft. A margin is normally required between the limit design speed and the speed at which flutter or divergence occurs (usually taken as 1.15). Bearing, fitting, and casting factors are often employed by the designer in analysis of those structural elements. Stress-concentration factors are also in common use. All of these are like-

wise important in designing elements for heated structures. In addition, however, other factors concerned with thermal phenomena will probably evolve for use in providing local design conservatisms in the affected structural elements. These may be used as individual parameter safety factors to cover inaccuracies in boundary-layer temperature analyses, heat-transfer coefficient, stress allowables at elevated temperatures, creep-allowable data, and thermal-stress analyses. If the 1.5 ultimate factor of safety is discarded as recommended, a new "buckling factor" of 1.25 times limit load is recommended as a safety factor for structural components designed for instability rather than yield failures.

Should it be considered desirable to impose a general ignorance factor on heated aircraft design—with the attendant loss-of-performance penalty—it is considered more rational to provide this at the design yield level. The 1.15 yield factor of safety of MIL-A-8629 (4), by which all limit loads are increased to obtain the design yield load, might accordingly be desirable and not impose an unrealistically high penalty. Such a factor would have the rational design purpose of providing a theoretically true and usable buffer or safety region between an intended maximum operating condition and the design strength level. It would likewise provide a region wherein experimental flight testing to fully demonstrate placarded operating limits could trespass with at least analytical assurance of accomplishing safe flight.

The foregoing discussion of safety factor is concerned only with the broad general aspects of this important element of structural criteria. Detailed, numerical-value consideration of safety factors to cover the individual parameters or analyses is beyond the scope of this paper.

(*c*) *Maximum Load-and-Temperature Combinations.* The selection of combinations of load-and-temperature conditions must be based upon examination of one or more mission profiles or flight trajectories for the particular aircraft. It can perhaps be shown that the most severe temperature conditions occur relatively infrequently, and for such conditions a very moderate load factor can be assumed to be required. Just as with aircraft gust loads, which are assumed imposed only on 1 *g* level-flight conditions, it might be reasonable to require design for maximum temperatures at, say, only a 2 *g* "sustained" maneuver for a 7 *g* fighter. Since exposed surfaces experience elevated temperatures as a function of angle of attack as well as Mach number and other parameters, we might therefore calculate maximum temperatures at angles of attack corresponding to maneuvers of 1 ± 1 *g* sustained for, say, 10 sec. At these calculated maximum temperatures we might impose the maximum limit airloads, assuming this to be applied for an insignificant time as far as temperature is concerned (representing, for example, a short period gust-load application).

A typical Mach number-altitude operating diagram might then appear as shown in Fig. 3. Here is presented a hypothetical design altitude and speed envelope for a 5 *g* airplane, and superimposed upon it are analytically determined permissible *g*-lines based on a single maximum temperature developed at a critical area on the airplane as a result of the indicated h, **M**, and α held for some specific permissible time. By this means the design temperature-and-load combinations are defined, and at the same time the pilot is given an indication of sustained-maneuver operating limits induced by the elevated temperatures.

In the case of vehicles which are operated over specific flight trajectories, a precise determination of critical load-and-temperature condition combinations is in order. For such aircraft the conventional *V*-*g* and **M**-*h* diagrams—which provide envelopes of operating regimes—must give way to time versus load factor (*t*-*n*) diagrams. Associated with these there must be

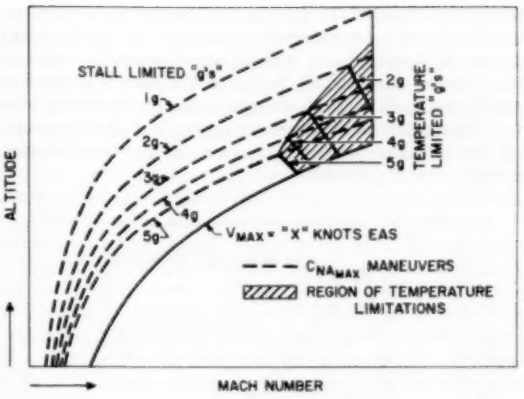

FIG. 3 MACH NUMBER, ALTITUDE, AND PERMISSIBLE ACCELERATION

time histories of Mach number, altitude, GW, q, design gust load, programmed load factor, transient-correction load factor, and prime-structure temperatures. Such a diagram for a programmed hypothetical rocket is illustrated in Fig. 4. Here again we would assume the maximum gust load to be imposed in combination only with the programmed-trajectory maneuver; and likewise, the transient-correction load factor is imposed on

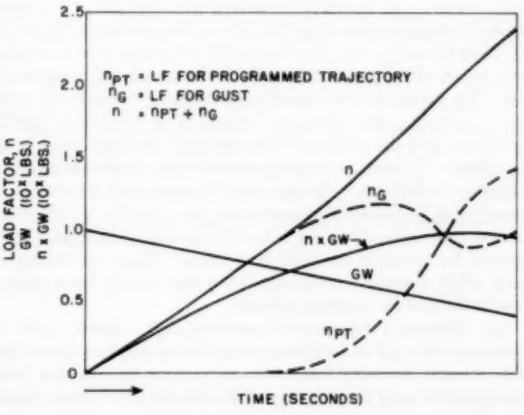

FIG. 4 LOAD FACTOR AND GW VERSUS TIME

the programmed-trajectory maneuver with no gust acting. Both the gust and the transient-correction maneuver have negligible effect upon structural temperatures, and hence design temperatures are calculated for the programmed trajectory. To provide for further conservatism, two or more design *t*-*n* and associated diagrams could be established, thereby again defining an envelope of operating regimes within which the flight trajectories for the vehicle might be established.

(*d*) *Thermal-Gradient and Load Combinations.* To a great extent, the combinations of externally applied loads and thermal gradients in the structure are determined by the criteria defined in the preceding section. Type of structure, insulation, and/or cooling may partially or totally eliminate thermal gradients, and hence this parameter cannot be defined realistically until a proposed design is determined. On the other hand, it should be well understood that the precise maximum temperature conditions may not be the most critical particularly from a permissible-

deformation standpoint. Furthermore, arbitrary assumption of superposition of maximum thermal gradient upon maximum temperature in design of any element would almost always be an unduly severe conservatism, from a peak stress and minimum allowable standpoint. It therefore remains for the initial stages of a design analysis to determine appropriate thermal-gradient and load combinations, based upon temperature-time histories of representative flight plans.

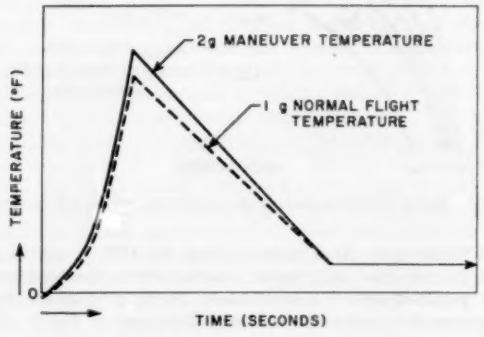

FIG. 5 TEMPERATURE VERSUS TIME AT TYPICAL STATION

In Fig. 5 is shown a typical design temperature-time history at one station on an aircraft. It is seen that the dashed line represents the temperatures experienced in a representative flight trajectory, while the solid line represents the temperatures expected as a result of a 2 g maneuver held for some selected time, say, 10 sec. By comparison of curves such as these, for adjacent structural elements, the time of occurrence of maximum thermal gradients and the concurrent design load condition may be determined. If such a loading-and-thermal gradient condition becomes unrealistically severe, either from a load or deformation standpoint, permissible maneuvering load and/or speed criteria would then be scrutinized carefully during preliminary design phases for possible downward revision. These conditions not only affect thermal-stress analysis but also provide basic data for insulation and/or cooling analyses.

(*e*) *Elevated-Temperature Operating Life.* Apart from the transient changes in temperature gradients and associated thermal stresses resulting from time at various temperature levels, the totals of such times have a direct effect upon material allowables due to creep. If we consider a simple case, where a structural element is loaded in the same manner every time elevated temperatures occur, it is evident that after some point the structure is no longer serviceable because of the permanent sets accumulated which disturb aerodynamic characteristics. For such a structure, therefore, we can establish (*a*) a temperature versus time-duration spectrum representing a typical flight; (*b*) average load experienced at each of the temperature and time values; (*c*) required number of such flights; and (*d*) permissible total deformation which may occur in that structure. When all of the foregoing are known the element cross-section area can then be determined either for the limit load in the cold condition, or for the permissible accumulated creep deformation.

Such a task as is outlined in the foregoing, when multiplied by the vast number of structural elements involved and complicated by stress concentrations and redundancies, becomes a virtually impossible task. Furthermore, most elements are not just subjected to one-direction loadings—load reversals enter into the picture. For example, the rudder-and-fin loads can be expected to occur equally to the right and to the left. It accordingly becomes evident that if possible some large—but conservative—simplification is mandatory at least for preliminary and initial-design-stage analyses. One such an approach is defined by the following criteria:

1 The design life of the aircraft shall be X number of flights, during which Y number of total hours at maximum temperature and limit load at that temperature are experienced (the Y can be broken into two parts; namely, a small number at maximum temperature, and a large number at a lower, sustained elevated temperature).

2 For the maximum-severity temperature-and-load conditions, the design allowable shall be that which corresponds with Z per cent permanent set for the applicable load(s) and temperature(s) held for the time specified in item 1.

3 Aeroelastic and deflection analyses, performed to demonstrate adequate rigidity, shall include both deformations due to thermal stresses and permanent creep deformations equivalent to those calculated to exist at the end of the design life specified in item 1 based on the criteria in item 2.

It can be seen from the foregoing that varying degrees of conservatism can be introduced in the selection of Y and Z. If Z is made 0.2 per cent, the creep criterion is as conservative as our present room-temperature yield criterion, and can be considered in a similar way. On the other hand it might be possible to show that Z can be 0.5 per cent for most designs without causing severe hardship; if so, the penalty introduced by "life" and "creep" is appreciably reduced.

Qualifications to the foregoing rough-and-ready criteria can be made by "rational analysis" where it is noted that the conservatism and cost of such simplified criteria are too severe. On the other hand the obvious advantages of permitting a structural design to proceed without total dependence upon a complex rigidity and deflection analysis are too great to be dismissed for the majority of cases. With the suggested criterion a stress analysis and structural design may proceed, as soon as the criteria have been assumed and the temperature levels calculated.

It should be noted here that if the arbitrary ultimate factor of safety is not discarded, an appreciable obstacle to design exists owing to lack of allowable data. In order to follow conventional practice in the application of the ultimate factor of safety, it would be necessary to obtain a new group of creep data. By rights, we would have to measure creep at various temperatures, per cent elongations, and times as before, but in addition at each of the combinations shown we would require a short-time load determination of ultimate strength. To eliminate this we might use directly the failing-load versus time curve, but this might be a very severe governing criterion.

CONCLUSIONS

A structural design "philosophy" for heated aircraft structures has been outlined. It is our belief, however, that the greatest progress in this direction will be achieved concurrently with development of actual hardware designs, when contractual criteria requirements are crystallized into model specifications. Our conclusions at this time are summarized as follows:

1 Structural criteria for aircraft consist of an interrelated framework of safety factors, limit-design conditions, aircraft-life assumptions, design-material allowables, qualification tests, and quality-inspection procedures. The assumptions utilized in the past for the first three of these are considerably affected by thermal conditions; for the last three, data and techniques change, but the criteria philosophy remains essentially the same. The present criteria problem, therefore, is to define new design assumptions and relationships for safety factors, limit condi-

tions, and aircraft life which are necessary as a result of aerodynamic heating effects.

2 The limit-condition basis for formulating structural criteria presently used in aircraft design is considered to be especially realistic and usable in elevated-temperature design. Limit conditions presently in use must be extended and altered to include consideration of temperature and time parameters. The following axiom (which has been tacitly accepted for many years) must be applied in establishing detailed limit conditions for each new design:

Sustained operating conditions may have superimposed upon them maximum-expected severity conditions, but two or more distinct types of maximum-severity conditions are not considered to be combined except in unusual design situations where such occurrences are reasonably probable.

Representative limit-condition combinations are described in items (*c*) and (*d*) of the preceding section.

3 The "normal-temperature" structure ultimate factor of safety of 1.5 should be discarded, because the way to apply it and the additional safety it provides are both exceedingly dubious. Conservatisms in each of the physical characteristics and design calculations must, on the other hand, be introduced in a complementary manner in the analyses, and substantiated in tests. This may be accomplished by use of individual parameter safety factors. If an over-all safety factor is desired, it is recommended that it be introduced at the yield level by making design yield load equal to 1.15 times the limit load (with all other parameters held constant); such a factor provides a measurable and comprehensible safety margin above a limit operating condition.

4 Thermal gradients dictate that transient variations must be considered in establishment of limit conditions of load and temperature; creep phenomena dictate that the specifying of a total aircraft life becomes mandatory, and that in turn is a governing parameter in determining elevated-temperature material allowables used in calculating cross-sectional areas. Accordingly, normal-temperature load conditions are analyzed with normal-temperature yield allowables; elevated-temperature load conditions are analyzed with creep allowables based on a selected aircraft life at those loads and temperatures using an arbitrary permissible creep-set. The conservatism of the selected creep-set must be verified analytically by a deflection-combined-with-deformation aeroelastic analysis. A sample creep criterion is presented in (*e*) of the preceding section.

5 Limit-condition combinations for heated aircraft structural designs are many times more numerous than for normal-temperature structures. It is considered impractical to define specific condition combinations now that temperature and time parameters are superimposed upon the conventional load parameters. Load-factor and associated criteria used presently in normal-temperature aircraft design continue to be applicable, however, and provide the basic source of loading conditions for synthesis of heated aircraft criteria. It is recommended that for heated aircraft a general criteria framework and fundamental principles such as are discussed in this paper be emphasized in future criteria specifications, rather than attempt to define specific load-and-temperature values, and condition combinations.

Acknowledgment

For their valuable criticism and suggestions during the preparation of this paper, the author wishes to extend his appreciation to Messrs. L. K. Fero, A. Schnitt, and W. H. Dukes; Dr. M. A. Brull; and other engineers of the Bell Aircraft Structures Section.

BIBLIOGRAPHY

1 Military Specification MIL-S-5700 (USAF), "Structural Criteria, Piloted Airplanes," December 14, 1954.

2 "Factor of Safety and Working Stress," by C. R. Soderberg. Trans. ASME, vol. 52, 1930, part 1, Paper No. APM—52-2, pp. 13–28.

3 "Is the Present Aircraft Structural Factor of Safety Realistic?" by G. N. Mangurian, *Aeronautical Engineering Review*, vol. 13, September, 1954, pp. 63–75.

4 Military Specification MIL-A-8629 (Aer), "Airplane Strength and Rigidity," August 28, 1953.

5 "Airplane Airworthiness," CAA CAR-04a, April 7, 1950.

6 "Structural Design for Aerodynamic Heating," by W. H. Dukes and A. Schnitt, USAF WADC TR-55-305, October, 1955.

7 "Strength of Metal Aircraft Elements," Air Force-Navy-Civil Bulletin ANC-5, March, 1955.

Discussion on Safety-Factor Requirements for Supersonic Aircraft Structures[1]

By G. M. GOLDMAN,[2] STRATFORD, CONN.

This paper deals with the safety-factor aspects of design rather than any discussion of design-criteria conditions. It covers essential items concerning certain present safety-factor aspects, new problems caused by the advent of heated aircraft structures, and the ideas of Air Force engineers as to the procedure necessary to provide adequate safety reserves in the design of new high-speed aircraft.

Discussion of Problems

SINCE a thorough understanding of certain fundamental aspects of structural design is necessary before we attempt to resolve special problems associated with heated aircraft structures, the author will discuss briefly the requirement aspects of our present-type aircraft as they influence the choice of factor of safety.

This subject was ably discussed by Mr. Mangurian of Northrop, in a paper presented before the Institute of the Aeronautical Sciences in June, 1954, and by other members of the industry. Mr. Mangurian has presented a good historical account of the factor-of-safety concept and of its design implications. Since the Air Force is the purchaser of the equipment and naturally has ideas which differ from those of the producer, there are areas of disagreement. Let us briefly run through the major items of the factor-of-safety concept as we know them today.

Table 1 presents in tabular form the points established by Mr. Mangurian in his discussion together with the author's opinion of their present status. These points are chosen because they

TABLE 1 GENERAL DESIGN PROBLEMS

Item	Validity
Allowance for no yielding at limit load	No
Allowance for defects in workmanship	Yes (−)
Allowance for variations in material	Yes
Allowance for design uncertainties	Yes
Aeroelastic	
Fatigue	
Flutter	
Dynamic effects	
Complexity	
Loading spectra	
Allowance for exceeding design maneuver limit	Yes

adequately cover the field and are not being discussed in any sense as a form of rebuttal.

Yield to Ultimate Stress Ratio. In general, whatever influence the ratio of yield to ultimate stress had upon the original choice of factor of safety no longer should be considered. While there are definite indications that the usage of aluminum alloys will continue, and that a portion of this will be in the 24S-T (user), die-forging, and casting materials, the trend is toward material with a higher yield to ultimate ratio.

Workmanship. There has been considerable improvement over the years in the workmanship of production aircraft. While there still remain some occasional cases of bad workmanship, the probability of such faults is rather low. Yet, this can be truly said only in connection with the aluminum alloys and current aircraft steels. Can we safely assume that we will not have a repetition of this item as we go to new fabrication methods, new super-tough alloys, new bonded honeycomb material, or such new materials as titanium carbide or Inconel? It seems rather illogical to think that we will never again have poor workmanship during periods of introduction of new materials or new fabrication techniques. It is logical, however, to expect a smaller degree of trouble as our over-all production knowledge increases.

Quality of Materials. Again, there has been a marked improvement in the quality of materials. However, new production requirements, extensive use of subcontractors, and use of new materials have created as many new problems as have been solved. We do not hesitate to use the B-values for material allowables from the ANC-5 Bulletin because of this improvement in materials. Yet, not so long ago, West Coast prime contractors were receiving 24S-T (user) parts from local heat-treating sources that were found to have portions below minimum. In certain cases, only 65 per cent of the parts checked met the minimum guaranteed strength values. The figure on B-values would have been even lower; however, this happens to be an area where B-values are not used. This condition eventually resulted in a reduction of the allowable strength values for the material because of the inability to obtain proper processing equipment.

As we broaden our production base, we find more areas wherein the present high aircraft standards are not met. The introduction of new materials with coincident new processes of manufacture or fabrication also introduces areas for variation. Parts cut cross grain from extrusions were used on one airplane with no apparent reluctance; yet later on, when fatigue failures occurred, this procedure was discarded as being too dangerous. The titanium-hydrogen contamination problem, which caused considerable trouble on one airplane recently, is an excellent example of the problems with new materials. The condition was not due to any particular failure other than use of a new and relatively untried material. The existence of the 1.5 safety factor played a large part in the decision by Air Force structures personnel to allow the continued flight of the airplane in question with parts of doubtful strength. It is not believed to be at all safe or wise to assume that we do not need a factor to allow for variation in usable material properties. In fact, we may need an allowance greater than the present increment to permit the desired rapid excursions into flight regimes which will require new and untried materials.

Design Requirements. There have been consistent efforts within the WADC in recent years to decrease the number of design requirements and to rationalize their severity. Perhaps the most important lesson derived therefrom is the realization of how little we really know of the design requirements for the future. We have learned that as we cut down on one requirement we must very carefully examine and perhaps even increase others. The over-all requirement of the past apparently worked well as long as it was wrapped up in one package, but as we single out one

[1] This paper was prepared while the author was Chief, Design Criteria Section, Structures Branch, Aircraft Laboratory, WADC, Wright-Patterson Air Force Base, Ohio.

[2] Head, Operations Analysis Section, Advanced Development Division, AVCO Manufacturing Corporation.

Contributed by the Aviation Division and presented at the Aviation Division Conference, Los Angeles, Calif., March 14–16, 1956, of The American Society of Mechanical Engineers.

Note: Statements and opinions advanced in papers are to be understood as individual expressions of their authors and not those of the Society. Manuscript received at ASME Headquarters, January 20, 1956. Paper No. 56—AV-18.

particular area for refinement, we find that we have introduced new difficulties into other areas. Thus we must be very wary of saying that we have overcome certain design uncertainties and have the situation in hand. Actually, we have; but it is certain we will be faced with others just as important in the future.

The author recalls one item several years ago when prominent industry engineers stated that the old 5-deg yaw condition at dive speed was much too severe, and would never be realized in the future. The author agreed with them but now finds we were all wrong for we have had cases of yaw far beyond the 5-deg value at speeds well above the old dive speeds. It is important to realize that it did happen, but even more so to acknowledge that it happened in spite of our decision that it never would. The fact that it was caused by some unforeseen stability phenomenon does not excuse us but rather should make us be more careful in the future.

While we have conquered some of the problem areas listed, others have not been solved, and it is certain that still others will be added to the list in the future. Since the design of the airframe cannot wait until all of these design problems are resolved, certain safety allowances must be made.

Design-Limit Load Factor. The last item is important or not, depending on one's field of endeavor. It is safe to say that there have been very few cases where transport or very heavy-type-bomber classes have consistently exceeded their design limits. It is likewise an established fact that trainers and fighters exceed the design limits quite frequently. Therefore either an allowance must be provided for this overshoot or the design-limit load factors must be established sufficiently high to prevent it. The author will limit further discussion on this lengthy subject to only a few brief remarks.

Allowance. It is reasonable under the present design system that the amount of allowance should vary for different types of airplanes. Whether it should be a fixed load-factor increment or a percentage value is the point that must be determined.

Limit-Design Concept. Under the present regime of training and operation of certain types of aircraft, any load-factor value picked as a design limit could be exceeded. It is conceivable, however, that with the proper training or with g limiting devices, a pilot could be taught to stay within a set value and thus the factor-of-safety increment could be reduced or eliminated. This chosen value would, of course, have to provide a fair margin above the mission requirements in order to allow for unexpected cases. The author has been working on such a concept which he calls the "limit-design concept." To date, he finds the limit load-factor values required are so high that very few would accept them if they were ever published. This is, however, a fruitful area for further study.

Design Maneuver Limit. The choice of design maneuver limit is a difficult one. It can be one value for a combat mission of one type; it must be a different value for a secondary mission and must be still another for use in training activities. Until such time as conditions permit the use of an aircraft for only that case for which it was designed, there must be a margin for this variety of use. While we may not always agree with some of the uses assigned to a particular aircraft, the condition does occur. As long as it occurs, regardless of the reasons, it must be considered. We, as the purchaser's engineering staff, cannot hide our heads in the sand and say we will not design for it, for such attitude leads only to a high repair rate. Therefore certain types will require a sizable allowance for conductance of flight regimes which are often more severe than those for the primary design purpose.

Allowance for Future Requirements. It is unfortunate that the tactics and armament people cannot predict in advance the way they will fight the next war and just exactly how their proposed equipment will function. As a result, it is quite possible that certain special fighters may be overdesigned for the primary mission. While this is regrettable and may cause a design penalty, it certainly is not logical to expect the structural designer to reduce his strength to be equivalent to a fire-control system not yet in existence, and it would be of little value in the end, for our tactical people will find some configuration that will use up all the available strength in the airframe. Therefore it appears dangerous to set an arbitrary maneuver-limit value or to reduce a factor of safety when it goes against the grain of all accumulated statistics.

Thus at present, an allowance for exceeding design maneuver limit must be provided.

Problems of the Hot Plane

The foregoing items have been mentioned because they are of importance to the airplane design, whether it be a "cold" or "hot" airplane. To these must be added the specific problems which are engendered from the aerodynamic heating associated with high-speed flight. As they are introduced, the physical area in which they fall, and therefore the area requiring design allowance, will be outlined. After summation, an attempt will be made to derive one rational procedure which will provide adequately for all items.

Under present cold conditions, it appears necessary to go to a load-time spectrum concept in order to cover both static and repeated load problems. For the future airplane, it appears necessary to stipulate a design criterion in terms of a three-dimensional concept, namely, the load-time-temperature spectrum. This immediately introduces at least three areas for design allowances; load factor for the operational aspect of loads, time for the duration of load at temperature, and temperature itself for errors in speed or trajectory calculations. No one chosen allowance will cover all these phases adequately. There must be a strength reserve, time reserve, and heat reserve.

This is an appropriate place to introduce a rather important matter for our next generation of airplanes. The answer to the item should logically come from the Air Force itself. Yet, to date, the matter has not been resolved satisfactorily. The point put simply is—do we use an insulated type of structure, an artificially cooled type, or a mass-heat-sink type? Undoubtedly, there is a good bit to be said for either type from the design standpoint. At the same time, the user's practical standpoint must be considered.

The insulated type of structure is intended to protect specifically the load-carrying members from the heat. As such it restricts the structure to essentially one load level for a given weight. It may vary slightly with speed, but the capability remains essentially constant. The artificially cooled type, either evaporation cooling or mechanical refrigeration system, likewise is essentially a constant-strength-level airplane.

On the other hand, the mass-sink-type structure represents a very flexible aircraft from a tactical standpoint, with an almost unlimited usage. It can become a low-factored bomber defense airplane at very high speeds, an air-superiority weapon at moderate speeds, or a high-factored fighter bomber at relatively low speeds. All this flexibility is achieved by the control of speed, hence control of temperature and hence control of load capability at a given constant weight. While the choice of design is quite important to the tactical user, it is doubly important to the structural designer, for it defines the problem areas facing him. The tolerances or design reserves would be considerably different in the three cases. Thus the choice of a particular type of structure will influence a portion of the "margin of safety" designed into the airplane.

Structural Temperatures. Next on the list is the question of

the structural temperatures themselves. As usual, each designer has his particularly favorite way of calculating adiabatic wall temperature from the speed and boundary-layer conditions. Use of various recovery and heat-transfer factors influences the value of skin temperature. Further, much is to be learned about the effect of structural cold or hot spots on the boundary layer, molecular dissociation, and other similar items required for determining the heat transfer. Here again, the choice of an insulated or heat-sink-type structure affects the heat-transfer characteristics. So much is yet unknown about this general temperature problem that an allowance for mistakes or unknowns is a must.

Heat conductance through continuous members, transfer to other members across joints or gaps, or radiation to internal members are the primary ways in which the heat corresponding to the structural temperature can be carried away from the skin contact surface. Predictions of conductance and radiation are probably quite well in line, although certain refinements undoubtedly will be required. We cannot say as much for heat transfer through joints where surface finish of the faying surface, anodizing, paint primer, trapped air, tank sealant, and even faying-surface pressures due to rivets or bolt installation can affect the results materially. Therefore a finite allowance must be made for errors in heat transfer and thus temperature and temperature gradients within the members.

The thermal stresses occurring in the structural members as a result of the temperature gradient in the member or the differential expansions caused by the various heat levels of adjacent members cannot be calculated with the required accuracy at this time owing to the many unknowns facing resolution. The prime variable in this case is again the temperature since stress calculations are probably more precise than the heat calculation. Some allowance must be made in this area until such time as our capability in the field of thermal analysis improves.

Thermal and Flight Load Stresses. The combination of thermal stresses with flight load stresses presents a rather involved, although not necessarily difficult, problem. Phasing of the loads with the temperature will depend on the thermal lag of the system and the operational use of the aircraft. This will require a rather lengthy analysis of the potential flight profiles in order to determine all possible critical combinations. It is entirely possible that a particular member could be under a tension stress from flight conditions, while at the same time under a compression stress from thermal effects. Of course it would be unsound to apply a factor to a resultant stress. In fact, any value so derived conceivably could be less than the flight load stress at a speed where temperature effects were virtually nonexistent. This indicates need for application of any required factor prior to combination of stresses and a knowledge of the conditions of combination. Again, the structure—be it heat, sink, or insulated type—will influence any factors chosen.

Properties of Materials. The behavior of material properties as a function of exposure to temperature is a subject that has been and is being studied at great length. Although there is considerable knowledge on the subject, difficulty in its use can be foreseen. The data now published concern values for continuous heating and loading but also are considered applicable to intermittent heating when total time at temperature is the same. Actual aircraft use does not fit this classical case. The exposure of materials will consist of a total integration of many short-time exposures of various time, temperature, and load levels. Therefore considerable judgment must be used in deriving a finite value from combination of these variable conditions in order to enter the presently known property curves and select an allowable stress level. Since this judgment is made by a human, some tolerance must be allowed.

Likewise, then, we become concerned over the prediction of creep effects of a composite structure, fatigue of materials at elevated temperatures, and such questions as: Does creep outmode fatigue and make it no longer of any concern in a heated design, or, does metal fatigue increase the creep rate? Any of the questions of this nature are dependent on variations in time, temperature, and stress.

There are additional problems such as thermal buckling of plates and skin areas between supports. This is of considerable concern, for an acceptable level of thermal buckling must be determined. This is necessary from a consideration of the allowable stress and the aerodynamic performance loss due to drag increases. Some tolerance must be provided in this area.

Approach to Safety Allowance

Up to this point we have discussed most, if not all, of the important points of concern in the structural analysis. Table 2 gives a summary of the items considered, and the design parameters or variables involved in each case. The next step then is to determine a sound method of providing for the required safety allowance. It is not necessarily true that all of the items listed

TABLE 2 DESIGN PROBLEMS INCLUDING TEMPERATURE EFFECTS

Item	Area for allowance
No yielding at limit load	.....
Defects in workmanship	Stress
Variation in material	Stress
Design uncertainties:	
Aeroelastic	Deflections introducing loads
Fatigue	Number of cycles or variation of load level
Flutter	Stiffness
Dynamic effects	Deflections introducing loads
Complexity	Stress
Loading spectra	Load factor
Exceeding design maneuver limit	Load factor
Elevated-temperature aspects of loading spectra	Time at temperature Temperature (errors in speed or trajectory)
Type of heat sink or insulated structure	Not definable—variable effects
Structural heating calculations	Temperature
Heat conductance or transfer through joints	Temperature
Thermal stresses from temperature gradients or thermal expansions	Temperature
Combination of flight and thermal stresses	Load factor
Decay in material properties	Stress
Creep	Time-stress-temperature
Thermal buckling	Time-stress-temperature

will require an allowance contained in a safety factor as such. It is quite possible that certain of these areas can be covered by conservatism and design procedures in routine stress analysis. Since it is only logical to avoid use of an arbitrary safety factor wherever possible, considerable efforts must be made to filter out those items which can be covered adequately in analysis.

This, in essence, brings us up to date. A procedure for providing the necessary safety allowance has not yet been derived. However, advances have been made and considerable resolution of thoughts has occurred. A summary of the items in Table 2 will show the following:

Stress	6
Deflections (introducing loads)	2
Stiffness (flutter)	1
Load factor	3
Time	3
Temperature	6
Speed	1

Regarding item 3 of the tabulation, there is already in existence in flutter and divergence requirements a safe margin of 1.15 on maximum speed. Therefore this item has not and will not in the future be contained in any values generated in structural criteria specifications. If other items are found to be covered by

other existing or planned requirements, they likewise will not be duplicated.

It will be agreed that no one arbitrary selected value will cover properly the remaining cases and their possible critical combinations. Thus it can be said that the present system of factor-of-safety stipulation is inadequate for future aircraft. It appears then, that the only acceptable procedure is a return to the older method of applying margins to the individual items, with this margin carried through the calculations. The easiest way would be to choose an arbitrary value, say, X per cent, and apply it at the initial level of occurrence of the proper parameters. However this is not a step which can be taken without considerably more study since it is quite possible that these margins would compound to unrealistically high values. It is likewise necessary to determine that the resulting design level is one which is within the limit of usage of the aircraft that is physically possible, and not one which represents an impossible flight condition or unachievable stress, flight duration, or deformation condition. Thus it will be necessary to determine the set of trial margins, follow them through a design problem and determine the degree to which they compound or conflict. This involves appreciable work not possible prior to the date of this presentation.

At present we can decide only the type of safety procedure believed necessary, but cannot yet assign values to its individual components. The Air Force earnestly solicits suggestions on this proposed procedure or on any others which may appear more appropriate. Until such procedure can be finally derived, however, we must rely on our present procedure with whatever actual safety it provides.

Some Structural Penalties Associated With Thermal Flight

By J. W. MAR[1] and L. A. SCHMIT,[2] CAMBRIDGE, MASS.

In designing aircraft for high-speed flight, the structural designer is confronted by many factors which tend to increase the weight. As Prof. R. L. Bisplinghoff[3] points out, the static strength of the structure still appears to be the most important design requirement for high-speed, manned, fighter-type aircraft of the foreseeable future. In subsonic aircraft, the margin of static strength is measured by comparing the stresses caused by maneuvering with the permissible stresses which the material can carry. In high-speed supersonic aircraft, the static strength must take into account not only the thermal stresses but also the degradation in the mechanical properties of the material which accompany elevated temperatures. This paper investigates the short-time static strength of the structure as it is subjected to the combined action of maneuvering loads and internal heat flow.

Nomenclature

The following nomenclature is used in the paper:

C_p = specific-heat capacity, Btu/lb deg R

h = heat-transfer coefficient, boundary layer to skin, Btu/sq ft-sec-deg R

h_0 = initial value of heat-transfer coefficient, boundary layer to skin, Btu/sq ft-sec-deg R

h_r = contact joint heat-transfer coefficient, Btu/sq ft-sec-deg R

k_1 = reduction in E at elevated temperature

k_2 = reduction in F_{cy} at elevated temperature

k_3 = reduction in F_{tu} at elevated temperature

k_4 = reduction in F_{su} at elevated temperature

l_r = effective joint-contact length, ft

$2l_s$ = length of skin, ft

l_w = length of web, ft

t = time, sec

$\bar{t} = \dfrac{\kappa_s}{l_s^2}\, t$ = nondimensional time

$\omega_1, \omega_2, \omega_3$ = per cent increases in skin material

$\omega_4, \omega_5, \omega_6$ = per cent increases in web material

x = co-ordinate location along skin, ft

$\bar{x} = \dfrac{x}{l_s}$ = nondimensional co-ordinate location along skin

y = co-ordinate location along web, ft

$\bar{y} = \dfrac{y}{l_w}$ = nondimensional co-ordinate location along web

E = modulus of elasticity, psi

F_{cy} = compressive yield stress, psi

F_{su} = ultimate shear stress, psi

F_{tu} = ultimate tensile stress, psi

K = thermal conductivity, Btu/ft-sec-deg R

$P = \dfrac{(h_r l_r) l_r}{2\delta_s K_s}$ = a nondimensional parameter

T_{amb} = ambient or undisturbed free-stream temperature, deg R

T_0 = uniform initial temperature, deg R

T_{aw} = adiabatic wall temperature, deg R

$(T_{aw})_e$ = extreme value of T_{aw} during flight history, deg R

T_s = skin temperature, deg R

$\bar{T}_s = \dfrac{(T_s - T_0)}{[(T_{aw})_e - T_0]}$ = nondimensional skin temperature

T_w = web temperature, deg R

$\bar{T}_w = \dfrac{(T_w - T_0)}{[(T_{aw})_e - T_0]}$ = nondimensional web temperature

$\Omega = \dfrac{[(T_{aw})_e - T_{aw}]}{[(T_{aw})_e - T_0]}$ = complementary nondimensional adiabatic wall temperature

$\psi = \dfrac{h}{h_0}$ = nondimensional heat-transfer coefficient

α = coefficient of thermal expansion, in/in-deg F

$\beta = \dfrac{K_s \delta_s}{h_0 l_s^2}$ = a nondimensional parameter

Δ = increment

δ_s = skin thickness, ft

δ_w = web thickness, ft

$\theta = \dfrac{(h_r l_r) l_w}{\delta_w K_w}$ = a nondimensional parameter

$\lambda = \dfrac{\kappa_s l_w^2}{\kappa_w l_s^2}$ = a nondimensional parameter

ρ = weight density, pcf

σ = stress, psi

σ_{cr} = buckling stress, psi

σ^T = thermal stress, psi

$\phi_s = \dfrac{[(T_{aw})_e - T_s]}{[(T_{aw})_e - T_0]}$ = complementary nondimensional skin temperature

$\phi_w = \dfrac{[(T_{aw})_e - T_w]}{[(T_{aw})_e - T_0]}$ = complementary nondimensional web temperature

Subscripts

amb = ambient

aw = temperature in flow at the adiabatic wall

0 = initially, that is at $t = 0$

s = of the skin or skin material

w = of the web or web material

---

[1] Assistant Professor, Department of Aeronautical Engineering, Massachusetts Institute of Technology. Assoc. Mem. ASME.

[2] Research Engineer, Aeroelastic and Structures Research Laboratory, Department of Aeronautical Engineering, Massachusetts Institute of Technology.

[3] "Some Structural and Aeroelastic Considerations of High-Speed Flight," by R. L. Bisplinghoff, the Nineteenth Wright Brothers Lecture, *Journal of the Aeronautical Sciences*, vol. 23, April, 1956, pp. 289–321.

Contributed by the Aviation Division and presented at the Aviation Conference, Los Angeles, Calif., March 14–16, 1956, of The American Society of Mechanical Engineers.

Note: Statements and opinions advanced in papers are to be understood as individual expressions of their authors and not those of the Society. Manuscript received at ASME Headquarters, January 18, 1956. Paper No. 56—AV-9.

Introduction

The structural design of aircraft takes on an added dimension when thermal flight is encountered. For the conventional (circa 1950–1955) aircraft, the strength of the structure is governed by the familiar V-n diagram. This diagram which has the benefit of many years of gradual evolution concisely defines the maneuvering loads which the aircraft will experience. The factors of safety which are now in usage are also closely related to the V-n diagram. With the advent of high-speed flight, the aircraft structure in addition to carrying the flight loads must also absorb great quantities of thermal energy.

It is apparent, therefore, that there need to be formulated additional design conditions which will augment the present V-n diagram. Two questions which must be answered are:

1 What types of flight missions will impose the most severe aerodynamic heating effects on the structure?

2 How are these effects to be superimposed with the familiar maneuvering loads?

From the customer's point of view, it would appear that restrictions on the use of the aircraft for structural reasons would be difficult to accept. On the other hand, there is the problem of the additional weight required to sustain the thermal loads. The formulation of thermal-structural-design criteria, the use of the aircraft, and the choice of a safety factor all hinge on the weight of the airframe.

The effects of the resulting increases in temperature encompass a field ranging from the well-known deterioration of the mechanical properties of the material to the less known phenomenon of creep. New modes of structural behavior can be expected.

Thermal stresses are induced by temperature gradients as the heat energy generated in the boundary layer is transferred to the interior of the structure. The magnitude of the thermal stresses depends upon the severity of the temperature gradients. If the aircraft changes its speed and altitude so that changes in the boundary layer occur in a relatively gradual manner, then small thermal stresses can be expected. If the converse is true, then large thermal stresses can be expected. Consequently, it is the transient nature of any given flight mission which accentuates the thermal effects on the static strength. The structural designer must therefore investigate those flight missions which are the most highly transient. Whether or not these are used as the basis for design depends upon the weight penalties which must be paid as measured against the decrease in flight-mission capabilities.

Various flight missions of an extremely transient character have been formulated. The aircraft structure is represented by various box beams, and these have been flown, figuratively speaking, through the various missions. Approximations have been made to simplify the heat-transfer equations. Aluminum 2024 S-T, titanium Ti-150A, and Inconel X are the materials which are considered. Transient temperature and stress distributions have been obtained. With these data, the structural penalties which accompany thermal flight have been assessed.

The additional problem in the design of an airplane which entails a tremendous amount of computation is the calculation of the temperature distribution. Even the simplest temperature-distribution problem results in equations which cannot generally be solved in closed form. Under such circumstances the use of numerical procedures is dictated. Without the aid of a high-speed digital computer, the solutions would require an almost prohibitive number of man-hours. The M.I.T. Whirlwind I digital computer has been used for the calculations in this paper.

The Flight Mission

The two main parameters which define the convective heat transfer to an airplane are the adiabatic wall temperature, T_{aw}, and the heat-transfer coefficient h. These are dependent upon the Mach number $\mathbf{M}$, and altitude A, of the aircraft once certain assumptions are made.[4,5] For a given Mach number, the adiabatic wall temperature and the heat-transfer coefficient increase with decreasing altitude. An airplane which is initially cruising at high altitudes will experience the most severe combination of adiabatic wall temperature and heat-transfer coefficient as it descends rapidly while at the same time it is increasing its Mach number. By trading altitude for speed the airplane is able to increase its forward speed at substantially higher acceleration than is possible in level flight.

The dive from altitude will raise the surface temperature of the airplane very rapidly, relative to the internal structure. Thus, the skin will be subjected to thermal compression while the webs will be under thermal tension. A converse situation can exist. If an airplane has been cruising for a long period of time at a high Mach number and then very rapidly decelerates, the surface of the airplane will experience cooling. This induces tension stresses in the skin and compressive stresses in the webs. Decelerations in level flight, which are larger in magnitude than the forward accelerations, are possible with airplanes of the near future.

Table 1 gives pertinent data for the flight missions which are considered. There are three dive missions and two level-flight deceleration missions. Mission C is a dive from 60,000 to 30,000 ft in 30 sec with a change in Mach number from 1 to 3. Mission D is the same as Mission C except that the changes in altitude and acceleration occur in a period of 60 sec. Missions E and F

[4] "Introduction to the Transfer of Heat and Mass," by E. R. G. Eckert, McGraw-Hill Book Company, Inc., New York, N. Y., 1950.

[5] "Convective Heat Transfer to Structures in Supersonic Flight," by J. A. Quinville and J. D. Revell, Northrop Aircraft, Inc., Hawthorne, Calif., 1954.

TABLE 1 TABULATION OF FLIGHT-HISTORY DATA

Flight mission	Time interval, sec	A, altitude variation, ft	$\mathbf{M}$, Mach number variation	h, heat-transfer coefficient Btu per hr-deg R-ft^2	T_i, deg F	T_∞, deg F
C	$0 \leq t \leq 30$	$60000-1000t$	$1 + \frac{1}{15}t$	$14 + \frac{101}{55}t$		
	$t \geq 30$	30000	3	69	1	601
D	$0 \leq t \leq 60$	$60000-500t$	$1 + \frac{1}{30}t$	$14 + \frac{101}{110}t$		
	$t \geq 60$	30000	3	69	1	601
E	$0 \leq t \leq 30$	30000	$3 - \frac{7}{60}t + \frac{1}{600}t^2$	$73 - t$		
	$t \geq 30$	30000	1	43	601	22
F	$0 \leq t \leq 60$	30000	$3 - \frac{7}{120}t + \frac{1}{2400}t^2$	$73 - \frac{1}{2}t$		
	$t \geq 60$	30000	1	43	601	22
G	$0 \leq t \leq 60$	$60000-500t$	$1 + \frac{25}{60}t$	$14 + \frac{61}{60}$		
	$t \geq 60$	30000	3.5	75	1	837

are the deceleration cases which occur at 30,000 ft with the Mach number changing from 3 to 1 in 30 and 60 sec, respectively. Mission G is the same as D except that the final Mach number is 3.5. All of the flight missions are assumed to continue at the final Mach number and altitude for an indefinite period of time. The airplane is also assumed to be initially at a uniform temperature corresponding to the initial adiabatic wall temperature. This means the airplane structure is initially in a thermally stress-free condition.

The specification of the time history of adiabatic wall temperature is given by the relation[4,5]

$$T_{aw} = \left[1 + r\left(\frac{\gamma - 1}{2}\right) M^2\right] T_{amb} \quad \ldots\ldots\ldots [1]$$

where

r = recovery factor = 0.88 (assumed)

γ = ratio of specific-heat capacities of air = $\frac{C_p}{C_v}$ = 1.4 (assumed constant)

T_{amb} = ambient temperature corresponding to altitude A

As can be seen in Table 1, the time-history of the heat-transfer coefficient is approximated by a straight line. The heat-transfer coefficient is a complicated function of many parameters. Once certain assumptions[4,5] have been made, charts such as those in reference 5 can be made. These reduce the heat-transfer coefficient to a function of the altitude, the Mach number, and the location of the transition point. In these studies, the transition point is assumed fixed, and the chordwise variation of the heat-transfer coefficient has been neglected. Also it has been assumed that the boundary layer is turbulent. With these assumptions Fig. 1 shows the difference between the assumed linear variation and the variation for Missions F and G based on reference 5. In view of the present state of knowledge, these assumptions appear reasonable. However, further investigations probably will need to be conducted.

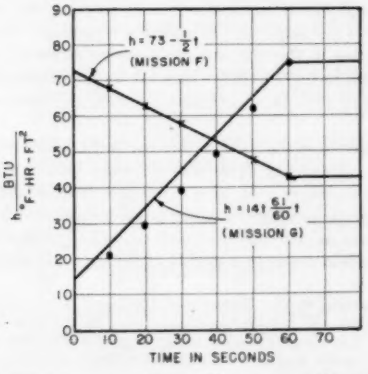

FIG. 1 APPROXIMATION OF TIME HISTORY OF HEAT-TRANSFER-COEFFICIENT VARIATION

THE AIRPLANE STRUCTURE

The wing structure of a high-speed aircraft will in general consist of many cells (Fig. 2).[3] There will be both a structural and a thermal interaction between the cells. It will be necessary for the purposes of this study to neglect both types of interaction. As far as the stress analyses are concerned, the structure can be represented by a simple box, Fig. 3. The temperature calculations are based on a T-section (see Fig. 4), which is composed of a piece of skin for the flange and a web for the stem. A contact

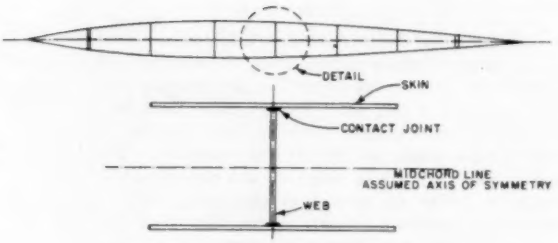

FIG. 2 TYPICAL WING CROSS SECTION

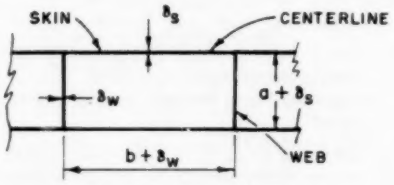

FIG. 3 STRUCTURAL BOX

TABLE 2 DIMENSIONS OF STRUCTURAL BOX

	a, in.	b, in.	δ_s, in.	δ_w, in.
Aluminum I	3.6	7.6	0.4	0.4
Titanium I	2.75	5.75	0.25	0.25
Inconel I	2.33	4.83	0.17	0.17
Aluminum II	3.6	7.8	0.40	0.2
Titanium II	2.75	5.875	0.25	0.125
Inconel II	2.33	4.915	0.17	0.085

NOTE: See Fig. 3.

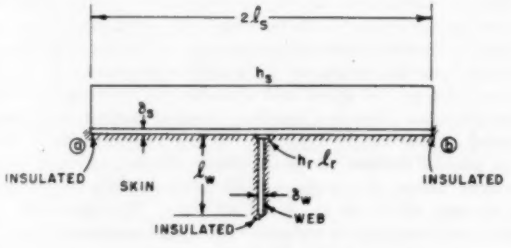

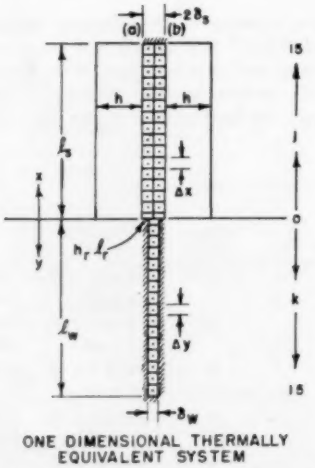

FIG. 4 SCHEMATIC REPRESENTATION OF THE SYSTEM

TABLE 3 T-SECTION MODEL DIMENSIONS, MATERIAL THERMAL PROPERTIES, AND NONDIMENSIONAL PARAMETERS

	K	κ	C_p	ρ	l_s	l_w	δ_s	δ_w	l_r	h_r *	P	β	λ		h_o	β	$E\alpha$
	BTU / ft-hr-°F	ft^2 / hr	BTU / lb	lbs / $(ft)^3$	in	in	in	in	in	BTU / ft^2-hr-°F					BTU / ft^2-hr-°F		lbs / in^2-°F
Aluminum Alloy (2024-T3) Model I	73	2.06	0.205	172.8	3.5	1.9	0.40	0.40	3.0	130	1.948	2.115	0.2947	Accel.	14	2.043	129.3
														Decel.	73	0.3919	
Aluminum Alloy (2024-T3) Model II	73	2.06	0.205	172.8	3.7	1.85	0.40	0.20	2.0	130	1.373	2.745	0.2500	Accel.	14	1.828	129.3
														Decel.	73	0.3507	
Titanium Alloy (Ti-150A) Model I	9	0.243	0.129	286.8	2.625	2.0	0.25	0.25	2.25	130	14.24	21.70	0.5805	Accel.	14	0.2794	80
														Decel.	73	0.0536	
Titanium Alloy (Ti-150A) Model II	9	0.243	0.129	286.8	2.75	1.97	0.25	0.125	1.5	130	9.946	28.48	0.5125	Accel.	14	0.2546	80
														Decel.	73	0.0488	
Inconel X Model I	9.16	0.168	0.105	518.4	2.185	1.665	0.17	0.17	1.873	130	14.24	21.70	0.5805	Accel.	14	0.2794	241.8
														Decel.	73	0.0536	
Inconel X Model II	9.16	0.168	0.105	518.4	2.289	1.640	0.17	0.085	1.249	130	9.946	28.48	0.5125	Accel.	14	0.2546	241.8
														Decel.	73	0.0488	

* For typical values refer to "Thermal Resistance of Aircraft Structure Joints," by C. D. Coulbert and C. Liu, WADC TN 53-50, University of California, Berkeley, Calif., June, 1953.

$K_s = K_w = K$; $\kappa_s = \kappa_w = \kappa$; $C_{ps} = C_{pw} = C_p$

resistance which has no heat capacity joins the web and skin. Thus, by neglecting the interaction, a cell can be isolated from the wing for purposes of stress analysis and a T can be isolated for temperature calculations. It should be noted that symmetry of the structure and of the heat input is assumed about both vertical and horizontal axes. In addition, the adiabatic wall temperature and the heat-transfer coefficient are assumed uniform over the flange of the T, i. e., over the skin area.

Table 2 summarizes the pertinent dimensions which are required for the stress calculations. Table 3 summarizes the pertinent dimensions which are required for the temperature calculations.

The Transient-Temperature Distribution

Statement of the Problem. Heat enters the system shown in Fig. 4 by forced convection through the boundary layer along the surface of the skin exposed to the external flow. The heat-transfer coefficient h and the adiabatic wall temperature T_{aw} are both considered uniform over the exposed surface of the T-section and each is assumed to be a known function of time. Internal heat transfer is assumed to occur solely by conduction through the structural material. The contact joint connecting the skin and web presents an impedance to the flow of heat. This impedance is approximately accounted for by the use of a joint heat-transfer coefficient h_r, valid over an effective joint contact length, l_r. The skin and web are both assumed thin in the thermal sense and hence the conductive heat flow is essentially one-dimensional. In other words, the temperature gradients in the thickness direction are neglected while the temperature gradients along the lengths of both skin and web are considered. The initial temperature distribution in the T-section is assumed uniform, and the variation in thermal properties with temperature of the skin, web, and contact joint are neglected.

The foregoing assumptions permit the following mathematical formulation for the system shown in Fig. 4. The heat-balance equation for any point along the skin is

$$h(T_{aw} - T_s) + K_s\delta_s \frac{\partial^2 T_s}{\partial x^2} = \rho_s C_{ps}\delta_s \frac{\partial T_s}{\partial t} \quad [2]$$

The heat-balance equation for any point along the web is

$$K_w\delta_w \frac{\partial^2 T_w}{\partial y^2} = \rho_w C_{pw}\delta_w \frac{\partial T_w}{\partial t} \quad [3]$$

The initial condition is

$$T_w = T_s = T_0 \text{ when } t = 0 \quad [4]$$

The boundary conditions at the insulated ends can be expressed as follows:

When $x = l_s$ $$\frac{\partial T_s}{\partial x} = 0 \quad [5]$$

When $y = l_w$ $$\frac{\partial T_w}{\partial y} = 0 \quad [6]$$

The boundary conditions at the contact joint, based on the assumption that the heat capacity of the joint can be neglected, are as follows.

When $x = y = 0$

$$2\delta_s K_s \frac{\partial T_s}{\partial x} = h_r l_r (T_s - T_w) \quad [7]$$

When $x = y = 0$

$$-\delta_w K_w \frac{\partial T_w}{\partial y} = h_r l_r (T_s - T_w) \quad [8]$$

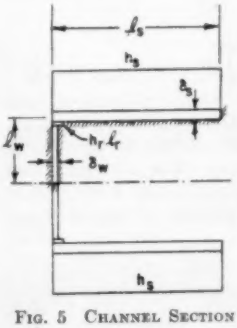

Fig. 5 Channel Section

Note that the foregoing formulation of the transient-temperature-distribution problem for a T-section, which is one half of a doubly symmetric I-section, is applicable to an angle section which is one half of a symmetrical channel section (see Fig. 5), or to an angle section which is one quarter of a doubly symmetric rectangular box section (see Fig. 6), provided Equation [7] is replaced by Equation [7a].

When $x = y = 0$

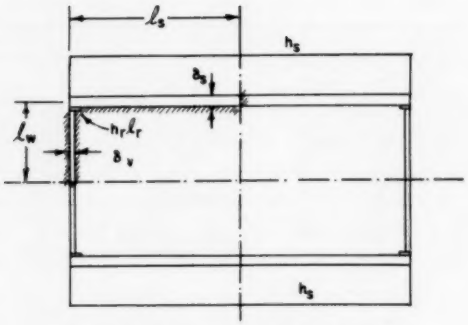

FIG. 6 RECTANGULAR-BOX SECTION

$$\delta_s K_s \frac{\partial T_s}{\partial x} = h_r l_r (T_s - T_w) \quad [7a]$$

Nondimensional Formulation. It is advantageous to nondimensionalize the formulation of the problem so as to reduce the number of parameters to a minimum. This will increase the usefulness of the numerical results obtained.

Let $(T_{aw})_e$ = extreme value of T_{aw} during the flight history
$(T_{aw})_e = (T_{aw})_{max}$ for accelerations
$(T_{aw})_e = (T_{aw})_{min}$ for decelerations

Let

$$\Omega(l) = \frac{[(T_{aw})_e - T_{aw}(l)]}{[(T_{aw})_e - T_0]} \quad [9]$$

where

$$l = \left(\frac{\kappa}{l_s^2}\right) t$$

Since the variation of T_{aw} with time and the initially uniform temperature T_0 are given, it is evident that for any particular case $\Omega(l)$ is known.

Let h_0 = heat-transfer coefficient at $l = 0$

and

$$\psi(l) = \frac{h(l)}{h_0} \quad [10]$$

Similarly it is evident that for any particular case $\psi(l)$ is known and is the nondimensional heat-transfer coefficient.

The problem defined by Equations [2] through [8] can be expressed in nondimensional form by introducing the nondimensional variables ϕ_s, ϕ_w, $\bar{x}$, $\bar{y}$, and l; the nondimensional parameters β, P, θ, and λ; and the nondimensionalized flight-history data represented by $\Omega(l)$ and $\psi(l)$

$$\frac{\partial^2 \phi_s}{\partial \bar{x}^2} = \frac{\partial \phi_s}{\partial l} + \left(\frac{\psi}{\beta}\right)(\phi_s - \Omega) \quad [11]$$

$$\frac{\partial^2 \phi_w}{\partial \bar{y}^2} = \lambda \frac{\partial \phi_w}{\partial l} \quad [12]$$

When $l = 0$

$$\phi_s = \phi_w = 1 \quad [13]$$

When $\bar{x} = 1$

$$\frac{\partial \phi_s}{\partial \bar{x}} = 0 \quad [14]$$

When $\bar{y} = 1$

$$\frac{\partial \phi_w}{\partial \bar{y}} = 0 \quad [15]$$

When $\bar{x} = \bar{y} = 0$

$$\frac{\partial \phi_s}{\partial \bar{x}} = P(\phi_s - \phi_w) \quad [16]$$

When $\bar{x} = \bar{y} = 0$

$$\frac{\partial \phi_w}{\partial y} = \theta(\phi_w - \phi_s) \quad [17]$$

The formulation given by Equations [11] through [17] is applicable to a T-section. For an angle section which is either one half of a symmetrical channel section or one quarter of a doubly symmetrical rectangular box section, the formulation given by Equations [11] through [17] is applicable provided Equation [16] is replaced by Equation [16*a*] (see Figs. 5 and 6).
When $\bar{x} = \bar{y} = 0$

$$\frac{\partial \phi_s}{\partial \bar{x}} = P'(\phi_s - \phi_w) \quad [16a]$$

where

$$P' = \frac{h_r l_r l_s}{\delta_s K_s}$$

Geometric Scaling Conditions. Assuming a solution of the nondimensional system has been obtained for a specific structure with skin material A and web material B subjected to a prescribed flight history, it is of interest to consider under what conditions this same nondimensional solution of the thermal problem would be valid for a structure with skin material C and web material D subjected to the same prescribed flight history. Since $\Omega(l)$ and $\psi(l)$ are to remain unchanged, it is required that

$$\frac{K_s^{(A)}}{[l_s^{(A)}]^2} = \frac{K_s^{(C)}}{[l_s^{(C)}]^2} \quad [17a]$$

where the superscript A refers to the skin material A of structure I and the superscript C refers to the skin material C of structure II (see Fig. 7). Now if the diffusivities of materials A

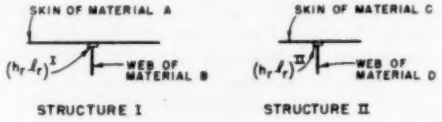

FIG. 7 STRUCTURES OF DIFFERENT MATERIALS

and C are related by a constant C_1

$$K^{(C)} = C_1 K^{(A)} \quad [18]$$

then Equation [17*a*] yields the following geometric condition

$$l_s^{(C)} = \sqrt{C_1}\, l_s^{(A)} \quad [19]$$

Similarly, since the parameters β, P, λ, and θ are to remain unchanged it is required that

$$\frac{K_s^{(A)} \delta_s^{(A)}}{h_0 [l_s^{(A)}]^2} = \frac{K_s^{(C)} \delta_s^{(C)}}{h_0 [l_s^{(C)}]^2} \quad [20]$$

$$\frac{(h_r l_r)^{(I)} l_s^{(A)}}{2\delta_s^{(A)} K_s^{(A)}} = \frac{(h_r l_r)^{(II)} l_s^{(C)}}{2\delta_s^{(C)} K_s^{(C)}} \quad [21]$$

$$\frac{\kappa_s^{(A)}[l_w^{(B)}]^2}{\kappa_w^{(B)}[l_s^{(A)}]^2} = \frac{\kappa_s^{(C)}[l_w^{(D)}]^2}{\kappa_w^{(D)}[l_s^{(C)}]^2} \quad [22]$$

$$\frac{(h_r l_r)^{(I)} l_w^{(B)}}{\delta_w^{(B)} K_w^{(B)}} = \frac{(h_r l_r)^{(II)} l_w^{(D)}}{\delta_w^{(D)} K_w^{(D)}} \quad [23]$$

where the superscript A refers to the skin material A of structure I, the superscript B refers to the web material B of structure I, the superscript C refers to the skin material C of structure II, the superscript D refers to the web material D of structure II, the superscript I refers to structure I, and the superscript II refers to structure II (see Fig. 7).

Assuming the following relations between the material properties of structures I and II

$$\left.\begin{aligned} \kappa^{(C)} &= C_1 \kappa^{(A)} \\ \kappa^{(D)} &= C_2 \kappa^{(B)} \\ K^{(C)} &= C_3 K^{(A)} \\ K^{(D)} &= C_4 K^{(B)} \end{aligned}\right\} \quad [24]$$

Equations [20] through [23] yield the geometric conditions stated by Equations [25] through [28]

$$\delta_s^{(C)} = \frac{C_1}{C_3} \delta_s^{(A)} \quad [25]$$

$$(h_r l_r)^{(II)} = \sqrt{C_1}\,(h_r l_r)^{(I)} \quad [26]$$

$$l_w^{(D)} = \sqrt{C_2}\, l_w^{(B)} \quad [27]$$

$$\delta_w^{(D)} = \frac{\sqrt{C_1}\sqrt{C_2}}{C_4} \delta_w^{(B)} \quad [28]$$

For the special case where the skin and web of structure I are both of material A, and the skin and web of structure II are both of material C the geometric conditions given by Equations [19], [25], [26], [27], and [28] still apply if C_2 is replaced by C_1, C_4 is replaced by C_3, B is replaced by A, and D is replaced by C.

Structures of different materials subjected to the same flight history which satisfy the geometric conditions stated by Equations [19], [25], [26], [27], and [28] have the same nondimensional temperature-distribution solution.

Finite-Difference Formulation. Numerical solutions of the nondimensionalized problem defined by Equations [11] through [17] are obtained by employing a finite-difference formulation in conjunction with a digital computer. The skin is divided into n elements of nondimensional length

$$\Delta\bar{x} = \frac{1}{\left(n + \frac{1}{2}\right)}$$

and the web is divided into m elements of nondimensional length

$$\Delta\bar{y} = \frac{1}{m + \frac{1}{2}}$$

as shown in Fig. 4, where $n = m = 15$. If the second difference approximation is used for the first derivatives

$$\left(\frac{\partial\phi_s}{\partial\bar{x}} \text{ and } \frac{\partial\phi_w}{\partial\bar{y}}\right)$$

at $x = y = 0$, and the first difference approximation is used elsewhere, the uncoupled finite-difference formulation of the problem defined by Equation [11] through [17] is readily obtained.

The Thermal-Stress Distribution

The thermal stresses are determined as if the wing were infinitely long and of constant cross section. Based on this assumption, the thermal stresses in the beam can be considered as the superposition of three effects:[6]

1 A stress of magnitude $E\alpha\Delta T$
2 A stress due to an axial load of magnitude $\int E\alpha(\Delta T)dA$
3 A stress due to a bending moment of magnitude $\int E\alpha(\Delta T)ZdA$

where α is the coefficient of thermal expansion and ΔT is the temperature change with respect to the initially uniform temperature T_0. It is evident that the symmetry of the heat input and the structure result in a symmetrical temperature response which eliminates the bending-moment term in the thermal-stress expression and hence there remains

$$\sigma^T = -E\alpha\Delta T + \frac{\int E\alpha(\Delta T)dA}{\int dA} \quad [29]$$

where $E\alpha$ is assumed to be constant and the superscript T identifies a thermal stress.

Equation [29] can be particularized in the following way for application to the finite-difference-element system shown in Fig. 4 (see also Fig. 3)

$$\sigma_j^T = -E\alpha[(T_{sw})_e - T_0](1 - \phi_j) + \frac{F}{A_t} \quad [30]$$

$$\sigma_k^T = -E\alpha[(T_{sw})_e - T_0](1 - \phi_k) + \frac{F}{A_t} \quad [31]$$

$$F = E\alpha[(T_{sw})_e - T_0]\left\{2(\Delta A_s)\sum_{j=1}^{15}(1 - \phi_j) + \Delta A_w \sum_{k=1}^{15}(1 - \phi_k) + \Delta A_s(1 - \phi_{j=0}) + \frac{\Delta A_w}{2}(1 - \phi_{k=0})\right\} \quad [32]$$

where

σ_j^T = thermal stress at jth skin-element location
σ_k^T = thermal stress at kth web-element location
$\Delta A_s = \delta_s \Delta x$ = cross-sectional area of skin elements
$\Delta A_w = \delta_w \Delta y$ = cross-sectional area of web elements
A_t = total cross-sectional area of T-section

A Whirlwind I digital computer program, which, given $E\alpha$, ΔA_s, ΔA_w, $[(T_{sw})_e - T_0]$, A_t, and l_s^2/κ_s, computes the eighteen pertinent times in seconds, the values of F/A_t, σ_s^T at $j = 15$, and σ_w^T at $k = 15$, for each of the eighteen times using the ϕ-distributions previously calculated and stored in the computer, is employed in determining the thermal stresses. It is of interest to note that the ϕ-distributions stored in the computer can be used to obtain thermal-stress solutions for sections of various materials provided the geometric conditions of Equations [19], [25], [26], [27], and [28] are satisfied.

The Structural Penalties

In undertaking the design of a high-speed airplane, the structural designer would like to have some knowledge of the additional structural material which is necessary in order to permit the airplane to withstand the same maneuvering loads at high speed that it can at low speeds. If the airplane is to be restricted in its mission capabilities at higher speeds, then this is equivalent to letting the decrease in strength dictate the usage of aircraft.

[6] "Theory of Elasticity," by S. Timoshenko and J. N. Goodier, McGraw-Hill Book Company, Inc., New York, N. Y., second edition, 1951.

A measure of the margin of static strength can be obtained by comparing the total stress due to maneuver and temperature with the allowable stress at the elevated temperature. The aircraft-wing structure has been idealized to a one-cell monocoque beam (see section Airplane Structure). It will be assumed that the structural function of the skin is to carry the applied bending moments and that of the webs is to carry the shear. This concept of an airplane wing serves as a basis for the evaluations which are to follow.

To determine the additional structural material which can be attributed directly to the absorption of thermal energy would involve a prohibitive amount of work if the usual design procedure were followed. An inverse process is used in the present study. It is assumed that the structures as represented by the box beams have been designed. These beams are then flown in the different flight missions and hence experience certain transient temperatures and thermal stresses. The combination of maneuver stress and thermal stress is not to exceed the allowable stress. Hence, the permissible stresses caused by maneuvering can be assigned the difference between the allowable stress and the thermal stress. This permissible maneuvering stress can be translated into a bending moment or shear flow. If the airplane is assumed to be in a subsonic environment, then the amount of structure necessary to carry this bending moment or shear flow can be calculated on the basis of room-temperature properties. In this manner, the weight penalties can be estimated.

Calculations such as described in the preceding paragraph have been performed for aluminum-alloy, titanium-alloy, and Inconel-alloy beams. As regards the skin, the allowable stress will be either the compressive yield stress or the plate-buckling stress. Buckling will be calculated from the formula

$$\sigma_{cr} = 3.62E\left(\frac{\delta_s}{b}\right)^2 \quad [33]$$

The bending moment which can be carried is given by

$$M = (k_2F_{cy} - \sigma_s^T)(\delta_s ab) \quad [34]$$

or

$$M = (k_1\sigma_{cr} - \sigma_s^T)(\delta_s ab) \quad [35]$$

where k_1 is the per cent reduction in the modulus of elasticity and k_2 is the per cent reduction in the compressive yield stress which accompanies high temperatures. Formulas [34] and [35] assume a state of uniform stress in the skin.

The structural designer in choosing allowable stresses can base these on properties existing at room temperature, the maximum adiabatic wall temperature, or some intermediate temperature. If the design is based on room-temperature values, then the thickness of the skin which is necessary to carry the foregoing bending moment is given by

$$\delta_1 = \frac{M}{F_{cy}ab} \quad [36]$$

or

$$\delta_1 = \frac{M}{\sigma_{cr}ab} \quad [37]$$

Since the final design thickness is δ, the per cent increase in the amount of compressive material in order to keep the combined maneuver and thermal stress below the permissible elevated-temperature value is given by

$$\omega_1 = \frac{\delta - \delta_1}{\delta_1} \times 100 \quad [38]$$

Similarly, if the design is based on properties which are permissible at some intermediate temperature, the corresponding formulas are

$$\delta_2 = \frac{M}{k_2(T)F_{cy}ab} \quad [39]$$

or

$$\delta_2 = \frac{M}{k_1(T)\sigma_{cr}ab} \quad [40]$$

$$\omega_2 = \frac{\delta - \delta_2}{\delta_2} \times 100 \quad [41]$$

where $k_2(T)$ and $k_1(T)$ are chosen at the appropriate temperature.

If the design is based on properties which are permissible at the maximum temperature which can be expected, the formulas become

$$\delta_2 = \frac{M}{k_2(T_m)F_{cy}ab} \quad [42]$$

or

$$\delta_3 = \frac{M}{k_1(T_m)\sigma_{cr}ab} \quad [43]$$

$$\omega_3 = \frac{\delta - \delta_3}{\delta_3} \times 100 \quad [44]$$

The webs of high-speed airplanes will experience normal stresses due to the temperature gradients. For flight missions which involve acceleration, the normal stress is tensile. The following interaction formula between shear and tension will be used

$$\left(\frac{q/\delta_\omega}{k_4F_{su}}\right)^{1.6} + \left(\frac{\sigma_\omega^T}{k_3F_{tu}}\right) = 1 \quad [45]$$

where q is the permissible shear flow due to maneuvering loads and k_3 and k_4 are the per cent reductions in tension ultimate and shear ultimate, respectively, which accompany elevated temperatures.

The web thickness necessary to carry the shear flow at room-temperature-property values is given by

$$\delta_4 = \frac{q}{F_{su}} \quad [46]$$

The per cent increase in web thickness which is necessitated by thermal stress and elevated temperature is

$$\omega_4 = \frac{\delta - \delta_4}{\delta_4} \times 100 \quad [47]$$

Similarly, if the properties for design are based on an intermediate temperature, the required thickness is

$$\delta_5 = \frac{q}{k_4(T)F_{su}} \quad [48]$$

and the corresponding per cent increase in web thickness is

$$\omega_5 = \frac{\delta - \delta_5}{\delta_5} \times 100 \quad [49]$$

If the properties at the maximum expected temperature are used, then the formulas are

$$\delta_6 = \frac{q}{k_4(T_m)F_{su}} \quad [50]$$

$$\omega_6 = \frac{\delta - \delta_6}{\delta_6} \times 100 \quad [51]$$

For flight missions which involve deceleration, the skins are in tension and the webs are in compression. Since the tension ultimate stress of the aircraft materials is higher than the compressive yield stress, there will be no weight penalties, in general, associated with the presence of tension thermal stresses in the skin. This assumes the wing structure to be symmetrical about the mid-chord. The webs, however, may need to be thicker. It is assumed that the interaction formula applicable to the webs has the following form

$$\left(\frac{q/\delta}{k_4 F_{su}}\right)^{1.5} + \left(\frac{\sigma_\omega{}^T}{k_2 F_{cy}}\right) = 1 \quad \ldots\ldots\ldots\ldots [52]$$

or

$$\left(\frac{q/\delta}{k_4 F_{su}}\right)^{1.5} + \left(\frac{\sigma_\omega{}^T}{k_1 \sigma_{cr}}\right) = 1 \quad \ldots\ldots\ldots\ldots [53]$$

where $\sigma_\omega{}^T$ is now a thermal compressive stress. With this change in the calculation of q, Formulas [46] through [51] can be used.

Figs. 36 through 50 summarize the calculations made for the different beams. Since the thermal stresses and the temperatures are transient in nature, the per cent increases in thickness have been plotted against time. The curves can be interpreted as the structural penalty which accompanies thermal flight. In other words, the elevated temperatures and thermal stresses require an increase in structural weight as indicated. Again it should be noted that these results are obtained by an inversion of the usual design procedure which proceeds from loads to the final structure. In effect, these calculations proceed from the final structural design to the loads.

The curves for ω_2 and ω_3 require some additional explanation These curves as defined are based on the property values at some intermediate temperature. Strictly speaking there are families of such curves. The two bounding curves for the ω_2 family are ω_1 and ω_3. For the ω_3 family, the bounding curves are ω_4 and ω_5. The ω_2 and ω_3 curves, which are actually plotted, base the k_1, k_2, and k_4 factors necessary for the calculation of δ_2 and δ_3 on the instantaneous temperatures.

The mechanical properties which are used in the calculation of the structural penalties are summarized in Figs. 51, 52, and 53. Certain liberties have been taken in arriving at the k_1, k_2, k_3, and k_4 variations with temperature. What is required are so-called short-time properties and these are not readily available.

The thermal stresses $\sigma_\omega{}^T$ and $\sigma_s{}^T$, which are used in the structural evaluations, are the maximum which occur in the web and the skin, respectively. Also, the reductions in mechanical properties are assessed at the maximum temperature which exists in the web or skin, respectively. These instantaneous maximum stresses and temperatures are the ones which have been plotted in the stress and temperature history curves.

The calculations for the increase in skin and web thicknesses have been made only for the configuration in which the skin and web thicknesses are equal. As can be seen the difference in stress level between configurations I and II is not sufficiently large to alter the results significantly.

It is evident that the webs of a multicell wing will require the largest increase in thickness in order to permit safe thermal flight. The low value of $E\alpha$ for titanium in conjunction with its high strength shows to advantage. On the other hand, the very high value of $E\alpha$ for Inconel X nullifies to a certain extent the high strength which Inconel X possesses at elevated temperatures. The large thermal diffusivity which aluminum possesses minimizes the thermal stresses and enables it to compete reasonably well with the other two materials despite its inherently lower strength.

Discussion of Results

Figs. 8 through 14 present the temperature-time histories for the structural configuration in which the web and skin thicknesses are equal. Figs. 15 through 18 show similar results for the configuration in which the web is one half the thickness of the skin. The curves labeled skin 15 refer to a point midway between the webs, the points labeled skin 0 and web 0 are located at the web-skin junction, and web 15 is a point in the middle of the web.

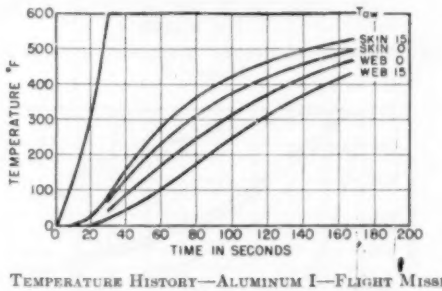

Fig. 8 Temperature History—Aluminum I—Flight Mission C

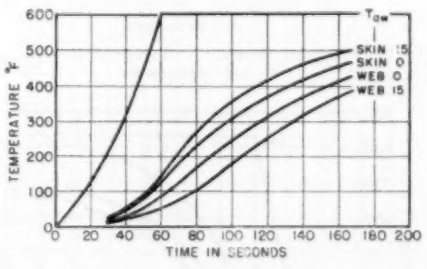

Fig. 9 Temperature History—Aluminum I—Flight Mission D

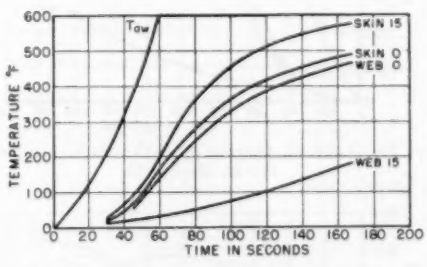

Fig. 10 Temperature History — Titanium I — Inconel I — Flight Mission D

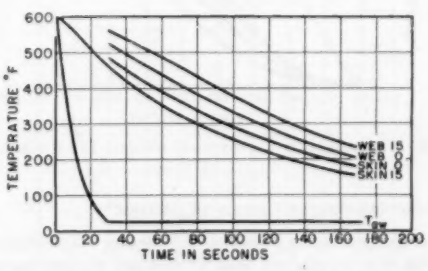

Fig. 11 Temperature History—Aluminum I—Flight Mission E

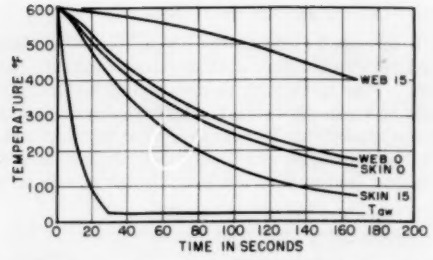

FIG. 12 TEMPERATURE HISTORY—TITANIUM I—INCONEL I—FLIGHT MISSION E

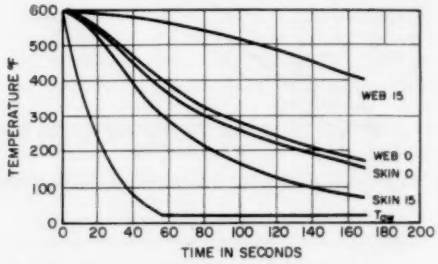

FIG. 13 TEMPERATURE HISTORY — TITANIUM I — INCONEL I — FLIGHT MISSION F

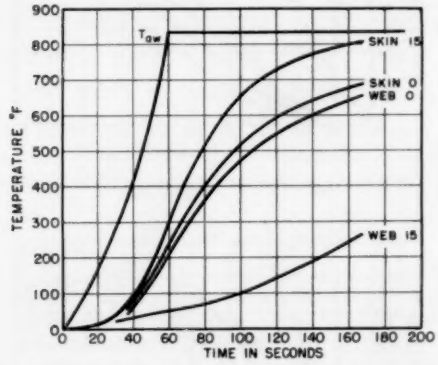

FIG. 14 TEMPERATURE HISTORY — TITANIUM I — INCONEL I — FLIGHT MISSION G

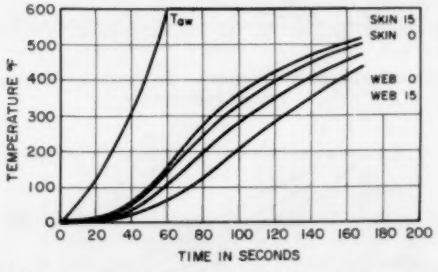

FIG. 15 TEMPERATURE HISTORY—ALUMINUM II—FLIGHT MISSION D

The following observations are of interest:

1 A comparison of Figs. 8 and 9 discloses that flight mission D which is more gradual than C does not change the temperature response of the aluminum structure to a significant extent.

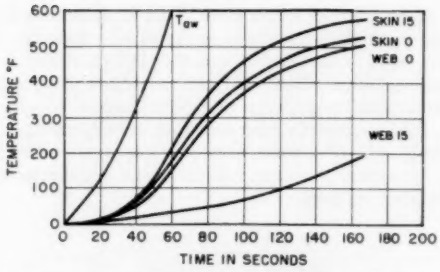

FIG. 16 TEMPERATURE HISTORY — TITANIUM II — INCONEL II — FLIGHT MISSION D

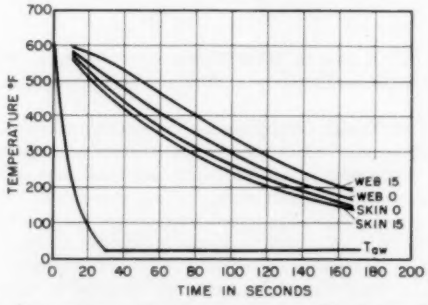

FIG. 17 TEMPERATURE HISTORY—ALUMINUM II—FLIGHT MISSION E

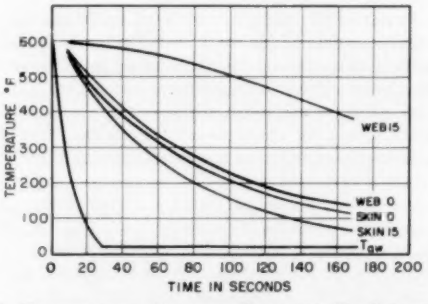

FIG. 18 TEMPERATURE HISTORY—TITANIUM II—INCONEL II—FLIGHT MISSION E

2 The discontinuity in temperature at the web-skin junction is due to the presence of the structural joint between the two. Note that the discontinuity is larger for the aluminum beam than for the Inconel X or titanium beams. This can be ascribed to the fact that a joint which is primarily a function of geometry rather than material will have relatively more effect on the better conducting material.

3 The effect of thermal diffusivity is graphically illustrated by the existence of much larger temperature differences between points skin 15 and web 15 for the titanium and Inconel beams than for the aluminum beam.

4 The deceleration-flight missions cause temperature differences which are of the same order of magnitude as that caused by the acceleration-flight missions; that is, a level-flight deceleration from Mach 3 to Mach 1 in 60 sec causes temperature differences which are approximately the same as those caused by a dive mission which accelerates the aircraft from Mach 1 to Mach 3 in 60 sec.

5 The change in structural configuration from Case I to Case II does not change the temperature response substantially.

Figs. 19 through 35 present the stress-time history of the points for which temperature time histories are presented. These are elastic stresses caused by the existence of a temperature gradient in a very long beam of uniform cross section. An examination of the curves discloses the following points of interest:

1 The stresses are mainly compressive in the skin and tensile in the web for the dive-flight missions, while the converse is true for the deceleration missions. Since the thermal stresses must form a self-equilibrating system, there is a marked peripheral variation in stress.

2 Despite the fact that the temperature gradients are quite large, a low coefficient of thermal expansion keeps the thermal stresses at relatively low values in a titanium wing.

3 The relatively large values of Young's modulus and the thermal-expansion coefficient of Inconel X result in stresses which are very high relative to mechanical properties of the material.

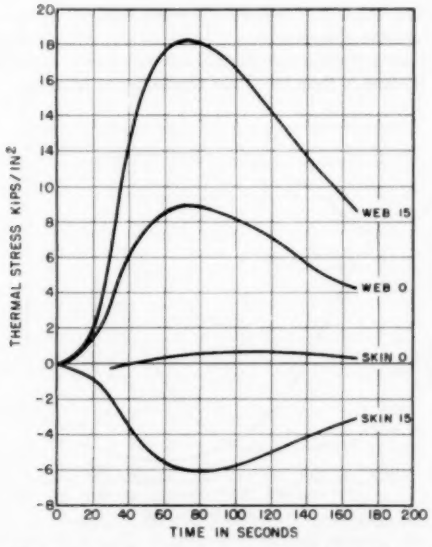

FIG. 19 STRESS HISTORY—ALUMINUM I—FLIGHT MISSION C

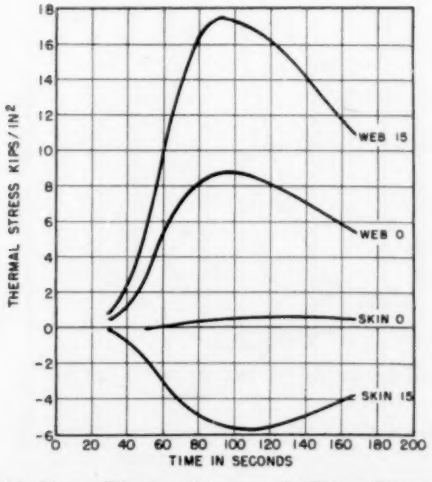

FIG. 20 STRESS HISTORY—ALUMINUM I—FLIGHT MISSION D

4 The thermal stresses are not very sensitive to the difference in average acceleration. Thus, flight missions C and E which are completed in 30 sec do not induce significantly different stresses from missions D and F which are completed in 60 sec.

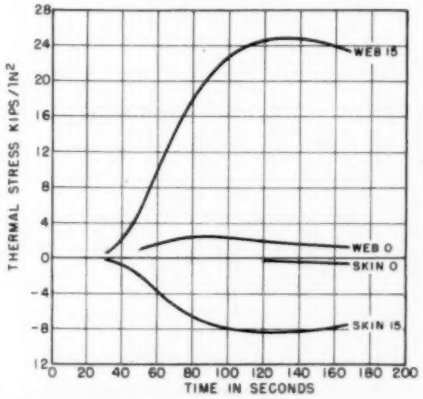

FIG. 21 STRESS HISTORY—TITANIUM I—FLIGHT MISSION D

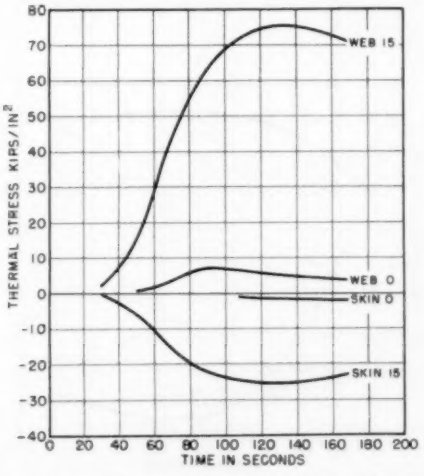

FIG. 22 STRESS HISTORY—INCONEL I—FLIGHT MISSION D

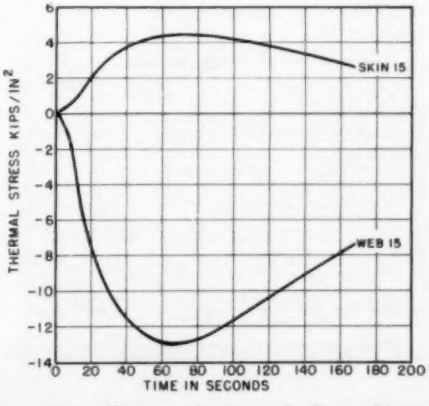

FIG. 23 STRESS HISTORY—ALUMINUM I—FLIGHT MISSION E

5 Configuration II, in which the web thickness is one half of the skin thickness, shows peak tensile stresses which are somewhat higher than those shown for Configuration I in the dive missions. The peak compressive stresses (in the dive mission) are approximately one half as large for Configuration II as for Configuration I.

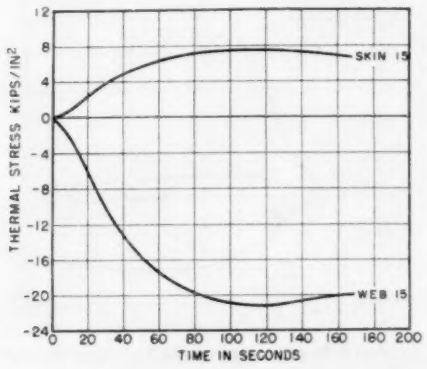

FIG. 24 STRESS HISTORY—TITANIUM I—FLIGHT MISSION E

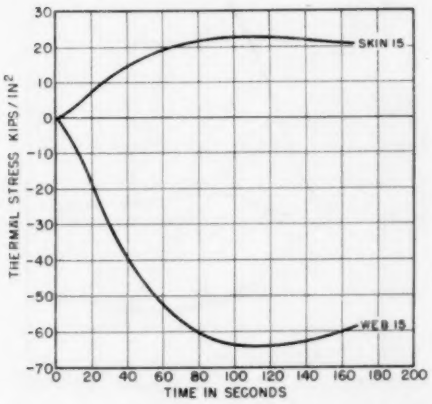

FIG. 25—STRESS HISTORY—INCONEL I—FLIGHT MISSION E

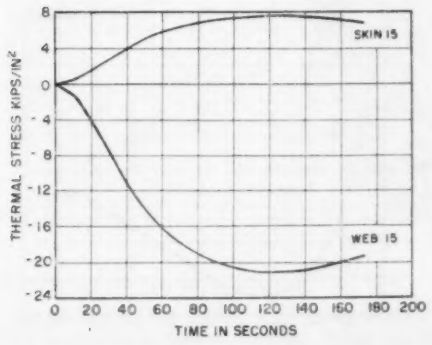

FIG. 26 STRESS HISTORY—TITANIUM I—FLIGHT MISSION F

6 In the deceleration-flight missions the change in web thickness from Configuration I to Configuration II produces slightly larger peak compressive stresses but tensile stresses which are only approximately 50 per cent as large.

Figs. 36 through 50 display the structural penalties associated with the various flight missions. Calculations have been made only for Configuration I. These curves show percentage increase in skin and web thicknesses plotted against time. Actually the peak values are of the greatest interest, but the shapes of the curves are also informative.

A few general comments can be made:

1 It is interesting to note that the curves for the aluminum beams in the dive missions are quite flat even though the stress-time curves were peaked rather sharply. This can be attributed to the decrease in material properties at the higher temperatures which occur time-wise after the peak thermal stresses.

2 The penalties which are presented for the Inconel X beams indicate that Inconel X is not a desirable material for the range of Mach numbers considered. It also is seen that a structural design which will minimize thermal stresses will be more important for Inconel X than for either aluminum or titanium.

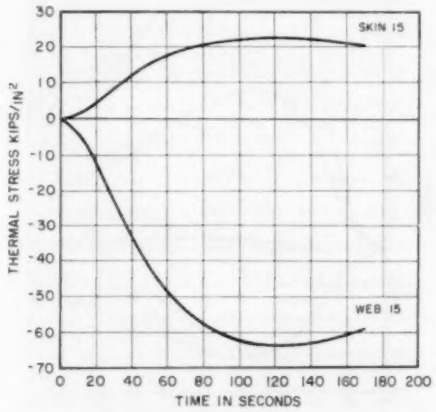

FIG. 27 STRESS HISTORY—INCONEL I—FLIGHT MISSION F

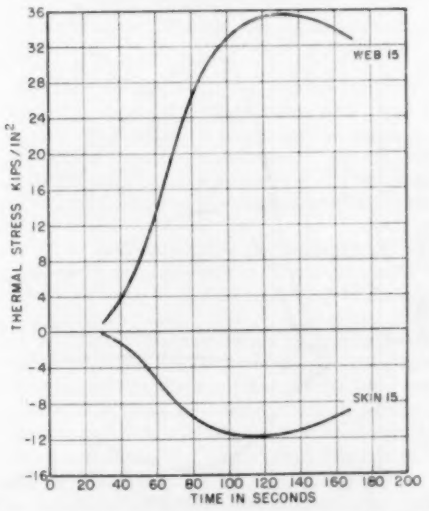

FIG. 28 STRESS HISTORY—TITANIUM I—FLIGHT MISSION G

3 Titanium shows to advantage for the flight missions considered. Since titanium has much better properties than aluminum, it appears possible that flight in the range up to Mach 3.5 can be achieved with a titanium airframe at about the same ratio of structural-to-gross weight which now exists for room-temperature aircraft.

4 The shear-carrying elements, i.e., the webs, will necessitate the largest increases in thickness.

5 A design for the web based upon material properties at the maximum adiabatic wall temperature may be overly conservative since it may not be possible for the airplane to fly for a sufficiently long period of time to attain the maximum adiabatic wall temperatures in the web.

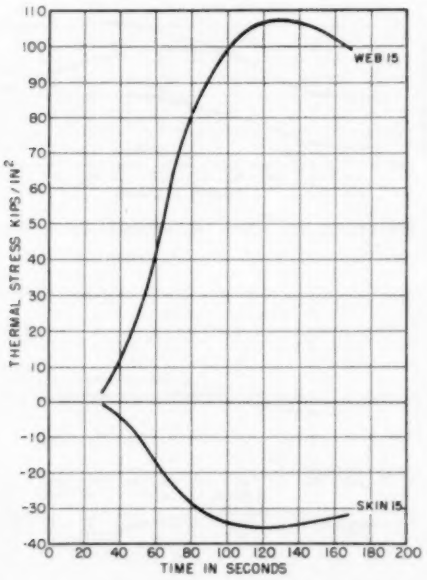

FIG. 29 STRESS HISTORY—INCONEL I—FLIGHT MISSION G

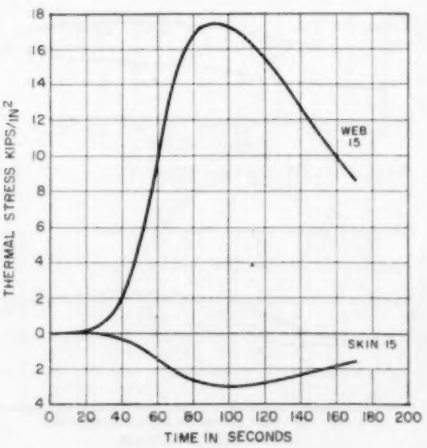

FIG. 30 STRESS HISTORY—ALUMINUM II—FLIGHT MISSION D

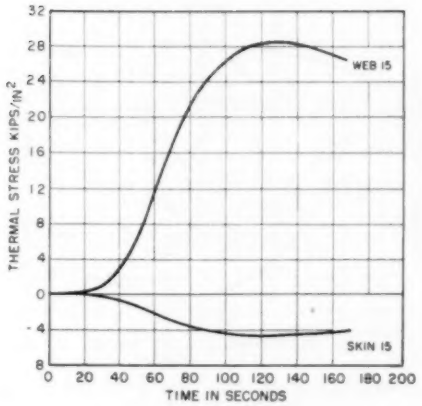

FIG. 31 STRESS HISTORY—TITANIUM II—FLIGHT MISSION D

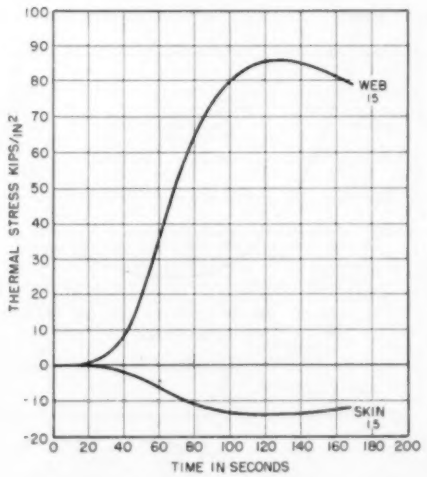

FIG. 32 STRESS HISTORY—INCONEL II—FLIGHT MISSION D

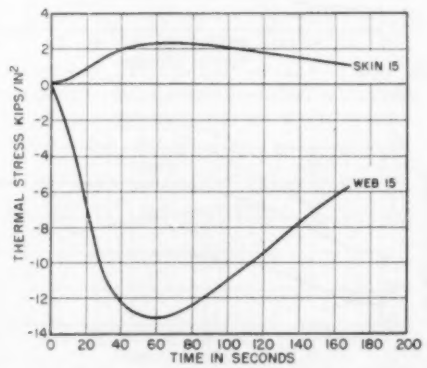

FIG. 33 STRESS HISTORY—ALUMINUM II—FLIGHT MISSION E

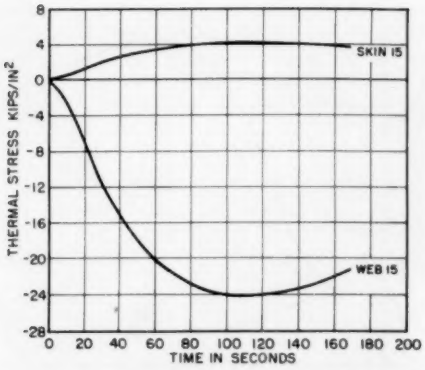

FIG. 34 STRESS HISTORY—TITANIUM II—FLIGHT MISSION E

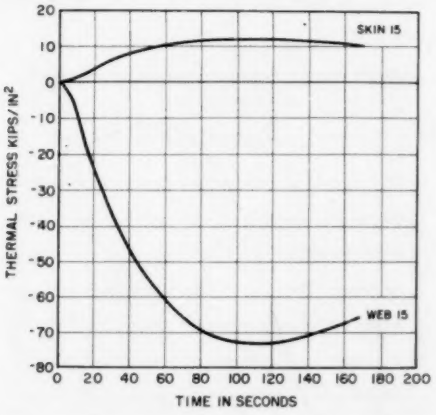

FIG. 35 STRESS HISTORY—INCONEL II—FLIGHT MISSION E

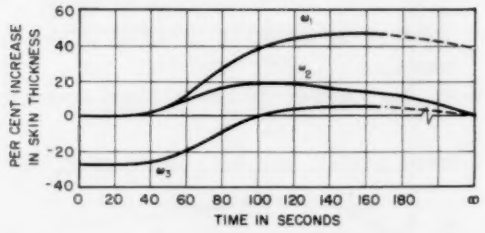

FIG. 36 STRUCTURAL PENALTIES—ALUMINUM I—FLIGHT MISSION C

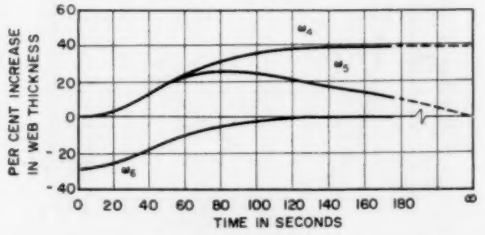

FIG. 37 STRUCTURAL PENALTIES—ALUMINUM I—FLIGHT MISSION C

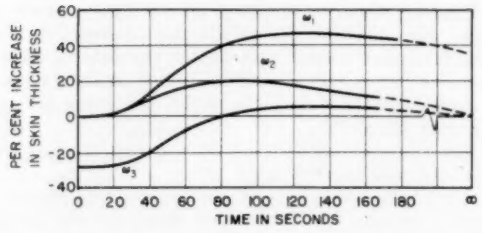

FIG. 38 STRUCTURAL PENALTIES—ALUMINUM I—FLIGHT MISSION D

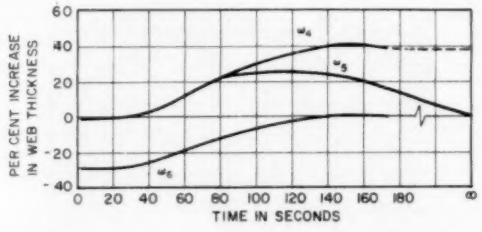

FIG. 39 STRUCTURAL PENALTIES—ALUMINUM I—FLIGHT MISSION D

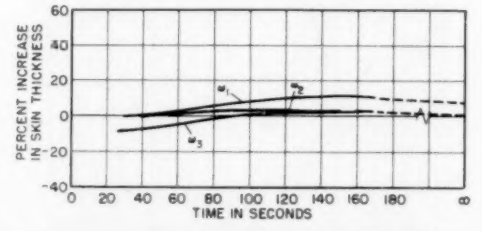

FIG. 40 STRUCTURAL PENALTIES—TITANIUM I—FLIGHT MISSION D

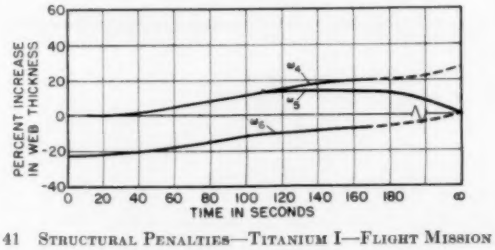

FIG. 41 STRUCTURAL PENALTIES—TITANIUM I—FLIGHT MISSION D

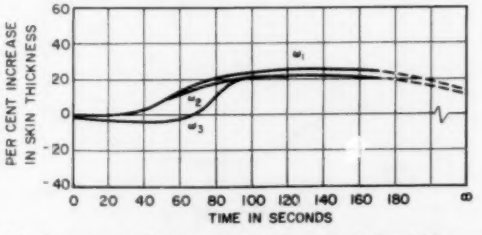

FIG. 42 STRUCTURAL PENALTIES—INCONEL I—FLIGHT MISSION D

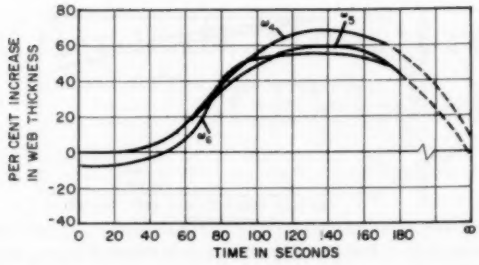

FIG. 43 STRUCTURAL PENALTIES—INCONEL I—FLIGHT MISSION D

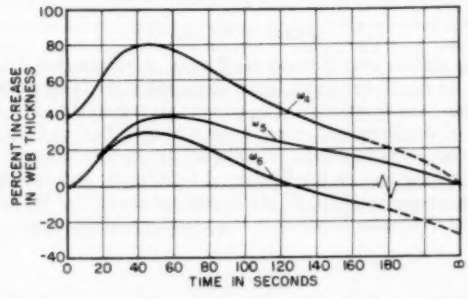

FIG. 44 STRUCTURAL PENALTIES—ALUMINUM I—FLIGHT MISSION E

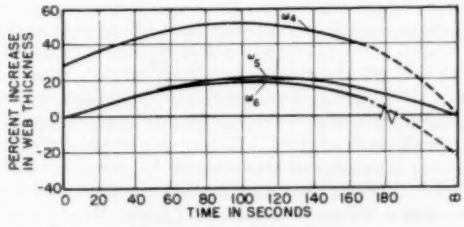

FIG. 45 STRUCTURAL PENALTIES—TITANIUM I—FLIGHT MISSION E

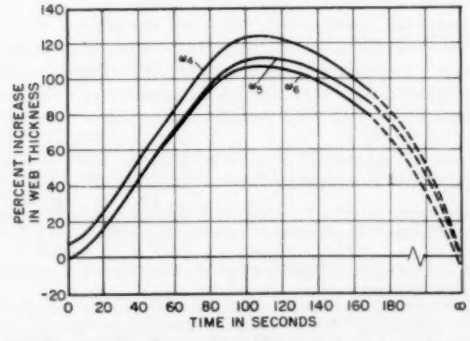

FIG. 46 STRUCTURAL PENALTIES—INCONEL I—FLIGHT MISSION E

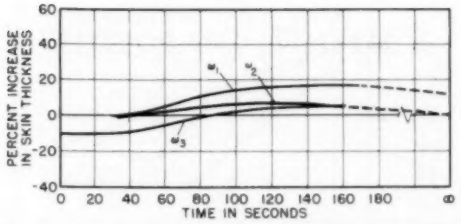

FIG. 47 STRUCTURAL PENALTIES—TITANIUM I—FLIGHT MISSION G

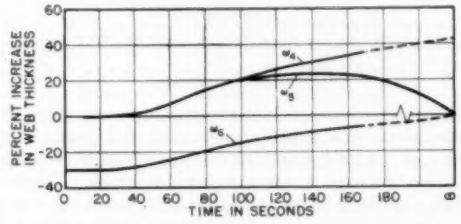

FIG. 48 STRUCTURAL PENALTIES—TITANIUM I—FLIGHT MISSION G

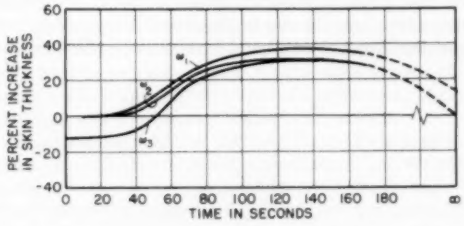

FIG. 49 STRUCTURAL PENALTIES—INCONEL I—FLIGHT MISSION G

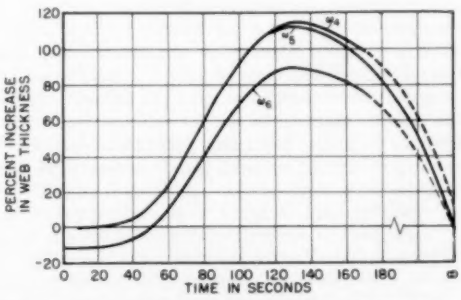

FIG. 50 STRUCTURAL PENALTIES—INCONEL I—FLIGHT MISSION G

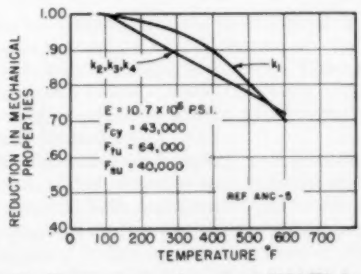

FIG. 51 PROPERTIES OF ALUMINUM 2024-T3 ALLOY

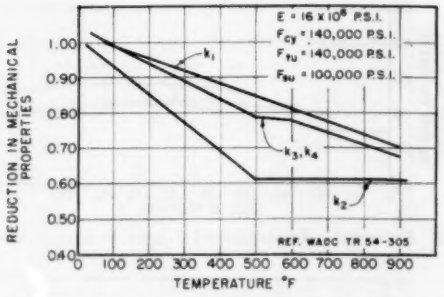

FIG. 52 PROPERTIES OF TITANIUM TI-150A ALLOY

CONCLUSIONS

In arriving at values for the structural penalties, peak thermal stresses have been superimposed with the peak maneuvering stresses. Actually, as has been pointed out, there is a significant stress gradient in the peripheral direction. The effect of this stress gradient on structural behavior is not too well understood and needs to be investigated both experimentally and analytically. On the basis of the results which have been obtained, it does not appear unreasonable to add a dive-flight mission and a deceleration-flight mission to the present V-n diagram in such a manner that peak thermal and maneuvering effects will superimpose. Such a design requirement confronts the structural designer with a positive challenge; that is, the airframe should be designed with sufficient strength and efficiency so that compromises in the use of the aircraft are unnecessary.

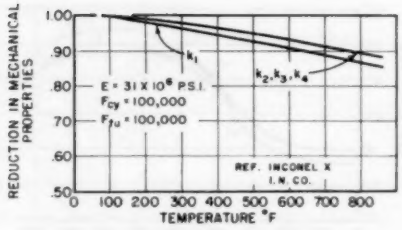

FIG. 53 PROPERTIES OF INCONEL X

ACKNOWLEDGMENTS

The authors wish to thank the Bureau of Aeronautics, Department of the Navy, under whose sponsorship the basic computer program was developed. The authors are indebted to Mr. R. A. Carl of the Bureau of Aeronautics who was Project Officer for Contract NOas 54-831-c. Thanks are due to the Office of Naval Research for making the Whirlwind I digital computer available. The co-operation of Dr. F. M. Verzuh and the staff of the M.I.T. Digital Computer Laboratory is gratefully acknowledged.

Aircraft Structural Testing Techniques at Elevated Temperatures

By R. C. BROUNS[1] and R. B. BAIRD,[2] DAYTON, OHIO

The object of this paper is to review some of the test-system requirements and problems associated with structural testing of aircraft at elevated temperatures. A brief description of loading methods used for the past generation of aircraft is presented. The requirements of an elevated-temperature test facility are established on the basis of the need for simultaneous heating and loading of an aircraft structure. Heating devices such as heating blankets, strip heaters, film heaters, induction coils, radiant heating coils, and infrared lamps which are being investigated by the Wright Air Development Center are discussed in relation to methods of attaching loads. Complications caused by simultaneous heating and loading are illustrated by a discussion of two structural tests performed at the Wright Air Development Center. A description is also given of an electronic computer developed to program the aerodynamic heating of a structure.

Introduction

THE development of supersonic aircraft and missiles has presented many complex problems to the designer and the structural test engineer. One of the most serious of these is aerodynamic heating. Flight and wind-tunnel tests have shown that the structure of a supersonic aircraft is heated to such an extent that both the thermal stresses and changes in material properties must be allowed for in design.

The aircraft designer must account somehow for the various temperature distributions which can occur in flight. He is faced with a complicated and tedious task, for in spite of the abundance of information which is now available (1–12),[3] a stress distribution due to nonuniformity of temperatures and material properties throughout the structure superimposed upon a stress distribution due to aerodynamic loads, presents a problem which defies solution.

Even for simple designs it must be agreed that there is no substitute for proof testing the final article. Design complications introduced by aerodynamic heating make this an even greater requirement. One common technique in structural research is the use of models and similarity parameters. However, attempting to relate model test results with the full-scale article is certain to present difficulties in cases where both the aerodynamic loads and temperature distributions must be duplicated simultaneously. Although continued work in this field is necessary, it alone will not be sufficient. Past experience has shown that the only reliable method of determining the structural integrity of aircraft and the validity of design practices is through the performance of comprehensive ground static and dynamic tests on full-scale aircraft and components. Therefore, present-day structural test procedures will have to be modified to duplicate aerodynamic heating as well as aerodynamic loading.

The need for developing static and dynamic testing techniques for use in the structural verification of supersonic and hypersonic aircraft was realized by the Air Research and Development Command a number of years ago. As a result, in 1952, the Wright Air Development Center was directed to design, construct, and place into operation a pilot plant for elevated-temperature structural testing research. The primary purpose of this pilot plant is to determine the various methods and techniques required to conduct elevated-temperature structural tests on complete aircraft or components. In addition, the results of the pilot-plant program are being used to establish design criteria necessary for the development, construction, and operation of a larger facility capable of testing full-scale aircraft at elevated temperatures.

This paper discusses some of the investigations which are being conducted by, or under the direct supervision of the Wright Air Development Center to provide methods and techniques for testing aircraft structures under simultaneous heat and load application. A practical type of approach is attempted because the end result must be hardware. Present testing techniques are reviewed briefly, the requirements of a loading and heating system are specified, and heating systems which are under development are discussed in relationship to satisfactory methods of attaching loads to the structure. Owing to space and time limitations, requirements for rapidly recording test data and controlling various load-versus-time programs will not be discussed. However, both rapid loading and controlling equipment and rapid temperature-recording equipment are being developed under Wright Air Development Center sponsorship. A program to develop high-speed strain-recording equipment is being delayed pending the development of a satisfactory high-temperature strain gage. High-temperature strain-gage research is presently being performed by the National Bureau of Standards under joint U. S. Navy and Wright Air Development Center sponsorship.

Loading Methods for Past Generation of Aircraft

For the past generation of aircraft, the structural test engineer has been primarily concerned with duplicating the load distribution occurring in flight or landing maneuvers. Consequently, he has had considerable latitude in selecting ways of jigging[4] the aircraft or aircraft components and in selecting methods of attaching loads to the structure.

Perhaps the oldest method of loading, used primarily for wing and tail sections, is that of lead or sand bags distributed on the structure to simulate both aerodynamic and inertia forces. A more common method developed at the Wright Air Development Center is the use of hydraulic struts attached to steel-backed sponge-rubber "tension patches" which are cemented to the air-

---

[1] Captain, USAF, Aircraft Laboratory, Wright Air Development Center, Air Research and Development Command, Wright-Patterson Air Force Base.

[2] Project Engineer, Aircraft Laboratory, Wright Air Development Center, Air Research and Development Command, Wright-Patterson Air Force Base.

[3] Numbers in parentheses refer to the Bibliography at the end of the paper.

Contributed by the Aviation Division and presented at the Aviation Division Conference, Los Angeles, Calif., March 14–16, 1956, of The American Society of Mechanical Engineers.

Note: Statements and opinions advanced in papers are to be understood as individual expressions of their authors and not those of the Society. Manuscript received at ASME Headquarters, January 18, 1956. Paper No. 56—AV-15.

[4] In structural testing terminology, a jig is the array of steelwork required to support the aircraft or parts of the aircraft for test purposes.

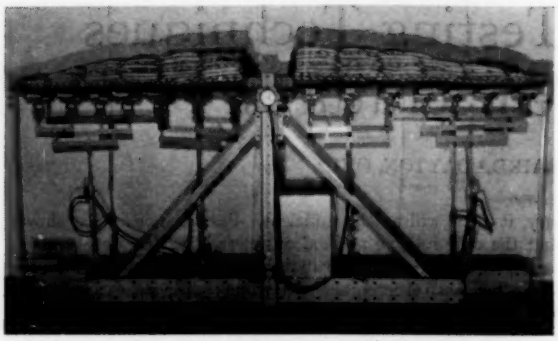

FIG. 1 EXAMPLE OF SHOT AND PATCH LOADING

craft skin. Both of these loading methods are illustrated in Fig. 1. As an alternative to the tension-patch method, some aircraft industries attach loads to wing spars, ribs, or heavy skin with metal fasteners such as eyebolts or specially designed adapters. Both of the latter two methods are satisfactory, and with suitable modifications can be adapted to structural testing at elevated temperatures.

TEST-SYSTEM REQUIREMENTS

The structural test engineer of the future, when testing supersonic aircraft, will be faced with a more serious problem than applying the correct load distribution to an aircraft. He must find a suitable method of applying both the air loads and the heating effects which are simultaneously experienced in flight. The loading portion of the task seems relatively easy. The heating problem is incomparably more complex, but solvable with sufficient ingenuity and equipment. In designing a combined system, the engineer soon realizes that neither the loading nor the heating can be considered an independent entity, but that each must be considered in relationship to the other.

Knowing the general configuration and behavior of airplane structures, and keeping uppermost in mind that a reliable test program must provide for reasonable duplication in the laboratory of the loads and heating which occur in flight, some of the basic requirements of an elevated-temperature structural test facility can be listed. These are:

(*a*) Any heating system used to simulate aerodynamic heating must be considered in conjunction with a method of load attachment to the aircraft structure. This requirement exists because the heat and load must be applied to the same surfaces. In other words, a method must be found which will allow two objects to occupy the same space at the same time.

(*b*) The heating unit must either be flexible or articulated so that it will deflect with the aircraft structure. Aircraft structures experience deflections which may be exceedingly large. As an example, wing-tip deflections, from maximum up to maximum down, of 18 ft, were measured during the static test program on the B-47 airplane.

(*c*) The heating and loading system must permit the duplication of boundary conditions; i.e., air and inertia loads in the case of loads, and heat input to the airframe in the case of aerodynamic heating. Striving to duplicate a stress or thermal analysis serves no logical purpose in proof testing of aircraft.

(*d*) The heating system must permit variations in heating-power density both in space and as a function of time.

(*e*) The heating units must not noticeably affect the strength of the structure.

(*f*) The heating units must be light in weight so as not to offer a large inertia load during rapid load tests.

(*g*) The system must provide for safety to personnel, ease of control, data recording, and reasonable cost.

These are the major requirements. Others could be added for specialized test conditions. The remainder of this paper will be devoted to a discussion of a few of the investigations which are being conducted by the Air Force to meet these requirements and some of the results which have been realized.

TESTS USING CONDUCTION-HEATING METHODS

Heat transfer by conduction requires that the two bodies experiencing a heat exchange be in intimate contact. Types of contact heaters which are being investigated by the Wright Air Development Center for suitability in simulating aerodynamic heating are heating blankets, strip heaters, and electrically conducting metallic or nonmetallic sprayed-on coatings.

Heating Blankets. The most common type of heating blanket consists of an electric resistance wire embedded in a flexible, electrically nonconducting matrix such as rubber or plastic. An experimental heating pad consisting of nichrome wire embedded in a 15 × 36-in. layer of silicone rubber is being produced for the U. S. Air Force by the Connecticut Hard Rubber Company.

Target values are to produce a blanket $^1/_{16}$ in. thick, operating up to 220 volts, and capable of producing temperatures of 500 F in a heated specimen. Pads of various sizes will be tailored to fit the aircraft surface, and the electric power varied to each pad independently to match the aerodynamic heating occurring in flight maneuvers. Power control for heating blankets, as well as for the other types of conduction heaters, should be possible using automatic computers and saturable reactor-control units of the type described later in this paper under the section on Computer Control of Heating.

One requirement for successful conduction heating is good contact between the heating blanket and the heated surface. Obviously, any material between the heater coils and the heated surface will reduce the heating efficiency. A blanket with a minimum of thermal insulation on the side in contact with the surface being heated is essential. It is also desirable to hold the blanket in position with uniformly applied external pressure, instead of using a cement. In practical test work, however, this procedure creates a complicated design and fabrication problem because of interference between pressure pads required to hold heating blankets against the aircraft surface and loading attachments required for tension application of aerodynamic loads. Loading a structure by pressure loading, that is, pushing on the structure, appears impractical for several reasons; i.e., danger of damaging the resistance wire in the heating blanket, danger of binding the hydraulic cylinders or failure of the loading struts under heavy column loads, and the possibility of movement in the point-of-load application.

The Wright Air Development Center is investigating methods of bonding heating blankets to aircraft surfaces using various types of adhesives. The scheme for simultaneous heating and loading is shown in Fig. 2. Obviously, this scheme will require a heating blanket and adhesives of considerable strength. A system capable of supporting 50 psi for 25 hr at 500 F has been established as the objective.

Thus far, efforts to obtain a successful bond between electric heating blankets and aircraft surfaces have not been too successful. The principal difficulty with many adhesives, and particularly the epoxy resins, is that they will not adhere well to silicone rubber. Silicone adhesives require a lengthy curing cycle of approximately 45 hr with the blanket and adhesive under continuous pressure while the temperature is raised in steps to a

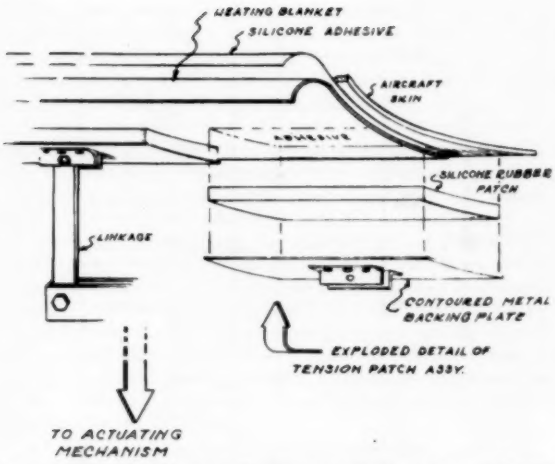

FIG. 2 EXPLODED VIEW OF HEATING AND LOADING SYSTEM USING HEATING BLANKETS

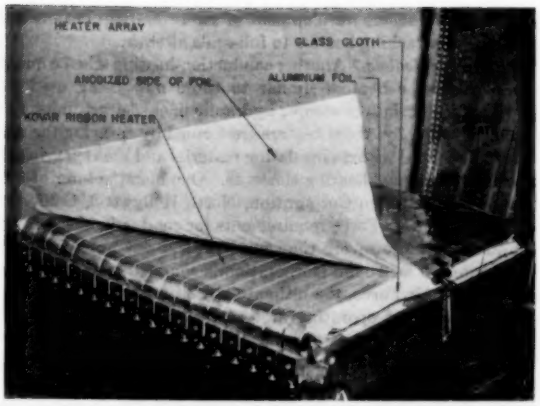

FIG. 3 UNIVERSITY OF COLORADO STRIP HEATER

maximum of about 480 F. Pressure application is a simple matter, and is best obtained by evacuating the air from a sealed silicone-rubber sheet covering the heating blanket. On the other hand, producing the temperatures required for curing silicone adhesive is difficult for large structures such as wings which will not fit into ordinary ovens. Perhaps the only solution is to use the electric heating blanket to supply the local temperatures required for curing the adhesive, and heating the opposite airfoil surface or adjacent areas by other means to avoid buckling of the structure by large thermal stresses. Radiant heating lamps have been used successfully for this purpose.

A serious problem in curing silicone adhesives, using heat from the heating blanket, is the formation of trapped gas bubbles during curing. This causes local hot spots and charring of the rubber blanket. Perforating the rubber blanket may solve this problem. Poor curing of silicone adhesive has been experienced in many cases, but eventually this may be overcome by modified curing cycles or better heat control. Tests have shown that good bonds between aluminum and silicone rubber can be obtained by curing the silicone adhesive in a controlled oven. For example, samples have supported 50 psi at 400 F for 30 hr.

Power densities obtained with silicone-rubber heating blankets, bonded to a structure with silicone-rubber adhesive, have been approximately 1 kw per sq ft with 90 per cent heating efficiency. Tests so far indicate that much larger power densities eventually will be possible with this type of blanket. The maximum temperature obtainable appears to be about 450 F, limited primarily by the strength of the silicone-rubber adhesive under a loading system of the type shown in Fig. 2. Heating blankets of this type will be limited to tests under steady-state conditions or transient-temperature conditions where the required heat-flow rate is low.

The techniques required for successful use of conduction-heating pads to simulate aerodynamic heating are still largely undeveloped, and will have to come primarily from experimental work. Investigations will be required into the effect of variations in pad and adhesive thickness upon heat-transfer rates, the effect of heating pads upon the strength of the structure, and changes in material properties of the structure under test due to the heat required for curing of adhesives. In addition to the difficulties already mentioned, such as bonding and obtaining a compatible load-attachment system, conduction-heating methods are plagued by the danger of electrical shorts to loading attachments or to the aircraft structure, the difficulty of replacing or repairing bonded pads, and the fact that inspection of a structure covered with pads is impossible.

Strip Heaters. For the purposes of this paper, a strip heater is distinguished from a heating blanket only in the sense that the heating element and electrical insulation of a strip heater do not form an integral unit.

A type of strip heater built and tested by the University of Colorado (18) for the Air Force consists of a 1-mil-thick Kovar ribbon insulated by a 1-mil anodic film of aluminum oxide (Al_2O_3) formed on one face of a 3 to 5-mil-thick aluminum foil, Fig. 3. The anodic film faces the heater, while the other surface of the foil lies in contact with the surface to be heated. The back of the heater is insulated by several layers of fiberglas cloth. Good contact between the heater and the heated surface is maintained by rubber pads subjected to a pressure of 1 psi or more.

A final evaluation of the Kovar strip heater has not been completed, but results so far have been very promising. During tests at the University of Colorado on a small wing panel, a heater-input power of about 85 kw per sq ft was realized with 240 volts across each heater. The heating efficiency was found to be above 90 per cent. The high heating efficiency permits operation of this type of heater at maximum power input without the heater reaching the oxidation temperature of Kovar (about 800 F). The present state of the art is such that temperatures in excess of 600 F can be produced in a heated structure.

Load application to an aircraft structure, employed simultaneously with heating by the Kovar conduction heater, is a problem which has not been investigated thoroughly. However, the loading difficulties discussed in connection with heating blankets apply to conduction-heating methods in general. The only immediately evident solution is to use a system of point loads with wires or cables passing through the Kovar heater and attached either directly to the aircraft skin or to internal members. Electrical insulation is certainly a problem which must be overcome. As mentioned earlier in this paper in connection with heating blankets, pressure (or compression) loading to simulate air loads does not appear desirable. If suitable procedures are developed to bond strip heaters to aircraft surfaces, an alternate loading system, using tension patches similar to those shown in Fig. 2 can be used.

The investigation of heating and loading systems using strip heaters such as the Kovar type is by no means complete. Further efforts are being directed toward obtaining better electrical insulating materials so that both the operating voltages and maximum obtainable temperatures can be raised. Other phases of the

investigation include development of sandwich-strip heaters and methods of attaching heaters to full-scale aircraft.

Film-Type Heaters. Another conduction-heating scheme makes use of film-type heaters similar to those now being used extensively for air-intake scoops, hydraulic lines, defrost units, and so on. Essentially, these heaters are formed by spraying the surface to be heated with an insulating material and then spraying on a series of electrical heating elements. One manufacturer of film heaters is Electrofilm Corporation, North Hollywood, Calif.

Because the Air Force requirements for conduction heaters are considerably more severe than most present-day applications of film heaters, Electrofilm Corporation is conducting an investigation for the Air Force, the ultimate objective being to produce a heater capable of operating at temperatures up to 500 F and capable of power inputs to a heated surface of 30 kw per sq ft. This power density is at least six times that available in most film heaters of today. In addition to other detailed requirements, the heating film and the bonding used to attach the film heater to the surface being heated must be capable of supporting a tensile load of 50 psi in a direction normal to the surface at 500 F for at least 25 hr. Again the plan is to apply loading to the structure being tested by use of metal-backed silicone-rubber tension patches glued to the film heaters, similar to the method shown in Fig 2. Loading wires or cables passing through the film heaters and attached to the aircraft skin or to internal members also can be used for loading if electrical-insulation problems can be solved.

No results on the film-heater study are available at the present time.

Induction-Heating Methods

Although induction heating is in common use today, particularly in the steel industry, many technical problems must be solved before the basic principles involved will be wholly adaptable to elevated-temperature testing of full-scale aircraft. The discussion in this paper will be limited to methods by which induction heating can be used in conjunction with loading systems to simulate the flight environment. Technical problems such as optimum design of work coils, mutual coupling between adjacent work coils and power leads, radio-frequency interference, development of power-control systems, and the like, are still under investigation for the Air Force by agencies such as the University of Florida and the Polytechnic Institute of Brooklyn. Even the results obtained so far (13, 14) would fill several volumes the size of this paper.

In simple terms, induction heating takes place by the following process: A changing magnetic field induces eddy currents within an electrically conducting material. The flow of current in a material with a finite resistance requires the expenditure of energy which appears in the form of heat.

An essential element in the simulation of aerodynamic heating is that the heat must enter the surfaces which are normally exposed to air flow in flight. This requirement is easily met in conduction and radiant heating. In the case of heating by induction, where the heat is generated within the material, good simulation of aerodynamic heating can be produced only if this heat is generated in the outer layers of the aircraft skin. Fortunately, the depth of radio-frequency (R-F) penetration is inversely proportional to the square root of the frequency-conductivity product. Therefore, an appropriate frequency can be selected, assuming that the conductivity as a function of temperature is known for the material being heated, and a desirable depth of penetration is selected. A depth-of-penetration criterion selected by the University of Florida for good simulation of aerodynamic heating is that a minimum of 80 per cent of the heating shall occur within $^1/_3$ the thickness of the surface being heated. Fig. 4 from reference (13) was drawn using this criterion and the rules for penetration of R-F fields. The minimum frequency selected, of course, must be satisfactory for the highest temperature produced in the heated material during a particular test.

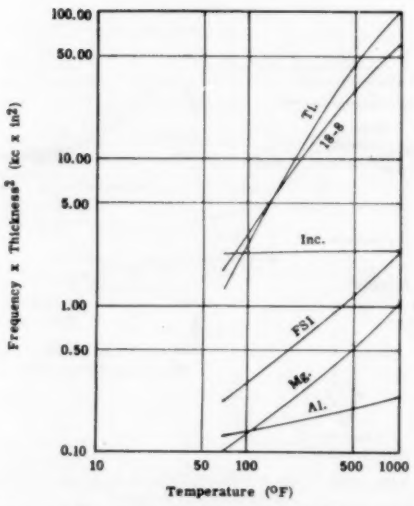

Fig. 4 Minimum Satisfactory Frequency × Thickness² Versus Temperature for Various Structural Materials

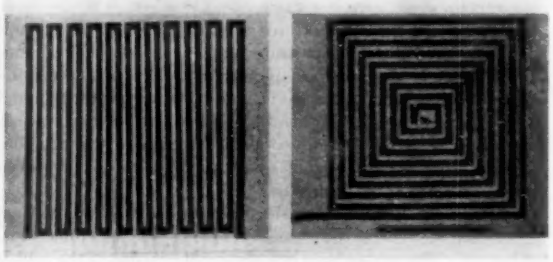

Fig. 5 Zig-Zag and Spiral Work Coils

Because of the large flat surfaces involved in aircraft structures, wrap-around induction coils are impractical for entire surfaces, especially those which must be heated according to different programs. Pancake coils consisting of wide flat conductors lying close to a structure to be heated appear to be the most practical. Two types tested by the University of Florida are shown in Fig. 5. These coils produce uniform power densities, can be designed to have efficiencies which approach the theoretical maximum, and will follow contours of a surface if correctly applied. Power densities can be varied over the area covered by a pancake work coil by varying the width of conductors. However, in practice it undoubtedly will be more practical to cover a large surface with many individual coils, each encompassing a relatively small area, and possibly operating at different power levels. Experimental work at the University of Florida (13) indicates that power densities of the order of 200 kw per sq ft may be achieved with a proper combination of frequency and design of the air-cooled coils. Some of the limitations are the melting point of the coil material, heat-storage capacity and cooling rate of the work coil, and length of time of tests.

Pancake work coils can be held in position against the surface being heated by sheets of insulation and silicone-rubber pressure pads. These pressure pads also can be used to apply the forces necessary to simulate aerodynamic loads on small-scale struc-

tures not subject to severe loads. However, as mentioned earlier in this paper, compression loading is not considered favorably for structures subject to large deflections or heavy loads. In a joint test program by the University of Florida and the Glenn L. Martin Company on a small wing panel, the Glenn L. Martin Company used a combination of compression loading with pressure pads and tension loading with "bicycle-spoke" loading wires (13, 15). In this case the loading wires were passed through the induction heating coil and attached to compression pads and button heads on the inside of the airfoil.

Experimental work to date on induction-heating methods has brought out at least two important points; i.e., that it is possible to develop an induction-heating system which can be used simultaneously with loading to simulate high-temperature flight conditions, but that the developmental work required and the expense will be considerably greater than for either conduction or radiant heating. Induction heating offers the advantages of high heating power density and high temperatures, perhaps well over 1000 F, with low thermal inertia.

Radiant-Heating Methods

The discussion so far has shown that considerable experimental work is still required to develop heating and loading methods for aircraft structural testing using either conduction or induction-heating methods. Knowledge of radiant heating is far more extensive and structural testing with radiant heating already has become a reality.

A distinct advantage of radiant heating is that a very high source temperature is available with some types of radiant-heating elements. Since the net radiant-heat flow between two bodies depends upon the difference of the fourth powers of the absolute temperatures, it is apparent that high power densities may be obtained in a structure being heated by radiation. Consequently, considerable research has been directed toward the application of radiant-heating methods to structural testing of aircraft at elevated temperatures. This research has included investigations of such radiant-heating devices as open-coil windings of nickel-chromium wire in parabolic reflectors and infrared lamps. Some of the more important aspects will be discussed.

Nickel-Chromium Heating Elements. Various configurations of nickel-chromium heating elements have been investigated with a fair degree of success. By placing a 30-in-long nichrome V-helical element at the focal point of a parabolic reflector, as shown in Fig. 6, very uniform heating was obtained. The heating element has

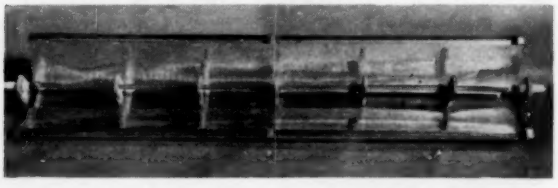

Fig. 6 Parabolic Reflector With Helical-Wound Nichrome Heating Element

been operated successfully at 2200 F in a normal atmosphere for long periods of time. The heating-power density obtained with the parabolic reflector was limited to about 1 kw per sq ft, primarily because of the wide spacing of the nichrome elements. With closely spaced helical coils, heater-power densities of over 20 kw per sq ft are possible.

This type of radiant-heating device has at least two major disadvantages. One is that the large thermal inertia makes shielding of the specimen necessary during heat-up for tests in which duplication of heating as a function of time is important. The use of a shield is impractical in most cases because it interferes with the loading mechanism. Numerous loading rods, cables, or wires must extend through the heater and be attached to the structure to apply distributed loads. Where time of heating is of no importance, such as in a "soak" test or equilibrium-temperature condition, this type of heater may be used satisfactorily. The other disadvantage is that the maximum temperature of nichrome heating elements is limited to about 2200 F in a normal atmosphere. This characteristic restricts their use to tests requiring relatively low heat-transfer rates.

Infrared Lamps. The previous discussions have shown the desirability of obtaining a radiant-heating device with a low thermal inertia and a very high element temperature. Infrared heating lamps meet these requirements. Their heat-up time is very short, and experiments have shown that most commercially available lamps may be operated at more than 300 per cent overload for short periods of time. The decrease in life caused by overloading is not considered a serious problem because severe transient heating conditions are of short duration.

Because of their favorable characteristics, various types of commercially available lamps have been investigated by the Wright Air Development Center with the following results:

1 250-watt infrared lamp. Ordinary 115-volt, 250-watt infrared heating lamps, as illustrated in Fig. 7, have been operated successfully at a power level of approximately 1000 watts. The main disadvantage is that they cannot be mounted close together because of their circular shape. This in turn, prevents the attainment of an even heat distribution. In addition, high power densities are not possible because of the low power capacity of the lamps themselves.

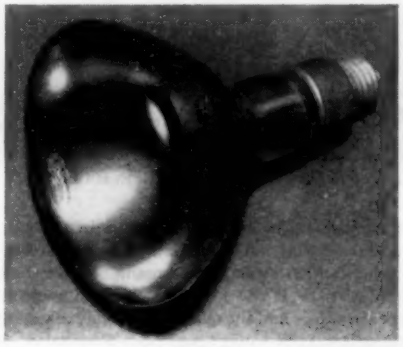

Fig. 7 Infrared Heating Lamp, 250 Watt

2 General Electric T-12 lamps. The General Electric T-12 infrared lamp, illustrated in Fig. 8, is approximately 1¼ in. diam and 14 in. long. The normal rating is 2500 watts at 115 volts. During tests performed at the Wright Air Development Center, these lamps have been operated successfully at 220 volts which produced a power output of approximately 7250 watts.

T-12 lamps were used successfully by the Wright Air Development Center to duplicate a transient heating condition on a small wing panel. This panel was identical to one tested by the NACA in its Wallops Island blow-down wind tunnel, and the temperatures obtained were due entirely to aerodynamic heating. The panel was fabricated from 24S-T aluminum alloy and had a 20 × 20-in. planform, multiple spars, and 0.064-in. skin.

For duplication of the heating condition, 18 General Electric T-12 lamps were arranged in a 24S-T aluminum alclad reflector as shown in Fig. 9. Two such reflectors were fabricated and mounted on opposite sides of the test panel. The specimen area was divided into five chordwise controllable areas and the power was

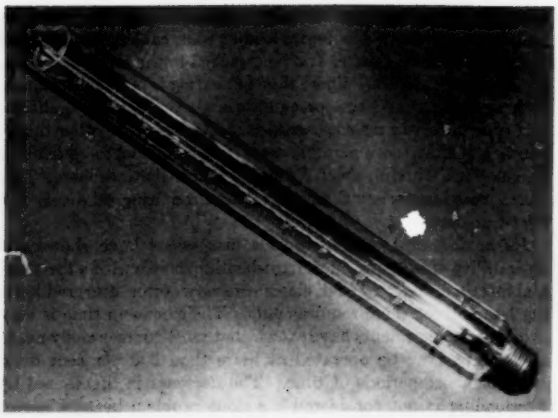

FIG. 8 INFRARED HEATING LAMP—GENERAL ELECTRIC T-12

FIG. 9 REFLECTOR WITH GENERAL ELECTRIC T-12 LAMPS

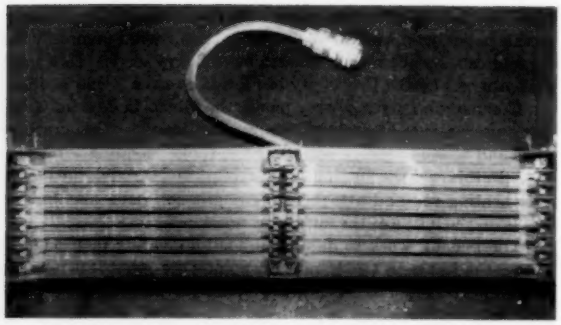

FIG. 10 BASIC REFLECTOR UNIT WITH GENERAL ELECTRIC T-3 LAMPS

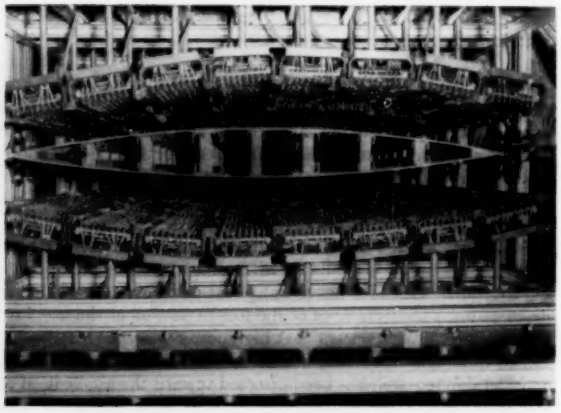

FIG. 11 RADIANT-HEATING OVEN

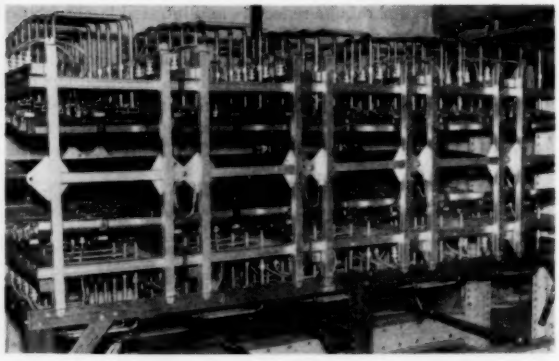

FIG. 12 RADIANT-HEATING OVEN

regulated in each area so as to obtain a chordwise power distribution. All temperature and strain data were recorded on Century oscillographs, but no attempt was made to load the structure. Heating rates of 50 F per sec were obtained near the leading edge of the structure, and the over-all efficiency of the heating system was approximately 55 per cent.

3 General Electric T-3 lamps. From the results of a radiant-heating research contract with Research, Inc., Minneapolis, Minn. (17), it was determined that the General Electric T-3 tubular, clear quartz, infrared lamp is one of the most suitable for elevated-temperature structural testing. This lamp is approximately $^3/_8$ in. diam and $11^3/_4$ in. long. Because of their small size, a large number of lamps can be placed in a small area. Normal rating is 1000 watts at 230 volts, but very satisfactory results have been obtained by operating this lamp at 460 volts giving a power output of 3000 watts.

The basic reflector unit in use at the Wright Air Development Center is shown in Fig. 10. It is 1 sq ft in area (6 × 24 in.) and contains 16 T-3 lamps. Therefore, a maximum lamp power density of 48,000 watts per sq ft may be obtained at 460 volts. The reflectors are part of the Wright Air Development Center radiant-heating oven shown in Fig. 11. This oven, manufactured by Research, Inc., contains five sections of 16 reflectors each, or a total of 80 reflectors. Fig. 12 illustrates that the oven sections are hinged together so they will deflect in relationship to each other. Thus the oven will follow the deflection of a structure being tested and will maintain a constant spacing between the lamps and the heated surface. Provisions also have been made in the basic reflector unit to permit adjustment of the reflectors up and down as well as in a chordwise direction. This feature is illustrated also in Fig. 12. The efficiency of the radiant-heating oven has been found to be approximately 65 per cent when the surface being heated is coated with a solution of graphite in lacquer and the distance between the lamps and work surface is 3 in.

Loading With Radiant Heating. Although infrared heating is a desirable method of heating aircraft structures, it is not entirely without difficulties. Owing to the very nature of infrared heating,

loading attachments to the structure must cover a minimum amount of surface area in order to prevent excessive shielding of the structure from the heating lamps. Neither tension patches nor shot bags can be used with radiant heating because they cover surface areas which must be heated.

The only possible method of loading which will meet the requirements is a system using wires or small-diameter rods attached directly to the specimen. These rods or wires must be long enough to extend either through or around the reflectors. Load linkages and hydraulic cylinders, which are commonly used to apply the distributed forces, Fig. 1, can be attached to the loading wires or rods outside of the heated area and may be of any convenient form.

In most cases, the type of structure determines how loading wires or rods are attached. If access to the inside of the structure is possible, loading rods may be attached to pads on the inside of the skin. If the test aircraft is completely assembled and access to the internal structure is difficult, other attachment methods must be used. Threaded fittings, such as eyebolts, can be screwed into drilled and tapped holes in thick aircraft skin. Blind fasteners, such as B. F. Goodrich Rivnuts, can be installed in aircraft skin which is too thin for drilling and tapping. Loading rods can then be screwed into the Rivnuts, making use of their internal threads.

The load-attachment methods discussed have been used by the Wright Air Development Center, but more extensive test work will be required before their reliability and load limitations are established definitely.

Test of the Douglas Nose Cone. The method used for a recent test will be described to illustrate the flexibility of T-3 lamps and the load and data-recording complications caused by heating requirements. The structure tested was a nose cone approximately 30 in. long, fabricated from 0.072-in-thick 61S aluminum alloy. To duplicate the transient heating condition, the conical reflector shown in Fig. 13 was fabricated from polished 0.064-in. 24S-T

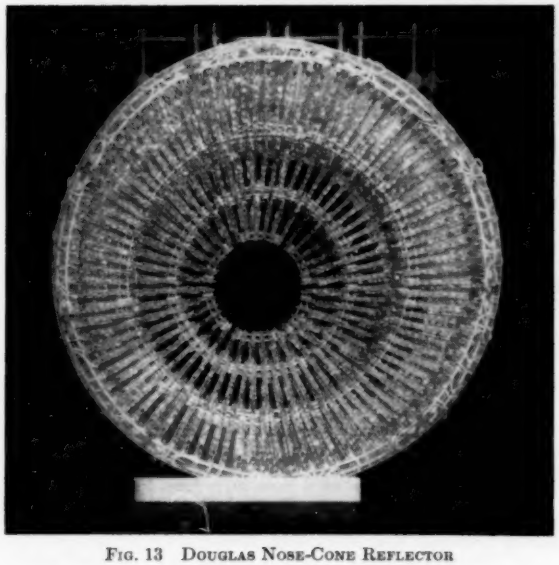

FIG. 13 DOUGLAS NOSE-CONE REFLECTOR

aluminum alloy. A total of 186 T-3 lamps were mounted inside the reflector.

The required temperature distribution for the test was obtained by varying the power input to each of the three rows of T-3 lamps. With the nose cone coated with Sauereisen No. 7W

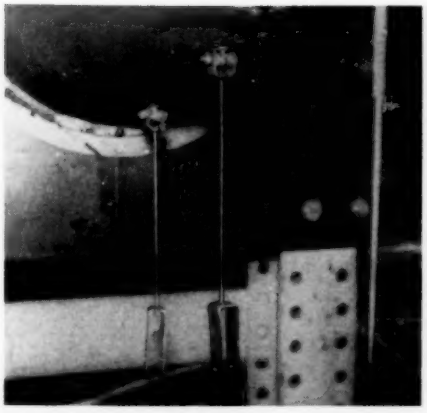

FIG 14 LOADING ATTACHMENT, DOUGLAS NOSE CONE

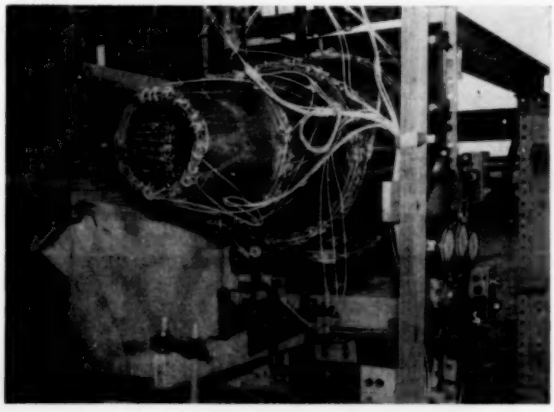

FIG. 15 TEST SETUP, DOUGLAS NOSE CONE

Special cement to increase absorptivity, heating rates of 150 F per sec were obtained near the nose of the cone.

The load-attachment method is shown in Fig. 14. Eyebolts were installed in the skin of the cone with nuts on the inside; $^3/_{16}$-in. steel rods which passed through the reflector were then attached to the eyebolts by means of a swivelling mechanism. Loads were applied prior to heating.

Deflection measurement was the most difficult problem because the short time of the test run (about 10 sec) prevented visual recording. The problem was solved by using high-speed movie cameras to photograph Ames dials which were connected to the cone by means of wires passing over small pulleys. Fig. 15 shows the complete test setup, including the Ames dials and loading struts which are outside the heated area.

COMPUTER CONTROL OF HEATING

One of the requirements of a heating system mentioned earlier in this paper is that it must provide for duplication of boundary conditions. This means that the rate of heat flow into the structure, which is determined at any instant by the boundary-layer temperature T_{aw}, the convective heat-transfer coefficient h, and the skin temperature T_s, must be duplicated as a function of time. A computer developed for this purpose by Research, Inc., Minneapolis, Minn., is in use at the Wright Air Development Center. A prototype model is shown in Fig. 16.

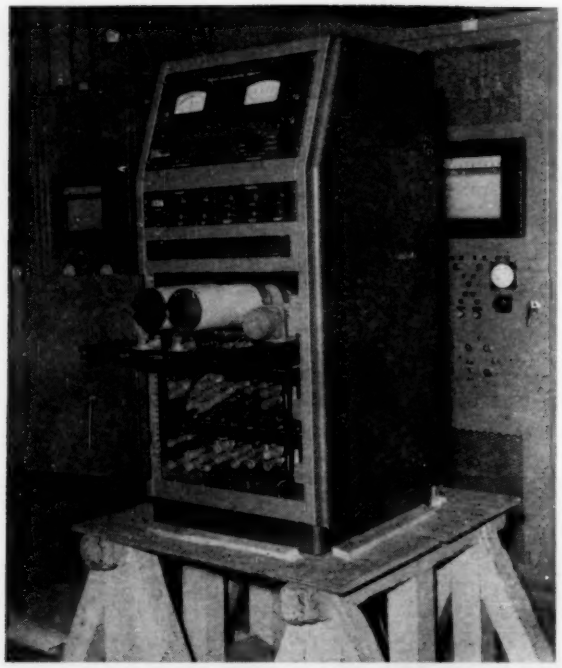

FIG. 16 HEATING-CONTROL COMPUTER, PROTOTYPE MODEL

actually being delivered to the surface of the structure by the heating system. If a difference exists, the computer instantaneously transmits an electronic signal to a power controller which adjusts the output of the heating system.

The power controllers in use at the Wright Air Development Center are of the saturable-reactor type and are shown in Fig. 17. Included in each of these controllers is a recorder which records the temperature of the thermocouple used for power control. Since there are 40 power-control units of 75 kva capacity each at the Wright Air Development Center, 40 heat-control computers are being fabricated for use with these power controllers. With this arrangement, 40 separate areas may be heated simultaneously according to 40 different heating programs entered into the computers.

Although the heat-control computers were designed to operate with saturable reactor-type power controllers, only slight modifications are required to permit operation with other power controllers such as ignitrons, motor-driven powerstats, and the like.

BIBLIOGRAPHY

1 "A Design Manual for Determining the Thermal Characteristics of High-Speed Aircraft," by H. A. Johnson, M. W. Rubesin, F. M. Sauer, E. G. Slack, and L. Possner, AAF Technical Report 5632, 1947.

2 "The Transient Temperature Distribution in a Wing Flying at Supersonic Speeds," by Joseph Kaye, *Journal of the Aeronautical Sciences*, vol. 17, 1950, pp. 787–807.

3 "Computing Surface Temperatures at High Speeds," by N. L. Dyste and R. A. Seban, AF Technical Report 6177, July, 1950.

4 "Comparison of Theoretical and Experimental Heat-Transfer Characteristics of Bodies of Revolution at Supersonic Speeds," by Richard Scherrer, NACA Technical Report 1055, 1951.

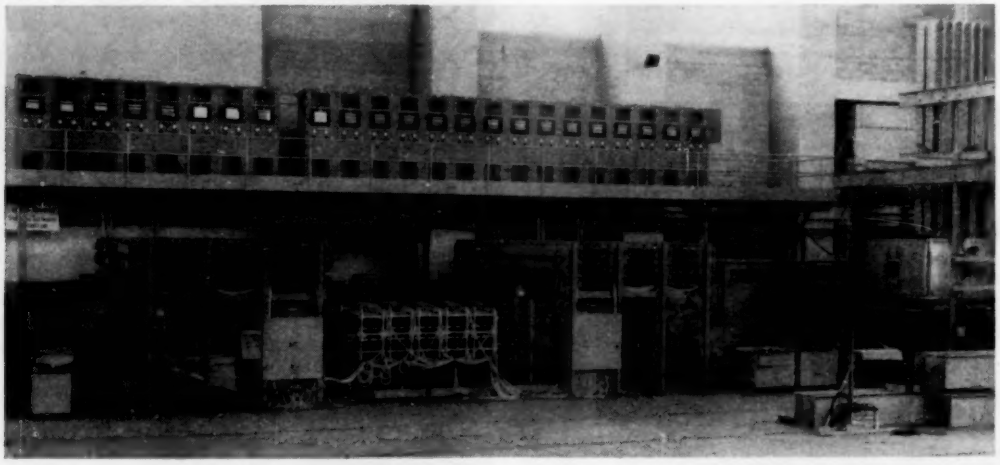

FIG. 17 WADC ELEVATED-TEMPERATURE TEST FACILITY

Without going into too many technical details, the operation of the computer is as follows: The convective heat-transfer coefficient and the boundary-layer temperature are assumed to be known as a function of time, and are entered into the computer on input drums. The skin temperature of the surface being heated is monitored by a thermocouple, and is also fed into the computer. By combining these three items of information, the computer solves the equation, $Q = h(T_{aw} - T_s)$, which determines the heating rate which should be realized at any instant. This value of heat flow can be considered the instantaneous "power required" from the heating system. The computer, in turn, compares the power required to the electrical power

5 "A Determination of the Laminar, Transitional, and Turbulent-Boundary-Layer Temperature-Recovery Factors on a Flat Plate in Supersonic Flow," by J. R. Stalder, M. W. Rubesin, and T. Tendeland, NACA Technical Note 2077, June, 1950.

6 "Effect of Pressure on Thermal Conductance of Contact Joints," by M. E. Barzelay, Kin Nee Tong, and G. F. Holloway, NACA Technical Note 3295, May, 1955.

7 "Strength of Metal Aircraft Elements," ANC-5, issued jointly by Departments of the Air Force, Navy, and Commerce, U. S. Government Printing Office, Washington, D. C., March, 1955.

8 "Tensile Properties of 7075-T6 and 2024-T3 Aluminum Alloy Sheet Heated at Uniform Temperature Rates Under Constant Load," by G. J. Heimerl and J. E. Inge, NACA Technical Note 3462, July, 1955.

9 "Determination of Transient Skin Temperature of Conical

Bodies During Short-Time, High-Speed Flight," by Hsu Lo, NACA Technical Note 1725, October, 1948.

10 "Turbulent-Heat-Transfer Measurements at a Mach Number of 1.62," by M. J. Brevoort and B. Rashis, NACA Technical Note 3461, June, 1955.

11 "An Account of Research Information Pertaining to Aerodynamic Heating of Airframe," by J. F. Brahtz and Allan Dean, WADC Technical Report 55-99, part 2, Bibliography, vols. 1–5, Wright Air Development Center, March, 1955.

12 "Behavior of a Cantilever Plate Under Rapid-Heating Conditions," by L. F. Vosteen and K. E. Fuller, NACA RM L55E20c, July 25, 1955.

13 "Induction Heating Methods of Aircraft Structures Testing," by R. W. Sampson and project staff, final report submitted by University of Florida to Wright Air Development Center under Contract AF18(600)-682, August 15, 1955.

14 "Theory and Experiment in the Solution of Structural Problems of Supersonic Aircraft," by N. J. Hoff, M. Bloom, F. V. Pohle, et al, WADC Technical Report 55-291, Wright Air Development Center, September, 1955.

15 "Combined Airload and Thermal-Shock Test Program," by V. J. Pleskacs and A. Runyon, final report submitted by the Glenn L. Martin Company to Wright Air Development Center under Contract AF18(600)-792, August, 1955.

16 "Rapid Radiant-Heating Tests of Multiweb Beams," by J. N. Kotanchik, A. E. Johnson, Jr., and R. D. Ross, NACA Technical Note 3474, May, 1955.

17 "Research Into the Application of Radiant Heating to the Structural Testing of Aircraft at Elevated Temperatures," by J. S. Berman, final report submitted by Research, Inc., Minneapolis, Minn., to the Wright Air Development Center, under Contract AF33(616)-2162, June 30, 1954.

18 "Simultaneous External Loading and Conduction Heating," by F. C. Wals and K. D. Wood, final report submitted by University of Colorado to Wright Air Development Center, under Contract AF 18(600)-396, February 1, 1955.

Some NACA Research on Effect of Transient Heating on Aircraft Structures

By J. E. DUBERG,[1] LANGLEY FIELD, VA.

A brief presentation is made of some of the radiant-heating apparatus developed by the National Advisory Committee for Aeronautics (NACA) to simulate aerodynamic heating of aircraft structures. Some results of the effects of thermal stresses on the stiffness and deflection of aircraft structures are demonstrated by tests incorporating the radiant-heating apparatus.

Introduction

IT IS generally recognized that the most important effect of aerodynamic heating is the existence of high temperature in the airframe. These high temperatures depreciate the structural properties of the materials of which the aircraft is made and in general lead to increased structural weight. It is also true that during the heating process there is a nonuniform distribution of temperature throughout the structure. The external surfaces heat the most rapidly and the internal structure lags behind an amount dependent upon the exact details of the construction. There arises from the nonuniform temperature distributions a distribution of thermal stresses.

The heating which a particular aircraft will experience depends upon its flight plan. It is possible, however, to make an estimate of the maximum heating an aircraft might experience at a given Mach number and altitude by computing the initial heating rate associated with an instantaneous acceleration to that Mach number at that altitude. In Fig. 1 is summarized the heating rate so computed for a wing structure at a distance of 1 ft from its leading edge. The wing skin is assumed to be at ambient-air temperature and as a result its maximum heating rates are independent of the details of the structure. It is clear from the figure that if such heating is to be simulated in the laboratory it is necessary to produce heating rates of the order of 100 Btu/sq ft-sec.

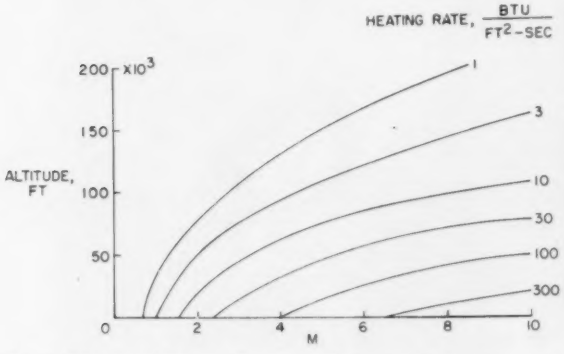

FIG. 1 MAXIMUM HEATING RATE AS A FUNCTION OF ALTITUDE AND MACH NUMBER FOR AN INSTANTANEOUSLY ACCELERATED WING SECTION

The law of radiation states that from a black body the heat output

$$q = 0.481 \left(\frac{T}{1000}\right)^4$$

in which q is measured in Btu/sq ft-sec and T is measured in degrees Rankine. Heat outputs of the order of 100 Btu/sq ft-sec can therefore be obtained by electrically heating elements to about 4000 R.

It is the purpose of this paper to discuss some of the techniques which the NACA has developed for producing such heating rates and to illustrate their applications by presenting the results of some tests

Heating Apparatus

Carbon-Rod Radiators. One of the most readily available materials that can be heated to sufficiently high temperatures to simulate aerodynamic heating is carbon. It is commercially available in a number of forms which can be made into heating elements. One of the most useful forms is that of the rod which can be so disposed to heat a given shape of surface. In Fig. 2 is shown a carbon-rod radiator which has been used to heat large flat surfaces. (A more complete description is given elsewhere.[2])

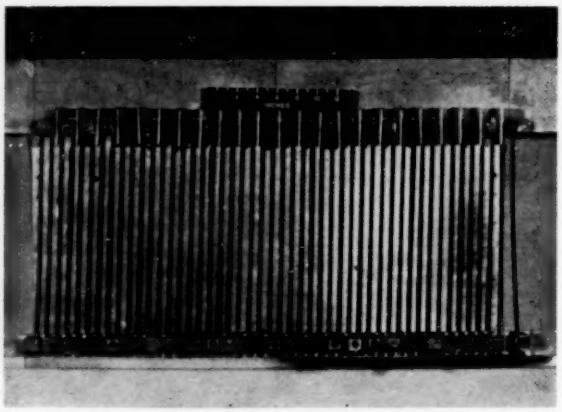

FIG. 2 HEAT RADIATOR CONSTRUCTED OF CARBON-ROD HEATING ELEMENTS

The basic heating element is a $^3/_8$-in-diam carbon rod operating at a temperature of about 4600 F. Electric power is supplied to the ends of the rods through machined-graphite terminal blocks. Rods in the radiator can be spaced as close as 1 in. and assembled in arrays sufficiently large to heat the test specimens. When heated to 4600 F, the useful life of the rods is about 3 min because of the considerable evaporation of the material from the rod.

[1] Chief, Structures Research Division, Langley Aeronautical Laboratory, National Advisory Committee for Aeronautics.

Contributed by the Aviation Division and presented at the Aviation Division Conference, Los Angeles, Calif., March 14–16, 1956, of THE AMERICAN SOCIETY OF MECHANICAL ENGINEERS.

NOTE: Statements and opinions advanced in papers are to be understood as individual expressions of their authors and not those of the Society. Manuscript received at ASME Headquarters, January 18, 1956. Paper No. 56—AV-16.

[2] "Rapid Radiant-Heating Tests of Multiweb Beams," by J. N. Kotanchik, A. E. Johnson, Jr., and R. D. Ross, NACA TN 3474, September, 1955.

Because the rods require 10 to 15 sec to reach operating temperature, a thermal shield is interposed between the specimen and the radiator during the heat-up time. The shield is withdrawn to expose the specimen to radiant heat and is replaced when the desired surface temperature on the structure is reached. The temperature of the radiating elements is so much higher than the surface of most test specimens that, as a result, surface temperatures of the specimen rise linearly with time during the heating period. If it is desired to maintain a given surface temperature after the initial heating, it is possible to do so by applying a reduced voltage to the rods and to continue to expose the specimen to heat.

Typical values of energy radiated by the rod are from 1 to 2 kw per inch of rod when they are new and about one half of these values at the end of their useful life. Fig. 3 shows the results of

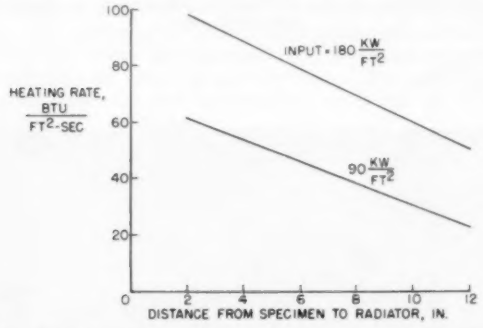

FIG. 3 EFFECT OF DISTANCE FROM RADIATOR ON HEATING RATES PRODUCED BY CARBON-ROD RADIATOR. RECEIVER: AN ALUMINUM-ALLOY SHEET COATED WITH FLAT BLACK LACQUER. RADIATOR SIZE: 20 × 24 IN.

tests made to determine the amount of energy received on a particular surface for two power inputs to the radiator shown in Fig. 2. A reflector made of $^1/_4$-in aluminum-alloy plate has been placed behind the radiator to direct the heat forward. The test specimen was an aluminum-alloy sheet 20 × 24 in. painted with flat black lacquer. Painting an aluminum surface with black lacquer increases the absorptivity by a factor of approximately 5. For the radiator-specimen arrangement used, the heat received on the surface decreased approximately linearly with distance. For close spacing of the radiator and specimen, efficiencies of the order of 50 per cent are obtained.

Although carbon-rod radiators are simple to construct and relatively inexpensive, they have the serious drawback that practical radiators are bulky and have considerable thermal inertia. As a consequence, they have been useful only for the production of high uniform rates of heating. A more desirable radiant heater would be one which had a sufficiently small thermal inertia so that its heat output could be controlled on a time scale suitable for actual aircraft.

Quartz-Lamp Heat Radiators. A heat radiator which has a low thermal inertia is the tungsten-filament lamp, type T-3, produced by the General Electric Company. This lamp is commercially available in nominal lengths of 10 and 25 in. and operating voltages of 220 and 440, respectively. They consist of a coiled tungsten-wire filament with a $^3/_8$-in-diam clear-quartz tube filled with argon gas.

The tungsten filament is supported at intervals and power is supplied through nickel terminal wires. A nominal rating of the lamps is 100 watts per in. and the life of the lamps is about 5000 hr. When the lamps are operated at approximately two times their nominal voltage, the power output is increased to approxi-

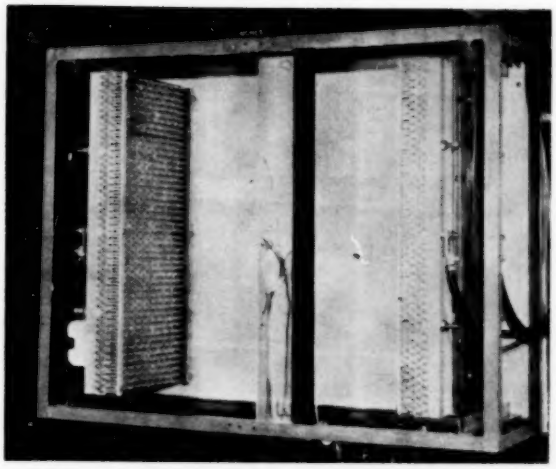

FIG. 4 HEAT-RADIATING UNITS CONSTRUCTED WITH A DOUBLE-BANK QUARTZ-LAMP HEATING ELEMENT

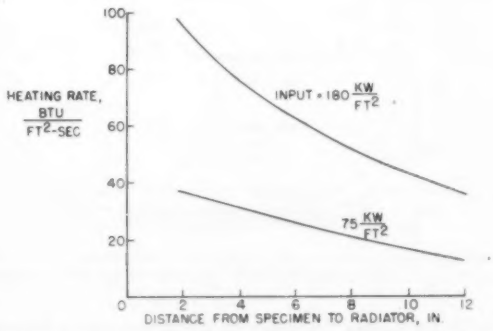

FIG. 5 EFFECT OF DISTANCE FROM RADIATOR ON HEATING RATES PRODUCED BY A DOUBLE-BANK QUARTZ-LAMP HEAT RADIATOR. RECEIVER: AN ALUMINUM-ALLOY SHEET COATED WITH FLAT BLACK LACQUER. RADIATOR SIZE: 10 × 24 IN.

mately 3 times the normal rating. There is a considerable reduction of average life, but it is then possible to obtain maximum heating rates of the order of those produced by the carbon-rod radiators.

A typical installation is shown in Fig. 4 in which the specimen is heated by two radiators, one on each side of the specimen. The radiators have been assembled into an array consisting of two rows of lamps. The lamps in each row are spaced at $^1/_2$-in. intervals and the lamps in the rear row are staggered one-half-lamp spacing with respect to the lamps in the front row. In each array a reflector is placed behind the lamps.

Control of the heat input to a test specimen can be achieved by varying the distance between the lamps and the specimen, the surface finish of the specimen, or the power input to the lamps. The fast response of the quartz lamps makes them readily adaptable to automatic control equipment and thus has made this type of heating equipment suitable for obtaining realistic temperature distributions and histories.

The heating rates experienced by a 10 × 24-in. black-lacquered aluminum-alloy sheet heated on one side by one of the radiator arrays of Fig. 4 are shown in Fig. 5. Maximum heating rates and efficiencies are of the same order as those obtained with the carbon-rod assemblies.

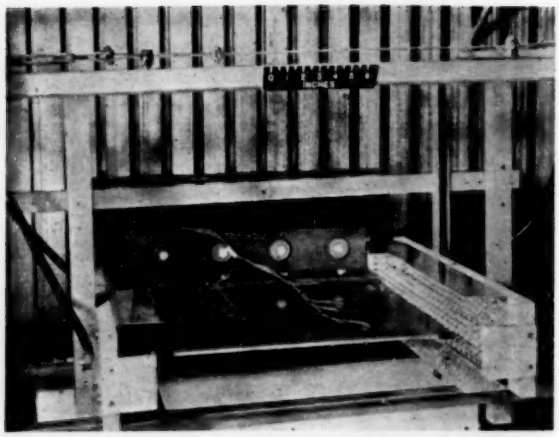

FIG. 6 VIBRATION TEST OF SOLID PLATE SUBJECTED TO RAPID HEATING BY RADIATION FROM QUARTZ-LAMP HEAT RADIATORS

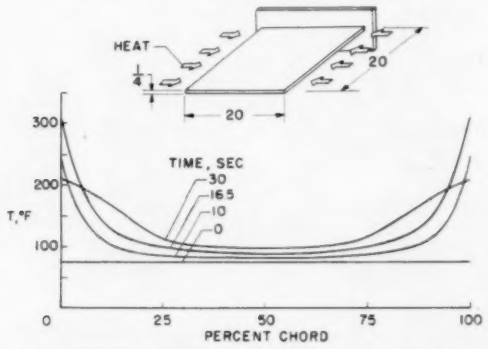

FIG. 7 CHORDWISE TEMPERATURE DISTRIBUTION OF A RADIANTLY HEATED PLATE

APPLICATIONS TO STRUCTURES RESEARCH

Vibration Tests of a Thermally Stressed Plate. A structural problem which can arise from thermal stresses is the reduction in effective stiffness of the structure against certain loadings. Probably the most severe occurrence of this effect takes place in thin solid plates of the form found in some missile wings. Thermal gradients can occur in such wings because of the variation of aerodynamic heat-transfer coefficients over the surface of the wings or because of the variation in thickness of such wings. An experimental verification of this effect has been given.[3] The experimental setup is shown in Fig. 6. A $^1/_8$-in. aluminum plate 20 in. square was cantilevered from a massive base. Two arrays of quartz-tube heaters arranged so as to heat the opposite unsupported edges developed thermal gradients in the wing similar to those encountered in flight. In flight the thermal gradients could have developed because of a chordwise change in thickness. In this experimental setup the chordwise variation is established by the location of the heaters at the leading and trailing edges.

The temperature distributions which were established in this plate are shown in Fig. 7. The wing was at room temperature at time zero. During the initial heating phase the temperatures of the leading and trailing edges rose rapidly to a maximum of 315 F in $16^1/_2$ sec at which time the heating was stopped. After the heating stopped, the leading and trailing edges cooled as the heat flowed into the interior of the plate. At time 30 sec, the temperature of the leading and trailing edges had fallen to 220 F and the interior had risen approximately 20 deg above room temperature.

[3] "Behavior of a Cantilever Plate Under Rapid-Heating Conditions," by L. F. Vosteen and K. E. Fuller, NACA RM L55E20c, July 25, 1955.

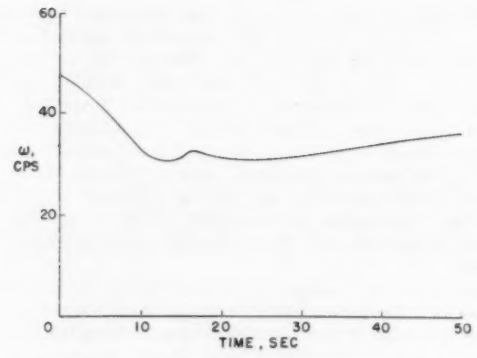

FIG. 8 HISTORY OF FIRST TORSION FREQUENCY OF RADIANTLY HEATED PLATE

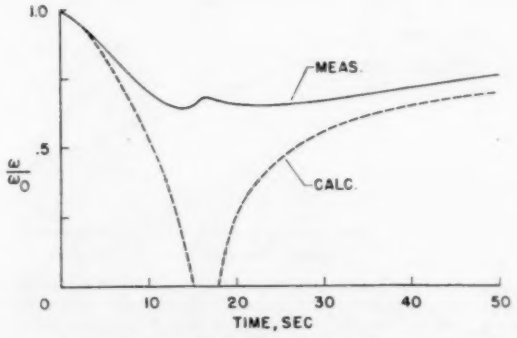

FIG. 9 COMPARISON OF EXPERIMENTAL FREQUENCY HISTORY OF HEATED PLATE WITH CALCULATED HISTORY FOR FIRST TORSION MODE

During the heating and cooling processes the plate was vibrated in its first torsion mode and its natural frequencies observed. The history of the variation of the first torsion frequency is shown in Fig. 8. It indicates that during the initial period of heating the torsion frequency decreases to a minimum and then rises slightly. During the period in which the wing is not exposed to heat, there is first a slight drop in frequency and then a gradual rise toward the original natural frequency as the temperature becomes more uniform.

A theoretical analysis of the plate behavior was made in which an approximate distribution of thermal stresses was obtained from the experimental temperature distribution. These stresses were incorporated in a vibration analysis of the plate based on small-deflection plate theory. A comparison of the results obtained by this theory with the experimental data is given in Fig. 9. Such an analysis predicts a rapid decrease in the plate-torsion frequency with heating, and further indicates that for this plate the temperature distribution was such as to decrease the torsion frequency to zero which is interpreted as plate buckling in the torsion mode. During the unheated phase the analysis predicts a gradual return to the original natural frequency. The experimental results agree with the analysis only during the initial heat-

ing and the latter stage of cooling. In the intermediate region in which the small-deflection analysis predicts almost a complete loss of stiffness, the plate still retains a considerable amount of its original stiffness. More recent studies have shown that this discrepancy is due to neglect of initial imperfections and finite displacements of the plate. Incorporation of these in the analysis substantially improves the comparison between the experimental and calculated results.

Buckling Tests of Box-Beam Covers. The wings of supersonic aircraft will experience thermal stressing as well as the usual load stressing. The wing skins during heating will be at a higher temperature than the interior web system. If the web is of the conventional solid-web type, compressive thermal stresses will exist in the wing skin. These compressive stresses when combined with load stresses will increase the stresses on the upper side of the wing and decrease those on the lower side. If the combination of load stresses and thermal stresses is sufficiently large, the possibility of buckling of the compression skins exists.

An experimental investigation in which thermal stresses and load stresses are combined has been made. The test setup employing carbon-rod heat radiators is shown in Fig. 10. A small

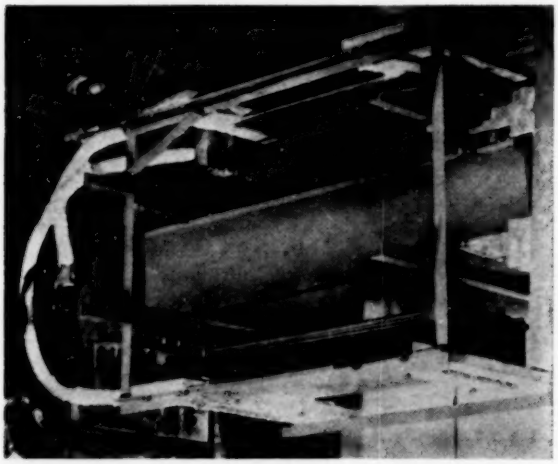

FIG. 10 TEST SETUP FOR RAPIDLY HEATED BOX BEAM LOADED AT TIP BY CONCENTRATED MOMENT

box beam was cantilevered from the support on the left and loaded at its tip on the right by a bending moment whose magnitude was fixed by dead-weight loading apparatus. The test procedure was to apply a moment which would produce a certain stress level. A shield was interposed between the heaters and the beam covers and the radiators brought up to temperature. The shield was withdrawn so as to expose both top and bottom covers to a practically constant rate of heating. Continuous records were made of the temperature distribution throughout the box as well as deflections of the beam. In Fig. 11 are shown two distributions of temperature around the perimeter starting at the web center line and extending to the center of the cover. These temperatures are those which exist when the compression cover buckled. The upper curve is for a test in which the dead-weight moment produced a nominal stress of 9.8 ksi and the lower curve when the nominal stress in the cover was 22 ksi. It is obvious that a much smaller temperature difference can produce buckling when the beam cover is more highly stressed.

The heating experienced by these beams is such that the covers are essentially at a uniform high temperature and the webs at a uniform lower temperature. A simple theoretical stress analysis

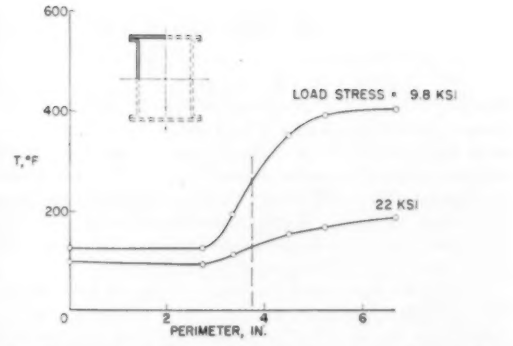

FIG. 11 TEMPERATURE DISTRIBUTION IN COVER AND WEB OF BOX BEAM AT BUCKLING FOR LOAD-STRESS LEVELS OF 9.8 AND 22 KSI

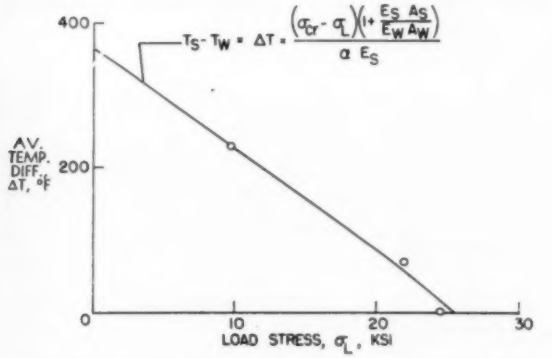

FIG. 12 COMPARISON OF EXPERIMENTAL AND THEORETICAL INTERACTION CURVE FOR BUCKLING UNDER COMBINED LOAD AND THERMAL STRESS

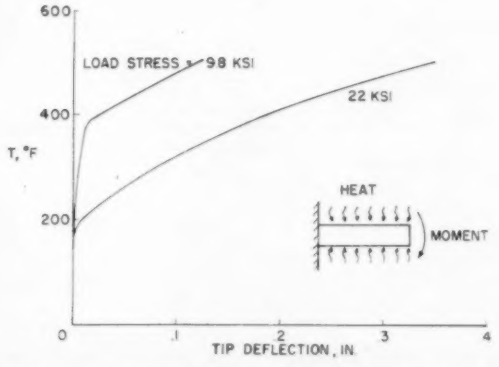

FIG. 13 ADDITIONAL DEFLECTIONS CAUSED BY HEATING AND BUCKLING OF BOX BEAM LOADED WITH CONSTANT TIP MOMENT

can then be made in which it is assumed that the thermal stresses are uniformly distributed at one stress level in the covers and at another in the webs. If these thermal stresses are added to the load stresses, a prediction can be made of the combinations of load stress and temperature differentials between web and cover that will produce buckling. These results can be expressed by an equation which states that at buckling the average temperature difference between skin and web is

$$T_S - T_W = \Delta T = \frac{(\sigma_{cr} - \sigma_L)\left(1 + \frac{E_S A_S}{E_W A_W}\right)}{\alpha E_S}$$

The first term of the numerator is the difference between the plate-buckling stress and the load stress; the second term contains the ratio of the products of Young's modulus and cross-sectional area for the cover plates and web. The denominator is the product of the coefficient of thermal expansion α and Young's modulus of the cover. A comparison of this simple analysis with the experimental buckling results obtained for these tests is shown in Fig. 12. The agreement is quite good.

An interesting aspect of the test results is the deflection of the beam during a heating cycle. In Fig. 13 is shown a plot of the variation of the tip deflection of the beam with skin temperature for two load-stress levels. Deflections do not include those that occurred when the beam was first loaded. During the first part of the heating of the covers little or no change in tip deflection occurs. This is to be expected because the heating is symmetrical top and bottom. When the cover buckles, further heating is accompanied by an increase in the tip deflection which is approximately proportional to the change in cover temperature. This change in deflection is due to the dissymmetry in the stiffness of the box that occurs when one cover buckles. As the box continues to heat beyond buckling the tendency is for the two covers to expand equally. The cool web is more effective in restraining the buckled cover than the unbuckled one. As a result, a curvature of the beam is produced which is approximately proportional to the excess of the cover temperature over the temperature at buckling.

Conclusion

The radiant-heating apparatus which has been described and the two applications to structures research which have been shown represent some preliminary efforts directed toward assessing the effects of thermal stresses on aircraft structures. More effort is needed on this problem and it is hoped that this presentation induces others to explore this field.

Utilization of Solar Furnaces in High-Temperature Research

By POL DUWEZ,[1] PASADENA, CALIF.

This paper presents a theoretical discussion of the performances of a parabolic-type solar furnace. Maximum temperature and maximum heat flux attainable at the focus are presented for furnaces of different diameter-to-focal length ratios. It is shown that the optical quality of the parabolic reflector is the most important factor for obtaining high heat fluxes. With present-day technology, the heat flux is limited to 600 Btu/sq ft/sec, but this figure could be raised to 2300 Btu/sq ft/sec by improving the optics.

Introduction

THE high heat fluxes to which supersonic aircraft are subjected bring up very complex thermal-stress problems to the aircraft designer. As usual in aircraft construction, theoretical stress analysis must be supplemented by carefully designed experiments. One of the new problems in the experimental field is to reproduce the very high heat fluxes in the laboratory before performing expensive flight tests. In order to achieve high heat fluxes through radiant energy, high-temperature sources are required. Since such sources must make use of solid materials, the highest attainable temperature is dictated by the melting point of these materials. Among the elements, graphite (sublimes at 3600 C) and tungsten (melts at 3380 C) are the most practical high-temperature radiators. Since the sun provides a source of radiant energy at a temperature of 5800 K, its use in connection with high flux problems offers definite possibilities.

Principles of Solar-Furnaces Design

The main function of a solar furnace is to collect a certain amount of sun radiation and concentrate it into a small area. This concentration may be achieved by the use of lenses or by means of parabolic reflectors. Although lens furnaces have been built (as, for example, the California Institute of Technology furnace designed by Hale and built in 1930), it is quite easy to demonstrate that from a practical point of view parabolic reflectors should be used, especially for large furnaces. This type of furnace only will be discussed in this paper.

When a parabolic reflector has its axis in the direction of the sun, an image of the sun is formed in the focal plane of the parabola. Knowing that the apparent diameter of the sun is 32 min of arc, the size d of the image (see Fig. 1) is given by

$$d = f \tan 16' = f/107.3 \quad [1]$$

in which f is the focal length of the parabola. A sharp image can be achieved, provided the ratio of the focal length to the diameter of the parabolic mirror is large, which is the case in an astronomical telescope. In a solar furnace this ratio should be as small as possible, since the highest possible concentration of radiation within the sun's image is desired.

Instead of focal length-to-diameter ratio, it is more convenient to consider the angular aperture of the mirror. The angle called θ in the following discussion is the angle between the axis of the parabola and a line joining the focus of the parabola to any point on the mirror (Fig. 1). At the rim, this angle has a certain value θ_r which determines the angular aperture. The rim angle may vary from 0 to a maximum of 90 deg.

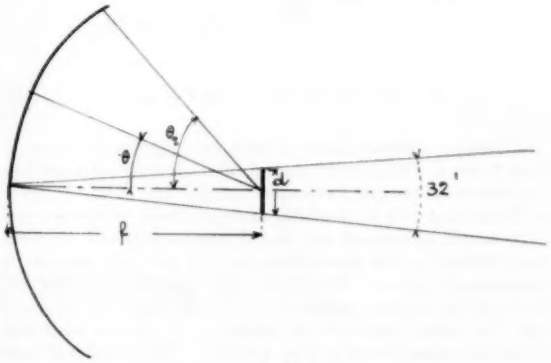

Fig. 1

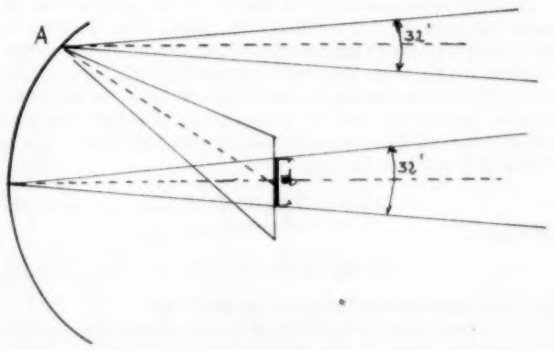

Fig. 2

Concentration Efficiency and Concentration Ratio. The contribution of any portion of the parabola to the total amount of radiation falling within the sun's image in the focal plane may be computed. If θ is the angle corresponding to a point A, Fig. 2, a cone of light with an angle of 32 min falling on the parabola is reflected as a 32-min-angle cone whose axis passes through the focus of the parabola. The intersection of this reflected cone with the focal plane is an ellipse whose large diameter is greater than the diameter of the sun's image. Hence some of the light contributed by an element of mirror around point A is falling outside the sun's image. For a furnace having a given focal length-to-diameter ratio, or a given rim angle θ,

[1] Professor of Mechanical Engineering, California Institute of Technology.

Contributed by the Aviation Division and presented at the Aviation Division Conference, Los Angeles, Calif., March 14–16, 1956, of The American Society of Mechanical Engineers.

Note: Statements and opinions advanced in papers are to be understood as individual expressions of their authors and not those of the Society. Manuscript received at ASME Headquarters, January 18, 1956. Paper No. 56—AV-17.

it is possible to calculate the ratio of the amount of energy received within the sun's image to the total energy received on the focal plane. This ratio, designated by η_c, is called the concentration efficiency.

To compute the concentration efficiency it is necessary to define the physical conditions at the focus. It is indeed obvious that any solid body placed around the focus will have an effect on the flux received since this body will remit some of the radiation it receives. The emissivity coefficient of the solid body will therefore enter into the computation. Two simple cases will be considered in the following discussion. In the first case, a cavity behaving like a black body (emissivity = 1) is placed at the focus and has a circular opening with a diameter equal to that of the sun's image. In the second case, a flat-plate receiver is placed in the focal plane and is assumed to behave according to Lambert's law $\epsilon = \epsilon_n \cos\theta$, in which ϵ is the emissivity coefficient in a direction θ and ϵ_n is the emissivity coefficient in a direction normal to the surface. In these two cases the concentration efficiencies are given by[2]

$$\eta_c = \left(\frac{1 + \cos\theta}{2}\right)^2 \quad \ldots\ldots [2]$$

$$\eta_c = \frac{\epsilon_n}{6}(1 + \cos\theta)(1 + \cos\theta + \cos^2\theta) \quad \ldots\ldots [3]$$

A graphic representation of these two relations is given in Figs. 3 and 4. As the rim angle θ_r of the furnace increases, the concentration efficiency decreases rapidly and is of the order of 20 per cent only for a 90-deg-angle parabola.

It should be pointed out that Equations [2] and [3] have been derived on the assumption that the parabolic reflector is geometrically perfect. Practically, the larger the rim angle, the more difficult it becomes to achieve a high degree of accuracy, and the actual concentration efficiency is always somewhat below the values shown in Figs. 3 and 4. This question of ideal versus actual conditions in solar furnaces will be discussed later.

Another useful parameter in evaluating the performances of solar furnaces is the concentration ratio. This number is defined as the ratio of the heat flux within the sun's image at the focus to the heat flux that would be reflected by a plane mirror facing the sun and having the same reflectivity as the parabolic mirror. As in the case of concentration efficiency, the concentration ratio depends on the conditions at the focus. For a black-body cavity it is given by

$$c = 46.2 \times 10^3 \sin^2\theta \quad \ldots\ldots [4]$$

and by

$$c = 30.7 \times 10^3 (1 - \cos^2\theta) \quad \ldots\ldots [5]$$

for a flat-plate receiver following Lambert's law.

A graph showing the variation of the concentration ratio with rim angle is shown in Fig. 3 for a black-body cavity. For a flat-plate receiver, the curve shown in Fig. 4 has been computed assuming $\epsilon_n = 1$ and hence represents the most favorable conditions at the focus, leading to the maximum concentration ratio.

Maximum Attainable Temperature. The maximum temperature that can be obtained in a solar furnace is also of great interest and can be computed. Although the actual temperature of the sun is several millions of degrees, the radiation spectrum received near the earth corresponds to that of a black body at 5800 K. That is called the effective temperature of the sun. In terms of this temperature T_s, the maximum temperature attainable in a parabolic-type furnace is given by

$$T_m = \frac{T_s}{14.65}(\eta c)^{1/4} = T_s \eta^{1/4} (\sin\theta)^{1/2} \quad \ldots\ldots [6]$$

for a black body

$$T_m = \frac{T_s}{14.65}\left(\frac{\eta c}{{}^2/_3\,\epsilon_n}\right)^{1/4} = T_s[\eta(1 - \cos^3\theta)]^{1/4} \quad \ldots\ldots [7]$$

for a flat-plate receiver.

In these equations η is the only symbol which has not been described previously and requires some explanation. Assuming that a solar furnace could be built outside the earth atmosphere and with a parabolic surface having a perfect reflectivity, η would be equal to unity. In this case the flux received by the parabola would be the solar constant $p_0 = 2$ cal/cm²/min and this flux would be reflected without losses. Actually, the flux received on the earth p is less than the solar constant because of atmospheric absorption and the reflectivity of the mirror is less than 1. The coefficient η is defined as the product of p/p_0 and the reflectivity coefficient of the parabolic mirror. If additional reflecting surfaces are involved in the construction of the furnace (as, for example, when a flat mirror is used to track the sun), the reflectivity coefficients of these surfaces also enter into the product and further decrease the value of η.

Curves showing the variation of the maximum attainable temperature with the rim angle of a parabolic furnace are reproduced in Fig. 3 for a black body and in Fig. 4 for a flat-plate receiver. In these two graphs η has been taken as unity, which means that the temperatures shown are those that would be obtained with a geometrically perfect parabola, having 100 per cent reflectivity and located outside the earth atmosphere. Under these ideal conditions the temperature attained with a 90-deg rim-angle furnace is the effective temperature of the sun. The maximum flux obtainable within the sun's image, also under these ideal conditions, may be computed by multiplying the solar constant by the concentration ratio corresponding to a rim angle of 90 deg. This flux is 92,000 cal/cm²/min (5640 Btu/sq ft/sec) for a black body and 62,000 cal/cm²/min (3800 Btu/sq ft/sec) for a flat-plate receiver. These flux values, as well as the temperature of the sun, are maximum values that no solar furnace will ever reach.

Estimated Practical Performances of Parabolic Furnaces

The most important factors which were idealized in the foregoing analysis are atmospheric absorption of solar radiation, reflectivity of the parabolic mirror, and geometrical accuracy of the parabolic surface. The effect of atmospheric absorption and of reflectivity are easy to discuss because they can be measured.

Atmospheric absorption is just the ratio of the actual flux received at the furnace site to the solar constant p_0. The flux received can be measured with a pyroheliometer. This instrument should be designed properly so that it measures the flux at normal incidence and does not include the diffused sky radiation. It appears that the atmospheric absorption may represent about 20 per cent in many parts of the world, so that flux on the earth may be about 0.80 p_0. The reflectivity of the mirror also can be measured and a coefficient as high as 0.85 is conceivable. As a consequence, a practically attainable value for the coefficient would be $0.80 \times 0.85 = 0.68$. With a geometrically perfect parabolic reflector, the actual flux within the sun's image may therefore be 0.68 times the flux computed on the basis of the analysis presented early in the paper. The

[2] A more detailed study has been presented in a report "Theoretical Considerations on Performance Characteristics of Solar Furnaces," by Eugene Loh, Pol Duwez, N. K. Hiester, and T. E. Tietz, prepared by Stanford Research Institute, under the sponsorship of the Office of Scientific Research, Air Research and Development Command, USAF, Baltimore, Md.

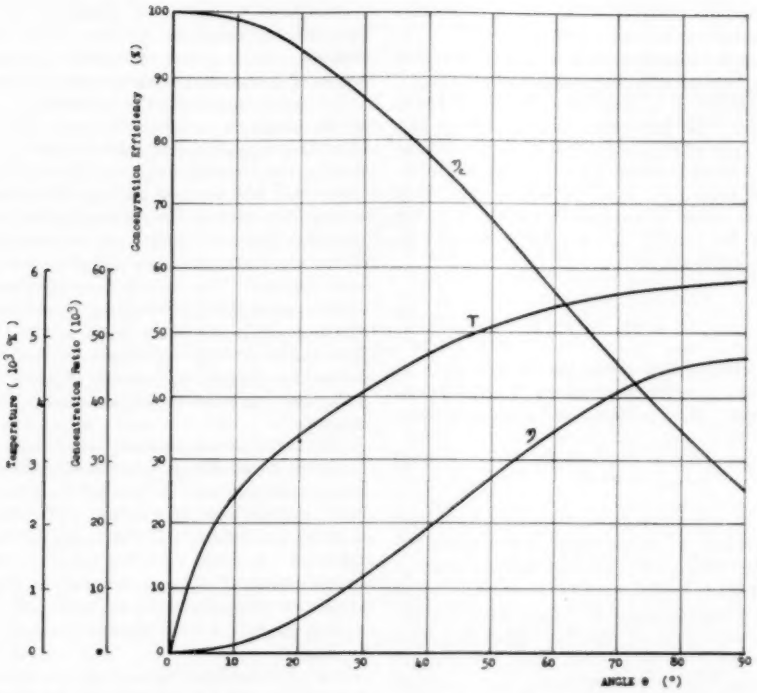

FIG. 3 CONCENTRATION EFFICIENCY η_c, CONCENTRATION RATIO η, AND MAXIMUM ATTAINABLE TEMPERATURE T AS FUNCTIONS OF θ FOR A BLACK-BODY CAVITY AT THE FOCUS

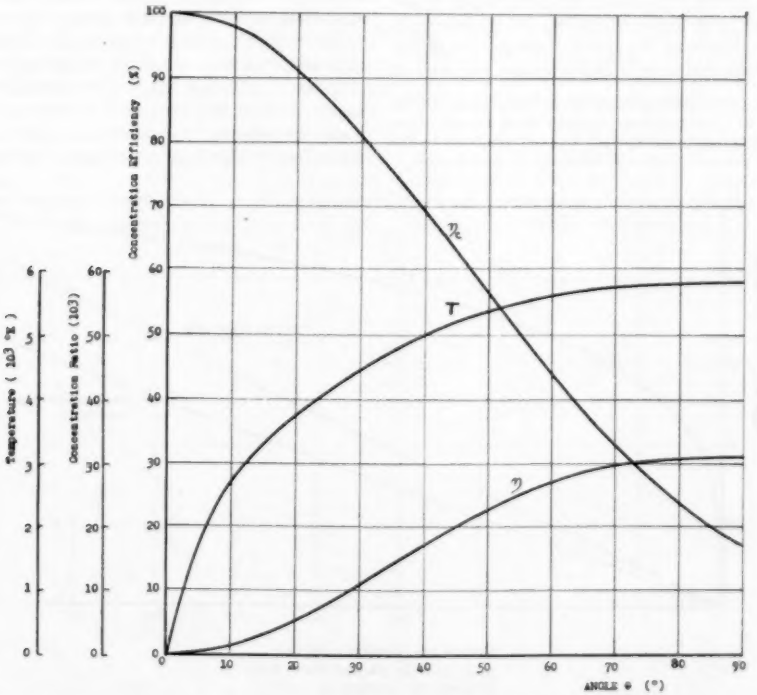

FIG. 4 CONCENTRATION EFFICIENCY η_c, CONCENTRATION RATIO η, AND MAXIMUM ATTAINABLE TEMPERATURE T AS FUNCTIONS OF θ FOR A FLAT-PLATE RECEIVER AT THE FOCUS

maximum temperature obtainable will be 4900 K; namely, 0.845 times the temperature under ideal conditions.

The effect of the geometrical perfection of the parabolic mirror is not easy to estimate, because it is not possible mathematically to define the optical quality of a parabolic reflector. When a furnace is built, however, the flux within the sun's image can be measured, and the ratio of this actual flux to the theoretical flux that should be obtained knowing the conditions of atmospheric absorption and reflectivity, may be determined. This ratio may be called the index of geometrical perfection of the parabolic mirror. On the basis of the analysis presented previously, this ratio γ is expressed by

$$\gamma = \frac{p_{act}}{\eta\ 92.4 \times 10^3 \sin^2 \theta} \quad [8]$$

in which p_{act} is the measured flux within the sun's image. If, instead of measuring the flux, the temperature T_{act} of a blackbody cavity is measured, γ may be expressed by the equation

$$\gamma = \left(\frac{T_{act}}{T_s}\right)^4 \frac{1}{\eta} \frac{1}{\sin^2 \theta} \quad [9]$$

This second method of measuring γ is not recommended for two reasons: (*a*) Equation [9] is valid only if no heat is lost through the walls of the cavity, a very difficult condition to satisfy in practice; (*b*) the index γ is very sensitive to small errors on the temperature since it is proportional to the fourth power of the temperature. The measurement of the flux within the sun's image is free from these two objections. This measurement can be made with a water-cooled calorimeter and with a minimum of heat losses, and in addition, the index γ varies linearly with the measured flux.

It is unfortunate that no data have been published on the measurements of the actual flux within the sun's image of the few furnaces which are presently in operation, and consequently it is very difficult to determine the order of magnitude of the coefficient γ for existing furnaces.[3] Temperatures obtained in various furnaces have been measured (or generally estimated) by several investigators, but because of the fourth-power relationship, this is a very unreliable method for evaluating the degree of geometrical perfection of a mirror.

In order to emphasize the importance of the optical accuracy of the mirror, a numerical example will be discussed briefly. First, it is apparent from the curves shown in Figs. 3 and 4 that beyond a certain angle θ of about 60 deg the concentration ratio does not increase rapidly. Practically this increase is even smaller because the accuracy of the parabola is the poorest when the angle θ is large. It will therefore be assumed that 60 deg is a practical maximum value for the rim angle of a parabolic furnace. For such a furnace, with an atmospheric-absorption coefficient of 0.80 and a reflection coefficient of 0.85, the flux within the sun's image and the maximum attainable temperature are plotted versus the index of geometrical perfection in Fig. 5. The linear relationship between flux and γ is just a graphical representation of the definition of the index γ.

The curve of temperature versus index of geometrical perfection γ shown in Fig. 5, is a striking illustration of the fourth-power radiation law. It is indeed quite interesting to see that with a rather poor geometrical perfection (index of the order of 0.15) temperatures in the neighborhood of 3000 K can be achieved. In order to cover the range from 3000 to 4600 K, which would be of great interest for fundamental studies of refractory compounds like carbides, nitrides, and borides, the optical quality of the reflecting parabola must be considerably increased.

For the aeronautical engineer interested in obtaining high heat fluxes, the optical quality is also of the utmost importance. A solar furnace capable of a temperature of 3000 K is not very spectacular in so far as flux is concerned, since, according to the curves of Fig. 5, the flux within the sun's image would be only 7000 cal/min/cm² (420 Btu/sq ft/sec). On the other end of the scale, if an index of geometrical perfection 0.75 could be achieved, the flux would be 35,000 cal/cm²/min (2100 Btu/sq ft/sec). This last figure is interesting to consider as the very maximum heat flux that could be obtained with a high-accuracy parabolic reflector. Higher figures that may have appeared in semiscientific literature must be regarded as highly speculative.

[3] Complete and accurate measurements have been reported by J. Farber at the Tucson Conference on Applied Solar Energy, Oct. 31, 1955, but the manuscript of this lecture was not available to the author at the time the present paper was required for publication.

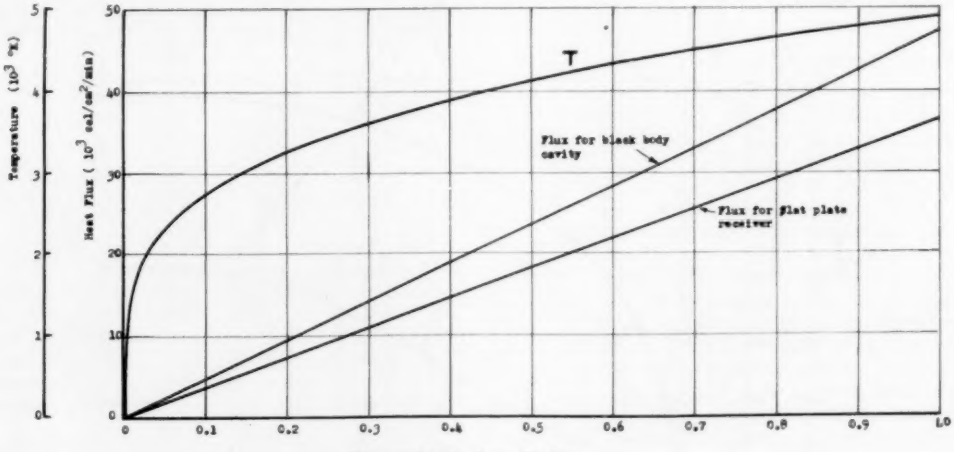

Rim angle of mirror, 60 deg
Atmospheric transmission, 0.80
Reflectivity coefficient, 0.85

FIG. 5 HEAT FLUX AND MAXIMUM ATTAINABLE TEMPERATURE AS FUNCTIONS OF INDEX OF GEOMETRICAL PERFECTION OF A PARABOLIC MIRROR

Effect of Solar-Furnace Size on Performances

In the preceding analysis all the parameters involved in solar-furnace design are dimensionless. Only one of these parameters, namely, the index of geometrical perfection, is seriously affected by size. A parabolic reflector may be made of one piece, or may be divided into segments. The one-piece reflector (either glass or metal) cannot be built beyond a certain size. At the present time there are glass parabolic reflectors up to 6.5 ft diam and one aluminum reflector of 10 ft diam. The cost of such units must rapidly increase with size and beyond a certain diameter (which might be around 15 ft), the one-piece reflector is practically impossible to build.

The performances of the one-piece-reflector furnaces which have been in operation are difficult to establish because of the lack of flux measurements and the unreliability of the estimated temperatures. It appears improbable, however, that the existing furnaces have an index of geometrical perfection greater than about 0.35. Better furnaces, with improved optical quality, could certainly be built with diameters up to 200 in. If the index of geometrical perfection could be increased to 0.80, both the temperature (4600 K) and the heat flux (37,500 cal/cm²/min) that could be obtained, would make such a furnace an ideal tool for fundamental research on highly refractory materials.

Because of the limitation in the sun's image size, one-piece solar-furnace reflectors may be of little interest to the aircraft engineer who wants to subject rather large structural elements to high heat fluxes. The size of the image being about 1/200 of the diameter of the parabola (assuming the rim angle to be 60 deg) the limiting size would be about 1 in. for a 200-in. reflector. Relatively large parabolic reflectors must therefore be considered for testing structural elements. The parabola in this case must be built of segments. The largest furnace of this type at the present time has been built by F. Trombe at the Laboratoire de l'Energie Solaire in Mont-Louis in the French Pyrennées. The parabolic reflector is about 35 ft in diameter and is made of 3500 individual glass elements. The size of the sun's image is approximately 2.5 in. diam. Although the measured flux has not been reported in the literature it may be estimated to be less than 9000 cal/cm²/min (550 Btu/sq ft/sec) since the maximum temperature reported by Trombe is about 3300 K. On the basis of these figures, the index of geometrical perfection of the furnace would be 0.20 or less (see Fig. 5). These relatively poor focusing conditions in a larger furnace might be improved, but higher efficiency will complicate the design of the furnace and considerably raise the cost of construction.

Conclusions

Solar furnaces may be used for fundamental research on high-temperature materials or for studying the effect of high heat fluxes on materials and structures. For high-temperature-material research, maximum performances in reaching the highest possible temperature are required. A research furnace for this purpose may be relatively small (up to 10 ft at present and perhaps up to 15 ft in the future) with a sun's image less than 1 in. in diameter. In the existing furnaces, it appears that temperatures up to about 3500 K have been reached. Many of the most interesting materials which cannot be melted in more conventional laboratory furnaces would require still higher temperatures. The value of solar furnaces as research tools would be greatly increased if they could produce temperatures up to 4600 K. As shown in the paper, this goal can be achieved only by increasing the optical quality of the reflecting parabolic mirror. It is believed that there is no physical limitation in building such high-quality mirrors, but their cost might be very high.

High temperature in a solar furnace means high heat flux, and the high-performance furnace capable of reaching 4600 K would have a flux of 37,500 cal/cm²/min (2300 Btu/sq ft/sec). Such a small furnace, however, with a sun's image diameter equal at the most to 1 in. may not be of great interest to the aircraft structural engineer. A high heat-flux area of at least 6 in. and possibly 12 in. (this would mean a 200-ft parabolic mirror) may be required before solar furnaces are considered useful tools in solving structural problems associated with high-speed aircraft. For large furnaces of this type, the present state of the art indicates that the maximum flux attainable is about 9000 cal/cm²/min (550 Btu/sq ft/sec). It would not be wise to say that these performances cannot be improved by better design, but because of the complete lack of experience in solar-furnace construction in this country, it is probable that many costly and frustrating attempts to build large high-performance furnaces will be made before successful results are obtained.

Acknowledgment

The author wishes to thank Dr. Eugene Loh of the Stanford Research Institute, to whom he is indebted for the analytical work on solar-furnace performances.

Description and Prediction of Human Response to Aircraft Thermal Environments

By CRAIG L. TAYLOR,[1] LOS ANGELES, CALIF.

The power and weight requirements of refrigeration equipment constitute a real limitation of aircraft performance at the present stage of aircraft development from the standpoint of thermal tolerance. Since man is the weak link among the components of the aircraft system, a clear understanding of the responses of humans to heat is vital to the achievement of an optimal balance between air conditioning and performance characteristics of the airplane. To obtain the highest combined fitness of man and aircraft for the exigencies of modern air warfare, it is necessary to abandon the time-honored concept that human thermal comfort must be assured, and to substitute the principle of maintaining the physiological and performance effectiveness of the crew for the limited period of the particular flight duration. When this duration is to be many hours, the efficiency criterion will probably demand an environment which also meets the traditional comfort standards.

The Biotechnical Problem

THE man-in-aircraft problem involves a constellation of systems, of which man himself is the most complex. It is necessary to seek the maximum idealization of these interacting factors so that a practical solution can be reached. To a satisfactory approximation the thermal variables can be separated from other environmental influences, such, for example, as oxygen pressure, noise or lighting, and attention focused upon the man-clothing-environment system. Briefly, the factors are as follows:

Environmental:

- Air and wall temperatures
- Rate of air movement and air pressure
- Wall emissivities and geometric configuration
- Water-vapor pressure (humidity)
- Solar radiation

Bodily state:

- Posture, activity level, and metabolic rate
- Sweat output and circulatory heat convection
- Resultant surface and deep body temperatures

Clothing:

- Thermal insulation
- Vapor-diffusion resistance
- Air permeability
- Degree of ventilation via clothing apertures

We can deal with these factors in a quantitative fashion, by determining a body thermal parameter with which can be related, on the one hand, the heat and mass-transfer processes in the system and, on the other hand, the physiological and psychological state. Finally, of course, it must be possible to predict the degree of thermal strain in the man and the probability of his satisfactory performance under this strain.

Bodily Thermal Responses and States

For an understanding of the problem it is necessary to outline some of the modes of thermal response of the body, and the physiological states resulting from a range of thermal loads including those which are both within and beyond its adaptive capacity.

Metabolic Rate and Work. Internal (or metabolic) heat production is a function of many physiological conditions and stimuli but the principal controlling factor is the level of activity. It is obvious that as metabolic rate is elevated through activity, a large part of the task of heat regulation will be to transfer this heat outward to the skin and to convey it away by the heat-loss mechanisms. These facts are graphically displayed in Fig. 1

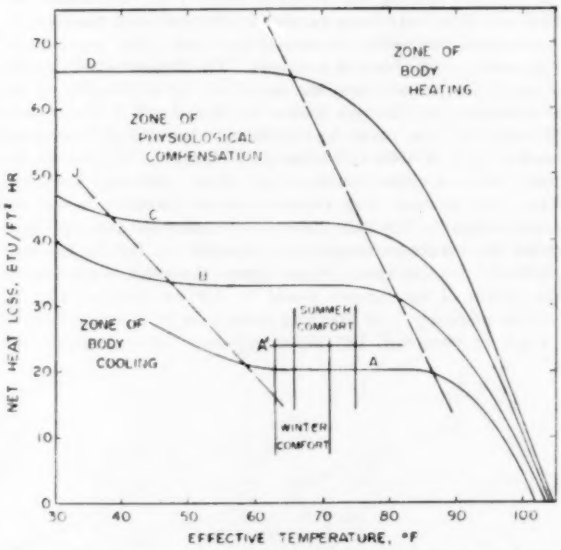

FIG. 1 COMFORT AND TOLERANCE CHART FOR REST AND WORK CONDITIONS

(Activity levels are *A*, sitting at rest, 20 Btu/sq ft-hr; *A'*, manual work, sitting, 24 Btu/sq ft-hr; *B*, light work, standing, 33 Btu/sq ft-hr; *C*, moderate work, 42.5 Btu/sq ft-hr; *D*, hard work, 65.5 Btu/sq ft-hr. Net heat loss = $q_m \pm q_s$.)

where it is shown that activity level sets the metabolic level and the required heat exchange. Curve *A'*, at 24 Btu/sq ft hr, is representative of a pilot's energy expenditure.

Modes of Heat Exchange With Environment. From a purely physical point of view, the human body can be considered to be a warm body of irregular geometry, behaving approximately as a Planckian radiator, and having varying moistness of surface.

[1] University of California.

Contributed by the Aviation Division and presented at the Aviation Division Conference, Los Angeles, Calif., March 14–16, 1956, of THE AMERICAN SOCIETY OF MECHANICAL ENGINEERS.

NOTE: Statements and opinions advanced in papers are to be understood as individual expressions of their authors and not those of the Society. Manuscript received at ASME Headquarters, January 5, 1956. Paper No. 56—AV-3.

The equations for radiant, convective, and evaporative heat-transfer rates are of familiar and conventional form, and introduce no basically new concepts. However, coefficients must be evaluated experimentally and, although many measurements have been made, it cannot be said that a full quantitative formulation has yet been achieved. Therefore, because of the complex of interacting factors, maximum dependence must be placed upon experimental studies in which both sweat rate and evaporation rate are separately determined.

Physiological Regulation of Thermal Exchanges. The possession of a body-temperature regulation system is one of the important evolutionary acquisitions of man. This system is capable of varying the internal-heat production, the heat conduction within the body, the skin temperature, and the sweat output, to preserve a near constancy of deep body temperature. The central mechanisms of control may, in very elementary terms, be compared to a dual thermostatic control which activates both heater and cooling units. Its setting is about 98.6 F in resting and mild-activity conditions, but apparently shifts to about 102 F in heavy exercise. The "thermostat" is, in fact, a nerve center or centers within the brain, controlled by nervous sensing elements which react both to central blood temperature and to body-surface temperature. Effector nerves actuate skin blood-vessel constrictor-dilator responses, sweat-gland output, shivering, and so on, to bring about the indicated correction of body thermal state.

Various temperature functions come into play when high thermal stresses are placed upon the body. Shivering occurs when mean body temperature is depressed about 2 deg F below the "neutral" condition of deep and skin temperatures of 98.6 F and 92 F, respectively. As a result, metabolic rate is increased in an attempt to supply cooling demand with greater heat flow and thus preserve the body temperature. At high combinations of temperature and humidity, a general increase of heart output and blood circulation strives vainly to convey heat to the surface, and thereby to ameliorate the thermal stress. Beyond the effective limits of body-temperature regulation, the symptoms of thermal breakdown occur.

The Thermal "Steady States." Actually, the human body does not exhibit a precisely steady state in any of its processes, and the biological usage of the term is of limited validity. In thermal matters, therefore, one must be content with a relative approach to the steady state. As shown in Fig. 1, the zone of physiological compensation is quite broad, and defines conditions which man can tolerate for many hours, if not indefinitely.

One may define an even narrower zone of thermal "neutrality" and relative comfort. A large amount of investigation has been made by psychologists, physiologists, and engineers to define the temperature, humidity, and air-movement conditions under which persons are thermally comfortable. It is evident that the results of such studies provide specifications for heating, ventilating, and air-conditioning practice. Over a period of 30 years the ASHVE laboratory has made important contributions to this subject, and the "Effective Temperature Scale and Comfort Zones" have become the standards of practice in the United States and many other parts of the world.[2] The comfort zones defined by these studies differ slightly from summer to winter.

Beyond the comfort zones but within the zones of compensation are the states of compensated hyper and hypothermia. Under heating and cooling loads of considerable magnitude, the body achieves a near-steady state of temperature, lasting for hours. The thermal state ranges far beyond the conditions for comfort, but the body temperatures, whether low (hypothermia) or high (hyperthermia), are kept at fairly constant level and compensation may be said to be achieved. The environmental and activity conditions under which these thermal states occur are difficult to define precisely, since clothing, health, acclimatization, etc., are additional modifiers.

The Thermal-Transient States. When the heat load or cooling load upon man reaches magnitudes which exceed the capacity of the thermal regulatory system to achieve compensation, there will ensue rates of body thermal storage, positive or negative, which continue until the voluntary tolerance limit is reached. If there is no escape from these extreme conditions, or if one persists because of unusual motivation and in spite of intense thermal distress, the phenomena of hyper or hypothermic breakdown, collapse, and bodily injury occur. Beyond these generalizations the detail and pattern of events in heat and cold differ markedly.

Of the transient zones the hyperthermic zone is of prime interest here. Up to a point, which will be defined later, the human body can withstand the rising internal temperature. Its regulatory mechanisms, including sweating and increased blood circulation strive to compensate for the unbalanced heat load, but ultimately fail so that performance decrement and physiological collapse ensue.

Biothermal Analysis System

Graphic displays of human response under thermal and activity loads, such as that shown in Fig. 1, while presenting a part of the picture, have a number of serious shortcomings. For example, the effects of radiant exchange and of clothing, other than those of the original experiments, cannot be calculated. Moreover, a more detailed treatment of the transient zones is necessary to formulate time-tolerance curves.

The analysis system, reported by Blockley, et al.,[3] is based upon a long series of experimental studies and the appropriate heat-transfer formulations, both in terms of the physical environment and body heat storage. The physiological and psychological condition of the man can then be expressed graphically by means of tolerance curves derived from correlation with heat storage.

Environmental Variables. The group of environmental variables can be combined into two quantities, namely, a reference operative temperature and an operative transfer coefficient, by a procedure which is outlined in Fig. 2. In the basic reference these steps are presented in detail, with computation aids in the form of charts and tables to simplify the procedure. An illustrative example must suffice here: Given the conditions of cabin wall temperature 200 F, cabin air temperature 100 F, cabin altitude 8000 ft, air velocity over the man 200 fpm, vapor pressure 0.6 in. Hg standard solar radiation load.

Reference operative temperature = 149 F

Operative transfer coefficient = 3 Btu/sq ft hr deg F

These two quantities, together with the clothing insulation and skin temperature, provide the means for calculating the rate of heat flow to the body by radiation and convection. The total heat load is the sum of this inflow and the metabolic heat production of the body itself. Total heat load is linearly related to reference operative temperature as shown in Fig. 3. The rate of heat loss can be computed from a knowledge of the resistance to vapor diffusion of the clothing and surrounding air, the vapor pressures and temperatures existing in the air and at the skin,

[2] "Heating, Ventilating, and Air Conditioning Guide," American Society of Heating and Ventilating Engineers, New York, N. Y., 1955.

[3] "The Prediction of Human Tolerance for Heat in Aircraft: A Design Guide," by W. V. Blockley, J. W. McCutchan, and C. L. Taylor, WADC Technical Report No. 53-346, Wright Air Development Center, 1954

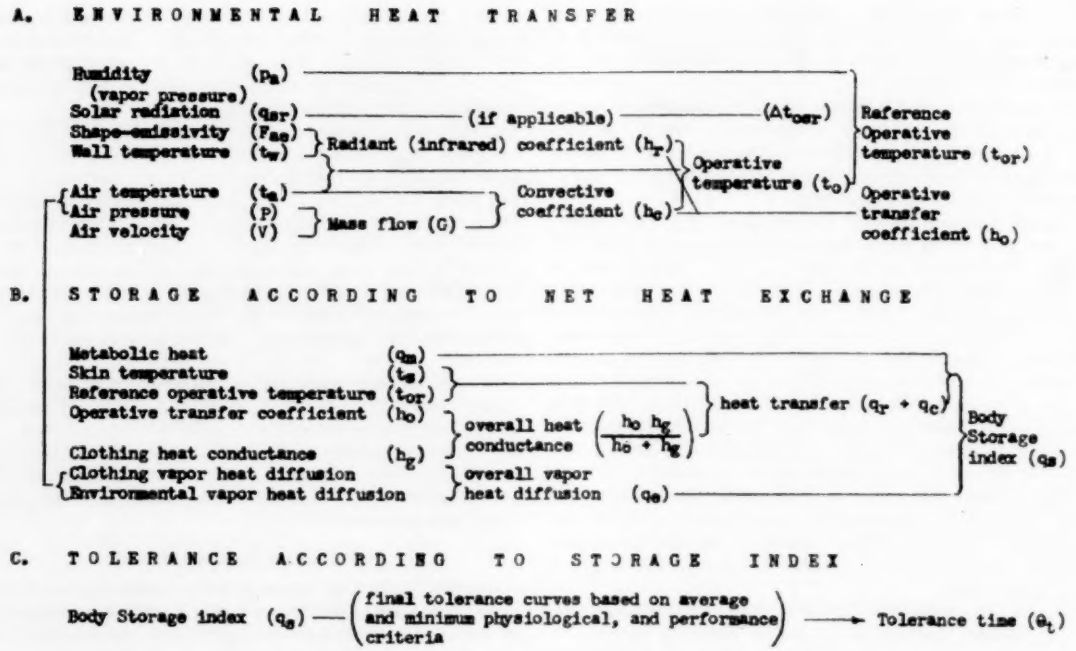

FIG. 2 DESCRIPTIVE OUTLINE OF BIOTHERMAL SYSTEM

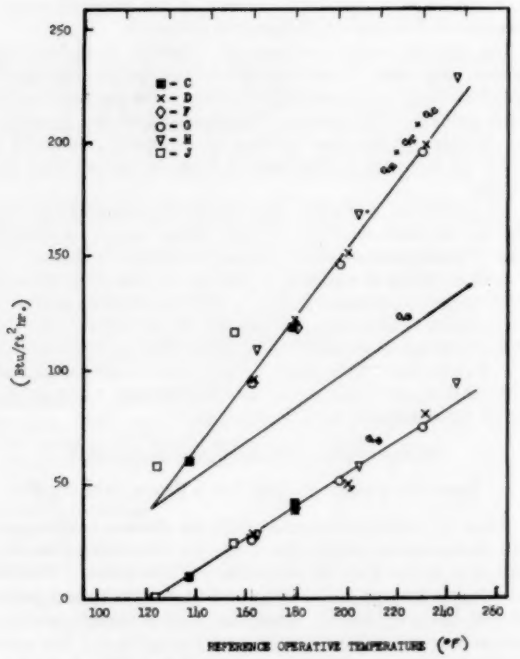

FIG. 3 MAJOR HEAT-EXCHANGE TERMS ACCORDING TO REFERENCE OPERATIVE TEMPERATURE
(Mean values for UCLA experimental series C through J shown by characteristic symbols.)

and the diffusivity of water vapor in air for the particular pressure, altitude, and temperatures concerned. The difference between heat load and heat loss represents heat storage, which may be used as a general body parameter for the prediction of tolerance limits.

Body Heat-Storage Index. It has been found that exposures to widely varied thermal-stress conditions can be correlated on the basis of the rate of rise of body temperature. Use of the standard weighting factors, two thirds and one third for rectal and average skin-surface temperature, respectively, appears to give a satisfactory approximation of the average body temperature. For exposures in which the heat stress is tolerable only for an hour or less, body temperature thus computed rises linearly with time after a brief initial adjustment period. When environments are compared, it is found that the rate of rise of body temperature is a linear function of reference operative temperature, all other conditions such as clothing, activity level, and so on, being equal. Rate of rise of body temperature is easily converted to a rate of heat storage by applying values for body mass, area, and specific heat; we prefer to term the resultant number a body heat-storage index, since it cannot be proved that the particular weighting factors used to obtain body temperature are precisely correct and valid for all transient-temperature changes. Fig. 3 shows the basic experimental relation of heat storage, calculated from body temperature rise, to reference operative temperature. In heat-balance calculations made for the collected UCLA experimental series, it also has been shown that heat storage computed by difference from heat gain and loss terms agrees well with the storage index based on weighted body temperature.[3]

The intercept on the zero storage line in Fig. 3 is 116 F which defines the lower limit of transient response, and the upper limit of the compensable zone.

Time Limits of Tolerance and Performance. For heat-stress conditions tolerable for up to 3 hr it has been found that in general the product of storage index and tolerance time is a constant. By implication, then, it appears that the body can accept a fixed quantity of heat beyond that associated with comfortable equilibrium conditions before reaching a state of incipient col-

lapse. For our experimental data, covering a range of temperatures and tolerance times from 140 to 250 F and from 1½ hr to 20 min, respectively, the average value of this constant is 28.4 Btu/sq ft. For application to the design of aircraft, we also have established a minimum value of 20.4 Btu/sq ft which pertains to the least heat-resistant individuals among our experimental subjects.

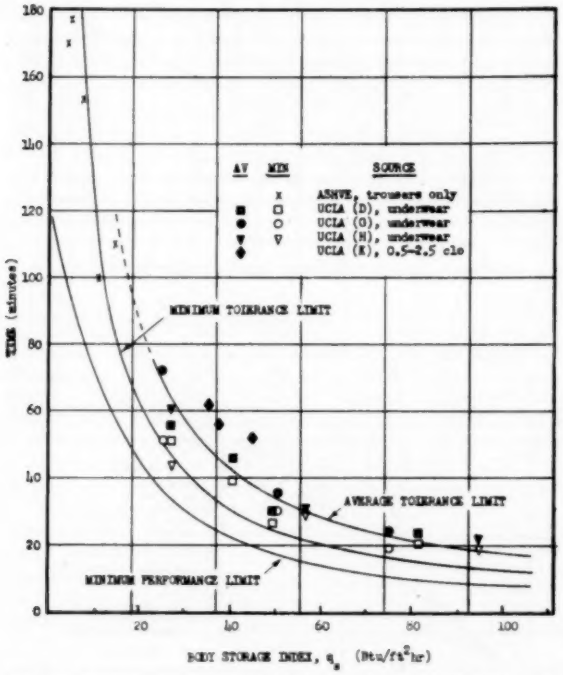

FIG. 4 PERFORMANCE AND TOLERANCE LIMITS: AVERAGE AND MINIMUM TIMES AS A FUNCTION OF BODY STORAGE INDEX

In Fig. 4 these two values of the storage-time product are represented by curves labeled average and minimum tolerance limit, respectively. The closeness of fit to the experimental data is apparent. The definition of the physiological state at the tolerance limit is as follows: (*a*) Presence of symptoms of heat exhaustion, such as, faintness, nausea, dyspnea, tingling in the extremities, mental distraction and confusion, compulsive restlessness; (*b*) heart rate in excess of 140 beats per minute.

This tolerance limit thus has the meaning of a survival extreme, and for full recovery rapid cooling is required. The assumption of an initial state of thermal comfort is implicit in the statement of these tolerance times, and they are valid only for single isolated exposures. The effect of repeated exposure to heat stress, more frequent than once every other day, has not been investigated.

Upon reaching the tolerance end-point state, the subject's ability to perform a complex psychomotor task, such as piloting an aircraft, is impaired, sometimes severely.

The lower curve in Fig. 4 indicates the expected minimum duration of unimpaired performance, based on the subjects in the UCLA experiments who showed the earliest onset of deterioration in their simulated instrument-flight task. These data covered the range of storage index from 24 to 85 Btu/sq ft hr and extrapolation to lower storage rates, representing less severe stress conditions, is based on studies in the literature conducted mainly in warm humid environments.

GRAPHIC SOLUTION OF BIOTHERMAL PROBLEMS

It has been shown that body-heat storage constitutes a parameter by which environmental influences can be correlated with human tolerance and performance limitations. The outline in Fig. 2 shows the nature of the interrelated variables, while reference[3] gives, both mathematically and graphically, the calculations. However, McCutchan[4] has reduced a large portion of this system to a graphic display for aircraft designers, and H. A. Mauch, of Wright Air Development Center, has further modified the display to permit the whole calculation to be made on a single chart. In this form it is now being incorporated in the Handbook of Instructions for Aircraft Designers.

Method of Graphic Solution. The computation chart (Fig. 5) provides, in sections I–VI, a solution for the largest portion of the environmental influence in terms of a standard operative temperature, and a heat-transfer coefficient. Two additional conditions modify the effect; namely, clothing and low barometric pressure. Clothing affects the thermal state of man by delaying body-heat storage above 140 F of reference operative temperature, and by augmenting it below this temperature. Low barometric pressure reduces heat transfer and increases vapor transfer through the clothing. Both result in reducing body-heat storage. These effects and their interactions are brought into the solution in sections VII and VIII, so that finally one enters section IX with a body heat-storage figure and from the applicable curve reads the minimum tolerance time or minimum performance time.

It will be noted that a compensable zone is provided in the portion of section IX below zero storage. Depending upon altitude this zone is bounded, for any clothing, in the reference operative, temperature range of 105 to 110 F. Experimentally, as pointed out previously, the zero storage line is determined at 116 F. However, there are uncertainties about its exact placement and the lower values given by the chart represent a factor of safety.

Limits and Cautions in Applying Computation Chart. While seven years of experimental study in the temperature range 120 to 240 F form the basis of the biothermal prediction system, and all basic modes of variation have been measured, still many of the permutations and combinations have not been subjected to test. However, factors of safety have been built in by taking the most conservative choices when necessary and the predictions should always err on the safe side.

Some of the further limitations imposed by the conditions of the experimental background are as follows:

1 Activity characteristic of light manual work, sitting, is the highest metabolic rate studied.

2 Medically normal and healthy young men, aged 18 to 36, served as subjects.

3 Interactions with other environmental and aviation stresses, such as noise, hypoxia, and G-forces, have not been investigated.

4 All experiments were single exposures for a given day, and there are no certain means for predicting the effects of repeated exposures within the time range of minutes or hours.

5 Comfort is not guaranteed; it is assumed that men will be willing to undergo discomfort, and, with objective attitude, accept the challenge of the calculated stress.

SUMMARY

The physiological and biophysical basis of human response to high environmental temperatures is discussed, and the state of adaptation, whether compensated or noncompensated, has been graphically displayed.

In the range of compensation, both comfort and noncomfort

[4] "Notes on the Revision of the HIAD," by J. W. McCutchan, Memo Report No. 12, University of California, Los Angeles, Calif.

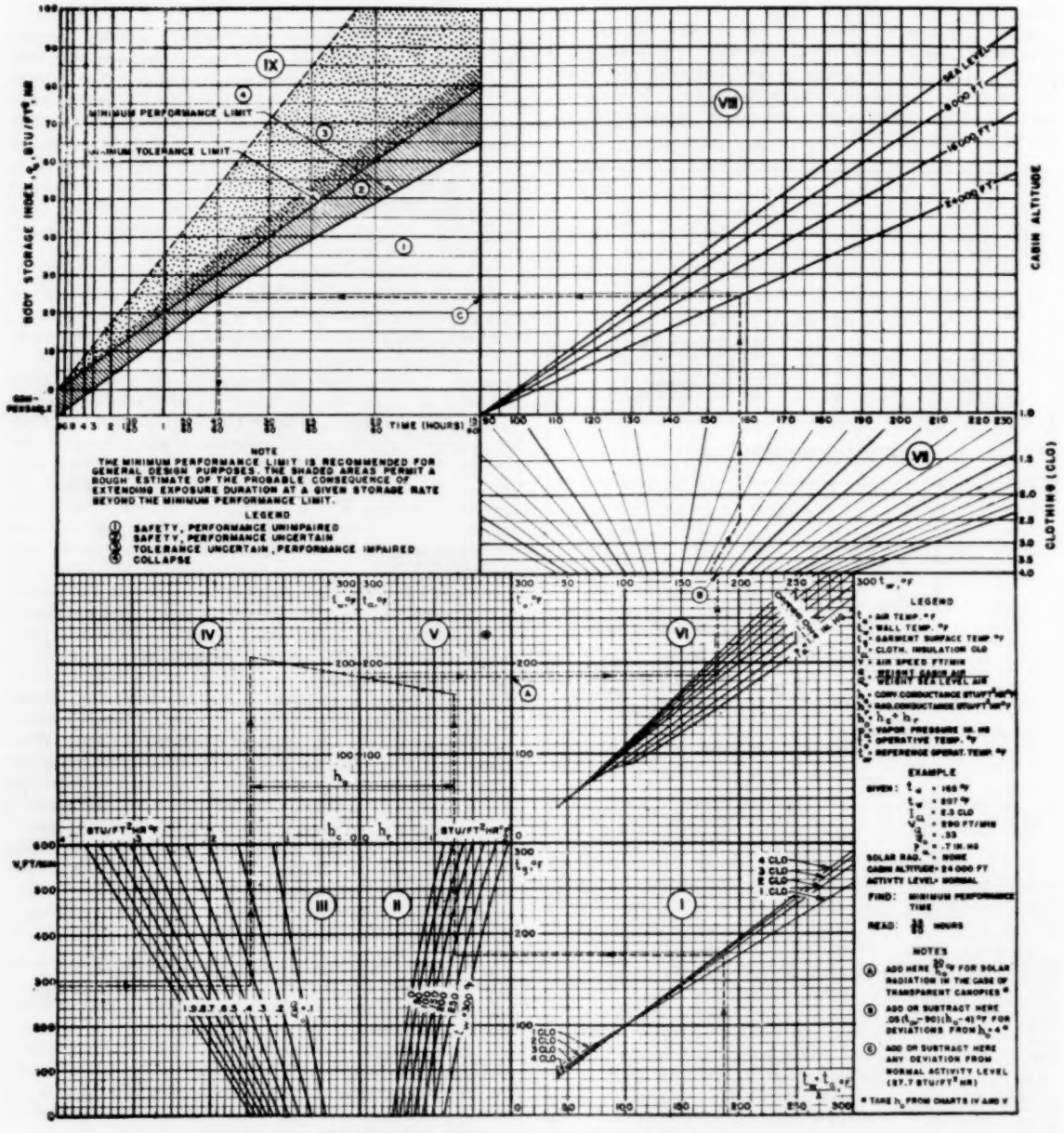

FIG. 5 GRAPHIC COMPUTATION OF THERMAL TOLERANCE

steady states are to be expected. Depending upon the clothing worn, and the conditions of altitude, humidity, etc., the upper margin of the compensable zone is about 110 F.

The man-clothing-environment system has been analyzed by use of biophysical heat-transfer formulations which take into account experimentally determined body heat and temperature parameters. Chief among these is a heat-storage index which is calculable from the conditions of environment and clothing. Time-tolerance and time-performance relationships with the heat-storage index have been experimentally determined.

A prediction chart has been prepared for the use of aircraft designers, which permits a rapid calculation of tolerance and performance times for a wide range of environment and clothing conditions.

Oronite High Temperature Hydraulic Fluids 8200 and 8515

By N. W. FURBY,[1] R. L. PEELER,[1] AND R. I. STIRTON[2]

Aircraft hydraulic fluids and hydraulic fluid systems have entered a new era. The advent of guided missiles and the fantastic increase in speed and operating altitude of aircraft make present requirements for fluids and systems far more severe than was imagined 15 years ago. This paper presents data on two outstanding fluids developed for use over a wide temperature range. These fluids, Oronite High Temperature Hydraulic Fluids 8200 and 8515, have pushed top operating temperatures upward some 300 deg F without reducing performance at low temperatures.

Hydraulic Fluid Requirements

THE primary function of a hydraulic fluid is to transmit energy from an energy source to an energy-utilizing device. For this reason, hydraulic fluids are also called power-transmission fluids. The liquids used as hydraulic fluids are largely organic materials. Thus the specification requirements established for hydraulic fluids have been limited by the properties of available organic liquids.

Hydraulic fluids must have many of the same properties important for lubricating oils and other industrial fluids. These include adequate viscosity at high temperature, good low-temperature fluidity, good lubricity, oxidation stability, and compatibility with hydraulic-system components. These and additional requirements are included in the list of 22 properties for "Recommended Characteristics of Hydraulic Fluids" (Table 1) recently furnished to ASTM by Vickers, Inc. Table 1 applies to hydraulic fluids in general. However, hydraulic fluids are used in many specialized fields, and the relative importance of these properties differs with the service. Thus Mr. Taplin of Vickers recently furnished Technical Committee "N" of ASTM Committee D-2 with comments on "Problems Related to Hydraulic Fluids in Servomechanisms." Properties in order of importance for servomechanisms were given as bulk modulus, lubricity, viscosity index, viscosity, specific gravity, foaming tendency, specific heat, and thermal conductivity.

TABLE 1 RECOMMENDED CHARACTERISTICS OF HYDRAULIC FLUIDS*

1 A good lubricant with presently available materials for bearings and sealing surfaces.
2 High viscosity index; i.e., small change in viscosity over a wide temperature range (—70 to +500 F).
3 Inert to presently used materials for hydraulic equipment, paint, metals, plastics, seal material, neutral.
4 Viscosity to be compatible with present hydraulic fits and clearances.
5 Stable with time and usage, high resistance to mechanical shear, long service life.
6 Nontoxic, both as a fluid and after decomposition. (Liquid or vapor.)
7 High bulk modulus.
8 Ability to purge itself of air readily (low foaming).
9 Low specific gravity.
10 Low cost and high availability.
11 Nonflammable to a reasonable degree.
12 Low air absorption.
13 High heat-transfer coefficient.
14 Low vapor pressure and high boiling point, residual film to remain oily.
15 Low coefficient of expansion with temperature.
16 Good dielectric and insulation properties.
17 Nonhydroscopic and low solubility in water.
18 Compatible with present hydraulic fluids, up to at least 10 per cent dilution.
19 High specific heat.
20 Odorless or at least a pleasant odor.
21 Viscosity change with pressure and velocity to be low.
22 Clear, transparent liquid with a distinctive color.

* By Vickers, Inc.

TABLE 2 TYPICAL COMPOSITION AND PROPERTIES OF MIL-O-5606 HYDRAULIC FLUID

Composition, Wt. %	
Highly Treated Light Gas Oil Fraction	60-80
Highly Treated Heavy Gas Oil Fraction	15-30
Viscosity Index Improver (Alkyl Methacrylate Polymer)	4-8
Oxidation Inhibitor	0.1-0.5
Red Dye	1 ounce/100 gallons
Important Properties (Typical)	
Viscosity at -65°F, cs	2130
100°F	14
400°F	1.9
Pour Point, °F	-90
Low Temperature Stability	Must meet detailed test requirements
Oxidation and Corrosion Stability	
Evaporation	
Shear Stability	
Rubber Swelling	

Aircraft hydraulic fluids generally are considered to comprise one class of fluid. But different types of aircraft may have different fluid requirements. Establishing these requirements is a major problem at the beginning of a fluid development program. As the program proceeds, the data may indicate a revision of objectives. The solution of these problems is greatly facilitated by co-operative activities, such as the SAE and ASTM committees.

Performance requirements for aircraft fluids were relatively mild in the early 1940's. At that time the temperature maximum was 160 F. Requirements were met satisfactorily by a readily available petroleum-base composition (Specification MIL-O-5606). Typical composition and important require-

[1] Richmond Laboratory, California Research Corporation, Richmond, Calif.
[2] Oronite Chemical Company, San Francisco, Calif.
Contributed by the Aviation Division and presented at the Aviation Division Conference, Los Angeles, Calif., March 14–16, 1956, of THE AMERICAN SOCIETY OF MECHANICAL ENGINEERS.
NOTE: Statements and opinions advanced in papers are to be understood as individual expressions of their authors and not those of the Society. Manuscript received at ASME Headquarters, January 23, 1956. Paper No. 56—AV-22.

TABLE 3 TARGET PROPERTIES FOR HIGH TEMPERATURE HYDRAULIC FLUIDS[a]

	Phase I	Phase II	Phase III	MIL-O-5606 Fluid[b]
Viscosity at -65° F, cp	2500 max.	-	2500 max.	1900
-40° F, cp	-	2500 max.	-	-
300° F, cp	3.5 min.	-	-	-
400° F, cp	-	3.5 min.	3.5 min.	1.35
Vapor Pressure at 200° F, mm	-	-	-	3.0
Vapor Pressure at 300° F, mm	3.0 max.	-	-	-
Vapor Pressure at 400° F, mm	-	3.0 max.	3.0 max.	230
Pour Point, °F	-75 max.	-75 max.	-75 max	-90
Appearance	Clear	Clear	Clear	Clear
Odor	Not nauseating or irritating			O.K
Evaporation	Must meet detailed test requirements			
Low Temperature Stability				
Hydrolytic and Corrosion Stability				

[a] See reference, footnote 3.
[b] Typical properties.

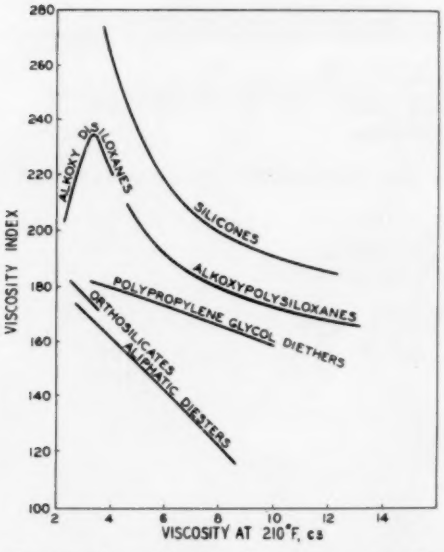

FIG. 1 VISCOSITY INDEX-VISCOSITY RELATIONSHIP FOR SYNTHETIC FLUIDS

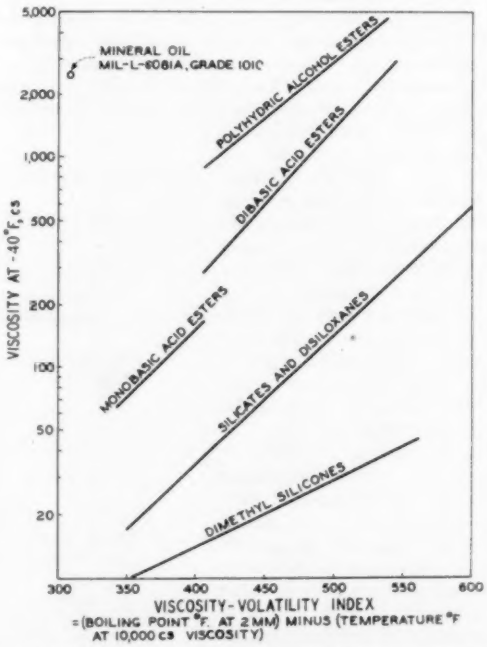

FIG. 2 VISCOSITY-VOLATILITY CHARACTERISTICS OF SYNTHETIC FLUIDS

ments of the 5606 fluid are shown in Table 2. About 25-million gallons of this specification fluid have been used in the past 15 years.

During the late 1940's, aircraft and missile designs clearly showed the need for fluids operable beyond the temperature range of 5606 fluid. The Air Force decided that there was not enough commercial incentive for the development of satisfactory fluids in time for use in prototype equipment. Hence the Air Force sponsored several research programs to search for new fluid base materials and to develop adequate hydraulic fluids, hydraulic pumps, and elastomers for use in the range of —65 to 400 F. Property requirements for the fluids are shown in Table 3 in comparison with the properties of a typical MIL-O-5606 fluid.[3] The more severe requirements are apparent, especially those of viscosity and volatility. The desired goal (Phase III) appeared so difficult to attain that the Air Force set up the two intermediate goals (Phases I and II). California Research Corporation undertook the fluid development aspect of this program.

Early in this program it became apparent that only a very few organic liquids had the desired properties. Two of the most important properties of base materials for hydraulic fluids are viscosity index and volatility. Characteristics related to these properties for several organic fluids are shown in Figs. 1 and 2. The widely used synthetics, such as esters of dibasic acids and derivatives of polyglycols, do not meet the requirements. Silicones have satisfactory physical properties but have poor steel-on-steel lubricity. The organic silicate esters, particularly the disiloxanes, have excellent physical properties but had been rejected in earlier work because of poor hydrolytic stability.

[3] "Development of a High Temperature Aircraft Hydraulic Fluid," WADC Technical Report 54-191, December, 1954.

An extensive program was carried out in synthesizing and testing many silicate compounds to obtain improved hydrolytic stability and other properties. Relatively stable compounds were prepared, and oxidation and hydrolysis-inhibiting additives were discovered. A disiloxane was chosen for the base stock because its viscosity-temperature properties are markedly superior to those of an orthosilicate of the same viscosity, as shown in Fig. 1. The viscosity index was further increased by the use of a very effective viscosity-index improver. The resulting fluid essentially met the Phase III properties. This fluid was designated MLO-8200 by Wright Air Development Center (WADC). A fluid of the same composition is now available commercially from the Oronite Chemical Company as Oronite High Temperature Hydraulic Fluid 8200.

In test work with packings, the Air Force found that the 8200 fluid did not cause sufficient swell in rubbers developed for use at 400 F. The inclusion of 15 per cent diester increased swell to the desired range. A fluid designated 85/15 resulted and was recommended for use with available rubbers in the temperature range —65 to 400 F. A fluid of the same composition is now commercially available as Oronite High Temperature Hydraulic Fluid 8515. The properties of Oronite Fluids 8200 and 8515 are listed in Tables 4 and 5. The 8200 fluid has better compatibility with available rubbers at 550 F than does the 8515 fluid. Therefore the 8200 fluid is recommended for operating temperatures above 400 F.

The important properties of the Oronite fluids are discussed separately in the following sections.

Properties of Oronite Fluids

Viscosity-Temperature Properties. Our experience has shown that viscosity is important in lubrication at high temperatures. The high viscosity of the Oronite fluids at high temperature minimizes lubrication failures due to excessively thin fluid films. In addition, system leakage and internal pump leakage are minimized.

The viscosity-temperature relationships for these fluids are shown in Fig. 3. Typical MIL-O-5606 fluid tests and the requirements of Specification MIL-H-8446 (USAF)[4] are shown for comparison. Both Oronite fluids have viscosity-temperature slopes considerably better than the 5606 fluid and both comply with the viscosity requirements of the 8446 specification, as shown in Table 6.

Shear Stability. Initial high viscosity at high temperatures and high viscosity index are without value if excessive viscosity loss occurs due to the shearing forces inherent in a hydraulic system. This quality is becoming more important as closer tolerances cause more severe shearing. The Oronite fluids have outstanding resistance to permanent shear breakdown, as shown in Fig. 4. Our data indicate that the breakdown obtained in approximately 20 min in the sonic oscillator test[5] corresponds to that obtained in the MIL-O-5606 5000 cycle (Pesco gear pump) shear-stability test. At this severity, the Oronite fluids lost less than 5 per cent of their original viscosity at 100 F, as compared to a 14 per cent loss for the 5606 fluid.

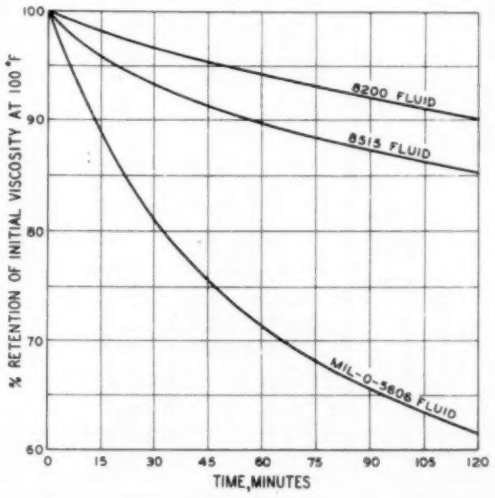

Fig. 4 Shear Stability for Oronite High Temperature Hydraulic Fluids (Sonic Oscillator 10,000 Cycles per Sec)

Vapor Pressure. Low pressures at high altitude and high operating temperatures can cause excessive evaporation of fluid

[4] Specification MIL-H-8446 (USAF) is for "Nonpetroleum Base Aircraft Hydraulic Fluid" and "covers the requirements for an aircraft hydraulic fluid for the temperature range of −65 to 400 F."

[5] "Determination of the Shear Stability of Non-Newtonian Fluids," by N. D. Lawson, ASTM Special Technical Publication No. 182, Appendix, September, 1955.

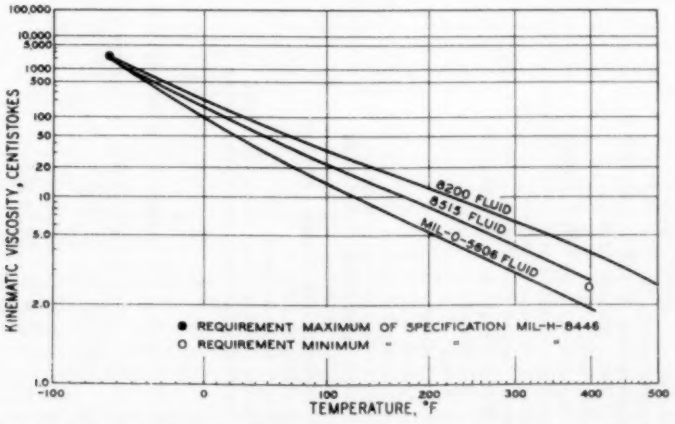

Fig. 3 Kinematic Viscosity Versus Temperature for Oronite High Temperature Hydraulic Fluids

TABLE 4 ORONITE HIGH TEMPERATURE FLUID 8200

Typical Properties

Specific Gravity, 20°C/4°C	0.931
Flash Point, °F	405
Fire Point, °F	450
Viscosity at -65°F, cs	2490
Viscosity at 100°F, cs	34.4
Viscosity at 210°F, cs	11.78
Viscosity at 400°F, cs	3.82
Neutralization No.	0.05
Evaporation, 6-1/2 hr. at 400°F (Spec. MIL-L-7808B)	22.3
Pour Point, °F	below -100
Compatibility with MIL-O-5606	compatible
Low Temperature Stability, 120 hr at -65°F	pass
Vapor Pressure at 400°F, mm Hg	1.2
Oxidation and Corrosion, 72 hr. at 400°F	
Metal Weight Change, mg/cm^2	
Aluminum	-0.02
Steel	-0.05
Beryllium-copper	+0.04
Silver	-0.04
Viscosity change at 100°F, %	-20
Neutralization No. increase	0.5
Sludge, gumming, insolubles	none
Hydrolytic Stability, 48 hr. at 200°F	
Copper weight change, mg/cm^2	-0.03
Insolubles, %	0.05
Viscosity change at 100°F, %	+2.1
Neutralization No. increase, fluid	0.10
Neutralization No. increase, water	0.03

TABLE 6 VISCOSITY AND VISCOSITY-TEMPERATURE SLOPE

Fluid	Viscosity at 400°F, cs.	Viscosity at -65°F, cs.	ASTM Viscosity-Temperature Slope 100°F to 210°F	ASTM Viscosity-Temperature Slope -65°F to 400°F
5606	1.9	2130	0.49	0.54
8515	2.6	2360	0.44	0.48
8200	3.8	2490	0.38	0.42
8446 (Spec.)	2.5[1] min.	2500 max.	-	0.49

[1] "Fluids with centistoke values between 1.0 and 2.5 at 400°F will not be eliminated on this requirement alone."

TABLE 5 ORONITE HIGH TEMPERATURE FLUID 8515

Typical Properties

Specific Gravity, at -65°F		0.982
at 60°F		0.930
at 350°F		0.809
Autogenous Ignition Temperature, °F		760
Fire Point, °F		450
Flash Point, °F		410
Pour Point, °F		Below -100
Viscosity, at -65°F, cs		2357
at 100°F, cs		24.30
at 210°F, cs		8.11
at 350°F, cs		3.36
at 400°F, cs		2.64
Precipitation No.		0
Neutralization No.		0.02
Evaporation, 6-1/2 hr. at 350°F, % evaporated		6.1
Low Temperature Stability,		
168 hr. at -65°F	Gelling	None
	Crystallization	None
	Solidification	None
Vapor Pressure, at 350°F mm Hg		0.2
at 400°F mm Hg		1.0
Oxidation and Corrosion, after 72 hr. at 400°F		
Metal Weight Change, mg/cm^2		
Aluminum		-0.04
Steel		+0.04
Copper		-0.05
Silver		-0.06
Visible Corrosion		None
Viscosity Change, % at 210°F		-28.4
Acid Number Increase		0.56
Insolubles		None
Hydrolytic Stability, after 48 hr. at 200°F		
Copper weight change, mg/cm^2		0
Visible Corrosion		None
Insolubles, %		0.04
Viscosity change, %		-1.2
Acid No. increase, fluid		0.10
Hygroscopic Tendency, 100% Relative Humidity at 120°F, % Water Increase after 100 hr., % weight		0.051

Adiabatic Bulk Modulus, at 76°F

Pressure, psig	Modulus, psi
0	218,000
3000	252,000
5000	279,000

Shear Stability, sonic oscillator at 10,000 cps. % of Initial Viscosity at 100°F after 2 hr.	85
Specific Heat, at 81°F, Btu/lb./°F	0.47
Thermal Conductivity, at 77°F, Btu/hr.-sq. ft.-°F/ft.	0.090

TABLE 7 HYDROLYTIC STABILITY AT 200 F

	MIL-H-8446 Test			51-F-21 Test	
	Specification	8200 Fluid	8515 Fluid	Specification	8200 Fluid
Copper Wt. change, mg/sq cm	± 0.5 max	-0.01	Nil	-0.2 max.	+0.03
Etching, pitting, corrosion	None	None	None	None	None
Insolubles, %	0.5 max.	0.05	0.04	0.5 max.	0.09
Viscosity change at 210°F, %	± 20 max.	+2.1	-1.2	0 to +25	+6
Neutralization No. fluid	0.5 max.	0.10	0.10	0.5 max.	Nil
Neutralization No. water	0.5 max.	0.03	0.10	-	-
Color, ASTM	-	-	-	5 max.	4

TABLE 8 OXIDATION AND CORROSION STABILITY IN THE RANGE OF 250 TO 400 F

	8200 Fluid			8515 Fluid	
Temperature, °F	250	347	400	350	400
Time, Hours	168	72	72	72	72
Metal Wt. change, mg/sq cm					
Aluminum	-0.03	Nil	-0.02	+0.01	-0.04
1020 Steel	-0.04	Nil	-0.02	+0.02	+0.04
Copper	Nil	+0.05	+0.01	+0.05	-0.05
Magnesium	Nil	-	-	-	-
Cadmium	Nil	-	-	-	-
Silver	-	Nil	-0.04	+0.02	-0.06
Beryllium-copper		-	-0.04	-	-
Viscosity Change at 210°F, %	+9.5	+8.0	-20	+4.4	-28
Neutralization Number	0.38	0.47	0.56	0.58	0.56
Insolubles	None	None	None	None	None

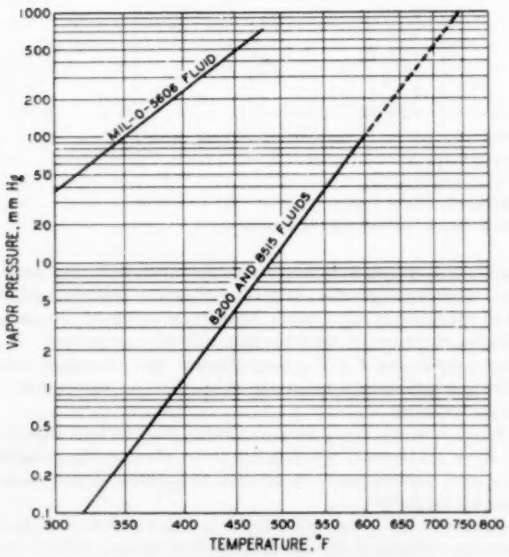

FIG. 5 VAPOR PRESSURE VERSUS TEMPERATURE FOR ORONITE HIGH TEMPERATURE HYDRAULIC FLUIDS

from exposed surfaces, leading to "spiral" failure of O-rings. The low vapor pressures of the Oronite fluids (Fig. 5) reduce evaporation and pump cavitation under these conditions. Low vapor pressure also materially reduces fire hazard due to flammable vapors. At 400 F, the vapor pressure of the Oronite fluids is only 0.5 per cent that of 5606 fluid.

Hydrolytic Stability. Water is often found in hydraulic systems of aircraft and in fluid-storage containers. Therefore the effect of water on hydraulic fluids is of considerable importance, especially with silicate-ester-base fluids. Some of these esters have poor resistance to chemical breakdown in the presence of water. The finely divided, solid silica resulting from hydrolysis plugs orifices and filters and jams moving parts. Both of the Oronite fluids show essentially no insolubles formation, viscosity change, or corrosion of copper in the standard hydrolytic stability test (48 hr at 200 F, Specification MIL-H-8446 [USAF]). The 8200 fluid showed excellent stability under the severe hydrolysis conditions of the oxidation and corrosion test of Specification 51-F-21 (Ord). Thus, after 336 hr at 200 F in the presence of water and a large amount of copper catalyst, there was essentially no change in the fluid except for 6 per cent viscosity increase. The foregoing data are summarized in Table 7.

Hydrolytic stability tests at WADC at 400 F in a pressure vessel showed that, as expected, all of the silicate and disiloxane fluids tested hydrolyzed severalfold more rapidly at 400 than at 200 F. The significance of hydrolytic stability at 400 F as related to service is being studied. The trend toward providing sealed dry systems for high temperature hydraulic applications is very desirable.

Oxidation and Corrosion Stability. The Oronite fluids have excellent oxidation stability and are noncorrosive to the metals of high temperature hydraulic systems. Table 8 summarizes tests over the range 250 to 400 F. These data show that both fluids are essentially inert to aluminum, 1020 steel, copper, and silver in oxidation and corrosion tests at temperatures as high as 400 F. No insoluble material or sludge is formed. Viscosity decreases in the tests at 400 F. However, the fluids remain usable because this effect is offset by the relatively high initial viscosities of the Oronite fluids.

Thermal Stability. Thermal stability is one of the most important properties of materials for high temperature use because it limits maximum operating temperatures. The Oronite fluids show excellent thermal stability. In one series of tests this property was measured by holding the fluid in a glass system with metal catalysts under an inert atmosphere at several test

TABLE 9 THERMAL STABILITY IN THE RANGE OF 400 TO 700 F

	8200 Fluid					MIL-O-5606 Fluid
Temperature, °F	400	500	550	600	700	500
Time, Hours	72	1	1	1	1	1
Viscosity change at 100°F, %	+0.8	+0.4	-1.4	-16	-44.2	-19
Viscosity change at 210°F, %	-	+0.1	-2.5	-16	-45.4	-20
Neutralization No. Increase	0.1	Nil	Nil	Nil	0.9	0.1
Evaporation, %	0.6	0.4	0.4	0.4	2.4	-
Insolubles	None	None	None	None	None	
Metal Wt. change, mg/sq cm						
Aluminum	Nil	Nil	Nil	+0.01		
Iron	+0.01	+0.03	Nil	+0.01		
Copper	Nil	Nil	+0.01	+0.01		

TABLE 10 EFFECT ON RUBBER

	8200 Fluid		8515 Fluid	
	Volume Change, %	Hardness Change, Durometer Numbers	Volume Change, %	Hardness Change, Durometer Numbers
158°F, 168 Hours				
MIL-P-5516 type[1]	-5.0	+6	-3.7	+1
Rubber H[2]	-0.2	+2	+0.3	-
Rubber L[3]	+1.2	-1	+11.6	-4
Rubber R[4]	-6.4	+2	+20.1	-2
Parco 351-70	-4.0	+3	+8.5	-10
Parco 363-70	+2.7	-2	+15.0	-
Linear KCX-70X	+2.5	-1	+14.0	-8
250°F, 70 Hours				
Rubber L	+4.0	-	+13.1	
Rubber R	+6.5	-1	+22.0	-4
Parco 351-70	-1.5	+2	+11.8	-4
Parco 363-70	+4.7	-1	+16.4	-7
Linear KCX-70X	+5.3	+3	+23.3	-7

[1] Commercial compound used with MIL-O-5606 fluid.
[2] Standard unplasticized Buna N stock for diester fluids.
[3] Standard unplasticized Buna N stock for MIL-O-5606 fluid.
[4] Standard unplasticized Neoprene WRT stock for silicate ester fluids.

temperatures. At the end of the test period the fluid was inspected for property changes. Data for the 8200 and 5606 fluids are given in Table 9. These data show no significant change in the 8200 fluid below 550 F for test periods of 1 hr. No corrosion of the metal catalysts was noted at 600 F. By comparison, the viscosity of 5606 fluid was reduced by 20 per cent after 1 hr at 500 F. The viscosity of the 8200 fluid decreased in the tests above 550 F. Again, the final viscosity of the 8200 fluid is relatively high because of its high initial viscosity.

Effect on Rubber. Rubber-swell data are summarized in Table 10. The 8515 fluid swells and softens rubbers more than does the 8200 fluid. The amount of swelling desirable for rubbers is controversial, although the limit for Specification MIL-H-8446 is 25 ± 5 per cent swell of either Rubber L or Rubber R in the 250 F test.

O-rings made from Parco Compound 363-70 were used successfully with the 8200 fluid in pump tests at 400 F. The other commercial rubber compounds shown in Table 10 are available for use with silicate ester-type fluids.

A few immersion tests at 400 F were performed. The results were variable, depending upon test conditions. The presence of air had a marked effect, probably because of oxidation of both rubber and fluid. Further study is needed of the variables involved in high temperature immersion tests.

Effect on Paints, Plastics, and Electrical Insulation. Spillage and leakage of hydraulic fluid in airplanes are practically unavoidable. Therefore the effect of fluids on paints, plastics, and electrical insulation is important. Some types of organic esters have a high solvent power for these materials of construction. Notable examples are found among diesters and phosphate esters. Silicate esters have a relatively mild effect on paints and electrical insulation.

There is no standardized test for the effect of hydraulic fluids on these substances, but data are being obtained by immersion of typical painted surfaces, plastics, and electrical insulations in the Oronite fluids.

Compatibility. Compatibility of new fluids with 5606 fluid is necessary because of the widespread use of this specification product. Inadvertent mixing of new fluids with 5606 fluid is apt to occur. Also, it is desirable in some instances merely to flush a system with the new fluid when 5606 fluid is to be replaced. If the fluids are not compatible, precipitation or separation of insolubles may occur. The separated material usually consists of concentrated viscosity-index improver. This gummy material plugs lines and causes trouble in many parts of the system

Oronite 8200 and 8515 fluids have good compatibility with 5606 fluid. Blends of 10, 50, and 90 per cent concentration of each Oronite fluid in 5606 fluid were prepared and stored at −65 F for 1 week. In no case was there any precipitation or separation of insolubles or gummy material. A light cloudiness

TABLE 11 SPECIFIC HEAT AND THERMAL CONDUCTIVITY AT 86 F

	8200 Fluid	8515 Fluid	MIL-O-5606 Fluid
Specific Heat, Btu/lb, °F	0.47	0.47	0.46*
Thermal Conductivity, Btu/hr, sq ft, °F/ft	0.089	0.090	0.076

*Estimated from "Thermal Properties of Petroleum Products," Bureau of Standards Miscellaneous Publication No. 97.

was evident, similar to that for 100 per cent 5606 fluid under the same conditions. At room temperature, all of the blends were clear.

Foaming. The Oronite fluids foam more readily than 5606 fluid. A larger volume of foam is formed which requires a longer time to disappear. Experience has shown that foaming is not a problem in properly designed systems. In particular, discharge into the sump should be below the liquid level. In completely closed systems foaming cannot occur.

Density. The density of hydraulic fluid determines the weight of fluid which must be carried. Also, density is important in hydrodynamic ram effects. The densities of the Oronite fluids (Fig. 6) are about halfway between the densities of 5606 fluid and water. However, the Oronite fluids are considerably less dense than the phosphate-ester and water-base hydraulic fluids used in aircraft.

Compressibility. The compressibility of hydraulic fluid influences static rigidity of the system and the time-lag in transmission of fluid-pressure changes. Low compressibility (high bulk modulus) is desired. Bulk modulus of the Oronite fluids is approximately 5 per cent lower than for 5606 fluid as shown in Fig. 7.

Specific Heat and Thermal Conductivity. Removal of heat from the hydraulic systems of supersonic aircraft is a serious problem. Fluids having high specific heat and high thermal conductivity permit smaller heat exchangers. As compared to 5606 fluid, the Oronite fluids have about the same specific heat and approximately 15 per cent higher thermal conductivity. Data obtained at 86 F are given in Table 11.

Toxicity. Toxicity tests of alkyl-silicate esters have shown these compounds to be relatively harmless. Quantitative toxicity tests of the Oronite fluids have not been performed. However, these fluids have been handled without special precautions for nearly 3 years with no harmful effects. No skin irritation or respiratory effect has appeared during this time. The low vapor pressures of the Oronite fluids result in low concentrations of fluid in the air of confined spaces and reduce the possibility of inhalation of significant amounts of fluid vapors.

Performance in Pumps and Hydraulic Systems. Over 20 pump tests were performed on silicate-ester fluids during the development program at California Research Corporation. Excellent pump performance at 160 F was obtained employing regular aircraft pumps. Attempts to operate these pumps at 400 F were not successful because of mechanical factors, notably dimensional instability. Finally, a conventional pump was reworked to improve dimensional stability above 160 F. Employing 8200 fluid, this pump performed satisfactorily in runs of 20 hr each at 250, 300, 350, and 400 F. The 400 F test was terminated by loss of the fluid at a defective hose connection with resultant pump damage.

Pumps designed for use at high temperatures are only now becoming commercially available. These will permit further evaluation of fluid performance by reducing failures due solely to mechanical factors.

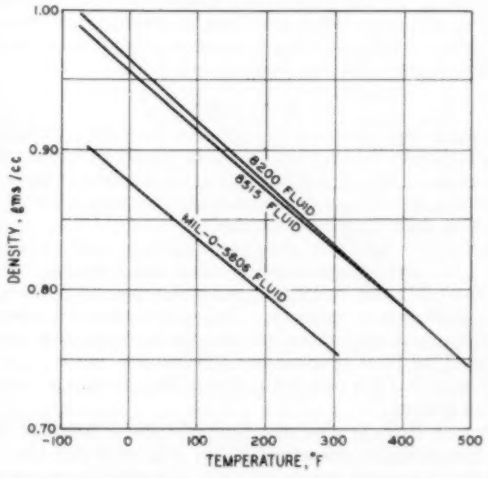

FIG. 6 DENSITY VERSUS TEMPERATURE FOR ORONITE HIGH TEMPERATURE HYDRAULIC FLUIDS

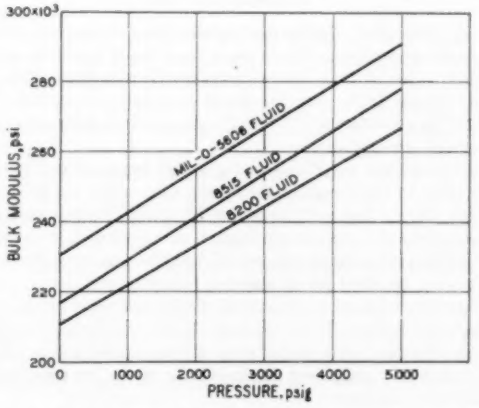

FIG. 7 ADIABATIC BULK MODULUS AT 76 F FOR ORONITE HIGH TEMPERATURE HYDRAULIC FLUIDS

Cost and Availability. Currently developmental quantities of 8200 and 8515 fluids are available. Six to eight weeks' notice is required for quantities larger than 100 gal. The availability will be improved when volume requirements warrant full-scale commercial production.

The current price for the 8200 fluid is $35 a gallon and for the 8515 fluid, $30 a gallon. These prices reflect the high manufacturing costs of pilot-scale production. Significant price reductions already have been made. Further reductions, even for

pilot-scale production, will be made when warranted by additional experience.

Future Developments. The numerous and difficult problems in the development of complete high temperature hydraulic systems are industry-wide. All materials of the system, including hydraulic fluid, rubbers, plastics, and metals, must be mutually compatible. The choice of elastomers and the design of seals, heat exchangers, and other components depend upon the type of fluid used. The establishment of a fluid specification, based on available fluids, and its acceptance by the industry will facilitate design of other parts of the hydraulic system. Also, choosing the type of fluid will permit the industry to obtain the extensive fluid-property and performance data on which to base fluid improvement. It is hoped that Specification MIL-H-8446 (USAF), recently issued, will serve these purposes.

Conclusion

Oronite High Temperature Hydraulic Fluids 8200 and 8515 are outstanding in the following properties important for operation of high-speed aircraft and guided missiles: Viscosity at high temperatures, viscosity index, shear stability, volatility, oxidation and corrosion stability, thermal stability.

Hydrolytic stability of the Oronite fluids is excellent as compared to many silicate-ester-base fluids and lubricants. Compatibility with 5606 fluid is good, and rubber compounds which appear satisfactory are available. Data on performance in pumps at high temperatures indicate satisfactory performance in pumps designed for these temperatures. Foaming is greater than for 5606 fluid, but this does not appear to be a problem in well-designed systems.

Oronite High Temperature Hydraulic Fluids 8200 and 8515 are now available commercially. It is believed that they will provide exceptional service over a wide temperature range and will contribute to the success of supersonic flight.

Discussion

G. R. Keller.[6] In the past several years three series of high-temperature hydraulic fluids have been made available on the market. One of these series comprises Oronite fluids 8200 and 8515. These fluids were developed on a research contract with WADC in accordance with specifications which were established a number of years ago.

In establishing specifications for a high temperature hydraulic fluid prior to the design of the systems for which the fluid is intended, certain assumptions had to be made. Later information caused some of these assumptions to be questioned; however, it is clear that the persons who established the original requirements did a very excellent job of guessing future trends.

Experience gained in the design of high temperature hydraulic systems has indicated that some of the properties which originally appeared important actually were of less significance and others which had previously been assumed to be trivial became items of considerable concern.

Early in the design of high temperature hydraulic systems it became obvious that an entirely closed system would be required to minimize tendencies toward oxidation of the hydraulic fluid. The closing of the system made it very easy to design systems having pressurized pump inlets. A review of the areas in which lubricity of the fluid is critical shows that most of the problems are related to pumping. Another item on which the thinking of the hydraulic designer has changed is the concept of self-ignition temperature of the fluid. It has been surprisingly easy to show that the ASTM testing methods for self-ignition temperatures yield values which are quite misleading. Simple heating of bulk oil has initiated burning at oil and ambient temperatures well below the ASTM self-ignition temperature of each of the silicate hydraulic fluids.

Information on these discoveries has been fed back regularly to the fluid manufacturers and is being used to modify the fluid design. It has become quite apparent, for instance, that the thermal stability of a fluid which is to be used in a high temperature system is of more importance than oxidative stability. The absence of any opportunities to build up a hydrodynamic wedge in a pump cylinder renders the importance of high viscosity at high temperature to be related only to pump efficiency and not to lubricity. It appears that the lubricating ability of the fluid under the boundary or thin film conditions is of greater importance than high viscosity. Certainly it has been demonstrated time and again that hydraulic fluids having viscosities of less than one centistoke can be pumped successfully and efficiently. The use of closed systems and the pressurization of the pump inlet has minimized the effect of high vapor pressure. Conceivably, even fluids having vapor pressures in the order of several atmospheres at 400 F could be used with the systems and components now available.

A great deal has been said and written on the subject of hydrolytic stability of high temperature hydraulic fluids. It is very easy to demonstrate that when water is added to a working hydraulic system which uses a silicate-ester fluid there is a point at which the shearing effect of the pump will develop siliceous gels. These gels contaminate the system and clog the filters. The question as to the seriousness of this effect hinges entirely on the type of treatment these systems will get in service. It has, however, been shown that silicate-ester systems can be operated in the open during extremely rainy weather without any serious contamination from water. Ground equipment can be designed to protect the hydraulic fluid from the effect of rain and atmospheric water vapor. There is no question but that any systems which use fluids which are susceptible to hydrolysis will have to be handled much more carefully than systems which use petroleum oil. Whether this is an unsurmountable difficulty or merely a sticky design problem remains to be seen.

The designers of these hydraulic fluids are to be congratulated for producing fluids which, even though they have some drawbacks, appear to be useful, workable, hydraulic fluids. As recently as three years ago it did not appear conceivable that we would today have as many as three competitive high temperature hydraulic fluids. The great advances that have been made in high temperature hydraulic technology in recent years have been due, in no small measure, to the efforts of the chemists who developed these synthetic oils.

P. S. Kleven.[7] These observations are from the viewpoint of an airframe designer. The Oronite 8515 fluid is being used for all hydraulic systems, totaling about 200 HP, in the B-58 supersonic bomber designed at the Fort Worth Division of Convair. This is a piloted long-range aircraft in which it is expected hydraulic systems may operate at sustained temperature of 350 F hydraulic fluid temperature. It is also significant that the temperature-range requirement extends to minus 65 F.

This paper notes that hydraulic systems and fluids have entered a new era. This is true beyond the mere necessity of new materials doing the old job under new conditions. The first and most pressing problem, upon being confronted with high temperatures, has been to simply obtain system survival. The objective should then be extended to provide characteristics of high quality.

For high temperature, fluid properties acquire changed relative

[6] G. R. Keller, Autonetics, Division of North American Aviation, Inc., Bellflower, Calif.

[7] Design Group Engineer, Convair, Division of General Dynamics Corporation, Fort Worth, Texas.

importances. Fluid development should follow lines of appropriate emphasis.

High temperatures are generally associated with high-speed supersonic flight. In this flight range full power (not boost) hydraulic flight control is the rule and typically comprises the principal hydraulic load. High temperature therefore usually includes flight control problems as inherently simultaneous.

High over-all stiffness is very important for servo actuation. High temperature materially decreases bulk modulus.

Foaming can be of concern as it would also reduce effective bulk modulus. System design for self-purging can, however, readily minimize this problem.

Full-power flight control means that safety is entirely dependent upon continuous hydraulic function. Reliability is therefore more vital than ever. Again, however, greater stringency of demand is accompanied by conditions tending to have adverse effects. Several properties, such as materials compatibility and lubricity, can be involved here. Presuming reasonable initial properties enabling feasible equipment design, deterioration due to shear and temperature breakdown may be dominant. Although accepted practices of eliminating air by use of an entirely closed system and by inert-gas charging of connected pneumatic services are of considerable aid, air to cause oxidation is still introduced in initial solution and by maintenance exposure.

Hydraulics for flight controls require a large air-borne fluid content. Fluid density therefore controls appreciable weight. Thermal expansion rate, its effect amplified by extended temperature range, governs weight for contraction reserve and expansion space. Piston separator airless reservoirs for high temperature are of much heavier construction than conventional ordinary temperature designs.

High temperatures are associated with heat-disposal problems. The rate of heat generation either establishes temperature level or the extent of cooling apparatus.

Pump losses represent a major heat source. Viscosity and bulk modulus are significant influences, both of which are degraded by elevated temperature.

Flight controls ordinarily utilize underlapped control valves and heat resistant actuator piston rings. Since these are sized for high power, appreciable heat results from the incident leakages. Viscosity affects this leakage.

Hydraulic actuation takes place at low thermodynamic efficiency. Compressibility here determines heating.

Temperature rise for any heat rate and flow is a direct function of specific heat. The total effect must of course also take account of density.

With multiplication factors for rework and maintenance loss, fluid cost for system charging is high. A secondary effect of high cost is that development testing can be expected to suffer constriction when the large number of equipment suppliers involved in any project is considered.

This paper discusses two types of fluids. It is believed that the 8515 will eventually be displaced by the better viscosity 8200 when improved packing materials become available. Oronite 8515 is in use by Convair principally because of the necessity for imparting −65 F capability to existing synthetic rubber.

D. H. Moreton.[8] The authors are to be congratulated on an excellent presentation of their development program for the military high-temperature hydraulic fluids. We have no specific experience with their fluids but we are in general agreement with their comment on fluid requirements for high temperature hydraulic systems. Several statements made, we feel, could stand some amplification, however. In their discussion of vapor pressure, the statement was made that too high a vapor pressure in the fluid can lead to evaporation from exposed surfaces and to spiral failure of "O" rings. While we heartily agree that low vapor pressure is a very desirable and necessary characteristic, and agree further that cases have been found where spiral failure of "O" rings could be induced by the evaporation of fluid from exposed rods, the thought should not be left that spiral failure always occurs from this cause. Spiral failure has been found many times under conditions of fully flooded lubrication and, unfortunately, a practical solution to its elimination is still unavailable.

Under the subject of hydrolytic stability a statement is made that some of the silicate esters have poor resistance to chemical breakdown in the presence of water and that the result of this can be finely divided solid silica which will plug orifices and filters and jam moving parts. Our experience would lead us to agree fully that this type of ester is sensitive in this regard and as a practical matter so little difference exists between any of the fluids which we have observed so far, that it becomes almost imperative that water be kept out of such systems. For that matter, water has never been an acceptable contaminant with any hydraulic fluids and invariably results in rusting and general corrosion damage to delicate components. We cannot agree with the authors that solid silica results from this hydrolysis. The results which we have observed would classify the breakdown product as a soft gelatinous jell-like material which would require almost complete pyrolysis to result in a truly solid particle. While a chemical defense of the authors' description might be established, the inference of a hard abrasive particle which we believe is left by this description is an incorrect one as far as our results show. We have observed the plugging of filters due to this jell-like material. It would be difficult to conceive of it jamming a component where any reasonably large forces were involved. We are in complete concurrence that the important point is to keep the water out. Due to its extremely high vapor pressure at temperatures in the 400 F range, any appreciable quantity of water could lead to system malfunction regardless of fluid decomposition effects.

As a final point, we believe a word of caution is in order on viscosities. Here is a characteristic of hydraulic fluids where a compromise must be considered as higher temperatures are encountered. Unfortunately, in the pumping of these fluids at high pressures, considerable shear force is unavoidable. The results of high shearing force on fluids are heat. The higher the viscosity the more heat is generated and the more work has to be performed. Since heat is the thing we are trying to dissipate, it seems logical to attempt to minimize the generation of it. This can be achieved by using as low a viscosity as the system will permit from the standpoint of fluid-film lubrication and internal leakage. This compromise should always be considered. To strive for high viscosities alone as a method of minimizing leakage and accomplishing fluid-film lubrication beyond that which is absolutely necessary is merely an invitation to perform more work at the pump in order to get the same amount of work out of the slave unit.

Authors' Closure

The three discussers represent extensive experience in their fields and we appreciate their comments.

We certainly agree with Mr. Keller that it is necessary to modify fluid requirements as experience is gained with new fluids and equipment. His recommendation of sealing the system for optimum performance at high temperature is highly desirable. The thermal stability of silicate-base fluids is superior to the oxidative and hydrolytic stabilities. If air and water can be excluded, the maximum operating temperature can be raised by at least 150 F.

[8] Douglas Aircraft Company, Inc., Santa Monica, Calif.

Although there is no hydrodynamic wedge in piston lubrication, there is, nevertheless, a hydrodynamic component. Approach of the piston to the cylinder wall requires displacement of the hydraulic fluid. This displacement is resisted by both the inertia and viscosity of the fluid. The lubrication and wear of pistons and cylinders have been investigated in internal-combustion engines.[9] Wear is in general inversely proportional to kinematic viscosity. Below a viscosity threshold, wear increases even more rapidly as viscosity decreases.

Mr. Kleven's comments on the fluid and system properties affecting high temperature operation are very interesting. The importance of heat rejection to the fluid and the many sources of this heating are clear. We also believe that use of the 8200 fluid is preferable if compatibility with seals is not critical.

We agree with Mr. Moreton that evaporation from actuator rods is not the only cause of spiral O-ring failure.

Hydrolysis of silicate-base hydraulic fluids can lead to a variety of products, depending to a considerable extent on the amount of water present. Either polysiloxane "gels" or hydrated silica may be formed. The latter, an effective grease thickener, may not appear as the familiar white powder but can form gels.

The effect of viscosity on the performance of hydraulic systems is an extremely important subject, although there is some confusion as to the role played by viscosity in system operation. Consider three major items where viscosity is important:

1 Leakage or "slip" is inversely proportional to viscosity.
2 Drag on moving parts is directly proportional to viscosity.
3 Flow losses are dependent on system design and Reynolds number.

Wilson[10,11] has derived equations for the leakage and power loss between parallel plates of width b, length l, separation h, and velocity V under a pressure differential Δp. Assuming the fluid to have constant viscosity μ, the equations are

Slip flow $$Q_s = \frac{(\Delta p)bh^3}{12\mu l}$$

Power loss $$P_L = \frac{(\Delta p)^2 bh^3}{12\mu l} + \frac{\mu V^2 bl}{h}$$

For a piston pump of n cylinders of bore D, stroke L, diametral clearance d, rotating at $30\omega/\pi$ rpm, these equations become

Slip flow $$Q_s = \frac{n(\Delta p)\pi D d^3}{192\mu l}$$

Power loss $$P_L = \frac{n(\Delta p)^2 \pi D d^3}{192\mu l} + \frac{n\mu\pi D\omega^2 L^2 l}{4d}$$

Thus, the slip flow varies inversely with viscosity, as does the power loss in parts that are largely stationary or slow moving. In pumps, in addition, drag affects power loss. At high temperature, where heat rejection and performance are critical, the importance of the slip heating of the fluid relative to the drag heating increases because of reduced fluid viscosity. For feasible pump parameters, slip heating becomes of major importance. Further reduction of pump clearance to reduce heat rejection is limited by the adverse effect on an already critical lubrication problem. Therefore, a decrease in fluid viscosity reduces pump delivery and increases slip heating. As the displacement of the pump must be increased to offset the increased leakage, adding further to the heat generated, the low viscosity fluid is penalized twice.

Consideration of the effect of the viscosity-temperature coefficient on slip flow[10,12] shows that a low viscosity-temperature coefficient (high viscosity index) is desirable. A fluid with a low coefficient does not lose viscosity excessively while being heated by flow through the slip passages, and as a result maintains a high resistance to leakage.

At high temperatures, flow in high-performance, aviation hydraulic systems is in a region of high Reynolds number. Investigation[13] of flow in this region in straight tubing showed the friction factor f to be inversely proportional to the fourth root of Reynolds number. Expansion and contraction factors are independent of Reynolds number, while fitting factors are only slightly dependent on Reynolds number.

Therefore, considering all major effects at high temperatures, heat rejected to the fluid decreases as the viscosity of the fluid increases. As heat rejection is one of the critical problems of these hydraulic systems, use of the fluid with the highest viscosity at high temperature offers real advantages in systems design and operation.

[9] "Motor Oils and Engine Lubrication," by C. W. Georgi, Reinhold Publishing Corporation, New York, N. Y., 1950, p. 375.
[10] "Clearance Design in Hydraulic Pumps and Motors," by W. E. Wilson, *Machine Design*, vol. 26, October, 1954, pp. 249–256.
[11] "Rotary-Pump Theory," by W. E. Wilson, Trans. ASME, vol. 68, 1946, pp. 371–384.
[12] "Design of Optimum Clearances in Positive-Displacement Pumps and Motors," by W. E. Wilson, Trans. ASME, vol. 78, January, 1956, pp. 117–122.
[13] "Investigation of the Fundamental Characteristics of High Performance Hydraulic Systems," by J. E. Campbell, USAF Technical Report No. 5997, 1950, p. 87.

Mass Flowmeter for In-Flight Refueling

By C. F. TAYLOR,[1] WEST LYNN, MASS.

A new mass flowmeter for in-flight refueling of jet aircraft is described. This flowmeter incorporates very large capacity in a compact rugged unit of unusually high accuracy. Other features are lightweight, low pressure drop, no rotating fluid seals, and fast response to sudden changes in fuel flow rate. This has been achieved by applying the angular momentum principle to obtain a mechanical torque that is linearly proportional to mass rate of flow.

Introduction

THE angular momentum-type mass flowmeter[2] is fast becoming a standard in the measurement of fuel flow to the engines of jet aircraft. It is a major contribution to the art in recent years and has almost unlimited applications. In answer to recent demands in air-to-air refueling, a new, large-capacity (600,000 lb per hr) flowmeter of this type has been developed. At rated flow, which exceeds that of a powerful fire-engine pump, a tank car would be emptied in about 7 min. Nevertheless, the application requires a compact, rugged unit of low pressure drop and unusually high accuracy. Only the most reliable apparatus can be tolerated in in-flight refueling systems.

In prolonged flight and long-range missions of modern jet aircraft, in-flight refueling is mandatory. Considerable emphasis is placed on efficiency, economy, and speedy completion of the refueling cycle. Continuous and precise indication of total pounds of fuel transferred and mass flow rate are required. These objectives can be realized through a measurement system comprising a flowmeter transmitter, an indicator, and associated equipment such as an amplifier and a power supply. Described in this paper is a flowmeter transmitter shown in Fig. 1 that is capable of meeting the stringent requirements imposed on the in-flight refueling operation.

Devices for Measuring Fuel Transferred

Fuel transferred can be measured by the existing quantity gages on the receiver aircraft. A serious handicap is faced in this approach, however, because attitude variations of the plane and fast transients make it exceedingly difficult to secure instantaneous indication to the required precision. Special equipment is necessary to measure flow rate in addition to that required to relay information to the tanker plane under radio blackout conditions.

Flowmeter transmitters that provide signals not primarily proportional to mass flow rate, such as those of the positive-displacement and venturi types, are at serious disadvantage. Fuel-quantity gages in modern aircraft are calibrated in mass (pounds) rather than in volumetric units. Consequently the signal from flowmeters of these types must be compensated automatically or

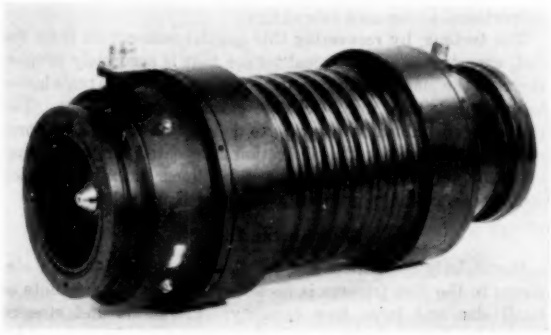

Fig. 1 Mass Flowmeter for In-Flight Refueling

corrective calculations must be made. This requires auxiliary equipment including fragile densitometric-sensing elements. In addition to such auxiliary equipment, emergency bypass valves are often needed to maintain flow under certain conditions of malfunction.

The angular momentum-type flowmeter provides a signal that is linearly proportional to mass flow rate. No auxiliary compensating equipment is required, pressure drop is low, and no damage is incurred by overloads well in excess of rated capacity.

Principle of Operation[3]

The principle of operation is that of adding a constant angular momentum to each unit mass of fuel and then obtaining a mechanical torque proportional to mass rate of flow by recovering this angular momentum. This torque is converted to mechanical displacement from which an electrical signal is derived.

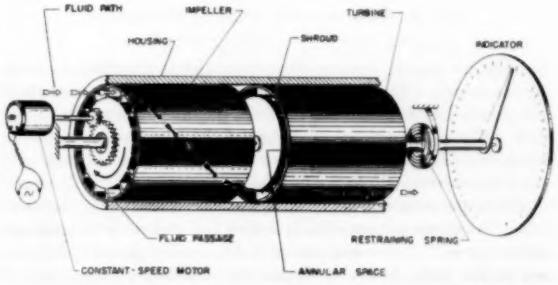

Fig. 2 Schematic Drawing Showing Operating Principle of Mass Flowmeter

The flow-sensing elements are two similar rotors placed coaxially end to end with small axial spacing, Fig. 2. Each rotor comprises a pair of concentric cylinders with radial vanes dividing the annular space between them into a number of identical flow passages. These rotors are enclosed in a common cylindrical housing with which the radial clearances are small enough to prevent appreciable fuel flow around the rotors. The upstream and

---

[1] Advance Engineer, Inertial Guidance Systems, Instrument Department, General Electric Company.

[2] "Fuel Mass Flowmeter Meets Needs of Aircraft Operation," by R. F. Buckley and H. T. Wrobel, *Aviation Age*, December, 1953, p. 136.

Contributed by the Aviation Committee of the Instruments and Regulators Division and presented at the Aviation Division Conference, March 14–16, 1956, of The American Society of Mechanical Engineers.

Note: Statements and opinions advanced in papers are to be understood as individual expressions of their authors and not those of the Society. Manuscript received at ASME Headquarters, January 19, 1956. Paper No. 56—AV-20.

[3] "The Momentum Principal Measures Mass Rate of Flow," by V. A. Orlando and F. B. Jennings, Trans. ASME, vol. 76, 1954, p. 961.

downstream rotors are referred to as "impeller" and "turbine," respectively.

The impeller is driven at a constant speed to impart to each unit mass of fuel a constant angular momentum independently of fuel density, viscosity, and flow rate. During a unit time interval the total angular momentum delivered to the fuel is, therefore, proportional to the mass rate of flow.

The turbine, by recovering this angular momentum from the fuel, experiences a mechanical torque that is accurately proportional to the mass rate of flow in accordance with Newton's law—torque equals time rate of change of angular momentum. The turbine is restrained by a spring to deflect through an angle proportional to torque. This deflection is repeated through a magnetic coupling in a hermetically sealed linear transducer which converts deflection to proportional output-signal voltage.

Mechanical Design

Particularly close attention to the mechanical design of elements in the flow passage is necessary to meet requirements of small size and large flow capacity. Vibrations and stresses caused by fluid turbulence and viscosity have to be reduced by careful streamlining. As shown in Fig. 3, contours of the flow

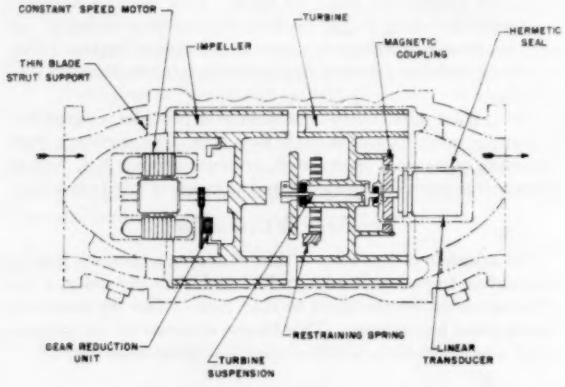

Fig. 3 Cross-Section View of Flowmeter

passage are smooth with no abrupt changes in direction or cross-sectional area. The inner mechanisms are supported on struts of thin-blade design to present the least possible obstruction to fuel flow. These precautions in design of the flow passage not only minimize vibrations and stresses but also reduce substantially the pressure drop across the flowmeter.

The impeller is driven by a three-phase synchronous motor of which the stator is hermetically sealed and the rotor is a permanent magnet. Power required of this motor is reduced by imparting to the fluid, before it enters the impeller, a component of velocity in the direction of impeller rotation. This is accomplished at the inlet housing by disposing the thin supporting struts angularly to the axis of the flowmeter. By taking advantage of mechanical energy in the fuel, a compact and lightweight meter is achieved with substantial gain in performance resulting from high impeller speed.

The turbine is supported by graphite sleeve bearings and stainless-steel pivots to maintain accurate radial alignment with low friction. Performance of these bearings is not affected by normal fuel contamination nor mechanical shock and vibrations expected in operation. End-thrust loading on the turbine is transmitted directly to the case by the novel suspension-spring element shown in Fig. 4. This construction permits no axial

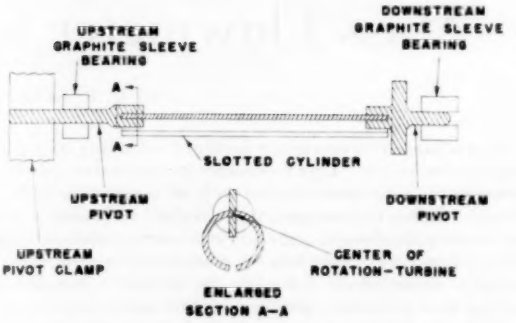

Fig. 4 Turbine Bearings and Suspension Spring

freedom of motion and not only insures precise axial alignment of the turbine but also eliminates end-thrust bearings and their associated friction errors and wear. Notwithstanding unusually severe end-thrust loading caused by viscous drag forces at high flow rates, exceptionally good calibration accuracy and stability are realized.

Electrical Design

The electrical wiring diagram is shown in Fig. 5. All components are contained within the flowmeter and are sealed from the fuel. The system for generating and calibrating the flowmeter-output signal is energized from the 115-volt, 400-cps power source of the aircraft. The output signal leads the excitation voltage by 15 electrical degrees and is proportional to mass rate of flow. The constant of proportionality is 1.000 volt per 1000

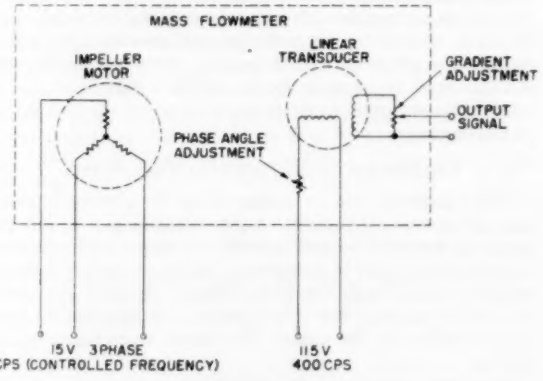

Fig. 5 Schematic Wiring Diagram

lb per min flow rate, precise calibration and phase relations being obtained through simple resistance adjustments. Through proper selection of circuit parameters, ambient temperature and self-heating effects of electrical components have negligible influence on operating characteristics; thus a highly stable system is realized without special temperature-compensating elements.

Power Supply

The power supply energizes the impeller motor with three-phase alternating current at a controlled frequency of 4 cycles per sec (cps). It comprises a direct-current timing motor which drives a separately energized commutator element at constant speed. The commutator converts direct current to three-phase alternating current. Radio frequencies are eliminated by an electrical filtering network. Constant frequency is obtained

by monitoring the timing motor with a spring-and-balance-wheel arrangement.

Performance

General design and performance characteristics are shown in Table 1. All mechanical and electrical adjustments are completed at the factory so that interchangeability of flowmeter transmitters in refueling system is realized. Fuel bleeding, purging, and priming are not required under any operating conditions. No warm-up time is necessary so that the flowmeter is ready for immediate use at any time after installation.

TABLE 1 DESIGN AND PERFORMANCE DATA

Rated capacity, lb per hr	600,000
Overload capacity, lb per hr	1,000,000
Physical dimensions:	
Length, in.	16
Diameter, in.	7¼
Weight, lb	18
Pipe diameter, in.[a]	4
Power requirements, watts	35
Pressure drop (at 240,000 lb per hr), psi	1.0
Scale-error	See Fig. 6
Hydrostatic pressure, psi	500

[a] This flowmeter can be supplied with adapters for a 3-in. line.

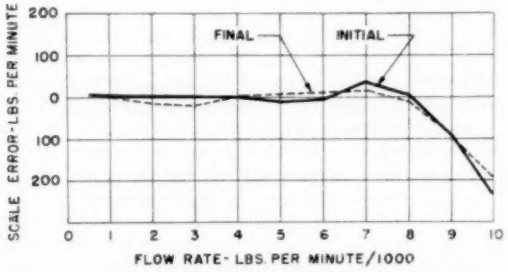

Fig. 6 Performance of Sample

Calibration of a sample is shown in Fig. 6, in which scale error is plotted versus true mass-flow rate. Errors due to bearing friction, mechanical and electrical hysteresis, and self-heating effects are below 5 lb per min at any flow rate. Excellent linearity is demonstrated by the fact that errors are less than 1 per cent of measured flow rate over 90 per cent of the scale range. Extreme precision is not required near full scale because such high flow rates occur only under emergency conditions. Accurate linearity over the normal working range is dictated by functional design of the measurements system. The importance of holding errors to a small per cent of "measured flow rate" lies in the cumulative characteristic of the basic measurement—total pounds of fuel transferred equals flow rate multiplied by time. Linearity of this meter is sufficiently close to permit totalizing pounds of fuel transferred within 1 per cent regardless of quantity or duration of refueling cycle for any flow rate within the normal operating range.

Calibration stability is shown by repeatability of measurements in a controlled series of tests conducted over an extended period of time. Results of such a series of tests are shown in Fig. 7, which is a curve of standard deviation[4] of the output signal, expressed in per cent of point, versus flow rate. Standard deviation is only about ¼ per cent over the greater part of the scale range. The larger values near the scale extremities reflect difficulties of measurement whose effects were inseparable from scale errors of the flowmeter. This series of tests covered several months during which the accumulated operating time exceeded 50 hr. The initial and final calibration curves, Fig. 6, show that there was no

[4] Standard deviation is the root-mean-square of deviations of individual readings from the average of the readings.

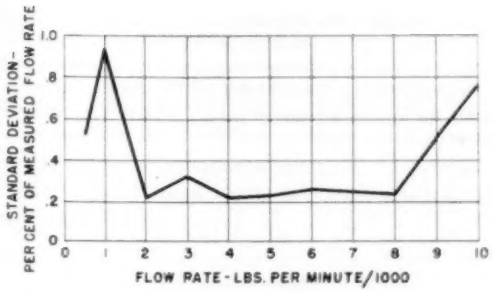

Fig. 7 Measured Stability

calibration drift within the measurement accuracy of the test equipment during these tests.

Owing to the nature of its application, the flowmeter for air-to-air refueling has to respond quickly and accurately to sudden changes in flow. Stringent requirements are imposed by relatively short refueling cycles during which flow rate is subject to unusually large and rapid variations. Careful balance of design parameters is required to obtain best results because response characteristics of the mass flowmeter are related in complex fashion to flow rate. This is illustrated in the curve of response time versus flow rate shown in Fig. 8. It is worth noting that transient oscillations in the output signal caused by sudden changes in flow de-

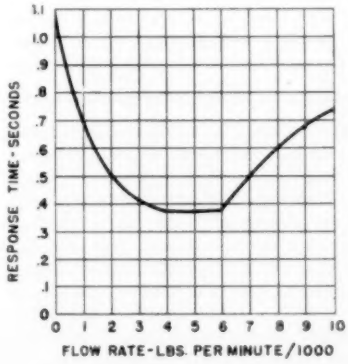

Fig. 8 Response Characteristic

cay so rapidly that they have no detectable effect on the measurement of fuel transferred. Tests show that response time (time for the output to come and remain within ±1.0 per cent of steady indication) is less than 1 sec following a sudden change of any direction or magnitude within rated capacity. These excellent dynamic-response characteristics permit accurate measurement of total pounds of fuel transferred regardless of how rapidly the tanker plane fuel-control valves are operated.

Conclusion

Speedy completion at maximum efficiency in air-to-air refueling requires precise and continuous indications of total quantity of fuel transferred and mass flow rate. The angular-momentum-type flowmeter is ideally suited to this application. It generates a signal that is linearly proportional to mass rate of flow independently of density, viscosity, and other properties of the fuel. Consequently no auxiliary compensating equipment is required. Although the design is mechanically simple, it is both compact and rugged besides exhibiting good accuracy and stabil-

ity of calibration. Other features are low pressure drop, negligible friction, and self-heating errors, no rotating-fluid seals, and fast response to sudden changes in flow. Notwithstanding the unusual severity of conditions encountered in air-to-air fuel transfer, the flowmeter has proved to be an important and reliable component in the successful completion of the refueling operation.

Acknowledgments

The author is indebted to Messrs. James Townsend, Guy Lai, and Chief Warrant Officer George Fels of the U. S. Air Force's Flight Control Laboratory, Wright Air Development Command at Dayton, Ohio, for their encouragement, technical advice, and guidance. Precision mass-flow testing at the high flow rates required was performed using the facilities of the Flight Control Laboratory, which is one of the few such facilities in the country for high flow-rate testing.

Noise, Vibration, and Measurement Problems, Resulting From Fluid-Flow Disturbances

By R. L. SOLNICK[1] and R. H. BISHOP,[2] WHITTIER, CALIF.

This paper has been prepared to give the reader a general understanding of the noise, vibration, and measurement problems resulting from fluid-flow disturbances. The occurrence of these problems in power plants has been given particular attention.

Nomenclature

The following nomenclature is used in the paper:

- A = projected area of obstacle (perpendicular to direction of flow)
- B = constant, dependent on configuration
- c = velocity of sound
- C_d = discharge coefficient for annular orifice, about 0.5
- C_k = dimensionless coefficient which may be called the von Karman coefficient, normally assumed ≈ 1
- C_t = a constant (approximately 0.20 for cylinders where the Reynolds number is between 2×10^2 and 2×10^5)
- d = orifice diameter, ft
- D = diameter of pipe, ft
- D_c = diameter of cylinder, ft
- f = frequency of vibrating object, cycles per sec (cps)
- f_m = frequency corresponding to most intense noise component, cps
- g = acceleration due to gravity
- F_k = von Karman force
- I = intensity of noise, watts/cm^2
- K = ratio of specific heats of gas
- p_c = absolute pressure in cylinder at instant of time when valve open area is S_v
- p_m = pressure difference indicated by meter
- p_0 = average absolute pressure in pipe
- p_r = amplitude of sound-wave pressure at distance r along axis of disk
- p_v = sound-wave pressure in exhaust pipe at instant when valve open area is S_v
- p_w = pulse (wave) pressure in discharge or suction nozzle at any instant
- P = pulse-pressure amplitude at orifice
- r = distance from center of disk, ft (r must be greater than Sf/c)
- S = cross-sectional area of pipe or disk
- S_c = cross-sectional area of compressor piston
- S_v = open area of valve at any instant
- u = fluid velocity (appropriate units)
- u_c = piston velocity at any instant
- $\rho u^2/2$ = stagnation pressure
- y = vibration amplitude of disk, ft
- $2y$ = total excursion of disk during vibration
- ρ = density of fluid, gm/cm^3

[1] Principal Research Engineer, Research Division, The Fluor Corporation, Ltd. Assoc. Mem. ASME.

[2] Senior Research Engineer, Research Division, The Fluor Corporation, Ltd. Mem. ASME.

Presented at the March, 1955, meeting of the Power and Fuels, Oil and Gas Power Division, Metropolitan Section of The American Society of Mechanical Engineers.

Note: Statements and opinions advanced in papers are to be understood as individual expressions of their authors and not those of the Society. Manuscript received at ASME Headquarters, March 22, 1956.

Introduction

Fluid-flow disturbances are of vital interest to the engineer. Under some conditions these disturbances may be desirable as, for example, in the increase of heat transfer resulting from turbulence or in the creation of musical notes, but in most cases they are not.

The undesirable effects of fluid disturbance are the subject of this paper, especially where these effects lead to noise, vibration, and measurement problems. The authors have attempted to summarize information which they have accumulated while pursuing various problems of this nature. Most of this experience has been in connection with gaseous fluids, although the basic approaches used would apply to liquids as well.

Various Sources of Fluid Disturbances

All fluid disturbances are potential sources of measurement error, noise, and vibration. Certain types of these disturbances are particularly bothersome in this respect and may be classified according to their origin under the headings which follow.

Reciprocating Compressors. Here the disturbance results from alternate compression and expansion of the fluid in a confined space. The disturbance normally appears as a pulse traveling at the speed of sound (itself a function of the gas properties) in the compressor suction and discharge piping.

Internal-Combustion Engines. There are two types of fluid disturbances associated with the internal-combustion engine:

(*a*) That which appears as a sound wave in the intake combustion-air piping as a result of rapid expansion of the gas in a confined space.

(*b*) That which results from the burning of a gaseous mixture in a confined space, and appears in the exhaust line as a sound wave.

As used in the preceding paragraphs, both the terms, "pulse" and "sound wave" describe a fluid-wave type of disturbance, the distinguishing factor being that the pulse is normally thought of in connection with a "closed" system as opposed to an "open" system for the sound wave.

Turbulence. During turbulent flow, low and high-pressure zones are formed in a random fashion. These zones are the sources of the sound waves which are associated with turbulent flow. In addition, these disturbances also may cause vibration of surfaces in or containing the fluid. These vibrating surfaces will then become sources of sound waves themselves.

Aerodynamically Induced. This is the type of disturbance associated with flow around a cylinder or similar section and is known as a vortex. A series of these vortexes shed from the down-

stream side of a cylinder is normally referred to as a von Karman vortex trail. These vortexes, in themselves, do not necessarily cause difficulty, but signal the presence of an unstable fluid-flow condition which gives rise to unbalanced forces acting on the cylinder. These forces, in turn, may cause serious vibration problems if the frequency at which they occur happens to coincide with the natural frequency of the structure. Under the proper conditions, shifting of the low-pressure zone associated with the vortexes from one side of the cylinder to the other may cause difficulty in itself, especially in combination with a resonant chamber. In this instance, vibration of the cylinder is not the problem, but rather it is the production of intense standing-pressure waves.

Steinman (1)[3] has proposed a second type of aerodynamically-induced vibration which always occurs under resonant conditions and does not involve the vortex phenomenon. In his opinion, this type of aerodynamically-induced oscillation was responsible for the destruction of the Tacoma Narrows Bridge on November 7, 1950.

Vibrating Members. As a solid object vibrates it causes alternate expansion and compression of the fluid surrounding it because of fluid inertia. This condition gives rise to the formation and propagation of sound waves. The member itself may be set into vibration by various means such as unbalanced mechanical forces, fluid disturbances, magnetic forces (2), and so on.

Formulas Used to Predict Amplitude and Frequency of Disturbances

In new *reciprocating-compressor* installations it is necessary to design pulsation-eliminating devices without benefit of actual pulse measurements. For this reason it is necessary to predict from known information the fundamental pulse amplitude and frequency which will exist in a particular compressor-piping arrangement. Predicting the fundamental frequency is not too difficult since, in most instances, it is simply related to the speed of the compressor, the number of single or double-acting cylinders, and the crank phase angle. The pulse amplitude resulting from a specific compressor installation is not as easy to predict. An equation developed by the authors for this purpose is

$$\frac{p_w}{p_0} = K(S_e/S)(u_e/c)$$

(See Appendix 1 for derivation.)

This formula was checked experimentally on both a 15-hp and 175-hp reciprocating compressor under various operating conditions and the results indicated good correlation. It should be pointed out that the formula assumes an infinite extension of constant-diameter pipe downstream of the compressor. In practice, of course, this is not usually the case, and the task of theoretically predicting the pulse where discontinuities exist in the downstream piping is a very difficult one. Considerable work is being done by the authors along these lines, and it is hoped that the results of this work may be published in the near future.

A method for predicting sound amplitudes and frequencies emanating from *internal-combustion-engine* exhausts also was developed in a fashion similar to that for compressors. This equation for the ratio of sound-wave pressure to average fluid pressure is

$$p_e/p_0 = (1.4)KC_d(S_e/S)(K-1)^{-1/2}[(p_e/p_0)^{(K-1)/K} - 1]^{1/2} \quad [1]$$

(See Appendix 1 for derivation.)

[3] Numbers in parentheses refer to the Bibliography at the end of the paper.

All items with the exception of S_e and p_e can be obtained with little or no difficulty. In most instances the engine manufacturer would be able to supply values for S_e and p_e, but in the event that he could not, it is not too difficult to predict maximum limiting values. The maximum pressure in the cylinder under most circumstances would be equal to the pressure at the time of firing (cylinder approximately at top of stroke). This value should certainly be available from the manufacturer since it is required by him in order to design the cylinder properly. Of course the maximum open area of the valve would not occur at the instant of maximum pressure but at some time after the piston has passed bottom dead center. The pressure in the cylinder at bottom dead center could be calculated from the maximum pressure by use of the gas laws and, as a limiting assumption, maximum valve opening could be assumed to occur at this point. This formula has been used to predict the exhaust-gas-sound pressure amplitude for a 150-hp diesel engine and good correlation was obtained.

The occurrence of noise resulting from *turbulent* flow is very common. Intake-air ducts, gas lines, steam lines, pressure-reducing valves, and fans are only a few of the sources of this type of noise. As mentioned previously, this type of flow actually may give rise to two different types of noise. One type originates in the fluid itself and is a function of the statistical pressure fluctuations of the fluid. The other is that resulting from the vibration of bodies in or containing the fluid which are set in motion by the fluid disturbances. From work done by the Air Force (3), the frequency and intensity of noise emanating from the fluid itself can be expressed by the following formulas, respectively

$$f_n = 3(u/D) \quad [2]$$

$$I = B\rho u^3 \quad [3]$$

Formula [2] was developed by plotting a dimensionless frequency parameter fD/u versus over-all sound level (Fig. 1) and then

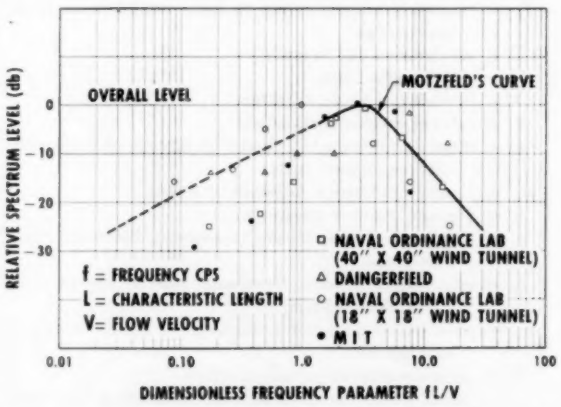

Fig. 1 Correlation of Experimental Data With Motzfeld's Curve—Dimensionless Frequency Parameter fL/V Versus Sound Level

setting this parameter equal to the value at which maximum sound level occurred. Examination of Fig. 2 indicates the broad frequency spectrum obtained. This is logical when one recalls the conditions giving rise to this type of disturbance; i.e., random pressure fluctuations in a flowing fluid.

Since the constant B in Equation [3] can be determined only by experiment, the usefulness of this equation lies principally in being able to make comparisons of sound intensities for varying fluid densities and velocities.

The noise emanating from the surfaces in and/or containing the

turbulent fluid will be dependent on the surface characteristics and will be discussed under Vibrating Members.

Aerodynamically-Induced Disturbances, known as vortexes, are shed at a definite frequency from alternate sides of a cylinder placed in a fluid stream, as depicted in Fig. 2. Strouhal (4) in 1878 published a formula based on observation alone which predicted the frequency at which these vortexes were shed

$$f = C_1(u/D_c) \quad [4]$$

Referring to Fig. 2, it can be seen that the velocity on the "vortex side" of the cylinder is greater than that on the opposite side

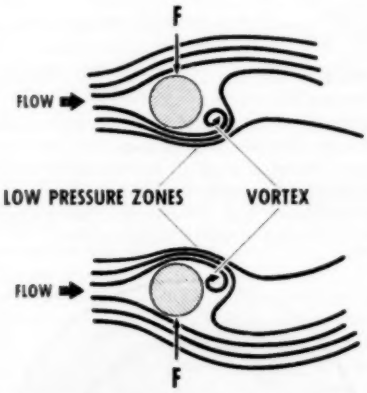

FIG. 2 CHANGE OF RESULTANT FORCE F ON CYLINDER WITH SHIFTING OF VORTEX DOWNSTREAM OF CYLINDER

which, in turn, means that the pressure will be lower on the vortex side. This gives rise to an unbalanced force which then reverses its direction as the vortex is shed and another vortex builds up on the opposite side of the cylinder. A theoretical analysis of this subject was made by von Karman in 1911 (4), and the following equation for the force involved was developed on the basis of dimensional analysis

$$F_k = C_k(\rho u^2/2g)A \quad [5]$$

Vibrating Members are probably the most common source of sound energy. These members may be set into motion physically such as when an object is struck, or the vibrations may be induced as in the case of a pipe wall set into motion by fluid flowing turbulently inside the pipe. In either case the sound waves emanate from a surface and are radiated to the surroundings. A mathematical derivation has been carried out in order to determine the sound pressure generated in a gas by a vibrating disk which is part of an infinite plane. The ratio of the sound-wave pressure to the average fluid pressure resulting from this arrangement can be expressed by a relatively simple formula

$$p_r/p_0 = (6.28)(f/c)^2KSy/r \quad [6]$$

Equation [6] is almost self-explanatory, but it might be pointed out that the quantity (Sy) is the same as the volume of gas displaced by the disk during one half of its total excursion in a cycle of periodic motion. It can be proved that the pressure p_r defined by Equation [6] also represents the sound pressure at any point off the axis at a distance r from the center of the disk, provided the wave length λ (or c/f) of the sound vibration is greater than the diameter of the disk.

It is also of interest to substitute some numerical values for the symbols in Equation [6] to get an idea as to the order of magnitude of the sound-pressure level resulting from vibrating surfaces. Assume

p_0 = 10^6 dynes/cm^2 = approximate value of atmospheric pressure
f = 1000 cps vibration frequency
c = 1137 fps for air at 80 F
K = 1.4 for air
S = 1.0 sq ft area of disk
r = 10 ft distance from disk
y = 0.001 ft = 0.012 in.
λ = c/f = 1137/1000 = 1.14 ft wave length

Then, from Equation [6]

$$p_r/p_0 = \frac{(6.28)(1.4)(10^{-3})}{(1.14)^2(10)} = (0.675)(10^{-3})$$

and the sound pressure p_r is only $(0.675)(10^{-3})$ times atmospheric pressure. Thus

$$p_r = 675 \text{ dynes/cm}^2$$

This is a rather small pressure compared to atmospheric, but nevertheless it represents an extremely intense sound wave. The pulse pressure existing in a zero decibel sound wave is only

$$p_1 = 2.8\,(10^{-4}) \text{ dynes/cm}^2 \text{ (amplitude — not rms value)}$$

Thus

$$p_r/p_1 = (6.75/2.8)(10^6) = 2.4(10^6)$$

and the pressure at 10 ft from the disk is 2.4 million times as intense as the pressure corresponding to a zero decibel sound wave. Since the power in a sound wave is proportional to the square of the pressure, the sound power 10 ft from the disk, W_r, is

$$W_r/W_1 = (2.4)^2 10^{12} = (5.7)(10^{12}) = (p_r/p_1)^2$$

or 5.7 trillion times as great as in a zero decibel sound wave. In decibels this ratio can be expressed as

$$(W_r/W_1)_{db} = 10 \log_{10} [(5.7)10^{12}]$$

or

$$(W_r/W_1)_{db} = 127.5 \text{ decibels}$$

A sound wave more intense than 120 decibels is actually painful to the ear, especially at the relatively high frequency of 1000 cps. Thus the vibration amplitude of only 0.012 in. which seems rather small, is in reality very dangerous at the high frequency of 1000 cps.

INSTRUMENTATION USED IN DETECTING FLUID DISTURBANCES

In detecting fluid disturbances of interest here, some sort of pressure transducer is required, since in all cases the disturbances are characterized by recurrent pressure fluctuations. These pressure transducers take various forms and use different methods for changing pressure variation into a varying electrical signal. They may be classified according to the electrical characteristic used to produce this varying electrical signal and fall logically into the following categories: (*a*) Resistive, (*b*) capacitive, (*c*) magnetic, (*d*) piezoelectric, (*e*) electronic. In addition, there has been developed recently (5) a transducer based on the gas-discharge principle. The magnetostrictive (magnetic), unbonded strain gage (resistive) shown in Fig. 3, and crystal (piezoelectric) types are the ones most frequency used by the authors. All three of these transducers take the form of a high-pressure diaphragm and case type of unit which may be screwed into a pipe wall. The crystal type of pickup is used also in the form of a microphone as, for instance, in the sound-level meter. In general, its use is re-

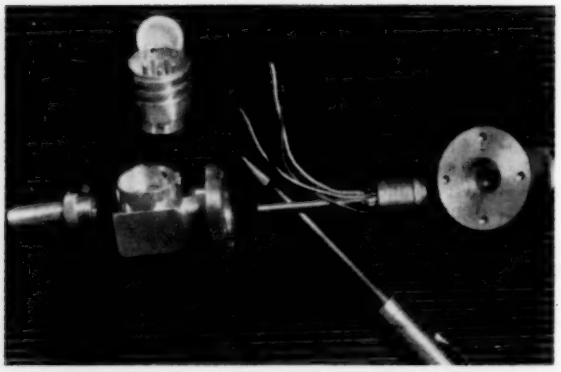

FIG. 3 TYPICAL UNBONDED STRAIN-GAGE-TYPE PRESSURE TRANSDUCER SHOWN DISASSEMBLED FROM SPECIAL CASE

stricted to temperatures below 120 F and low pulse amplitudes, whereas the unbonded strain-gage type may be used at temperatures as high as 250 F. The magnetostrictive type is capable of operation at temperatures as high as 1000 F. Recently, some of the manufacturers have appreciably raised the upper operating temperature limit of the unbonded strain-gage type by circulating water or air through passages in the transducer casing. As the reader may well imagine, considerable time could be spent on the subject of the transducer itself, but time and space do not permit and it is actually unnecessary since a considerable amount of literature (6) has already been published on this subject.

To this point the discussion has been limited to the conversion of a pressure signal to an electrical one. This electrical signal in most cases must be amplified and in some instances also integrated in order to be observed on an oscilloscope or meter, or recorded by an oscillograph. Recording of pressure fluctuations is normally limited to higher pulse amplitudes. For small-amplitude pressure waves, such as encountered in sound problems, the sound-level meter and analyzer and octave-band analyzer are used. On some occasions, it is necessary to measure vibrations in order to isolate the cause of the sound or pulse, and for this work the vibration meter and analyzer are used.

Often it is necessary to take considerable electronic equipment into the field in order to analyze a sound, vibration, or pulsation problem effectively. A well-equipped mobile laboratory is highly desirable in these instances and the authors have been fortunate in having such a laboratory available for their use.

DETRIMENTAL EFFECTS OF FLOW DISTURBANCES

Vibration is probably the most familiar and destructive effect of fluid-pressure disturbances. Rupture of high-pressure pipe lines due to pulsation-induced vibrations, with its serious consequences, is not unusual in the gas-transmission field. Most engineers are familiar with other examples such as vibrating internal-combustion-engine exhaust pipes, rattling windows, vibrating sheet-metal duct walls, vibrating floors, "galloping" suspension bridges, and many others. All of these are, of course, highly undesirable.

Measurement of pressure drop, pressures, and flow can be extremely difficult under pulsative flow conditions (7). Many engineers have observed vibrating pressure-gage needles and what appeared to be a negative pressure drop in a pipe run. Both of these phenomena are a result of pulse action on the recording instruments and their associated lines. One very interesting problem which the authors have encountered concerns the use of orifice meters under pulsative flow conditions. It was found that errors in flow measurement as great as 23 per cent for undamped, and $3\frac{1}{2}$ per cent for damped meter lines could result. A damped meter line is defined as one in which the pulse pressure at the meter is less than 5 per cent of the pressure difference recorded by the differential meter itself. The damped-line error may be expressed as

$$\frac{\text{True flow rate}}{\text{Indicated flow rate}} = 1.0 - (0.25)(P/p_m)^2 \left[1 + (0.85)(Kp_0/p_m)^{1/2}(D/d)^{-2}\right]^{-2}$$

(See Appendix 2 for derivation.)

The undamped line error may be expressed as

$$\frac{\text{True flow rate}}{\text{Indicated flow rate}} = [1.0 - (0.7)(1/K)(D/d)^4(p_0/p_m)(P/p_0)^2]^{1/2}$$

(see Appendix 2 for derivation) assuming that there is no phase difference between the two instrument lines.

The accurate measurement of pressure under pulsative-flow conditions usually requires damped gage lines also, since judging the center of oscillation of a rapidly moving needle is difficult even if one assumes that the needle faithfully responds to the actual pressure fluctuations. Fig. 4 shows a differential-pressure recorder chart indicating effects of pulsative flow.

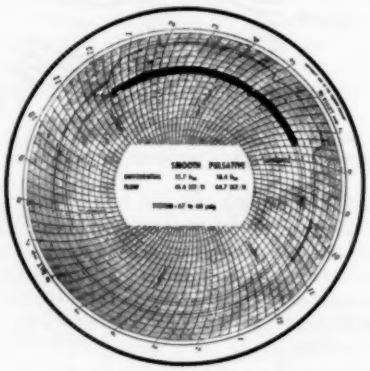

FIG. 4 DIFFERENTIAL-PRESSURE RECORDER CHART SHOWING EFFECTS OF PULSATIVE FLOW

Although no difficulty has been encountered by the authors, it is very likely that errors exist in the measurements of fluid temperature and velocity under certain pulsative-flow conditions.

Serious physiological damage can result from intense fluid disturbances in the form of sound. Probably even more common and costly to industry is the mental problem posed by disturbing noises. In most cases, these sounds do not inflict bodily damage but seriously impair the workers' efficiency. Vibrations resulting from fluid disturbance seldom cause physical harm, but again affect the workers' efficiency. Many of the sound and vibration surveys in which the authors have become involved were a direct result of complaints by employees or nearby neighbors.

The change of process effectiveness as a result of pulsative flow is an area in which so little work has been done that it is impossible to evaluate its effect intelligently. However, enough has been accomplished to know that there is some effect, sometimes desirable and sometimes undesirable. Probably much more will be done in this field in the near future. Such items as combustion (8), heat transfer, and mass transfer are certain to come under further investigation.

Theoretically, the pressure drop of a fluid flowing in a pipe under pulsative-flow conditions should be greater than the same

quantity of fluid flowing in the same pipe under uniform flow conditions. Experimentally, this has been found to be the case and may amount to a severalfold increase depending on the pulse amplitude. The additional pumping horsepower required under these conditions may become an important economic consideration especially if large quantities of fluid are pumped, as is the case in the gas-transmission industry.

There is considerable evidence that engines and compressors, operating under conditions whereby reflected pulse waves may communicate with the cylinders, suffer a loss in efficiency. The major obstacle to evaluating this effect quantitatively is the lack of an accurate, easy-to-use horsepower indicator. Without an effective means of determining horsepower and valve action accurately, it is impossible to evaluate the effect of pulsative flow on engine and compressor operation. The authors are currently doing work along these lines and it is hoped that effective evaluating techniques soon will be developed.

Methods for Attenuating Disturbances or Eliminating Effects

Pulsation dampeners, exhaust-gas mufflers, and intake combustion-air silencers are devices commercially available for handling fluid-flow disturbances caused by engines and compressors. No attempt will be made to discuss the complex factors affecting the design of these units.

Most turbulent noise may be treated with the use of some type of sound-absorbing material. In most instances where the sound is generated inside a container, the acoustical material may be applied either externally or internally. In the case of valve noise it is usually more convenient to apply the treating material externally. One good example of the type of problem often encountered involves noise generated by the regenerator blowoff of a fluid catalytic-cracking unit in which high-temperature flue gas is ejected to the atmosphere through a large stack. Flow control of the gas is obtained by a slide valve which in one installation was placed approximately 15 ft below the exit of a 72-in-diam stack. A pressure drop of approximately 6 psi was being taken across the valve and it was at this point that the severe noise was being generated. The noise was seriously affecting the morale of the operating personnel and there is no doubt that complaints would have been registered from nearby residents if such had existed. This problem was solved by first placing two perforated trays in the existing stack as shown in Fig. 5 for the purpose of converting the low to high-frequency noise. Once all the noise was converted to the high-frequency range, it was possible to attenuate it by using acoustically lined duct downstream of the plate. With this arrangement, the noise level was reduced approximately 15 decibels (db) in the immediate vicinity of the stack and the objectionable roar which previously existed was eliminated completely. This type of silencer also could be used for such applications as steam blowoff silencing.

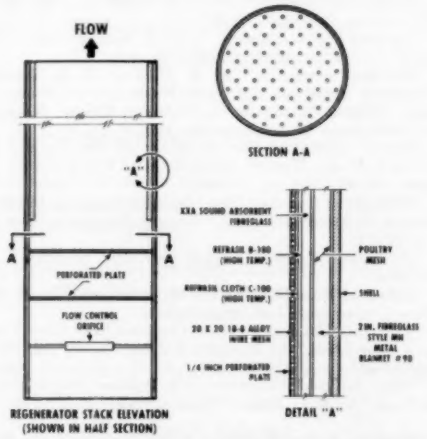

Fig. 5 Silencer Used for High-Temperature (1100 F) Exhaust Gases From Catalytic-Cracker Regenerative Unit

The technique of handling vibrations or pulses resulting from conditions identified by aerodynamically-induced vortexes is completely different from that just outlined. There are basically three methods for handling the problem:

1 Streamlining of the body so as to eliminate formation of the vortexes.

2 Applying some sort of baffle so as to prevent the vortexes from acting in phase.

3 Bracing of the structure subject to vibration.

The first method, in most cases, is the most costly and impractical. The use of baffles to prevent resonance is a practical solution and has been applied successfully in at least two instances by the company with which the authors are associated:

1 Virtual elimination of the vibrations occurring on a 30-in. gas pipeline suspension bridge across the Colorado River (9).

2 Elimination of a serious vibration problem resulting from a pulse condition in the low-temperature superheater-economizer section of a 920,000 lb/hr steam generator.

The "galloping" pipeline bridge referred to was being set into vibration by unbalanced, in-phase forces characterized by von

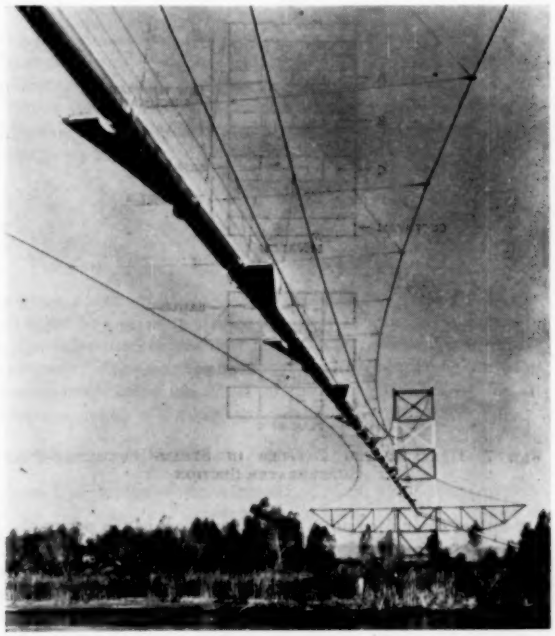

Fig. 6 Pipeline Suspension Bridge With Baffles Used to Prevent Aerodynamic Oscillations

Karman vortex trails and caused by a 4 to 6 mph wind passing across the cylindrical pipeline section. This problem was solved with the use of baffles placed on the bridge, as shown in Fig. 6, to prevent "in-phase action" of the unbalanced forces. It also could have been solved by mechanical bracing (10).

The steam-generating-unit problem also was solved by means of baffles (11), but this will be discussed more fully later.

Many other examples of aerodynamically-induced vibrations for structures such as smokestacks (4), chemical-processing columns (12), highway suspension bridges (1), and antennas may be found in the literature.

Mechanical bracing is often used to reduce noise and vibration by increasing the stiffness of the structure. This increased stiffness reduces the displacement caused by the application of a given force. The higher stiffness also increases the resonant frequency which in turn often results in higher-frequency vibrations or sound. Sometimes these higher frequencies are permissible and are almost always more easily attenuated. Certainly in the case of sound the higher-frequency noise is more easily dealt with since relatively simple acoustical treatment usually will suffice. This method of reducing energy or converting it to a more easily attenuated form should also be considered. Often, however, as in the case of severe pulsative flow in pipeines, mechanical bracing is unsatisfactory.

Noise and Vibration Problems in Power Plants

One example in this category is the problem which occurred at a large steam-generating plant. Here a severe pulsing condition existed in the superheater-economizer section of the boiler. This condition was caused by a periodically varying pressure (von Karman vortexes) induced by gases flowing across a cylindrical cross section, coupled with acoustically resonant chambers. The problem was solved with the use of baffles, as shown in Fig. 7, to deresonate the chamber.

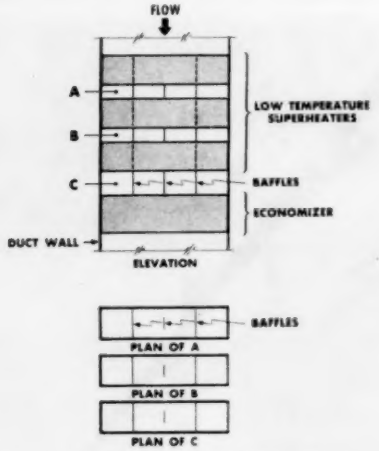

Fig. 7 Deresonating Baffles in Steam-Generating-Plant Superheater Section

Most of the noise and vibration problems in the power-plant field with which the authors are familiar (excluding that mentioned in the foregoing), are caused by turbulent-flow conditions. Typical of these turbulent-noise sources are forced-draft-fan inlets, fuel-gas regulators, boiler blowoff tank vents and safety-valve-discharge pipes, cooling-tower fans, air-discharge openings in motor housings, high-velocity flow in natural-gas lines, throttled flow in feed-pump recirculation lines, steam manifolding, and air-compressor intakes.

These various examples are actual problems which were encountered by several of the major power companies on the West Coast. One problem concerning a main steam-line vibration was very interesting and probably is worth some discussion. The source of the vibration was traced to a point in the main steam line where two $5^1/_2$-ft, 14-in. stub lines had been installed opposite each other for possible future expansion. It was found that the broad noise spectrum which was generated by the turbulent flow of steam in the line caused resonant conditions to exist at this point. The frequency of vibration was equal to that calculated for a closed-end organ pipe $5^1/_2$ ft long. The problem was solved by removing one of the stub connections and plugging the opening (a model was used to arrive at this solution). Although the authors were not involved in this problem, and learned of it through a report published by the company concerned, it is our feeling that the reason the resonance occurred with two stub connections and not with one is that it would appear to be easier to excite a half-wave rather than a quarter-wave type of resonance. Another way of looking at this is to consider that each stub in itself was excited to a minor degree by the turbulent noise, but when two stubs with identical acoustical characteristics were placed directly opposite each other they were even more actively excited. It would be similar to having two strings individually excited and also interconnected so that motion of one induced motion in the other.

In general, it can be said that noise resulting from turbulent flow is the type most frequently occurring in the power industry, but fortunately it can be dealt with rather easily in most cases since this type of noise is usually in the higher-frequency range and is susceptible to treatment with acoustical materials. Where difficult vibration problems are encountered, it probably would be wise to look for turbulent noise in combination with some sort of resonant chamber. In these cases, some type of baffling usually will suffice to correct the condition.

Although rather simple treatment will suffice to solve most power-plant noise problems, the number of these problems requiring solution will increase with the increasing use of outdoor stations (13, 14). These outdoor stations, like many of the oil and gas-industry installations, will bring complaints from nearby residents even though the noise levels are much lower than those considered satisfactory from an employee standpoint.

Acknowledgment

The authors wish to express appreciation to Mr. O. H. Hedrich for his help in obtaining information concerning sound and vibration problems in power plants. The comments of other Fluor personnel relative to the content of the paper are also acknowledged with thanks.

Bibliography

1 "Suspension Bridges," by D. B. Steinman, *American Scientist*, vol. 42, July, 1954, pp. 397–438.

2 "Keeping Products Quiet," by D. F. Muster, *Product Engineering*, vol. 25, December, 1954, pp. 140–145.

3 "Physical Acoustics," by R. H. Bolt, L. L. Beranek, and R. B. Newman, Handbook of Acoustic Noise Control, WADC Technical Report 52-204, Wright Air Development Center, Wright-Patterson Air Force Base, Ohio, December, 1952.

4 "Recent Technical Manifestations of von Karman's Vortex Wake," by J. P. den Hartog, Proceedings of The National Academy of Science, vol. 40, 1954, pp. 155–157.

5 "Transducer Based on Gas-Discharge Principle Paves Way for Advances in Measurement Field," *Western Electronics News*, October, 1954, pp. 20–21.

6 "Transducer," second edition, published by Allen B. Dumont Laboratories.

7 "Effect of Pulsation on Gas Measurement," by C. F. Yates, The Fluor Corporation, Ltd., unpublished.

8 "Pulsating Combustion: An Old Idea May Give Tomorrow's Boilers a New Look," by Howard Kallen, *Power*, vol. 98, August, 1954, pp. 88–91.

9 "Wind-Induced Vibration of a Pipeline Suspension Bridge, and Its Cure," by R. C. Baird, Trans. ASME, vol. 77, 1955, pp. 797–804.

10 "Pipeline Bridge Stabilized With Diagonal Rope Stays," by D. B. Steinman, *Civil Engineering* (N. Y.), vol. 22, March, 1952 pp., 25–27.

11 "Pulsation-Induced Vibration in Utility Steam Generation Units," by R. C. Baird, *Combustion*, vol. 25, April, 1954, pp. 38–44.
12 "Aerodynamic Vibration of Tall Cylindrical Columns," by R. C. Baird, The Fluor Corporation, Ltd., unpublished.
13 "Trends in Utility Plants," *Power*, vol. 98, mid-September, 1954, p. 39.
14 "How Do the Operators Like Outdoor Power Plants?" *Power Engineering*, vol. 58, June, 1954, pp. 68–70.

Appendix 1

Pulse Amplitudes in Piping

Pulse Pressure Amplitude in Compressor Piping (Fig 8)

du_c = compressor piston-velocity change
du = velocity change of gas in pipe near valve
S_c = cross-sectional area of piston
S = cross-sectional area of pipe

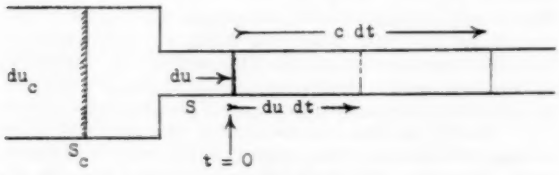

Fig. 8

From the necessity for continuous mass flow of gas across the change of areas between the compressor cylinder and the pipe

$$du = du_c(S_c/S) \quad \ldots\ldots [7]$$

A given portion of gas near the pipe entrance moving at the additional velocity du will move an additional distance $du\,dt$ in the time dt. The disturbance propagates down the pipe at the speed of sound c, and therefore the gas beyond a distance $c\,dt$ (at $t = 0 + dt$) from the reference location ($t = 0$) remains at constant velocity and is not affected by the change in piston velocity at time $t = 0$. Thus the gas in between is relatively compressed, or "condensed" by the fractional amount

$$-dv/v_0 = (du\,dt)/(c\,dt) = du/c \quad \ldots\ldots [8]$$

in which v_0 is the initial volume of gas and $-dv$ is the reduction in volume produced by the change of velocity du at the time $t = 0$.

For an adiabatic change of state of a perfect gas

$$-dv/v_0 = K^{-1}(dp/p_0) \quad \ldots\ldots [9]$$

where

K = ratio of specific heats of gas
$K = C_p/C_v$
dp = change of pressure of gas
p_0 = absolute pressure of gas
v_0 = initial volume of gas

Equation [9] follows from differentiating the equation of state for adiabatic reversible changes of a perfect gas

$$pv^K = \text{const} \quad \ldots\ldots [10]$$

Substituting the value of $-dv/v_0$ from Equation [9] into Equation [8] gives

$$dp/p_0 = K\,du/c \quad \ldots\ldots [11]$$

Substituting the value of du from Equation [7] into Equation [11]

$$dp/p_0 = K(S_c/S)(du_c/c) \quad \ldots\ldots [12]$$

Integrating both sides of Equation [12]

$$(p - p_m)/p_0 = K(S_c/S)(u_c/c) \quad \ldots\ldots [13]$$

in which p_m is the absolute pressure at the instant when the piston velocity u_c is equal to zero.

Define $p - p_m = p_w$ = wave pressure in pipe at any instant. Then from Equation [13]

$$p_w/p_0 = K(S_c/S)(u_c/c) \quad \ldots\ldots [14]$$

Internal-Combustion-Engine Exhaust-Pulse Pressure (Fig. 9)
Let

S_v = open area of valve for flow of gas at any instant
S_e = cross-sectional area of exhaust pipe

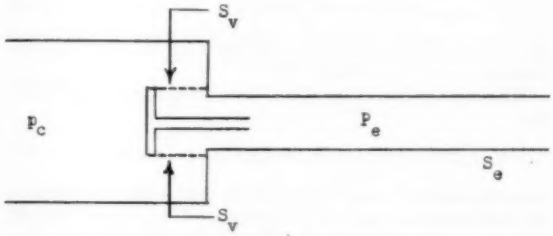

Fig. 9

The pulse pressure in the pipe at any instant during the cycle depends on the open area of the valve S_v and on the cylinder pressure p_c at a given instant.

From the generalized Bernoulli law for variable density, in differential form, the fluid pressure p and velocity u in the valve passage are related according to

$$\left.\begin{aligned} -dp &= (0.5)\rho d(u^2) \\ \text{or} \qquad -\rho^{-1}dp &= (1/2)d(u^2) \end{aligned}\right\} \quad \ldots\ldots [15]$$

in which ρ is the fluid density and du is the fluid-velocity change produced by a pressure change dp. Let the pressure and density in the valve-passage end near the exhaust pipe be p_e and ρ_e, respectively. The pressure and density at any point along the valve passage are related according to the equation of state for an adiabatic change of a perfect gas

$$\rho^{-1} = (p_e/p)^{1/K}\rho_e^{-1} \quad \ldots\ldots [16]$$

where K is the specific-heat ratio C_p/C_v, and p and ρ are, respectively, the pressure and density of the gas at any point along the valve passage between the cylinder and the exhaust pipe.

Substituting the value of ρ^{-1} from Equation [16] into Equation [15] gives

$$-(0.5)d(u^2) = \rho_e^{-1}p_e^{1/K}p^{-1/K}dp \quad \ldots\ldots [17]$$

Integrating Equation [17] from $p = p_e$ (at the exhaust pipe) to $p = p_c$ (in the cylinder) gives

$$(0.5)(u_e^2 - u_c^2) = \rho_e^{-1}p_e^{1/K}\int_{p_e}^{p_c} p^{-1/K}\,dp$$

neglecting energy losses due to viscosity and heat conduction

$$(0.5)(u_e^2 - u_c^2) = K(K-1)^{-1}(p_e/\rho_e)[(p_c/p_e)^{(K-1)/K} - 1] \quad \ldots\ldots [18]$$

Since the flow velocity u_v in the valve-passage end near the exhaust pipe is much greater than the flow velocity u_c in the cylinder, Equation [18] may be written approximately as

$$(0.5)u_v^2 = K(K-1)^{-1}(p_e/\rho_e)[(p_c/p_e)^{(K-1)/K} - 1] \quad [19]$$

The velocity of sound c in the exhaust pipe is

$$c = (Kp_e/\rho_e)^{1/2} \quad [20]$$

Taking the square root of both sides of Equation [19], and using Equation [20] gives

$$u_v/c = (1.41)(K-1)^{-1/2}[(p_c/p_e)^{(K-1)/K} - 1]^{1/2} \quad [21]$$

The mass rate of flow of fluid M_v through the annular valve passage area S_v is

$$M_v = C_d S_v \rho_e u_v \quad [22]$$

in which C_d is the discharge coefficient for the annular valve passage with cross-sectional area S_v.

The mass-flow rate of gas along the exhaust pipe of cross section S_e is

$$M_e = S_e \rho_e U_e \quad [23]$$

where U_e is the velocity of flow of the fluid in the exhaust pipe. By conservation of matter the two mass-flow rates M_v and M_e must be equal, and Equations [22] and [23] therefore lead to the condition that

$$U_e = C_d u_v (S_v/S_e) \quad [24]$$

The wave pressure in the exhaust pipe p_w is related to the fluid-flow velocity U_e in the exhaust pipe, and is obtained by integrating Equation [11]

$$p_w/p_e = KU_e/c \quad [25]$$

in which

$$p_w = p - p_m$$

where p_m is the absolute pressure when $U_e = 0$, and p is the absolute pressure for any other value of U_e.

Substituting the value of U_e from Equation [24] into Equation [25] gives

$$p_w/p_e = KC_d(S_v/S_e)(u_v/c) \quad [26]$$

Substituting the value of u_v/c from Equation [21] into Equation [26]

$$p_w/p_e = (1.4)KC_d(S_v/S_e)(K-1)^{-1/2}[-1 + (p_c/p_e)^{(K-1)/K}]^{1/2}$$

Appendix 2

Flow Measurement Errors Due to Pulsating Gas Pressure

Meter With Undamped Pressure Lines. When a differential-pressure gage is used with an orifice plate to measure a pulsating flow, the pressure lines are ordinarily undamped and the pressure fluctuations both above and below the orifice plate are transmitted with undiminished amplitude to each side of the differential-pressure transducer element. The differential-pressure transducer element itself is ordinarily damped, however, and therefore it indicates an average value of the various differential pressures which reach the element during a complete cycle. If the pressure lines to the differential-pressure gage are short, there is no phase shift in going from the pipe to the gage, and the pressures at the gage-transducer element are therefore assumed to be the same as the pressures near the orifice plate in the pipe, both in amplitude and in phase. At any instant of time, the pressure difference across the transducer results in a force which tends to move the indicator of the gage, but the indicator will not follow rapid fluctuations, especially if it is damped. Hence only the average value of the fluctuating force is indicated by the meter, and all the purely oscillatory components are damped out by the inertia and friction of the transducer element of the differential-pressure gage. In other words, all the sinusoidal components of the Fourier representation of the variable pressure are not indicated by the meter because the average value of each sinusoidal component (over a complete cycle) is zero.

The correct average flow rate is not indicated by the meter because it indicates the average pressure-difference across the orifice plate during a cycle. As will be shown later, the pressure-difference across an orifice plate at any instant is approximately proportional to the square of the fluid flow rate through the orifice at that same instant of time. Therefore the meter deflection indicates approximately the average of the squares of all the different flow rates which occur during a complete cycle of the oscillating motion of the fluid. The true flow rate, of course, is by definition equal to the average value of all the different flow rates that occur during a complete cycle of the pulsating-fluid motion. The flow inferred from the meter is the square root of the average of the squares of the various flow rates occurring during a cycle. In general, this RMS (root-mean-square) flow rate inferred from the meter is not equal to the true average flow rate. Therefore a correction must be applied, which can be measured experimentally or calculated approximately. The following calculation is made with the assumption of short undamped pressure lines from the pipe to the differential-pressure meter. It will be shown later that the use of damped lines to the meter will result in a much smaller error in the indicated flow rate. Moreover, when the pressure lines are damped there is no length limit, since no phase shift is thereby introduced between the pipe and the meter, and therefore no pressure wave-form distortion can occur between the pipe and the meter. This results because no oscillating pressure reaches either side of the gage.

In order to deduce the correct average flow rate, it is necessary to know the relation between pressure difference and flow rate at each instant during one complete cycle of the oscillatory fluid motion through the orifice. Once this is known, the total flow during a complete cycle can be found by integrating the flow rates at all instants of time during a cycle. A rigorous analysis of this problem requires solving the complete nonlinear differential equation of fluid flow, including both the steady average component and the oscillating component. The total acceleration of an element of fluid, du/dt, can be resolved into two components; (a) the "autonomous" acceleration $\partial u/\partial t$, and (b) the "convective" acceleration $u\partial u/\partial x$ (for one-dimensional flow along a tube). The convective acceleration term can occur even with a steady flow.

For example, fluid is accelerated in passing by a constriction in a pipe, even though the flow velocity u, at any single location along the pipe, is steady; i.e., does not change with time. The autonomous acceleration is the velocity change of any fluid element occurring at a fixed point in space. The convective acceleration is the velocity change which occurs as a result of the change of location of a single element of fluid. The convective acceleration $u\partial u/\partial x$ is nonlinear in u, as can be seen by rewriting it as $(1/2)(\partial u^2/\partial x)$. When the fluid-flow differential equation is integrated for steady flow, the term $\partial u/\partial t$ is zero because the autonomous acceleration of all fluid elements is zero for steady flow, by definition, since at any one location in space the flow velocity does not change with time. The result of the integration is the well-known Bernoulli formula

$$p_2 - p_1 = (1/2)\rho(u_1^2 - u_2^2)$$

where

p_1 = pressure at orifice
p_2 = pressure upstream of orifice
ρ = fluid density
u_1 = fluid velocity at orifice
u_2 = fluid velocity upstream of orifice

The fluid velocity at the orifice cannot be calculated merely by multiplying the upstream fluid velocity by the ratio of the pipe cross-sectional area to the orifice area, because the fluid contracts to make a smaller cross section than the actual orifice area. When the foregoing formula is used to relate the pressure drop across an orifice to the effective flow velocity averaged over the area of the orifice, it is necessary to know the value of an empirical correction factor called the discharge coefficient

$$u_a S = F_p C_D S[2\rho^{-1}|p_t|]^{1/2}[1 - (d/D)^4]^{-1/2} \ldots\ldots [27]$$

where

C_D = discharge coefficient
$|p_t|$ = absolute value of pressure difference across orifice at time t
F_p = 1.0 when p_t is positive
F_p = —1.0 when p_t is negative
ρ = density of fluid
$u_a S$ = volume flow rate of fluid at time t
u_a = "effective" velocity of fluid, averaged over area of orifice
S = area of orifice
D = diameter of pipe
d = diameter of orifice

Since the autonomous-acceleration term $\partial u/\partial t$ (due to nonsteady flow) has been assumed equal to zero in the derivation of Equation [27], it is clear that the formula cannot be absolutely accurate when the flow velocity u changes with time (at any fixed location in the pipe) as necessarily occurs under conditions of pulsating pressure and velocity. The error in Equation [27] comes about because of the neglected autonomous-acceleration term $\partial u/\partial t$ which results in an additional pressure drop across the orifice when the flow velocity changes with time. To evaluate the resulting error with complete accuracy requires solving a nonlinear-wave equation derived from both the autonomous and the convective accelerations. However, it has been shown by others that the nonlinear convective acceleration term can be neglected to a first approximation in the derivation of the usual acoustic wave equation, which is linear. It can be shown that this linear-wave equation is sufficiently accurate whenever the total fluid velocity is small everywhere compared to the velocity of sound. This will be the case if the steady component of the fluid velocity is small compared to the velocity of sound, provided also that the pulse-pressure amplitude is small compared to the static pressure. When the pulse-pressure amplitude is small compared to the static pressure, the corresponding oscillating component of the fluid velocity will have an amplitude which is small compared to the velocity of sound, as can be shown from the specific impedance relation

$$p/u = \rho c = Kp_0/c$$

where

p = amplitude of pulse pressure in traveling wave
u = amplitude of oscillating component of gas-particle velocity
p_0 = average absolute pressure of gas
c = velocity of sound in gas
ρ = density of gas
K = ratio of specific heats of gas

Since both the steady and the oscillating components of the gas-particle velocity are assumed to be small compared to the velocity of sound, it follows that the linear acoustic-wave equation will give a sufficiently accurate description of the wave motion. Therefore the additional pressure drop due to the autonomous acceleration $\partial u/\partial t$ can be calculated from the linear acoustic-wave equation alone, without including the nonlinear convection-acceleration term. This autonomous acceleration is due to pulsative-flow conditions. Hence, finally, the pressure drop indicated by Equation [27] can be corrected approximately by the inclusion of an additional pressure drop calculated from the linear acoustic-wave equation. In order to estimate the pressure drop across the orifice due to oscillating fluid flow through the orifice, it is necessary to solve the linear acoustic-wave equation $\partial^2\phi/\partial t^2 = c^2\nabla^2\phi$. In spherical co-ordinates, a well-known solution is

$$\phi = A_\phi r^{-1} e^{i(\omega t - kr)} \ldots\ldots [28]$$

$$-\partial\phi/\partial r = \text{radial velocity of fluid, by definition} \ldots [29]$$

in which ϕ is the "velocity potential" and r = distance from origin.

Equation [28] represents waves emitted from a "point source." Since the actual source in the present case is the orifice, it should be assumed that the orifice is fairly small compared to the pipe diameter. Relatively high fluid velocities will then occur only near the source, and for this reason the influence of the pipe walls can be neglected. If the orifice diameter d is nearly as large as the pipe diameter D the "velocity of approach" correction factor

$$k_v = [1 - (d/D)^4]^{1/2} \qquad \text{(see Equation [27])}$$

becomes important because the distance r from the origin is equal to $D/2$ at the nearest points on the inside of the pipe wall. Evidently, when $d = D$ there is no orifice and hence no orifice impedance, and the correction factor becomes zero in this instance. Actually, it is the "kinetic energy of approach" that is significant, and this is proportional to the square of the fluid velocity in the pipe. Hence the ratio of the squares of the cross-sectional areas of pipe and of orifice becomes the ratio of the fourth powers of the orifice and pipe diameters. It will be assumed that k_v is approximately equal to 1.0 in the subsequent analyses.

In Equations [28] and [29]

A_ϕ = arbitrary constant
ϕ = velocity potential at distance r and time t
r = distance from origin
$\omega = ck = 2\pi f$
c = velocity of sound
$k = 2\pi/\lambda$
λ = wave length
$f = c/\lambda$
f = frequency of oscillation
$i = (-1)^{1/2}$

Substituting the value of ϕ from Equation [28] into Equation [29]

$$u_r = -\partial\phi/\partial r = (ik + r^{-1})\phi \ldots\ldots [30]$$

in which u_r is the radial velocity of the fluid at distance r from the origin.

The excess pressure p due to a sound wave is given by a well-known formula

$$p = \rho \partial\phi/\partial t \quad [31]$$

where ρ is the fluid density. Substituting the value of ϕ from Equation [28] into Equation [31] gives the pulse pressure

$$p = i\omega\rho\phi = i(\rho c)k\phi \quad [32]$$

Dividing Equation [32] by Equation [30] gives the specific impedance p/u_r of a spherical wave at distance r from the origin

$$p/u_r = (\rho c)(ikr)(1 + ikr)^{-1} \quad [33]$$

in which ρc is the specific impedance of a plane wave. Consider an orifice of radius r_0 in an infinite plane, and assume that r_0 is small compared to one quarter of the wave length. Let the fluid velocity in the orifice be u_z. Consider a spherical surface of radius r_0 such that the edge of the orifice is a great circle on the spherical surface. The surface area of each hemispherical surface is twice the surface area of the orifice. Therefore the flow velocity u_z is twice the velocity u_{r0} at the hemispherical surface (by continuity of the volume flow through each surface). Thus from Equation [33] on one side of the orifice

$$(p_1/u_z) = (0.5)(\rho c)(ikr_0)(1 + ikr_0)^{-1} \quad [34]$$

But on the other side of the orifice, the excess pressure p_2 is 180 deg out of phase with the excess pressure p_1

$$(p_2/u_z) = -(0.5)(\rho c)(ikr_0)(1 + ikr_0)^{-1} \quad [35]$$

because if the fluid velocity at any instant is directed into one region, it is necessarily directed out of the other region. The total pressure difference p across the orifice at any time is the difference between the excess pressures p_1 and p_2

$$p = p_1 - p_2 = \text{pressure drop across orifice due to autonomous acceleration of fluid} \quad [36]$$

Thus from Equation [36] the specific impedance is

$$p/u_z = (\rho c)(ikr_0)(1 + ikr_0)^{-1} \quad [37]$$

The corresponding specific impedance p_i/u_z associated with the convective acceleration described by Equation [27] is given approximately by

$$p_i/u_z = (\rho c)(p_i/p_0)^{1/2} \quad [38]$$

(p_0 = average absolute pressure)

in which the discharge coefficient C_d is assumed to be 0.60, and the pipe diameter D is much greater than the orifice diameter d. If r_0 is much smaller than one quarter of the wave length, kr_0 can be neglected compared to 1.0, and Equation [37] becomes

$$p/u_z = ikr_0\rho c \quad [39]$$

The absolute value of Equation [39] is

$$p/u_z = kr_0(\rho c) \quad [40]$$

where p is the pressure drop across the orifice due to the autonomous fluid acceleration alone.

The flow velocity u_z is the same in Equation [38] and in Equation [40], but the corresponding pressure differences across the orifice are very different for usual frequencies and orifice diameters. To see this, divide Equation [40] by Equation [38]

$$p/p_i = (\pi d/\lambda)(p_0/p_i)^{1/2} \text{ (since } kr_0 = \pi d/\lambda) \quad [41]$$

Equation [41] shows that the pressure drop p due to the autonomous acceleration of the fluid in the orifice is negligibly small compared to the pressure drop p_i due to the convective acceleration of the fluid in the orifice unless the pressure drop p_i is very small compared to the average absolute pressure p_0. For example, assume that $p = p_i$, so that the pressure drop due to the convective acceleration is equal to the pressure drop due to the autonomous acceleration; Equation [41] becomes

$$p_i/p_0 = (\pi d/\lambda)^2 \quad [42]$$

Suppose the orifice diameter d is 2 in. and the frequency is 50 cycles per sec (cps). Let the velocity of sound be 1400 fps. Then the wave length λ is 28 ft or 336 in. Then $\pi d/\lambda$ is 1/53.5 and p_i/p_0 is 1/2870. Thus in this example the autonomous pressure drop p can be neglected for any values of convective pressure drop p_i greater than $p_0/2870$. In an 800-psi system, for example, the autonomous effect will be negligible for any orifice meter reading much greater than 800/2870 = 0.28 psi. In any usual orifice-metering arrangement the pressure difference across the orifice will be much greater than 0.28 psi, probably about 1.0 psi to 10.0 psi, when used with an 800-psi system.

The final conclusion is that for fundamental frequencies less than 50 cps, the autonomous acceleration of the fluid in a 2-in. orifice can be neglected, and the pressure drop is correctly represented by Equation [27] at any instant of time during the cycle of oscillation. A slight error could arise from the higher harmonic frequencies composing a complex wave-form.

For orifices larger than 2 in. diam, Equation [42] shows that the wave length λ must be increased in proportion, and therefore the corresponding frequency limit must be proportionately lowered below 50 cps, for the same limiting orifice-pressure drop ratio p_i/p_0 (in this case 1/2870). Evidently it is necessary to solve the complete nonlinear wave equation for flow through relatively large orifices at relatively high fundamental frequencies of oscillating flow. This problem is not treated in the present discussion.

Since the reliability of Equation [27] has now been established for a certain range of conditions, it is possible to calculate the maximum indicated error in flow rate due to pulsations, by assuming that the pressure drop and flow rate at any instant are in phase with each other and are related by Equation [27] during a cycle of the pulsative flow.

At any instant, the fluid velocity u_i in the pipe corresponding to the average fluid velocity u_a in the orifice is determined by the necessity for continuity of fluid flow in the pipe and in the orifice, which requires

$$u_a = u_i(D/d)^2 \quad [43]$$

Substituting the value of u_a from Equation [43] into Equation [27] and assuming that $C_d = 0.6$

$$p_i = (1.39)F_p\rho u_i^2[(D/d)^4 - 1] \quad [44]$$

which may be expressed as

$$p_i = F_p R\rho u_i^2 \quad [45]$$

where

$$R = (1.39)\,[(D/d)^4 - 1] \quad [46]$$

When the fluid velocity u_i is constant, Equation [45] becomes

$$p_c = R\rho u_0^2, \quad [47]$$

where u_0 is the constant velocity and p_c is the constant pressure difference across the orifice.

In Equation [45] define u_i as

$$u_i = u_0 + uW \quad [48]$$

in which W is the wave-shape factor, and u is the amplitude of the velocity fluctuation.

For a sinusoidal wave of frequency f

$$W = \sin(2\pi ft) \quad [49]$$

For a sinusoidal wave, the average pressure difference during a cycle can be easily calculated from Equations [45], [48], and [49]

$$p_t = F_p R\rho(u_0 + u \sin\theta)^2 \quad [50]$$

$$\theta = 2\pi ft, \text{ by definition} \quad [51]$$

The pressure difference p_t is the pressure difference at the meter at any instant during a cycle of the wave motion, since there is no loss of pressure in the lines from the orifice flange taps to the meter. The pressure difference p_m which will be observed on the meter is the average value of p_t over one cycle of the wave motion from $\theta = 0$ to $\theta = 2\pi$. This is found from Equation [50] with no difficulty provided u/u_0 is less than 1.0, because in this case the fluid velocity u_t at any instant is always positive, as indicated by Equations [48] and [49]. With this restriction F_p is always 1.0 by definition and the average value of p_t is found from Equation [50] to be

$$p_m = (p_t)_{avg} = (2\pi)^{-1}\rho R \int_0^{2\pi} (u_0 + u \sin\theta)^2 d\theta \quad [52]$$

Evaluating the integral in Equation [52] gives

$$p_m = \rho R u_0^2 + (0.5)\,\rho R u^2 \quad [53]$$

Dividing Equation [53] by Equation [47]

$$p_m/p_c = 1 + (0.5)(u/u_0)^2 \quad [54]$$

The ratio of the indicated flow rate to the true flow rate is found by taking the square root of both sides of Equation [54]

$$\frac{\text{Indicated flow}}{\text{True flow}} = (p_m/p_c)^{1/2} = [1 + 0.5\,(u/u_0)^2]^{1/2} \quad [55]$$

The greatest value that u/u_0 can have is 1.0, because the derivation is not valid if u/u_0 is greater than 1.0. The value $u/u_0 = 1.0$ when substituted into Equation [55] gives

$$\left(\frac{\text{Indicated flow}}{\text{True flow}}\right)_{max} = (1.5)^{1/2} = 1.23 \quad [56]$$

Thus the indicated flow rate is higher than the true flow rate by 23 per cent for this case. By a process of dividing the cycle of the oscillatory motion into separate parts, it is possible to obtain a result corresponding to Equation [54] which applies when u/u_0 is greater than 1.0, although this is usually only of academic value because the corresponding errors (larger than 23 per cent) cannot be corrected accurately enough by theory. It is important, however, to express the values of u and u_0 in terms of easily measurable quantities.

If there are no standing waves, there is a simple relation between the pulse-pressure amplitude P and the associated fluid velocity amplitude u

$$u = cP(Kp_0)^{-1} \quad [57]$$

since the characteristic wave impedance ρc can be written as Kp_0/c because $c^2 = Kp_0/\rho$ in which

K = ratio of specific heats of gas
p_0 = average absolute pressure
c = velocity of sound
ρ = density of gas

Also, from Equation [47], Equation [53] can be written as

$$p_m = p_c + 0.5\rho R u^2 \quad [58]$$

Dividing both sides of Equation [58] by p_m

$$p_c/p_m = 1 - 0.5\rho R u^2/p_m \quad [59]$$

Substituting the value of u from Equation [57] and the value of R from Equation [46] into Equation [59] gives

$$p_c/p_m = 1 - 0.7(Kp_0p_m)^{-1}P^2[(D/d)^4 - 1] \quad [60]$$

If D/d is fairly large $(D/d)^4 - 1$ is nearly equal to $(D/d)^4$, and the true flow rate divided by the indicated flow rate is found by taking the square root of both sides of

$$p_c/p_m = 1 - 0.7(Kp_0p_m)^{-1}P^2(D/d)^4 \quad [61]$$

$$\frac{\text{True flow}}{\text{Indicated flow}} = [1 - 0.7(Kp_0p_m)^{-1}P^2(D/d)^4]^{1/2} \quad [62]$$

Meter With Damped Pressure Lines. The previous case assumed no damping in the instrument lines, and perfectly damped differential-pressure gage element. Suppose, on the contrary, that the pressure pulsation in each line is damped before it reaches the differential pressure-registering element of the meter. In this case, one line to the meter will be at the average pressure just upstream of the orifice, and the other line will be at the average pressure just downstream of the orifice. It is not necessary to describe the exact method of providing the damping in each of the lines as this will be different for each installation. Regardless of the method, however, the meter will give the same reading, provided only that the amount of the pulse damping is sufficiently complete. With this assumption, the meter must indicate directly the difference between the average upstream pressure, and the average downstream pressure. This is not the same as the average of the pressure differences (between upstream and downstream) which occur during a cycle, such as was indicated in the previous case, when the meter lines were undamped. In fact, it will be shown that the error in the average flow rate inferred from the meter with damped lines is much less than the error in the average flow rate inferred from the meter with undamped lines. It is necessary to describe the average flow rate as "inferred," because any differential-pressure gage obviously cannot indicate any sort of a flow rate directly. From theory (Equation [27] for steady flow) it has been demonstrated that the flow rate is proportional to the square root of the pressure difference actually indicated by the meter.

With damped lines, the meter indicates the difference between the average upstream pressure and the average downstream pressure. This is not equal to the average of the square roots of the pressure differences between upstream and downstream, as would be required to obtain a correct reading under the assumptions of the present problem. It is assumed here, as in the previous case (with undamped lines) that the autonomous-acceleration term is negligible. Therefore the use of Equation [27] is still suitable for relating pressure and flow at any instant during a cycle.

By definition, let

$$\left.\begin{aligned} P_1W + p_1 &= \text{pressure upstream of orifice at any instant} \\ P_2W + p_2 &= \text{pressure downstream of orifice at any instant} \end{aligned}\right\} \quad [63]$$

Then the pressure difference p_t across the orifice at any instant is

$$p_t = p_m + (P_1 - P_2)W \quad [64]$$

$p_m = p_1 - p_2$ = difference of average values of upstream and downstream pressures . . . . . [65]

p_1 = average value of upstream pressure
p_2 = average value of downstream pressure
P_1W = pulsating component of upstream pressure at any instant
P_2W = pulsating component of downstream pressure at any instant
W = wave-shape factor (= sin θ for sine wave)

When both the pressure lines to the differential-pressure meter are completely damped, the pressure p_m is the pressure indicated by the meter. The corresponding steady-flow velocity which would produce the same meter reading is u_m, where by analogy with Equation [47]

$$p_m = \rho R u_m^2 \quad [66]$$

but in this case u_m is not the true average flow velocity, because there is an additional "rectified" component which results from averaging the square root of the variable pressure difference across the orifice during a complete cycle of the wave motion. In other words, the true value of the average flow rate is found by integrating the fluid velocity u_t over a complete cycle. Substituting the value of p_t from Equation [45] into Equation [64] gives

$$F_p \rho R u_t^2 = p_m + (P_1 - P_2)W \quad [67]$$

Since p_m is the known meter reading with damped lines, it would be possible to calculate u_t from Equation [67] if only a value of $(P_1 - P_2)W$ could be found at each instant during a cycle of the wave motion. This requires a knowledge of the exact value of pulse pressure at each instant both above and below the orifice. Unfortunately, the difference $(P_1 - P_2)W$ is very small relative to P_1W because P_1W is nearly equal to P_2W. Only P_1W or P_2W, separately, can be measured directly without special instruments, and it is desirable to be able to predict flow-rate errors from a previous estimate of the general pulse-pressure level in the region of the orifice, without knowing $(P_1 - P_2)W$. Therefore it is desirable to eliminate the unknown value of $(P_1 - P_1)W$ from Equation [67] and express u_t in terms of P_1 or P_2 only. This requires determining an additional relationship between P_1, P_2, and u_t. From the characteristic wave impedance ρc, if there are no standing waves in the system, it is possible to deduce a fluid velocity u_1 or u_2, associated with a pulse pressure P_1 or P_2, which would occur in a long pipe with no orifice plate. The actual fluid velocity u_t can only be estimated, without explicitly solving the complete nonlinear partial-differential wave-and-flow equation.

The values of Wu_1 and Wu_2 are determined from

$$Wu_1 = F(\rho c)^{-1} P_1 W \quad [68]$$

$$Wu_2 = F(\rho c)^{-1} P_2 W \quad [69]$$

$F = 1.0$ when average flow and pressure waves travel in the same direction

$F = -1.0$ when average flow and pressure waves travel in opposite directions

For example, $F = 1.0$ when the orifice plate is in the discharge line of a compressor and $F = -1.0$ when the orifice plate is in the suction line of a compressor. Here W = wave-shape factor. Using the same notation as in the previous analysis with undamped meter lines, let u_0 represent the average value of u_t during the cycle, which corresponds to the true flow rate

$$(u_t)_{avg} = u_0 \quad [70]$$

At any instant during a cycle, the actual fluid velocity u_t will be different from u_0. It will not be $u_0 + Wu_1$, nor will it be $u_0 + Wu_2$, but a good estimate is found by assuming an average value

$$u_t = u_0 + 0.5(u_1 + u_2)W \quad [71]$$

Since the pipe has the same diameter upstream and downstream from the orifice, u_t must have the same value both upstream and downstream from the orifice.

Substituting the values of Wu_1 and Wu_2 from Equations [68] and [69] into Equation [71] gives

$$u_t = u_0 + (2\rho c)^{-1}(P_1 + P_2)WF$$

or

$$2\rho c u_t = (2\rho c)u_0 + (P_1 + P_2)WF \quad [72]$$

Adding Equation [67] to Equation [72] with $F = 1.0$ gives an equation containing only the upstream-pulse pressure WP_1 and the unknown pressure difference $W(P_2 - P_1)$ has been eliminated

$$F_p \rho R u_t^2 + 2\rho c u_t - (p_m + 2\rho c u_0 + 2P_1W) = 0 \quad [73]$$

Adding Equation [67] to Equation [72] with $F = -1.0$ also eliminates $W(P_2 - P_1)$. However, it gives an equation identical to Equation [73] except that $+P_1W$ is replaced by $-P_2W$

$$F_p \rho R u_t^2 + 2\rho c u_t - (p_m + 2\rho c u_0 - 2P_2W) = 0 \quad [74]$$

Since the upstream pulse pressure WP_1 is nearly equal to the downstream pulse pressure WP_2, an average pressure "amplitude" P may be used in place of either P_1 or P_2, where

$$P = 0.5(P_1 + P_2) \quad [75]$$

and the flow velocity u_t may be found from a single equation containing FP which reduces to Equation [73] when $F = 1.0$ and to Equation [74] when $F = -1.0$

$$F_p \rho R u_t^2 + 2\rho c u_t - (p_m + 2\rho c u_0 + 2FPW) = 0 \quad [76]$$

As in the previous calculation of flow error with undamped pressure lines to the dp meter, only positive values of the instantaneous fluid velocity u_t will be considered in the present analysis. Therefore $F_p = 1.0$ by definition, in Equation [76].

It is convenient to express the pulse pressure P in Equations [75] and [76] in terms of a fluid velocity u defined as

$$u = 0.5(u_1 + u_2) \quad [77]$$

From Equations [75], [68], and [69], since $F = F^{-1}$, substituting into Equation [77]

$$FP = \rho c u \quad [78]$$

Using Equations [78] and [66], Equation [76] becomes

$$R u_t^2 + 2c u_t - (R u_m^2 + 2c u_0 + 2ucW) = 0 \quad [79]$$

in which the density ρ has been eliminated by division since it occurs in each term of the resulting equation. It should be observed that the velocity u may be either positive or negative according to the value of F in Equation [78] which may be either $+1.0$ or -1.0.

Since it has been assumed that the fluid velocity u_t is always positive, it is necessary to determine the condition under which u_t will always be greater than zero, using Equation [79]. Let $u_t = 0$ in Equation [79]. The result is

$$R u_m^2 + 2c u_0 + 2uc \sin\theta = 0 \quad [80]$$

in which W has been replaced by $\sin\theta$ for a sinusoidal wave.

Solving Equation [80] for $\sin^2\theta$ gives

$$\sin^2\theta = (u_0/u)^2[1 + 0.5R(u_m/u_0)(u_m/c)]^2 \quad [81]$$

In this formula u_0 is unknown but does not differ greatly from u_m when the flow-rate error is small. Evidently, when u_0 is greater than u, the right-hand member will be greater than 1.0 because the term containing u_m^2 is always positive. Thus it will be assumed that $(u/u_0)^2$ and $(u/u_m)^2$ are each less than 1.0. Under this condition, the fluid velocity u_t is always positive. Solving Equation [79] for u_t gives

$$u_t = -c/R + [(c/R)^2 + u_m^2 + 2u_0c/R + 2ucR^{-1}\sin\theta]^{1/2} \quad [82]$$

The known value of u_m can be used as a standard velocity. Dividing both sides of Equation [82] by u_m gives

$$u_t/u_m = -b + [(1+b)^2 + 2Ab + 2(u/u_m)b\sin\theta]^{1/2} \quad [83]$$

$$A = (u_0 - u_m)/u_m \quad [84]$$

$$b = c(Ru_m)^{-1} \quad [85]$$

In Equation [84] A is approximately equal to the relative fractional flow-rate error, which will be shown to be about three or four per cent. Factoring the quantity $(1+b)^2$ from the square root in Equation [83] gives

$$u_t/u_m = -b + (1+b)(1+B+x)^{1/2} \quad [86]$$

$$x = 2b(1+b)^{-2}(u/u_m)\sin\theta \quad [87]$$

$$B = 2Ab(1+b)^{-2} \quad [88]$$

The maximum value of $|B|$ occurs when $b = 1$, as can be shown by differentiating $b(1+b)^{-2}$ and setting the derivative equal to zero. Then the maximum value of $|B|$ is (0.50) $|A|$. Therefore the value of $|B|$ is always less than about 0.02 since $|A|$ is less than about 0.04 as will be proved later. Therefore B can be neglected compared to 1.0 in Equation [86]. The result is

$$u_t/u_m = -b + (1+b)(1+x)^{1/2} \quad [89]$$

Equation [89] also can be written in another form by algebraic rearrangement, which gives

$$u_t/u_m = 1 - (1+b)[1 - (1+x)^{1/2}] \quad [90]$$

This form is more convenient in terms of the average integral which will be used to determine the average value of u_t during a cycle. The average velocity $(u_t)_{avg}$ corresponding to the true flow rate is the average value of u_t over one cycle, from $\theta = 0$ to $\theta = 2\pi$. Integrating both sides of Equation [90] from $\theta = 0$ to $\theta = 2\pi$ and dividing both sides of the resulting equation by 2π gives

$$(u_t)_{avg}/u_m = 1 - (1+b)(1 - I_b) = u_0/u_m \quad [91]$$

in which

$$I_b = (2\pi)^{-1}\int_0^{2\pi}(1+x)^{1/2}d\theta \quad [92]$$

where x is defined by Equation [87]. The greatest value that $|x|$ can have is 0.5, as it was shown (following Equation [88]) that the maximum value of $b(1+b)^{-2}$ occurs when $b = 1.0$. Therefore $(1+x)^{1/2}$ can be expanded into an absolutely convergent power series in terms of x by the binomial theorem and each term of the resulting power series can be integrated from $\theta = 0$ to $\theta = 2\pi$, as indicated by Equation [92]. The series is

$$(1+x)^{1/2} = 1 + (1/2)x - (1/8)x^2 + (1/16)x^3 - (5/128)x^4 + \cdots \quad [93]$$

Define

$$x = y\sin\theta \quad [94]$$

From Equation [87]

$$y = 2(u/u_m)b(b+1)^{-2} \quad [95]$$

Inserting the value of $(1+x)^{1/2}$ from Equations [93] and [94] into Equation [92] and evaluating the resultant integrals

$$1 - I_b = (0.0625)y^2(1 + 0.234\,y^2 + \text{-------}) \quad [96]$$

The value of y^2 cannot exceed 0.25 because $(u/u_m)^2$ is assumed less than 1 and it has already been shown that the maximum value of y occurs when $b = 1.0$. Then the term $0.234\,y^2$ cannot exceed (0.25)(0.234), or 0.059, which produces a relative fractional difference of less than 6 per cent, if the value of $1 - I_b$ in Equation [96] is replaced by

$$1 - I_b = (0.0625)y^2 \quad [97]$$

Substituting the value of y from Equation [95] into Equation [97]

$$1 - I_b = (0.25)(bu/u_m)^2(1+b)^{-4} \quad [98]$$

The value of b is found from Equation [85]. Substituting the value of R from Equation [46], and the value of u_m from Equation [66] gives

$$b = (0.85)(Kp_0/p_m)^{1/2}[(D/d)^4 - 1]^{-1/2} \quad [99]$$

in which use has been made of the formula for the velocity of sound $c^2 = Kp_0/\rho$.

Substituting the value of b from Equation [85], the value of u from Equation [78], and the value of u_m from Equation [66] into the expression bu/u_m in Equation [98]

$$bu/u_m = cu(Ru_m^2)^{-1} = FP/p_m \quad [100]$$

Therefore Equation [98] becomes

$$1 - I_b = (0.25)(P/p_m)^2(1+b)^{-4} \quad [101]$$

Substituting the value of $1 - I_b$ from Equation [101] into Equation [91] gives

$$u_0/u_m = 1 - (0.25)(P/p_m)^2(1+b)^{-2} \quad [102]$$

Substituting the value of b from Equation [99] into Equation [102] gives

$$u_0/u_m = \frac{\text{true flow}}{\text{indicated flow}} = 1 - (0.25)(P/p_m)^2[1 + (0.85)(Kp_0/p_m)^{1/2}(D/d)^{-2}]^{-2} \quad [103]$$

in which $[(D/d)^4 - 1]^{-1/2}$ has been replaced by its approximate value $(D/d)^{-2}$, and where

- P = pulse-pressure amplitude at orifice (= half peak-to-trough value)
- p_m = pressure difference across orifice, indicated by meter with damped lines
- p_0 = average absolute pressure
- K = ratio of specific heats of gas
- D = pipe diameter
- d = orifice diameter

From Equation [100], since $b = 1.0$ and $u/u_m = 1.0$ under the maximum pulse conditions assumed in deriving Equation [102], it follows that $P/p_m = 1.0$. Then Equation [102] shows that

$$(u_0/u_m)_{max} = \left(\frac{\text{true flow}}{\text{indicated flow}}\right)_{max} = 1 - \frac{0.25}{8}$$

$$= 1 - 0.031$$

which corresponds to a 3.1 per cent error in flow rate under the maximum pulse conditions assumed in the derivation. Including the correction term $0.234\ y^2$ in Equation [96] would indicate 3.3 per cent error under these conditions.

Appendix 3

Sound-Wave Radiation From a Vibrating Surface

From equation (4.17), chapter 4, of "Acoustics," by Leo L. Beranek (McGraw-Hill Book Co., New York, 1954), for a vibrating disk in an infinite plane

$$p_r = F_D u_m f \rho_0 S/r \quad \ldots\ldots [104]$$

When the wave length is greater than the diameter of the disk, the directivity factor

$$F_D = 2J_1(ka \sin \theta)/(ka \sin \theta)$$

is nearly equal to 1.0. For any wave length, the factor F_D is also equal to 1.0 on the axis (where $\theta = 0$). In the foregoing

p_r = amplitude of pulse pressure at distance r from center of disk
u_m = maximum velocity of surface of disk
f = frequency of vibration of disk
ρ_0 = density of gas
S = surface area of disk
r = distance from center of disk to point at which pressure is measured
k = $2\pi/\lambda$
λ = wave length = c/f
c = velocity of sound
θ = angle between axis and line from center of disk to point where pressure is measured
$J_1(y)$ = Bessel function = $y/2$ for small y
a = radius of disk

Since

$$c^2 = Kp_0/\rho_0$$

where p_0 is the average absolute pressure and K is the specific-heat ratio C_p/C_v, it follows that

$$\rho_0 = Kp_0/c^2 \quad \ldots\ldots [105]$$

Also

$$u_m = 6.28 x_m f \quad \ldots\ldots [106]$$

where x_m is maximum excursion of the disk from its average position. Substituting the value of ρ_0 and u_m from Equations [105] and [106] into Equation [104] gives

$$p_r/p_0 = (6.28)(f/c)^2 K S x_m/r \quad \ldots\ldots [107]$$

Effect of the Volute on Performance of a Centrifugal-Pump Impeller

By R. D. BOWERMAN[1] and A. J. ACOSTA[2]

An experimental study of volute influence on radial flow-impeller performance was conducted by operating a single impeller with three different sets of volute vanes. In each case, over-all performance was measured and an internal-flow study within the volute was made. The results show that at their respective design flow rates the influence of the volutes is least and the deviation of performance from the free-impeller operation is small. At off-design flow rates there are major changes in the impeller performance resulting from the presence of the volutes. Large real fluid effects, coupled with a nonuniform velocity pattern at the impeller exit, result in a flow through the volute that does not resemble a potential flow. Even so, the fluid losses through the volute are comparatively small.

Nomenclature

The following nomenclature is used in the paper:

A_2 = outlet area of impeller
b = impeller-passage height
c = absolute fluid velocity
c_m = absolute meridional component of fluid velocity
c_u = absolute tangential component of fluid velocity
C = static-head coefficient = $H_s g/u_2^2$
g = gravitational constant
H_T = total head (referenced to total head at impeller inlet)
H_S = static head (referenced to total head at impeller inlet)
Q = flow rate
r = radius from impeller axis
r_v = radial co-ordinate of volute vane
R_e = Reynolds number = $r_2^2\omega/\nu$
T = torque
u = impeller tangential velocity = ωr
β = impeller-vane angle
β_v = volute-vane angle
η = efficiency = $\dfrac{\phi\psi}{\tau}$
θ = angular co-ordinate of volute vane; absolute angular co-ordinate
ρ = fluid density
τ = torque coefficient = $\dfrac{T}{\rho A_2 u_2^2 r_2}$
ϕ = flow-rate coefficient = $c_{m2}/u_2 = Q/A_2 u_2$
ϕ_x = impeller-design flow-rate coefficient
ψ = total-head coefficient = $H_T g/u_2^2$
ω = angular velocity of impeller
ν = kinematic viscosity

Subscripts

1 = impeller inlet (β_1)
2 = impeller outlet (β_2, r_2, u_2, A_2, c_{m2})
i = impeller only (ψ_i, η_i)
p = "whole pump" (impeller with volute) (ψ_p, η_p)
x = design quantity (ψ_x, ϕ_x, η_x)
v = refers to volute quantity (ψ_v, C_v)

Introduction

The pump-research program of the Hydrodynamics Laboratory of the California Institute of Technology has been directed towards determining basic design information by systematically studying the performances of pump components and by correlating performance with internal-flow phenomena. Previously, extensive work has been conducted on centrifugal impellers operated with a vaneless diffuser; i.e., an annular passage of constant breadth. Thus, polar symmetric conditions existed for the impeller over the complete range of flow rates. An impeller operated in this manner is herein termed a free impeller. In the present work, effects of the volute case on the aggregate pump have been studied by successively combining three simplified two-dimensional volute shapes with a single impeller (previously studied as a free impeller) and conducting over-all performance and internal-flow experiments on the combinations.

The information sought can be divided roughly into two categories: (*a*) the over-all performance for comparison of the different impeller-volute combinations and determination of the volute effect on the impeller itself; and (*b*) the nature of the flow through the volute, its agreement with potential theory, and its correspondence with the features of the over-all performance. At a given speed of rotation, the over-all performance is described completely by the head and torque as functions of flow rate from which the water power and efficiency can be calculated. The flow in the volute is determined by measurements of the total-head and static-head distributions from which velocity can be calculated.

With regard to the over-all performance of the impeller-volute combinations, a distinction is made between impeller performance based on averaged head measurements made at the impeller exit and pump performance based on averaged head measurements made at the volute exit. Furthermore, as the definition of pump performance indicates, the "pump" of this test is not directly comparable to a commercial pump, as the latter also includes final collection of the discharge into a single pipe with the consequent additional adjustment of the flow pattern to uniform pipe flow. Thus, the complete pump is subject to additional mixing losses which are not accounted for in the volute losses reported here. It should be noted also that, unlike commercial tests, the torque resulting from disk friction and other mechanical losses is not included in the present tests.

Design and Construction

The impeller employed in the investigation was a two-dimensional design with a 20-deg inlet angle and a 23.5-deg outlet angle, and has been described thoroughly in previous publications (1, 2,

[1] Research Engineer, U. S. Industries Research & Development Corporation, Los Angeles, Calif. Assoc. Mem. ASME.
[2] Assistant Professor of Mechanical Engineering, California Institute of Technology, Pasadena, Calif. Assoc. Mem. ASME.

Contributed by the Hydraulic Division and presented at a joint session of the Hydraulic and Gas Turbine Power Divisions at the Semi-Annual Meeting, Cleveland, Ohio, June 17–21, 1956, of The American Society of Mechanical Engineers.
Note: Statements and opinions advanced in papers are to be understood as individual expressions of their authors and not those of the Society. Manuscript received at ASME Headquarters, March 16, 1956. Paper No. 56—SA-45.

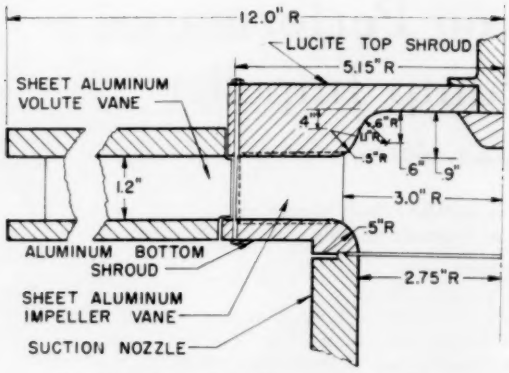

FIG. 1(a) AXIAL CROSS SECTION OF TEST PUMP

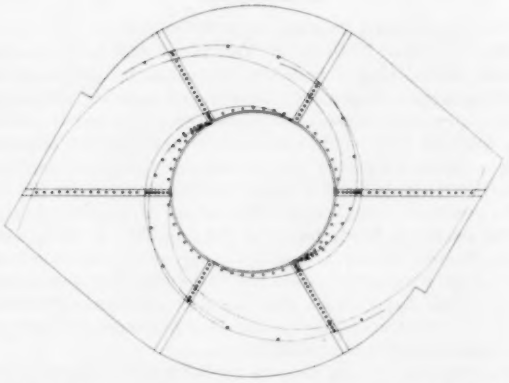

FIG. 1(b) LAYOUT OF VOLUTE VANES IN DIFFUSER SHROUDS. POSITION OF PIEZOMETER TAPS SHOWN AS FOLLOWS:
○ Indicates static tap
● Indicates static tap and total-head probe

FIG. 2 ASSEMBLY VIEW OF PUMP COMPONENTS

3).[3] The two-dimensional volute cases were formed by fitting the volute vanes between parallel diffuser shrouds, as seen in Figs. 1(*a*), (*b*), and 2. Double-volute construction was chosen to meet space limitations and to make an added study of flow symmetry. It should be noted that the volute vanes extend inward quite close to the impeller vanes. This close proximity is not common in commercial designs; however, for the purposes of this study, the maximum effect of the volutes was desired.

The volute-vane shapes were derived by considering the elementary theory of constant angular momentum. In two dimensions this yields the equation of the familiar logarithmic spiral

$$r_v = r_2 e^{\frac{\phi_x \eta_x}{\psi_x}\theta}$$

where r_v and θ are the radial and angular co-ordinates of the volute vane, ϕ and ψ are dimensionless coefficients of the flow rate and head, respectively, and η is the efficiency. Calculation of a volute shape was made by choosing a volute-design flow rate ϕ_x and taking the corresponding ψ_x and η_x data from the free-impeller characteristics. The ratio $\phi_x\eta_x/\psi_x$ which is the tangent of the volute-vane angle is also the tangent of the actual flow-discharge angle from the impeller at the chosen flow rate. The three sets of volutes resulted from the choice of ϕ_x equal to 75, 100, and 120 per cent of the free-impeller design point, ϕ_x. All pertinent dimensions and design constants are given in Table 1.

The volute vanes were formed of $^1/_8$-in. aluminum sheet, 1.2 in. wide, bent to match metal templates cut to the r_v and θ-co-ordinates. The vane leading edges were rounded. The templates also were used to scribe the vane positions on the diffuser shrouds and the vanes were held in position with screws. A single set of shrouds was made to accommodate all three sets of vanes.

EXPERIMENTAL WORK

Test Program. The following experiments were made on each of the impeller-volute combinations:

I Static-head measurements around the impeller periphery.

II Total-head measurements at the radial probe stations in the volute passage. Total-head measurements were made at five elevations.

III Input-torque measurements.

Additional pressure-distribution measurements on the volute vanes and tuft studies in the volute passages were made but are not reported herein.

Instrumentation. The Laboratory facilities have been described thoroughly in previous publications (1, 2) and will not be further recorded here. The static-pressure measurements of Test I were made by means of 42 static piezometer taps (0.020 in. in diam) that were spaced around the impeller periphery $^3/_{16}$ in. from the impeller exit.

The total and static-pressure data needed in Test II were measured by static holes and total-head probes set into brass inserts which were set into radial slots machined in the top shroud. Separate inserts for static and total-head measurements were used. The angular direction and elevation of the total-head probes were maintained by pouring melted wax around the base of the probes. The total-

[3] Numbers in parentheses refer to the Bibliography at the end of the Paper

TABLE 1 TABLE OF CONSTANTS

Volute equation: $r_2 = r_{2c}\frac{\phi\eta}{\psi}\theta$

Impeller-vane angles: $\beta_1 = 20°$, $\beta_2 = 23.5°$
$r_2 = 5.15$ in. $b = 1.2$ in. $\phi_x = 0.1170$

Per cent free-impeller design point	ϕ_x*	ψ_x*	η_x*	$\frac{\phi_x\eta_x}{\psi_x}$	β_v, deg	Volute designation
75	0.0878	0.568	0.920	0.143	8.1	75% volute
100	0.1170	0.475	0.925	0.2278	12.8	100% volute
120	0.1404	0.405	0.915	0.3163	17.6	120% volute

Running Clearances

Radial: 0.005 – 0.008 in. Volute tongue:
Inlet seal: 0.004 in. 0.015 in. from impeller shrouds
0.020 in. from impeller vanes

* Measured free-impeller characteristics, ψ measured $^1/_{16}$ in. from impeller exit.

head-tube proportions were slightly unusual. The design and calibration are given in Fig. 3. The location of the static-pressure holes and inserts for total and static-pressure determination is shown in Fig. 1(*b*). The completely instrumented volute is shown in Fig. 4, together with the multi-tube manometers used to read the pressure signals.

All pressure measurements were referenced to the total head at the inlet of the impeller.

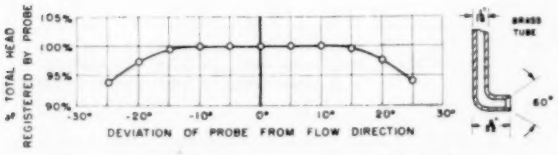

FIG. 3 ANGLE SENSITIVITY OF TOTAL-HEAD PROBES

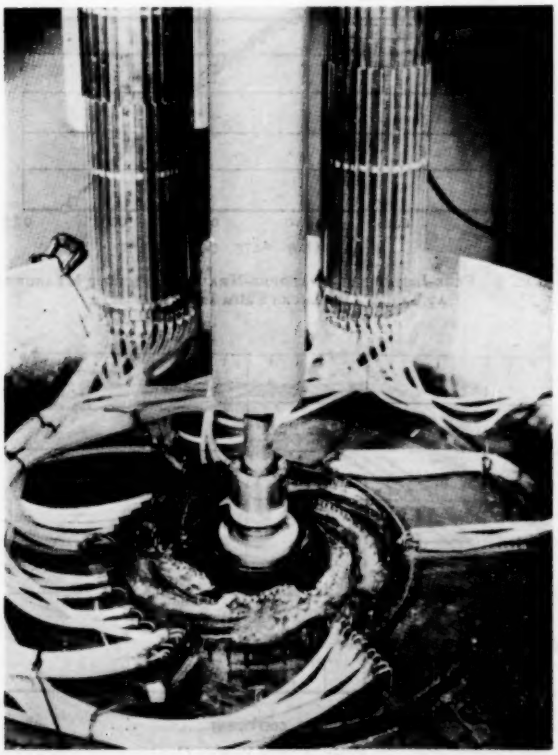

FIG. 4 ASSEMBLY OF PUMP COMPONENTS

Torque measurement was accomplished by balancing the reaction torque of the motor case with weights suspended over a pulley from a lever arm. The balance position was indicated by a Statham displacement gage and fixed-bridge circuit.

Procedure. All tests were conducted at 150 rpm over an established set of flow rates. To minimize the effect of probe interference, all static-head data were taken independently of the total-head data and total-head data were taken with the probes evenly divided between the two volute passages to maintain flow symmetry.

The torque tests required careful technique as the bridge drift and general laboratory vibration contributed to scatter in the readings. As the torques involved at the low rpm were small (0.2–0.5 ft-lb), the percentage error was large. Continual checks were made on the bridge zero and statistical methods were applied to the taking of each reading. As only the torque due to the impeller-vane action was wanted, the tare torque which included the motor windage and the fluid-disk friction on the outside of the impeller had to be measured. This was done by running the impeller empty but with a temporary basin holding water atop the impeller, simulating the operating condition. Duplication of actual running conditions was difficult and the reading was sensitive, but identical technique was employed for all the torque tests. Estimated final torque error is within ±2 per cent.

RESULTS AND DISCUSSION

Presentation of Data. All quantities are reported as dimensionless coefficients as defined in the nomenclature. The curves of Figs. 5(*a*), (*b*), and (*c*) represent the impeller head as a function of the angular position from the volute tongue. Each of these values is the average of five head readings taken over the breadth of the impeller. The over-all impeller head is the average of the data of Fig. 5 and it should be recognized that these averages cannot be accurate where the curves differ widely. The over-all pump head (Fig. 13) was obtained by an integrated average of the head values over the volute exit. Velocity coefficients were calculated from the difference in total head and static head, and it was necessary to assume that the static head at the top shroud was a representative of that across the passage depth.

With regard to free-impeller-head values, some explanation is required as to the manner in which they were obtained. In Fig. 6, curves *A* and *B* are the result of earlier work on the impeller where curve *A* represents measurements made $^1/_{16}$ in. away from the impeller-vane exit and curve *B*, $^3/_8$ in. away. The difference of these curves was considered in reference (1), wherein at low flow rates it was decided that large mixing losses occur immediately following the impeller exit. Values from curve *A* were used in calculating the volute shapes. The data for curve *C* were currently taken in an identical manner as the data with volutes; i.e., $^5/_{32}$ in. away from the impeller exit. Curve *C*, generally in accord with curves *A* and *B*, is taken as the free-impeller performance for comparison with the data of the volutes.

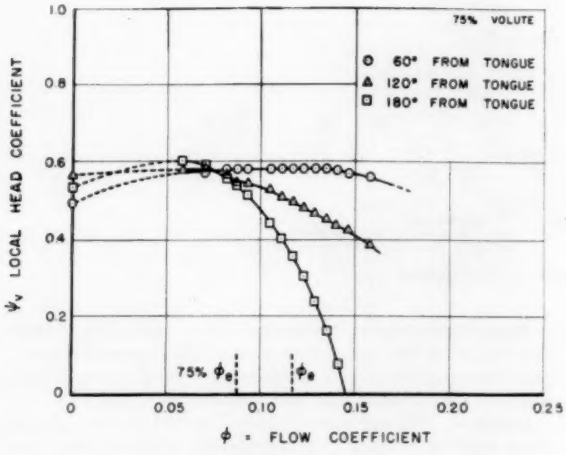

Fig. 5(a)

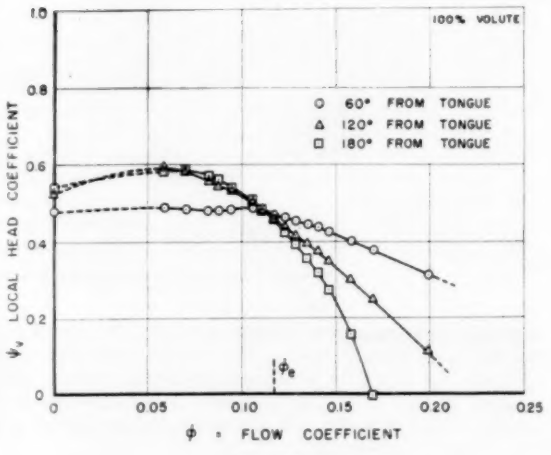

Fig. 5(b)

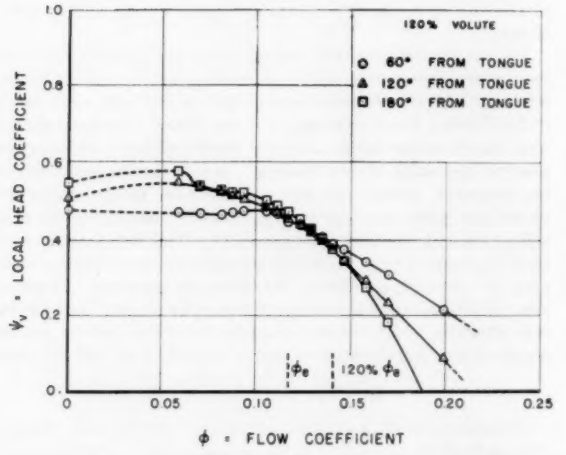

Fig. 5(c)

FIGS. 5(a, b, c) IMPELLER-HEAD COEFFICIENT MEASURED AT 60, 120, 180-DEG POSITIONS FROM VOLUTE TONGUE FOR THREE VOLUTE SHAPES

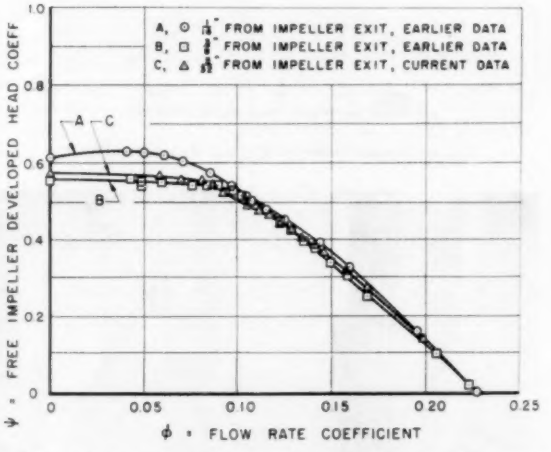

FIG. 6 FREE-IMPELLER DEVELOPED-HEAD COEFFICIENT MEASURED AT THREE DISTANCES FROM IMPELLER EXIT

Effect of Volutes on Performance

Over-All Results. The experimental results show that the volute shape is quite prominent in determining the performance characteristics of a pump. The significant result is that the performance is controlled by the influence of the volute shape on the impeller operation rather than by the addition of losses to the fluid within the volute. Conclusive evidence that the impeller operates differently with different volute shapes is found in the torque curves (Fig. 7). Although there is not too much difference in the torque curves at low flow rates, above $\phi = 0.09$ the curves are distinct, and at ϕ above 0.14 there is considerable variance. The 75 and 100 per cent combinations generally require somewhat greater torque than the free impeller, whereas the 120 per cent combination torque requirement is about the same as the free impeller.

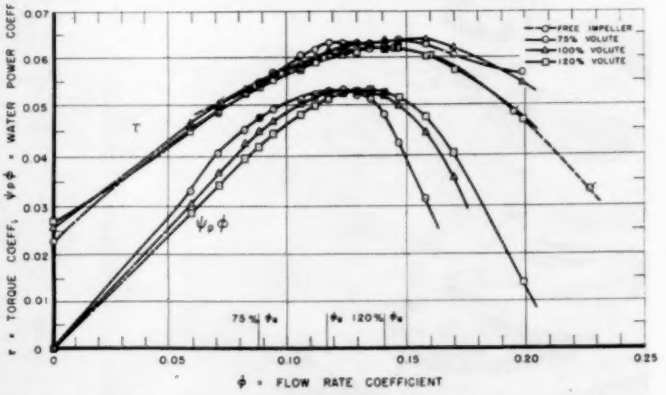

FIG. 7 TORQUE COEFFICIENT AND PUMP WATER POWER COEFFICIENT FOR THREE VOLUTE SHAPES

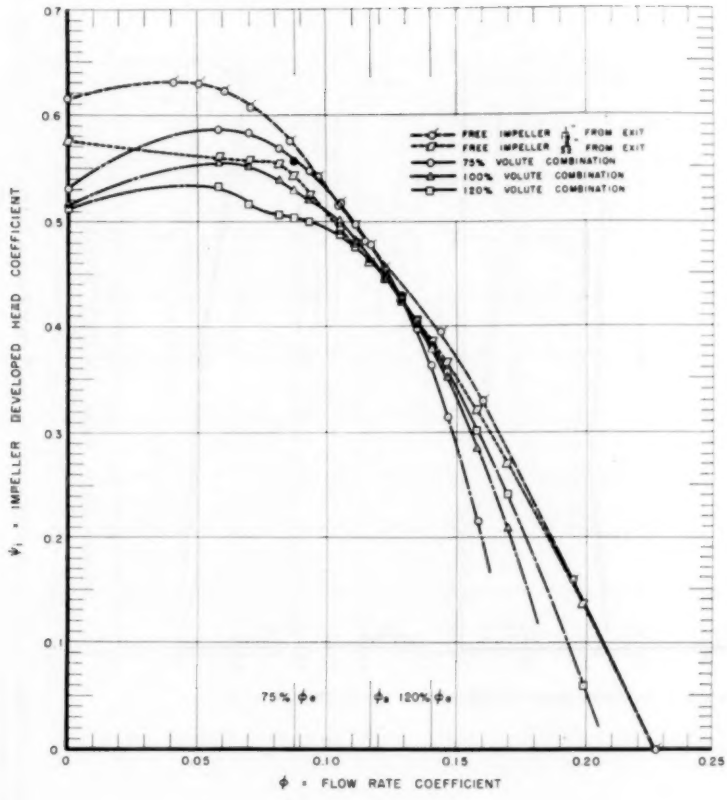

FIG. 8 IMPELLER DEVELOPED-HEAD COEFFICIENT FOR THREE VOLUTE SHAPES AND FREE IMPELLER

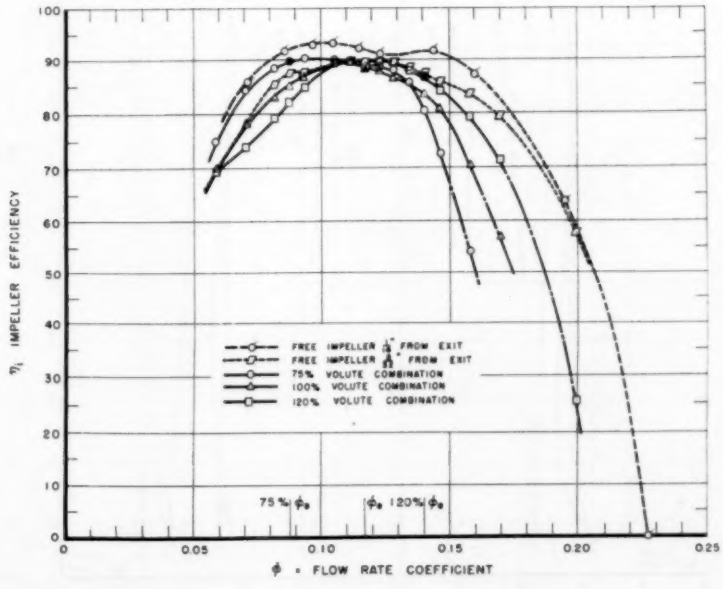

FIG. 9 IMPELLER EFFICIENCY FOR THREE VOLUTE SHAPES AND FREE IMPELLER

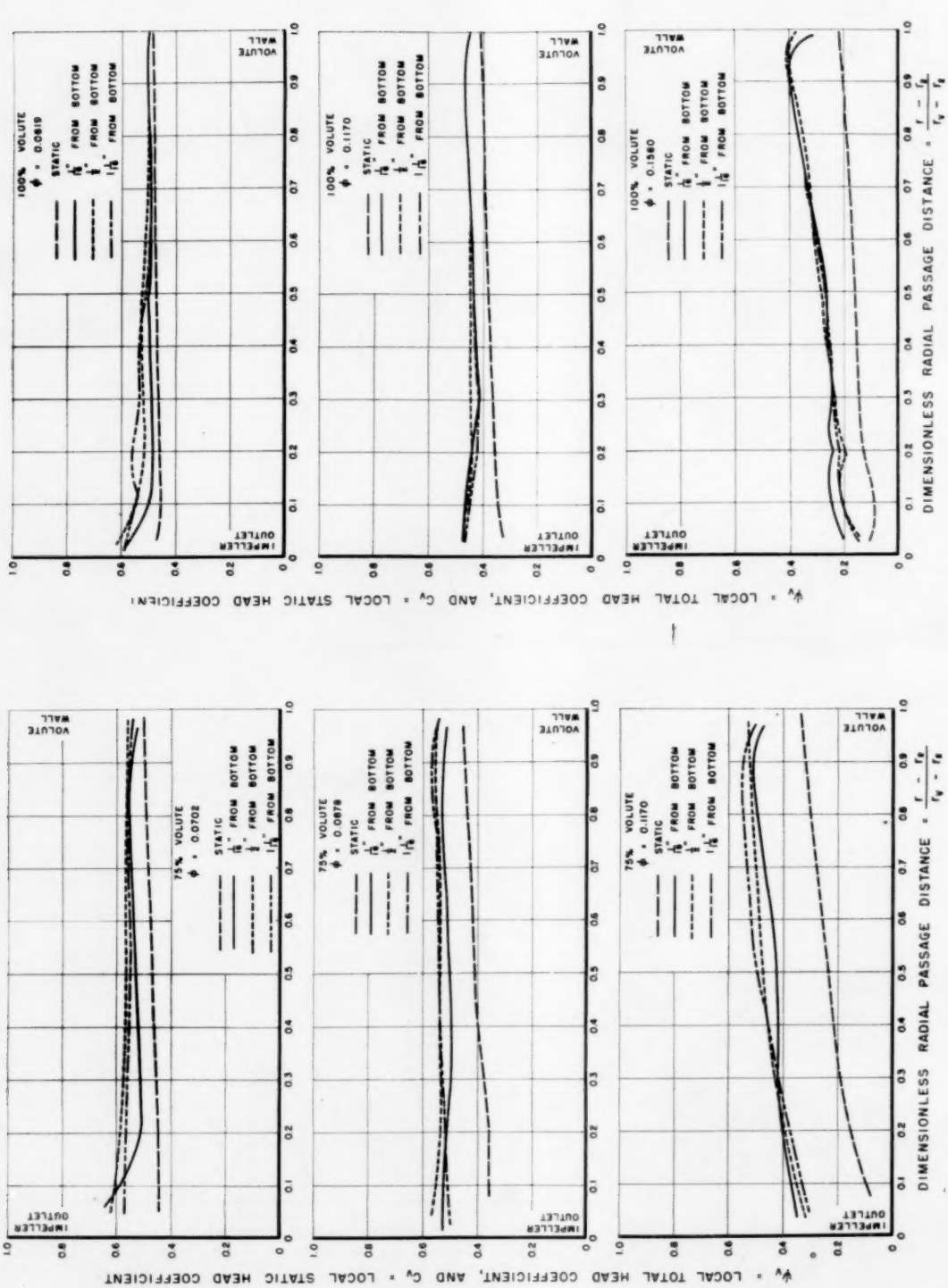

FIGS. 10(*a*, *b*, *c*) LOCAL STATIC-HEAD COEFFICIENT AND LOCAL TOTAL-HEAD COEFFICIENTS AT THREE LEVELS FROM BOTTOM SHROUD FOR THREE VOLUTE SHAPES AT SELECTED FLOW-RATE COEFFICIENTS

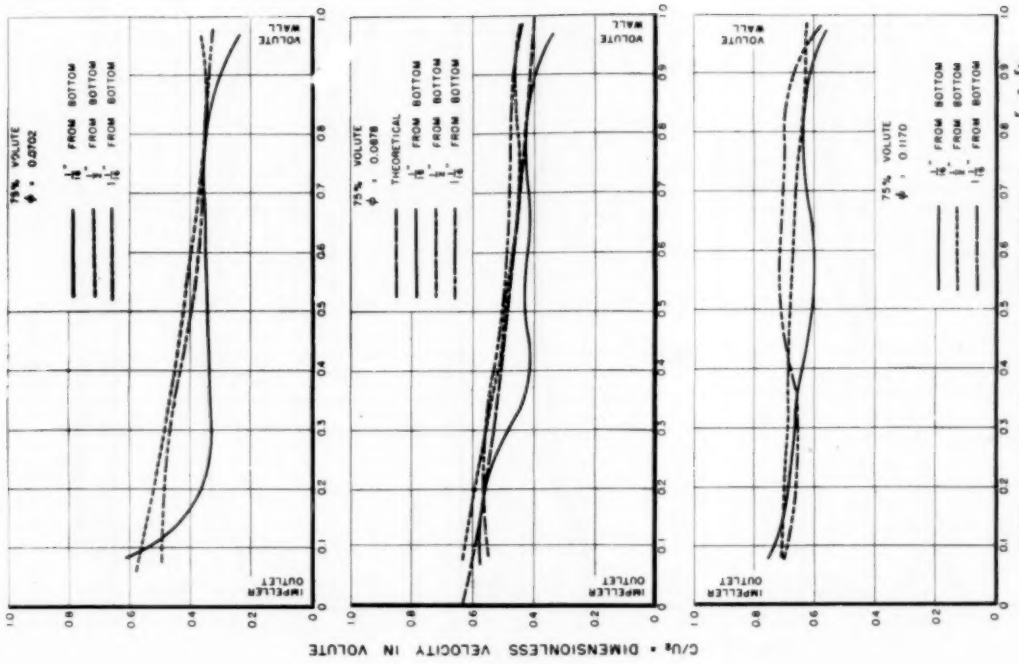

FIGS. 11(*a*, *b*, *c*) HORIZONTAL VELOCITY PROFILES AT THREE LEVELS FROM BOTTOM SHROUD AT VOLUTE EXIT (180 DEG FROM TONGUE) FOR THREE VOLUTE SHAPES AT SELECTED FLOW RATES

Fig. 11(*a*)

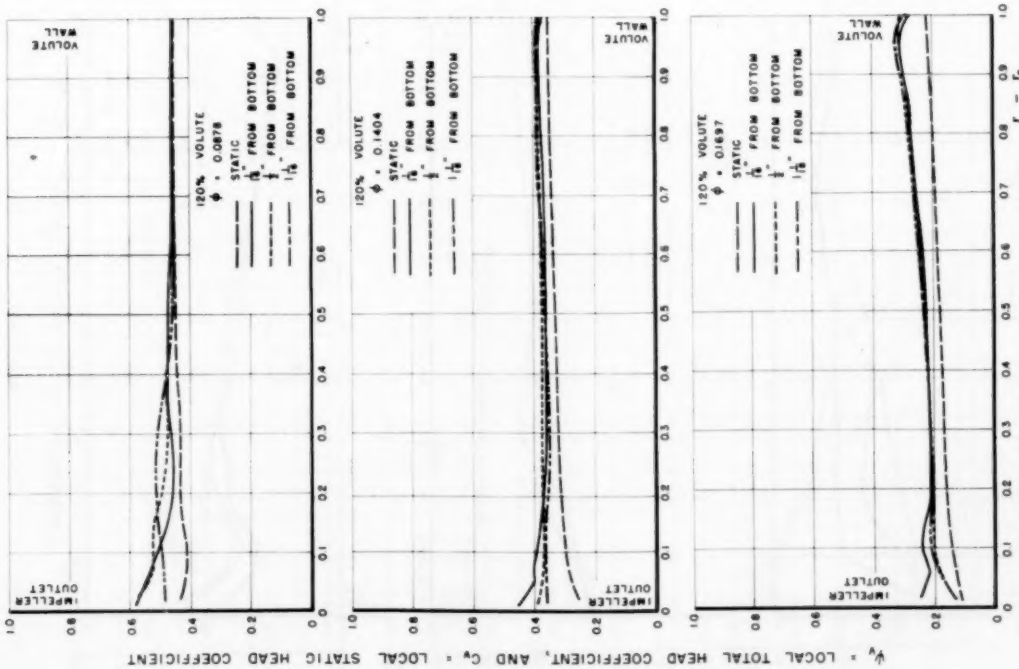

Fig. 10(*c*)

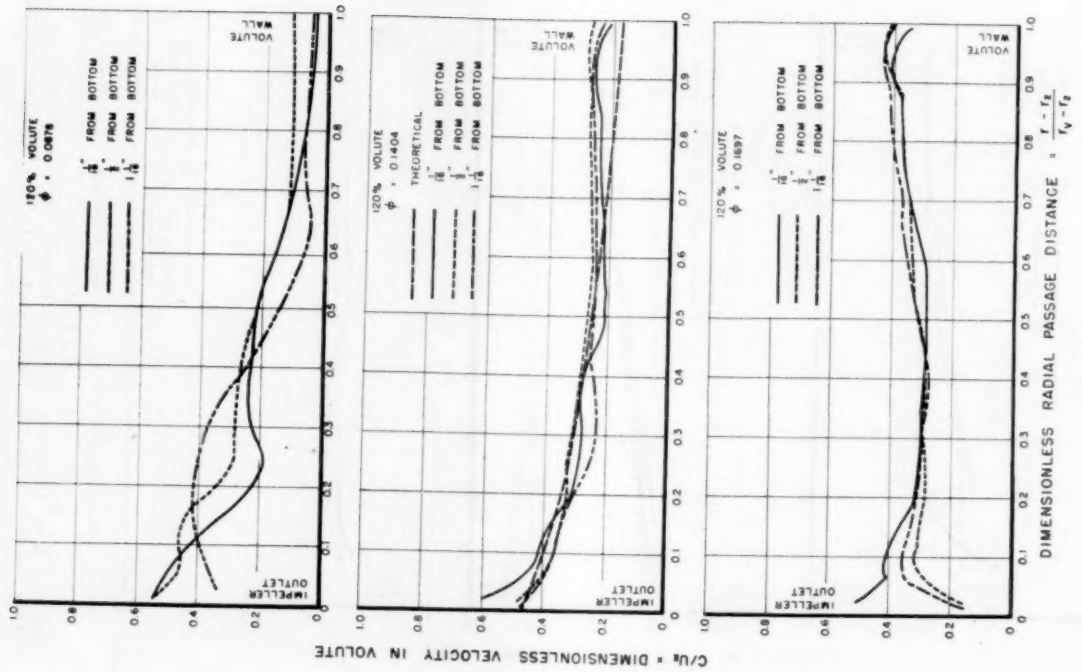

Fig. 11(c)

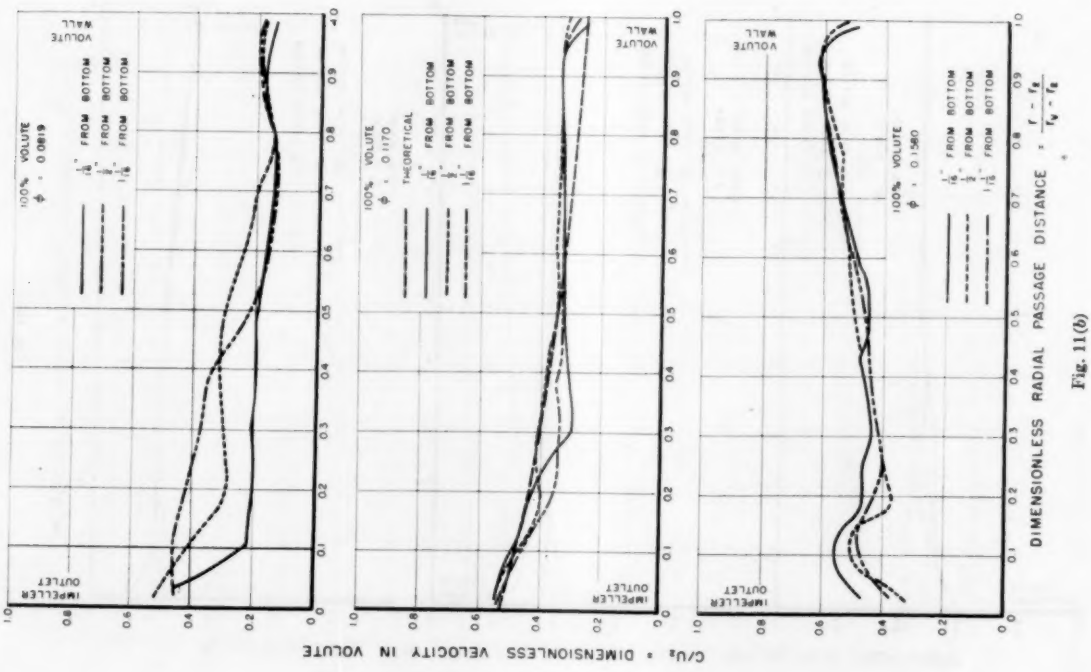

Fig. 11(b)

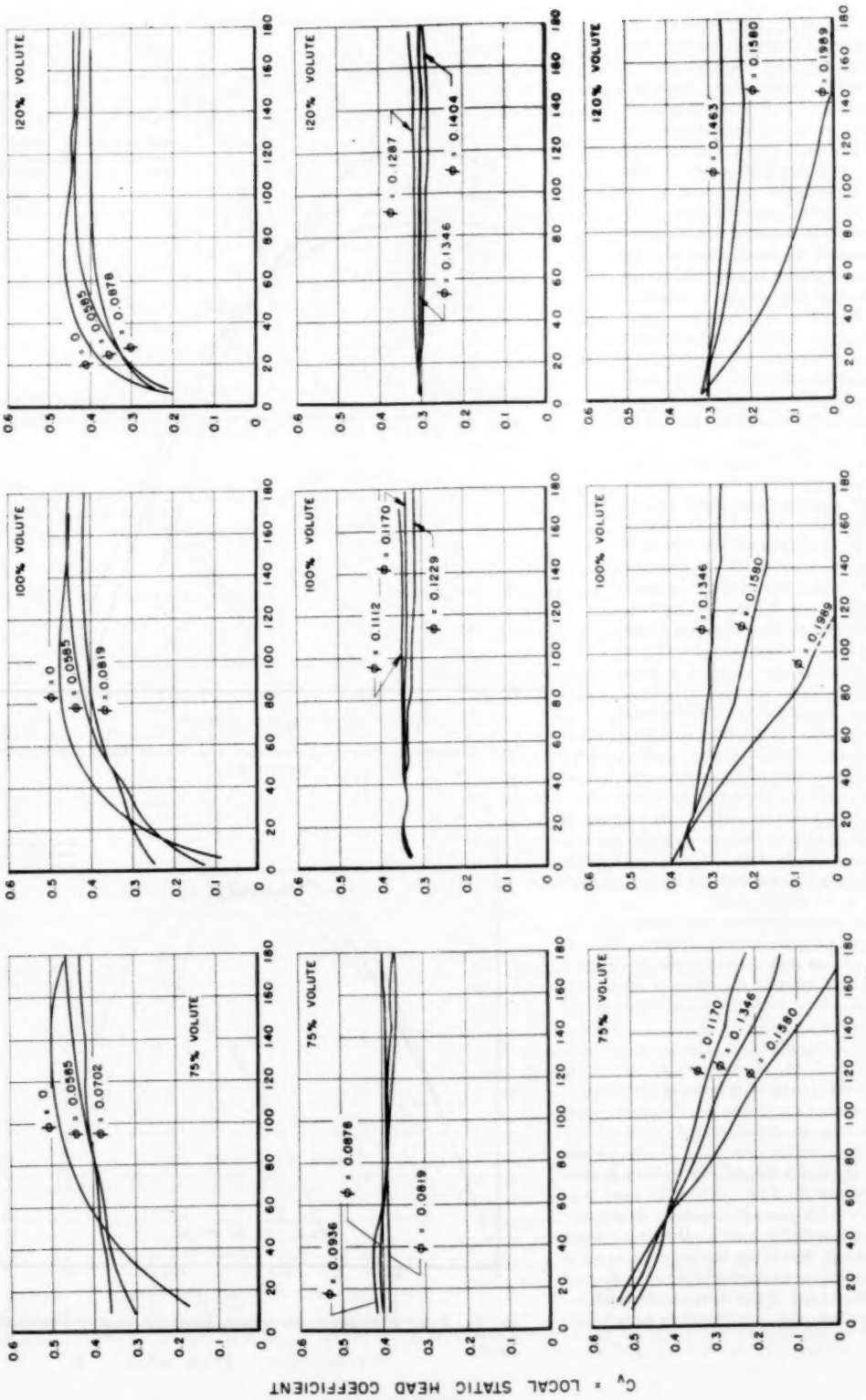

FIG. 12 STATIC-HEAD COEFFICIENT AROUND IMPELLER PERIPHERY FOR THREE VOLUTE SHAPES AT SELECTED FLOW-RATE COEFFICIENTS

Additional evidence of volute effect on impeller performance is given by the impeller-head curves (Fig. 8). The heads are similar over the span of the design points; however, at low flow rates and high flow rates, there are large differences in the head curves. In general, it can be concluded that each volute causes different loss distribution within the impeller and immediately following it for these reasons: At very low flow rates each of the four cases must have a different impeller loss because the heads are quite different even though there is little change in the torque. At high flow rates, the impeller heads of the 120, 100, and 75, per cent combinations successively decrease and are lower than the free-impeller values; however, the torques progressively increase, all being as high or higher than the free-impeller requirement. The impeller-efficiency curves (Fig. 9) reflect the effect of these losses.

Effect of Volutes at Design Points. The operation of each volute-impeller combination is optimum at approximately the individual volute design flow rate. The heads produced by the 100 and 120 per cent combinations are almost the same as the free-impeller head measured $^{5}/_{32}$ in. away from the impeller exit. At the flow rate $0.75\phi_o$, the free-impeller head measured at $^{5}/_{32}$ in. away is below that measured $^{1}/_{16}$ in. away, and the 75 per cent volute combination produced a head between these two free-impeller values. Evidently in the 75 per cent case the presence of the volute alleviates the conditions causing the losses immediately following the impeller.

The internal-flow data also support the fact that the volutes operate best at their design points. In each case, the radial surveys of total and static head and their consequent velocity distributions are smooth, Figs. 10 and 11, and the impeller total heads, measured at the various angular positions, Fig. 5, are nearly equal.

Likewise, the static pressure distribution around the impeller periphery is quite uniform, Fig. 12. These results indicate that the volute can be designed without taking into account the effect of friction, at least for the relatively high Reynolds numbers (2.4×10^5) of these tests.

Complete Pump Performance. The pump-performance curves (Figs. 7, 13, 14) are seen to be not significantly different from the impeller-performance curves. There are some losses as the fluid passes through the volute, as demonstrated by the total-head curves compared in Fig. 15. At the volute-design points, the losses through the volutes in each case are approximately 3 per cent of the total head of the impeller (which amounts to about 20 per cent of the volute exit-velocity head). However, except at the volute-design flow rates, the losses incurred in the volute are of a lesser magnitude than the changes in impeller performance of the three volute combinations. All impeller-volute combinations have nearly

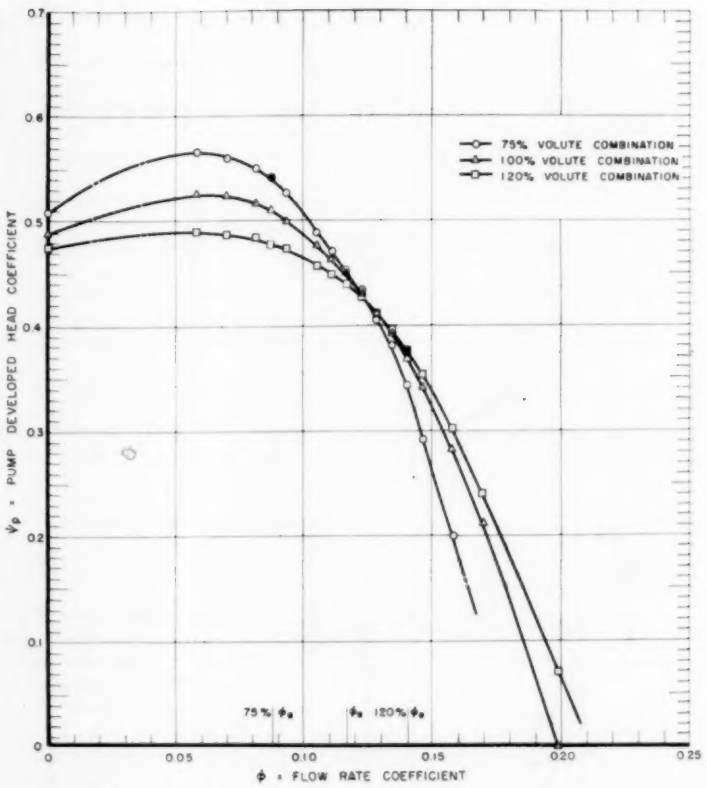

FIG. 13 PUMP DEVELOPED-HEAD COEFFICIENT FOR THREE IMPELLER-VOLUTE COMBINATIONS

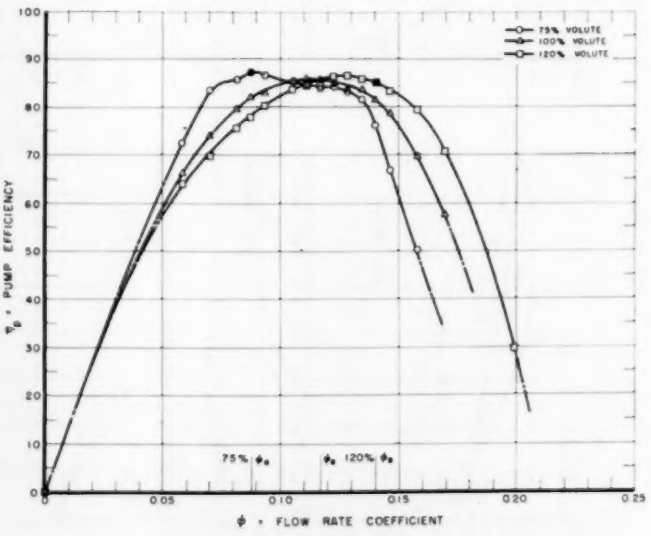

FIG. 14 PUMP EFFICIENCY FOR THREE IMPELLER VOLUTE COMBINATIONS

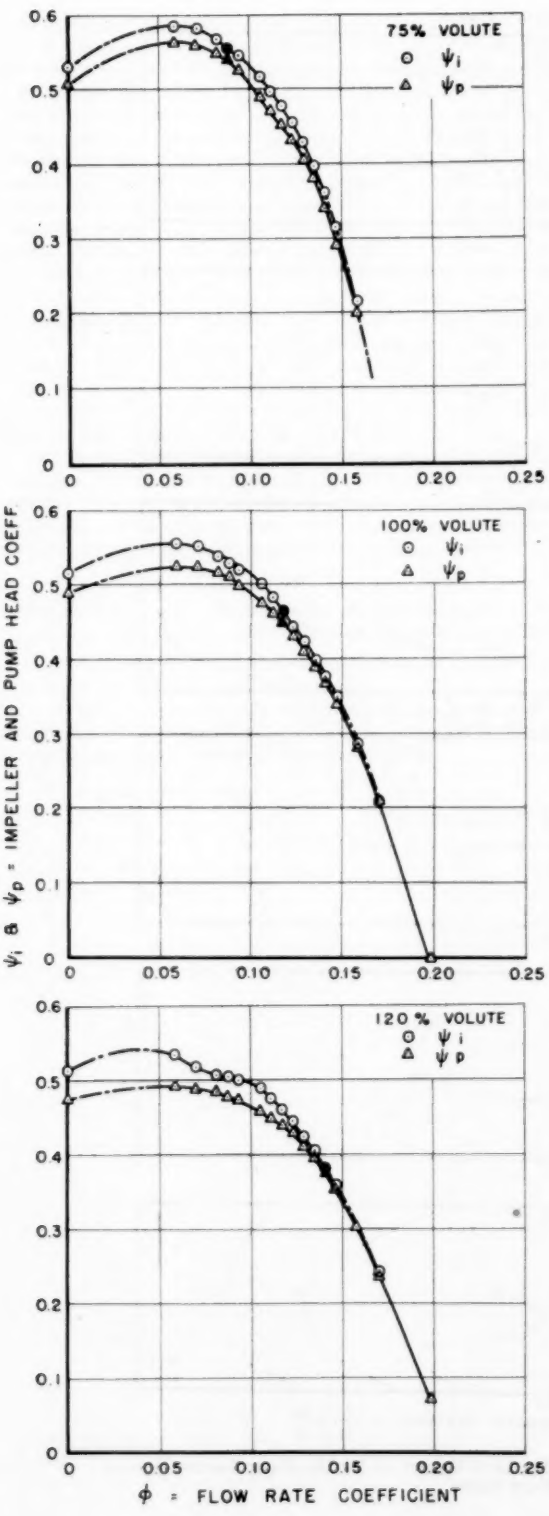

equal best efficiency (about 87 per cent) which is probably due to the fact that the design points of the volutes are within the high-efficiency region of the free impeller. It is not likely that a volute designed below the high-efficiency region of the impeller would give good performance.

Flow Patterns Through the Volute. As happens in many other flow problems, the flow in the volute has an approximate potential flow static-pressure distribution, but the velocity distribution is not at all that predicted by theory. The local total and static-head curves and horizontal velocity-profile plots, Figs. 10 and 11, show that at design points the velocity diminishes to some degree with increasing radius to about one third of the volute-passage width, and from there on to the volute vane it is nearly constant. Potential flow requires the velocity to diminish inversely as the radius. Furthermore, over the entire range of flow rates there appears to be a region of high-velocity flow along the concave side of the volute vane that would not ordinarily be expected. It is believed that this result is due to a secondary flow of the high-energy fluid coming from the impeller-shroud boundary layer. Considerable flow disturbance is caused by this discharged-impeller boundary layer, as can be seen in Figs. 10, 11, and 16. The effect is notably more pronounced on the bottom surface as the bottom impeller shroud has a larger diameter. The fluid elements with varying total energy necessarily mix at the impeller exit, and this process accounts for some of the observed losses.

Discussion

It would be of interest to be able to predict, roughly, the direction and magnitude of the volute-impeller interference effects. Early investigators, e.g., Straszacker (4), have made attempts in this direction by assuming the absolute flow to be irrotational and inviscid, so that potential theory could be used. Straszacker was concerned chiefly with the flow and streamline picture at the impeller exit rather than with performance calculations.

At off-design conditions high velocities can occur at the volute tongue and these disturbances may cause substantial deviations in the velocity pattern. If the impeller is considered to have an infinite number of blades, it can be shown (5) that these deviations will give rise to a nonuniform total head around the periphery of the impeller and, as a consequence, the flow leaving the impeller will not be irrotational. The same conclusions also may be obtained if the impeller is considered to have a finite number of vanes; however, the discussion proceeds more easily with an infinite number of vanes.

The influence of the volute on the impeller performance (from an elementary point of view) comes from the nonuniform distribution of radial velocity around the impeller. If it may be assumed that the infinite number of vanes perfectly guides the relative flow, then the torque required can be determined from the momentum law. From this computation it is easy to show that any variation in radial velocity around the impeller leads to a decrease in required torque. If the impeller efficiency were unchanged, the impeller head would thus be reduced.

The foregoing deduction is not borne out by the present experiments. Practically all cases show an increase in the torque required by the impeller. It must be concluded that either the foregoing simple picture is inadequate or the principal assumption, i.e., that the flow is perfectly guided by the impeller vanes, is erroneous. Probably both situations occur. In potential flow, with a finite number of blades, the Kutta condition is applied at the impeller tips and replaces the perfect guidance of the infinite-vane case. The presence of the volute tongue gives rise to

Fig. 15 Impeller and Pump-Head Coefficients Compared for Three Volute Shapes; ψ_i Denotes Impeller Head; ψ_p Denotes Pump Head

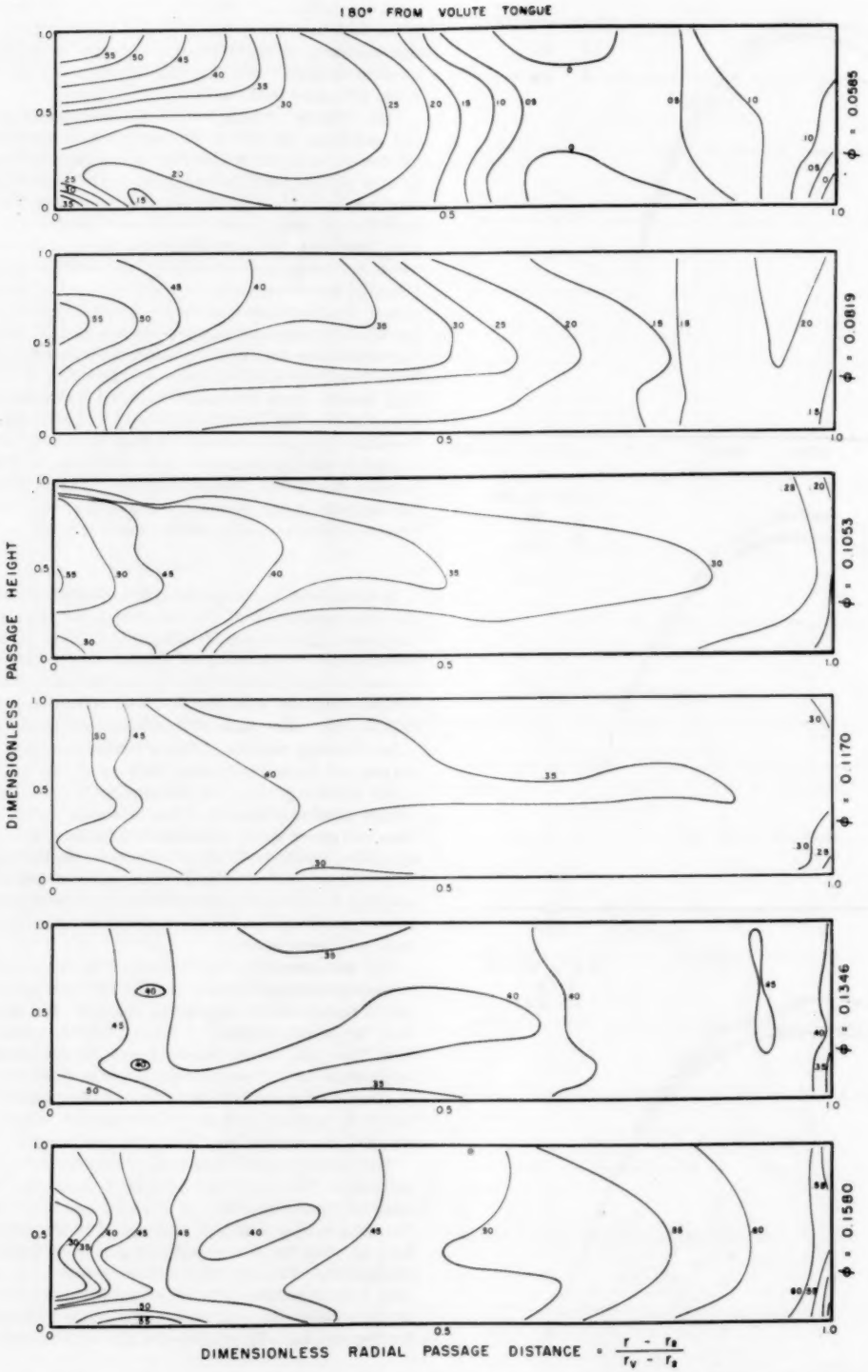

FIG. 16 VELOCITY CONTOURS (c/u_2 = CONST) FOR 100 PER CENT VOLUTE AT 180 DEG FROM VOLUTE TONGUE AT SELECTED FLOW RATES

trailing vorticity and nonsteady flow patterns in both the relative and absolute flow patterns. Their precise influence on torque is not known, although the situation is qualitatively similar to the infinite-vane case. Since the volute vanes were only about $^1/_{16}$ in. from the impeller, enormous nonsteady disturbances could occur there, and it does not seem unreasonable that the real fluid flow cannot always adjust itself to stream smoothly off the blade tips. If the condition of perfect guidance (for an infinite number of blades) is relaxed, then it is possible for an increase in torque to occur. This result also follows from the intuitive notion that near the volute tongue, the absolute flow leaving the impeller is determined by the volute-vane angle. Thus, at high flow rates, the tangential component of absolute velocity (and thus torque) would be greater than in the free-impeller case. If it were not for a simultaneous decrease in impeller efficiency, a larger average head would result. An inspection of Fig. 5 does show that the head measured 60 deg from the volute tongue is consistently high for the high flow rates and low for the low flow rates, showing that the head there is controlled by the volute vanes.

This discussion is admittedly speculative in part and should be subjected to further investigations. It appears, however, that potential theory cannot be used to describe the flow at off-design conditions. At the present time no satisfactory method of accounting for off-design performance is available.

Conclusions

From a series of experiments on a two-dimensional impeller and simplified volute shape, the following observations can be made:

1 For efficient operation, the volute must be matched to the impeller at the desired design flow rate.

2 At the design point of the volute, its influence is relatively small and it can be designed without considering the effect of friction at the Reynolds numbers of these experiments.

3 At off-design conditions large changes in pump performance occur that are due primarily to changes in impeller performance.

4 There are large real fluid effects in the volute flow that arise from the discharge of the rotating boundary layer into the volute channel. The resulting velocity distributions are only qualitatively similar to a potential flow; i.e., constant angular momentum at design conditions and depend markedly on flow rate.

In the present experiments, the maximum influence of the volute vanes has been studied. The degree of volute-impeller interference is, of course, dependent upon the spacing between them. It is hoped that investigation of this variable, as well as that of Reynolds number, will be undertaken in the future.

Acknowledgment

This work was supported by the Office of Naval Research. Reproduction in whole or part is permitted for any purpose of the United States Government.

BIBLIOGRAPHY

1 "Evaluation of a Two-Dimensional Centrifugal Pump Impeller," by J. H. Beveridge and D. A. Morelli, ASME Paper No. 50—A-147, unpublished.

2 "Pressure Distributions on the Vanes of a Radial Flow Impeller," by D. A. Morelli, Transactions of the Heat Transfer and Fluid Mechanics Institute, 1950, p. 73; Stanford University Press, Stanford, Calif., 1950.

3 "An Experimental Study of Centrifugal Pump Impellers," by A. J. Acosta and R. D. Bowerman, California Institute of Technology, Hydrodynamics Laboratory Report No. E-19.8, August, 1955.

4 "Die Ermittlung der Strömungsverhaltnisse in Spiralgehausen," by R. Strasznacker, *Ingenieur-Archiv*, VI-3-1935, pp. 157–182.

5 "Effect of the Volute on Performance of a Centrifugal Pump Impeller," by R. D. Bowerman, California Institute of Technology, Hydrodynamics Laboratory Report No. E-19.7, March, 1955.

Pressure Drop and Flow Characteristics of Short Capillary Tubes at Low Reynolds Numbers[1]

By FRANK KREITH[2] AND RAYMOND EISENSTADT[3]

The pressure drop and flow characteristics of short capillary tubes have been investigated experimentally for length-to-diameter ratios varying from 0.45 to 18 at diameter Reynolds numbers ranging from 8 to 1500. In the range of the dimensionless modulus $(L\mu)/(VD^2\rho)$ from 4×10^{-3} to 3 to 10^{-1}, the experimental data agree within 15 per cent with a mathematical theory by Langhaar (1).[4] At a value of $(L\mu)/(VD^2\rho)$ of about 0.3 the experimental data approach the Poiseuille laminar-flow theory (2). For very short tubes ($L/D < 0.5$) the experimental results deviate from Langhaar's theory at values of $L\mu/VD^2\rho$ less than 4×10^{-3}, and at $L\mu/VD^2\rho$ equal to 5×10^{-4}, the pressure drop is twice as large as that predicted by Langhaar's theory (1). The experimental results for tubes having very short aspect ratios are in agreement with data obtained by Zucrow (12) with short square-edged jets. It was found that the flow rate $\dot{Q}$ through a short capillary tube can be related empirically to the over-all pressure drop $\overline{\Delta p}$ raised to a power N. The exponent N is a function of the length-to-diameter ratio L/D varying from 0.5 at L/D equal to 0.45 to 0.91 at L/D of 18. The trend of the curve suggests an asymptotic approach to unity, the exponent for Poiseuille-type flow. The results of this study have application to: (*a*) Simulating flow through screens, doors, cracks, and fissures in small-scale model testing of buildings in atmospheric wind tunnels. (*b*) Automatic control devices where capillary tubes are used as hydraulic resistances in a larger line and in nozzle-flapper combinations. (*c*) Heat pumps and air-conditioning equipment where short capillary tubes are used as two-way control valves. (*d*) Flow through compact heat exchangers and porous materials.

Nomenclature

The following nomenclature is used in the paper:

C = orifice coefficient, defined by Equation [10]
D = diameter of tube, in.
g_c = 32.2 ft-lb_M/lb_F — sec^2
$\bar{f}_{APP}$ = integrated apparent friction coefficient, defined by Equation [8]
k = characteristic flow exponent, defined by Equation [1]
L = length of tube, in.
N = characteristic pressure-drop exponent, $1/2k$
p = static pressure, psf
Δp = static pressure drop, psf
$\overline{\Delta p}$ = total pressure difference between reservoirs connected by capillary tubes, psf or in. H_2O
$\dot{Q}$ = volumetric flow rate, cfm
V = mean velocity, $9.6\,\dot{Q}/\pi D^2$, fps
x = distance from the inlet section, illustrated in Fig. 4.
Re_D = Reynolds number, $0.8\dot{Q}\rho/\pi D\mu$, dimensionless
μ = dynamic viscosity, lb_M/ft-sec
ρ = mass density, lb_M/ft^3

Introduction

It is usual to express the pressure drop of an incompressible fluid flowing through a duct or an orifice as a function of velocity by a relation of the type

$$\frac{\Delta p}{\rho} = 4\bar{f}_{APP}\frac{L}{D}\left(\frac{V^2}{2g_c}\right) \simeq \text{const}\left(\frac{V^2}{2}\right)^k \quad \ldots\ldots [1]$$

where the exponent k in Equation [1] depends upon the flow system. For some common flow systems Equation [1] yields the following relations between pressure loss and velocity:

1 Orifices, screens, or grids (above critical Reynolds number, $\bar{f}_{APP}$ = const)

$$\Delta p \sim V^2, k = 1 \quad \ldots\ldots [2]$$

2 Turbulent flow in ducts ($\bar{f}_{APP} = \text{const}/Re_D^{0.2}$)

$$\Delta p \sim V^{1.8}, k = 0.9 \quad \ldots\ldots [3]$$

3 Fully developed laminar flow in ducts ($\bar{f}_{APP} = \text{const}/Re_D$)

$$\Delta p \sim V, k = 0.5 \quad \ldots\ldots [4]$$

While numerous investigations have been made to determine the flow characteristics of the foregoing systems in fully developed laminar and turbulent flow, the data available for laminar flow in short tubes are scant and inconclusive. A survey of available experimental data and analytical investigations on laminar flow in the inlet zone of ducts (2 to 7) is contained in reference (8).

The interest in this flow regime arose originally as a result of the need to simulate various types of flow through screens, doors, windows, and the like, in tests of small-scale models of buildings in an atmospheric type of wind tunnel.

It is well known that the pressure drop of a fluid under laminar-flow conditions in short tubes is considerably larger than the value predicted from the Poiseuille law. This is a result of the changes in the velocity profile occurring near the tube entrance. When a fluid enters a duct, the fluid particles adjacent to the

[1] This paper reports work done under contract with the Chemical Corps, U. S. Army, Washington, D. C.

[2] Associate Professor of Mechanical Engineering, Lehigh University, Bethlehem, Pa. Assoc. Mem. ASME.

[3] Assistant Professor, Department of Mechanical Engineering, Union College, Schenectady, N. Y.; formerly, Assistant Professor of Civil Engineering, Lehigh University. Assoc. Mem. ASME.

[4] Numbers in parentheses refer to the Bibliography at the end of the paper.

Contributed by the Hydraulic Division and presented at the Semi-Annual Meeting, Cleveland, Ohio, June 17–21, 1956, of The American Society of Mechanical Engineers.

Note: Statements and opinions advanced in papers are to be understood as individual expressions of their authors and not those of the Society. Manuscript received at ASME Headquarters, January 17, 1956. Paper No. 56—SA-15.

wall are slowed down by the viscous forces while the particles in the inner core are not directly affected by these forces for some distance from the entrance. Under the influence of the frictional forces the thickness of the retarded fluid layer grows. Since the mass-flow rate remains constant, it is necessary for the fluid in the inner core to speed up until finally a parabolic velocity distribution is reached some distance from the entrance. The change in momentum of the fluid in the inner core can only be produced by a force over and above that which is required to overcome the friction between the fluid and the pipe wall. This force shows up as an increase in the pressure difference required to move a given quantity of fluid through a short tube.

The superposition of the pressure drop resulting from the momentum change upon the pressure drop caused by the tractive forces at the wall of a duct offers the possibility of obtaining various values of the exponent k in Equation [1] by a proper balance between the two mechanisms. Thus, by a proper selection of the length-to-diameter ratio, it is possible to simulate various types of flow system, even if the reduction in scale of the prototype results in length dimensions for openings in the model which produce purely laminar flow.

Numerous other engineering problems involve laminar flow through ducts having such short length-to-diameter ratios that a parabolic velocity profile cannot be established. For example, in recent designs of heat pumps and air-conditioning equipment (11), short capillary tubes have been used to replace more complicated two-way control valves. Also in the design of pneumatic instruments and compact heat exchangers or regenerators such entrance effects may be appreciable.

Object

The purpose of this investigation was as follows:

1 Determine experimentally the pressure drop characteristics (i.e., k) of capillary tubes having small length-to-diameter ratios.

2 To provide experimental data for laminar flow through tubes in the range of the dimensionless quantity $(L/D\mathrm{Re}_D)$ from 4×10^{-4} to that value of $(L/D\mathrm{Re}_D)$ where the Poiseuille law holds.

Apparatus and Experimental Procedure

A schematic flow diagram of the equipment used in this investigation is shown in Fig. 1. Compressed air from a large settling chamber passes through a needle valve, filter, and air drier to the test section. The test section consists of two 6-in-diam pipes between which a thin plate of aluminum or lucite is tightly clamped with rubber gaskets and flanges. At the inlet side, a baffle plate is installed in the pipe to dissipate the kinetic energy of the incoming stream.

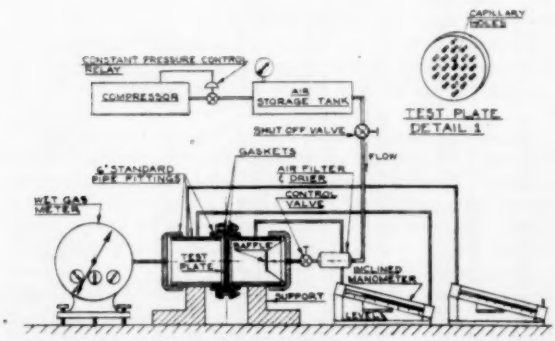

Fig. 1 Schematic Diagram of the Experimental Apparatus

Capillary holes of about $^1/_{32}$ or $^1/_{64}$ in. were drilled and reamed perpendicular to the face of the circular plate. The entrance and the exit of the holes were square-edged with sharp corners. Plate thickness of about $^1/_{64}$, $^1/_{32}$, $^1/_{16}$, $^1/_8$, $^1/_4$, and $^1/_2$ in. were used to obtain the desired length-to-hole diameter ratios.

It was decided to use several capillary holes in a parallel arrangement (see detail in Fig. 1) instead of a single hole, for two principal reasons: (*a*) The flow rate through a single capillary hole is exceedingly small and the available flowmeter would not have been suitable. (*b*) It is rather difficult to measure the diameter of a single capillary hole accurately and a larger number of holes offers a better means of obtaining a more reliable "average" size. It was arbitrarily decided to use 50 holes per plate. The holes were drilled about one or two thousandths of an inch undersize and then reamed to the final diameter. The size of the holes was measured by means of "go" and "no-go" gages, different in diameter by 0.001 in. Test data were reduced on the basis of a hole diameter halfway between the two gage diameters and, for purposes of evaluating the accuracy of the results, it was assumed that the diameter of an average hole was known to within 0.0005 in. on a 20:1 odd basis.

In order to ascertain whether or not the material or its roughness has an effect on the results, some of the earlier tests were first performed with the holes drilled in lucite plates and then repeated with aluminum plates. Since no effect could be observed only lucite plates were used in the later stages of the work because the transparent material permitted visual inspection of the holes.

To insure that there was no interference effect between the emerging air streams, check runs were made during which one half of the holes were plugged. It was found that the spacing of the holes had no effect on the results.

The principal data consisted of measurements of flow rate, pressure, and temperature in the downstream chamber of the test rig, and the differential pressure across the plate containing the capillary holes. The flow rate was measured by means of a stop watch and a vane-type wet flowmeter which had been calibrated carefully before the test program was initiated. The pressure and temperature on the downstream side of the holes were measured by means of an inclined manometer and a mercury-in-glass thermometer, respectively. The differential pressure (or the total pressure drop) was measured by means of an inclined manometer with a precision level.

Each test was repeated at least twice and the data were accepted only if the results agreed to within 3 per cent. Special care was taken at low flow rates where the differential-pressure measurements were the source of the largest potential uncertainty.

The pressure in the supply tank was not affected measurably by the outflow as would be expected from the small amount of air involved in any one test run. Therefore no pressure regulator was required.

Accuracy of Results

The accuracy of the experimental results was determined in accordance with a method suggested by Kline and McClintock (9) for single-sample experiments. Table 1 presents the percentage accuracy of the results in terms of uncertainty intervals based on 20-to-1 odds. This means that the odds are 20 to 1 against the per cent error in any one value of a result exceeding the stated percentage. The uncertainty intervals in the table are based on a combination of statistics and judgment, and they should be regarded as best estimates rather than absolute values. It is believed however that the accuracy of the final correlation of the data, represented by the curve drawn through all of the

experimental points (Fig. 5) is considerably better than the percentage figures for individual test points in Table 1.

TABLE 1 UNCERTAINTY INTERVAL FOR ANY ONE VALUE ON A 20-TO-1 ODDS BASIS

Result	Low differential pressure, 1/64 in. diam	Low differential pressure, 1/32 in. diam	High differential pressure, 1/64 in. diam	High differential pressure, 1/32 in. diam
$\overline{\Delta p}$	5	5	2	2
$\overline{\dot{Q}}$	1/4	1/4	1/2	1/2
$\overline{\Delta p/{}^1/_2 \rho V^2}$	11	8	8	5
$\overline{L/DRe_D}$	1/2	1/2	1	1

Results and Discussion

The test results are tabulated in Table 2 and are presented in Fig. 2 in the form of curves in which the flow rate per tube is plotted against the total pressure drop between the reservoirs. Each of the curves represents the data obtained in a series of tests with one particular test section (e.g., one capillary tube). Inspection of Fig. 2 shows that the curves for tubes of larger aspect ratios (L/D) have steeper slopes than those of smaller aspect ratios. The slope of each curve was measured and the results are plotted in Fig. 3 with the slope as ordinate and the aspect ratio as abscissa. The resulting curve shows that the exponent N in an equation of the type

$$\dot{Q} = \text{const } \Delta p^N \quad [5]$$

increases from 0.5 at an aspect ratio approaching zero, to 0.91 at an aspect ratio of about 17. The exponent N in Equation [2] is related to k, the exponent of the velocity head in Equation [1] by

$$N = 1/2k \quad [6]$$

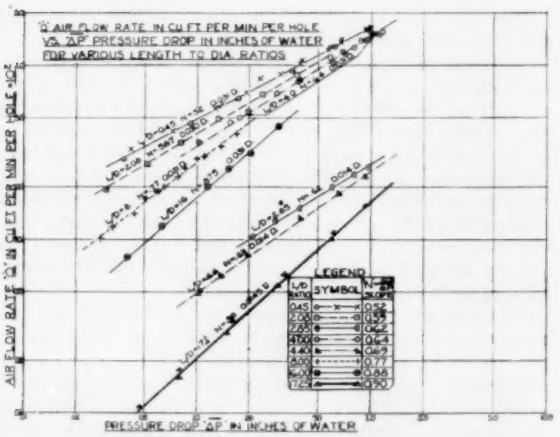

Fig. 2 Air Flow Rate Versus Pressure Drop in Capillary Tubes of Various Length-to-Diameter Ratios

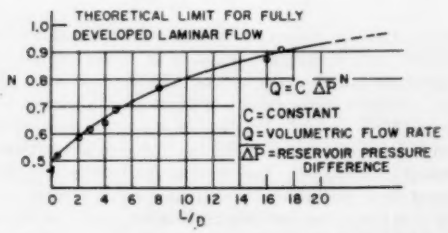

Fig. 3 Characteristic Flow Exponent N Versus Length-to-Diameter Ratio for Laminar Flow

Hence, the trend of the curve in Fig. 3 suggests an asymptotic approach to an exponent of unity, a value predicted from the Poiseuille law. The curve in Fig. 3 can be used to simulate, within the range of the variables shown in Fig. 2 and Table 2,

TABLE 2 EXPERIMENTAL DATA OF FLOW AND PRESSURE DROP IN SHORT CAPILLARY TUBES

$\overline{\Delta p}$ in. H_2O	$\overline{\dot{Q}}$ cfm × 10^2	V fps	$\overline{L/D}$	$\overline{\Delta p / \frac{1}{2g_c}\rho V^2}$	$\overline{L/DRe_D}$ × 10^2	Comments
0.091	0.465	14.60	0.45	1.92	1.97	Test rig 1
0.172	0.650	20.3	0.45	1.89	1.41	
0.35	0.938	29.3	0.45	1.84	0.99	
0.615	1.265	39.7	0.45	1.76	0.73	
0.073	0.435	13.6	0.45	1.78	2.12	Test rig 2
0.140	0.615	19.2	0.45	1.71	1.50	
0.136	0.622	19.5	0.45	1.63	1.47	
0.253	0.840	26.3	0.45	1.66	1.10	
0.40	1.070	33.5	0.45	1.61	0.86	
0.57	1.28	40.0	0.45	1.61	0.72	
0.67	1.40	43.9	0.45	1.58	0.656	
0.93	1.63	51.1	0.45	1.61	0.562	
0.042	0.333	10.4	0.45	1.75	2.76	Test rig 3
0.128	0.565	17.6	0.45	1.87	1.64	
0.193	0.697	21.85	0.45	1.825	1.32	
0.300	0.886	27.8	0.45	1.75	1.034	
0.391	1.020	31.9	0.45	1.735	0.90	
0.560	1.240	38.9	0.45	1.675	0.740	
0.672	1.355	42.4	0.45	1.68	0.68	
0.930	1.62	50.7	0.45	1.64	0.567	
0.975	1.66	52.0	0.45	1.635	0.560	
0.030	0.193	6.56	2.08	3.17	21.0	
0.081	0.360	12.25	2.08	1.45	11.3	
0.133	0.490	16.7	2.08	2.18	8.25	
0.052	0.272	9.25	2.08	2.75	15.1	
0.238	0.677	23.0	2.08	2.04	6.00	
0.376	0.880	30.0	2.08	1.89	4.60	
0.581	1.120	38.2	2.08	1.82	3.62	
0.21	0.104	16.1	2.85	3.62	25.2	
0.39	0.152	23.8	2.85	3.11	17.0	
0.60	0.200	31.8	2.85	2.51	12.7	
0.80	0.236	36.8	2.85	2.66	11.0	
0.96	0.260	40.4	2.85	2.67	10.0	
0.285	0.128	20.0	2.85	3.24	20.3	
0.102	0.361	11.3	4.0	3.63	22.7	Aluminum plate
0.155	0.475	14.9	4.0	3.18	17.3	
0.195	0.550	17.2	4.0	2.98	14.9	
0.286	0.702	22.0	4.0	2.67	11.7	
0.390	0.835	26.1	4.0	2.58	9.8	
0.595	1.06	33.0	4.0	2.44	7.7	
0.975	1.37	43.0	4.0	2.38	6.0	
0.020	0.118	3.7	4.0	6.67	70.0	
0.87	1.41	44.0	4.0	2.01	5.85	Lucite plate
0.68	1.21	38.0	4.0	2.14	6.75	
2.60	2.46	77.1	4.0	1.95	3.33	
1.50	1.82	59.1	4.0	1.94	4.35	
1.10	1.50	47.0	4.0	2.25	5.45	
1.15	1.56	49.0	4.0	2.17	5.30	
0.70	1.17	36.7	4.0	2.33	7.00	
0.93	1.42	44.5	4.0	2.10	5.76	
0.175	1.51	16.0	4.0	3.13	16.0	
0.38	0.82	25.8	4.0	2.57	9.9	
0.79	1.28	40.2	4.0	2.20	6.37	
0.96	1.45	45.5	4.0	2.10	5.64	
2.8	2.63	82.5	4.0	1.86	3.10	
4.5	3.40	108.0	4.0	1.75	2.38	
0.057	0.031	4.75	4.4	11.4	131.0	Lucite plate
0.105	0.051	7.9	4.4	7.7	79.0	
0.196	0.081	12.6	4.4	5.76	50.0	
0.396	0.132	20.5	4.4	4.25	30.7	
0.920	0.228	36.5	4.4	3.10	17.2	
0.655	0.184	28.5	4.4	3.63	22.0	
0.137	0.062	9.6	4.4	6.72	65.0	
0.102	0.049	7.6	4.4	8.00	82.1	
0.058	0.187	5.87	8.0	7.6	88.0	Lucite plate
0.100	0.289	9.05	8.0	5.63	57.6	
0.078	0.226	7.1	8.0	7.1	72.0	
0.044	0.139	4.36	8.0	10.5	119	
0.060	0.189	5.93	8.0	7.75	87.0	
0.065	0.199	6.05	8.0	8.1	85.0	
0.170	0.408	12.8	8.0	4.7	40	
0.028	0.101	3.16	8.0	12.7	163	
0.051	0.173	5.42	8.0	7.85	96.0	
0.086	0.256	7.7	8.0	6.61	66.5	
0.033	0.118	3.7	8.0	11.0	139	
0.110	0.298	9.35	8.0	5.7	54.7	
0.04	0.079	2.48	16.0	29.6	425	Lucite plate
0.085	0.160	4.96	16.0	15.6	200	
0.153	0.255	8.0	16.0	10.8	128	
0.293	0.421	13.2	16.0	7.65	77.8	
0.485	0.580	18.2	16.0	6.62	58.4	
0.06	0.119	3.7	16.0	20.9	277	
0.115	0.200	6.25	16.0	13.3	164	
0.205	0.313	9.8	16.0	9.65	105	
0.035	0.0073	1.06	17.25	142	2,230	Lucite plate
0.150	0.029	4.22	17.25	38.2	562	
0.295	0.054	7.85	17.25	21.6	302	
0.595	0.100	14.5	17.25	12.85	165	
0.99	0.149	21.6	17.25	9.58	110	
0.047	0.011	1.59	17.25	86.0	1,490	
0.160	0.034	4.95	17.25	29.5	480	
0.610	0.111	16.2	17.25	10.50	146	
0.935	0.156	22.7	17.25	8.25	105	
0.320	0.063	9.15	17.25	17.2	260	

various types of flow characteristics, since it is possible to obtain any value of k between 0.5 and 1.0 by a proper choice of the length-to-diameter ratio. The curve also shows that entrance effects can be appreciable in capillary tubes even at length-to-diameter ratios as large as 50.

The experimental data can also be correlated by means of an analysis originally proposed by Langhaar (1). The pressure drop between a reservoir and a downstream section in the tube x (Fig. 4) can be broken into three parts, or

$$p - p_x = \Delta_1 p + \Delta_2 p + \Delta_3 p \quad [7]$$

where

$(p - p_x)$ = drop between reservoir and a downstream section x
$\Delta_1 p$ = pressure drop between reservoir and inlet cross section ($x = 0$)
$\Delta_2 p$ = drop in pressure due to increase in kinetic energy in length x
$\Delta_3 p$ = pressure drop due to frictional loss in length x

If the stream tube between the reservoir and the section $x = 0$ is frictionless and has a bellmouth shape, the velocity at the inlet is approximately uniform (1, 7) and equal to the mean velocity V. Thus the pressure drop between the reservoir and the inlet section equals one velocity head according to Bernoulli's equation, or

$$\Delta_1 p = \frac{1}{2g_c} \rho V^2$$

Using the Navier-Stokes boundary-layer equations and Helmholtz's principle of least dissipation the remaining two pressure-drop terms, $\Delta_2 p$ and $\Delta_3 p$, have been evaluated by Langhaar (1) who showed that there exists for streamline flow in the transition length of tubes a unique relationship between $(\Delta_2 p + \Delta_3 p)$ and a single parameter $(x/D\mathrm{Re}_D)$. His results are shown graphically in Fig. 5 where

$$(\Delta_2 p + \Delta_3 p)/(\rho V^2/2g_c)$$

is plotted versus $(x/D\mathrm{Re}_D)$. The pressure-drop term $(\Delta_2 p + \Delta_3 p)$ also can be expressed in terms of a pipe-friction factor (8) by the equation

$$\frac{\Delta_2 p + \Delta_3 p}{\frac{1}{2g_c}\rho V^2} = \frac{p_0 - p_x}{\frac{1}{2g_c}\rho V^2} = 4 f_{APP} \frac{x}{D} = \phi\,(x/D\mathrm{Re}_D) \quad [8]$$

where f_{APP} is an integrated apparent friction coefficient defined by Equation [8] and ϕ denotes a functional relation. The integrated apparent friction coefficient f_{APP} includes the effects of the viscous shearing stress as well as the change in velocity head or momentum flux caused by the change of the velocity profile between the inlet section ($x = 0$) and the section where p_x is measured.

With capillary tubes of the size used in this study it was not possible to obtain local static-pressure measurements. Instead, the pressure difference between the reservoirs upstream and downstream of the tubes were measured. To compare the experimental results with Langhaar's theory it was assumed that the static pressure at the outlet of the tube is equal to the downstream reservoir pressure (10). It was further assumed that as the fluid enters a tube it forms a stream tube having the shape of a bellmouth so that the assumptions regarding the term $\Delta_1 p$ are valid. Then the pressure difference between the reservoirs $\overline{\Delta p}$ is related to $p_0 - p_L$ by the relation

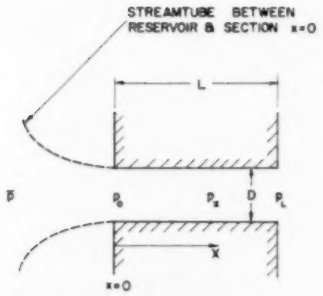

FIG. 4 SKETCH ILLUSTRATING NOMENCLATURE FOR TRANSITION FLOW

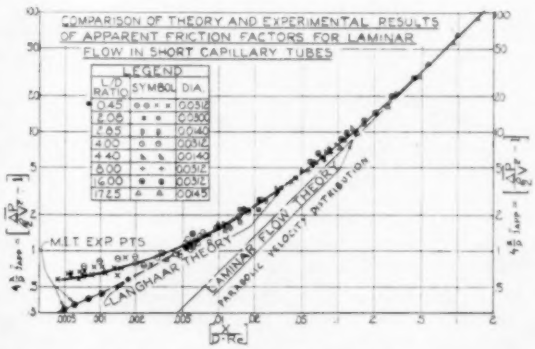

FIG. 5 COMPARISON BETWEEN THEORY AND EXPERIMENTAL RESULTS FOR LAMINAR FLOW IN SHORT CAPILLARY TUBES

$$\frac{\overline{\Delta p}}{\frac{1}{2g_c}\rho V^2} - 1 = \frac{p_0 - p_L}{\frac{1}{2g_c}\rho V^2} \quad [9]$$

The experimental results are shown in Fig. 5 where $\overline{\Delta p}/(\rho V^2/2g_c) - 1$ is the ordinate and $(L/D\mathrm{Re}_D)$ is the abscissa. Also shown on this graph are the analytical curve of reference (1), the Poiseuille relation for fully established laminar flow, and the averaged experimental results of reference (8). These experimental data were obtained with water and air in the entrance section of a 1.25-in-ID tube with a bellmouth entrance. The diameter Reynolds numbers Re_D used in reference (8) were large and resulted in turbulent flow downstream from the transition section.

Inspection of the data points and the curves of Fig. 5 shows that the experimental data for laminar flow in capillary tubes agree within the uncertainty interval (see Table 1) with the analysis of Langhaar (1) at values of the dimensionless quantity $(x/D\mathrm{Re}_D)$ greater than 4×10^{-2}, but deviate considerably at smaller values of $(x/D\mathrm{Re}_D)$. The test runs in this regime were repeated with three different test sections to verify the results.

The reason for the discrepancy between Langhaar's theory and the experimental results at $(x/D\mathrm{Re}_D)$ less than 4×10^{-2} can be found by examining the assumptions regarding $\Delta_1 p$. It was assumed that the stream tube formed by the fluid entering a tube has a bellmouth shape and that the velocity at the entrance section is uniform and equal to the average velocity V. However, even at very low Reynolds numbers small eddies form behind a sharp edge entrance and cause a vena contracta with some

friction losses. These losses, which are not considered in Langhaar's analysis, affect the over-all pressure drop appreciably when the tubes are so short that the total pressure drop between the reservoirs is of the order of one velocity head. Since the test data at $(x/D\mathrm{Re}_D)$ less than 4×10^{-3} were obtained in tubes having square-edged entrances and aspect ratios L/D of 0.45, the experimentally measured pressure losses are larger than those predicted by Langhaar's analysis. The geometry of these short tubes actually approaches that of an orifice for which the flow rate can be related by Torricelli's equation in the form

$$\dot{Q} = C \frac{\pi D^2}{48} \sqrt{\left(2g_c \frac{\overline{\Delta p}}{\rho}\right)} \quad [10]$$

The orifice coefficient C for the capillary tubes with an L/D ratio of 0.45 was found to be 0.76 ± 0.03 in the Reynolds-number range Re_D between 100 and 800. This result is in agreement with data obtained by Zucrow (12) in the same Reynolds-number range with benzol flowing through square-edged jets having an aspect ratio L/D of 0.33.

The experimental results obtained in the range of large values of $(x/D\mathrm{Re}_D)$ approach those predicted from the Poiseuille laminar-flow theory for a parabolic velocity distribution at values of $(x/D\mathrm{Re}_D)$ equal to 0.3.

Conclusions

From an experimental study of the flow characteristics of short capillary tubes the following conclusions can be drawn:

1 Measured values of the pressure drop between reservoirs upstream and downstream of capillary tubes with square-edged entrances are in agreement with Langhaar's theory for $(L/D\mathrm{Re}_D)$ larger than 4×10^{-3} and (L/D) larger than 2.

2 Measured values of the reservoir pressure drop for tubes having an aspect ratio L/D equal to 0.45 are considerably larger than those predicted by Langhaar's theory, but can be correlated by the usual orifice equation. The orifice coefficient for the range of Reynolds numbers Re_D between 100 and 800 was found to be 0.76 ± 0.03.

3 By proper selection of length-to-diameter ratios of short capillary tubes it is possible to simulate various flow characteristics in small-scale models for tests in atmospheric wind tunnels or in pneumatic control devices.

BIBLIOGRAPHY

1 "Steady Flow in the Transition Length of a Straight Tube," by H. L. Langhaar, *Journal of Applied Mechanics*, Trans. ASME, vol. 64, 1942, pp. A-55–58.

2 "Recherches expérimentales sur le movement des liquides dans les tubes de très petits diametres," by J. L. M. Poiseuille, *Memories des Savants Étrangers*, vol. 9, 1846, pp. 433–444.

3 "Hydrodynamique," by J. Boussinesq, *Comptes Rendus*, t. 110, 1890, pp. 1160, 1238; t. 113, 1891, pp. 9, 49.

4 "Die Entwicklung der Laminaren Geschwindigkeitsvertielung und ihre Bedeutung für Zähigkeitsmessungen," by L. Schiller, *Zeitschrift für angewandte Mathematik und Mechanik*, band 2, heft 2, 1922, pp. 96–106.

5 "Modern Developments in Fluid Dynamics," Fluid Motion Panel of the Aeronautical Research Committee, et al., edited by S. Goldstein, Clarendon Press, Oxford, England, 1938, pp. 304–308.

6 "Experimental Investigation of the Effects of Cooling on Friction and on Boundary Layer Transition for Low Speed Gas Flow at the Entry of a Tube," by S. J. Kline and A. H. Shapiro, NACA TN 3048, November, 1953.

7 "Applied Hydro- and Aeromechanics," by L. Prandtl and O. G. Tietjens, McGraw-Hill Book Company, Inc., New York, N. Y., first edition, 1934, pp. 27, 139–143.

8 "Friction Coefficients in the Inlet Length of Smooth Round Tubes," by A. H. Shapiro and R. Smith, NACA TN 1785, November, 1948.

9 "Describing Uncertainties in Single-Sample Experiments," by S. J. Kline and F. A. McClintock, *Mechanical Engineering*, vol. 75, 1953, pp. 3–8.

10 "The Dynamics and Thermodynamics of Compressible Fluid Flow," by A. H. Shapiro, Ronald Press, 1953.

11 "Capillary Tube Improves Heat Pump Design," by G. L. Biehn, *Heating and Ventilating*, vol. 51, no. 2, February, 1954, pp. 75–79.

12 "Discharge Characteristics of Submerged Jets," by M. J. Zucrow, Bulletin No. 31, Purdue Engineering Experiment Station, 1928.

Discussion

M. A. Rivas, Jr.[5] The experimental data presented in the paper are quite valuable due, in particular, to the care taken by the authors in their experiments. However, the writer takes exception to the lack of emphasis on what constitutes the governing design parameter for laminar flow in tubes (or capillaries). As has been shown by theoretical and experimental investigations (the authors' references (1), (3), (4), (5), and reference[6] of this discussion), the sole parameter which governs the flow is $L/D/\mathrm{Re}_D$ or $\mathrm{Re}_x/\mathrm{Re}_D{}^2$.

In particular, the writer is disturbed by the correlation presented in Fig. 3 of the paper where the exponent N in equation [5]

$$\dot{Q} = \text{const.}\ \overline{\Delta p}^N \quad [5]$$

is depicted as a function of L/D alone. It will be shown that it is legitimate to write an expression as given by Equation [5], but that N, however, in this expression is a function of $L/D/\mathrm{Re}_D$ and not of L/D.

It is easily shown (e.g., from Equations [8] and [9]) that the total pressure drop between the two reservoirs (assuming that, as the fluid enters the tube, it forms a stream tube having the shape of a bellmouth—for a detailed discussion of flow on bellmouth entries (see reference[7] of this discussion) is given by

$$\overline{\Delta P} = \left(1 + 4\bar{f}_{\mathrm{APP}} \frac{x}{D}\right) \frac{1}{2} \rho V^2 \quad [11]$$

or

$$\overline{\Delta P} = \left(1 + 4\bar{f}_{\mathrm{APP}} \frac{x}{D}\right) \frac{1}{2} \rho \left(\frac{Q}{A}\right)^2 \quad [11a]$$

transposing

$$Q = \frac{A}{\sqrt{(\rho/2)}} \frac{\overline{\Delta P}^{1/2}}{\sqrt{(1 + 4\bar{f}_{\mathrm{APP}} x/D)}} \quad [12]$$

For laminar flow in tubes (see Figs. 4 and 5 in reference[6] or Fig. 5 of the paper),

(*a*) If $(x/D)/\mathrm{Re}_D$ is very small $< 10^{-5}$

then

$$4\bar{f}_{\mathrm{APP}} \frac{x}{D} \ll 1$$

and therefore, from Equation [12]

---

[5] First Lieutenant, USAF, Directorate of Research, Fluid Dynamics Research Branch, Aeronautical Research Laboratory, Wright Air Development Center, Air Research and Development Command, Wright-Patterson Air Force Base, Ohio. Assoc. Mem. ASME.

[6] "Friction Factor in the Laminar Entry Region of a Smooth Tube," by A. H. Shapiro, Robert Siegel, and S. J. Kline, Proceedings of the Second U. S. National Congress of Applied Mechanics, June, 1954, pp. 733–741.

[7] "On the Theory of Discharge Coefficients for Rounded-Entrance Flowmeters and Venturies," by M. A. Rivas, Jr. and A. H. Shapiro, Trans. ASME, vol. 78, 1956, pp. 489–498.

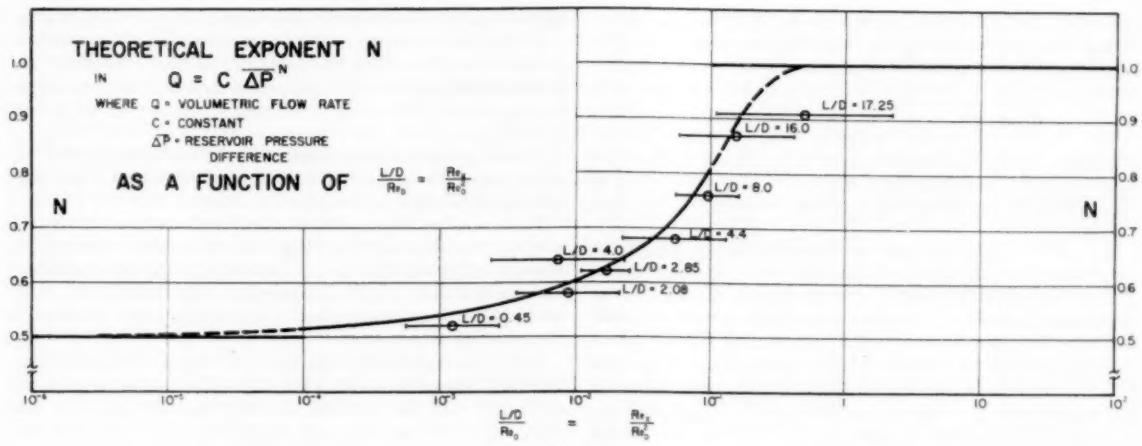

FIG. 6

$$Q \sim \overline{\Delta P}^{1/2}; \quad N = 1/2$$

The same result is obtained if $4\bar{f}_{APP}(x/D)$ is constant.

(*b*) If $(x/D)/\mathrm{Re}_D$ is high >0.5

then

$$4\bar{f}_{APP}\frac{x}{D} \gg 1$$

and therefore, from Equation [12]

$$Q \sim \frac{\overline{\Delta P}^{1/2}}{\sqrt{\left(4\bar{f}_{APP}\frac{x}{D}\right)}}$$

but since, in this range

$$4\bar{f}_{APP}\frac{x}{D} = \frac{64\,\frac{x}{D}}{\mathrm{Re}_D} \sim \frac{1}{V} \sim \frac{1}{Q}$$

we then have

$$Q \sim \frac{\overline{\Delta P}^{1/2}}{\frac{1}{Q^{1/2}}} \quad \text{or} \quad Q \sim \overline{\Delta P}; \quad N = 1$$

(*c*) If $10^{-2} < \dfrac{x}{D}\Big/\mathrm{Re}_D < 0.5$

$$Q \sim \frac{\overline{\Delta P}^{1/2}}{\sqrt{\left(1 + 4\bar{f}_{APP}\frac{x}{D}\right)}}$$

but since

$$4\bar{f}_{APP}\frac{x}{D} = \varphi_1\left(\frac{\frac{x}{D}}{\mathrm{Re}_D}\right)$$

also

$$1 + 4\bar{f}_{APP}\frac{x}{D} = \varphi_2\left(\frac{\frac{x}{D}}{\mathrm{Re}_D}\right)$$

In particular we could define an exponent n such that

$$1 + 4\bar{f}_{APP}\frac{x}{D} \sim \left(\frac{\frac{x}{D}}{\mathrm{Re}_D}\right)^n \quad \ldots\ldots [13]$$

or

$$1 + 4\bar{f}_{APP}\frac{x}{D} \sim \left(\frac{1}{Q}\right)^n \quad \ldots\ldots [13a]$$

Substituting Expression [13*a*] into [12]

$$Q \sim \frac{\overline{\Delta P}^{1/2}}{\left(\frac{1}{Q}\right)^{n/2}} \quad \ldots\ldots [14]$$

or

$$Q \sim \overline{\Delta P}^{\frac{1/2}{1-n/2}} = \overline{\Delta P}^N \quad \ldots\ldots [15]$$

where

$$N = \frac{1/2}{1 - n/2} \quad \ldots\ldots [16]$$

The exponent n can be calculated readily from the curve given in Fig. 5 of the authors' paper; however, the curve in Fig. 5 in reference[6] has been used instead, since it is in a form that yields a greater accuracy. Having calculated n, N is readily computed from Equation [16]. The results of these calculations are presented in Fig. 6.

The apparently successful correlation given by the authors in their Fig. 3 is explained as follows: If, from the authors' Table 2 and from their Fig. 3, we construct Table 3 and plot these data on Fig. 6 in the manner shown, where each solid horizontal line represents for each L/D the range of $(L/D)/\mathrm{Re}_D$ at its corresponding N-value, and each circle represents the mean value of the $(L/D)/\mathrm{Re}_D$ range, we can see how the authors were able to arrive at the smooth correlation shown in their Fig. 3. Therefore, it was quite

TABLE 3

L/D	Range of $L/D/\mathrm{Re}_D$		N
0.45	2.76×10^{-2}	5.60×10^{-4}	0.52
2.08	2.1×10^{-2}	3.62×10^{-3}	0.58
2.85	2.52×10^{-2}	1.1×10^{-3}	0.62
4.0	2.27×10^{-2}	2.38×10^{-3}	0.64
4.4	1.31×10^{-1}	2.2×10^{-3}	0.68
8.0	1.63×10^{-1}	5.47×10^{-2}	0.76
16.0	4.25×10^{-1}	5.8×10^{-2}	0.87
17.25	2.25	1.1×10^{-1}	0.91

fortuitous that the authors chose such an $(L/D)/\mathrm{Re}_D$ range for each of their L/D's, and had they extended the range of $(L/D)/\mathrm{Re}_D$ extensively for any of the L/D's chosen they would have observed a variation in the value of N for each value of the L/D's used.

One concludes from the foregoing that, although it is permissible to write an expression as given by Equation [5] of the paper, N in this expression must be regarded as a function only of $(L/D)/\mathrm{Re}_D$, the important sole parameter which governs the flow in tubes.

In regard to the deviations from tube-flow theory observed for low values of L/D, $(L/D = 0.45)$, the writer agrees with the authors that this is the result of a vena-contracta effect due to the sharp-edged entrance. This effect undoubtedly exists just as well in sharp-edge-entry tubes with the larger L/D's, but the effects become obscured by the wall-friction losses being of a much larger magnitude for tubes with larger L/D's. It is suggested that a systematic investigation, in which $(L/D)/\mathrm{Re}_D$ is kept constant and L/D (in this low-value range) is varied, would be extremely valuable. The present state of the art does not provide the designer with the criterion to distinguish at what values of L/D, for a particular $(L/D)/\mathrm{Re}_D$ range, deviations from tube-flow theory should be expected for tubes with sharp-edged entries.

A. H. Shapiro.[8] It is essential to the unambiguous interpretation of the experimental results given in this paper to appreciate that they refer to a capillary tube into which the flow is introduced from a large space via a square-edged orifice. Consequently the pressure drop depends both on the flow in the orifice and the flow in the capillary. Viewed in this light, the experimental results are less likely to be applied to circumstances in which they are not valid.

For example, it is true that the single dimensionless parameter, $x/D\mathrm{Re}_D$, governs the entire flow when the flow at the entrance of the capillary is uniform, and that it thus controls the dimensionless pressure drop in the capillary, $2\Delta p/\rho V^2$, for such a uniform entry. But, for a given orifice geometry, the governing number for the orifice is simply Re_D, and the latter controls the dimensionless pressure drop as the flow accelerates into the orifice. Furthermore, Re_D controls the character of the flow entering the capillary, and thereby the pressure drop in the latter. From all this we are forced to conclude that the dimensionless pressure drop for the entire system depends on two dimensionless groups, say

$$\frac{\Delta p}{\frac{1}{2}\rho V^2} = f\left(\frac{x}{D\mathrm{Re}_D}, \frac{x}{D}\right) \quad [17]$$

rather than on $x/D\mathrm{Re}_D$ alone.

Accordingly, Fig. 5 of the paper must be used with some caution, for a more extensive series of tests, perhaps with less scatter, would surely reveal on this chart a series of curves, one for each value of x/D. The authors obtained what seems to be a single curve only because of the experimental circumstance that an increase in x/D was accompanied by a general increase in the experimental values of $x/D\mathrm{Re}_D$.

This point may be elucidated by considering two extremes. If x/D is very small, say less than 0.10, the effect of x/D itself vanishes, the system behaves like a sharp-edged orifice, and $2\Delta p/\rho V^2$ depends only on Re_D. Thus, if several orifices with very small (but different) values of x/D were tested, each would yield a different curve on the chart of $2\Delta p/\rho V^2$ versus $x/(D\mathrm{Re}_D)$, but all would yield the same curve on a chart of $2\Delta p/\rho V^2$ versus Re_D.

At the other extreme, consider large values of x/D, say always greater than 100. Then the nature of the inlet is relatively inconsequential, and all the experimental data may be expected to be in agreement with Langhaar's theory, even for very low values of $x/D\mathrm{Re}_D$.

The foregoing discussion suggests that it would be of interest to carry out further systematic experiments with the goal of establishing the individual curves of x/D in Fig. 5.

To the authors' account of theoretical and experimental work on laminar flow in tube entries, it might be added that in reference (6) several additional theories are presented. One in particular, based on the theory of thin, laminar boundary layers, is especially accurate for very small values of $x/(D\mathrm{Re}_D)$, where Langhaar's theory seems to be in error.

The best experimental data for short tubes are those of reference (6), also given in reference (8). They are in remarkable agreement with the theories, differing from the latter by less than 1 per cent in the range of $x/(D\mathrm{Re}_D)$ between 10^{-3} and 10^{-2}.

J. F. D. Smith.[9] The authors of this paper have been loose in their dimensional treatment of the subject. The units specified are quite inconsistent and awkward. For example, in Equation [1] the authors divide a pressure drop in pounds (force) per square inch by a mass density in pounds (mass) per cubic foot. In the same equation V is given as a velocity in feet per second. The part in parentheses $(V^2/2)$ is raised to a variable power k, which means that the friction coefficient has dimensions in this case which vary with k.

The writer would suggest that the authors revamp the units and equations to insure dimensional consistency and rigor. For example, any factor raised to a variable power, as in this equation, must be dimensionless if no other dimensions are changed elsewhere.

This is not to be construed as a criticism of the results, but is a plea for a more satisfactory and rigorous mathematical presentation.

J. R. Sproat.[10] A paper was presented at the Appalachian Gas Measurement Short Course held at West Virginia University in August, 1955. Simple working formulas were developed by the writer for determining the dimensions of capillary tubes required to produce desired flow rates for gases and liquids. The concluding remarks of that paper may be of interest to those contemplating further investigations or use of capillaries:

"In the design of a capillary, the Reynolds number should be calculated to determine if the flow is laminar. If the Re_D is found too high, using the available diameter tube, it may be necessary to divide the flow, say in 10 parallel tubes.

"Roughness of the bore has no effect on the flow rate, because there is no flow at the wall of the tube.

"The capillary should be calibrated with dry air or a known gas such as nitrogen; boiled or distilled water. After calibration the capillary can be used on any other fluid if its viscosity is known. The flow will vary inversely as the viscosity; i.e., as the viscosity increases the flow decreases. Calibration is necessary due to the fact that the flow varies as the fourth power of the diameter and it is difficult to obtain tubing with exact bore through the entire length of section.

"If the capillary is to be coiled, calibration should be made after coiling.

[8] Professor of Mechanical Engineering, Massachusetts Institute of Technology, Cambridge, Mass.; presently, Visiting Professor of Applied Thermodynamics, Engineering Laboratory, University of Cambridge, Cambridge, England. Mem. ASME.

[9] Dean, Division of Engineering, Iowa State College, Ames, Iowa.

[10] Measurement Engineer, Carbide and Carbon Chemicals Company, So. Charleston, W. Va. Mem. ASME.

"The differential pressures should range from 20 to 300 inches of water.

"The length should be greater than 50 times the diameter.

"The area preceding the inlet should be at least 20 times the capillary area.

"A filter or screen should be installed upstream of the capillary.

"The temperature affects the diameter of the capillary and the viscosity of the flowing fluid; therefore, for accurate work a temperature bath or some suitable means should be provided to maintain uniform temperature of both capillary and fluid.

"Since the flow varies inversely as the viscosity, once the capillary has been calibrated with a fluid of known viscosity, such as air, nitrogen, or water, the viscosity of any other fluid may be determined. Several makes of viscosimeters use this method as a means of calculating viscosity.

"The capillary has many uses as a measuring device, especially for a small quantity of gas or liquid. They are accurate, inexpensive, and simple to construct."

Authors' Closure

The authors wish to thank the discussers for their interest in the paper. Some of the comments are pertinent and valuable and the authors will attempt to answer, as far as possible, the questions raised.

Lieutenant Rivas' comments represent a valuable contribution to the paper, but unless the assumptions made in the course of his analytical derivation of the flow exponent N are understood clearly, the application of his results could lead to erroneous conclusions. His assertion that the flow exponent N depends solely on the parameter $(L/D)/\mathrm{Re}_D$ is not entirely true. As pointed out explicitly in the paper as well as in Professor Shapiro's discussion, and implicitly also in the last paragraphs of Lieut. Rivas' discussion, the pressure drop in flow through short capillary tubes into which the flow is introduced from a large space via a square-edged orifice depends on L/D as well as Re_D, or $[(L/D)/\mathrm{Re}_D]$. Fig. 3 is an empirical correlation and therefore applies only within the range of the variables investigated. Its primary purpose is to show that by selecting appropriate values of L/D, flow exponents ranging from about 0.5 to 1.0 can be attained. The actual value of L/D required to obtain a specific value of N for a specified, but limited, range of Reynolds numbers Re_D depends also on the Reynolds-number range.

Lieut. Rivas' analysis can be used to predict N when $\Delta_1 p$ in Equation [7] of the paper is sufficiently small compared to $(\Delta_2 p + \Delta_3 p)$ so that deviations of the actual value of $\Delta_1 p$ from the assumed value of one velocity head are negligible. However, for small values of L/D, irrespective of the value of $(L/D)/\mathrm{Re}_D$, the theoretical curve shown in Fig. 6 does not apply because vena-contracta effects which are not considered in the analysis become important.

To elucidate this point and to illustrate the vena-contracta effects at least qualitatively, Fig. 7, based on Fig. 5 and Equation [16], has been prepared. In this figure curves of N, calculated on the assumption that $\Delta_1 p = \rho V^2/2g_c$, are shown as a function of L/D. Each curve is for a given value of Re_D. The crosses represent the experimental values of N from Fig. 3 and the accompanying vertical lines show the range of Reynolds numbers covered in the tests (see Table 2). The circles represent values of N calculated from experimental data reported by Linden and Othmer[11] for aspect ratios of 0.20, 0.30, and 0.58 in the Reynolds-number range indicated by the accompanying vertical lines.

An examination of Fig. 7 shows that N depends both on L/D and Re_D or $(L/D)\mathrm{Re}_D$. The observed values of N represent average values for a specific length-to-diameter ratio over a limited Reynolds-number range. The experimental values agree fairly well with the predicted values for $L/D > 2$. Fig. 7 further shows, as pointed out by Lieut. Rivas, that if a much wider range of Reynolds numbers had been covered with any of the test sections, the relation between $\overline{\Delta p}$ and $\dot{Q}$ could not have been approximated by a single straight line. It is also apparent that for small values of L/D the experimental results deviate appreciably from the values predicted by Lieut. Rivas' analysis. For very small values of L/D the data of Linden and Othmer yield values of N below 0.5 which is the lower limit of the analysis. For the purpose of relating $\overline{\Delta p}$ to $\dot{Q}$ empirically, it would therefore appear acceptable, and maybe even preferable, to treat N, the flow exponent for the system investigated, as a function of L/D within a limited, but specified, range of Reynolds numbers rather than to treat N solely as a function of $(L/D)/\mathrm{Re}_D$ as suggested by Lieut. Rivas.

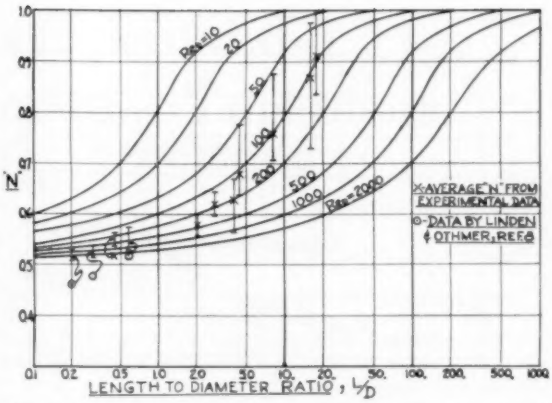

Fig. 7 Theoretical and Experimental Flow Exponent N Versus Length to Diameter Ratio for Various Reynolds Numbers

It should also be noted that in Fig. 5 of footnote 6 which was used by Lieut. Rivas for his calculations, no experimental data for $(L/D)/\mathrm{Re}_D$ above 1×10^{-3} are shown. In the range of $(L/D)/\mathrm{Re}_D$ between 1×10^{-3} and 5×10^{-1} in which the boundary-layer flow gradually merges into fully developed Poiseuille flow and the variation of N takes place, the results of the various theories shown differ by as much as 10 per cent from one another.

In an effort to determine which of the theories is valid in the range of the experimental results of this investigation, the experimental data are compared in Fig. 8 of this closure, with the analytical results summarized by Shapiro, et al.,[6] which was published after this paper was submitted. The solid line represents the average of the results of this investigation for tests with $(L/D) > 4$. As predicted by Shapiro, et al.,[6] the experimental results agree in the range of $(L/D)/\mathrm{Re}_D$ between 5×10^{-3} and 5×10^{-1} more closely with results obtained by differential-equation methods (1 and 5) than with results calculated by integral methods.

Professor Shapiro's comments emphasize succinctly the importance of the entrance conditions. In an effort to shed more light on the pressure drop, the authors reviewed available data, including those for very small values of L/D where conditions approach flow through a sharp-edged orifice.[12]

An incidental observation made in the course of this study is that orifice coefficient in the laminar-flow range may be affected

[11] "Air Flow Through Small Orifices in the Viscous Region," by H. R. Linden and D. F. Othmer, Trans. ASME, vol. 71, 1949, pp. 765–.277

[12] "Orifice Coefficients for Reynolds Numbers From 4 to 50,000," by H. W. Iversen, Trans. ASME, vol. 78, 1956, pp. 359–364.

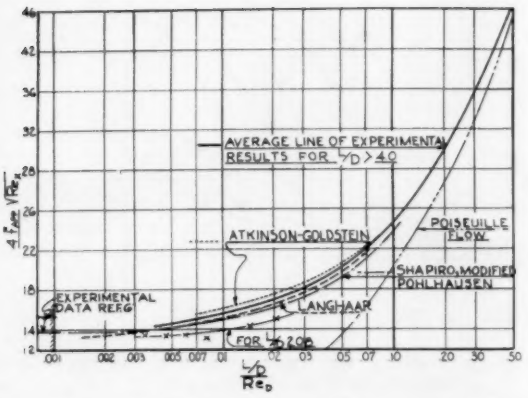

FIG. 8 COMPARISON OF THEORETICAL AND EXPERIMENTAL RESULTS FOR INTEGRATED APPARENT FRICTION FACTOR

by L/D variations even when L/D is of the order of 0.1. The ISA and ASME codes specify the maximum thickness of orifice plates, t, as a fraction of the pipe diameter, D_p; i.e., $t < 0.02\ D_p$. For a small orifice in a large pipe it is therefore quite possible that the pressure drop through the orifice, although designed according to specifications, will deviate from the results predicted from a simple orifice equation (e.g., footnote 8). To safeguard against such deviations it is suggested that the maximum orifice thickness be specified in terms of the orifice diameter.

The information available to-date is unfortunately insufficient to give quantitative answers to the questions raised by Professor Shapiro's valuable and pertinent comments which, however, are broader in scope than the limited objectives for which the tests reported in this paper were conducted. Qualitatively, we can conclude that only for conditions when $\Delta_1 p$ in Equation [7] is of the order of $(\Delta_2 p + \Delta_3 p)$ will deviations from the pressure drop predicted from Equation [9] and Fig. 5 be appreciable.

The authors agree with Lieut. Rivas and Professor Shapiro that additional experiments, especially at Reynolds numbers between 500 and 2100 and in the low L/D range, are desirable. The tests reported by the authors were conducted within the scope of a large research project in the course of which experimental data for flow of air through capillary tubes in the pressure-drop range of 0.03 and 2.0 in. water were required. These conditions yield $(L/D)/\mathrm{Re}_D$ values between 1×10^{-3}, the maximum value for which data were available and 0.5, the value at which Poiseuille flow is approached. The data were published simply because they fall into a range of variables in which no experimental results were heretofore available. When comparing the accuracy of the experimental results of this study with those of Shapiro, et al.,[6] it is well to keep in mind that the pressure drop, which more than any other measurement limits the accuracy of the apparent friction coefficient at low Reynolds numbers, is much smaller in the range of variables covered by the authors than in the range of variables covered by Shapiro, et al. The original equipment was returned to the sponsor at the termination of the contract, but an improved version is at present being built at Union College to conduct further tests along the lines suggested by the discussers.

Dean Smith's comments regarding the units and the dimensional treatment of the subject seem to have been prompted by an error in the preprint of this paper, where instead of the proportional sign an equal sign was used in Equation [1]. Equation [1] is dimensionally consistent as shown and the parameters $\Delta p/(\rho V^2/2g_c)$ and $(L/D\mathrm{Re}_D)$ are dimensionless quantities. One could, of course, express ρ in slugs/ft^3 instead of lb$_M$/ft^3 and thereby eliminate the explicit use of g_c. This choice of units may be more satisfactory to some, but it would not affect the mathematical rigor.

Mr. Sproats comments on the application of capillary tubes to flow measurements will be of value to those contemplating the use of capillaries for this purpose. It would seem, however, that the minimum length should be specified in terms of $(L/D)/\mathrm{Re}_D$ instead of L/D. The experimental results of this study confirm theoretical predictions[8] which show that for the centerline velocity to approach the Poiseuille value within 1 per cent, $(L/D)/\mathrm{Re}_D$ must be at least 0.3, but probably close to 0.6. With the lower figure as a limit, the minimum length-to-diameter ratio required to establish a parabolic velocity profile at Re_D of 2000 is 600, which is twelve times larger than the value suggested by Mr. Sproats.

Orifice-Metering Coefficients and Pipe Friction Factors for the Turbulent Flow of Lead-Bismuth Eutectic

By H. A. JOHNSON,[1] J. P. HARTNETT,[2] W. J. CLABAUGH,[3] and L. FRIED[4]

Pipe friction factors and orifice-metering coefficients are reported for the turbulent flow of lead-bismuth eutectic and are found to be in satisfactory agreement with the results for water flow when compared on the usual dimensionless basis.

Nomenclature

The following nomenclature is used in the paper:

A_o = area of orifice, sq ft
D = inside diameter of pressure-drop test pipe, ft
f = Weisbach friction factor defined as $f = \dfrac{(\Delta p/\Delta L)}{(\rho u^2/2g_c D)}$
g_c = conversion faction, 4.17×10^8 lb_m ft/lb_f hr^2
H = head loss across orifice, ft lb_f/lb_m of flowing fluid
K = orifice flow coefficient, defined as $K = \dfrac{W}{A_o\sqrt{2g_cH}}$
u = mean fluid velocity, fph
W = mass rate of flow, lb_m/hr
$\Delta p/\Delta L$ = pressure drop per unit length of pipe, psf/ft
ϵ = surface roughness of pipe, ft
ν = kinematic viscosity, ft^2/hr
ρ = fluid density, lb_m/ft^3

Introduction

Liquid metals, because of their low vapor pressure and high thermal conductivity, have appeared promising for use in nuclear power plants. As a result, considerable engineering information for liquid metals has been accumulated. The purpose of this paper is to report some additional engineering data, more specifically pipe friction factors and orifice-metering coefficients, which may be of use to those designing a liquid-metal system.

A knowledge of the friction factor is necessary to calculate the pumping power requirements for any given system. A review of the literature indicated only one previously reported investigation of friction factors of liquid metals (1).[5] The present investigation presents friction factors for turbulent flow of lead-bismuth, thereby allowing a comparison with this earlier reported work. In addition, friction factors were obtained for water flow in the same tubes making possible direct comparison of water friction factors with those for liquid metals.

In many liquid-metal systems it is either necessary or desirable to determine the liquid flow rate, and consequently flowmetering equipment is necessary. It is realized that there are many disadvantages in the use of orifice meters in permanent liquid-metal installations; however, the low cost and availability of such a device may sometimes offset these disadvantages, particularly in small-scale or experimental investigations. The use of such orifice meters for liquid metals is reported in references (2 to 7). Generally these orifices have not been calibrated directly with the liquid metal, but rather it was assumed that the flow coefficients for liquid metals were equivalent to those for water when compared on the usual dimensionless basis. However, it has been suggested in reference (6) that nonwetting may result in a different calibration for those liquid metals which do not wet the orifice surface. Therefore it was felt worth while to investigate the problem directly.

Apparatus and Test Procedure

Lead-Bismuth Flow Circuit. The lead-bismuth flow circuit, as shown in Fig. 1, consisted essentially of a centrifugal pump submerged in a closed sump tank, an orifice-metering section, the pressure-drop test section, a calibrated volume tank, and the necessary piping. Nichrome resistance wire was wrapped around all of these components to permit preheating the system above the melting temperature of lead-bismuth (257 F) before operation. Provisions were made to evacuate the system and to maintain a helium-gas atmosphere over the molten metal at all times.

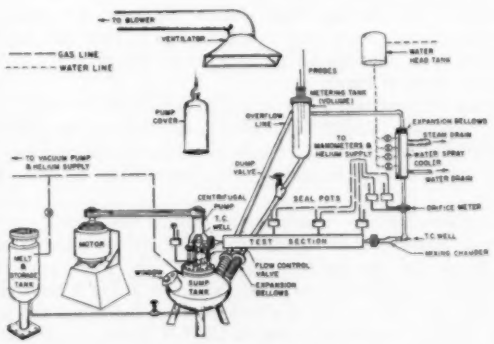

Fig. 1 Lead-Bismuth Flow Circuit

The belt-driven centrifugal pump, expressly built for this system, was a vertical-shaft, end-suction volute type which operated submerged in the lead-bismuth. The sump tank was ellipsoidal in shape to minimize the required metal charge and, at the same

---

[1] Professor of Mechanical Engineering, University of California, Berkeley, Calif. Mem. ASME.

[2] Associate Professor of Mechanical Engineering, University of Minnesota, Minneapolis, Minn. Assoc. Mem. ASME.

[3] Engineer, Atomic Power Equipment Department, General Electric Company, San Jose, Calif. Assoc. Mem. ASME.

[4] Product Design Engineer, Light Military Electronic Equipment, General Electric Company, Utica, N. Y. Assoc. Mem. ASME.

[5] Numbers in parentheses refer to the Bibliography at the end of the paper.

Contributed by the Hydraulic Division and presented at the Semi-Annual Meeting, Cleveland, Ohio, June 17–21, 1956, of The American Society of Mechanical Engineers.

Note: Statements and opinions advanced in papers are to be understood as individual expressions of their authors and not those of the Society. Manuscript received at ASME Headquarters, January 26, 1956. Paper No. 56—SA-16.

time, to insure a reasonably constant suction head on the pump during the metering period.

The pump discharged through a bellows-sealed flow-control valve and then through the pressure-drop test section to the vertical orifice-metering section. From the metering section the fluid flowed through the cooler and into a horizontal line carrying the fluid over to the calibrated volume tank which normally emptied into the sump. During the metering period the dump valve was closed. An overflow line from the top of the volume tank served to return the fluid to the sump in case the dump valve was not opened before the volume tank was filled completely.

On shutdown the system was secured by using helium pressure to force the liquid lead-bismuth into the isolated melt tank. The melt tank also served in preparing the eutectic from pigs of lead and bismuth.

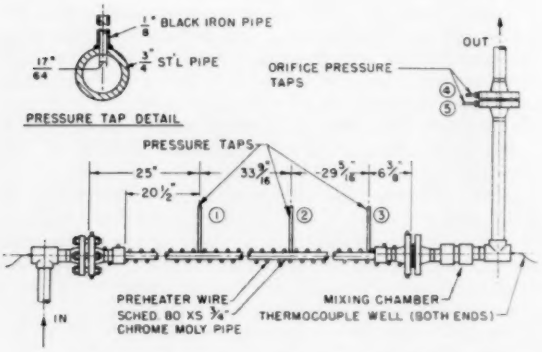

FIG. 2 PRESSURE-DROP TEST SECTION NO. 1

Pressure-Drop Test Section—No. 1. The first pressure-drop test section, designated as No. 1, is shown in Fig. 2 and consisted of an $87^1/_4$-in. length of $^3/_4$-in., schedule 80 XS seamless pipe of 5 per cent chromium, $^1/_2$ per cent molybdenum (0.742 in. ID, 1.050 in. OD). The pipe was welded at the two ends to socket reducers, which in turn were welded to $1^1/_2$-in. ring-joint flanges. This $94^1/_4$-in. unit was flanged into the permanent lead-bismuth loop as shown in Fig. 1.

The first pressure tap was located $21^1/_2$ in. from the entrance of the $^3/_4$-in. pipe, thereby allowing 29 pipe diameters as a hydrodynamic calming section. The two remaining taps were located at distances of $33^9/_{16}$ in. and $62^7/_8$ in., respectively, from the first tap.

The pressure taps were made by drilling $^{17}/_{64}$-in. holes in the pipe at the noted positions, taking precautions to insure no burrs on the inner pipe surface. Standard $^1/_8$-in. pipes were then welded in position over the holes. As shown in Fig. 1, these pipes in turn were welded into the bottom of the individual seal pots. The seal pots were connected to the 8-ft mercury manometers through appropriate valving. For each run, three separate pressure-drop values were obtained, across taps 1–2, 2–3, and 1–3, thereby giving an indication of the reliability of the test measurements.

Pressure-Drop Test Section—No. 2. The second pressure-drop test section, Fig. 3, was of the same material and of the same length as section No. 1; however, the location and construction of the pressure taps were altered. The first tap was located $20^1/_8$ in. from the entrance, a distance of 27 tube diameters. The remaining taps were positioned $31^1/_8$ in. and $62^1/_4$ in., respectively, from the first one.

Orifice-Metering System. The orifice-metering section, shown in Fig. 4, consisted of the orifice flanges, the orifice plate, and the upstream and downstream sections of pipe. A duplicate section

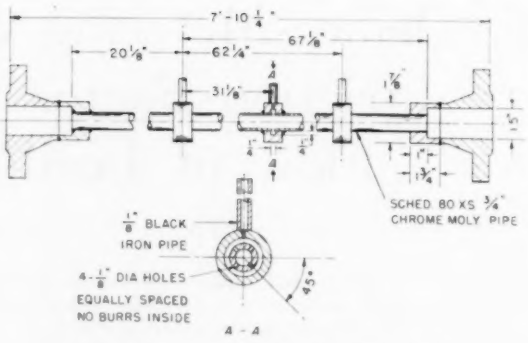

FIG. 3 PRESSURE-DROP TEST SECTION NO. 2

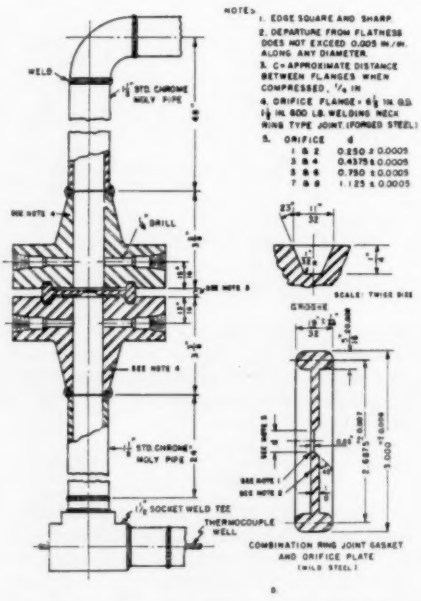

FIG. 4 ORIFICE-CALIBRATION ASSEMBLY

was assembled and used for the calibrations with water. The orifice flanges were of the $1^1/_2$-in. 600-lb, welding-neck, ring-joint type with ASME flange taps. The combination ring-joint gasket and orifice plate was so designed that the orifice plate conformed to the ASME specifications for a sharp-edged orifice. A total of eight orifices, two each of four sizes, were calibrated in both the water and lead-bismuth-metering sections.

In the lead-bismuth system, each flange tap was connected by a $^1/_8$-in. pipe to the bottom of a seal pot on which was mounted a lead-bismuth level indicator, Fig. 1. The pots were constructed of 4-in. lengths of 5-in. steel pipe with welded ends of 1-in. steel plate. The level indicator consisted of a hollow float with a thin stem extending upward into an 11-mm-OD, 3-mm-ID glass tube which in turn was glass-to-metal seal-welded to the pot. The liquid-metal level was controlled by introducing or removing helium through a suitable valving arrangement.

The seal pots were connected by steel tubing to the legs of an 8-ft mercury manometer made of 12-mm-high pressure pyrex tubing fitted into special stainless-steel manometer blocks. A trap on each manometer leg insured against the blowing of mer-

cury into the lead-bismuth system. The manometer could be isolated from the system by $^1/_8$-in. diaphragm valves in the line to each manometer leg.

Metering Tank. The metering tank was constructed of a 36-in. length of 8-in. extra strong chrome-moly pipe with a chrome-moly welding cap as the base and a slip-on welding flange for the top with the cover plate a tongue-and-groove blind flange. The inside diameter of this tank had been measured carefully at several positions along the length with inside micrometers. The lead-bismuth entered through a $1^1/_2$-in. pipe near the top and drained to the pump sump through a bellows-sealed Y-valve in the 2-in. line at the bottom of the tank. A 2-in. overflow pipe connected the top of the metering tank to the sump tank.

Three $^1/_4$-in. steel rods, 50 in. in length with conical tips, extended through the tank cover into the volume tank through Teflon-packed glands. To minimize the temperature of these glands, which served as pressure-tight connections and electrical insulators, they were mounted on $^1/_2$-in. pipes 5 in. above the cover. The rods, insulated from each other and from the tank, extended to different depths and could be adjusted to any desired vertical position. Since all three rods were the same length, the distance between probe tips could be determined from external measurements.

The external ends of the rods were connected to an electrical timer which was energized when the rising liquid metal contacted the lower rod and was stopped when it reached the upper one. A switch on the timer allowed selection of any two of the three probes for this metering process. Liquid surface waves were reduced by baffles which directed the flow down the side walls and by a 3-in. pipe surrounding the rods. There were no indications of entrapment of helium in the flowing metal as had been encountered in previous investigations (4).

Experimental Procedure. Periodically throughout the test program, the pressure-drop sections and the orifice meters were removed from the lead-bismuth circuit and, without cleaning, check runs with water were made. For these water tests the pressure differentials were measured with mercury-water or inverted water manometers over most of the test range. At low water-flow rates it was necessary to use a Prandtl manometer to measure the small deflections. Water-flow rates were determined directly by weighing. After such water tests the test surfaces were cleaned before placing the units back into the lead-bismuth circuit.

Pressure differentials in the liquid-metal testing were normally read on mercury manometers which were connected to the test sections as shown in Fig. 1. At low flow rates the small deflections made it necessary to use a cathetometer and abandon the mercury manometers. In these cases the cathetometer was sighted on the seal-pot floats which were open to a common helium pressure over the liquid-metal surface. Zeroing was accomplished at a no-flow condition by sighting on the seal-pot floats under a constant head of lead-bismuth.

Discussion of Results

Pipe Friction Factors. The friction-factor values for water flow through the two test sections, as shown in Fig. 5, are in agreement within 5 per cent over the Reynolds-number range of 10^4 to 2×10^5. This agreement also includes water data taken immediately after lead-bismuth operation, thereby indicating negligible effect of the liquid metal on the surface roughness of the pipe. The observed 5 per cent test scatter agrees with the calculated probable error based on the accuracy of instrumentation.

Visual inspection of the internal surface of the test section indicated that the chrome-moly surface more closely approximated a drawn-tube surface than that of a pipe. This is confirmed by

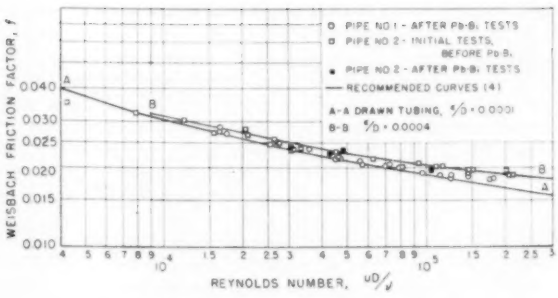

Fig. 5 Pipe Friction Factors—Water

the results shown in Fig. 5, where the experimental friction-factor results lie midway between the recommended values (6) for drawn tubing ($\epsilon/D = 0.0001$) and tubing with a relative roughness ϵ/D of 0.0004.

The friction-factor results for lead-bismuth eutectic flow are shown in Figs. 6 to 8. Although the predicted probable deviation is only 5 per cent, the test results for pipe No. 1 scatter ±20 per cent about the curve obtained from the water friction-factor measurements. This same scatter is observed for test section No. 2. The summary of all lead-bismuth tests is revealed in Fig. 8, where it is seen that the major portion of all the liquid-metal results lie in a region extending from 15 per cent above to 15 per cent below the experimental water friction-factor curve.

The observed spread in the liquid-metal data was not a completely random variation. In general, those data taken during a given test sequence, that is, on any given day of operation with no interrupting shutdown period, were consistent and would fall on a friction-factor curve roughly parallel to the one found for water. During the next sequence the general level of the results would

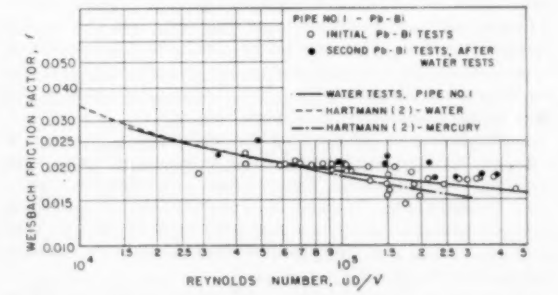

Fig. 6 Pipe Friction Factors—Lead-Bismuth Test Section No. 1

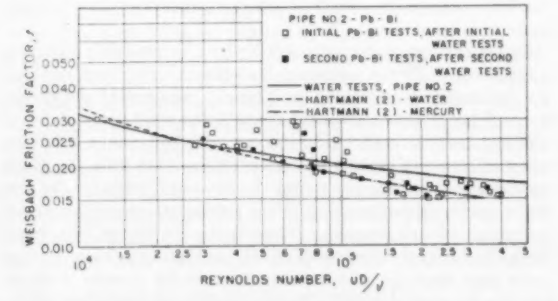

Fig. 7 Pipe Friction Factors—Lead Bismuth Test Section No. 2

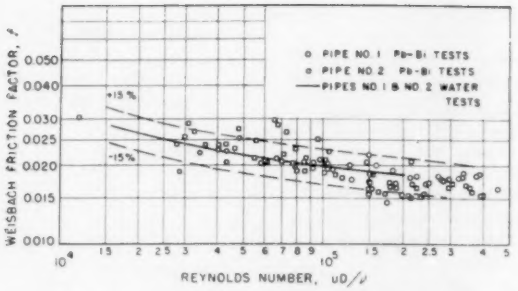

FIG. 8 PIPE FRICTION FACTOR—SUMMARY

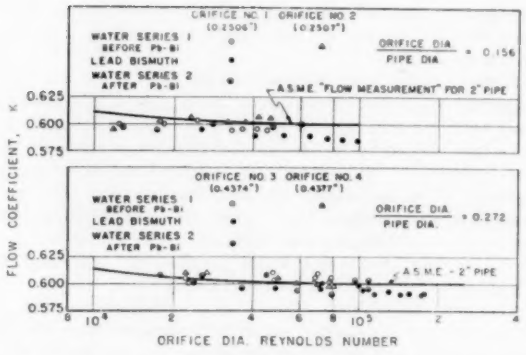

FIG. 9 ORIFICE-METERING COEFFICIENTS—ORIFICES 1–4

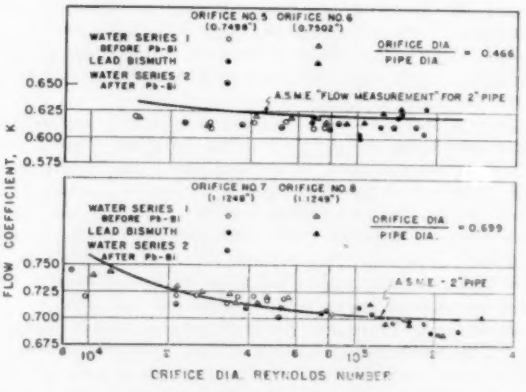

FIG. 10 ORIFICE-METERING COEFFICIENTS—ORIFICES 5–8

shift, either up or down, but the results would remain consistent throughout the sequence. Since the water tests before and after the liquid-metal tests were in agreement no major changes in surface roughness occurred during the lead-bismuth testing. If surface effects are responsible for the pressure-drop variation, such effects may be of the nature reported in reference (8) where local detachments at the wall surface of liquid metal flowing through a glass tube were observed.

Since the water tests were performed at 60 F, while the liquid-metal tests were at 400 F, the errors caused by the neglect of thermal expansion should be considered. The coefficient of thermal expansion for the chrome-moly pipe is 6×10^{-6} deg F^{-1} and thus accounts for a 1 per cent difference in the friction factors of liquid metal and water, a small value compared to the observed variations.

The results of Hartmann (1) are shown in Figs. 6 and 7 where it is seen that his water and mercury test ranges did not overlap. However his mercury data do indicate a smooth extension of his water results allowing the conclusion that friction-factor results for water and mercury are the same when compared at the same Reynolds number. This same general conclusion is substantiated by the present lead-bismuth tests; however, the shifting of the lead-bismuth friction-factor results from one test series to the next requires additional experimentation.

Orifice-Metering Coefficients. Eight orifice plates, two each of four sizes, in a $1^1/_2$-in. pipe with flange taps were calibrated with water and lead-bismuth. The resulting orifice-flow coefficients are presented in Figs. 9 and 10. The probable error, based on the instrumentation accuracy, was calculated to be $1^1/_2$ to 3 per cent at the maximum and minimum flow rates, respectively, for both water and lead-bismuth.

The reproducibility of the flow coefficients for duplicate orifices is demonstrated by the results of the water and lead-bismuth tests. As shown in Figs. 9 and 10, the flow coefficients for the duplicate orifices for each fluid are in agreement within $1^1/_2$ per cent.

The maximum water rate was limited by available pumping equipment, while the minimum lead-bismuth flow was fixed by the necessity of obtaining a readable manometer deflection. Accordingly, it was impossible to cover the same range of Reynolds numbers for both fluids. There was, however, a sufficient range of common values of Reynolds modulus with the three smaller-size orifices to show that the flow coefficients for the two fluids are in agreement within the calculated experimental accuracy of $1^1/_2$ to 3 per cent. There is also revealed in Figs. 9 and 10 the tendency for the lead-bismuth coefficients to be somewhat lower than those for water and to continually decrease with increasing Reynolds number. It was anticipated that minor differences would be found since separate orifice assemblies were used for the water and lead-bismuth tests. (The orifice meters, however, were interchanged between these units for the calibrations with both fluids.) In all cases, however, the agreement of the water and lead-bismuth coefficients is within the estimated accuracy of 3 per cent. It is concluded, therefore, that orifice-meter flow coefficients obtained with water will apply without correction for lead-bismuth at the same value of the orifice Reynolds number.

The smallest pipe for which the ASME reports coefficients is a 2-in. pipe. As shown in Figs. 9 and 10, the ASME recommended curve for the 2-in. pipe deviates from the values obtained in the present $1^1/_2$-in. pipe by only $1^1/_2$ per cent with the exception of orifices Nos. 7 and 8. These two large orifices yielded coefficients which are below the ASME curve below 20,000, but in this range the ASME values are suspected due to lack of supporting data. Thus the $1^1/_2$-in. pipe-flow coefficients may be predicted within $1^1/_2$ per cent by the ASME recommendations for a 2-in. pipe at orifice Reynolds numbers in excess of 20,000.

CONCLUSIONS

Pipe Friction Factors. Pipe friction factors for the turbulent flow of lead-bismuth eutectic agree with those for the flow of water when compared on the usual dimensionless basis. However, a relatively large unexplainable spread (±15 per cent) occurs in the results for lead-bismuth eutectic which requires further exploration.

Orifice-Metering Coefficients. When compared at the same orifice Reynolds number and for the same pipe size the flow coefficients for lead-bismuth eutectic and for water are equivalent for sharp-edged orifices with flange taps.

Acknowledgments

The authors acknowledge the able assistance of Messrs. J. Ingamells, E. D. Martin, and E. A. Conway throughout the test program. Profs. R. A. Seban and H. W. Iversen contributed valuable suggestions during the course of the work reported herein.

The sponsorship of the Atomic Energy Commission is gratefully acknowledged. The present paper is a summary of the reports, "Orifice Metering Coefficients for Lead-Bismuth Eutectic," December, 1953, and "Pipe Friction Factors for the Flow of Lead-Bismuth Eutectic," February, 1954, both reports by H. A. Johnson, J. P. Hartnett, W. J. Clabaugh, and L. Fried and printed as Institute of Engineering Research Reports, University of California, Berkeley, Calif.

BIBLIOGRAPHY

1 "A Comparison Between the Flow of Water and Mercury in Pipes With a View to Testing the Osborne Reynolds' Law of Similarity," by Jul. Hartmann, Danske Videnskabernes Selskabs Skrifter, series 8, vol. 10, no. 5, 1926, p. 385.

2 "Heat Transfer Coefficients for Liquid Mercury and Dilute Solutions of Sodium in Mercury in Forced Convection," by T. C. Doody and A. H. Younger, preprint for Heat Transfer Symposium at the 44th Annual Meeting, The American Institute of Chemical Engineers, December, 1951.

3 "Heat and Momentum Transfer in Turbulent Flow of Mercury," by S. E. Isakoff and T. B. Drew, preprint for Heat Transfer discussions, London, England, September, 1951.

4 "Heat Transfer to Molten Lead-Bismuth Eutectic in Turbulent Pipe Flow," by H. A. Johnson, J. P. Hartnett, and W. J. Clabaugh, Institute of Engineering Research Division Report, University of California, Berkeley, Calif., November, 1951.

5 "Heat Transfer to Mercury," by R. J. Musser and W. R. Page, MS thesis, Massachusetts Institute of Technology, Cambridge, Mass., May, 1947.

6 "Flow Metering of Molten Lead-Bismuth Eutectic," by R. A. Seban, W. T. Schrank, and D. Bartz, Institute of Engineering Research Division Report, University of California, Berkeley, Calif., May, 1949.

7 "Effect of Wetting on Heat Transfer Characteristics of Liquid Metals," by W. K. Stromquist, Department of Chemical Engineering, University of Tennessee, Knoxville, Tenn., AEC Contract AT-(40-1)-1310 Report, March, 1953.

8 "Effect of Wetting on Heat Transfer Characteristics of Liquid Metals," by R. M. Boarts, H. Chelemer, and B. Hoffman, University of Tennessee, Knoxville, Tenn., July 31, 1953.

9 "Power Test Codes," ASME, part 5, 1949, chapter 4, "Flow Measurement."

10 "Friction Factors for Pipe Flow," by L. F. Moody, Trans. ASME, vol. 66, 1944, pp. 671–684.

11 "The Direct Measurement of the Film Coefficient of Heat Transfer to Molten Sodium Metal in Forced Convection," by R. C. Quittenton, PhD thesis, University of Toronto, Canada, March, 1953.

Discussion

O. E. Dwyer.[6] The authors have gone a long way toward settling the question of whether or not the dynamical behavior of heavy metals in flow equipment is the same as that for ordinary fluids. Since degree of wetting was mentioned as a possible factor in distinguishing between the behavior of the two types of liquids, it would be desirable to have seen some discussion on this question, with reference to the experimental results. For example, to what extent, if any, did the Pb-Bi wet the pipe or the orifice edges? We at Brookhaven have found that, in the case of bismuth (about 200 ppm Zr and 100 ppm Mg) at 1000 F, high velocity is capable of effecting complete wetting on steels.

The authors state that when their apparatus was once running fairly constant results were obtained; but that from run to run duplicability was not nearly as good. We have observed the same phenomenon in a mercury loop at our laboratory; and the writer is of the opinion, in agreement with the authors' suspicion, that entrapped gas is mainly responsible; i.e., in the case of a nonwetting system. In this connection, it is significant to note that the friction-factor data for water scattered appreciably less than those for the Pb-Bi. It would have been interesting to determine the effect of wetting on duplicability from run to run, by adding an alkali or alkaline-earth metal to the Pb-Bi to induce wetting. The amounts needed would not have been enough to change the physical properties of the Pb-Bi.

R. R. Miller.[7] It is of interest that similar friction factors and orifice metering coefficients are found for the metals and water but, considering the properties of liquid metals in general, it is not surprising. The liquid metals are simpler in molecular structure and should be more ideal than the customary liquids. While we have done no work in connection with friction factors of flow and relatively little on viscosity, the most unusual phenomena are those attributed to the condition of nonwetting. This condition can be aggravated and perhaps extended by the occlusion of gases in liquids as found by Boarts, et al. (reference 8 of the paper), where decreases in density of mercury up to 12 per cent were found to be due to entrapped gases. It is not entirely clear from the present paper whether or not gases could be trapped during the operation of this apparatus. The entrapment of gases and nonwetting appear to be the only characteristics with which we are acquainted which could cause the variation in the friction factors. However, these would appear to cause variation only in one direction away from the water values and it does not appear to be a complete explanation of the effects found.

T. Trocki[8] and R. A. Edwards.[8] In this paper, the authors have contributed some significant experimental work and they are to be commended on it. The experimental program and the test equipment were quite adequate to meet their objectives.

One question which arises in our minds is why a simple permanent magnet, magnetic-type flowmeter was not investigated at the same time. For laboratory installation, a magnetic flowmeter should not be any more expensive than the orifice with its instrumentation. It would be valuable to have more calibrations of magnetic flowmeters by use of a metering tank.

Another question arises with regard to the control of temperature during these experiments. Some of the scatter may be accounted for by variation of temperature among different runs of the test.

Authors' Closure

The authors wish to express their appreciation to the discussers for bringing out some significant points which were not covered adequately in the paper. In answer to Dr. Dwyer's questions regarding wetting, visual inspection indicated that the lead-bismuth did not wet the pipe or orifice plates. No attempt was made to cause wetting by the use of additives, since after the pressure-drop tests it was planned to obtain heat-transfer data under nonwetting conditions. With regard to the question of entrapped gas raised by both Dwyer and Miller, it was pointed out in the paper that there were no indications of such a condition during the present tests. Several of the present authors had reported in 1951 (reference 4 of the paper) the severe effects of small amounts of entrapped gas on the heat-transfer performance of liquid metals and consequently extreme care was exercised to eliminate, or at least minimize, such effects during the present tests. However, it is possible that some small

[6] Head, Chemical Engineering Division, Brookhaven National Laboratory, Upton, Long Island, N. Y.

[7] Naval Research Laboratory, Washington, D. C.

[8] Atomic Power Equipment Department, General Electric Company, San Jose, Calif.

amounts of gas may have been in solution in the lead-bismuth and possibly these may come out of solution at the wall of the tube. If one postulates such an occlusion of gases to be responsible for the random behavior of the pipe-friction factors, it is difficult to understand why the orifice-metering coefficients were not influenced in a similar manner.

A magnetic-type flowmeter, as suggested by Messrs. Trocki and Edwards, was not tried in this Pb-Bi test loop since the authors had been advised early in the development of the meter, that its performance would be sensitive to a lack of wetting and the electrical output response poor for Pb-Bi, as compared with Na or Na-K. On the other hand, the authors certainly agree that calibrations of the magnetic flowmeter would have been worth while here since the metering-tank performance was quite satisfactory.

With reference to the suggestion that temperature variation may have contributed to the scatter, a review of the data reveals that 52 per cent, for test section 1, was observed in the temperature range 350 to 370 F; 10 per cent at 400 to 450 F; and for test section 2, 75 per cent at 370 to 390 F and 10 per cent at 400 to 415 F. The results for temperatures above 400 F showed the same scatter and could not be distinguished from the results for the temperature range 355 to 365 F. Although this indicates that temperature is probably not a cause for the excessive scatter, better temperature control is to be desired.

Predicting Performance of Large Steam Turbine-Generator Units for Central Stations

By H. HEGETSCHWEILER[1] and R. L. BARTLETT,[2] SCHENECTADY, N. Y.

The purpose of this paper is to provide the power industry with an up-to-date method for predicting the performance of large steam turbine-generator units.

The efficiency-calculation method given has been adjusted carefully to show a true comparison between machines of different types, sizes, steam conditions, reheat and nonreheat, and so on.

The level of performance obtained by use of this method is judged to be the highest justifiable for prediction purposes at the present state of the art. Fig. 1 shows the correlation of the method with recent representative test results.

Based upon the performance-calculation method presented in this paper, relative heat-rate curves have been prepared comparing the performance of various turbine-generator units at normal nameplate rating. A complete heat-balance diagram and an efficiency-calculation example are included illustrating the use of the method.

Nomenclature

The following nomenclature is used in the paper:

Turbine Types

CCSF (3600/1800) = cross-compound, single-flow; single 1800-rpm exhaust section is on a separate shaft.

CCDF (3600/1800) = cross-compound, double-flow; 1800-rpm double-flow exhaust sections are on a separate shaft.

CCQF (3600/3600) = cross-compound, quadruple-flow; parallel 3600-rpm TCDF reheat sections.

CC6F (3600/3600) = cross-compound, six-flow; parallel 3600-rpm TCTF reheat sections.

SC = single-casing; without crossover to single-flow exhaust section.

TCSF = tandem-compound, single-flow; single-flow exhaust section.

TCDF = tandem-compound, double-flow; double-flow exhaust section.

TCTF(1) = tandem-compound, triple-flow; triple-flow exhaust section. Bearing separates inlets to high-pressure and reheat sections.

TCTF(2) = tandem-compound, triple-flow; triple-flow exhaust section. No bearing between inlets to high-pressure and reheat sections. Bearing separates high-pressure end of reheat section into two parts joined by a crossover.

Definitions

Bowl = space immediately ahead of nozzles of a turbine stage.

Design flow = flow which turbine is expected to pass with control valves wide open.

Exhaust-pressure ratio = exhaust pressure/exhaust pressure at design flow. This may be estimated with sufficient accuracy by multiplying the throttle flow ratio by the *K*-factor given in Fig. 2.

Nameplate rating = generator output of turbine when operating at rated initial steam conditions, $3^1/_2$-in-Hg abs exhaust pressure, with 3 per cent evaporated feedwater makeup, and with a margin to design flow of 5 per cent to assure that shop tolerances on drawing areas, variations in flow coefficients from expected values, etc., will not prevent the turbine from meeting its capacity commitments.

Reheat turbine flow ratio = reheat turbine flow/design reheat turbine flow, numerically the same as the exhaust-pressure ratio.

Throttle flow ratio = throttle flow/design flow.

Velocity ratio = ratio of blade speed at pitch-line to steam velocity corresponding to available energy of stage.

Volume flow = weight flow in pounds per hour multiplied by initial specific volume in cubic feet per pound.

Symbols

AE = available energy or isentropic enthalpy difference, Btu/lb

EL = exhaust loss, Btu/lb

ELEP = expansion-line end point, Btu/lb

H = enthalpy, Btu/lb

H_c = condenser end point, ELEP plus corrected exhaust loss, Btu/lb

H_{iv} = enthalpy ahead of intercept valves, Btu/lb

H_m = mixed enthalpy, the enthalpy resulting when leakage steam is mixed with H_{iv}

HP = high pressure

H_t = throttle enthalpy, Btu/lb

H_{xs} = enthalpy at throttle entropy and exhaust pressure, Btu/lb

K = conversion factor to obtain approximate exhaust-pressure ratio from throttle flow ratio (Fig. 2)

LP = low pressure

M = per cent moisture in exhaust steam at expansion-line end point, per cent

N = number of parallel-flow sections at beginning of expansion

---

[1] Large Steam Turbine-Generator Department, General Electric Company. Mem. ASME.

[2] Large Steam Turbine-Generator Department, General Electric Company. Mem. ASME.

Contributed by the Power Division and presented at the Semi-Annual Meeting, Cleveland, Ohio, June 17–21, 1956, of The American Society of Mechanical Engineers.

Note: Statements and opinions advanced in papers are to be understood as individual expressions of their authors and not those of the Society. Manuscript received at ASME Headquarters, June 12, 1956. Paper No. 56—SA-52.

NR = nonreheat
P_{Bowl} = pressure immediately ahead of nozzles of first stage of a section, psia
PF = power factor
P_1 = pressure at exit from governing stage, psia
P_{iv} = pressure ahead of intercept valves, psia
P_t = throttle pressure, psia
P_x = exhaust pressure, psia
Q = flow in pounds per hour at beginning of expansion
R = reheat
S_{iv} = entropy ahead of intercept valves, Btu/lb deg F
S_m = mixed entropy, entropy corresponding to P_{iv} and H_m
S_t = throttle entropy, Btu/lb deg F
T_{iv} = temperature ahead of intercept valves of a reheat turbine, deg F
T_t = throttle temperature, deg F
v = specific volume in cubic feet per pound ahead of stop or intercept valves. If they are absent, use first-stage bowl specific volume
V = velocity, fps

Introduction

Over the years, the Large Steam Turbine-Generator Department of the authors' company has attempted to present basic data on the performance of large steam turbine-generator units to the power industry. The Warren-Knowlton paper of 1940[3] represented the first of these attempts to show relatively the over-all performance of turbine-generator units. The Elston-Knowlton paper in 1952[4] extended the area of application, and was based upon considerably more test data. The present paper again attempts to extend the area of application and usefulness. In particular, a system for predicting partial-load performance is included.

The performance-calculation system presented in this paper reflects a considerable increase in the available test data, particularly on modern reheat units, where few test data were formerly available.

A large number of these recent test results were analyzed and rationalized. These analyses were complemented by tests of components and models to obtain information in certain areas. Fig. 1 shows how test results of various representative types and sizes of large steam turbine-generator units compare with the method of calculation presented.

The method developed has been derived for steam turbines of wheel and diaphragm design. It is believed that it can be applied to turbines of other design philosophies with satisfactory results if proper consideration is given to the difference in design factors; e.g., internal and external packing leakages, degree of reaction, velocity ratios, arrangement of governing stages, and general quality of aerodynamic design of the steam flow path.

Theory Underlying the Method

A large steam turbine is actually not a single machine, but a series of relatively independent components referred to as stages. Logically, the over-all efficiency can be calculated by combining the performance of the individual stages, or, calculating it "stage by stage." Stage-by-stage calculation methods are being used by the authors' company to evaluate existing turbine designs. For purposes of predicting the performance of new units in the study and proposition stage, however, stage-by-stage calculation systems are usually extremely long and tedious since they require a detailed knowledge of the turbine design which is normally unavailable at that time.

As the Warren-Knowlton[3] and Elston-Knowlton[4] papers note, analysis of the test results indicates a remarkable consistency in the efficiency of groups of stages once the basic thermodynamic differences have been accounted for.

The method presented in this paper is based upon this underlying observation. In general, it assumes that given a pressure ratio and an initial volume flow, regardless of the initial condition of the steam, the stages designed will be similar in construction and will have essentially the same efficiency. A corollary of this assumption is that the same group of stages, operating under other initial conditions but with the same pressure ratio, will have the same efficiency. A turbine operating with various throttle flows typifies this condition and indicates the importance of this corollary. Minor variations from this rule have been detected and have been compensated.

As the volume flow increases, the height of the steam-path components must increase proportionately, and consequently, stage leakages, root and tip-interference losses, and rotation losses are reduced in their effect on the over-all steam-path efficiency. Thus, the greater the volume flow passing through a set of stages, the more efficient they may be expected to be. Test efficiencies of turbines with the same pressure ratio plotted against volume flow have a characteristically hyperbolic shape. In the method presented this hyperbolic shape is represented by assuming base efficiencies corresponding to infinite volume flows and subtracting from them quotients of constants divided by volume flows.

The prediction of efficiency for turbine sections preceded by multiple-admission governing stages is complicated by the effect of the governing stage. While the succeeding stages may still be analyzed using the constant-efficiency for constant-volume flow approach, the governing stage violates both the constant-pressure-ratio and the constant-volume-flow criteria. As a consequence, means must be formulated to take into account the change in governing-stage efficiency with the volume flow and pressure ratio, the effect of the governing-stage design-velocity ratio, the size of the governing stage, and the variation in the energy drop on the first stage relative to the energy drop on the succeeding stages. This latter effect must be taken into account not only as it varies from one turbine design to another but also as it varies from one throttle flow to another for the same design.

If the design-velocity ratio is standardized for single and double-row governing stages then the effect of the governing-stage velocity ratio may be considered as implicit in the base efficiencies and the volume-flow corrections. Velocity ratios at design flow of 0.5 for single-row governing stages and 0.31 for double-row governing stages were assumed.

Knowledge of the performance of a governing stage has little value when separated from the succeeding stages. Therefore, it was decided to treat the efficiency of turbine sections preceded by governing stages as a unit rather than to calculate the performance of the governing stage separately and factor in its effect afterward. An advantage of this approach is that a minimum of information about the governing stage is required. Since this required governing-stage information has a very small effect on the over-all performance it may be reasonably assumed without introducing significant errors. The effect of the governing stage is accounted for by the first-stage pitch-diameter corrections and noncondensing exhaust-pressure corrections, and is the major part of the partial-load correction for sections with governing stages.

Condensing turbine sections normally operate with their latter stages in the moisture region. Operation in the moisture region is substantially less efficient than in the superheat region. There is

[3] "Relative Engine Efficiencies Realizable From Large Modern Steam-Turbine-Generator Units," by G. B. Warren and P. H. Knowlton, Trans. ASME, vol. 63, 1941, p. 125.

[4] "Comparative Efficiencies of Central-Station Reheat and Nonreheat Steam-Turbine-Generator Units," by C. W. Elston and P. H. Knowlton, Trans. ASME, vol. 74, 1952, p. 1389.

an average reduction in stage efficiency of approximately 1 per cent for each per cent of average stage moisture as read from the expansion line. The correction curves for moisture and the correction to expansion-line end point for exhaust pressures other than 1.5-in-Hg abs account for the losses due to operation in the wet region.

Different types of turbines have somewhat different basic efficiencies owing to their construction. Among the characteristics which affect efficiency are pressure drops in crossover piping, the number of parallel exhaust sections, and changes in internal leakage due to inherent differences in shaft span and packing diameter. All of these factors have been lumped together in the form of "type" corrections.

The substitution of an 1800-rpm low-pressure section affects efficiency because of the differences in efficiency between 3600-rpm and 1800-rpm low-pressure sections. The procedure used to obtain this mixed efficiency has been to calculate the efficiency of the reheat section as if the whole were operating at 3600 rpm and then to apply the calculated difference between the two low-pressure sections to the 3600-rpm efficiency. The curve, "Efficiency Correction for Substitution of an 1800-rpm Section," gives the calculated difference between 3600-rpm and 1800-rpm low-pressure sections in curve form.

The method presented is based on operation at full-valve points where there is a minimum of throttling in the governing valves. In the early stages of design, it is difficult to predict accurately where the valve-intercept points will occur. It has become customary to draw "mean-of-the-valve-loop" performance curves which give the same average performance as a valve-loop curve would give. Efficiency-correction curves for mean-of-valve-loop performance are given for sections preceded by governing stages.

To simplify the use of this method, procedures to be followed have been outlined in tabular form in Table 1. The applicable procedure is selected from those listed at the top of the table, and the efficiency is calculated by following the sequence outlined in the column beneath it.

This calculation method may be applied to 50-cycle turbine-generator units by using a suitable type correction to account for design differences such as shaft span, packing diameter, and possible differences in average velocity ratio.

Expansion Lines

The method presented here predicts what are known as "internal efficiencies" or "expansion-line efficiencies." These internal efficiencies include all internal losses from ahead of the main-stop valves, reheat-intercept valves, or turbine-inlet flange to the outlet flange of the turbine section. They include thermodynamic losses within the equipment supplied by the turbine manufacturer except for exhaust loss of last stages in condensing sections. The latter is discussed under the heading of Exhaust Loss. Packing leakages and other external flows entering or leaving the turbine must be accounted for in the heat-balance calculations.

Internal "used energies" for determining end points of expansion lines are obtained by multiplying the "internal efficiency" by the isentropic enthalpy drop or "available energy" of the section. Thus, for noncondensing turbines with governing stages, the expansion-line end point may be obtained by multiplying the internal efficiency by the available energy from ahead of the main stop valves to the turbine-exhaust flange and subtracting this from the enthalpy of the steam ahead of the main stop valves.

For condensing turbines the available energy should be taken from ahead of the main stop valves, reheat-intercept valves, or equivalent inlet point, down to 1.5-in-Hg abs exhaust pressure. Owing to the treatment of exhaust loss, the expansion-line end point thus obtained is more or less fictional since no such measurable condition exists. To obtain the expansion-line end point for exhaust pressures other than 1.5-in-Hg abs, a direct Btu/lb difference in enthalpy is applied. This difference depends upon the efficiency of the turbine in that part of the moisture region.

Expansion lines are drawn on Mollier charts from the initial conditions ahead of the turbine section to the exhaust pressure and expansion-line end point. For performance calculations, the expansion lines are assumed to be loci of extraction steam points.

The shape of the expansion line is an integral part of this method since changes in the curvature of the expansion line will produce changes in the heat rate. All expansion lines are assumed to be drawn on the Mollier chart of Keenan and Keyes.[5]

Expansion lines for nonreheat units are drawn with Keuffel & Esser Curves No. 1864-41. The convex edge of the curve is placed with the rounded end of the curve projecting about 3.5 in. below the 1.5-in-Hg abs expansion-line end point. The upper end of the curve is positioned at the throttle enthalpy and at an entropy greater than that at throttle conditions by 0.007 entropy unit and 0.014 entropy unit for one-row and two-row governing stages, respectively, at design throttle flow. Partial-flow expansion lines are drawn from the calculated 1.5-in-Hg abs expansion-line end points keeping a constant entropy difference between the expansion lines. Fig. 20 shows the construction of expansion lines for nonreheat turbines with governing stage.

Expansion lines for the high-pressure section of reheat units are drawn as straight lines. The upper end of the expansion line for the high-pressure turbine may be taken at throttle enthalpy, and at an entropy greater than that at throttle conditions by 0.007 entropy unit and 0.014 entropy unit for one-row and two-row governing stages, respectively, at design throttle flow. Partial-flow expansion lines are drawn parallel to the design-flow expansion line through the calculated expansion-line end points. Fig. 18 shows the construction of these high-pressure turbine-expansion lines.

Expansion lines from reheat to exhaust of reheat units are drawn with Keuffel & Esser Curve No. 1864-31. The concave edge of the curve is positioned with the tip of the small end of the curve at the upper end of the expansion line and the lower edge passing through the 1.5-in-Hg abs exhaust-pressure expansion-line end point. Partial-flow expansion lines are drawn in the same manner. Fig. 19 shows the construction of expansion lines for the reheat section.

Exhaust Loss

The internal efficiency, by means of an expansion line, has been used as a measure of the internal losses of the turbine. It is very difficult, however, to distinguish at the exhaust end of the condensing section of a turbine as to where internal losses end and external losses begin. It has been implied earlier that this line was to be drawn at the exit from the last stage of the turbine but at the pressure existing at the condenser flange.

This division recognizes that losses occur between the last stage and the condenser which cannot be counted properly as internal losses. These losses are referred to as exhaust losses. They are made up primarily of the energy loss due to the velocity of the steam as it leaves the last stage, the pressure drop which normally occurs between the exit from the last stage and the condenser flange, and the losses which occur if the latter stages have insufficient pressure drop due to low volume flow, the assumption being, as stated previously, that the internal efficiency is independent of the state of flow. These component losses are referred to as the leaving loss, hood loss, and turn-up loss, respectively.

The magnitude of the exhaust loss was obtained by combining calculated leaving-loss and turn-up-loss data with hood-loss data

[5] "Thermodynamic Properties of Steam," by J. H. Keenan and F. G. Keyes, John Wiley & Sons, Inc., New York, N. Y., 1936.

obtained from model tests. The resulting exhaust-loss curves were then checked by running turbine-performance tests at various exhaust pressures and observing the correlation of the tests with the calculated performance data.

By treating exhaust loss in the manner outlined, it may be considered as an external loss; that is, it may be dealt with independently of the solution of the efficiency and flow calculations in the heat balance.

Mechanical and Generator Losses

The mechanical losses given in Fig. 25 include bearing losses, oil-pump losses, and shaft-grounding-device losses. All mechanical losses of the turbine plus the bearing losses for the generator are included. All units are assumed to have steam-sealed shaft packings.

The generator losses shown in Figs. 22, 23, and 24 include all mechanical and electrical losses of the generator except the bearing losses.

Packing Leakages

The method presented in this paper assumes that all leakages which flow to the feedwater heaters or which by-pass groups of stages are treated as external flows in heat-balance calculations.

Shaft-packing leakages used have been calculated by use of Martin's formula for leakage of steam through labyrinth seals.[6] Clearances assumed are based on average shaft packing clearances as measured on machines during normal overhauls. This packing leakage calculation procedure is substantiated by station performance tests.

Martin's formula is given in the Appendix. Information necessary to evaluate this formula for typical packings used by the authors' company for various types of turbines is included.

Comparative Heat Rates

The preparation of comparative heat-rate information, even with the aid of the data presented in this paper, is laborious. To assist those who wish closely calculated performance differences between various types and sizes of machines, comparative heat-rate curves are given for reheat turbine-generator units at normal nameplate ratings from 50,000 kw to 500,000 kw. The specific heat rates for any desired machine may be obtained by using the heat-balance example given in this paper as a base.

The relative heat rates given in Figs. 26, 27, and 28 are on a net basis to make comparisons between units at various initial pressures more realistic. A boiler-feed-pump efficiency of 70 per cent and a pump-motor efficiency of 95 per cent have been assumed throughout.

Conclusion

In this paper the fundamental concept of appraising turbine-stage performance by stage groups developed by Warren, Knowlton, and Elston has been followed. The basic efficiency factors and efficiency corrections have been re-evaluated in the light of more recent experience. Partial-load performance and extended and refined procedures have been introduced.

Additional comparisons of test results with the method presented here will indicate if and when further refinement may be necessary.

The method given, at its present stage of development, permits the realistic economic evaluation of relative performance of steam turbine-generator units.

Acknowledgments

No paper covering a field so comprehensive as that of turbine performance can be the work of a few individuals. The authors are indebted to the generations of General Electric Company turbine engineers who have developed the concepts and accumulated the data reflected in this paper. The work of H. W. Prust on the efficiency-prediction system and that of Miss J. Siwik on the relative heat-rate calculations have been particularly valuable.

[6] Articles on "Leakage of Steam Through Dummy Pistons," by H. M. Martin, *Engineering*, Jan. 10, 1908, and Jan. 3, 1919; also, see "Kent's Mechanical Engineering Handbook," John Wiley & Sons, Inc., New York, N. Y., vol. 2, 1950.

TABLE 1 EFFICIENCY CALCULATION PROCEDURES

(Note: All corrections are in per cent)

	3600-rpm Non-condensing Without Governing Stage	3600-rpm Non-condensing 1-Row Governing Stage	3600-rpm Non-condensing 2-Row Governing Stage	3600-rpm, Non-reheat Condensing 1-Row Governing Stage	3600-rpm, Non-reheat Condensing 2-Row Governing Stage	1800-rpm, Non-reheat Condensing 2-Row Governing Stage	3600-rpm Condensing Without Governing Stage	1800-rpm Condensing Without Governing Stage	3600/1800-rpm Condensing Without Governing Stage
Base Efficiency	Fig. 17	87.00	84.24	88.80	88.39	88.93	89.05	90.25	89.05
Efficiency Correction for Volume Flow		$\frac{1,005,200}{Q \times v} \times N$ Poorer	$\frac{2,173,800}{Q \times v} \times N$ Poorer	$\frac{331,000}{Q \times v} \times N$ Poorer	$\frac{412,000}{Q \times v} \times N$ Poorer	$\frac{761,000}{Q \times v} \times N$ Poorer	$\frac{730,620}{Q \times v} \times N$ Poorer	$\frac{1,365,380}{Q \times v} \times N$ Poorer	$\frac{730,620}{Q \times v} \times N$ Poorer
Efficiency Correction for Pitch Diameter of Governing Stage		Fig. 7							
Efficiency Correction for Exhaust Pressure		Fig. 6	Fig. 10						
Efficiency Correction for Type				TCDF BASE SC 0.0 TCTF 0.16 Poorer	TCDF BASE SC 0.0 TCTF 0.16 Poorer		TCDF BASE SC 0 TCSF .16 Poorer TCTF(1) .16 Poorer TCTF(2) .30 Poorer CCQF 0		CCSF 0.14 Poorer CCDF 0.14 Poorer
Efficiency Correction for Moisture				Fig. 14	Fig. 14	Fig. 14	Fig. 14	Fig. 14	Fig. 14
Efficiency Correction for Pitch Diameter of Governing Stage at Partial Load		Fig. 8							
Efficiency Correction for Partial Load		Fig. 9	Fig. 11	Fig. 4	Fig. 4	Fig. 4	Fig. 13	Fig. 13	Fig. 13
Efficiency Correction for Mean of Loops		Fig. 12	Fig. 12	Fig. 5	Fig. 5	Fig. 5			
Efficiency Correction for Substitution of an 1800-rpm Exhaust Section									Fig. 15

TABLE 2

EXAMPLE OF USE OF THE METHOD

Expansion line end points, mechanical, and generator losses used in the illustrative heat balance diagram given in Fig. 3 are worked out below with explanatory notes.

1. Basic assumptions

Turbine Nameplate Rating: 250,000 kw.

Turbine Type: Cross-compound double-flow, 3600/1800-rpm, 43 inch last-stage buckets, 247.6 sq ft total last-stage annulus area.

Steam Conditions: Initial 2400 psig, 1000 F, reheat 1000 F; exhaust pressure 1.0 in. Hg abs.

Feedwater Heating Cycle: Seven heaters, top heater connected to reheat point; heater terminal differences and heater arrangement as shown on Fig. 3; pressure drop from extraction stage to turbine flange three percent, pressure drop from turbine flange to heater five percent; final feedwater temperature approximately 470 F; no feedwater makeup; 10 percent reheat pressure drop.

Extraction Stage Pressures: Selected for optimum cycle performance and turbine stage design.

Leakage Flows: Calculated.

Load Point: Approximately 250,000 kw.

Estimated Throttle Flow Required: 1,559,000 lb/hr.

METHOD OF CALCULATION	EXAMPLE
2. Calculation of high-pressure turbine efficiency and expansion line end point	
Design Throttle Flow	Q = 1,770,000 lb/hr
Throttle Flow Ratio	TFR = 1,559,000/1,770,000 = 0.881 = 88.1 percent
Exhaust Pressure Ratio (Fig. 2) = K x Throttle Flow Ratio	Exhaust Pressure Ratio = 1.004 x 88.1 = 88.45 percent
Base Efficiency (Table 1:3600 Rpm, Noncondensing, 1-row Governing Stage)	Base Efficiency = 87.00 percent
Design Volume Flow = Design Throttle Flow x Specific Volume at 2400 psig, 1000 Degrees	Q x v = 1,770,000 x 0.3185 = 564,000 cu ft/hr
Correction for Volume Flow (Table 1)	Correction = -1,005,200 x N/Q x v = -1,005,200/564,000 = - 1.78 percent Eff_1 = 87.00 -0.0178 x 87.00 = 85.45 percent
Correction for Pitch Diameter of Governing Stage (Fig. 7), 36-inch Pitch Diameter Is Assumed	Correction = +0.22 percent at 36 inches Eff_2 = 85.45 + 0.0022 x 85.45 = 85.64 percent

TABLE 2 (*continued*)

METHOD OF CALCULATION	EXAMPLE
Correction for Exhaust Pressure (Fig. 6)	
$\frac{\text{Throttle Pressure}}{\text{Design Exhaust Pressure}}$; Where:	$\frac{P_t}{P_x} = \frac{2415}{542/0.8845} = 3.935$
Design Exhaust Pressure = Exhaust Pressure from Heat Balance Divided by Exhaust Pressure Ratio	Correction = -2.13 percent at 3.935 and 564,000 cu ft/hr $Eff_3 = 85.64 - 0.0213 \times 85.64 = 83.82$ percent
Correction for Pitch Diameter of Governing Stage at Partial Load (Fig. 8)	Correction = -0.14 percent at 88.45 percent and 36 inches $Eff_4 = 83.82 - 0.0014 \times 83.82 = 83.70$ percent
Correction for Partial Load Operation (Fig. 9)	Correction = -0.83 percent at 88.45 percent and 3.935 $Eff_5 = 83.70$ percent $- 0.0083 \times 83.70 = 83.01$ percent
Correction for Mean of Valve Loops (Fig. 12), Four Control Valves Assumed	Correction = -1.52 percent at 88.1 percent $Eff_6 = 83.01 - 0.0152 \times 83.01 = 81.75$ percent
Throttle Enthalpy (at 2415 psia, 1000 F)	$H_t = 1461.2$ Btu/lb
Available Energy to 542 psia	AE = 181.5 Btu/lb
Expansion Line End Point = $H_t - Eff_6 \times AE$	ELEP = 1461.2-0.8175 x 181.5 = 1312.8 Btu/lb
3. Calculation of reheat turbine efficiency and expansion line end point	
Design Reheat Turbine Flow	$Q = \frac{1,392,000}{0.8845} = 1,575,000$ lb/hr
$= \frac{\text{Estimated Heat Balance Reheat Turbine Flow}}{\text{Reheat Turbine Flow Ratio}}$	
Reheat Turbine Flow Ratio = High Pressure Turbine Exhaust Pressure Ratio	
Base Efficiency (Table 1: 3600/1800-rpm, Condensing, without Governing Stage)	Base Efficiency = 89.05 percent
Design Volume Flow = Design Reheat Turbine Flow x Specific Volume at 1000 F and at Design Pressure Ahead of Intercept Valves	Q x v = 1,575,000 x 1.535 = 2,420,000 cu ft/lb Design $P_{iv} = 488/0.8845 = 552$ psia Read v at 1000 F and 552 psia
Correction for Volume Flow (Table 1) Use one-half of Design Volume Flow for two Parallel Reheat Sections (N = 2)	Correction = $\frac{730,620 \times 2}{2,420,000} = -0.60$ percent $Eff_1 = 89.05 - 0.0060 \times 89.05 = 88.51$ percent
Correction for Turbine Type (Table 1)	Correction = -0.14 percent $Eff_2 = 88.51 - 0.0014 \times 88.51 = 88.39$ percent

TABLE 2 (*continued*)

METHOD OF CALCULATION	EXAMPLE
Correction for Moisture (Fig. 14)	Correction = +2.28 percent at 1000 degrees, 488 psia $Eff_3 = 88.39 + 0.0228 \times 88.39 = 90.41$ percent
Correction for Partial Load (Fig. 13)	Correction = -0.11 percent at 88.1 percent $Eff_4 = 90.41 - 0.0011 \times 90.41 = 90.31$ percent
Correction for 1800-rpm Section (Fig. 15)	
Crossover Volume Flow = Crossover Flow x Specific Volume at 125 psia and 1360 H. (Expansion Line at Assumed Crossover Pressure) Consider 2 LP Sections	Q x v = 1,319,626 x 5.275 = 6,961,000 cu ft/hr Q x v Per LP Section = 6,961,000/2 = 3,480, 500 cu ft/hr Curve Value = +1.16 percent
Available Energy Ratio (Read at S_{iv}) $= \frac{\text{AE of 1800-rpm Section}}{\text{AE of Reheat Turbine}}$	AE Ratio $= \frac{378}{564.4} = 0.67$
	Correction = +1.16 x 0.67 = +0.78 percent $Eff_5 = 90.31 + 0.0078 \times 90.31 = 91.01$ percent
Enthalpy Ahead of Intercept Valves (at 1000 F, 488 psia)	H_{iv} = 1519.9 Btu/lb
Available Energy to 1.5 in. Hg abs	AE = 564.4 Btu/lb
Expansion Line End Point at 1.5 in. Hg abs $= H_{iv} - Eff_5 \times AE$	ELEP at 1.5 in. Hg abs = 1519.9 - 0.9101 x 564.4 = 1006.2 Btu/lb
Moisture at Expansion Line End Point, 1.5 in. Hg abs	M at 1.5 in. Hg abs = 9.15 percent
Change in Expansion Line End Point from 1.5 in. Hg abs to 1.0 in. Hg abs (Fig. 16)	ΔELEP = -19.4 x (1-0.0915) = -17.6 Btu/lb
Expansion Line End Point at 1.0 in. Hg abs	ELEP at 1.0 in. Hg abs = 1006.2-17.6 = 988.6 Btu/lb
4. Exhaust loss, condenser end point enthalpy at 1.0 inch Hg abs	
Annulus Velocity $= \frac{Q \times v \times (1-M)}{3600 \times 247.6}$	$V = \frac{1{,}055{,}521 \times 652.3 \times (1-0.103)}{3600 \times 247.6} = 693$ ft/sec
Use Percent Moisture at Expansion Line End Point at 1.0 in. Hg abs	M at 1.0 in. Hg abs = 10.3 percent
Exhaust Loss (Fig. 21a)	Exhaust Loss = 12.0 Btu/lb
Corrected Exhaust Loss = Exhaust Loss x 0.86 x (1-M)	Corrected Exhaust Loss = 12.0 x 0.86 x (1-0.103) = 9.3 Btu/lb
Condenser End Point Enthalpy at 1.0 in. Hg abs = Expansion Line End Point + Corrected Exhaust Loss	H_C at 1.0 in. Hg abs = 988.6 + 9.3 = 997.9 Btu/lb

TABLE 2 (*continued*)

METHOD OF CALCULATION	EXAMPLE
5. Mechanical loss (Fig. 25)	
HP: Read at 250,000 kw, CC-HP LP: Read at 250,000 kw, CCDF-LP-43	HP Mechanical Losses = 710 kw LP Mechanical Losses = 760 kw
6. Generator loss (Fig. 22, 23, and 24)	
Generator Kva Rating = $\frac{\text{Gen. Output}}{0.919 \times \text{PF}}$ at 30 psig H_2 pressure Assume Conventionally Cooled Generator and Operation at 15 psig H_2 Pressure (See Notes on Fig. 22)	3600-rpm Generator 30 lb kva Rating $= \frac{128,571}{0.919 \times 0.85} = 164,614$ kva
Generator Loss = (Rated 30 psig H_2 kva) $\times \frac{\text{Factor 1}}{100}$ $\times \frac{\text{Percent of Rated 30 psig } H_2 \text{ kva}}{100}$ x Factor 2 x Factor 3	Generator Loss (3600) $= 164,614 \times \frac{1.06}{100} \times \frac{91.9}{100} \times 0.94 \times 1.00$ $= 1507$ kw
	1800-rpm Generator 30 lb kva Rating $= \frac{120,784}{0.919 \times 0.85} = 154,622$ kva
	Generator Loss (1800) $= 154,622 \times \frac{1.11}{100} \times \frac{91.9}{100} \times 0.94 \times 1.00$ $= 1483$ kw
7. Generator outputs	
Generator Output = Turbine Output – Mechanical Losses-Generator Losses	Generator Output of 3600-rpm Generator = 130,788 - 710 - 1507 = 128,571 kw Generator Output of 1800-rpm Generator = 123,027 - 760 - 1483 = 120,784 kw
8. Boiler feedpump power	
BFP Power = $\frac{\text{BFP Flow x BFP Enthalpy Rise}}{\text{BFP Motor Efficiency x 3412.75}}$ BFP Enthalpy Rise = $\frac{\text{Isentropic Enthalpy Rise at 326.3 F to 3020 psia}}{\text{BFP Efficiency}}$ (See Reference 4, Fig. 3)	BFP Power $= \frac{1,559,000 \times 13.4}{0.95 \times 3412.75} = 6,444$ kw

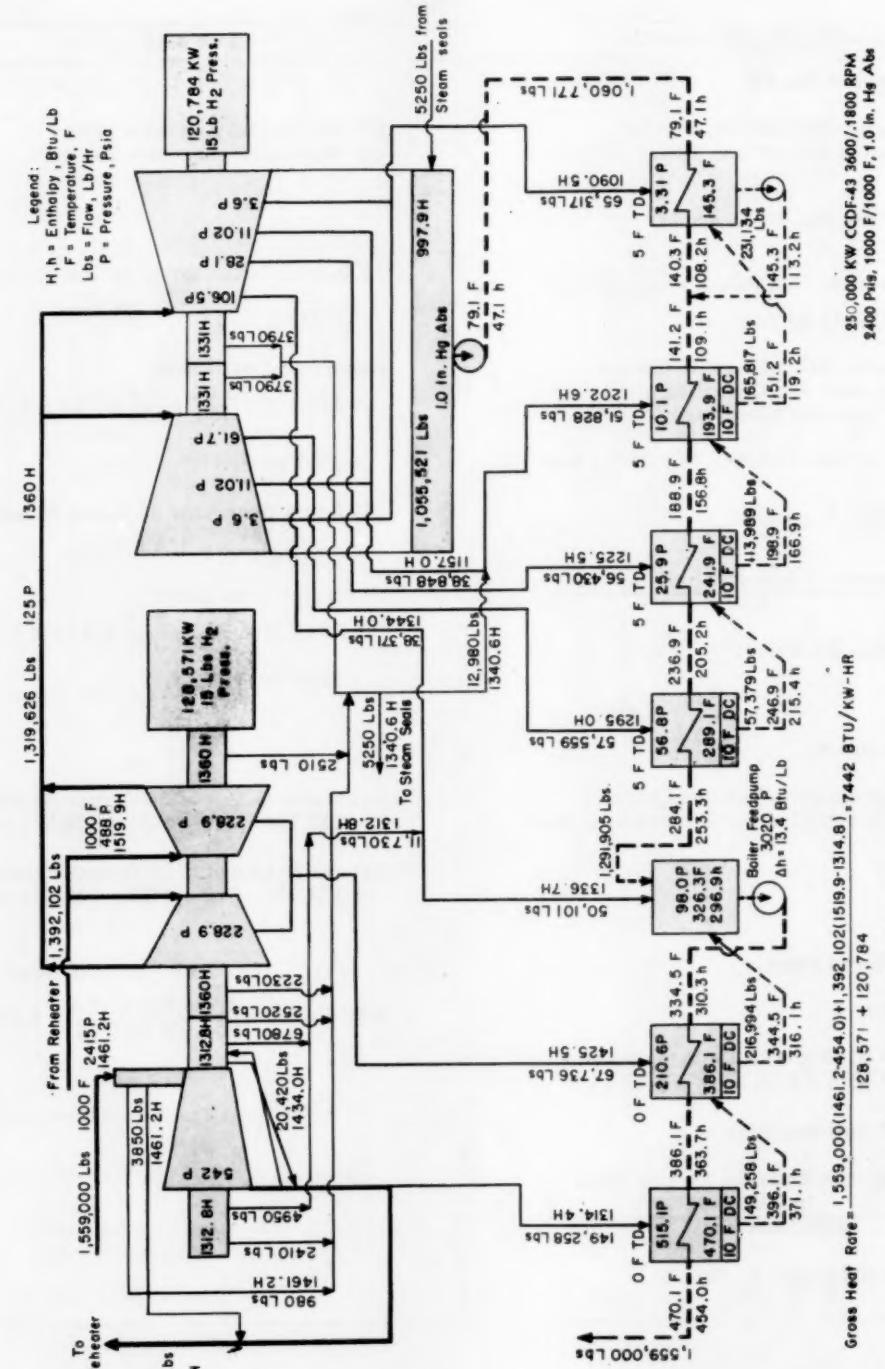

FIG. 3 HEAT-BALANCE DIAGRAM FOR ILLUSTRATIVE CALCULATION

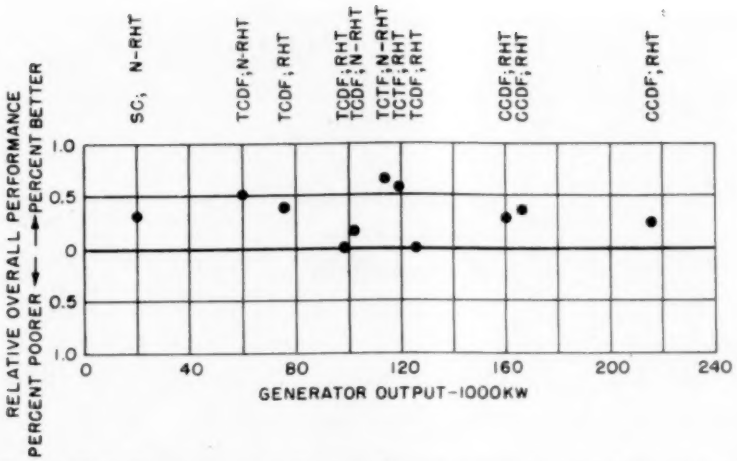

FIG. 1 TEST PERFORMANCE OF VARIOUS REPRESENTATIVE MODERN LARGE STEAM TURBINE-GENERATOR UNITS RELATIVE TO CALCULATED PERFORMANCE
(The comparisons shown on this curve are based on test points near rated load.)

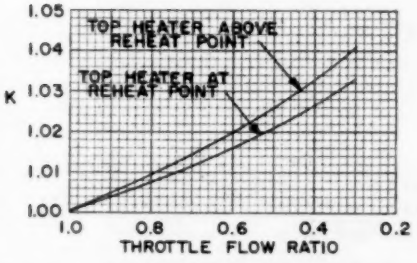

FIG. 2 CONVERSION FACTOR TO OBTAIN EXHAUST-PRESSURE RATIO FROM THROTTLE-FLOW RATIO

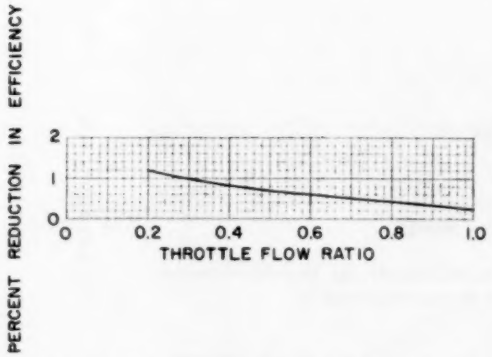

FIG. 5 NONREHEAT CONDENSING; EFFICIENCY CORRECTION FOR MEAN-OF-VALVE LOOPS

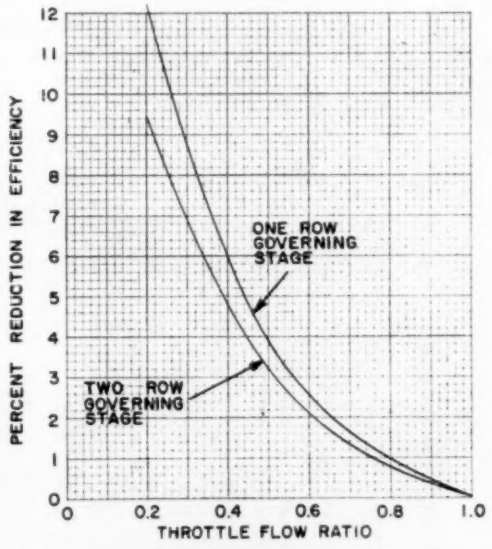

FIG. 4 NONREHEAT CONDENSING; EFFICIENCY CORRECTION FOR PARTIAL-LOAD OPERATION

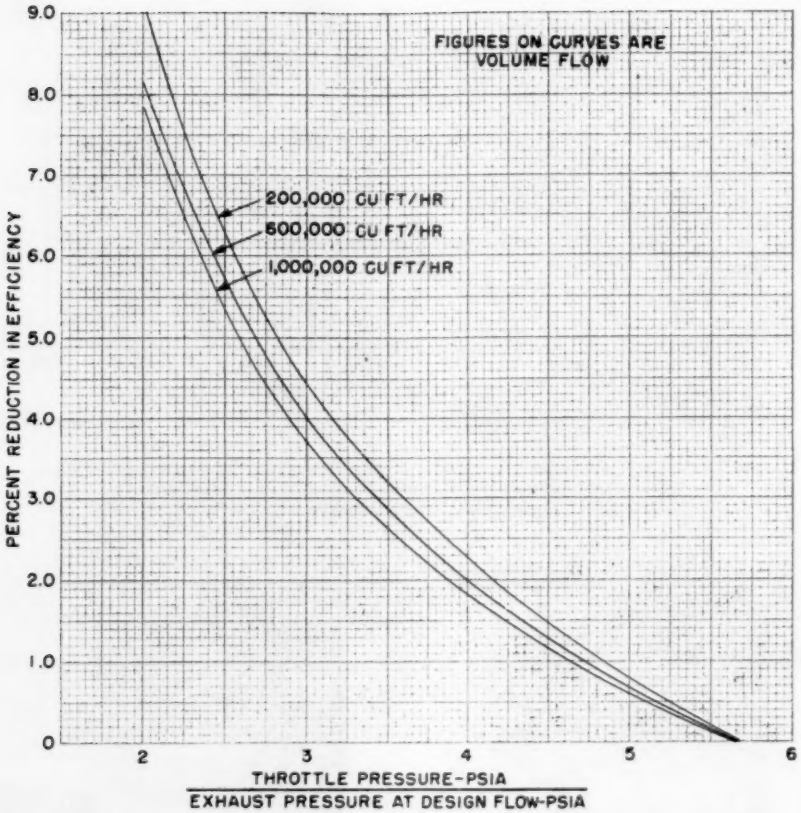

FIG. 6 3600-RPM, NONCONDENSING, SINGLE-ROW GOVERNING STAGE; EFFICIENCY CORRECTION FOR EXHAUST PRESSURE

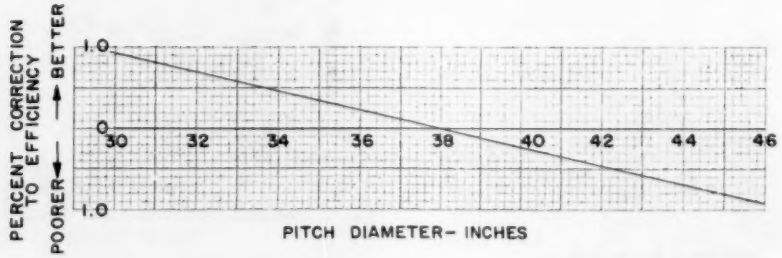

FIG. 7 3600-RPM, NONCONDENSING, SINGLE-ROW GOVERNING STAGE; EFFICIENCY CORRECTION FOR PITCH DIAMETER OF GOVERNING STAGE

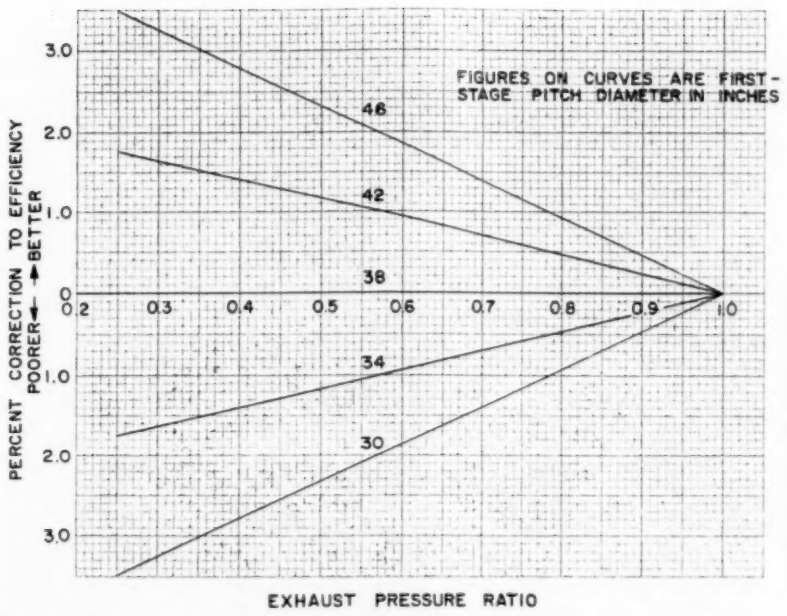

FIG. 8 3600-RPM, NONCONDENSING, SINGLE-ROW GOVERNING STAGE; EFFICIENCY CORRECTION FOR PITCH DIAMETER OF GOVERNING STAGE AT PARTIAL LOADS

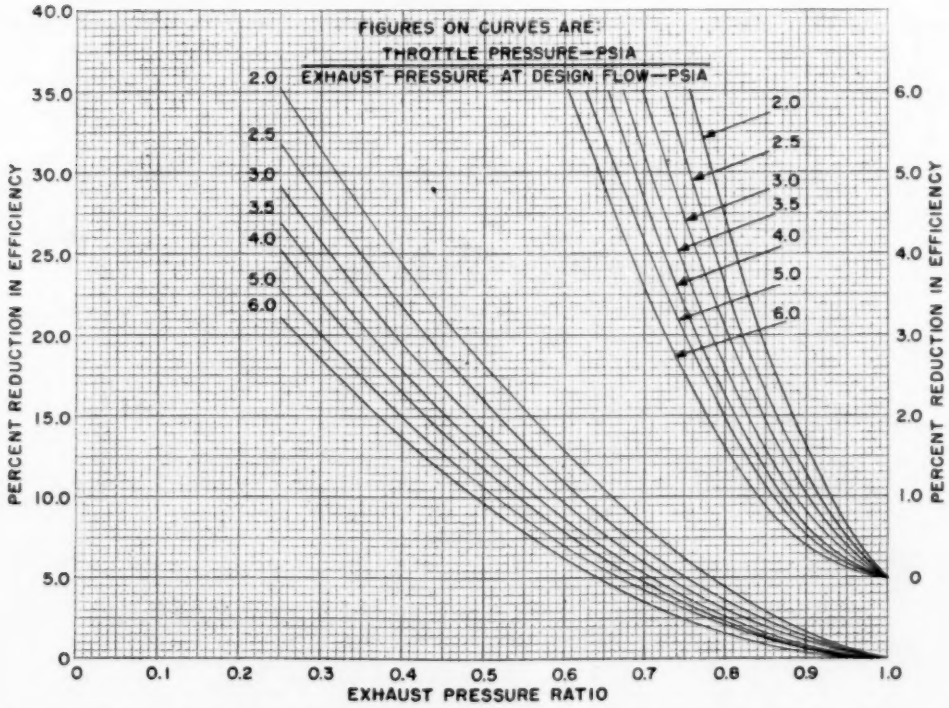

FIG. 9 3600-RPM, NONCONDENSING, SINGLE-ROW GOVERNING STAGE; EFFICIENCY CORRECTION FOR PARTIAL-LOAD OPERATION

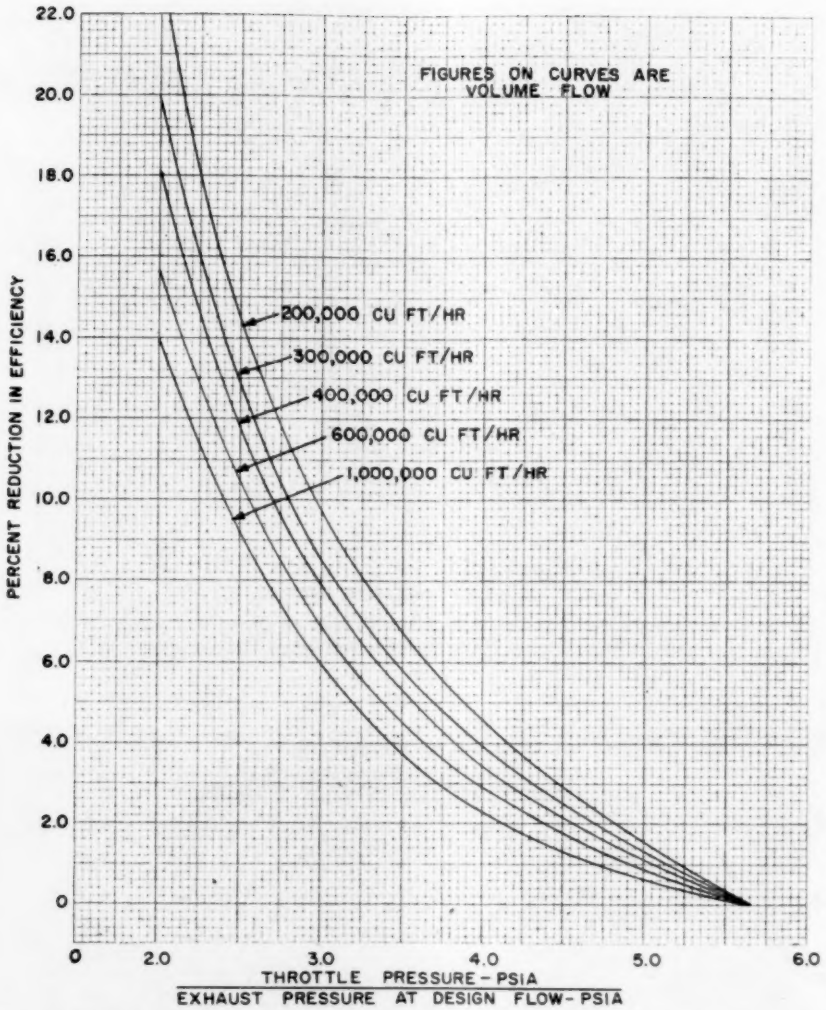

FIG. 10 3600-RPM, NONCONDENSING, DOUBLE-ROW GOVERNING STAGE; EFFICIENCY CORRECTION FOR EXHAUST PRESSURE

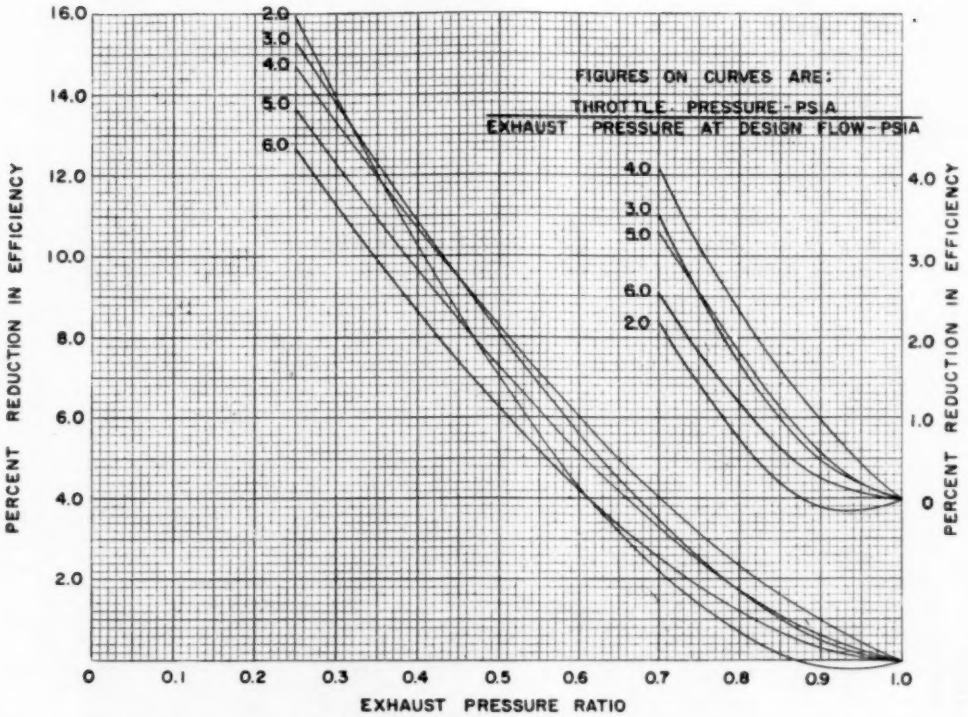

FIG. 11 3600-RPM, NONCONDENSING, DOUBLE-ROW GOVERNING STAGE; EFFICIENCY CORRECTION FOR PARTIAL-LOAD OPERATION

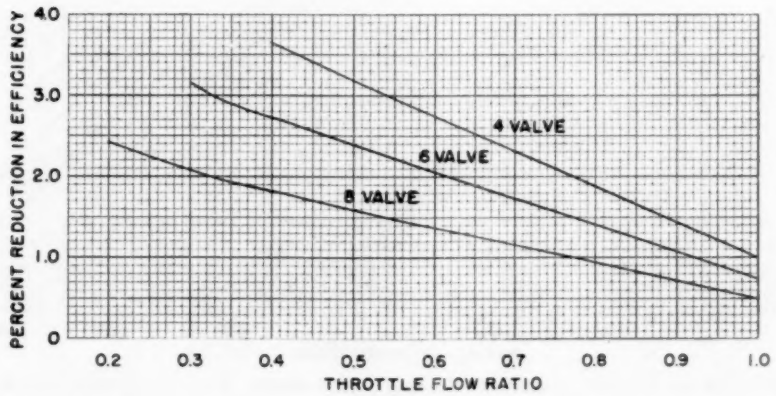

FIG. 12 3600-RPM, NONCONDENSING, SINGLE-ROW OR DOUBLE-ROW GOVERNING STAGE; EFFICIENCY CORRECTION FOR MEAN-OF-VALVE LOOPS

NOTE: This curve assumes a (reheat pressure/throttle pressure) ratio at design flow of 0.26. If this ratio is significantly at variance from 0.26 use: Per cent reduction in efficiency = (reheat pressure/throttle pressure) × (curve value/0.26)

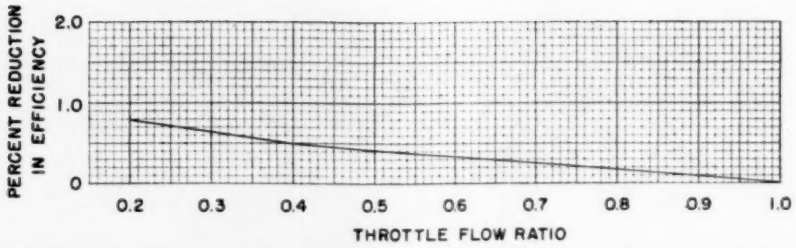

FIG. 13 3600-RPM AND 1800-RPM, REHEAT, CONDENSING SECTION; EFFICIENCY CORRECTION FOR PARTIAL LOAD

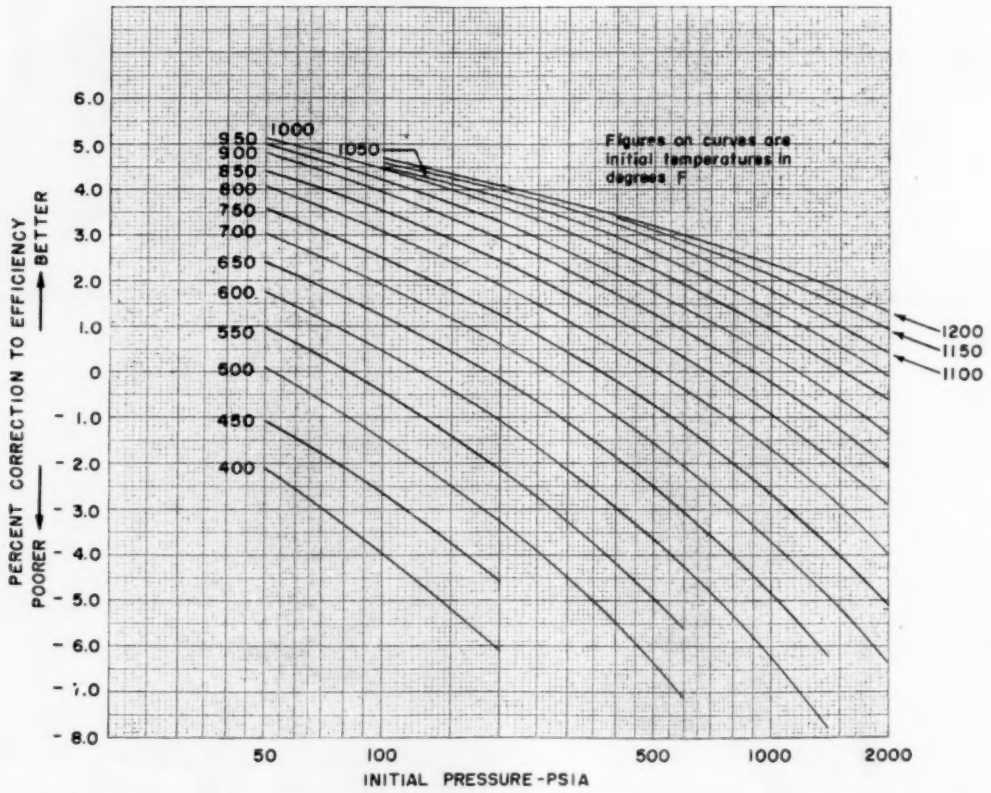

FIG. 14 3600-RPM AND 1800-RPM, REHEAT AND NONREHEAT, CONDENSING; EFFICIENCY CORRECTION FOR MOISTURE

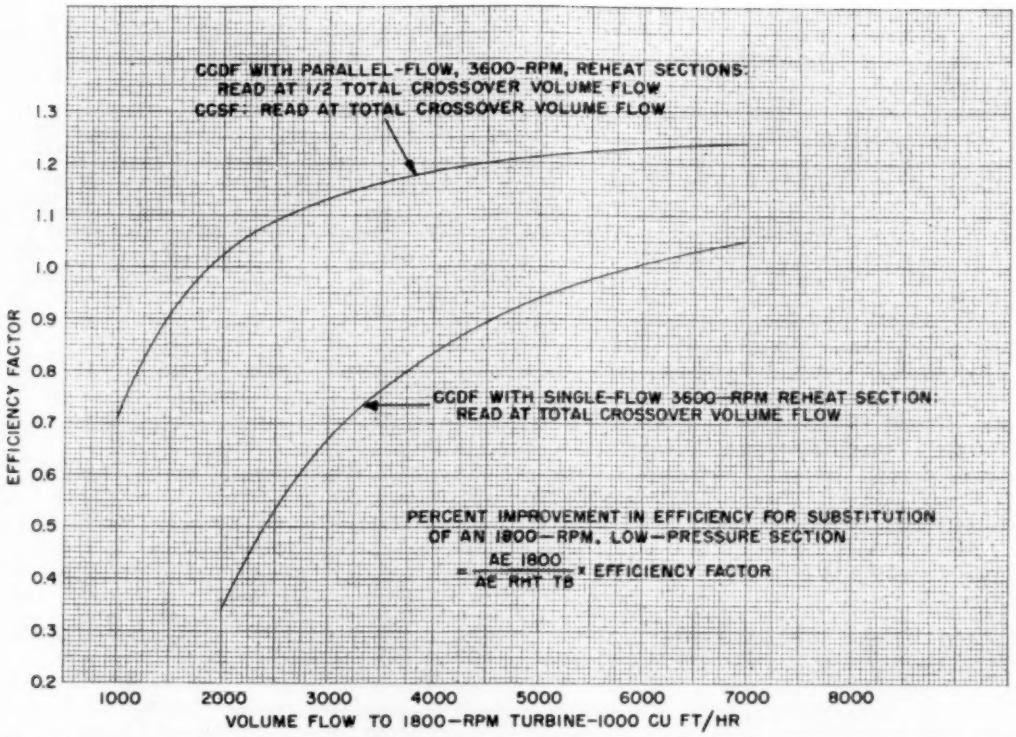

FIG. 15 3600-RPM AND 1800-RPM CROSS-COMPOUND, REHEAT AND NONREHEAT, CONDENSING; EFFICIENCY CORRECTION FOR SUBSTITUTION OF AN 1800-RPM CONDENSING SECTION

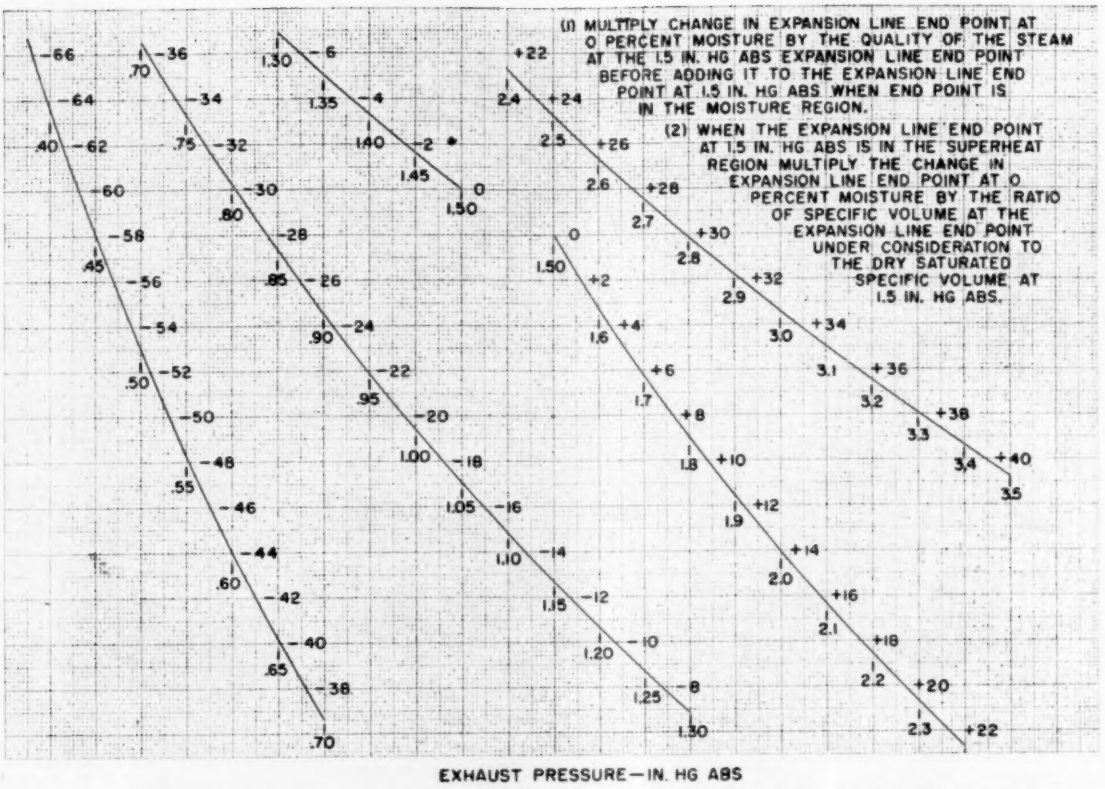

FIG. 16 3600-RPM AND 1800-RPM, REHEAT AND NONREHEAT, CONDENSING; CORRECTION TO EXPANSION-LINE END POINT FOR EXHAUST PRESSURES OTHER THAN 1.5-IN HG ABS

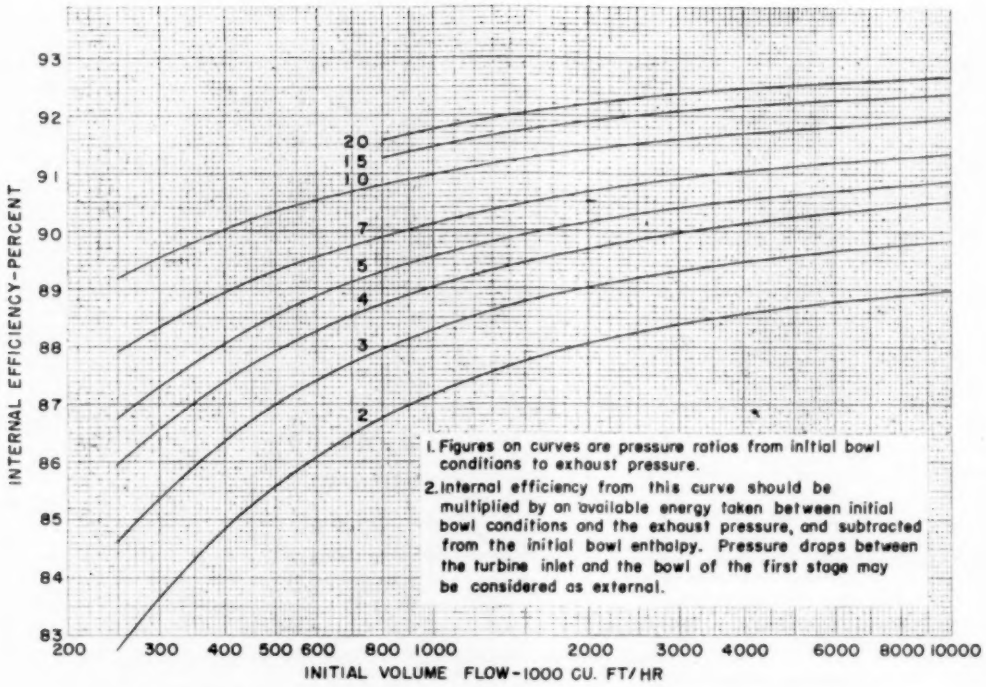

FIG. 17 3600-RPM, NONCONDENSING, WITHOUT GOVERNING STAGE; TURBINE EFFICIENCY

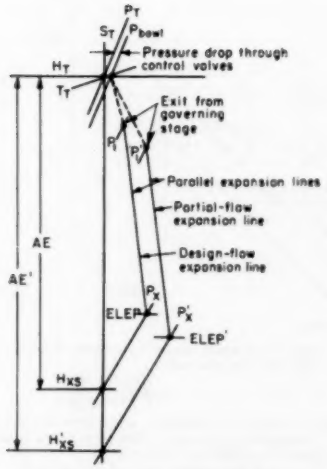

FIG. 18 CONSTRUCTION OF EXPANSION LINES FOR NONCONDENSING TURBINES WITH GOVERNING STAGE

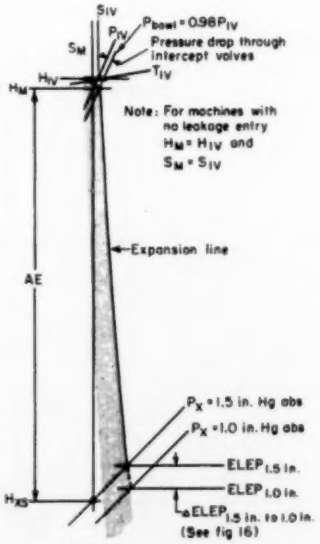

FIG. 19 CONSTRUCTION OF EXPANSION LINES FOR CONDENSING TURBINES WITHOUT GOVERNING STAGE

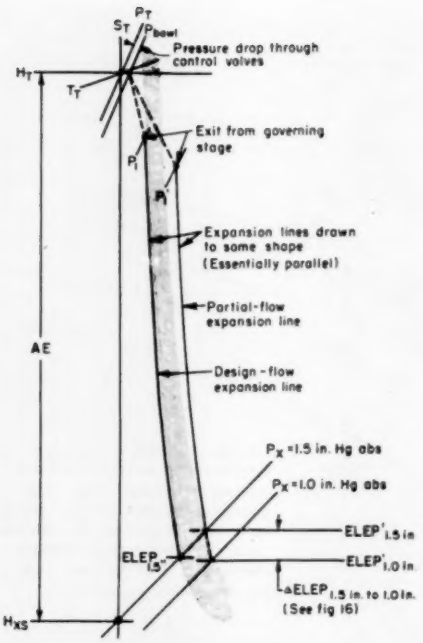

FIG. 20 CONSTRUCTION OF EXPANSION LINES FOR NONREHEAT CONDENSING TURBINES WITH GOVERNING STAGE

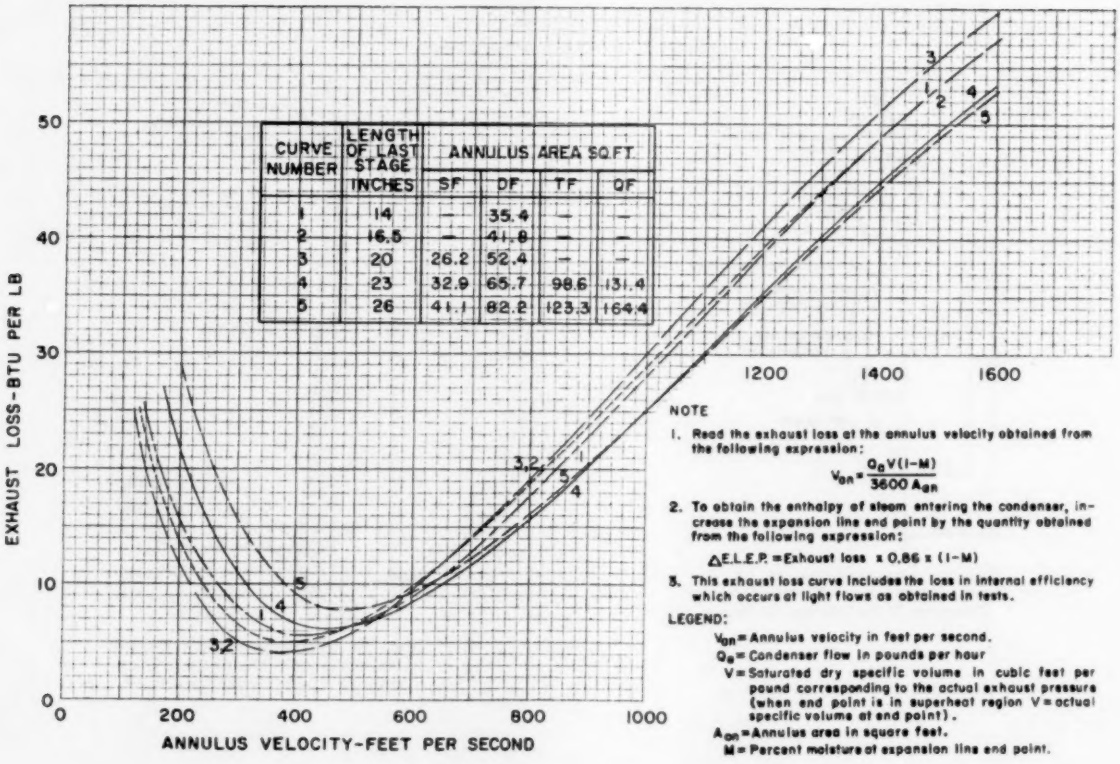

CURVE NUMBER	LENGTH OF LAST STAGE INCHES	ANNULUS AREA SQ FT SF	DF	TF	QF
1	14	—	35.4	—	—
2	16.5	—	41.8	—	—
3	20	26.2	52.4	—	—
4	23	32.9	65.7	98.6	131.4
5	26	41.1	82.2	123.3	164.4

NOTE

1. Read the exhaust loss at the annulus velocity obtained from the following expression:

$$V_{an} = \frac{Q_c V(1-M)}{3600\, A_{an}}$$

2. To obtain the enthalpy of steam entering the condenser, increase the expansion line end point by the quantity obtained from the following expression:

$\Delta E.L.E.P.$ = Exhaust loss x 0.86 x (1−M)

3. This exhaust loss curve includes the loss in internal efficiency which occurs at light flows as obtained in tests.

LEGEND:

V_{an} = Annulus velocity in feet per second.
Q_c = Condenser flow in pounds per hour
V = Saturated dry specific volume in cubic feet per pound corresponding to the actual exhaust pressure (when end point is in superheat region V = actual specific volume at end point).
A_{an} = Annulus area in square feet.
M = Percent moisture at expansion line end point.

FIG. 21 3600-RPM HIGH-PRESSURE SECTION, EXHAUST LOSS

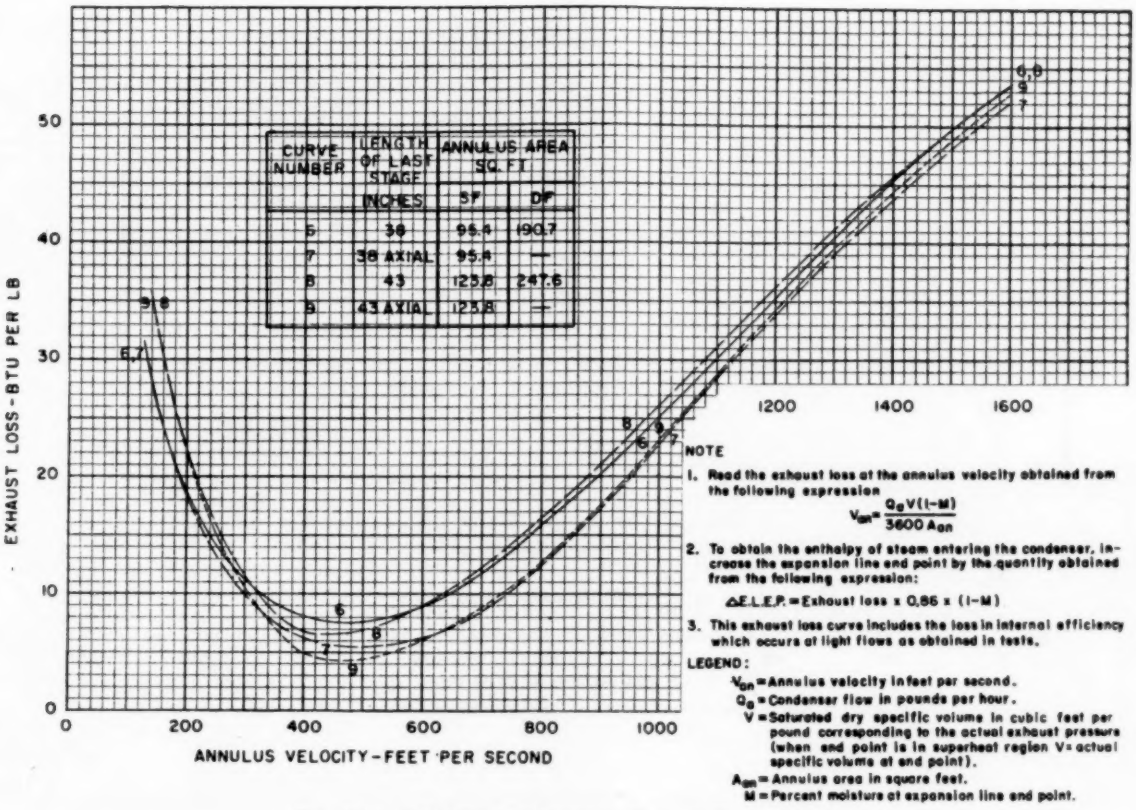

FIG. 21(a) 1800-RPM LOW-PRESSURE SECTION, EXHAUST LOSS

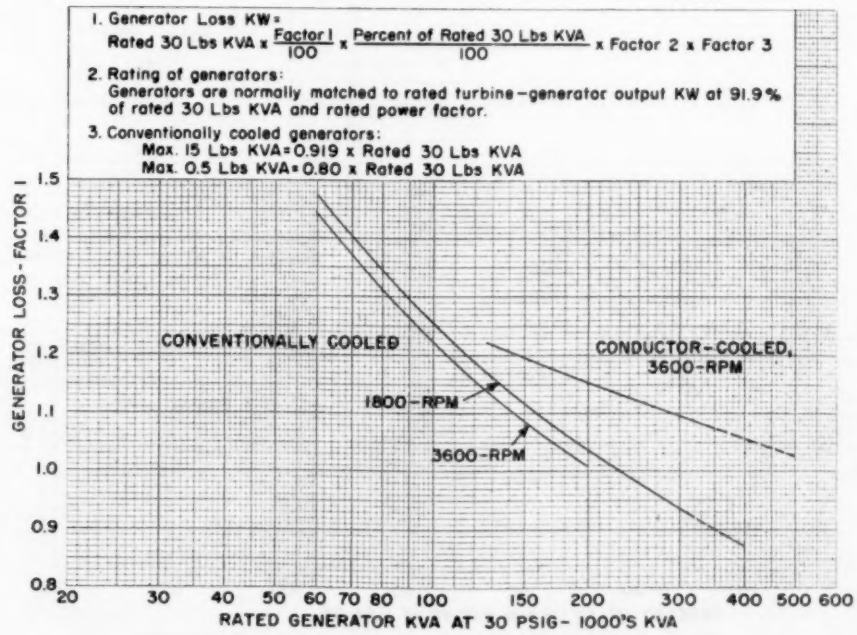

FIG. 22 GENERATOR LOSSES

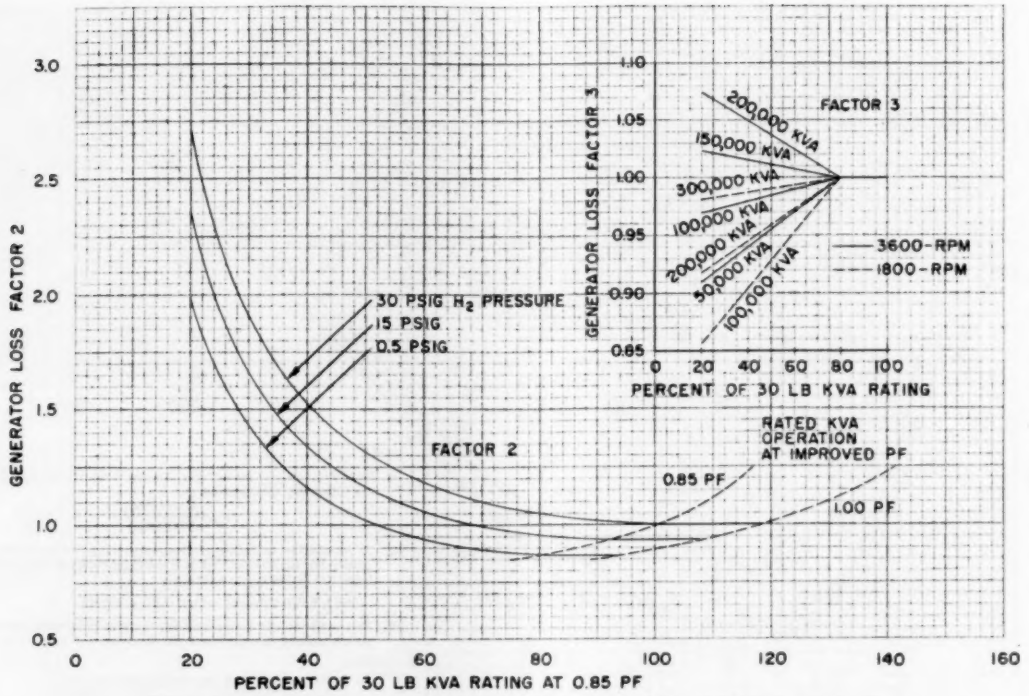

FIG. 23 GENERATOR-LOSS FACTORS; CONVENTIONALLY COOLED GENERATORS

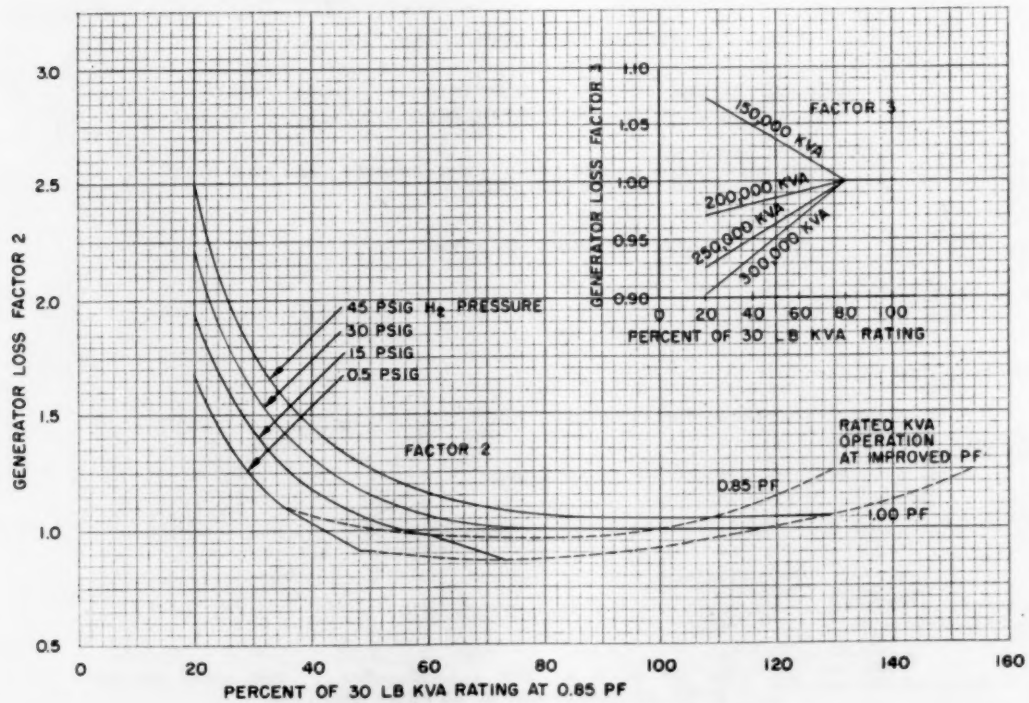

FIG. 24 GENERATOR-LOSS FACTORS; CONDUCTOR-COOLED GENERATORS

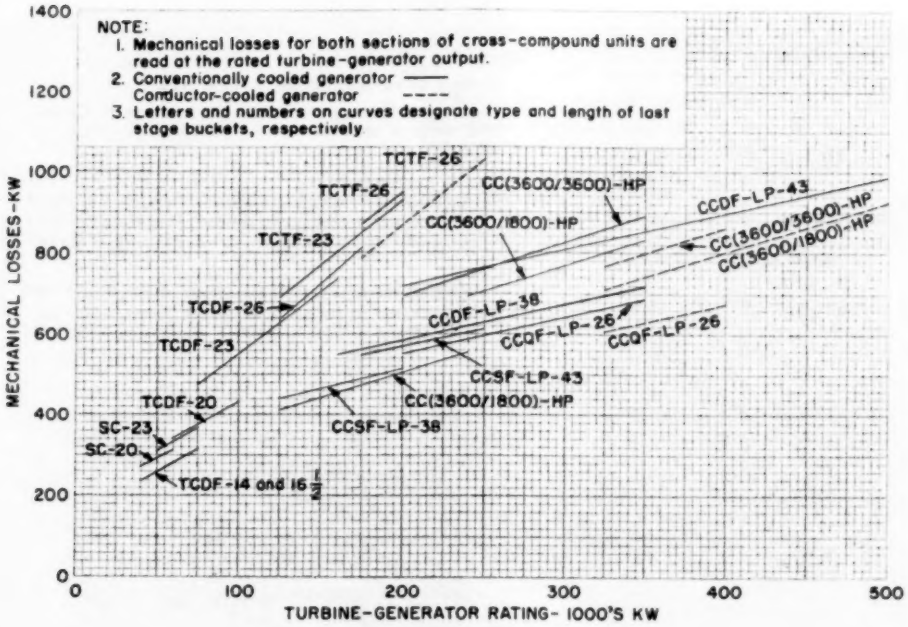

FIG. 25 REHEAT UNITS, MECHANICAL LOSSES

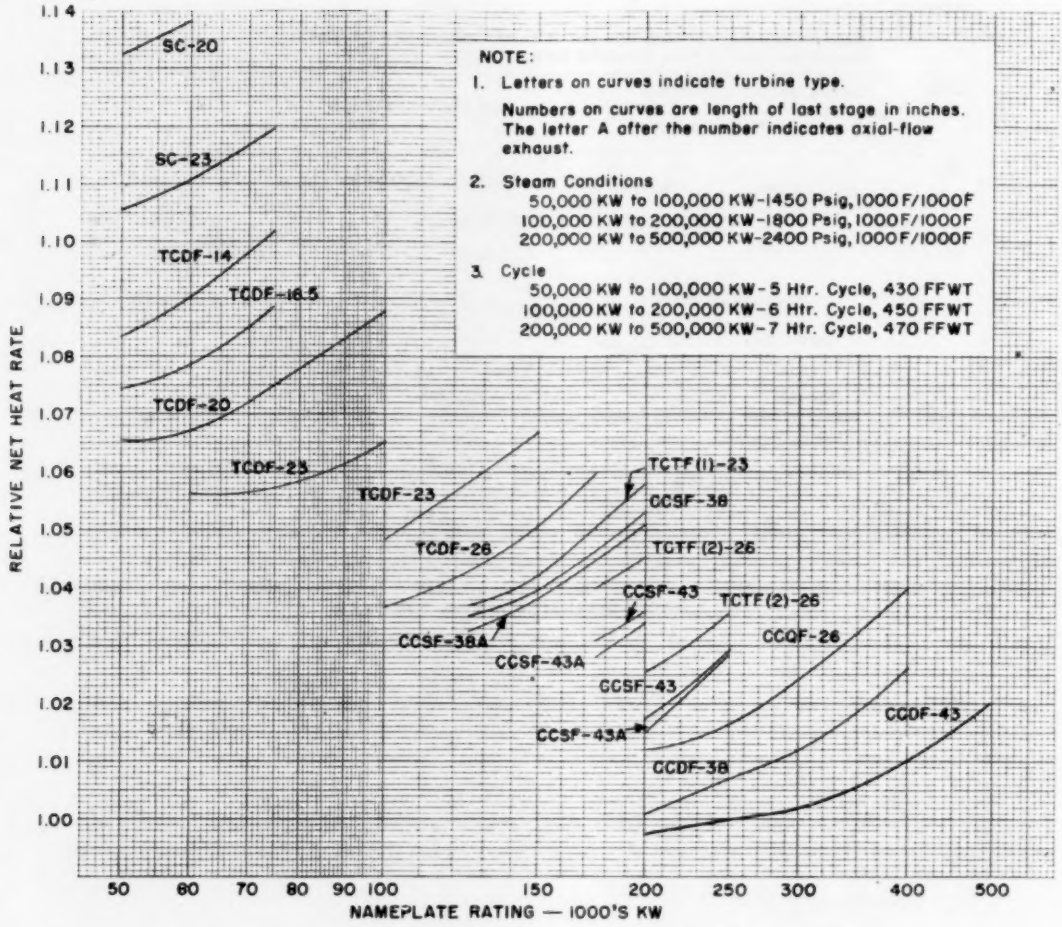

Fig. 26 Reheat Units, Relative Net Heat Rates at 1.0-In-Hg Abs Exhaust Pressure

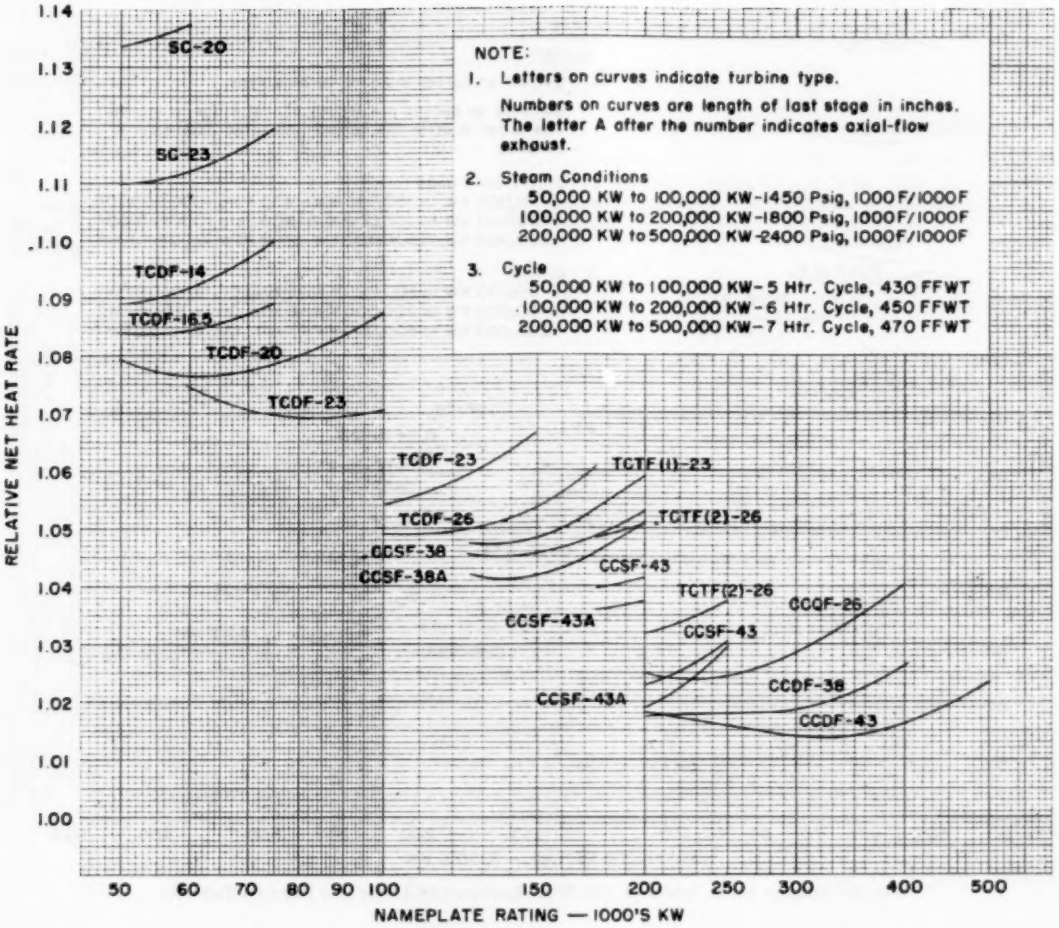

Fig. 27 Reheat Units, Relative Net Heat Rates at 1.5-In-Hg Abs Exhaust Pressure

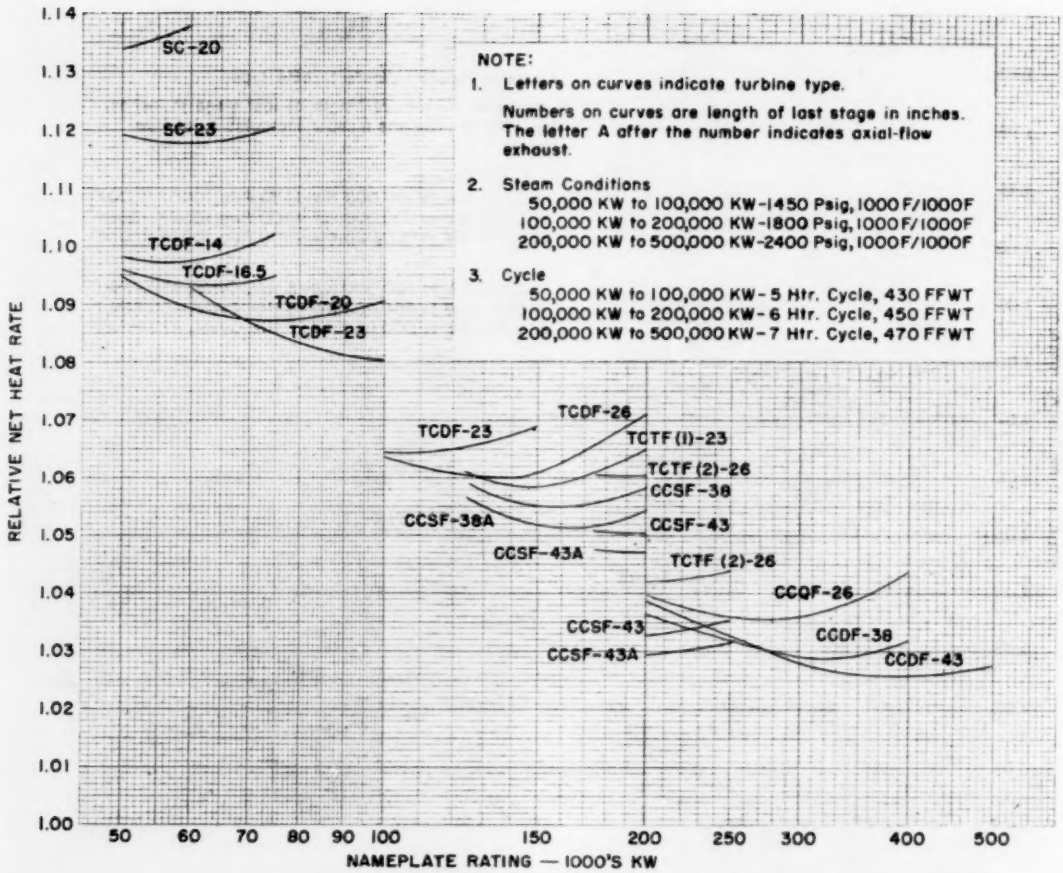

Fig. 28 Reheat Units, Relative Net Heat Rates at 2.0-In-Hg Abs Exhaust Pressure

Appendix

Calculation of Packing Leakage Flows

Martin's formula

$$F = 25KA\sqrt{\left[\frac{1-(P_2/P_1)^2}{N-\log_e(P_2/P_1)}\right]}\sqrt{\left(\frac{P_1}{v_1}\right)} = C\sqrt{\left(\frac{P_1}{v_1}\right)}$$

where

F = packing flow, lb/hr
K = factor for packing type (see Fig. 29)
A = leakage area, sq in.
$= \frac{\pi}{1000} \times$ packing diameter in inches $\times$ clearance in mils
P_1 = initial pressure, psia
P_2 = final pressure, psia
v_1 = initial specific volume, cu ft/lb
N = number of stationary teeth
C = packing constant from Table 3

Fig. 29 is based on results of packing-flow tests. Clearances assumed are measured on machines during normal overhauls.

Information for evaluating Martin's formula for typical packings used by the authors' company is given in the form of a constant C in Table 3.

Calculation of Valve-Stem Leakage Flows

Valve-stem leakage flows vary widely and are difficult to predict. The rough method of estimating these flows given in the following has been found to be sufficiently accurate for heat-balance-calculation purposes.

Total Valve-Stem Leakage

Reheat turbines: $F = 2 \times$ throttle pressure, psia
Nonreheat turbines: $F = 1.5 \times$ throttle pressure, psia

Second Valve-Stem Leakage

Reheat turbines: $F = 1.8 \times$ high-pressure section exhaust pressure, psia
Nonreheat turbines: $F = 1.5 \times$ highest extraction pressure, psia

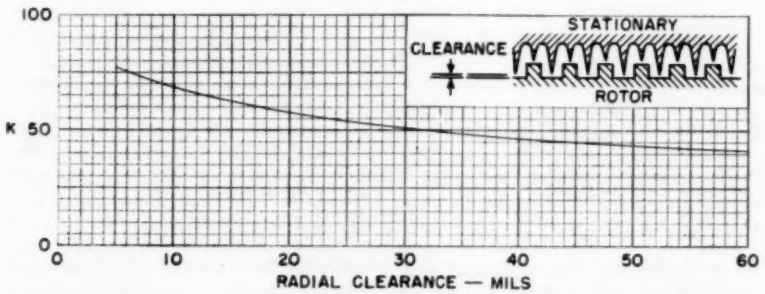

Fig. 29 High-Pressure Packings; K Versus Clearance for Interlocking Teeth for Use in Martin's Formula

TABLE 3 PACKING CONSTANT *C* FOR LARGE REHEAT TURBINE-GENERATOR UNITS

	SC	TCSF	TCDF	TCTF(1)	TCTF(2)	CCSF (3600/1800) Below 250,000 kw	CCSF (3600/1800) 250,000 kw	CCDF (3600/1800) Below 250,000 kw	CCDF (3600/1800) 250,000 kw to 500,000 kw	CC4F (3600/3600)
HIGH-PRESSURE SECTION—INLET END										
1. Packing leakage from first stage of high-pressure section to high-pressure section exhaust or to the reheat section bowl if they are not separated by a bearing	339	266	398	266	433	463	330	483	330	330
*2. Packing leakage from high-pressure section exhaust to approximately 100 psia		301		301			419		419	419
3. Packing leakage from approximately 100 psia to gland seal regulator at 18 psia		423		423			581		581	581
HIGH-PRESSURE SECTION—EXHAUST END										
*1. Packing leakage from high-pressure section exhaust to approximately 100 psia	464	321	506	321	646	409	332	426	332	332
2. Packing leakage from approximately 100 psia to gland seal regulator at 18 psia	650	533	722	533	1064	700	555	730	555	555
REHEAT SECTION—INTERMEDIATE PRESSURE—INLET END									Parallel flow	Parallel flow
1. Packing leakage from first reheat stage to approximately 100 psia		472		472			367			
2. Packing leakage from approximately 150 psia extraction line to 100 psia		519		519			466			
3. Packing leakage from approximately 150 psia extraction line to gland seal regulator at 18 psia		532		532			380			
REHEAT SECTION—INTERMEDIATE PRESSURE—EXHAUST TO FIRST CROSSOVER										
*1. Packing leakage from intermediate pressure reheat section exhaust to first crossover to approximately 100 psia					354	None	None	None	None	None
2. Packing leakage from approximately 100 psia to gland seal regulator at 18 psia for tandem-compound units or from crossover pressure for cross-compound units					652	364	365	636	458 Tb. End 516 Gen. End	458 Tb. End 516 Gen. End
REHEAT SECTION—INTERMEDIATE PRESSURE—INLET FROM FIRST CROSSOVER										
*1. Packing leakage from first stage of intermediate pressure reheat section inlet from first crossover to approximately 100 psia					671					
2. Packing leakage from approximately 100 psia to gland seal regulator at 18 psia					598					
1800-RPM SECTION—INLET FROM CROSSOVER										
1. Packing leakage from first stage of 1800-rpm section to gland seal regulator at 18 psia						671	671	1008	1008	

*Note: The first packing leakage in a series will be the sum of the flows to the packing leakoffs following it.

Discussion

W. E. Hopkins[7] and T. J. Whelan.[8] The authors are to be commended for their excellent presentation of basic turbine-generator design data. Their extension of the Warren-Knowlton and Elston-Knowlton data, to include part-load performance, conductor-cooled generator and sizes up to 500 mw, will be of great value to all those concerned with the design of steam power stations.

The writers' comments consist of questions that have come up during the past few weeks while using the data presented in connection with economic evaluations to determine size of unit and size of turbine-exhaust end.

The statement is made that the level of performance obtained by use of the data presented is judged to be the highest justifiable for prediction purposes at the present state of the art. It is not clear, however, whether this predicted level of performance takes into account a margin to take care of the usual uncertainties of manufacture and testing, in which case it might be expected to be comparable to the guaranteed level of performance.

Fig. 25 of the paper shows the mechanical losses for reheat units. However, no new data are presented for mechanical losses for nonreheat units. Would it be correct to assume that the data given in Fig. 13 in the Elston-Knowlton paper for mechanical losses for nonreheat units are still applicable?

The method presented requires that an assumption be made as to pitch diameter of the governing stage, and the number of control valves. Although these data have only a small effect on over-all performance, a brief discussion of the factors influencing their selection would be of interest and would be of assistance in making reasonable assumptions.

Figs. 26, 27, and 28 show relative net heat rates at 1.0, 1.5, and 2.0-in-Hg abs, respectively, for the several exhaust-annulus areas which may be selected for a given size of unit. If similar data at $3^1/_2$-in-Hg abs were available, they could be used to calculate relative design flow and, in turn, maximum expected capability at the lower exhaust pressures which must be considered in an evaluation to determine economic size of exhaust end.

The writers are hopeful that the presentation of the authors' paper will lead representatives of other large steam turbine-generator manufacturers to furnish similar data.

E. H. Krieg.[9] This paper is most stimulating and valuable to those engineers interested in selecting the most economical turbine-generator so that the plant may enjoy optimum economy.

To those who must "read while they run," Figs. 26, 27, and 28 can convey a remarkable story, such as comparisons between:

1 1450 psi and 1800 psi (both 1000/1000 F) on the 100-mw abscissa.

2 1800 psi and 2400 psi (both 1000/1000 F) on the 200-mw abscissa for TCTF-26 also CCSF-43 downflow and axial-flow turbines.

3 TCTF turbines with 23-in. and 26-in. buckets, also CCSF turbines with 38-in. and 43-in. buckets.

4 All types of turbines at 1-in., $1^1/_2$-in., and 2-in-Hg abs exhaust pressure.

Those who determine the plant performance and its economy know that the incremental dollar savings do not always balance the incremental headaches. To them a comparison of the Fig. 26 curves at 1 in. and the Fig. 28 curves at 2 in. will be of interest in highlighting the "loss" incurred when units with a large exhaust annulus operate at poor vacuums.

These curves will facilitate greatly comparisons between the many types of turbines available in this country, and the power industry is indebted to the authors for making these data available.

S. W. W. Mitchell.[10] The authors have presented an extremely fine paper, the scope and usefulness of which exceed that of any papers heretofore published on the determination of turbine-generator performance. They are to be commended for their excellent contribution to the industry.

It is quite apparent that considerable review and analysis of field and laboratory test results were necessary for the compilation of the basic efficiencies and correction factors enumerated in Table 1. We have been studying the relative efficiencies of one-row and two-row governing stages, utilizing results obtained from laboratory-controlled tests and by thermal determination during the over-all testing of large turbine-generator units of varied initial pressures and arrangements. The experience of many such tests indicates a smaller difference than that shown in the columns of Table 1 headed 3600 rpm, noncondensing. We are hopeful that further testing and study by the industry will result in a clarification of the efficiencies of these two types of governing stages.

J. A. Tillinghast.[11] The manufacturers of large steam turbine-generators have done a good job over the past years designing machines to utilize at equal or even better efficiencies the high temperatures and pressures which progressively have been utilized to obtain better thermodynamic-cycle performance. This paper gives a fine summary of the present state of these efficiency levels. We say present levels of efficiency because we know that the designers of turbines will not rest on their laurels but will continually improve performance even though facing problems such as the higher steam pressures that dictate, for instance, first stages that are too small for best flow proportions. An example of this is the 4500-psi Philo No. 6 machine on the American Gas and Electric System which, although admittedly of less than optimum capacity for its steam conditions, has first-stage buckets, which are only $^3/_8$-in. long and a second-stage diaphragm, which is approximately 4 to 5-in. thick.

This paper puts into easily workable form information which the designers of steam cycles can utilize to eliminate many variables which arise and which must be evaluated when a turbine is to be selected. The advantage of making information of this type generally available is that the large number of alternatives which should be considered can be condensed more easily, so that only the most promising ones need be given detailed study.

In selecting designs for large steam power plants we always expect to receive from turbine manufacturers machines with the best levels of internal efficiency economically possible in the state of the art at the time of the machine's purchase. With good internal efficiency, however, we must combine good cycle design to obtain the best over-all plant performance. Several good papers have been published recently on the effect of the initial steam conditions on cycle performance. These have dealt with some of the other parameters of cycle arrangement, such as number of reheats, reheat pressure, and so on. It would seem that a very worth-while paper could be written which would deal in a convenient, and perhaps to a degree approximate, manner, with other variables of cycle arrangement, which would not require detailed calculations for evaluation but which would allow the elimination

[7] Mechanical Engineer, Stone & Webster Engineering Corporation, Boston, Mass. Mem. ASME.

[8] Mechanical Division Engineer, Stone & Webster Engineering Corporation, Boston, Mass.

[9] Vice-President, Stone & Webster Engineering Corporation, Boston, Mass. Mem. ASME.

[10] Steam Division, Westinghouse Electric Corporation, So. Philadelphia, Pa.

[11] Staff Engineer, American Gas and Electric Service Corporation, New York, N. Y. Assoc. Mem. ASME.

of a large number of alternative arrangements which might be less than satisfactory. Variables of cycle design to which we refer are arrangements and spacing of feedwater heaters, particularly around reheat points, pressure drop in reheaters and extraction lines, location of boiler feed pumps at various temperature levels, effect of terminal temperature difference on feedwater heaters, use of drain coolers and drain pumps at various temperature levels, use of heat-recovery items, such as hydrogen coolers, GSLO condensers, and the like, in the condensate cycle, and other features.

Authors' Closure

The kind remarks of Messrs. Hopkins and Whelan are appreciated. The level of performance obtained by use of the data presented in this paper does take into account a margin to take care of the usual uncertainties of manufacture and testing. The order of magnitude of this margin is illustrated in Fig. 1. Rather than reading mechanical losses for nonreheat units from Fig. 13 in the Elston-Knowlton paper, the authors suggest the use of Fig. 25 of the paper presented here. Although the losses shown here are for reheat units, better consistency is insured this way. Specific information on losses of nonreheat units may be obtained from the authors.

Design considerations of turbine rotors and shells determine the diameters of governing stages. For 3600-rpm, HP turbines, the authors' company normally uses 38-in. pitch diameter governing stages at 1450 to 1800 psig initial pressure and up to 1050 F initial temperature. At steam conditions of 2400 psig and 1050 F 36-in. pitch diameters are favored. Higher initial temperatures tend to require reduced diameters, below 36 in. On supercritical pressure units where no particular pattern has been established as yet, 38-in. pitch diameters should be assumed at 1050 F initial temperature. At initial pressures as high as 1800 psig, the authors' company normally uses eight independent control valves. At 1800 psig, for larger sized units, the number of control valves has sometimes been reduced to six. Six valves have also been used on 2000 psig turbines, while higher initial pressures normally require four independent control valves. The largest sized units may require simultaneous opening of two or three control valves, thus reducing the effective number of admissions. The authors hope to find time to have estimating data prepared permitting the calculation of relative design flows and maximum expected capabilities and performance data at 3.5 in. Hg abs and other exhaust pressures, all consistent with the paper presented here.

Mr. Krieg's remarks are sympathetic and the authors are grateful.

The authors thank Mr. Mitchell for his gracious comments on the value of the paper. The difference in efficiency between turbines with one and two-row governing stages is based on performance tests of turbines and components built by the authors' company. It represents the most up-to-date comparative information available to them at the present time.

Mr. Tillinghast's stimulating remarks are much appreciated. Several people in the authors' company are continuously working on problems concerning the analysis of the performance of turbine feedwater heating cycles. Results are being made available to the industry periodically and the authors are confident that, with the aid of new calculating methods, such as high speed electronic computers, more accurate and more complete analysis of turbine feedwater heating cycles will soon be made possible.

The authors have noted that there has been some confusion regarding the assumption of standard design velocity ratios of 0.5 for single-row governing stages and 0.31 for two-row governing stages. These are the normal design conditions for large turbines built by the authors' company.

If the velocity ratio at design flow is other than 0.5 or 0.31, then an equivalent design flow should be obtained and used throughout the procedures in place of the design flow except in connection with Figs. 5, 12, and 13. For example, if a reheat unit, due to design considerations, has been designed with a velocity ratio less than 0.5 at design flow, the unit would be considered by the authors' paper to be operating at partial load, even though the unit were passing maximum flow. The following tables give multiplying factors which may be used to obtain equivalent design flows.

Single Row Governing Stages

W/V_0 at design flow	Equivalent pitch diameter[a] 34 in.	36 in.	38 in.	40 in.
0.42	1.070	1.082	1.092	1.100
0.44	1.048	1.056	1.062	1.068
0.46	1.030	1.034	1.038	1.042
0.48	1.014	1.016	1.018	1.020
0.50	1.000	1.000	1.000	1.000
0.52	0.988	0.986	0.984	0.982
0.54	0.977	0.973	0.970	0.967

Two Row Governing Stage

W/V_0 at design flow	Equivalent pitch diameter[a] 31 in.	34 in.	37 in.	40 in.
0.25	1.219	1.276	...	...
0.28	1.088	1.109	1.134	1.161
0.31	1.000	1.000	1.000	1.000
0.34	0.942	0.950	0.917	0.901
0.37	0.896	0.880	0.856	0.833
0.40	0.863	0.842	0.812	0.781
0.43	0.842	0.813	0.784	0.744

[a] Note: Equivalent pitch diameter

$$= \frac{\text{Pitch diameter} \times \text{rpm}}{3600} \times \sqrt{\frac{790}{P_t v_t \text{ at throttle condition}}}$$

A New Way to Simplify the Steam Power Plant

By H. A. KULJIAN[1] and W. J. FADDEN, JR.,[2] PHILADELPHIA, PA.

The purpose of this paper is to present a new approach to the ever-urgent problem of simplifying the installation and operation of steam power plants. Two alternative methods are involved, both of which combine regenerative feedwater heaters in a single shell. One integrates the closed-type heat exchangers; the other employs a new method of using open-type heat exchangers with intermediate locks. By either method, it is the conclusion of the authors that a saving in initial investment of from $10.00 to $15.00 per kilowatt will be obtained.

Introduction

MODERN power plants are notoriously complicated and appear to the layman as a baffling maze of various machines, heat exchangers, and tanks, all interlaced together with many pipes and valves of unknown functions. Yet, basically, all of this equipment in a steam power plant can be classified under three major groups; namely, the steam-generating unit, the turbogenerating unit, and the heat exchangers. All of the other equipment is either used to interconnect these, or contribute to their operation.

Modern Power-Plant Equipment

The steam-generating unit includes the economizer, air preheater, waterwalls, superheater, forced-draft fan, induced-draft fan, pulverizers, and furnace, in addition to the boiler itself. All of these are fairly compact in arrangement.

The turbogenerating unit includes the condenser and controls, and it, too, is compactly arranged.

But by contrast, the heat-exchanger equipment in a multistage bleeding installation usually includes several low-pressure heaters, a deaerating heater, high-pressure heaters with boiler feed pumps, and endless piping located wherever it can be squeezed in. The result is a complicated installation.

The importance of heat exchangers in attaining high thermal efficiency in modern plant operation is well known to all engineers. Going to higher and higher pressures and temperatures will not by itself answer the problem of better efficiencies for the steam power plant. This cannot be accomplished without the use of regenerative feedwater heaters.

In power plants, most machinery such as circulating water pumps, condensate pumps, boiler feed pumps, forced and induced-draft fans are all rotating apparatus, either pumping water or air into the boiler furnace, or sucking the products of combustion from the furnace. They make a considerable amount of noise and hum in the power plants. In the heat exchanger, however, there are no moving elements. Only fluids are in motion; one is the water which runs through the coils with fairly high velocity, at the rate of 6 or 8 fps, the other is steam, which is bled from the turbine connected to the shell of the heat exchanger, being condensed continuously, transferring its energy into the water, thereby increasing the thermal efficiency of the plant. If it were not for these heat exchangers, it would be impossible to use generated power so cheaply in our industries or in our homes.

While the supercritical-pressure stations constitute a radical change in power-plant practice, by far the greatest change now imminent is the use of nuclear energy for generating electric power. Naturally, more complex equipment will be added. It is, therefore, of paramount importance that the feedwater-heating cycle be kept as simple and as effective as possible.

Take for example a 150,000-kw unit. The condenser, with approximately 100,000 sq ft of condensing surface, is manufactured in a single shell. For the same size unit, eight single-stage heat exchangers are used with a combined total heating surface of less than one half that of the condenser.

The basic concept of incorporating all the stages of feedwater heating in a single compact shell reduces costs by:

(*a*) Greatly simplified piping.
(*b*) Reducing the number of engineering drawings.
(*c*) Reducing installation cost and time.
(*d*) Reducing building volume, particularly valuable floor space.

In the aggregate, these four economies indicate a total saving of from $10.00 to $15.00 per installed kilowatt.

Proposed New Heaters

Two types of combined heaters are offered for both power plants and industrial plants. The closed heater will be referred to as type K feedwater heater. The other is an open heater called type K-F. Each type will be described.

Type K Feedwater Heater. The type K feedwater heater is basically a series of closed shell-and-tube type heaters that have been combined in a single vertical shell, and factory-built and tested as a single unit. Flow is accomplished by pumping feedwater directly from the condenser hotwell through the coils of the stages directly to the suction of the boiler feed pumps. The suction-head requirements of the boiler feed pumps are satisfied by proper selection of the discharge pressure of the condensate booster pump. The tubes carrying the feedwater are arranged in flat spirals in the horizontal plane and are of such a size and number as to give the best heat transfer. Steam bled from the turbine at the desired point passes around these tubes to raise the temperature of the feedwater to the boiler and raise the over-all thermal efficiency of the power plant.

Operation of K Feedwater Heater. Figs. 1–4 and the accompanying description are based on a 150,000-kw turbogenerator 2000 psig, 1050 F, 1000 F reheat, with eight stages of extraction heating.

The type K feedwater heater, with its spiral-wound heat-exchanger tubes, consists of a tower-like, cylindrical shell partitioned into stages, one stage for each heater.

This feedwater-tower assembly stands in a vertical position on the condenser floor, as close to the turbogenerator as possible, with

---

[1] President, The Kuljian Corporation. Fellow ASME.
[2] Chief Mechanical Engineer, The Kuljian Corporation. Assoc. Mem. ASME.

Contributed by the Power Division and presented at the Semi-Annual Meeting, Cleveland, Ohio, June 17–21, 1956, of The American Society of Mechanical Engineers.

Note: Statements and opinions advanced in papers are to be understood as individual expressions of their authors and not those of the Society. Manuscript received at ASME Headquarters, February 21, 1956. Paper No. 56—SA-34.

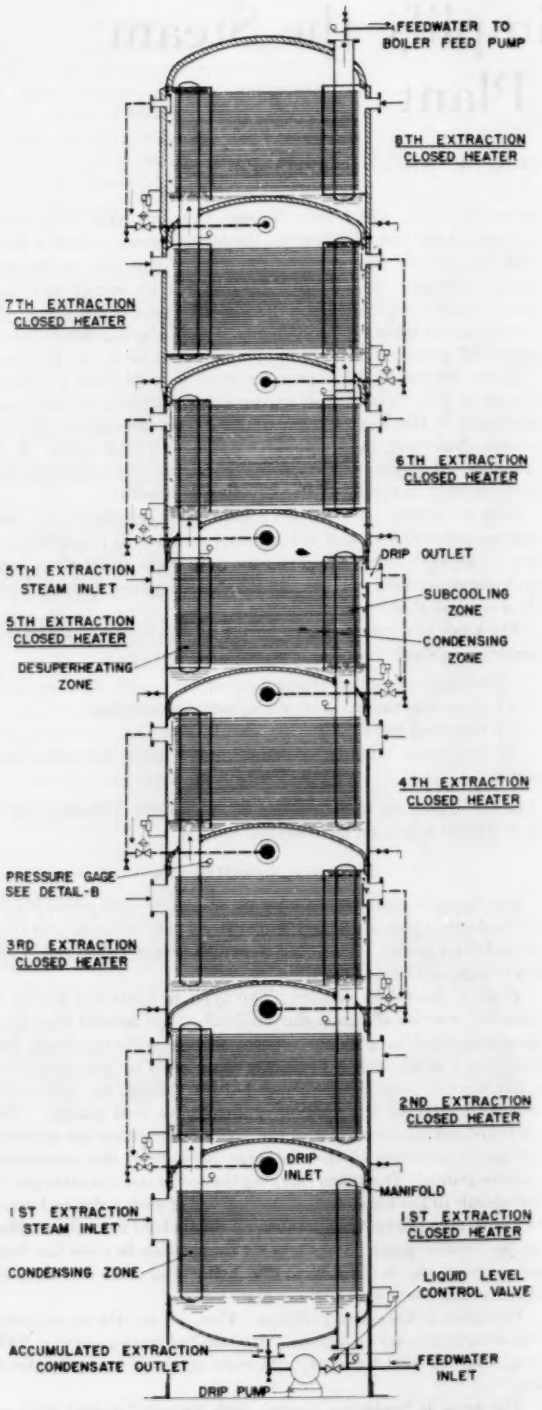

FIG. 1 K FEEDWATER HEATER FOR 150,000-KW TURBOGENERATOR, 2000 PSIG, 1050 F, 1000 F REHEAT; DIAMETER 10 FT, OVER-ALL HEIGHT 69 FT

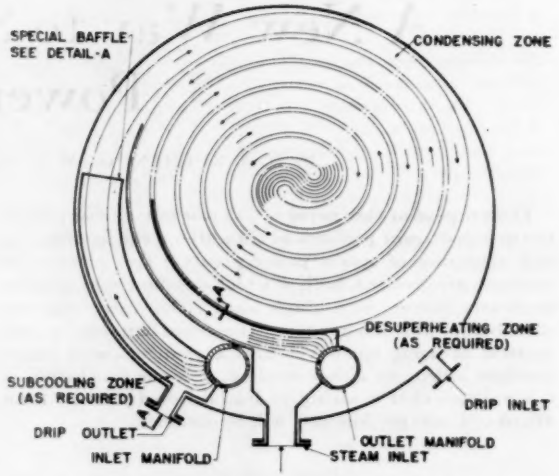

FIG. 2 PLAN OF TYPICAL EXTRACTION CLOSED HEATER

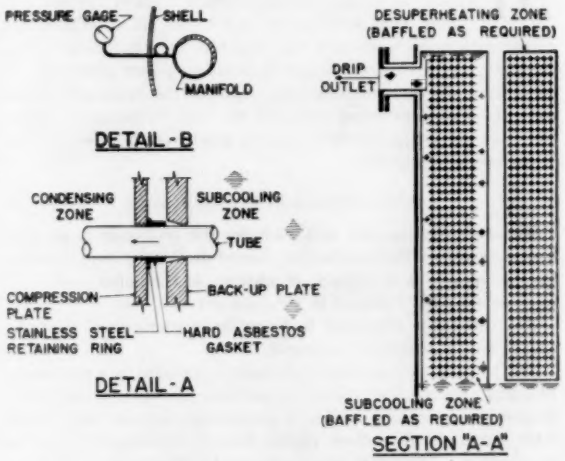

FIG. 3 DETAILS OF EXTRACTION CLOSED HEATER OF FIG. 2

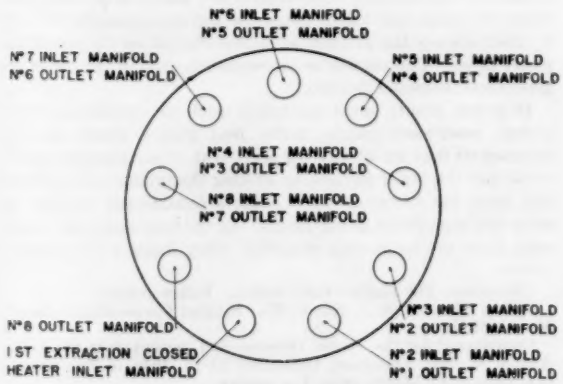

FIG. 4 ORIENTATION OF INLET AND OUTLET MANIFOLDS

the highest-pressure stage at the top. Condensed extraction steam is cascaded from each stage heater to the next lower pressure unit. The condensate level in each stage is maintained with a level-control valve. The accumulated extraction condensate from the lowest-pressure stage heater is pumped into the inlet manifold combining with the condensate booster-pump discharge. The stage-heater vents are also cascaded from one unit to the next lower pressure unit, finally cascading to the condenser.

Condensate from stage heaters, as well as from main condenser, enters the lowest-pressure stage-heater manifold at the bottom. It then passes through a number of parallel coils into another manifold which becomes the inlet manifold for the next higher pressure stage heater. These manifolds are entirely internal and are welded to the partition plates at one point only, to allow free expansion of the manifolds and coils without causing any appreciable stress. The remaining stages operate in a similar manner.

In high-pressure stages of the feed cycle, energy is kept at the highest possible temperature level by use of desuperheating and drain-cooling zones. In drain cooling, entering feedwater picks up heat from the leaving condensate before it is flashed to the lower-pressure heater and releases its heat at a lower temperature. The feedwater temperature is thereby raised a few degrees which it could not realize from the same heat in the lower-pressure heater. In the desuperheating zone, the leaving feedwater picks up heat from the incoming superheated steam, thereby raising the water temperature higher than the saturated-steam temperature corresponding to the pressure. The K feedwater heater includes both drain-cooling and desuperheating zones as required.

The cycle efficiencies obtained by using the type K feedwater heater are equal to those obtained by using conventional regenerative cycles.

Type K-F Feedwater Heater. The new type K-F feedwater heater uses standard tray-type open heaters and deaerating heaters, as now manufactured, which are combined in a vertical tower.

Flow from one heater to another is accomplished by gravity through a novel arrangement of receiving and discharging locks. A pair of locks is interposed between each heating stage. One lock is steam equalized to the heating stage immediately above and receives water from that stage by gravity flow. The other lock is steam equalized to the next heating stage and discharges water by gravity to that stage.

When a lock is emptied and the other is full, a transfer valve is automatically operated to interchange the functions of the locks so the full one discharges to the high-pressure stage and the empty one receives water from the low-pressure stage.

This operation continues with a frequency of transfer as required by the boiler load.

By this means water flows from the low-pressure stage to the high-pressure receiver without requiring pumps.

In the case of the open-type heater, feedwater is finely divided to mix with the extracted steam, since small particles present the most surface to absorb the vapor. Steam condenses on the water droplets heating them to a value approaching the boiling temperature. Direct-contact heaters remove all dissolved oxygen in excess of 0.03 ml per liter. When such a unit is designed to reduce the dissolved oxygen to 0.005 ml per liter, it becomes a deaerating heater.[3] Removal of dissolved gases depends on heating the feedwater to the boiling point, agitating it, and presenting as big a surface as possible to liberate the gas and absorb heat by condensing the steam.

In the type K-F heater, feedwater is fed into a series of trays and falls from tray to tray by overflowing. Steam completely envelops the trays, and heats and deaerates the feedwater along its path to the bottom of the shell. It is a well-known fact that direct-contact heating of feedwater has the advantage of 0 deg F terminal difference over that of indirect heating.

Operation of the Type K-F Feedwater Heater. The K-F feedwater-heater-tower assembly is also a completely factory-built and tested unit. It starts with the lowest-pressure heater at the top, progressing downward to the highest-pressure direct-contact heater and finally to the receiver at the bottom. The receiver is held at the same pressure as the highest extraction stage. The highest-pressure extraction steam is first desuperheated in the closed heater and enters the receiver at approximately saturated condition. The condensing zone for this closed heater is completely open to the steam space in the receiver. Condensed steam (drains) is automatically included in the receiver liquid space (refer to Figs. 5 and 6).

Inasmuch as the feedwater temperature at the boiler feed-pump suction is below that for vaporization, these pumps will not get steam bound but operate under a positive suction head at all times. With this design, net positive suction head for boiler feed pumps is no longer a station design factor.

Figs. 5 and 6 and the description which follows are based on a 150,000-kw turbogenerator, 1800 psig, 1000 F, 1000 F reheat, with seven stages of extraction heating. Refer to Fig. 7 for heat-balance diagram. The operation for the 150,000-kw unit is as follows:

Exhaust steam from the turbogenerating unit is condensed in the condenser and collected as condensate in the condenser hotwell. Make-up is added at this point. The condensate pumps discharge this condensate through the condensate control valve to the condensate inlet at the top of the heater. Condensate enters the first heater by spilling over the edges of inlet distributing troughs in weir fashion, requiring only a very low head. Condensate is then intimately mixed with steam by spilling over the heating trays. Steam from the first extraction enters the heater uncontrolled; along with vented steam from the receiving lock.

The remaining open heaters operate in the same manner as just described. No storage is provided within each heater, however, as the receiving lock in each case acts as an effective storage compartment. With the exception of the lowest-pressure heater which vents to the condenser, all other stage venting is taken care of by the equalizing steam connection.

The receiver contains two desuperheaters, one for the 6th extraction and one for the 5th extraction. A 7th extraction closed heater is also mounted within the receiver.

Suction to the boiler feed pump is taken from the receiver and discharged through the 7th extraction closed heater to the boiler.

Control System for K-F Heater. The control system for the K-F heater is designed to maintain a practically steady flow to each heater for a given load on the turbine, thus minimizing fluctuations in the extraction line pressures. Basically, the control system for each stage is made up of three elements: (1) primary demand, (2) correction for head variation, and (3) correction for flow to the succeeding stage.

Heat Balance for K-F Feedwater Heater. It is interesting to note that the heat rate for the regenerative cycle, when using the K-F feedwater heater combined with a closed heater, is better than that of the same cycle employing conventional closed heaters.

Fig. 7 is a heat balance for a 150,000-kw, 1800-psig, 1000 F, 1000 F reheat, 1½ in. Hg, preferred standard turbogenerator with seven stages of feedwater heating. With the exception of the direct-contact-heater terminal differences, the assumptions made were comparable to manufacturers' handbook assumptions; how-

[3] "Heat Exchangers" by B. G. A. Skrotzki and S. S. Waldron, *Power*, vol. 98, June, 1954, pp. 75–106.

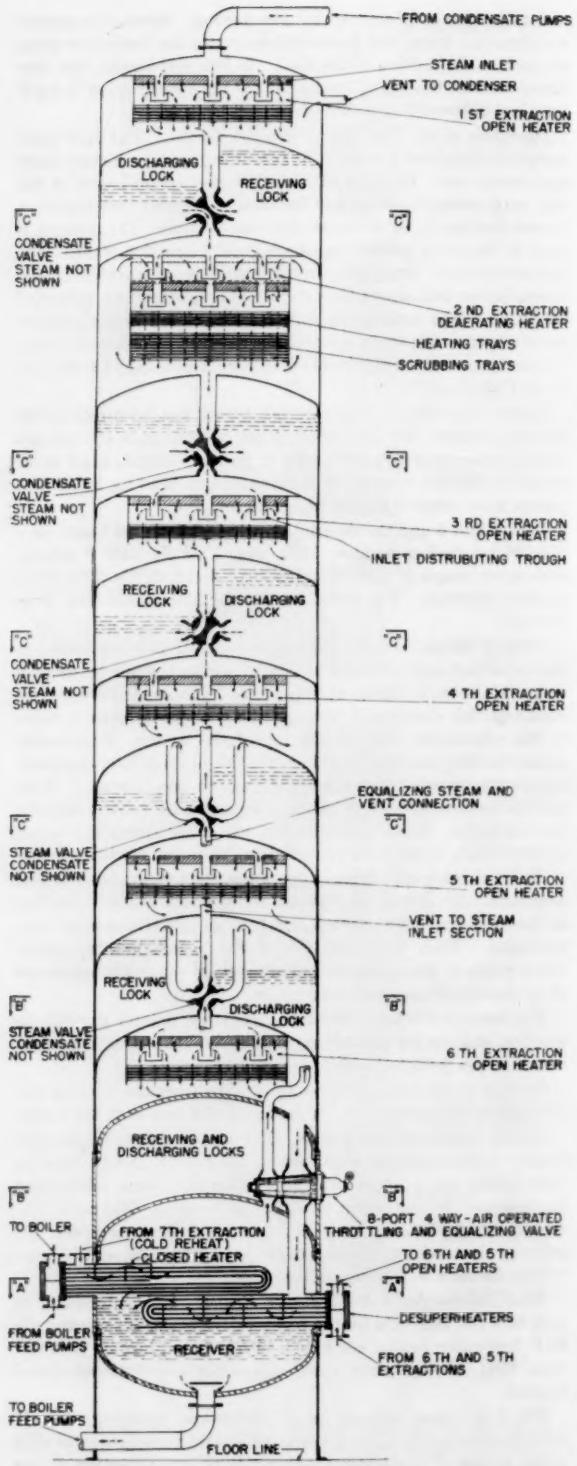

FIG. 5 K-F FEEDWATER HEATER FOR 150,000-KW TURBOGENERATOR 1800 PSIG, 1000 F, 1000 F REHEAT. DIAMETER 11 FT 6 IN., OVER-ALL HEIGHT 72 FT 6 IN.

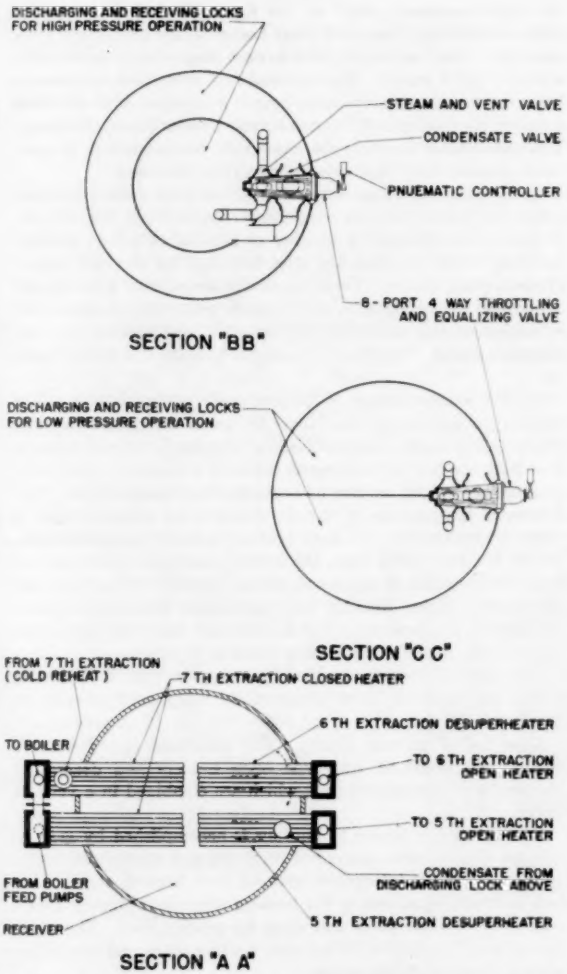

FIG. 6 SECTIONS THROUGH K-F FEEDWATER HEATER OF FIG. 5

ever, the heat rate for the K-F cycle is 0.425 per cent better than that found in the handbook.[4]

Assumptions:[5]

(*a*) Three per cent pressure drop turbine shell to extraction flange.

(*b*) Five per cent pressure drop extraction flange to heater.

(*c*) Boiler feed-pump power included.

(*d*) Nine hundred pounds per hour ejector steam.

(*e*) Generator H_2 pressure 0.5 psig.

(*f*) Zero per cent make-up.

(*g*) Ejector condensate leaves at 135 F.

It is possible in the foregoing heat balance to improve the heat rate still further by bettering the terminal difference of the high-pressure heater. The foregoing assumptions were made for comparison purposes. In the case of the 150,000-kw heat balance, the

[4] "Turbine Specialist's Data Book," General Electric Company, Scheneetady, N. Y., Steam Performance, 1954, sec. 404 TS, pp. 3, 4, 9; and curves, sec. 452 TS.

[5] "Thermodynamic Properties of Steam," by J. H. Keenan and F. G. Keyes, John Wiley & Sons, Inc., New York, N. Y., first edition, 1950.

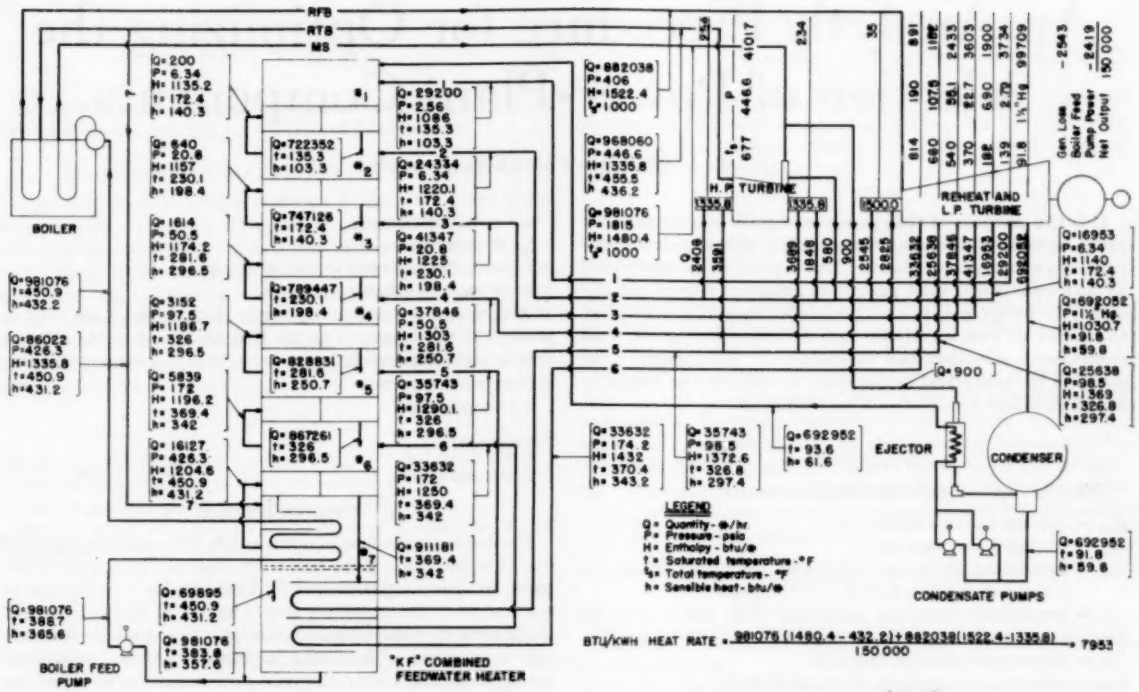

FIG. 7 HEAT-BALANCE DIAGRAM FOR 150,000-KW STEAM POWER PLANT

heat rate in Fig. 7 can be improved by approximately 8 Btu per kwhr by using the desuperheating coils for heater No. 6 to improve the terminal difference on heater No. 7.

Heat-balance studies of other size units indicate approximately $^1/_2$ per cent better heat rates than those found in the handbook, using the same assumptions.

INDUSTRIAL APPLICATION OF K-F LOCK FOR SINGLE DEAERATING HEATERS

So far in this paper, multistage open-type heaters and utility-type installations have been discussed.

The new K-F lock arrangement described is applied to the single deaerating-heater installation for industrial use. The heater can be located at the same level as the boiler feed pumps, thus eliminating expensive supporting structure. In addition, savings will be made in the reduction of the boiler-feed-pump horsepower and initial pump costs.

Where boiler-drum pressure is maintained on the boiler-feed-pump suction, pumping horsepower need only overcome static head plus friction drop in piping.

Maintenance of K and K-F Feedwater Heaters. Reliability and ease of maintenance of equipment are always foremost in the minds of power-plant operating personnel; however, design engineers sometimes lose sight of these problems. In the K and K-F heaters, emphasis has been placed on rugged design and simplicity of construction so that maintenance problems will be kept to a minimum.

In the type K-F feedwater heater, the valves and controls are of simple construction and should require very little attention. Both open and closed heaters are provided with access manholes in the shell for easy inspection and maintenance.

CONCLUSION

The last decade was a tremendously active and stimulating one in the power industry. But the power engineer's problem, production of the maximum amount of power with the minimum amount of fuel, is still the same.

The complicated feedwater heating apparatus in present-day power plants must be simplified. The use of a single, integrated, multiple heat exchanger will substantially reduce building size, piping systems, erection time, and many other costs. Both the types described in the foregoing are designed to meet this need for streamlining the modern power plant.

ACKNOWLEDGMENTS

The authors gratefully acknowledge the considerable assistance of E. S. Daugherty, Executive Vice-President, Cochrane Corporation; G. T. Hutchison, Chief Engineer, Cochrane Corporation; G. Stables, Jr., Sales Engineer, Hagan Corporation; J. B. Stevens, Manager Valve Sales and Engineering, Schutte and Koerting Company; E. H. Myers, Application Engineer, S. Morgan Smith Company, and many others in the preparation of this paper.

An Analytic Procedure for Optimizing the Selection of Power-Plant Components

By W. A. WILSON,[1] CAMBRIDGE, MASS.

It is the purpose of this paper to inquire into systematic procedures for optimizing the selection of equipment comprising a steam power plant. The inquiry is not motivated by any conviction that plants as designed depart significantly from optima, but rather stems from the belief that the labor of the inevitable cut and try process of final component selection can be reduced. It appears to be possible by analytical techniques to narrow the range in which detailed explorations are required.

Nomenclature

The following nomenclature is used in the paper:

A_{ex} = exhaust annulus area, sq ft
A_c = condensing surface, sq ft
c_{ex} = investment increment associated with unit change in exhaust annulus, \$/sq ft
c_c = investment increment associated with unit change in condenser heat-transfer capability, \$/(Btu hr deg F)
c_f = rate of fixed charges, (\$/yr)/\$
c_{op} = operating cost per unit of output, \$/kwhr
C_f = fixed charges, \$/yr
C_{op} = operating costs, \$/yr
h = enthalpy, Btu/lb
G = steam flow rate, lb/hr
I = capital investment, \$
L = load factor based on generator output
N = number of feedwater heaters
P = generator rating (and output for purposes of optimization analysis), kw
Q = heat transfer, Btu/hr
t = temperature, deg F
U = over-all coefficient of condensing heat transfer $\equiv \dfrac{Q_2}{(t_2 - t_c)A_c}$, $\dfrac{\text{Btu}}{\text{sq ft-hr-deg F}}$ for conventional plant
U^* = over-all coefficient of condensing heat transfer $\equiv \dfrac{Q_2}{(t_w - t_c)A_c}$, $\dfrac{\text{Btu}}{\text{sq ft-hr-deg F}}$ for cooling-tower plant
x = quality
η = efficiency
Turbine heat rate $\equiv \dfrac{\eta_g Q_1}{P}$, Btu/kwhr

Subscripts

( )$_b$ = boiler
( )$_c$ = circulating water
( )$_{ex}$ = exhaust system
( )$_g$ = generator
( )$_1$ = boiler (referring to heat addition to cycle)
( )$_2$ = turbine exhaust (state)
1, 2, 3, 4, 5, 6, 7—plant components (1, 2, 5, and 7 are fixed in price; 3 is the boiler. 4 is the feed heaters; 6 is the exhaust system including circulating water system, condenser, and turbine-exhaust annulus).
( )$_0$ = condensate

Superscript

( )^0 = stagnation

Optimum Defined

The economic problem of optimization is to minimize the total cost of performing a given task where that cost is the sum of two parts; (*a*) operating costs and (*b*) fixed charges. In the case of a power plant the former are closely related to the heat rate and the latter to the total capital investment. In general, the heat rate can be improved by increasing investment. In fact, aside from aesthetic considerations, the only justification for increased investment is reduction of operating cost. Presumably, then, there exists for a family of plants of particular capability and built to consistent standards of reliability and safety a relationship between operating cost and investment

$$c_{op} = f(I)$$

and

$$\frac{dc_{op}}{dI} = \dot{f}(I) \text{ (negative quantity)}$$

where

c_{op} = operating cost per unit output (\$/kwhr)

I = capital investment (\$)

If the rate of fixed charges is c_f (\$/yr)/\$, the yearly cost, dC_F(\$/yr), of an increment of investment is

$$dC_F = c_f\, dI \text{ (\$/yr)}$$

corresponding to an increment of operating cost, dC_{op} (\$/yr); and

$$dC_{op} = dc_{op}\, P\, L\, 24 \times 365$$
$$= 8760\, P\, L\, dc_{op}$$

where P is the generator rating in kw and L is the load factor based on that rating. An optimum investment is one for which the total of operating costs and fixed charges is indifferent to the investment; i.e.

$$\frac{dC_f}{dI}\, dI + \frac{dC_{op}}{dI}\, dI = 0$$

$$c_f\, dI + 8760\, PL \frac{dc_{op}}{dI}\, dI = 0$$

---

[1] Associate Professor of Mechanical Engineering, Massachusetts Institute of Technology. Mem. ASME.

Contributed by the Power Division and presented at the Semi-Annual Meeting, Cleveland, Ohio, June 17–21, 1956, of The American Society of Mechanical Engineers.

Note: Statements and opinions advanced in papers are to be understood as individual expressions of their authors and not those of the Society. Manuscript received at ASME Headquarters, April 9, 1956. Paper No. 56—SA-51.

or

$$\frac{dc_{op}}{dI} = f(I) = -\frac{c_F}{8760\,PL} \quad [1]$$

In order to select an appropriate investment I, it is only necessary to know the function $c_{op} = f(I)$ and its derivative.

Operating Cost as a Function of Investment

For each possible total investment I there are many combinations of component investments and corresponding variations in operating cost. This is not merely because it is possible to use inferior components; but, unless special precautions are taken, the investment may be unwisely distributed among them. Among the possible combinations which are equivalent in investment and in all other significant respects one will be best so far as operating cost is concerned. This combination is said to be balanced (1).[2] The function

$$c_{op} = f(I)$$

relates the operating cost to investment for balanced plants.[3] It should be noted that another constraint on this relationship is that it refers to plants having equal capabilities.

If each plant of a given class consists of n-components, we may write

$$I = I_1 + I_2 + \ldots\ldots + I_n \quad [A]$$

$$P = F(I_1, I_2, \ldots\ldots, I_n) \quad [B]$$

$$c_{op} = f(I_1, I_2, \ldots\ldots, I_n) \quad [C]$$

The problem is to find for each value of I the c_{op} of a balanced plant which produces a particular output P, that is, to minimize [C] subject to [A] and [B] being constants.

Given I, one of the independent component investments may be written in terms of I and the other $n - 1$ component investments. Given P another investment may be eliminated

$$I_1 = I - (I_2 + \ldots\ldots + I_n) \quad [A\text{-}1]$$

$$I_2 = F^*(I, P, I_3, \ldots\ldots, I_n) \quad [B\text{-}1]$$

$$c_{op} = f^*(I, P, I_3, \ldots\ldots, I_n) \quad [C\text{-}1]$$

If the problem could, in fact, be reduced to these terms, it would still remain to find for a series of values of I that combination of $I_3, \ldots, I_n$ which minimizes c_{op}.

The Three-Component Problem

If only three independent investments are involved, finding the minimum c_{op} for a given investment would be, in principle, a straightforward process of solving the relationship

$$\left(\frac{\partial c_{op}}{\partial I_3}\right)_{I,P} = 0 = f^*(I, P, I_3)$$

[Note that if only two components are involved there is no problem of balancing. The operating cost is a unique function of rated power and investment: $c_{op} = f^*(I, P)$.]

More Than Three Components

If there are four components it becomes necessary in general to establish the appropriate values of component I's by a more elaborate procedure. Since we are focusing our attention on a series of plants all having the same capability, the function

$$c_{op} = f^*(I, P, I_3, I_4)$$

which is presumably determinable may be thought of as a series of constant I surfaces in c_{op}, I_3, I_4 space. We wish to locate c_{op} (min) in each of these surfaces. The criterion for a minimum in any one such surface is

$$\left(\frac{\partial c_{op}}{\partial I_3}\right)_{I.P.I_4} = \left(\frac{\partial c_{op}}{\partial I_4}\right)_{I.P.I_3} = 0$$

Since with I and P constant both these derivatives are functions of I_3 and I_4, these conditions are sufficient to fix both of the latter quantities. If solutions are found in terms of I, then c_{op} (min) = c_{op} (balanced) can be found as a function of I.

Actually, we are seldom if ever in a position to write Equations [A], [B], and [C] in analytic form and are consequently unable to proceed in the straightforward way indicated to find c_{op} (balanced) as a function of I. The significance of this formal development is that it calls attention to the fact that the criterion for balance is indifference of operating cost to small transfers of investment from component to component where these transfers must satisfy not only the conditions

$$\sum_0^n \Delta I_i = 0 \text{ and } P = \text{const}$$

but also must be made in the most favorable way consistent with these restrictions.

Another conclusion is that, in the absence of analytic functions expressing the relationships of power output and operating cost to component investment, the problem of optimizing a plant comprising more than three components is indeed formidable. Fortunately, however, one can circumvent some of the difficulties. Certain techniques for doing so are outlined.

1 *Components whose selections do not influence the power output.* Such items as the coal-handling equipment, for example, can be chosen independently of the rest of the plant. Similarly the question of whether or not to add a given element of automation can be judged on its own merits; does it or does it not save enough in yearly payroll to support the annual fixed charges? Again, the problem of fuel storage can be separated from the remainder of the plant; that is, it can be optimized independently to provide fuel to the power plant at a minimum unit cost including fixed charges.[4]

2 *Components which co-operate with each other to produce a single common effect through which their influence is felt on the rest of the plant.* The circulating-water system and the condenser proper, for example, influence the plant only through their combined effect on the heat-transfer effectiveness of the latter. For this reason the condenser and its auxiliaries may be treated as a single component in so far as the plant as a whole is concerned. The pertinent economic relationship—effectiveness versus duty and investment—can be predetermined for the combination.

Beyond this, it is possible, as previously demonstrated (1), to define combinations of condensing system and turbine-exhaust annulus which are in balance independent of the choice of the remaining components. This combination may then be treated as a single component of the over-all plant. This is possible because the condenser and the exhaust annulus both influence the plant output and its fuel economy through their common

[2] Numbers in parentheses refer to the Bibliography at the end of the paper.

[3] All optimum plants are balanced, but whether a particular balanced plant is optimum or not depends on such economic factors as the rate of fixed charges, fuel cost, and load factor.

[4] Strictly speaking this determination is not entirely independent of the plant heat rate, but the influence of variations in fuel consumption with heat rate would be trivial indeed.

effect on the stagnation enthalpy of the steam leaving the last blade row.

3 *Components, the costs of which are determined solely by the ground rules and the plant rating.* The turbogenerator exclusive of the exhaust annulus is priced solely on the basis of inlet steam conditions and electrical output. From an economic point of view there is no freedom of choice in its selection once the plant generating capacity is set and the basic cycle fixed. One might expect the addition or subtraction of stages to be a mechanism for providing a range of turbine performance for a corresponding price range. In practice, this choice is not given to the customers of large turbogenerators.

4 *Components which are subject to modification only in finite steps.* As a practical matter many elements of the power plant fall into this category including the turbine-exhaust annulus which has been tacitly assumed to be indefinitely variable in order that it might be treated in combination with the condensing system (see item 2). Other items such as feed heaters are not conveniently represented as having continuous variability, and it may be necessary to optimize separately plants incorporating arbitrary numbers of heaters and then to choose between these optima. The point to be made here is that a component like a heater modifies not only the heat rate but also the exhaust and throttle flows and therefore the appropriate boiler and condenser-exhaust annulus investments. In principle, at least, it is not sufficient to compare the performances of plants which are identical except with respect to the number of heaters.

Application of the Method

Let us consider the problems of selecting the basic components for two 150-mw reheat plants. It will be assumed that the basic cycles are the same including the initial and reheat steam states, 1800 psi, 1050 and 1050 F. A "conventional" plant is to be favored with a copious supply of 60 F circulating water whereas the second must depend on a cooling tower operating with 50 F wet-bulb and 65 F dry-bulb air.[5] The fuel cost in each case is assumed to be \$0.30/10^6 Btu. The rate of fixed charges is taken as 14 per cent. An annual load factor of 0.80 is assumed to be an appropriate basis for equipment selection.

It is first necessary to enumerate the components of the plants and categorize them according to the foregoing classification. At the same time, the corresponding economic data will be assigned. The latter are considered realistic as to numbers and form but by no means general in either respect.

1 *Site,* including fuel storage and handling facilities; category 1. Its cost is independent (for any one plant) of small differences in component selection. It does not, therefore, enter the optimization problem.

2 *Structure,* category 3. It is convenient to classify as "structure" that part of the building, etc., which is independent of the selection of equipment. Obviously, the sizes of condenser, turbine exhaust, and boiler do affect structure, but it greatly simplifies matters to associate these effects with the responsible components. The basic structure, then, does not enter the optimization problem.

3 *Boiler-plant equipment,* category 4. Over the small range of capacities and feed-heating arrangements within which the optimum may be expected to lie the cost of the boiler may be assumed to be linear with heat release and to have a constant efficiency. We will assume the factor of proportionality and the efficiency as 5.6×10^{-3} \$/Btu/hr[6] and 0.88 per cent, respectively. (A reviewer of the original manuscript properly questions the assumption of independence of boiler cost per Btu/hr from final feed-water temperature.)

4 *Feedwater heaters,* category 5. It is assumed that heaters can be added for \$80,000 per heater. The effect of the number of heaters on heat rate is tabulated in Table 1 which is based on Salisbury's (2) data and a "base" turbine heat rate of 7880 Btu/kwhr for five heaters and an exhaust pressure of 1.5 in. Hg (3). A leaving loss of 10 Btu/lb is assumed to correspond to this heat rate.[7]

TABLE 1 EFFECT OF NUMBER OF HEATERS ON HEAT RATE

No. heaters	Feed temp, deg F	Reduction in turbine heat rate, Btu/kwhr
4	542	—64
5	561	0
6	575	46
7	585	82.5
8	593	112.
9	599	134.5
10	603	152

The effect of addition of heaters on the exhaust flow is approximated through the relationship

$$G_2 = \frac{(\text{turbine heat rate} - 3413)P}{\eta_g(h_2^\circ - h_0)} \quad \ldots\ldots\ldots [2]$$

For purposes of evaluating the economics of the heaters it is probably permissible to ignore the cross effects of the turbine-exhaust system so far as the evaluation of the change in exhaust flow G_2 is concerned. Therefore for $\eta_g = 0.98$

$$dG_2 = \frac{d(\text{turbine heat rate}) \times 150{,}000}{0.98\,(h_2^\circ - h_0)}$$

$$= \frac{153{,}000}{h_2^\circ - h_0}\, d(\text{turbine heat rate}) \ldots\ldots [3]$$

5 *Turbogenerator (less exhaust annulus),* category 3. This item is not variable once the basic cycle, design capability, and power factor are set. Since it is fixed, the price does not enter the optimization analysis. The condition curve or state line is assumed to be independent (except for its lower terminus) of the choice of other components. This curve is defined by assuming 2 : 1 pressure-ratio stages of 80 per cent efficiency, one point on the curve being the 12 per cent moisture 1.5 in. Hg condition (1). Fig. 1 plots the enthalpy h_2, and $(1 - x)_2$ as a function of p_2. Generator efficiency is assumed to be 98 per cent.

6 *Exhaust annulus and condensing system,* category 2. Fig. 2 is adapted from reference (1). It plots the exhaust annulus area per unit of exhaust flow G_2, versus the heat-transfer capability, A_eU, per unit of G_2 for the condenser. The ratio of unit costs of the annulus area and transfer capability is a parameter which is assumed to have the value 5.5×10^{-6} (Btu/hr deg F)/sq ft for the present case. The corresponding cost of annulus area is assumed to be 12,200 \$/sq ft making the unit cost of A_eU 6.71×10^{-3} \$/(Btu/hr deg F).[8]

---

[5] It is recognized that assignment of appropriate representative values of these temperatures is in itself a very subtle problem.

[6] Investment unit costs include engineering and erection overheads.

[7] In effect we are proceeding as though this heat rate had been calculated on the basis of a provisional choice of components.

[8] For a typical heat-transfer coefficient $U = 325$ (4) the corresponding cost of condenser area is 22.00 \$/sq ft. This is based on a two-pass condenser and the following definition of U

$$U \equiv \frac{Q_2}{(t_2 - t_e)}$$

where t_2 is the condensing temperature and t_e is the initial temperature of the circulating water. The coefficient as thus defined is very nearly constant for a particular circulating-water velocity (assumed to be balanced with the condenser surface) over the range 1.0 in. Hg to 3.0 in. Hg. The cost of the circulating-water system including intakes, screens, etc., is incorporated in the condenser cost as is the capitalized value of increments in the pumping power.

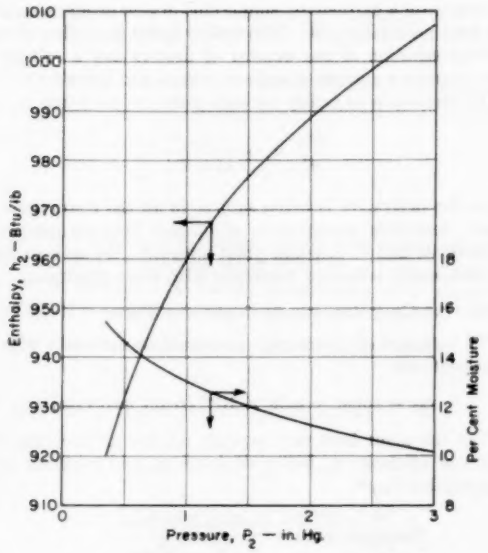

FIG. 1 PROPERTIES ALONG THE STATE LINE

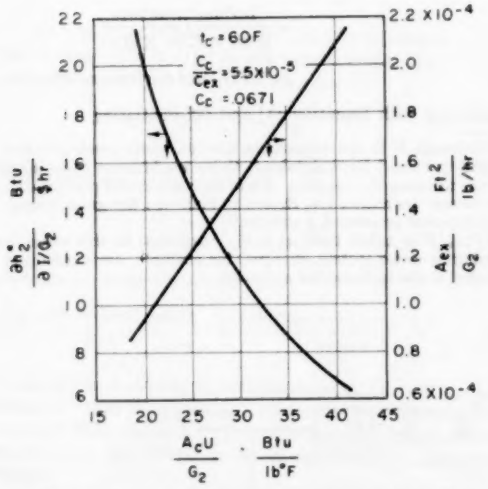

FIG. 2 PERFORMANCE OF BALANCED CONDENSER AND EXHAUST-ANNULUS AREAS FOR 60 F CIRCULATING WATER

A second set of curves on the same figure indicate indirectly the economic incentive for adding exhaust and condenser areas. For the assumed unit costs the rate of change of stagnation enthalpy leaving the last blade row with investment

$$\frac{\partial h_2^\circ}{\partial (I/G_2)}$$

is plotted against balanced heat-transfer capability, A_cU/G_2. Fig. 3 plots the condensing temperature versus A_cU/G_2 for balanced annulus areas.

For the case of the cooling tower it is possible first to balance the cooling tower-condenser combination; i.e., to find the appropriate distribution of investment between tower and condenser for any particular wet-bulb temperature as a function of condensing temperature. At the same time the balanced area per unit

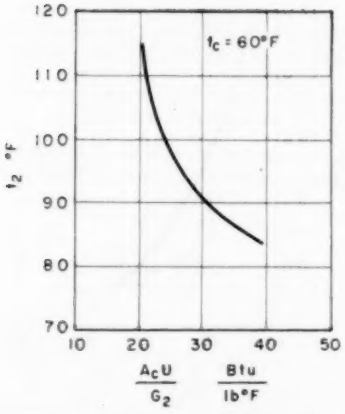

FIG. 3 CONDENSING TEMPERATURE VERSUS CONDENSER AREA (t_c = 60, c_e/c_{ex} = 5.5 × 10⁻⁵.)

of exhaust flow necessary to maintain that temperature would be found. The assumption is made here that the appropriate ratios between cooling-tower and condenser investment and capitalized fan and pump power costs is an invariant (at least for a fixed wet-bulb temperature). It is also assumed that over a reasonable range an over-all transfer coefficient

$$U^* \equiv \frac{Q_2}{(t_w - t_c)\,A_c}$$

is a constant. These assumptions lead to a fixed unit price for heat-transfer capability U^*A_c exactly analogous to the case of the conventional condensing system. An appropriate ratio between these unit costs has been deduced from data in a paper by J. Lichtenstein (5) to be approximately 3.5. Accordingly a value of $A_cU^* = 0.235$ \$/Btu deg F has been adopted for the illustrative purposes of this paper. This corresponds to a value of $c_e/c_{ex} = 19 \times 10^{-6}$. Fig. 4 has been constructed by the methods of reference (1) to relate balanced condenser and exhaust-annulus areas and to indicate the derivative of stagnation enthalpy h_2° with respect to investment per unit of exhaust flow,

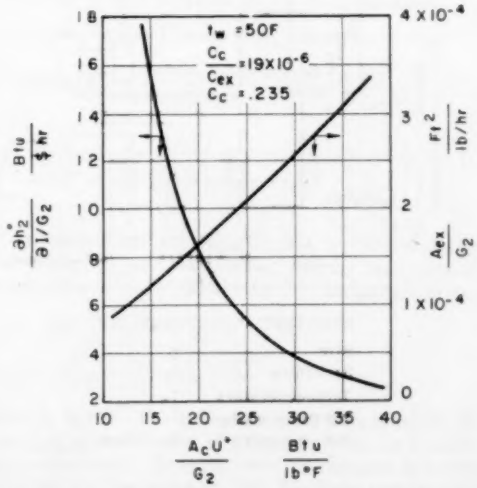

FIG. 4 PERFORMANCE OF BALANCED COOLING TOWER, CONDENSER, AND EXHAUST ANNULUS FOR 50 F WET-BULB TEMPERATURE

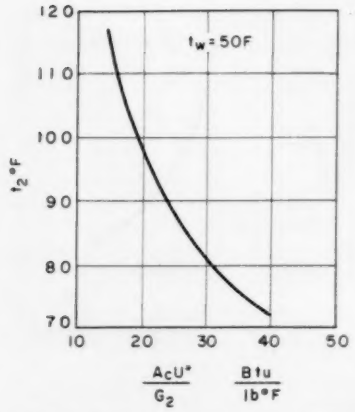

FIG. 5 CONDENSING TEMPERATURE VERSUS CONDENSER AREA (t_w = 50, c_c/c_{ex} = 19.0 × 10^{-6})

I/G_2, for this cost ratio. Similarly Fig. 5 plots the condensing temperature versus $A_c U^*/G_2$.

7 *All other items*, category 1. It is assumed that the foregoing listing includes all the significant variables from the standpoint of an economic analysis.

ANALYSIS

Fig. 6 summarizes the various assumptions made in the preceding paragraphs. It is seen that the items of investment which are variable from the standpoint of optimization are

I_3, boiler-plant equipment
I_4, feedwater heaters
$I_8 = I_{ex} + I_c$, exhaust annulus-condensing system

The problem consequently involves four components. It is reduced to a three-component problem by virtue of existing balancing relations for the exhaust annulus and condenser. Further, the economic cross effects between heaters and the other components are of a particularly simple kind in view of our assumption of a fixed per-heater cost. This results in the possibility of independent selection of the number of heaters and a subsequent two-component analysis of exhaust system and boiler.

The problem is to satisfy for each plant the condition

$$\frac{dc_{op}}{dI} = -\frac{c_F}{8760\,PL} \quad \ldots\ldots\ldots\ldots\ldots [1]$$

where the derivative is taken subject to all the restrictions discussed, including maintenance of balance between component investments and of constant plant output.[9] We seek to define the component selections consistent with these constraints.

OPERATING COST RELATED TO PLANT AND TURBINE HEAT RATES

The unit cost of operation is presumed to vary only with the plant heat rate

$$c_{op} = \text{const} + 0.30 \times 10^{-4}\,(\text{plant heat rate}) \quad \ldots\ldots [4]$$

Now the plant heat rate depends on the turbine heat rate, generator efficiency η_g, boiler efficiency η_b, and auxiliary power consumption P_{aux}[10]

$$\text{Plant heat rate} = \frac{\text{turbine heat rate}}{\eta_b \eta_g \left(1 - \frac{P_{aux}}{P}\right)}$$

$$= \frac{\text{turbine heat rate}}{0.88 \times 0.98 \times 0.94}$$

$$= 1.234\,(\text{turbine heat rate}) \quad \ldots\ldots [5]$$

Combining with Equation [4] and differentiating

[9] Although it is not important that an exact predetermined net capability should be maintained, there would seem to be no excuse for not utilizing the capacity of the turbogenerator purchased. For this reason the author has chosen to maintain the gross output, i.e., electric power generated, a constant.

[10] P_{aux}/P is taken fixed at 0.06; variations in this value due to circulating water-system changes, for example, are capitalized and included in the incremental unit costs.

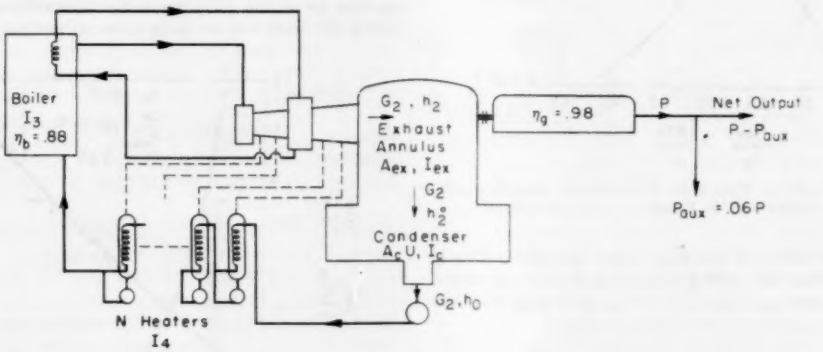

CONSTANT INVESTMENT		VARIABLE INVESTMENTS*	
Site	I_1	Boiler	I_3 = Const. + 5.6 × 10^{-3} × Heat Release
Structure	I_2	Heaters	I_4 = 8 × 10^4 × N
Turbogenerators	I_5	Exhaust Annulus	I_{ex} = 1.22 × 10^4 × A_{ex}
All Other Items Not Indicated	I_7	Condenser	I_c = .0671 × $A_c U$ or .235 $A_c U$*

*Includes: (1) Equipment Cost; (2) Engineering and Construction Overheads; (3) Capitalizations of Variations in P_{aux}; (4) Circulating Water Systems.

FIG. 6 SUMMARY OF ASSUMPTIONS FOR OPTIMIZATION ANALYSIS

$$\frac{dc_{op}}{dI} = 0.370 \times 10^{-6} \frac{d(\text{turbine heat rate})}{dI} \quad [6]$$

Turbine Heat Rate Related to Exhaust Conditions

The variation in generator output with $h_2°$ as G_2 and Q_1 remain constant is

$$P = \text{const} - \frac{G_2 \Delta h_2°}{3413} \eta_g \quad [7]$$

If the turbine heat rate is assumed to be independent of small changes in throttle flow, its dependence on $h_2°$ as P remains fixed can be calculated by finding its derivative with respect to $h_2°$ as the throttle (hence boiler) flow remains constant

$$\left(\frac{\partial(\text{turbine heat rate})}{\partial h_2°}\right)_P = \left(\frac{\partial(\text{turbine heat rate})}{\partial h_2°}\right)_{G_1}$$

Differentiating the definition of turbine heat rate

$$\left(\frac{\partial}{\partial h_2°} \frac{\eta_g Q_1}{P}\right)_{G_1} = \left(\frac{\partial}{\partial h_2°} \frac{\eta_g (\Delta h)_1 G_1}{P}\right)_{G_1}$$

$$= \frac{\eta_g G_1}{P} \left(\frac{\partial (\Delta h)_1}{\partial h_2°}\right)_{G_1} - \frac{\eta_g G_1 (\Delta h)_1}{P^2} \left(\frac{\partial P}{\partial h_2°}\right)_{G_1}$$

$$= \frac{\eta_g G_1}{P} \left(\frac{\partial (\Delta h)_1}{\partial h_2°}\right)_{G_1} - \frac{(\text{turbine heat rate})}{P} \left(\frac{\partial P}{\partial h_2°}\right)_{G_1}$$

For an infinite number of feed heaters $(\Delta h)_1$ is independent of $h_2°$, and this independence is very closely approximated when there is a reasonable number of heaters in the cycle; i.e.

$$\left(\frac{\partial (\Delta h)_1}{\partial h_2°}\right)_{G_1} \cong 0$$

Then if we differentiate Equation [7]

$$\left(\frac{\partial P}{\partial h_2°}\right)_{G_1} = -\frac{G_2}{3413} \eta_g$$

and substitute in the previous expressions

$$\left(\frac{\partial(\text{turbine heat rate})}{\partial h_2°}\right)_P = \frac{(\text{turbine heat rate})\, \eta_g G_2}{3413\, P} \quad [8]$$

(This relationship is slightly in error because of the assumption in Equation [7] that G_2 is constant. Actually the extraction for feed heating will depend on h_2. This effect has been calculated in a particular case and found to be of substantially negligible proportions.)

Turbine Heat Rate Related to Condenser and Exhaust Annulus Investments

In view of Equation [8]

$$\frac{\partial(\text{turbine heat rate})}{\partial I_s} = \frac{\partial(\text{turbine heat rate})}{\partial h_2°} \frac{\partial h_2°}{\partial I_s}$$

$$= \frac{\text{turbine heat rate}}{3413\, P} \eta_g G_2 \frac{\partial h_2°}{\partial I_s}$$

$$= \frac{\text{turbine heat rate}}{3413\, P} \eta_g \frac{\partial h_2°}{\partial \left(\frac{I_s}{G_2}\right)} \quad [9]$$

This latter derivative is taken for

$$h_2° = f(I_s/G_2) = f(I_c/G_2 + I_{ex}/G_2)$$

where the distribution of investments between I_c and I_{ex} is balanced. This is exactly the sort of data which has been adduced by the methods of reference (1) and recorded on Figs. 1 and 2.

Plant Investment Related to Condenser and Exhaust Annulus Investment

If we now note that for N = const the plant investment varies only with the exhaust system and the boiler investments

$$I = \text{const} + I_s + I_s$$

$$\frac{\partial I}{\partial I_s} = \frac{\partial I_s}{\partial I_s} + 1 \quad [10]$$

where

$$I_s = \text{const} + 5.6 \times 10^{-3} (\text{heat release}) \quad [11]$$

$$= \text{const} + 5.6 \times 10^{-3} \left(\frac{Q_1}{0.88}\right)$$

$$= \text{const} + 5.6 \times 10^{-3} \left(\frac{\text{turbine heat rate}}{0.88}\right) \left(\frac{P}{\eta_g}\right)$$

$$\frac{\partial I_s}{\partial I_s} = \frac{5.6 \times 10^{-3}}{0.88} \left(\frac{P}{\eta_g}\right) \left[\frac{\partial(\text{turbine heat rate})}{\partial I_s}\right]_P$$

Introducing Equation [9]

$$= \frac{5.6 \times 10^{-3}}{0.88} P \left(\frac{\text{turbine heat rate}}{3413\, P}\right) \frac{\partial h_2°}{\partial \left(\frac{I_s}{G_2}\right)}$$

$$= 1.87 \times 10^{-6} (\text{turbine heat rate}) \frac{\partial h_2°}{\partial \left(\frac{I_s}{G_2}\right)} \quad [12]$$

So in view of Equation [10]

$$\frac{\partial I}{\partial I_s} = \left[1 + 1.87 \times 10^{-6} (\text{turbine heat rate}) \frac{\partial h_2°}{\partial \left(\frac{I_s}{G_2}\right)}\right] \quad [13]$$

Operating Cost Related to Plant Investment

Finally, if we combine Equations [6], [9], and [13]

$$\frac{dc_{op}}{dI} = 0.370 \times 10^{-6} \left(\frac{\text{turbine heat rate}}{3413\, P}\right) \eta_g \left[\frac{\partial h_2°}{\partial (I_s/G_2)}\right]$$

$$\times \left[\frac{1}{\left(1 + 1.87 \times 10^{-6} (\text{turbine heat rate}) \left[\frac{\partial h_2°}{\partial (I_s/G_2)}\right]\right)}\right] \quad [14]$$

Since P is constant and $\partial h_2°/\partial(I_s/G_2)$ is a function of $A_c U/G_2$ which also fixes $h_2°$ and consequently turbine heat rate, the appropriate value of $(dc_{op})/(dI)$ as defined by Equation [1] establishes

$$\frac{A_c U}{G_2}, \frac{A_{ex}}{G_2}$$

and thence I_s, I_s, etc. Using the data in the form provided, the solutions for each combination of c_s/c_{ex} and N can be found by an iterative procedure. However, since the variation in turbine heat rate from the base value of 7880 Btu/kwhr corresponding to 5 heaters and a vacuum of 1.5 in. Hg is small, a very good approximation for the dc_{op}/dI relationship becomes

$$\frac{dc_{op}}{dI} = \frac{0.370 \times 10^{-6}}{3413} \times \frac{7880}{150 \times 10^{3}} \eta_g \left[\frac{\partial h_2^\circ}{\partial(I_s/G_2)}\right] \times \left[\frac{1}{1 + 1.87 \times 10^{-6} \times 7880 \left[\frac{\partial h_2^\circ}{\partial(I_s/G_2)}\right]}\right]$$

$$= 5.60 \times 10^{-12} \left[\frac{\partial h_2^\circ}{\partial(I_s/G_2)}\right] \left[\frac{1}{\left(1 + 0.015 \frac{\partial h_2^\circ}{\partial(I_s/G_2)}\right)}\right] \quad [15]$$

Criterion for Specifying Condenser and Exhaust Annulus

For the values of fixed charges, rating, and load factor assumed, Equation [1] becomes

$$\frac{dc_{op}}{dI} = -\frac{0.14}{8760 \times 150 \times 10^{3} \times 0.80} = -1.333 \times 10^{-10}$$

So

$$\frac{\partial h_2^\circ}{\partial(I_s/G_2)} \left[\frac{1}{1 + 0.015 \frac{\partial h_2^\circ}{\partial(I_s/G_2)}}\right] = \frac{-1.333 \times 10^{-10}}{5.60 \times 10^{-12}} = -23.8$$

or

$$\frac{\partial h_2^\circ}{\partial(I_s/G_2)} = -17.5$$

Specification of Condenser and Exhaust Annulus

This value of —17.5 for

$$\frac{\partial h_2^\circ}{\partial(I_s/G_2)}$$

defines, through Figs. 2 and 4, the condenser and annulus areas which are economically correct for the conventional plant and the cooling-tower plant. For the conventional plant these areas are

$$\frac{A_c U}{G_2} = 22 \text{ Btu/lb deg F}$$

$$\frac{A_{ex}}{G_2} = 1.05 \times 10^{-4} \text{ sq ft/lb/hr}$$

For the cooling-tower plant they are[11]

$$\frac{A_c U^*}{G_2} = 14.2 \text{ Btu/lb deg F}$$

$$\frac{A_{ex}}{G_2} = 1.17 \times 10^{-4} \text{ sq ft/lb/hr}$$

Selection of Feed Heaters

To justify the addition of a heater we must satisfy the condition

$$\left|\frac{\Delta c_{op}}{\Delta I}\right| \leq \left|-\frac{c_F}{8760\,PL}\right| \quad [1a]$$

where ΔI comprises not only the incremental heater cost but the concomitant changes in other component investments.

In view of Equation [6] this condition may be rewritten

$$\left|0.370 \times 10^{-6} \frac{\Delta(\text{turbine heat rate})}{\Delta I}\right| \leq \left|\frac{c_F}{8760\,PL}\right| \quad [16]$$

or putting in our assumed values for c_F, P, and I

$$|\Delta(\text{turbine heat rate})| \leq \left|-\Delta I \frac{0.14}{8760 \times 0.15 \times 10^{6} \times 0.80 \times 0.370 \times 10^{-6}}\right|$$

$$\leq \left|-\Delta I \times 0.360 \times 10^{-3}\right| \frac{\text{Btu/kwhr}}{\$} \quad [17]$$

For each proposed heater addition the Δ (turbine heat rate) is found from Table 1. The change in boiler investment is found from Equation [11] which together with Equation [5] yields

$$\Delta I_3 = 5.6 \times 10^{-3} \times 1.234\ \Delta(\text{turbine heat rate}) \times 150{,}000$$
$$= 1037\ \Delta(\text{turbine heat rate}) \quad [18]$$

The change in condenser investment is

$$\Delta I_c = \frac{A_c U}{G_2} \Delta G_2 c_c$$

and in exhaust-annulus investment

$$\Delta I_{ex} = \frac{A_{ex}}{G_2} \Delta G_2 c_{ex}$$

whence

$$\Delta I_s = \left(\frac{A_c U}{G_2} c_c + \frac{A_{ex}}{G_2} c_{ex}\right) \Delta G_2$$

For the two plants this yields

$$\Delta I_s \text{ (conventional)} = (22 \times 0.0671 + 1.05 \times 10^{-4} \times 1.22 \times 10^{4}) \Delta G_2$$
$$= 2.75\ \Delta G_2\ \$ \quad [19a]$$

and

$$\Delta I_s \text{ (cooling tower)} = (14.2 \times .235 + 1.17 \times 10^{-4} \times 1.22 \times 10^{-4}) \Delta G_2$$
$$= 4.77\ \Delta G_2\ \$ \quad [19b]$$

In both these expressions ΔG_2 may be found from Equation [3]

$$\Delta G_2 = \frac{153{,}000}{h^\circ_2 - h_0}\ \Delta(\text{turbine heat rate}) \quad [3]$$

For the purposes of this computation $(h_2^\circ - h_0)$ may be approximated by the value associated with the base plant; h_2 is found from Fig. 1, $(h_2^\circ - h_2) = 10$ and h_0 is found from the steam tables to be 59.7.

[11] See item 4 in preceding section.

TABLE 2 CALCULATION OF ECONOMIC JUSTIFICATION FOR ADDITIONAL FEED HEATERS

Change in number of heaters	Δ turbine heat rate	ΔG_2	ΔI_3 (boiler)	ΔI_s (condenser and exhaust annulus) Conventional	ΔI_s (condenser and exhaust annulus) Cooling tower	ΔI_s (heaters)	ΔI Conventional	ΔI Cooling tower	Minimum justified Δ turbine heat rate, $-\Delta I \times 0.360 \times 10^{-3}$ Conventional	Minimum justified Δ turbine heat rate, $-\Delta I \times 0.360 \times 10^{-3}$ Cooling tower
5 to 4	64	10560	+66100	+29000	+50400	−80000	15100	36500	5.43	13.1
5 to 6	−46	−7590	−47500	−20900	−36200	+80000	11600	−37000	4.17	−1.33
6 to 7	−36.5	−6020	−37700	−16550	−28800	+80000	25750	13500	9.26	4.85
7 to 8	−29.5	−4870	−30500	−13400	−23200	+80000	36100	29300	13.0	10.5
8 to 9	−22.5	−3710	−23200	−10200	−17700	+80000	46600	39100	16.8	14.1
9 to 10	−17.5	−2890	−18100	−7950	−13800	+80000	59950	48100	21.5	17.3

$$h_2^\circ - h_2 \approx 977 + 10 - 59.7 = 927.3 \text{ Btu/lb}$$

whence

$$\Delta G_2 \approx 165\ \Delta(\text{turbine heat rate}) \quad \ldots\ldots\ldots [20]$$

Table 2 is a computation of ΔI's corresponding to the Δ(turbine heat rate)'s based on the foregoing analysis. The decrease in turbine heat rate is seen to exceed $0.360 \times 10^{-3}\ \Delta I$ for the addition of the ninth heater in the conventional plant. A tenth heater is similarly justified for the cooling-tower plant.

Determination of Final Turbine Heat Rates

The heat rates of the optimized plants are found from turbine heat rates which are established by "correcting" the 7880 Btu/kwhr value (presumed to have been calculated accurately) for the base plant. From Table 1 we find the corrections for additional feed heaters to be —134.5 Btu/kwhr for the conventional plant and = —152.0 Btu/kwhr for the cooling-tower plant. The corrections due to the exhaust-system modifications are found using Equation [8]

$$\Delta(\text{turbine heat rate}) = \Delta h_2^\circ \frac{(\text{turbine heat rate})\ \eta_g G_2}{3413P} \quad \ldots [8]$$

Except for Δh_2° all the items on the right side of this equation may be given their values for the base plant. From Equation [2]

$$G_2 = \frac{(\text{turbine heat rate} - 3413)P}{\eta_g(h_2^\circ - h_0)}$$

So Equation [8] may be rewritten

$$\Delta(\text{turbine heat rate}) = \Delta h_2^\circ \frac{(\text{turbine heat rate})\ (\text{turbine heat rate} - 3413)}{3413\ (h_2^\circ - h_0)}$$

$$= \Delta h_2^\circ \frac{7880\ (7880 - 3413)}{3413 \times 927.3} = 11.2\ \Delta h_2^\circ$$

Figs. 3 and 5 indicate condensing temperatures of 103.5 and 115.2 F corresponding to the condenser areas chosen for the conventional and cooling-tower plants, respectively. Referring to Fig. 1, corresponding values of the stream enthalpy h_2 and final moisture $(1 - x)_2$ are found to be 991.5 Btu/lb and 11.1 per cent and 1006.9 Btu/lb and 10.2 per cent.

The specific volumes can be calculated directly from these data and introduced into the relationship

$$h_2^\circ - h_2 = \frac{\left(\dfrac{v_2}{A_{ex}/G \times 3600}\right)^2}{2gJ} \quad \ldots\ldots [21]$$

to determine leaving losses of 12 and 4.8 Btu/lb, respectively, for the conventional and cooling-tower plants. The corresponding stagnation enthalpies h_2° are 1003.5 and 1011.7. For the base plant $h_2^\circ = 987$. Thus Δh_2° (conventional) = 1003.5 — 987 = 16.5 and Δh_2° (cooling tower) = 1011.7 — 987 = 24.7. The corresponding corrections to the turbine heat rates are 185 and 277, respectively. Adding the corresponding corrections

Turbine heat rate = 7880 — 134.5 + 185
= 7930.5 Btu/kwhr for the conventional plant

Turbine heat rate = 7880 — 152.0 + 277
= 8005 Btu/kwhr for the cooling-tower plant

Assignment of Component Investments

We are now in a position to evaluate the increase in investments in the several components relative to the corresponding

TABLE 3 COMPARISON OF INVESTMENTS IN THREE PLANTS

① Plant	② Turbine HR, Btu/kwhr	③ Plant HR $1.234 \times$ ②, Btu/kwhr	④ Δ(Plant HR), Btu/kwhr	⑤ Heat release $150000 \times$ ③, Btu/hr	⑥ Δ(heat release), Btu/hr	⑦ ΔI_1 (boiler) $5.6 \times 10^{-4} \times$ ⑥, $	⑧ N No. heaters	⑨ ΔN	⑩ ΔI_2 (heaters) $80,000 \times$ ⑨, $	⑪ Q_2 THR $\times$ 3413, Btu/kwhr	⑫ $(h_2^\circ - h_0)$, Btu/lb
Base	7880	9723		1458 $\times 10^4$			5			4467	927.3
Conventional	7930.5	9785.3	62.3	1468 $\times 10^4$	9.34 $\times 10^6$	52.2 $\times 10^3$	9	4	320 $\times 10^3$	4517.5	932.4
Cooling tower	8005	9877.2	154.2	1482 $\times 10^4$	13.13 $\times 10^6$	73.5 $\times 10^3$	10	5	400 $\times 10^3$	4592	930.6

① Plant	⑬ $\frac{G_2}{150,000} \times \frac{⑪}{0.98}$, lb/hr	⑭ $A_c U/G_2$, Btu/lb deg F	⑮ c_e $/Btu/hr deg F	⑯ I_c (Condenser) ⑬ × ⑭ × ⑮, $	⑰ ΔI_c $	⑱ A_{ex}/G_2, sq ft/lb/hr	⑲ c_{ex}, $/sq ft	⑳ I_{ex} (ex annulus) ⑬ × ⑱ × ⑲, $	㉑ ΔI_{ex}, $	㉒ $\Sigma\Delta I$ ⑦ + ⑩ + ⑰ + ㉑, $	㉓ ΔC_p $(c_p \times \Delta I)$ 0.14 × ㉒, $/yr	㉔ ΔC_{op} 8760 × 150,000 × 0.80 × 0.30 × 10^{-4} × ④, $/yr
Base	737.3 $\times 10^4$	29.25	0.0671	1.447 $\times 10^6$		1.535 $\times 10^{-4}$	1.22 $\times 10^{-4}$	1.391 $\times 10^6$				
Conventional	741.6 $\times 10^4$	22.0	0.0671	1.095 $\times 10^6$	−353 $\times 10^3$	1.05 $\times 10^{-4}$	1.22 $\times 10^{-4}$	0.950 $\times 10^6$	−441 $\times 10^3$	−421.8 $\times 10^3$	−59100	19600
Cooling tower	755.3 $\times 10^4$	14.2	0.235	2.488 $\times 10^6$	1041 $\times 10^3$	1.17 $\times 10^{-4}$	1.22 $\times 10^{-4}$	1.078 $\times 10^6$	−313 $\times 10^3$	1201.5 $\times 10^3$	168300	48500

components of the base plant. Table 3 summarizes the necessary computations and makes the final comparisons.

Comparison of the final two columns indicates a net yearly saving of $39,500 for the balanced and optimized conventional plant as compared to the arbitrarily selected base plant. On the basis of the incremental unit component costs this saving is the consequence of adding $320,000 worth of heaters and $52,200 worth of boiler and reducing condenser and exhaust annulus investments by $352,000 and $441,000.

The corresponding comparison for the cooling-tower plant is less meaningful because the conditions imposed are different. The difference in condenser investment indicated in column 16 is probably in error because it is based on the assumption that the incremental unit costs are applicable to the entire condensing-investment. On the other hand, this does not invalidate the component choices dictated by the analysis.

Conclusions

The procedure outlined and illustrated in the foregoing is, of course, not the whole story with respect to the selection of power-plant components. It remains to choose an available exhaust annulus and to make other practical compromises as well as to perform a conventional heat balance. This method is, however, a straightforward analysis which includes the somewhat subtle interactions between the various component choices and narrows without resort to cut and try the limits within which the choices should be made.

BIBLIOGRAPHY

1 "An Approach to the Economic Problem of Matching Condenser Surface With Exhaust Annulus Area," by W. A. Wilson and L. G. Malouf, Trans. ASME, vol. 78, 1956, pp. 135–141.

2 "Steam Turbines and Their Cycles," by J. K. Salisbury, John Wiley & Sons, Inc., New York, N. Y., 1950.

3 "Thermal Performance of Modern Steam Turbines," by H. R. Reese and J. P. Carlson, *Mechanical Engineering*, vol. 74, 1952, pp. 205–211.

4 "Economic Determination of Condenser and Turbine-Exhaust Sizes," by E. H. Miller and A. Sidun, Trans. ASME, vol. 77, 1955, pp. 373–383.

5 "Economic Comparison of River and Cooling Tower Circulating Water Systems," by J. Lichtenstein, ASME Paper No. 54—SA-37, unpublished.

Applications of an Enthalpy-Fuel/Air Ratio Diagram to "First Law" Combustion Problems

By H. N. POWELL,[1] CINCINNATI, OHIO

An "absolute enthalpy" is defined which has the advantage that the enthalpies of different systems are similar and compatible quantities regardless of differences in state or chemical composition. An enthalpy-fuel/air ratio diagram for equilibrium state combustion gases is formulated using absolute enthalpies. On this diagram, virtually all processes which involve combustion and combustion product gases—and which are entirely within the scope of the first law of thermodynamics—can be represented by straight lines. Such a diagram therefore provides a very rapid and flexible method of solving many frequently occurring combustion problems. Procedures for handling the following typical problems are developed: Determination of adiabatic flame temperatures, theoretical heat releases, combustion efficiencies (from experimental temperature measurements), and the adiabatic mixing of two streams. Absolute enthalpy and heat-capacity data for $(CH_2)_y$-air (in 100 R increments) and $(CH_2)_y$-air (in 50 K increments) systems are tabulated for lean and rich composition ranges. Above $\sim$ 3000 R $\sim$ 1400 K the enthalpy and heat-capacity functions are pressure sensitive and the tabulated data are for 1 atm.

Nomenclature

The following nomenclature is used in the paper:

Superscript (°) indicates quantity is identified with the standard thermochemical reference temperature, $T° = 25$ C $= 77$ F.

Subscript ($_i$) indicates quantity pertaining to a previous fuel + air system to which additional fuel is added.

c_p = heat capacity of equilibrium mixture per unit weight of mixture

e = absolute internal energy per unit weight of mixture

f, f_s = fuel/air weight ratio, and the stoichiometric fuel/air weight ratio, respectively; dimensionless

f' = "effective" fuel/air weight ratio for η_f calculations

H_i = absolute enthalpy of the ith pure constituent, Btu per lb-mol of i

$H_{0i}° = H_i$ at $T = 0$ K $= 0$ R

h, h_A, h_F = absolute enthalpy of mixture, of air, and of fuel, respectively, Btu/lb

$(1 + f)h$ = absolute enthalpy of fuel + air mixture (burned or unburned) per unit weight of original air

$(1 + f)h'$ and $(1 + f)h''$ = "effective" enthalpies of fuel + dry air mixtures, per unit weight of original air, which are associated with the temperatures T' and T'', respectively

m, m_i, m_F = mean molecular weight of mixture, of pure species i, and formula weight of fuel, respectively; all in lb per lb-mol

$M = \dfrac{f}{f_s + f} = \dfrac{r}{1 + r}$ = fuel-air mixture proportion parameter

n_i = mol weights of pure constituent i per unit weight of mixture

$n_i' = (1 + f)n_i$ = mol weights of pure constituent i per unit weight of original air

p = pressure, atm

q = theoretical heat release per unit weight of mixture

$q_f°$ = fuel's heat of combustion, per unit weight of fuel at $p = 1$ atm and $T°$

$(1 + f)q$ = theoretical heat release per unit weight of original air

$(1 + f)q'$ = "effective" heat release per unit weight of original air for η_q calculations

$r = f/f_s$ = equivalence ratio

$T°$ = adiabatic combustion temperature for complete combustion, $\eta_f = \eta_q = 100$ per cent

T' = an experimentally determined combustion temperature

T'' = an experimentally measured temperature after the hot combustion gases have been cooled by addition of quench water

w = weight ratio of additional water to original dry air

x = H/C atom ratio of fuel

z_a and z_b = weight ratio of original air in (a) or (b) stream, respectively, to the total original air in the combined (a) and (b) streams

η_q = combustion efficiency defined on an "equivalent heat loss" basis

η_f = combustion efficiency defined on an "equivalent fuel consumption" basis

Introduction

There has long been a pressing need in many scientific and engineering fields for detailed data on the thermodynamic properties of combustion gases at high temperatures. The advent of the high-speed computer now makes it possible to carry out these evaluations on a scale which hitherto was completely impracticable. In view of these developments, it is important that the calculations be organized in a way which permits the greatest generality, flexibility, and clarity for subsequent applications to specific problems.

The object of the present paper is to develop and illustrate a particularly convenient and general method for dealing with several commonly occurring combustion problems which fall entirely within the scope of the first law of thermodynamics. The method largely depends on the availability of data which have been computed on an "absolute" reference state basis (to be

[1] Aircraft Gas Turbine Division, General Electric Company.

Contributed by the Gas Turbine Power Division and presented at a joint session of the Gas Turbine Power and Machine Design Divisions at the Semi-Annual Meeting, Cleveland, Ohio, June 17–21, 1956, of The American Society of Mechanical Engineers.

Note: Statements and opinions advanced in papers are to be understood as individual expressions of their authors and not those of the Society. Manuscript received at ASME Headquarters, April 25, 1956. Paper No. 56—SA-68.

defined). To date, only the tabulations prepared by S. R. Brinkley, Jr., and his various associates (1, 2, 3, 4),[2] have used this basis. It is hoped that the present paper will provide a sufficient incentive for a general use of the absolute reference state in future computations.

Part 1 deals with the formulation of the enthalpy-fuel/air ratio diagram in two forms and their use for constant-pressure combustion processes. Completely equivalent internal energy-fuel/air ratio diagrams can be constructed for constant volume processes as discussed at the end of Part 1.

Part 2 lists some h and c_p data for $(CH_2)_y$-air and $(CH_2)_y$-air combustion products.

1—THE ENTHALPY-FUEL/AIR RATIO DIAGRAM AND APPLICATIONS

The Enthalpy-Fuel/Air Ratio Diagram

The sense of the definition of absolute enthalpies is given by

$$\text{Absolute enthalpy} = \left\{\begin{array}{l}\text{sensible heat at}\\ T \text{ above that}\\ \text{at } T = 0\text{ R}\end{array}\right\} + \left\{\begin{array}{l}\text{heat of formation at } T = 0\text{ R}\\ \text{from the elements in their standard reference states at } T = 0\text{ R}\end{array}\right\}$$

in which the standard reference states for the elements of interest in hydrocarbon-air combustion gases are

A as A	(ideal gas)	pressure = 1 atm temperature = 0 R
N as N_2	(ideal gas)	
O as O_2	(ideal gas)	
H as H_2	(ideal gas)	
C as C_s	(graphite, solid)	

For a pure chemical constituent i, the foregoing definition is fulfilled by the identity

$$H_i = (H_i - H_{0i}^\circ) + H_{0i}^\circ \quad \ldots\ldots [1]$$

in which $(H_i - H_{0i}^\circ)$ is the sensible energy part and H_{0i}° is the heat of formation of the constituent from its elements at absolute zero. Both the sensible and "zero heat of formation" parts are listed in the NBS-API tables (5) for most of the chemical species of interest in hydrocarbon-air combustion gases. By way of illustration, we may calculate the H_i values of some typical pure constituents of combustion gases. For future convenience the H_i°'s which pertain to a particular temperature, T°, will be calculated (Table 1). The same procedure can of course be used to calculate the H_i°'s for any other temperature. It is noteworthy that H_{O_2} contains no chemical energy (heat of formation at absolute zero) term. In general this is true for all the species, O_2, N_2, A, H_2, and $C_{(s)}$ since, by definition, their reference state energy is zero. For a pure species, $h_i = H_i/m_i$.

TABLE 1 SOME VALUES OF H_i° AT THE REFERENCE TEMPERATURE, T°

T° = 298.17° K = 25° C = 77° F

(The source table designation in reference (5) is noted under each quantity.)

H_i°	=	$(H_i^\circ - H_{0i}^\circ)$ 0u	+	H_{0i}° 0w	=	H_i° cals/gm-mol	=	H_i° Btu/lb-mol
$H_{CO_2}^\circ$	=	2238.1	+	(−93968.6)	=	−91730.5	=	−165006.0
$H_{H_2O}^\circ$	=	2365.1	+	(−57104.3)	=	−54739.2	=	−98464.7
$H_{O_2}^\circ$	=	2069.8	+	0	=	+ 2069.8	=	+3723.1

The absolute enthalpy of a mixture is given by the simple additive relation

$$h = \sum_i n_i H_i \quad \ldots\ldots [2]$$

in which n_i is the number of mol weights of i per unit weight of mixture, and H_i is the absolute molal enthalpy of i as determined by Equation [1]. Upper case letters indicate a "per mol" basis and lower case a "per unit weight" basis.

Since, by definition, the energy content of the elements in their standard reference states (T = 0 R) is zero, this state establishes an absolute, zero-enthalpy, reference state for h which is common to all single or multiconstituent systems regardless of their chemical composition. And furthermore, as long as the H_i are correctly associated with the specified solid, liquid, or gaseous state of the respective i constituents, there is no restriction on the number of phases which are present in a given system in so far as the definition of h is concerned. It is not necessary that the system be homogeneous or that the constituents even be at the same temperature. Consequently, the absolute enthalpies of different fuel-air mixtures, burned as well as unburned—in fact, of any arbitrary composition involving any number of phases—are all similar and compatible quantities.

In dealing with combustion problems, particular interest centers on the h's which pertain to equilibrium states of the combustion products; i.e., those in which the n_i satisfy the free energy and material balance relationships for particular combinations of the independent variables. From a property-evaluation standpoint the four independent variables for equilibrium state hydrocarbon-air combustion gases are T, p, f, and the H/C ratio of the fuel. Computing machines render their greatest service in calculating the equilibrium n_i values.

The sensible-heat portion of the absolute enthalpy of an equilibrium mixture is always positive in sign, but the zero heats of formation of the principal combustion products, CO_2 and H_2O, are numerically large and negative in sign, so that the resulting absolute enthalpy may be positive or negative, depending on which of the two contributions is greater. Numerically speaking, the appearance of negative enthalpies is a characteristic feature which usually indicates the use of an "absolute" zero-enthalpy reference state.

In the ranges of temperature and pressure commonly of interest in combustion problems, all the constituents are in the gas phase and may be regarded with negligible error as individually obeying the ideal gas law; i.e., the H_i are functions of T alone. In very fuel-rich combustion gases, solid carbon may be present, but $H_{C(s)}$ is still dependent only on T. The net result is that for a fixed f, all departures from ideal equation of state behavior, in the sense that $(\partial h/\partial p)_T \neq 0$, and so on, are due to variations of the equilibrium n_i with T and p.

The absolute enthalpy of air may be obtained from enthalpy tabulations (6) which are referred to T = 0 R by merely subtracting 1.75 Btu/lb to account for the zero heat of formation of the 0.03 per cent CO_2; all other constituents having $H_{0i}^\circ = 0$.

Now consider Equation [2] as applying to an equilibrium system and multiply it through by $(1 + f)$

$$(1 + f)h = \sum_i n_i' H_i \quad \ldots\ldots [3]$$

in which $n_i' = (1 + f)n_i$. Note that since f is the fuel/air weight ratio, $(1 + f)$ is the weight of mixture per weight of original air (or oxidant), i.e., $(1 + f)h$ is the gross mixture enthalpy and n_i' is the equilibrium number of mols of i, both quantities on a per unit weight of original air (or oxidant) basis. At low to moderate temperatures the degree of dissociation is negligible or very small, with the result that the only sizable $(n_i'H_i)$ terms are those which pertain to the principal products of combustion, H_2O, CO_2, N_2, and so on. Therefore, when a hydrocarbon fuel is added to a fixed quan-

[2] Numbers in parentheses refer to the Bibliography at the end of the paper.

tity of original air, the changes in the amounts of hydrogen, carbon, and oxygen containing compounds in the final combustion products are proportional to the amount of added fuel, i.e., in differential form, $df \sim dn'_{CO_2} \sim dn'_{H_2O} \sim -dn'_{O_2}$ for lean mixtures, and $df \sim dn'_{CO} - dn'_{CO_2} \sim dn'_{H_2} - dn'_{H_2O}$ for rich mixtures.

Therefore, noting that the H_i are functions of T alone, isotherms of $(1 + f)h$ versus f will exhibit a linear relationship when the foregoing proportionalities are not appreciably disturbed by dissociation. When dissociation is appreciable, the isotherms depart from the straight-line relationship and a graphic picture is presented of the degree of dissociation and the conditions under which it occurs.

Fig. 1 shows an enthalpy-fuel/air ratio diagram containing isotherms of $(1 + f)h$ versus f for a $(CH_2)_y$-air system. Since the isotherms pertain only to equilibrium combustion products, the basic diagram is independent of all specific fuel properties except the H/C ratio. The figure was prepared from the data listed in Part 2. The values of $(1 + f)h$ at intersections of the isotherms with the $f = 0$ axis obviously must correspond to the enthalpy of pure air per unit weight of air. Since the fuel/air equivalence ratio r is proportional to f, the abscissa scale can be made to read in terms of either f or r.

In accord with the foregoing definition of h, the slope of the $(1 + f)h$ versus f isotherms is negative for lean mixtures due to the increasing amounts of CO_2 and H_2O with their large negative heats of formation, and also reflecting the fact that, as more fuel is burned, heat has to be removed from the combustion products to maintain them at the specified isotherm temperature. The sharp minimum in the V-shaped isotherms is at the stoichiometric fuel/air ratio f_s where, ideally speaking, all the free O_2 has been consumed. The positive slope of the isotherms in the rich region stems from the replacement of CO_2 and H_2O with CO and H_2 which have smaller heats of formation.

Although it is not readily apparent from Fig. 1, there is a slight curvature in certain portions of the solid-line isotherms. This effect is caused by the nitric-oxide equilibrium in lean mixtures and the water-gas equilibrium in rich mixtures. Since both these equilibria are equimolar, $(\partial m/\partial T)_p = 0$, $(\partial m/\partial p)_T = 0$ and the locations of the solid-line isotherms are independent of pressure; i.e., $(\partial h/\partial p)_T = 0$, and $(\partial c_p/\partial p)_T = 0$. Consequently, the ideal equation of state, $pv = RT/m$, is applicable in the solid line region of Fig. 1; $(1 + f)/m$ varies only (and linearly) with f (7).

At the higher temperatures indicated by the dotted-line isotherms, nonequimolar equilibria are important and make the location of the isotherms pressure dependent. The location of the boundary between the pressure-dependent and pressure-independent regions is somewhat arbitrary, but the indicated boundary at about 3000 R is conservative for most cases. The indicated dotted-line isotherms are those for 1 atm pressure.

The enthalpy-fuel/air ratio diagram, as illustrated in Fig. 1, constitutes the principal tool in the approach to "first-law" combustion problems as developed in the following sections. Similar diagrams may be made for the functions expressed by the equations

$$(1 + f)c_{p_f} = \sum n_i' C_{p_i} + \sum_i (\partial n_i'/\partial T)_p H_i \quad \ldots\ldots [4]$$

$$(1 + f)/m = \sum_i n_i' \quad \ldots\ldots [5]$$

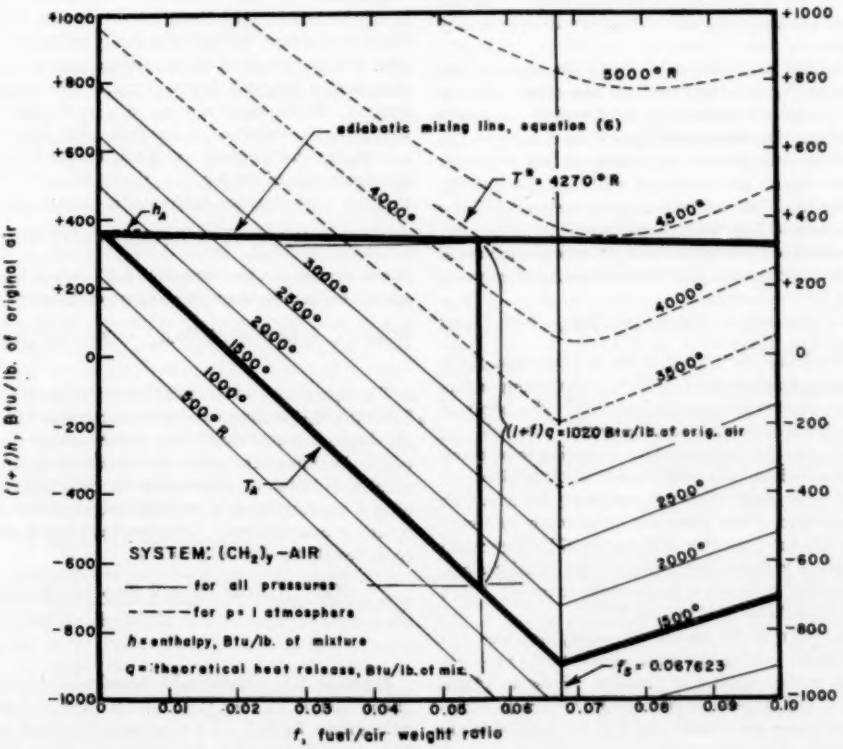

FIG. 1 DETERMINATION OF ADIABATIC FLAME TEMPERATURES AND THEORETICAL HEAT RELEASES
(For problem shown, initial air and fuel [kerosene] temperatures are T_A = 1500 R and T_F = 817 giving indicated results at f = 0.056.)

A more detailed discussion of these and other thermodynamic properties of combustion gases has been reported elsewhere (7).

Adiabatic Flame Temperatures

It is apparent from the definition of an adiabatic constant-pressure process that the absolute enthalpy of a post-combustion mixture must equal that of the same mass of precombustion mixture, independently of the degree of completion of reaction

$$(1 + f)h = h_A + fh_F \quad [6]$$

h_A and h_F are the absolute enthalpies (per unit weight of air and fuel, respectively) in the precombustion mixture and $(1 + f)h$ is the absolute enthalpy (per unit weight of original air) of the completely burned, unburned, or partially burned mixture. Now since the co-ordinates of the enthalpy-fuel/air ratio diagram are $(1 + f)h$ and f, a plot of Equation [6] yields a straight line. Spontaneous changes of composition and temperature are always possible if the gases are not in equilibrium; i.e., when $\eta < 100$ per cent. Therefore, the final temperature T^* for complete combustion can be associated only with an equilibrium state; i.e., for $\eta = 100$ per cent. The functional relationships between the equilibrium $(1 + f)h$ and T, however, are made explicit by the location of the isotherms, and the intersection of the Equation [6] "adiabatic mixing line" with these isotherms identifies the adiabatic T^* at each value of f. Fig. 1 shows such an adiabatic mixing line for a $(CH_2)_y$ kerosene-type fuel.

Since at $f = 0$, $T^* = T_A$, and $(1 + f)h = h_A$, the origin is at the intersection of the T_A isotherm with the $f = 0$ co-ordinate and consequently is independent of fuel variables, depending only on the air temperature, T_A. On the other hand, the slope of the line is equal to the fuel's enthalpy h_F and is therefore independent of the air temperature.

The most convenient procedure is to locate the origin of the line from the known T_A and then evaluate one other point by Equation [6] at an arbitrary value of f (say $f = 0.10$), using the value of h_A read from the diagram at T_A. Then a straight line drawn through these two points determines all the adiabatic flame temperatures which are consistent with the specified T_A and h_F. Any other initial air temperature may be dealt with by simply drawing a parallel line through the new T_A.

In case fuel is added to the products of a preceding combustion reaction (from a fuel of the same H/C ratio) the adiabatic mixing equation is

$$(1 + f)h = (1 + f_1)h_1 + (f - f_1)h_F \quad [7]$$

in which f is the final fuel/air ratio, f_1 is the fuel/air ratio of the preceding combustion reaction and $(1 + f_1)h_1$ is the corresponding absolute enthalpy per unit weight of original air. The origin of the Equation [7] line is at the intersection of the $(1 + f_1)h_1$ and f_1 co-ordinates. In case the products of the preceding combustion reaction are in equilibrium, this origin point also identifies the temperature T_1 of these gases. T_1 is not necessarily the adiabatic combustion temperature of the preceding combustion. As with Equation [6], the left-hand member of Equation [7] is linear with f and the independent variables pertaining to the initial gas and fuel enthalpies manifest themselves in the same manner. When $f_1 = 0$, Equation [7] reduces to Equation [6].

Since Equations [6] and [7] are merely energy balances, the location of an adiabatic mixing line with respect to the $(1 + f)h$ and f co-ordinates is independent of pressure. Pressure affects only the location of the dotted-line isotherms by which the adiabatic flame temperatures are determined, not the independently specified enthalpies.

In practice it may be desirable to account for the effects of additional water in the system which may be due to either moisture in the original air, or quench water added to the hot combustion products. In case the final temperatures are in the dotted-line region of the diagram, the additional moisture will participate in the chemical equilibria and prevent the problem from being handled with complete exactness without a reevaluation of the equilibrium-state properties. However, if the additional water is regarded as a simple diluent, the problem can be handled simply and without large error. The error is entirely negligible if the final "wet" temperature is in the solid-line region. Merely subtract the quantity $w\Delta h_{H_2O}$ from the adiabatic mixing line at the final f, (defined with respect to dry air). w is the weight of additional moisture per unit weight of dry air and Δh_{H_2O} is the increase in enthalpy of the water from its initial temperature (either as a vapor in the initial air or as quench water) to the final "wet" temperature. Since we are dealing with differences in enthalpy, they do not have to be on an "absolute" basis, ordinary steam-table values being suitable. The use of quench water for determining combustion efficiencies is discussed under Combustion Efficiencies.

The determination of h_F is the only aspect of the adiabatic mixing line which remains to be considered. It is convenient to refer h_F to a standard reference absolute enthalpy, $h_F°$, pertaining to a standard reference temperature for thermochemical data, $T°$ (usually 25 C = 77 F)

$$h_F = \Delta h_F + h_F° \quad [8]$$

Δh_F is the sensible heat of the fuel at the fuel temperature T_F relative to that at the reference temperature $T°$. Obviously, if any phase changes occur between $T°$ and T_F, the latent-heat contribution must be included in Δh_F. $h_F°$ is then a constant which is characteristic of a particular fuel. In the case of a pure substance it may be evaluated by Equation [1] from the NBS-API tables (5) or other sources. However, in many instances it is necessary to deal with a mixture of hydrocarbons such as kerosene for which there are no clear-cut thermochemical data except a heat of combustion. In the latter case $h_F°$ can be defined easily in terms of the heat of combustion of the fuel. The derivation is aided by performing an imaginary combustion of the fuel with the stoichiometric amount of oxygen; i.e., the reaction by which, in principle, the heat of combustion of the fuel is determined

$$(CH_x)_y + (y + xy/4)O_2 \rightarrow yCO_2 + xy/2\ H_2O$$

When carried out isothermally at $T°$ and at 1 atm pressure, the energy balance in terms of absolute enthalpies for this reaction is

$$H°_{F(1\text{ or }g)} + (y + xy/4)H_{O_2(g)}° = yH_{CO_2(g)}° + xy/2\ H_{H_2O(g)}° + Q_F° \quad [9]$$

The upper case letters indicate a mol basis for the enthalpies. Since the H_2O is considered to have remained on the vapor phase, $Q_F°$ is the so-called "low" heat of combustion on a per mol of fuel basis. Dividing through by the formula weight of the fuel, $m_F = (12.010 + 1.008x)y$, places both the enthalpy of the fuel and the heat of combustion on a per unit weight of fuel basis as indicated by lower-case letters. After rearrangement and simplification, there results the final expression

$$h_F° = \frac{H_F°}{m_F} = \left[\frac{H_{CO_2}° + x/2\ H_{H_2O}° - (1 + x/4)H_{O_2}°}{12.010 + 1.008x}\right]_{T°} + q_F° \quad [10]$$

Equation [10] permits $h_F°$ to be calculated from the known heat of combustion $q_F°$, the H/C ratio of the fuel x, and the three $H_i°$ values from Table 1. For a kerosene-type fuel with the empirical formula $(CH_2)_y$ and a heat of combustion of 18,630 Btu/lb, $h_F° = -553$ Btu/lb. For ethylene, also conforming to the formula $(CH_2)_y$, and with a heat of combustion of 20,276 Btu/lb,

$h_F^\circ = +1093$ Btu/lb. Note that, depending on the particular fuel, h_F° may be positive or negative which gives the adiabatic mixing line a corresponding positive or negative slope.

Fig. 1 illustrates the determination of T^* for the combustion of the aforementioned kerosene fuel at $T_F = 377$ F $= 837$ R with air at $T_A = 1500$ R, and with $f = 0.056$. With a mean liquid $c_{pF} = 0.5$ Btu/lb deg R, $h_F = -553 + 0.5(377 - 77) = -403$ Btu/lb. Note that the numerical value of h_F is so small that the adiabatic mixing line of Fig. 1 is almost horizontal. Usually the sensible heat contribution of the fuel Δh_F has only a very small influence on the slope.

Theoretical Heat Releases

The theoretical heat release for any mixture ratio at any particular set of conditions is defined as the amount of heat energy per unit weight of mixture, q, which is released by an isothermal, constant pressure, chemically complete combustion; i.e., it is the "useful" heat release of the reaction. In contrast, the standard heat of combustion of the fuel q_F° pertains only to the heat release of a complete oxidation to CO_2 and H_2O at the fixed standard reference temperature T°. Consequently, variable differences in temperature level complicate the general relation between q and q_F°, and furthermore, a complete oxidation to CO_2 and H_2O is not possible in rich mixtures. For these reasons q is not explicitly defined in terms of q_F°.

On the enthalpy-fuel/air ratio diagram, the theoretical heat release per pound of original air $(1 + f)q$ can be determined for any specific combustion process by "cooling" the gases along the final f co-ordinate from the adiabatic temperature T^* on the adiabatic mixing line, to the isotherm of the initial gas temperature, T_A (or T_1), Fig. 1

$$(1 + f)q = (1 + f)h - (1 + f)h_{T(A \text{ or } 1)} \quad [11]$$

When the initial fuel temperature $T_F = T_A$ (or T_1) this heat release is in exact accord with the foregoing definition of the theoretical heat release; when $T_F \neq T_A$ (or T_1), the $(1 + f)q$ contains the sensible heat brought into the system by the fuel at T_F relative to T_A (or T_1). For many applications it is precisely the quantity $(1 + f)q$ which is of interest regardless of how the heat was made available. In most cases the sensible heats involved are very small in comparison to the heat release of the combustion.

It is interesting to note that, whereas the maximum adiabatic flame temperatures are generally encountered somewhat to the rich side of the stoichiometric, the maximum heat release is at the stoichiometric because of the sharp change in the slope of the T_A (or T_1) isotherms in passing from lean to rich mixtures. It is also noteworthy that the heat release can be determined without knowledge of the T^* since the origin of the vertical cooling line must, under any circumstances, fall on the adiabatic mixing line. Furthermore, since the location of the adiabatic mixing line is independent of pressure, and since in most cases the T_A (or T_1) isotherm is in the solid line, pressure independent region, $(1 + f)q$ is correspondingly independent of pressure.

Combustion Efficiencies

A combustion efficiency can only be determined rigorously by performing a chemical analysis on a sample of the combustion gas. In practice, however, this procedure is frequently too laborious and time-consuming to be practicable. In addition, sometimes there is doubt as to whether the composition of the sample is the same as that of the parent, hot combustion gases. When the combustion can be assumed to be adiabatic, or when the heat-transfer losses can be accounted for, a widely used and much simpler alternative is to measure the temperature of the post-combustion gases. This temperature, in comparison to the theoretical adiabatic temperature, provides a measure of the undeveloped heat release. However, in order to calculate a combustion efficiency from this datum, it is necessary to assume some relationship between the temperature and the energy content of the incompletely burned mixture. Despite the lack of complete rigor which is implicit in making such an assumption, the temperature-measurement approach to combustion efficiencies is widely used because of its simplicity. Since different assumptions may yield different results from the same data, consistency and an understanding of the nature of a particular assumption are important.

The enthalpy-fuel/air ratio diagram readily lends itself to either of two methods, both of which have versions in common use.

The first method assumes that the c_p of the incompletely burned mixture is equal to that of the equilibrium mixture at the same T, and regards the undeveloped heat release as equivalent to a sensible-heat loss from the adiabatic-equilibrium state. With this assumption, the experimental T' can be associated with the T' isotherm on the diagram, Fig. 2, and η_q (the combustion efficiency defined on the "equivalent heat loss" basis) is the ratio of the "actual" $(1 + f)q'$ to the theoretical heat release, $(1 + f)q$

$$\eta_q = \frac{(1 + f)q'}{(1 + f)q} = \frac{(1 + f)h' - (1 + f)h_{T(A \text{ or } 1)}}{(1 + f)q} \quad [12]$$

$(1 + f)h'$ may be regarded as an "effective" enthalpy which is associated with the temperature T' but, because the combustion is adiabatic regardless of its degree of completion, $(1 + f)h$ is still the "true" adiabatic enthalpy. Now since the adiabatic mixing line is straight, and since the T_A (or T_1) isotherm is so nearly straight, a family of straight combustion-efficiency lines can be drawn in by a simple proportioning of the theoretical heat release at any arbitrary value of f. Fig. 2 shows such a family for $\eta_q =$ 100, 80, 60, 40, 20, and 0 per cent. Note that the generality in the definition of $(1 + f)q$ is preserved in the definition of η_q, i.e., it is directly proportional to the degree of achievement—in relation to what is theoretically achievable—at the particular conditions of interest. If, as is sometimes done, the combustion efficiency is related to the standard heat of combustion q_F° of the fuel, this is not the case.

At high values of η_q the inefficiency is usually due to incomplete combustion of CO and H_2, and since small amounts of these gases do not seriously alter the c_p of the mixture, the assumption concerning the equality of the c_p's, is reasonably realistic for high η_q's and becomes exact as η_q approaches 100 per cent. At low η_q's the method is formally consistent with that in the high range; when $T' = T_A$ or (T_1) the $\eta_q = 0$ line falls on the T_A (or T_1) isotherm.

For lean mixtures in which the final temperatures are not too high, the c_p is reasonably constant as is indicated by the approximately regular vertical spacing of the isotherms in Fig. 1, and Equation [12] may be given the frequently used form

$$\eta_q \simeq \frac{T' - T_{A \text{ or } 1}}{T^* - T_{A \text{ or } 1}} \quad [13]$$

In the high-temperature region, the c_p's increase so markedly that Equation [13] is inaccurate, yielding too high a value of η_q.

The second method assumes that a complete adiabatic combustion occurs in a mixture of fuel/air ratio f', and that these gases contain completely unreacted fuel in the amount $f - f'$, the total fuel/air ratio of the mixture being f.

The combustion efficiency on this "equivalent fuel consumption" basis, η_f, is again given by the ratio of the actual to the theoretical heat release

$$\eta_f = \frac{(1 + f')h' - (1 + f')h'_{T(A)}}{(1 + f)q} = \frac{f'}{f} \quad [14]$$

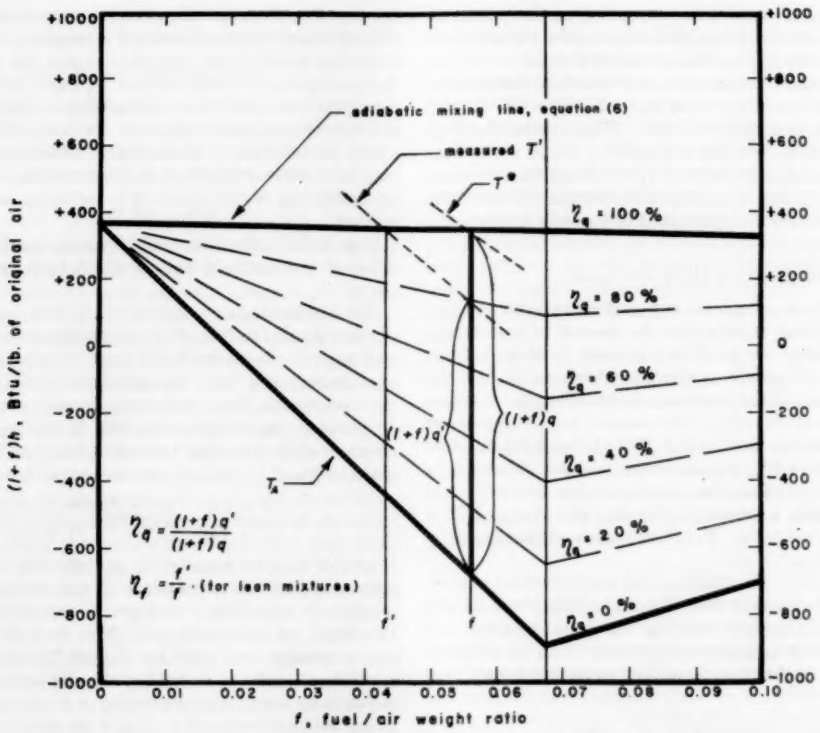

FIG. 2 DETERMINATION OF COMBUSTION EFFICIENCIES FROM MEASURED TEMPERATURES BY TWO METHODS
(Isotherms omitted for the sake of clarity.)

for fuel + air combustion processes. On the enthalpy-fuel/air ratio diagram, the f' value is determined by the intersection of the T' isotherm with the adiabatic mixing line as shown in Fig. 2. By the use of Equations [6] and [11] and a linear expression for the T_A isotherm, the second simple formulation in terms of f'/f can be derived easily.

When fuel is added to the products of a preceding combustion of fuel/air ratio f_1, the corresponding expression for η_f is

$$\eta_f = \frac{f' - f_1}{f - f_1} \quad \ldots\ldots\ldots\ldots\ldots\ldots [15]$$

At low combustion efficiencies, η_f has a reasonably realistic physical basis since under these conditions the combustion gases usually contain unburned and only partially oxidized hydrocarbons; it becomes exact as η_f approaches 0 per cent. At high η_f's the method is formally consistent with that in the low range; when $f' = f$, $\eta_f = 100$ per cent.

In summary, we see that two combustion efficiencies, η_q and η_f, have been defined on the basis of different physical assumptions which become exact at the opposite extremes, $\eta_q = 100$ per cent and $\eta_f = 0$ per cent. Furthermore, each is formally consistent with itself over the whole range from 0 to 100 per cent.

Now we note that, since only straight (or nearly straight) lines are involved in the application of either method to lean-mixture problems as shown in Fig. 2, it follows by geometry from the approximate parallelism of the isotherms that $\eta_q \simeq \eta_f$. It may therefore be concluded that for lean mixtures, either method gives a reasonably accurate numerical evaluation of the combustion efficiency over the complete range from 0 to 100 per cent in spite of the varying degrees of realism in their respective definitions.

In rich mixtures, when $T' \leqslant T^*$, $\eta_q \leqslant 100$ per cent, but $\eta_f \geqslant 100$ per cent. This latter somewhat disconcerting result stems directly from regarding the $f - f'$ amount of unburned fuel as a potential source of sensible heat, disregarding its role as a potential absorber of heat when present in rich mixtures owing to the highly endothermic reduction reactions which are then possible.

When a rich fuel + air mixture is burned the temperature increases and incomplete combustion is characterized by $T' \leqslant T^*$. Therefore, since the corresponding $\eta_q \leqslant 100$ per cent, the equivalent heat-loss method is recommended for determining the combustion efficiencies of rich fuel + air mixtures. On the other hand, when fuel is added to hot combustion products of a near stoichiometric mixture, the temperature decreases and an incomplete "combustion" of the added fuel is then characterized by $T' \geqslant T^*$ with the result, $\eta_q \geqslant 100$ per cent, and $\eta_f \leqslant 100$ per cent. Therefore, η_f may find application as a "cooling efficiency" when fuel is added to hot, near-stoichiometric combustion gases, using Equation [15].

A frequently used method of determining combustion efficiencies in high-temperature gases is to introduce a known amount of water and then measure the temperature of the cooled "wet" gases, T''. Since the decrease in the enthalpy of the hot combustion products, per unit weight of original air, is equal to the increase in the enthalpy of the quench water, per unit weight of original air, the effective enthalpy of the hot gases before quenching is therefore

$$(1 + f)h' = (1 + f)h'' + w(h''_{H_2O} - h_{H_2O(l)}) \ldots\ldots [16]$$

$(1 + f)h''$ is the enthalpy read from the T'' isotherm at f; w is the

weight ratio of quench water to original air and $(h''_{H_2O} - h_{H_2O(l)})$ is the enthalpy increase (determined from steam tables) associated with the temperature rise from the liquid water-injection temperature, $T_{H_2O(l)}$, to the measured T''. Combining Equations [12] and [16] yields

$$\eta_q = \frac{(1+f)h'' + w(h''_{H_2O} - h_{H_2O(l)}) - (1+f)h_{T(A \text{ or } 1)}}{(1+f)q} \quad \ldots [17]$$

An η_f efficiency also can be calculated from the same data by drawing a line parallel to the adiabatic mixing line and displaced downward by the amount $w[h''_{H_2O} - h_{H_2O(l)}]$. The intersection of this line with the T'' isotherm determines the equivalent fuel/air ratio, f'.

Note that it is unnecessary to deal with the prequench temperature T' either experimentally or analytically. Furthermore, if the final quench temperature T'' is in the solid-line region of the diagram the method is independent of pressure considerations.

Application to Combustion in Flowing Streams

The enthalpy-fuel/air ratio diagram and the previously developed application methods are applicable to combustion in flowing streams provided all h values are taken to be those of the stagnation state; i.e., Equation [6] is a total energy balance. Its intersections with the solid-line isotherms yield stagnation temperatures at any pressure, and its intersections with the dotted-line isotherms yield stagnation temperatures at a stagnation pressure equal to the pressure for which the isotherms were drawn. If the local velocity u is known, the static enthalpy is given by a downward displacement of $(1+f)u^2/2gJ$ from the Equation [6] line. The solid-line isotherms then yield static temperatures at any pressure and the dotted-line isotherms yield static temperatures at a static pressure equal to that for which the isotherms are drawn. This procedure merely represents the "first-law" aspects of converting kinetic into sensible energy and vice-versa. It introduces no restrictions and gives no information on the path between the two states or the relation of their pressures. All processes which involve the "second law" must be evaluated independently.

Adiabatic Mixing of Two Streams

Consider two streams with the stagnation enthalpy and fuel/air ratio co-ordinates $(1+f_a)h_a, f_a$ and $(1+f_b)h_b, f_b$ as shown by the (a) and (b) points in Fig. 3. In the case of two static systems all h's are static and pertain to the same pressure. Let z_a and z_b be defined as

$$z_a = \frac{\text{Weight of original air in } (a) \text{ stream}}{\text{Weight of original air in combined } (a) \text{ and } (b) \text{ streams}}$$

$$z_b = \frac{\text{Weight of original air in } (b) \text{ stream}}{\text{Weight of original air in combined } (a) \text{ and } (b) \text{ streams}}$$

from which

$$z_a + z_b = 1 \quad \ldots [18]$$

In the combined stream, the enthalpy per unit weight of original air, and the fuel/air ratio are consequently

$$(1+f)h = z_a(1+f_a)h_a + z_b(1+f_b)h_b \quad \ldots [19]$$

and

$$f = z_a f_a + z_b f_b \quad \ldots [20]$$

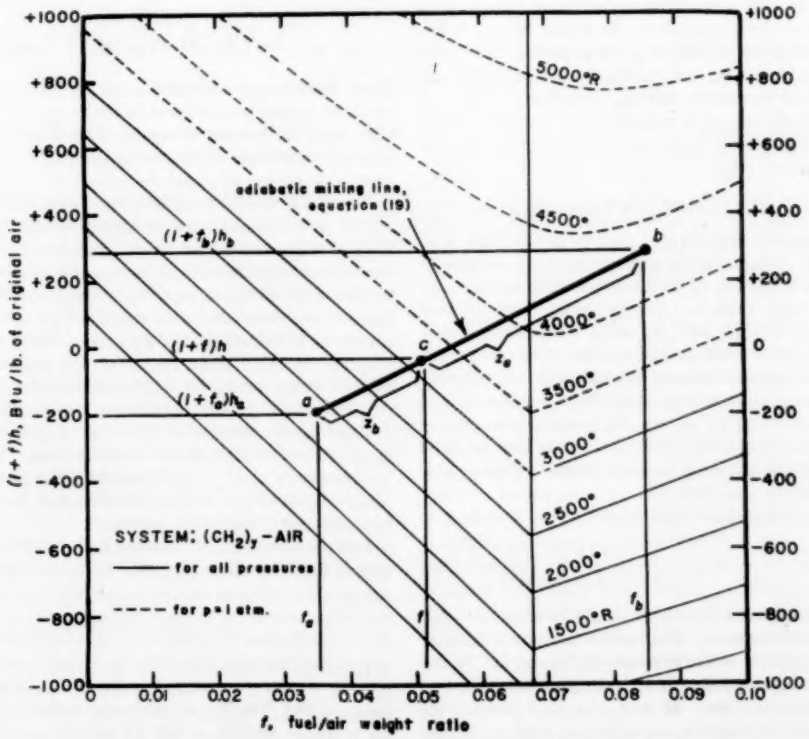

Fig. 3 Determination of Final State for Adiabatic Mixing of Two Streams
(Points a and b identify the initial stream conditions. Weight-ratio contributions of original air to combined stream, z_a and z_b, locate final state at point c.)

Equation [19] may be plotted on the enthalpy-fuel/air ratio diagram by simply drawing a straight line between the (a) and (b) end points. The $(1 + f)h$ and f for a particular z_a (or z_b) ratio is determined by a simple proportioning of the line (a) to (b) ("the lever rule") or, alternatively, by proportioning its projection on the ordinate or abscissa axes as shown in Fig. 3. Algebraically, this operation is expressed by the equations

$$\frac{(1 + f_b)h_b - (1 + f)h}{(1 + f_b)h_b - (1 + f_a)h_a} = z_a = \frac{f_b - f}{f_b - f_a} \quad \ldots\ldots [21]$$

or

$$\frac{(1 + f)h - (1 + f_a)h_a}{(1 + f_b)h_b - (1 + f_a)h_a} = z_b = \frac{f - f_a}{f_b - f_a} \quad \ldots\ldots [22]$$

which are derived by eliminating z_b or z_a, respectively, between Equation [18] and Equations [19] and [20].

There is no restriction as to whether the initial (a) and (b) streams are in equilibrium; i.e., as to whether or not the enthalpy and fuel/air ratio co-ordinates of the (a) and (b) streams also identify the temperatures T_a and T_b. Also there is no restriction as to whether or not chemical reactions accompany the mixing process, the only restriction being that the mixing is adiabatic. The final equilibrium temperature of the combined streams—implying complete mixing as well as chemical equilibrium—can be read from the intersecting isotherm.

A special case of this problem which frequently occurs in practice is that one of the streams is pure air; e.g., as in the case of a metered secondary air flow for an enclosed bunsen flame. Another example may be drawn from gas-turbine practice, in which it is customary to burn fuel in a near-stoichiometric, high-temperature zone, and then by dilution with additional air to cool the gases to a permissible turbine-inlet temperature. Such processes are easily handled by designating the (a) stream point as pertaining to pure air and locating it at $(1 + f_a)h_a = h_A$ on the $f = 0$ axis. Although there may be practical reasons for desiring to study such processes in steps, if the over-all process is adiabatic and if the h_A is the same for all steps, one can of course proceed directly to the final state by using Equation [6].

A Modified Enthalpy-Fuel/Air Ratio Diagram

The enthalpy diagram as illustrated and applied in Figs. 1, 2, and 3 is particularly convenient for engineering purposes since it deals in quantities which are of direct engineering significance; i.e., the fuel/air weight ratio and energy contents are referred to fixed quantities of original air. However, a limitation is that the fuel/air weight ratio scale on the abscissa does not permit an evenly weighted representation of the lean and rich composition ranges; i.e., the lean mixtures extend from $f = 0$ to $f = f_s$ and the rich from $f = f_s$ to $f = \infty$. By a simple co-ordinate transformation the enthalpy-fuel/air ratio diagram may be given another—and for some purposes a more elegant—form which solves this difficulty.

Let the fuel-air mixture parameter M be defined according to

$$M = \frac{f}{f_s + f} = \frac{r}{1 + r} = \frac{2 + {}^1/_2(\mathrm{H})/(\mathrm{C})}{(\mathrm{O})/(\mathrm{C}) + 2 + {}^1/_2(\mathrm{H})/(\mathrm{C})} \quad [23]$$

in which f_s is the stoichiometric fuel/air weight ratio and $r = f/f_s$ is the fuel/air equivalence ratio. The last formulation is in terms of the relative proportions of the elements C, H, and O. M has the following characteristics: $0 < M < {}^1/_2$ for lean mixtures, and ${}^1/_2 < M < 1$ for rich mixtures. $M = 0$, ${}^1/_2$, and 1 identify the respective pure-air, stoichiometric, and pure-fuel mixture proportions, thereby giving an equal weight to the lean and rich composition ranges. M differs from the similarly defined c function of S. R. Brinkley and co-workers only in that it is associated in an opposite manner with the lean and rich composition ranges.

The linearity of the adiabatic mixing line as given by Equation [6] is an essential feature which should be preserved in a new co-ordinate system.

Solve Equation [23] for f in terms of M

$$f = \frac{f_s M}{1 - M} \quad \ldots\ldots [24]$$

and substitute for f in Equation [6]. After rearrangement and simplification, there results

$$[1 - (1 - f_s)M]h = h_A + [-h_A + f_s h_F]M \quad \ldots\ldots [25]$$

from which it is seen that the essential linear nature of the adiabatic mixing line is preserved if it is plotted on the co-ordinates, $[1 - (1 - f_s)M]h$ versus M. Similarly, it can be shown easily that the linearity of the low to moderate temperature isotherms is also preserved with these co-ordinates. It is also seen that at the two extremes of pure air and pure fuel, Equation [25] reduces to

$$[1 - (1 - f_s)M]h = h_A \quad \text{(for } M = 0\text{, pure air)} \ldots [26]$$

$$[1 - (1 - f_s)M]h = f_s h_F \quad \text{(for } M = 1\text{, pure fuel)} \ldots [27]$$

The numerical ordinate scale in the new co-ordinate system is therefore identical with the $(1 + f)h$ scale in the old. As previously, at $M = 0$ it refers directly to the absolute enthalpy of pure air per unit weight of air, but at intermediate values of M it refers to a weight basis containing the factor $[1 - (1 - f_s)M]$ instead of $(1 + f)$. At $M = 1$ it refers to the enthalpy of the fuel per unit weight of air in a stoichiometric mixture, i.e.

$$f_s h_F = f_s \frac{\text{lb of fuel}}{\text{lb of air}} \; h_F \frac{\text{Btu}}{\text{lb of fuel}}$$

Now, since f_s depends only on the H/C ratio, a scale reading directly in h_F and proportional to the main $[1 - (1 - f_s)M]h$ scale may easily be located along the $M = 1$ ordinate. By using the thermal properties of the particular fuel of interest, a T_F scale may then be keyed to the h_F scale.

The points at which any isotherm intercepts the limiting $M = 0$ and $M = 1$ ordinates must be consistent with the equilibrium $h = h(T, p)$ relations for pure air and pure hydrocarbon, respectively. However, because a state of chemical equilibrium is approximated by only a few of the common hydrocarbon fuels, the $M = 1$ intercepts of fully extended isotherms need not coincide with the temperatures indicated by the T_F scale. Since h_F is defined on an absolute enthalpy basis, its use on the diagram is unaffected by whether or not the fuel is in chemical equilibrium; for a particular fuel such considerations are already implicit in the specification of $h_F°$ and known relation of T_F to h_F. Fig. 4 shows the isotherms extended to the limit of the available data. The sharp break in the isotherms at $M = 0.75$ indicates the boundary of the two-phase region of gas + solid carbon which extends to the $M = 1$ boundary for equilibrium systems.

It is apparent from Equations [26] and [27] that the adiabatic mixing line, Equation [25], may be located by simply drawing a straight line between the two points which identify the enthalpies (or temperatures) of the pure air and pure fuel on the $M = 0$ and $M = 1$ ordinates, respectively. And, as previously, the intersection of this line with the isotherms determines the adiabatic combustion temperature at each value of M. Fig. 4 shows an adiabatic mixing line for ethylene-air systems (for the conditions $T_A = T_F = 1000$ R $= 540$ F) and the resulting adiabatic combustion temperature at each value of M.

In case fuel is added to the products of a preceding combustion

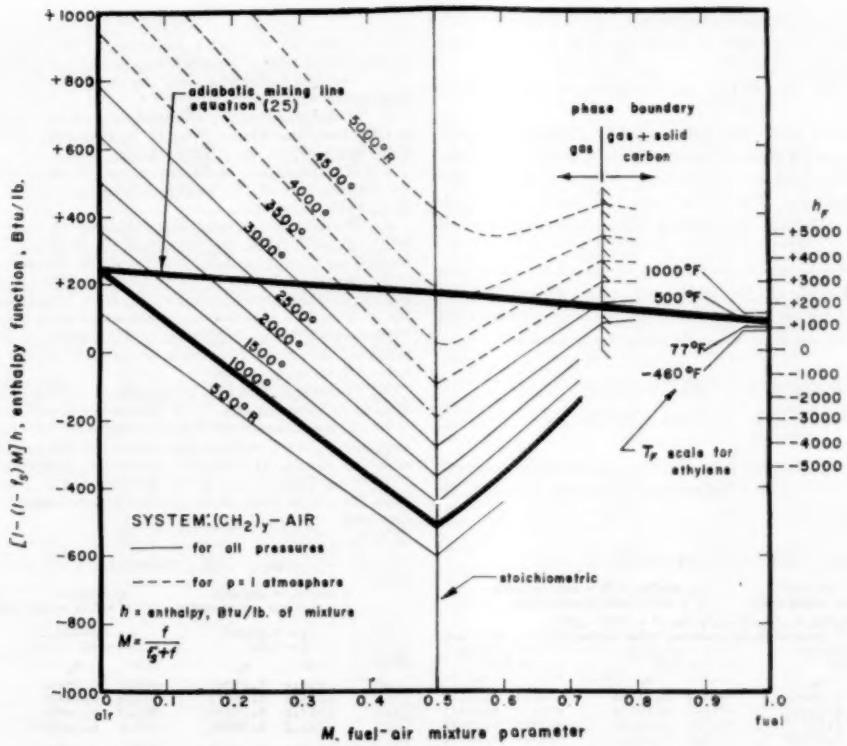

FIG. 4 MODIFIED ENTHALPY-FUEL/AIR RATIO DIAGRAM SHOWING SOLUTIONS FOR ADIABATIC FLAME TEMPERATURES
(For mixtures of air and ethylene initially at $T_A = T_F = 1000$ R.)

of mixture proportion M_1 (involving the same H/C ratio), the end points of the corresponding adiabatic mixing line are $[1 - (1 - f_s)M_1]h_1$ at M_1 and $f_s h_F$ at $M = 1$.

The theoretical heat release can be determined from the Fig. 4 diagram in the same manner as shown in Fig. 1, taking care to divide out the $[1 - (1 - f_s)M]$ factor when converting to a per unit weight of mixture basis. Similarly, families of η_g combustion-efficiency lines can be located with equal facility on the Fig. 4 type diagram. The treatment of η_f combustion efficiencies and two stream-mixing problems is complicated by the change in the mixture ratio variable.

In summary, the $(1 + f)h$ versus f co-ordinate diagram is more convenient for engineering purposes, especially since in power applications rich mixtures are rarely of interest. For more general laboratory and physical chemical use, the broader scope of the modified diagram is advantageous.

In Part 2, tables of $h = h(T, f)$ for $(CH_2)_y$-air and $(CH_3)_y$-air systems are presented for $p = 1$ atm. Since the temperature increments are rather small, large detailed diagrams of either the Fig. 1 or 4 type may be prepared from these data and used with relatively high accuracy.

CONSTANT VOLUME PROCESSES

Noting that, at $T = 0$, $H_{i0}° = E_{i0}°$, all the preceding developments hold for constant-volume processes if "absolute internal energy" is substituted for "absolute enthalpy" and "constant volume (or density)" is substituted for "constant pressure." In calculating the absolute internal energy of the fuel by Equation [10], care should be taken to use $E_i° = H_i° - RT°$ instead of the $H_i°$'s of Table 1, and also to use the standard heat of combustion of the fuel at constant volume instead of the indicated constant pressure value, $q_F°$. In general, internal energies of equilibrium systems can be calculated from the h data by $e = h - pv = h - RT/m$. While satisfactory at low temperatures when T is the only variable, in general, this procedure yields the set of $e = e(T, p, f)$ values instead of the more useful $e = e(T, v, f)$ set.

2—SOME h AND c_p DATA FOR COMBUSTION GASES OF TWO H/C *RATIOS*

Sources. The $(CH_2)_y$-air data are abstracted from reference (4) which contains similar data for a wide range of pressures. A discussion of the data and bases for the calculations in reference (4) is given in reference (7). The $(CH_3)_y$ data were computed by the same program which was used for reference (4). In all cases the primary source data are the NBS-API tables (5).

Note on Pressure Dependence. In the accompanying tables for the $(CH_2)_y$-air system, if at a fixed T, a change of p from 0.1 to 10 atm changes h by less than 1 Btu/lb (~3 R for a fixed h) the h is considered negligibly dependent on p. Equally complete data for estimating the effect of p in the $(CH_3)_y$-air system was not computed, but it is assumed to behave similarly at the same temperature. The same criterion applies less strongly to the c_p data.

The Fuel. These data are applicable to all fuels of the indicated H/C ratio, independently of their chemical structure. The Equation [10] formula for computing the reference state absolute enthalpy $h_F°$, from the "low" or net $q_F°$ is given at the beginning of each table.

The Air. Combustion is assumed to occur with a standard dry air of the following composition, as is consistent with reference (6)

N_2: 78.0881% O_2: 20.9495% A: 0.9324% CO_2: 0.0300%

and which gives it a mean molecular weight: 28.9666. For use with the accompanying combustion gas data, absolute enthalpies of air may be obtained by subtracting 1.75 Btu/lb from the reference (6) enthalpies. The same procedure can be used with the values from reference (8), noting that these tables neglect dissociation.

Units. Important uses in engineering applications led to the choice of English units for the $(CH_2)_y$-air data. The $(CH_3)_y$-air data were computed in the metric system using international calories. Conversions may be made with the formulas

$$h \text{ Btu/lb} = 1.798813\, h \text{ cal/gm}$$

$$c_p \text{ Btu/lb °R} = (0.999341) c_p \text{ cal/gm °K}$$

which are in accord with the values of the universal gas constant R, in the two systems: $R = 1.98588$ Btu/lb-mol deg R = 1.98719 cal/gm mol deg K.

BIBLIOGRAPHY

U. S. Bureau of Mines Reports of Investigation series on the "Thermodynamics of Combustion Gases," references (1), (2), and (3):

1 "General Considerations," by S. R. Brinkley, Jr., and B. Lewis, R. I. 4800, April, 1952.

2 "Temperatures and Compositions of the Combustion Products of Oxy-Acetylene Flames," by H. E. Edwards, R. W. Smith, Jr., and S. R. Brinkley, Jr., R. I. 4958, March, 1953.

3 "Temperatures of Methane-Air, Propane-Air, and Ethylene-Air Flames," by R. W. Smith, J. Manton, and S. R. Brinkley, Jr., R. I. 4983, June, 1953.

4 "Properties of Combustion Gases; System C_nH_{2n}—Air," by H. N. Powell, S. N. Suciu, and S. R. Brinkley, Jr., McGraw-Hill Publishing Company, Inc., New York, N. Y., vols. I and II, 1956.

5 "Selected Values of the Properties of Hydrocarbons," National Bureau of Standards Circular C461, U. S. Department of Commerce, 1947. The data of interest in combustion gases are also contained in: "Selected Values of Properties of Hydrocarbons and Related Compounds," American Petroleum Institute Project 44, Carnegie Institute of Technology, 1949.

6 "Tables of Thermal Properties of Gases," National Bureau of Standards Circular 564, U. S. Department of Commerce, 1955.

7 "Proceedings of the Gas Dynamics Symposium on Aerothermochemistry" (Northwestern University), article, p 273, by H. N. Powell and S. N. Suciu, Multicopy Corporation, Evanston, Ill., 1956.

8 "Gas Tables," by J. H. Keenan and J. Kaye, John Wiley & Sons, Inc., New York, N. Y., 1948; Chapman and Hall, Ltd., London, England.

$(CH_2)_y$—AIR COMBUSTION PRODUCTS

h Btu/lb. = enthalpy; c_p Btu/lb. - °R = heat capacity
f = fuel/air weight ratio; r = f/f_s = equivalence ratio

h°_f Btu/lb. = -19,183 + q°_f (at T° = 77°F = 25°C)

Above dotted line h is independent of pressure; below dotted line h is for 1 atm.

	f = 0.016906 r = 0.25		f = 0.033812 r = 0.50		f = 0.047336 r = 0.70	
T°R	h	c_p	h	c_p	h	c_p
600	-179.0	0.24440	-489.3	0.24822	-730.3	0.25119
700	-154.4	0.24620	-464.3	0.25054	-705.0	0.25391
800	-129.7	0.24847	-439.1	0.25324	-679.5	0.25695
900	-104.7	0.25118	-413.6	0.25632	-653.6	0.26031
1000	-79.4	0.25427	-387.8	0.25972	-627.4	0.26396
1100	-53.9	0.25759	-361.7	0.26335	-600.8	0.26779
1200	-27.9	0.26104	-335.1	0.26705	-573.8	0.27171
1300	-1.6	0.26450	-308.2	0.27074	-546.4	0.27569
1400	25.0	0.26790	-280.9	0.27441	-518.6	0.27947
1500	51.9	0.27125	-253.3	0.27800	-490.4	0.28325
1600	79.3	0.27450	-225.3	0.28149	-461.9	0.28693
1700	106.8	0.27758	-197.0	0.28480	-433.0	0.29040
1800	134.8	0.28051	-168.3	0.28794	-403.8	0.29371
1900	163.0	0.28332	-139.4	0.29094	-374.3	0.29685
2000	191.4	0.28602	-110.1	0.29380	-344.5	0.29983
2100	220.2	0.28861	-80.6	0.29655	-314.3	0.30268
2200	249.2	0.29111	-50.8	0.29917	-283.9	0.30539
2300	278.4	0.29354	-20.8	0.30170	-253.2	0.30798
2400	307.9	0.29590	9.4	0.30414	-222.3	0.31047
2500	337.6	0.29838	40.0	0.30673	-191.2	0.31310
2600	367.5	0.30078	70.8	0.30919	-159.8	0.31556
2700	397.7	0.30322	101.8	0.31167	-128.2	0.31804
2800	428.1	0.30575	133.0	0.31424	-96.3	0.32059
2900	458.9	0.30839	164.6	0.31693	-64.1	0.32327
3000	489.8	0.31119	196.4	0.31981	-31.6	0.32618
3100	521.1	0.31421	228.6	0.32300	-1.2	0.32945
3200	552.7	0.31756	261.1	0.32660	34.3	0.33325
3300	584.6	0.32114	293.9	0.33052	67.8	0.33733
3400	616.8	0.32497	327.0	0.33483	101.6	0.34244
3500	649.6	0.32991	360.8	0.34064	136.3	0.34922
3600	683.2	0.33649	395.6	0.34869	172.0	0.35876
3700	717.2	0.34372	431.0	0.35781	208.5	0.37000
3800	751.9	0.35182	467.2	0.36830	246.0	0.38341
3900	787.5	0.36170	504.6	0.38138	285.1	0.40036
4000	824.3	0.37373	543.5	0.39763	326.2	0.42160
4100	862.4	0.38834	584.3	0.41772	369.7	0.44792
4200	902.2	0.40573	627.3	0.44188	416.1	0.47944
4300	943.7	0.42610	672.9	0.47026	465.8	0.51604
4400	987.5	0.44984	721.5	0.50319	519.4	0.55765
4500	1033.8	0.47724	773.6	0.54079	577.4	0.60393
4600	1083.0	0.50850	829.8	0.58306	640.3	0.65445
4700	1135.6	0.54363	890.4	0.62959	708.4	0.70834
4800	1191.9	0.58242	955.8	0.67970	782.0	0.76465
4900	1252.2	0.62456	1026.3	0.73267	861.2	0.82259
5000	1316.8	0.66966	1102.3	0.78780	946.5	0.88158

$(CH_2)_y$—AIR COMBUSTION PRODUCTS

h Btu/lb. = enthalpy; c_p Btu/lb. - °R = heat capacity
f = fuel/air weight ratio; r = f/f_s = equivalence ratio

	f = 0.054098 r = 0.80		f = 0.060861 r = 0.90		f = 0.067623 r = 1.00	
T°R	h	c_p	h	c_p	h	c_p
600	-848.4	0.25765	-965.1	0.25408	-1080.3	0.25550
700	-823.0	0.25956	-939.6	0.25720	-1054.6	0.25880
800	-797.3	0.25874	-913.7	0.26056	-1028.5	0.26233
900	-771.2	0.26226	-887.4	0.26419	-1002.1	0.26610
1000	-744.8	0.26603	-860.8	0.26808	-975.3	0.27011
1100	-718.0	0.26997	-833.8	0.27213	-948.0	0.27426
1200	-690.8	0.27399	-806.3	0.27626	-920.4	0.27848
1300	-663.1	0.27801	-778.5	0.28037	-892.2	0.28269
1400	-635.1	0.28195	-750.2	0.28440	-863.8	0.28681
1500	-606.7	0.28582	-721.5	0.28836	-834.8	0.29086
1600	-577.9	0.28958	-692.5	0.29221	-805.5	0.29479
1700	-548.8	0.29315	-663.1	0.29586	-775.9	0.29850
1800	-519.3	0.29653	-633.3	0.29931	-745.8	0.30200
1900	-489.5	0.29973	-603.2	0.30257	-715.4	0.30529
2000	-459.3	0.30277	-572.8	0.30566	-684.8	0.30839
2100	-428.9	0.30567	-542.1	0.30859	-653.8	0.31133
2200	-398.2	0.30841	-511.0	0.31136	-622.5	0.31417
2300	-367.2	0.31102	-479.8	0.31398	-591.0	0.31692
2400	-336.0	0.31352	-448.3	0.31647	-559.1	0.31960
2500	-304.6	0.31615	-416.6	0.31906	-527.2	0.32229
2600	-272.9	0.31860	-384.6	0.32148	-494.8	0.32515
2700	-241.0	0.32105	-352.4	0.32389	-462.2	0.32828
2800	-208.8	0.32357	-319.9	0.32638	-429.3	0.33186
2900	-176.3	0.32624	-287.2	0.32904	-395.9	0.33609
3000	-143.6	0.32916	-254.1	0.33203	-362.1	0.34121
3100	-110.4	0.33250	-220.7	0.33557	-327.6	0.34752
3200	-76.9	0.33647	-186.9	0.33996	-292.4	0.35533
3300	-43.1	0.34108	-152.7	0.34534	-256.4	0.36479
3400	-8.9	0.34656	-118.0	0.35211	-219.5	0.37612
3500	26.1	0.35420	-82.3	0.36161	-181.2	0.39021
3600	62.4	0.36499	-45.2	0.37495	-141.1	0.40787
3700	99.7	0.37806	-6.8	0.39157	-99.2	0.42832
3800	138.1	0.39398	33.3	0.41198	-55.4	0.45154
3900	178.4	0.41412	75.6	0.43726	-8.9	0.47828
4000	221.0	0.43924	120.8	0.46780	40.4	0.50888
4100	266.5	0.47004	169.4	0.50378	93.0	0.54368
4200	315.4	0.50636	221.9	0.54445	149.3	0.58223
4300	368.0	0.54767	278.5	0.58887	209.6	0.62401
4400	425.0	0.59351	339.7	0.63640	274.2	0.66880
4500	486.7	0.64323	405.7	0.68654	343.3	0.71643
4600	553.6	0.69625	476.9	0.73903	417.4	0.76683
4700	626.0	0.75172	553.5	0.79340	496.7	0.81966
4800	704.0	0.80883	635.6	0.84921	581.3	0.87454
4900	787.7	0.86702	723.2	0.90620	671.5	0.93120
5000	877.3	0.92599	816.8	0.96427	767.5	0.98952

$(CH_2)_y$—AIR COMBUSTION PRODUCTS

h Btu/lb. = enthalpy
f = fuel/air weight ratio
c_p Btu/lb. - °R = heat capacity
r = f/f_s = equivalence ratio

	f = 0.071385 r = 1.10		f = 0.081118 r = 1.20		f = 0.101434 r = 1.50	
T°R	h	c_p	h	c_p	h	c_p
600	-1054.0	0.26018	-1027.9	0.26484	-950.6	0.28969
700	-1027.8	0.26389	-1001.2	0.26916	-921.0	0.30411
800	-1001.2	0.26822	-974.0	0.27489	-889.9	0.31945
900	-974.1	0.27352	-946.1	0.27280	-857.3	0.33341
1000	-946.4	0.27986	-917.3	0.29257	-823.4	0.34372
1100	-918.1	0.28675	-887.6	0.30248	-788.6	0.34991
1200	-889.0	0.29345	-856.8	0.31068	-753.5	0.35268
1300	-859.4	0.29930	-825.5	0.31649	-718.2	0.35310
1400	-829.2	0.30403	-793.6	0.32020	-682.9	0.35215
1500	-798.5	0.30777	-761.4	0.32251	-647.7	0.35066
1600	-767.6	0.31077	-729.1	0.32402	-612.8	0.34910
1700	-736.4	0.31324	-696.6	0.32510	-578.0	0.34770
1800	-704.9	0.31538	-664.1	0.32602	-543.2	0.34659
1900	-673.3	0.31733	-631.4	0.32691	-508.6	0.34581
2000	-641.5	0.31918	-598.7	0.32784	-474.1	0.34535
2100	-609.5	0.32096	-565.9	0.32884	-439.6	0.34518
2200	-577.3	0.32270	-532.9	0.32990	-405.1	0.34525
2300	-545.0	0.32438	-499.9	0.33101	-370.5	0.34553
2400	-512.5	0.32603	-466.8	0.33216	-336.0	0.34597
2500	-479.7	0.32765	-433.6	0.33336	-301.3	0.34657
2600	-447.0	0.32921	-400.2	0.33456	-266.8	0.34724
2700	-414.1	0.33072	-366.8	0.33575	-232.1	0.34799
2800	-381.0	0.33221	-333.2	0.33697	-197.3	0.34884
2900	-347.7	0.33368	-299.5	0.33821	-162.4	0.34979
3000	-314.3	0.33517	-265.6	0.33948	-127.4	0.35083
3100	-280.7	0.33677	-231.6	0.34085	-92.2	0.35199
3200	-246.9	0.33858	-197.4	0.34239	-57.0	0.35336
3300	-212.9	0.34070	-163.0	0.34415	-21.5	0.35496
3400	-178.7	0.34326	-128.6	0.34619	14.0	0.35685
3500	-144.2	0.34701	-93.8	0.34889	49.8	0.35926
3600	-109.2	0.35310	-58.7	0.35288	85.9	0.36247
3700	-73.4	0.36198	-23.1	0.35818	122.4	0.36647
3800	-36.6	0.37505	13.0	0.36524	159.2	0.37140
3900	1.8	0.39499	50.0	0.37542	196.7	0.37778
4000	42.6	0.42419	88.2	0.39039	234.8	0.38620
4100	87.0	0.46396	128.3	0.41239	274.0	0.39743
4200	135.8	0.51276	171.0	0.44337	314.4	0.41216
4300	189.8	0.56741	217.4	0.48484	356.6	0.43125
4400	249.3	0.62510	268.3	0.53739	400.8	0.45609
4500	314.7	0.68420	325.1	0.59974	448.0	0.48829
4600	386.1	0.74429	388.4	0.66928	498.8	0.52968
4700	463.5	0.80514	459.0	0.74276	554.3	0.58183
4800	547.0	0.86672	537.0	0.81761	615.5	0.64566
4900	636.7	0.92914	622.4	0.89252	683.7	0.72114
5000	732.8	0.99255	715.4	0.96711	760.0	0.80706

$(CH_2)_y$—AIR COMBUSTION PRODUCTS

h Btu/lb. = enthalpy
f = fuel/air weight ratio
c_p Btu/lb. - °R = heat capacity
r = f/f_s = equivalence ratio

	f = 0.118340 r = 1.75		f = 0.135246 r = 2.00		f = 0.169058 r = 2.50	
T°R	h	c_p	h	c_p	h	c_p
600	-852.0	0.28689	-755.5	0.29471	-570.7	0.31062
700	-823.0	0.29286	-725.8	0.29890	-539.6	0.31251
800	-793.3	0.30321	-695.6	0.30522	-508.2	0.31581
900	-762.2	0.31864	-664.6	0.31495	-476.4	0.32055
1000	-729.5	0.33560	-632.5	0.32741	-444.0	0.32691
1100	-695.3	0.34878	-599.1	0.34045	-411.0	0.33430
1200	-659.9	0.35652	-564.5	0.35067	-377.2	0.34172
1300	-624.1	0.35985	-529.1	0.35714	-342.7	0.34817
1400	-588.1	0.36042	-493.2	0.36036	-307.6	0.35313
1500	-552.1	0.35990	-457.1	0.36143	-272.1	0.35665
1600	-516.2	0.35824	-420.9	0.36140	-236.3	0.35906
1700	-480.4	0.35680	-384.9	0.36081	-200.3	0.36071
1800	-444.9	0.35553	-348.8	0.36012	-164.2	0.36195
1900	-409.3	0.35455	-312.8	0.35954	-127.9	0.36302
2000	-373.9	0.35388	-276.9	0.35916	-91.6	0.36405
2100	-338.6	0.35351	-241.0	0.35901	-55.1	0.36509
2200	-303.3	0.35341	-205.1	0.35909	-18.5	0.36621
2300	-267.9	0.35354	-169.2	0.35937	18.1	0.36739
2400	-232.6	0.35384	-133.2	0.35983	54.9	0.36864
2500	-197.2	0.35437	-97.2	0.36048	91.7	0.37004
2600	-161.8	0.35497	-61.3	0.36120	128.8	0.37136
2700	-126.3	0.35567	-25.2	0.36202	166.0	0.37274
2800	-90.8	0.35651	11.0	0.36299	203.3	0.37422
2900	-55.1	0.35746	47.4	0.36407	240.8	0.37581
3000	-19.3	0.35852	83.8	0.36529	278.5	0.37751
3100	16.6	0.35976	120.4	0.36669	316.3	0.37941
3200	52.7	0.36122	157.2	0.36835	354.4	0.38158
3300	88.9	0.36297	194.1	0.37034	392.7	0.38414
3400	125.3	0.36506	231.3	0.37272	431.2	0.38720
3500	161.9	0.36767	268.7	0.37567	470.1	0.39089
3600	198.8	0.37107	306.4	0.37942	509.4	0.39544
3700	236.1	0.37528	344.6	0.38403	549.2	0.40103
3800	273.9	0.38043	383.2	0.38970	589.7	0.40788
3900	312.2	0.38690	422.5	0.39671	630.9	0.41624
4000	351.3	0.39512	462.6	0.40544	673.0	0.42646
4100	391.3	0.40560	503.7	0.41631	716.2	0.43888
4200	432.5	0.41878	546.0	0.42967	760.9	0.45381
4300	475.2	0.43516	589.7	0.44590	807.1	0.47159
4400	519.6	0.45557	635.2	0.46561	855.3	0.49266
4500	566.4	0.48101	683.0	0.48949	905.8	0.51745
4600	616.0	0.51267	733.3	0.51834	958.9	0.54641
4700	669.2	0.55187	786.8	0.55303	1015.2	0.57997
4800	726.7	0.59993	844.1	0.59452	1075.0	0.61860
4900	789.4	0.65814	905.9	0.64385	1139.0	0.66277
5000	858.6	0.72752	973.1	0.70209	1207.8	0.71294

$(CH_2)_y$—AIR COMBUSTION PRODUCTS

h Btu/lb. = enthalpy
f = fuel/air weight ratio

c_p Btu/lb. - °R = heat capacity
r = f/f_s = equivalence ratio

	f = 0.202869 r = 3.00		f = 0.236680 r = 3.50		f = 0.270492 r = 4.00	
T°R	h	c_p	h	c_p	h	c_p
2500	267.7	0.38411	312.8		355.6	
2600	306.0	0.38378	352.9		397.2	
2700	344.4	0.38443	392.9		438.7	
2800	382.8	0.38569	433.1		480.4	
2900	421.5	0.38735	473.4		522.3	
3000	460.4	0.38932	513.9		564.3	
3100	499.4	0.39160	554.7		606.6	
3200	538.7	0.39424	595.6		649.2	
3300	578.3	0.39732	636.9		692.0	
3400	618.2	0.40100	678.6		735.3	
3500	658.5	0.40540	720.6		779.0	
3600	699.3	0.41075	763.2		823.3	
3700	740.7	0.41729	806.5		868.3	
3800	782.9	0.42528	850.5		914.0	
3900	825.9	0.43500	895.4		960.7	
4000	869.9	0.44675	941.5		1008.7	
4100	915.3	0.46087	988.9		1058.1	
4200	962.2	0.47769	1038.1		1109.4	
4300	1010.9	0.49756	1089.2		1162.7	
4400	1061.8	0.52084	1142.6		1218.5	
4500	1115.3	0.54791	1198.8		1277.2	
4600	1171.6	0.57902	1258.0		1339.2	
4700	1231.2	0.61445	1320.9		1405.0	
4800	1294.6	0.65440	1387.7		1475.1	
4900	1362.2	0.69905	1459.1		1550.1	
5000	1434.6	0.74847	1535.7		1630.5	

$(CH_2)_y$—AIR COMBUSTION PRODUCTS

h cals./gm. = enthalpy
f = fuel/air weight ratio

c_p cals./gm. - °K = heat capacity
r = f/f_s = equivalence ratio

h°_f cals./gm. = -11,804 + q°_y (at T° = 25°C = 77°F)

Above dotted line h is independent of pressure; below dotted line h is for 1 atm.

	f = 0.015532 r = 0.25		f = 0.031064 r = 0.50		f = 0.046590 r = 0.70	
T°K	h	c_p	h	c_p	h	c_p
300	-110.8	0.24525	-286.9	0.25022	-424.0	0.25489
350	-98.5	0.24654	-274.3	0.25197	-411.3	0.25628
400	-86.1	0.24822	-261.7	0.25406	-398.4	0.25860
450	-73.6	0.25030	-248.9	0.25648	-385.4	0.26130
500	-61.1	0.25274	-236.0	0.25923	-372.2	0.26429
550	-48.4	0.25548	-223.0	0.26226	-359.0	0.26753
600	-35.5	0.25846	-209.8	0.26549	-345.5	0.27096
650	-22.5	0.26155	-196.4	0.26882	-331.8	0.27449
700	-9.3	0.26468	-182.9	0.27220	-318.0	0.27806
750	3.9	0.26779	-169.2	0.27555	-304.0	0.28160
800	17.4	0.27084	-155.3	0.27885	-289.8	0.28509
850	31.0	0.27385	-141.2	0.28210	-275.4	0.28852
900	44.8	0.27677	-127.1	0.28526	-260.9	0.29186
950	58.7	0.27955	-112.7	0.28828	-246.3	0.29505
1000	72.8	0.28221	-98.3	0.29115	-231.4	0.29809
1050	86.9	0.28478	-83.6	0.29391	-216.4	0.30101
1100	101.2	0.28725	-68.8	0.29656	-201.3	0.30379
1150	115.7	0.28964	-53.9	0.29912	-186.1	0.30647
1200	130.2	0.29195	-38.9	0.30158	-170.7	0.30904
1250	144.9	0.29420	-23.8	0.30395	-155.2	0.31150
1300	159.6	0.29639	-8.5	0.30625	-139.5	0.31387
1350	174.5	0.29852	6.8	0.30848	-123.8	0.31616
1400	189.5	0.3008	22.3	0.3109	-108.0	0.3187
1450	204.6	0.3030	37.9	0.3132	-92.0	0.3210
1500	219.8	0.3053	53.5	0.3155	-75.9	0.3233
1550	235.1	0.3076	69.4	0.3179	-59.7	0.3257
1600	250.5	0.3100	85.3	0.3204	-43.4	0.3282
1650	266.1	0.3126	101.4	0.3231	-26.9	0.3309
1700	281.8	0.3153	117.6	0.3259	-10.3	0.3338
1750	297.7	0.3183	134.0	0.3291	6.5	0.3372
1800	313.6	0.3215	150.6	0.3327	23.5	0.3409
1850	329.8	0.3248	167.2	0.3363	40.5	0.3450
1900	346.0	0.3284	184.1	0.3404	57.8	0.3496
1950	362.6	0.3333	201.3	0.3461	75.5	0.3562
2000	379.6	0.3395	219.0	0.3537	93.8	0.3651
2050	396.8	0.3461	236.9	0.3620	112.3	0.3752
2100	414.2	0.3533	255.2	0.3712	131.3	0.3867
2150	432.0	0.3620	274.0	0.3824	150.9	0.4010
2200	450.4	0.3722	293.4	0.3960	171.4	0.4184
2250	469.3	0.3844	313.6	0.4124	192.8	0.4397
2300	488.9	0.3989	334.8	0.4322	215.5	0.4653
2350	509.3	0.4156	357.0	0.4551	239.5	0.4950
2400	530.5	0.4348	380.4	0.4817	265.1	0.5289
2450	552.8	0.4569	405.2	0.5120	292.4	0.5670
2500	576.3	0.4821	431.6	0.5463	321.8	0.6092
2550	601.1	0.5105	459.9	0.5846	353.4	0.6554
2600	627.4	0.5422	490.1	0.6268	387.4	0.7049
2650	655.3	0.5771	522.6	0.6725	423.9	0.7572
2700	685.1	0.6152	557.4	0.7213	463.1	0.8119
2750	716.9	0.6561	594.7	0.7727	505.0	0.8685
2800	750.8	0.6996	634.7	0.8265	549.9	0.9269

$(CH_2)_x$—AIR COMBUSTION PRODUCTS

h cals./gm. = enthalpy
f = fuel/air weight ratio
c_p cals./gm. - °K = heat capacity
r = f/f_s = equivalence ratio

	f = 0.049703 r = 0.80		f = 0.055916 r = 0.90		f = 0.062129 r = 1.00	
T°K	h	c_p	h	c_p	h	c_p
300	-491.4	0.25599	-557.9	0.25787	-623.7	0.25972
350	-478.5	0.25828	-545.0	0.26034	-610.6	0.26236
400	-465.9	0.26083	-531.9	0.26304	-597.4	0.26522
450	-452.4	0.26367	-518.6	0.26601	-584.1	0.26832
500	-439.1	0.26677	-505.2	0.26922	-570.6	0.27165
550	-425.7	0.27012	-491.7	0.27268	-556.9	0.27521
600	-412.1	0.27365	-478.0	0.27631	-543.1	0.27894
650	-398.3	0.27727	-464.0	0.28003	-529.0	0.28274
700	-384.4	0.28094	-449.9	0.28378	-514.7	0.28659
750	-370.2	0.28457	-435.6	0.28750	-500.3	0.29040
800	-355.9	0.28815	-421.1	0.29117	-485.7	0.29416
850	-341.3	0.29167	-406.5	0.29478	-470.8	0.29785
900	-326.7	0.29510	-391.6	0.29830	-455.8	0.30145
950	-311.8	0.29837	-376.6	0.30165	-440.7	0.30487
1000	-296.8	0.30150	-361.5	0.30485	-425.4	0.30813
1050	-281.7	0.30448	-346.1	0.30791	-409.9	0.31122
1100	-266.4	0.30733	-330.7	0.31081	-394.2	0.31414
1150	-250.9	0.31006	-315.0	0.31359	-378.4	0.31693
1200	-235.4	0.31267	-299.3	0.31623	-362.5	0.31962
1250	-219.7	0.31517	-283.5	0.31876	-346.5	0.32226
1300	-203.8	0.31757	-267.4	0.32117	-330.3	0.32482
1350	-187.9	0.31987	-251.3	0.32347	-314.1	0.32735
1400	-171.9	0.3224	-235.2	0.3260	-297.7	0.3299
1450	-155.8	0.3247	-218.8	0.3282	-281.2	0.3326
1500	-139.5	0.3270	-202.4	0.3305	-264.5	0.3353
1550	-123.1	0.3294	-185.9	0.3329	-247.7	0.3388
1600	-106.6	0.3319	-169.2	0.3354	-230.7	0.3426
1650	-90.0	0.3346	-152.5	0.3381	-213.4	0.3470
1700	-73.2	0.3375	-135.3	0.3412	-195.9	0.3522
1750	-56.2	0.3410	-118.2	0.3449	-178.2	0.3586
1800	-39.0	0.3450	-100.8	0.3493	-160.0	0.3663
1850	-21.7	0.3493	-83.3	0.3544	-141.5	0.3752
1900	-4.2	0.3545	-65.5	0.3608	-122.6	0.3856
1950	13.7	0.3619	-47.2	0.3698	-102.9	0.3986
2000	32.3	0.3718	-28.2	0.3819	-82.5	0.4146
2050	51.2	0.3834	-8.7	0.3964	-61.3	0.4326
2100	70.6	0.3969	11.4	0.4137	-39.2	0.4528
2150	90.8	0.4138	32.6	0.4349	-16.0	0.4798
2200	112.0	0.4343	55.0	0.4602	8.4	0.5019
2250	134.4	0.4593	78.7	0.4900	34.2	0.5314
2300	158.1	0.4890	104.1	0.5241	61.6	0.5643
2350	183.4	0.5229	131.3	0.5619	90.8	0.6002
2400	210.5	0.5610	160.3	0.6028	121.7	0.6390
2450	239.5	0.6031	191.5	0.6466	154.6	0.6805
2500	270.8	0.6487	225.0	0.6930	189.7	0.7249
2550	304.4	0.6975	260.8	0.7418	227.1	0.7721
2600	340.5	0.7490	299.2	0.7929	267.0	0.8220
2650	379.3	0.8028	340.1	0.8460	309.3	0.8745
2700	420.8	0.8584	383.7	0.9011	354.3	0.9295
2750	465.1	0.9158	430.2	0.9582	402.2	0.9871
2800	512.4	0.9750	479.6	1.0173	453.1	1.0473

$(CH_2)_x$—AIR COMBUSTION PRODUCTS

h cals./gm. = enthalpy
f = fuel/air weight ratio
c_p cals./gm. - °K = heat capacity
r = f/f_s = equivalence ratio

	f = 0.068342 r = 1.10		f = 0.074555 r = 1.20		f = 0.093194 r = 1.50	
T°K	h	c_p	h	c_p	h	c_p
300	-610.5	0.26478	-597.4	0.26979	-559.0	0.28454
350	-597.2	0.26767	-583.8	0.27296	-544.7	0.28899
400	-583.7	0.27083	-570.1	0.27651	-530.1	0.29542
450	-570.1	0.27445	-556.1	0.28090	-515.0	0.30585
500	-556.2	0.27870	-542.0	0.28648	-499.4	0.32039
550	-542.2	0.28361	-527.5	0.29330	-483.0	0.33568
600	-527.9	0.28903	-512.6	0.30086	-465.9	0.34788
650	-513.3	0.29464	-497.4	0.30831	-448.3	0.35566
700	-498.4	0.30009	-481.8	0.31492	-430.4	0.35974
750	-483.2	0.30506	-465.9	0.32027	-412.3	0.36126
800	-467.8	0.30942	-449.7	0.32435	-394.2	0.36128
850	-452.3	0.31320	-433.4	0.32742	-376.2	0.36060
900	-436.5	0.31648	-417.0	0.32977	-358.2	0.35968
950	-420.6	0.31925	-400.5	0.33161	-340.3	0.35874
1000	-404.6	0.32171	-383.8	0.33314	-322.3	0.35795
1050	-388.4	0.32392	-367.2	0.33449	-304.4	0.35737
1100	-372.2	0.32596	-350.4	0.33575	-286.6	0.35702
1150	-355.9	0.32788	-333.6	0.33697	-268.8	0.35689
1200	-339.4	0.32970	-316.7	0.33818	-250.9	0.35697
1250	-322.9	0.33144	-299.8	0.33938	-233.1	0.35722
1300	-306.3	0.33312	-282.8	0.34058	-215.2	0.35763
1350	-289.6	0.33474	-265.8	0.34179	-197.4	0.35816
1400	-272.9	0.3363	-248.7	0.3430	-179.5	0.3588
1450	-256.0	0.3378	-231.5	0.3442	-161.6	0.3595
1500	-239.2	0.3393	-214.3	0.3454	-143.6	0.3603
1550	-222.2	0.3408	-197.1	0.3466	-125.6	0.3612
1600	-205.1	0.3422	-179.7	0.3478	-107.5	0.3622
1650	-188.0	0.3436	-162.3	0.3491	-89.4	0.3632
1700	-170.8	0.3451	-144.8	0.3504	-71.2	0.3643
1750	-153.5	0.3468	-127.2	0.3518	-53.0	0.3657
1800	-136.1	0.3486	-109.6	0.3534	-34.6	0.3672
1850	-118.6	0.3508	-91.9	0.3552	-16.2	0.3689
1900	-101.0	0.3534	-74.1	0.3573	2.2	0.3709
1950	-83.3	0.3571	-56.2	0.3601	20.8	0.3735
2000	-65.2	0.3629	-38.0	0.3640	39.6	0.3768
2050	-46.9	0.3708	-19.7	0.3690	58.9	0.3809
2100	-28.1	0.3816	-1.1	0.3753	77.7	0.3857
2150	-8.7	0.3974	17.8	0.3840	97.1	0.3918
2200	11.7	0.4198	37.3	0.3959	116.9	0.3995
2250	33.4	0.4503	57.5	0.4127	137.1	0.4095
2300	56.9	0.4891	78.7	0.4358	157.9	0.4222
2350	82.5	0.5346	101.2	0.4684	179.4	0.4381
2400	110.5	0.5847	125.5	0.5097	201.7	0.4581
2450	141.0	0.6377	151.9	0.5541	225.2	0.4833
2500	174.2	0.6926	181.0	0.6109	250.2	0.5149
2550	210.2	0.7491	213.1	0.6745	276.8	0.5543
2600	249.1	0.8070	248.5	0.7430	305.7	0.6028
2650	290.9	0.8664	287.4	0.8143	337.3	0.6613
2700	335.7	0.9275	329.9	0.8873	372.0	0.7303
2750	383.6	0.9906	376.1	0.9616	410.4	0.8095
2800	434.8	1.0559	426.0	1.0371	453.1	0.8980

$(CH_2)_y$—AIR COMBUSTION PRODUCTS

h cals./gm. = enthalpy
f = fuel/air weight ratio
c_p cals./gm. - °K = heat capacity
r = f/f_s = equivalence ratio

	f = 0.108726 r = 1.75		f = 0.124258 r = 2.00		f = 0.155322 r = 2.50	
T°K	h	c_p	h	c_p	h	c_p
300	-527.8	0.30341	-479.8	0.30649	-387.3	0.32561
350	-512.2	0.31707	-464.4	0.31152	-370.9	0.32884
400	-496.0	0.33389	-448.6	0.31976	-354.1	0.33286
450	-479.0	0.34941	-432.3	0.33399	-337.6	0.33895
500	-461.1	0.36367	-415.1	0.35298	-320.4	0.34804
550	-442.6	0.37421	-397.0	0.37083	-302.7	0.35970
600	-423.7	0.38044	-378.1	0.38324	-284.4	0.37187
650	-404.6	0.38348	-358.8	0.38983	-265.6	0.38208
700	-385.4	0.38372	-339.2	0.39210	-246.3	0.38903
750	-366.3	0.38230	-319.6	0.39163	-226.7	0.39274
800	-347.2	0.38003	-300.1	0.38970	-207.0	0.39403
850	-328.2	0.37753	-280.6	0.38721	-187.3	0.39389
900	-309.4	0.37514	-261.3	0.38469	-167.6	0.39307
950	-290.7	0.37303	-242.2	0.38238	-148.0	0.39204
1000	-272.2	0.37129	-223.1	0.38045	-128.5	0.39110
1050	-253.6	0.36995	-204.2	0.37894	-108.9	0.39041
1100	-235.2	0.36898	-185.2	0.37784	-89.4	0.39001
1150	-216.7	0.36836	-166.3	0.37712	-69.9	0.38990
1200	-198.4	0.36803	-147.5	0.37673	-50.4	0.39007
1250	-180.0	0.36797	-128.7	0.37664	-30.9	0.39049
1300	-161.6	0.36812	-109.9	0.37679	-11.4	0.39112
1350	-143.2	0.36846	-91.0	0.37714	8.1	0.39192
1400	-124.8	0.3690	-72.2	0.3777	27.8	0.3930
1450	-106.4	0.3698	-53.3	0.3784	47.4	0.3940
1500	-87.9	0.3709	-34.5	0.3792	67.1	0.3951
1550	-69.4	0.3712	-15.5	0.3801	86.9	0.3964
1600	-50.8	0.3721	3.5	0.3811	106.7	0.3978
1650	-32.2	0.3732	22.6	0.3823	126.6	0.3994
1700	-13.5	0.3744	41.7	0.3836	146.6	0.4011
1750	5.2	0.3758	61.0	0.3852	166.8	0.4031
1800	24.1	0.3774	80.3	0.3870	187.0	0.4054
1850	43.0	0.3793	99.7	0.3892	207.3	0.4081
1900	62.0	0.3816	119.2	0.3918	227.8	0.4113
1950	81.1	0.3844	138.8	0.3949	248.4	0.4151
2000	100.4	0.3880	158.7	0.3988	269.3	0.4198
2050	119.9	0.3923	178.7	0.4036	290.4	0.4255
2100	139.6	0.3974	199.0	0.4092	311.9	0.4323
2150	159.7	0.4038	219.7	0.4161	333.7	0.4404
2200	180.0	0.4116	240.7	0.4245	355.9	0.4503
2250	200.9	0.4213	262.2	0.4348	378.7	0.4621
2300	222.2	0.4334	284.2	0.4473	402.2	0.4762
2350	244.2	0.4480	306.9	0.4622	426.4	0.4929
2400	267.1	0.4658	330.5	0.4800	451.5	0.5124
2450	290.9	0.4875	355.0	0.5013	477.7	0.5352
2500	315.9	0.5138	380.6	0.5266	505.1	0.5618
2550	342.3	0.5459	407.7	0.5587	533.9	0.5926
2600	370.6	0.5846	436.4	0.5923	564.4	0.6281
2650	400.9	0.6311	467.0	0.6343	596.8	0.6687
2700	433.8	0.6865	499.9	0.6835	631.4	0.7150
2750	469.6	0.7518	535.5	0.7409	668.4	0.7677
2800	509.1	0.8278	574.1	0.8075	708.2	0.8272

$(CH_2)_y$—AIR COMBUSTION PRODUCTS

h cals./gm. = enthalpy
f = fuel/air weight ratio
c_p cals./gm. - °K = heat capacity
r = f/f_s = equivalence ratio

	f = 0.186387 r = 3.00		f = 0.217452 r = 3.50		f = 0.248516 r = 4.00	
T°K	h	c_p	h	c_p	h	c_p
1400	121.8	0.4066	209.8	0.4279	297.8	0.4491
1450	142.2	0.4082	231.1	0.4271	280.1	0.3120
1500	162.6	0.4099	252.5	0.4274	282.4	0.3139
1550	183.1	0.4116	273.9	0.4285	304.7	0.3158
1600	203.8	0.4135	295.3	0.4300	327.1	0.3178
1650	224.5	0.4155	316.9	0.4319	349.6	0.3199
1700	245.3	0.4177	338.5	0.4341	372.2	0.3222
1750	266.3	0.4201	360.3	0.4367	395.0	0.3249
1800	287.3	0.4228	382.2	0.4398	417.9	0.3280
1850	308.6	0.4261	404.3	0.4434	440.9	0.3317
1900	330.0	0.4299	426.6	0.4477	464.2	0.3362
1950	351.6	0.4344	449.1	0.4528	487.7	0.3423
2000	373.4	0.4398	471.9	0.4589	511.6	0.3503
2050	395.6	0.4464	495.0	0.4663	535.7	0.3601
2100	418.1	0.4543	518.6	0.4752	560.3	0.3719
2150	441.0	0.4637	542.6	0.4858	585.5	0.3864
2200	464.5	0.4750	567.2	0.4985	611.2	0.4039
2250	488.6	0.4884	592.5	0.5135	637.7	0.4248
2300	513.4	0.5043	618.6	0.5312	665.0	0.4492
2350	539.0	0.5230	645.6	0.5518	693.4	0.4765
2400	565.7	0.5447	673.8	0.5757	723.0	0.5062
2450	593.6	0.5699	703.3	0.6034	754.0	0.5379
2500	622.8	0.5989	734.2	0.6351	786.5	0.5713
2550	653.5	0.6321	766.9	0.6710	820.8	0.6061
2600	686.1	0.6698	801.4	0.7116	857.2	0.6418
2650	720.6	0.7123	838.1	0.7570	895.9	0.6780
2700	757.3	0.7601	877.2	0.8074	937.1	0.7141
2750	796.7	0.8133	918.9	0.8631	981.2	0.7498
2800	838.8	0.8724	963.8	0.9240	1028.5	0.7848

The Influence of Lead on Metal-Cutting Forces and Temperatures

By M. C. SHAW,[1] P. A. SMITH,[2] E. G. LOEWEN,[3] AND N. H. COOK[4]

The effects of additions of lead and sulphur to steel upon tool-face friction F, cutting energy per unit volume u, and tool-face temperature $\bar{\theta}_t$ were investigated. By means of high-speed flash pictures of chips in the process of being formed, it was found that lead was effective in decreasing chip thickness at all speeds, but particularly at high speeds. Sulphur, on the other hand, was found most effective in this regard at tool temperatures (speeds) below about 900 F. It was found that certain cutting fluids (principally cutting oils) interfered with the action of lead and sulphur, and fluids that are normally effective on ordinary steels may give poorer results than air upon steels containing lead or sulphur. In all cases leaded steels were found to give lower values of F, u, and $\bar{\theta}_t$ than comparable nonleaded steels and the improvement due to lead was far greater than could be achieved from cutting fluids at speeds of 150 fpm and above. The paper ends with a note of warning that the results on F, u, and $\bar{\theta}_t$ cannot be used to predict tool life directly and an example is presented which illustrates this point.

IN MOST metal-cutting operations, the smoothness of the surface produced and the life of the cutting tool are the chief items of interest. For a given workpiece and tool geometry, the friction force F between chip and tool is a good measure of the tendency for a chip to weld to the tool. When such welding occurs, particles of built-up edge (BUE) are left behind on the finished surface and it will be rough. Invariably a decrease in friction force is accompanied by an improvement in surface finish. The friction force may be computed as follows (see Fig. 1 for a definition of the notation used)

$$F = F_p \sin \alpha + F_Q \cos \alpha \quad [1]$$

When metal is cut by a single-point tool, essentially all of the energy required is converted into heat. The total energy per unit volume of metal cut u is a good measure of the over-all performance of a cutting operation and is given by

$$u = \frac{F_p V}{Vbt} = \frac{F_p}{bt} \quad [2]$$

The mean temperature between the chip and the tool face ($\bar{\theta}_t$) is a significant quantity since it influences the rate of tool wear in an important way. This temperature may be measured by considering the chip-tool interface to be the hot junction of a thermoelectric circuit and measuring the thermoelectric emf generated when a cut is taken. While good correlation is usually found between tool life and tool-face temperature, this is not always the case, since other quantities are also of importance with regard to tool wear. When the size or stability of a BUE changes with cutting conditions, it is found that changes in tool life cease to follow changes in tool-face temperature, or changes in friction force F, or energy per unit volume u. While many workers have sought an alternate quantity to study in place of tool life, there appears to be no universally applicable method of evaluating tool life other than actually performing life tests on cutting tools.

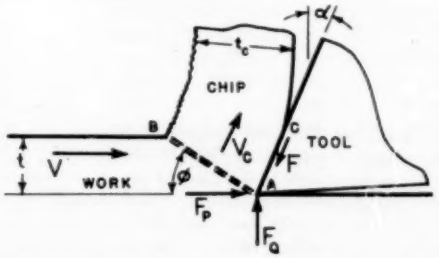

FIG. 1 CONDITIONS AT POINT OF CUTTING TOOL DURING CONTINUOUS CUTTING. WIDTH OF CUT ALONG CUTTING EDGE = b

In this study the influence of a wide variety of cutting conditions on the tool-face friction force F, the energy per unit volume u, and the tool-face temperature $\bar{\theta}_t$, have been investigated for identical steels with and without added lead. While a decrease in these quantities corresponds to an improvement in surface finish and in general an improvement in tool life, the latter may not be the case where loss of a protective BUE may cause the rate of tool wear to increase. An example of this sort of action will be presented at the end of the paper, from which it is evident that care must be exercised in inferring changes in tool life from changes in cutting forces, energy or tool-face temperature.

FREE-MACHINING ADDITIVES

Aside from cutting speed the most important method of altering tool-chip friction is by introducing a low-shear-strength solid material between the high points of sliding surfaces. This is normally accomplished in two general ways—by use of cutting fluids or by use of free-machining additions to steel.

A cutting fluid reduces friction either by reacting or chemadsorbing on the high points on the chip or tool to form a low-shear-strength layer that is not easily pushed aside. A good fluid will be perfectly stable toward all metals with which it comes in contact under ordinary conditions of temperature and pressure but must react quickly under the high pressures and temperatures encountered at the high points on the chip. Free-machining additives, on the other hand, are materials that are added to the metal cut in order to decrease the tendency for chips to weld to the tool.

The principal free-machining additives that have been used include sulphur, selenium, lead, tellurium, phosphorus, nitro-

[1] Professor of Mechanical Engineering, Massachusetts Institute of Technology, Cambridge, Mass. Mem. ASME.

[2] Associate Professor of Mechanical Engineering, Massachusetts Institute of Technology, Cambridge, Mass. Mem. ASME.

[3] Staff Engineer, The Taft-Peirce Manufacturing Company, Woonsocket, R. I. Mem. ASME.

[4] Assistant Professor of Mechanical Engineering, Massachusetts Institute of Technology, Cambridge, Mass.

Contributed by the Research Committee on Metal Processing and presented at the Semi-Annual Meeting, Cleveland, Ohio, June 17–21, 1956, of THE AMERICAN SOCIETY OF MECHANICAL ENGINEERS.

NOTE: Statements and opinions advanced in papers are to be understood as individual expressions of their authors and not those of the Society. Manuscript received at ASME Headquarters, March 13, 1956. Paper No. 56—SA-36.

TABLE 1 DESCRIPTION OF STEELS INVESTIGATED

Steel No.	Description	Chemical composition C	Mn	P	S	Pb	Amount of cold work % reduction in area
1	Hot-rolled B-1113 steel	0.12	0.84	0.084	0.27	0	Hot rolled
2	Same as 1 but cold drawn	0.12	0.84	0.084	0.27	0	6.1
3	Cold-drawn 4140 steel without lead	0.43	0.90	0.019	0.024	0	6.1
4	Same as 3 with lead added	0.43	0.90	0.019	0.024	0.15/0.35	6.1
5	Low-carbon cold-drawn, resulphurized OH steel without lead	0.09	0.97	0.049	0.29	0	6.1
6	Same as 5 with lead added	0.09	0.97	0.049	0.29	0.15/0.35	6.1
7	Same as 5 with additional sulphur	0.08	0.92	0.050	0.43	0	5.4
8	Same as 7 with lead added	0.08	0.92	0.050	0.43	0.15/0.35	5.4
9	Cold-drawn C-1213 steel	0.08	0.90	0.053	0.31	.....	6.1

TABLE 2 PHYSICAL PROPERTIES OF STEELS INVESTIGATED

Steel No.	Description	Bhn	Tensile YS (0.2% offset), psi	Ult. tens. stress, psi	Percent elong. per cent	Per cent red. in area	Charpy impact at 77 F, ft-lb
1	Hot-rolled B-1113 steel	109	...	.....	..	..	..
2	Same as 1 but cold drawn	146	...	.....	..	..	..
3	Cold-drawn 4140 steel without lead	207	90000	103500	13.3	30.0	7
4	Same as 3 but with lead added	197	86000	102500	19.3	37.5	36
5	Low-carbon cold-drawn resulphurized OH steel without lead	109	59000	64500	18.8	56.0	12
6	Same as 5 with lead added	111	56000	64,500	22.0	57.0	15
7	Same as 5 with additional sulphur	116	54000	62500	21.5	54.5	15
8	Same as 7 with lead added	109	52000	60000	20.2	55.5	18

gen, and graphite. The most common of these are sulphur in the form of manganese-sulphide particles, lead in its elementary form, and graphite principally in the form of the plates found in gray cast iron and graphitic tool steels and as nodules in ductile cast irons. Like cutting fluids, free-machining additives are thought to involve the formation of low-shear-strength contaminating films at points of contact and in this sense may be referred to as "internal lubricants." This designation emphasizes an important difference between a cutting fluid and a free-machining additive. For a fluid to be effective it first must penetrate to the tool point and then react to form a low-shear-strength layer. These are both time-consuming processes and it is not surprising to find that cutting fluids are far more effective in decreasing chip-tool friction at cutting speeds below 100 fpm than above. Since the free-machining additives are present on the chip surface when it is formed, the important time of penetration is saved and these materials are generally useful in reducing friction to higher speeds than are cutting fluids.

Lead was introduced as a free-machining additive to steel in amounts up to 1 per cent (the commercial amount of lead added is normally 0.15/0.35 per cent) in 1937 (1).[5] Several articles (2 to 15) appeared after this concerning such problems as segregation in the ingot, the microidentification of lead particles, the influence of lead on physical properties, and the influence on cutting and friction characteristics. These articles revealed that lead added to steel is very finely divided and usually in a homogeneous manner, that additions of lead have negligible influence on the physical properties of the steel but that the added lead significantly improves machinability and reduces sliding friction. A recent publication (16) discusses the characteristics of lead in steel and presents a theory for its action.

Steels Investigated

The steels investigated in this study are described in Table 1, and results of materials tests upon representative leaded and nonleaded steels are given in Table 2 and Fig. 2. From these data it is evident that lead in the amount normally added to steel has a very slight effect upon the physical properties. The yield and ultimate stresses are decreased less than 5 per cent by the addition of lead in all cases. However, this insignificant decrease in strength is accompanied by an increase in ductility. The leaded steels are seen to have impact strengths that are of the order of 20 per cent greater than those for the corresponding nonleaded steels. While these results are in general agreement with previously published findings, they do not agree with reference (14), where it was reported that both impact strength and ductility were lowered by additions of lead.

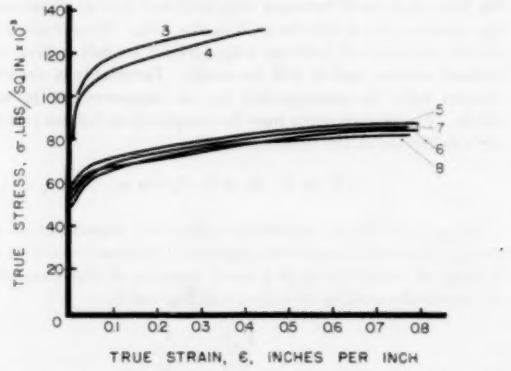

Fig. 2 True-Stress True-Strain Tensile Data for Leaded and Nonleaded Steels

(For description of steels see Table 1. In all cases standard ASTM specimens were used being 0.505 in. diam and 2-in. gage length.)

High-Speed Photographs

The high-speed photomicrographs of Figs. 4, 6, and 7 clearly show the influence of free-machining lead upon chip formation. These pictures were taken with a microscope-camera combination

[5] Numbers in parentheses refer to the Bibliography at the end of the paper.

while cutting, using a high-speed flash tube developed by Professor Edgerton at M.I.T. The duration of the flash was but a few microseconds thus enabling sharp photomicrographs of the surface of the highly polished workpiece to be obtained at all cutting speeds. The arrangement of tool and specimen was as shown in Fig. 3, the diameter of the workpiece being about 2 in. in each case. For all pictures shown here the rake angle was 15 deg and the feed rate was 0.008 in. per revolution (ipr).

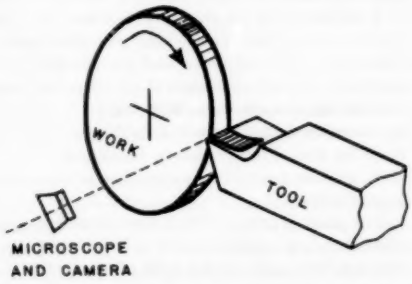

FIG. 3 ARRANGEMENT OF TOOL, SPECIMEN, AND CAMERA FOR OBTAINING HIGH-SPEED PHOTOMICROGRAPHS WHILE CUTTING

In Fig. 4 the improvement obtained by use of lead can be seen at a glance by comparing the chip thicknesses in the two series of pictures for identical steels with and without free-machining lead. The relative chip thicknesses are expressed quantitatively in the chip-thickness-ratio values given in Fig. 4; the greater this ratio, the thinner the chip and hence the better the cutting conditions. In all cases the leaded-steel chips are thinner than the corresponding nonleaded-steel chips indicating a smaller shear surface and hence less energy is required to form the chips. Both steels are seen to give thinner chips as the cutting speed is increased from the lower values. This is due to the decreased tendency for strong welds to form between the high points on chip and tool at the higher cutting speeds.

The nonleaded-steel chips (steel No. 5) are seen to intersect the uncut surface in a more or less sharp manner as in Fig. 5(*a*), indicating that shear strain is confined to a rather narrow band ABB′. On the other hand, the leaded steel (steel No. 6) appears to shear over a wider zone, particularly at the higher cutting speeds, as shown in Fig. 5(*b*). The increase in the volume ABB′ over which strain occurs should tend to decrease the cutting energy per unit volume u, as a consequence of the size effect. This suggests that part of the benefit associated with the use of lead may be attributable to an increase in the volume undergoing shear at any one time and not only due to a reduction of friction between chip and tool.

Unlike a cutting fluid, lead is seen to be effective in improving chip formation to the highest speeds. The added improvement obtained when lead is incorporated into a resulphurized steel accounts for the fact that practical cutting speeds may be in the range from 300 to 350 fpm for a leaded, resulphurized steel that would give the same HSS tool life at from 200 to 250 fpm when no lead is present.

Similar high-speed chip photographs are shown in Fig. 6 for steels Nos. 7 and 8 which have a higher sulphur content. Again the added lead is seen to be beneficial to chip

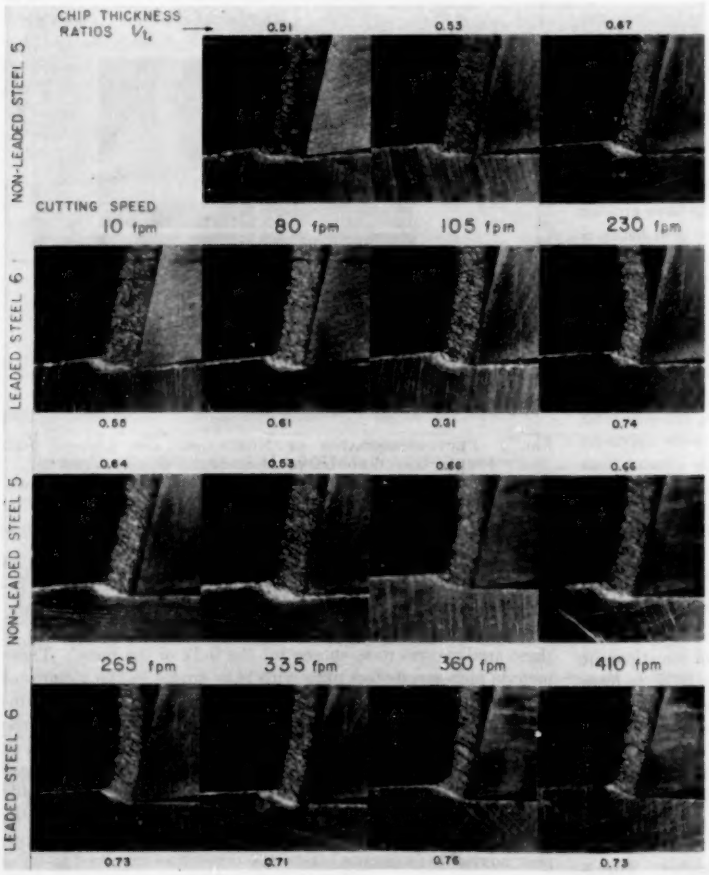

FIG. 4 PHOTOMICROGRAPHS OF NONLEADED AND LEADED STEELS OBTAINED USING HIGH-SPEED FLASH TUBE

(×40; rake angle, 15 deg; feed rate, 0.008 ipr; cutting fluid, none. Tool material, T-15 HSS. Steels Nos. 5 and 6 are resulphurized, low-carbon, open-hearth steels without and with lead added, respectively—see Table 1 for detailed specifications.)

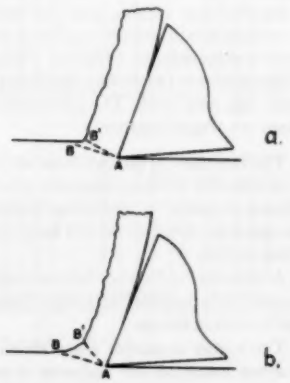

FIG. 5 DIAGRAMMATIC SKETCH SHOWING THE DIFFERENCE IN SHEAR VOLUME ASSOCIATED WITH STEEL (*a*) WITHOUT LEAD, AND (*b*) WITH LEAD AT HIGH CUTTING SPEED

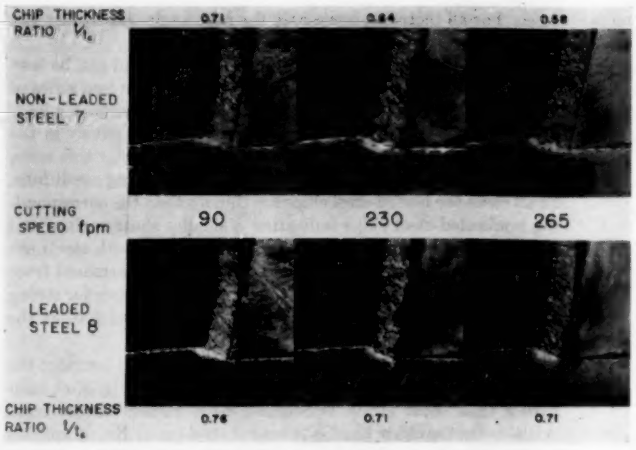

FIG. 6 PHOTOMICROGRAPHS OF NONLEADED AND LEADED HIGH-SULPHUR STEELS OBTAINED USING HIGH-SPEED FLASH TUBE

(×40; rake angle, 15 deg; feed rate, 0.008 ipr; cutting fluid, none. Tool material, T-15 HSS. Steels Nos. 7 and 8 are highly resulphurized, low-carbon, open-hearth steels without and with lead added, respectively—see Table 1 for detailed specifications.)

formation at all speeds. By comparing the photographs of steels Nos. 5 and 7 it is evident that while the additional sulphur in steel No. 7 is quite effective at 90 fpm, it appears to be less effective at higher speeds (above about 200 fpm). The same observation can be made when steels Nos. 6 and 8 are compared. Here the additional sulphur is seen to be most effective at 90 fpm but to have little effect on chip formation at 230 and 265 fpm.

The leaded-steel chips in Figs. 4 and 6 are seen to have greater curl than the corresponding nonleaded-steel chips and hence a smaller apparent area of contact between chip and tool. An increase in chip curl is found to accompany a decrease in the tool-face friction force as produced, for example, by a good cutting fluid. At the same time, the chips produced with decreased friction are found to be thinner and consequently the force between chip and tool will be less. The mean shearing stress along the tool face will therefore tend to decrease when tool friction is decreased owing to the decrease in the friction force, but will tend to increase because of the accompanying decrease in the apparent area of contact. Since the change in area is usually greater than the change in friction force we have the rather paradoxical result that the shearing stress along the tool face actually increases when cutting conditions are improved, as by use of a good cutting fluid or free-machining additive. Why then is it so desirable from the standpoint of surface finish that we cut with low friction between chip and tool? The answer may not be given in a word for there are several reasons:

1 The increased apparent shear stress (based on the apparent area) is valuable in decreasing the tendency for a BUE to form and hence is useful in providing improved surface finish. The higher apparent shear stress will keep the tool point swept clear of adhering metal.

2 A decrease in friction between chip and tool is always accompanied by a decrease in the total energy per unit volume u, as well as in cutting forces.

3 The higher apparent shear stress does not mean that the shear stress based on the real area of contact is higher. This is actually less since the ratio

$$\frac{\text{Real area of contact}}{\text{Apparent area of contact}}$$

decreased when cutting with lower friction and hence lower forces. It is the real shear stress and the real area of contact that are responsible for welding between chip and tool, and, since these are both less, the tendency for metal transfer will be less when cutting with decreased friction.

It therefore may be concluded that the greater curl that is evident in lead-containing chips is a good sign and indicates lower tool-face friction and generally better cutting conditions from the standpoint of surface finish. If the chips tend to curl tightly as they generally do with a leaded steel, chip curl can be of further significance; i.e., with regard to chip disposal. It is observed that there is a significantly greater tendency for leaded steel chips to break naturally owing to their greater tendency to curl than is the case for nonleaded chips.

The photographs in Fig. 7 show that lead is not only effective when added to a low-carbon resulphurized steel but can be equally useful with alloy steels.

TURNING EXPERIMENTS

From the practical point of view the performance of leaded low-carbon steels in the speed range from 100 to

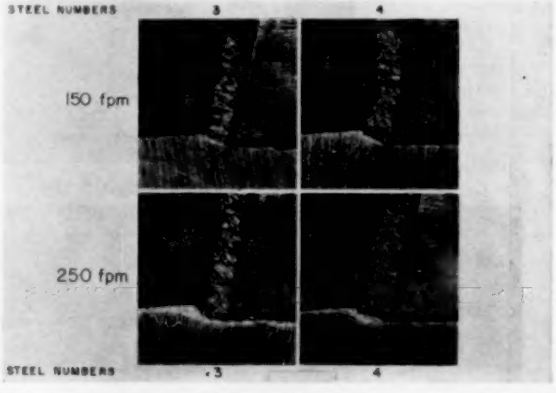

FIG. 7 PHOTOMICROGRAPHS OF NONLEADED AND LEADED 4140 STEELS OBTAINED USING HIGH-SPEED FLASH TUBE

(×40; rake angle, 15 deg; feed rate, 0.008 ipr; cutting fluid, none. Tool material, T-15 HSS. Specimens 3 and 4 are 4140 steels without and with lead, respectively—see Table 1 for detailed specifications.)

300 fpm is of primary interest, and turning tests covering this range of cutting speeds will now be considered. Owing to the increasing use of low-carbon leaded steels in automatic screw machines and turret lathes, machining conditions most common to these applications were chosen for the bulk of the tests. These include high-speed-steel tools with rake angles in the vicinity of plus 10 deg, resulphurized low-carbon steels both with and without lead, speeds in the vicinity of 250 fpm, light feeds in the finishing range from 0.002 to 0.010 ipr, light depths of cut in the finishing range from 0.02 to 0.10 in., and oil- and water-base cutting fluids. A few test results also are included for carbide tools and alloy-steel workpieces mainly to illustrate the versatility of lead in steel. Before considering these data, it would appear advisable to discuss briefly the difficulties involved in lathe testing, criteria available for use in making an evaluation of this sort, and the test procedure that was adopted in the present study.

Two major obstacles are encountered in lathe testing that make

it difficult to obtain representative and reproducible data when making a series of tests in which a single quantity such as cutting speed is varied. These are the BUE and the difficulty of grinding tools that give identical results. The BUE, if present in large size, gives data that vary randomly as the size of the BUE changes, and this makes it difficult to ascribe a representative value to a given set of test conditions. The BUE is most troublesome in those tests, involving low cutting speeds, large feeds, low rake angles, and for work materials, tool materials, and atmospheres that have a strong tendency to promote weld formation. Whenever possible it is preferable to evaluate a cutting parameter under conditions that give the smallest BUE. While the steels used in the present study are far from the worst encountered from the standpoint of BUE, nevertheless the test conditions have been chosen so that this difficulty will obscure the results as little as possible.

When a number of supposedly identical tools are prepared with careful control of grinding conditions, they frequently will yield cutting-force and temperature data that vary considerably. A few tools of a batch will deviate significantly from mean performance. The action of a given tool also will change as the tool wears. In order to minimize these difficulties it is best to preselect the tools to be used by testing them under a standard set of conditions to make sure they give results close to the mean of the batch and then obtain the data with as little cutting and hence as little wear on the tools as possible.

Whenever a newly sharpened tool is put into service, the data for the first fraction of an inch cut will show a rapid variation followed by a gradual trend that accompanies normal wear. It is therefore advisable to precondition all tools by cutting a small amount before taking data so that the initially rapid (although small) breakdown period is not included in the recorded data.

In all tests described in this paper the work materials were cut in close succession since the work material was the variable of major interest. Specimens 2 in. in diam by $^1/_2$ in. wide were arranged on a mandrel, as shown in Fig. 8, where the numbers refer

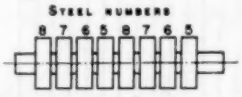

FIG. 8 ARRANGEMENTS OF SPECIMENS ON MANDREL FOR COMPARISON OF CUTTING CHARACTERISTICS OF LEADED AND NONLEADED FREE-MACHINING STEELS

to the steels tested (see Table 1). A single pass across the assembly thus yielded two sets of values for each steel tested with negligible tool wear between tests. By comparing values for identical tests it is possible to ascertain whether a BUE is causing erratic results, in which case additional cuts can be made. A cut of $^1/_2$ in. duration is far more than necessary to achieve temperature and force equilibrium and yet little enough that many tests can be made with the same tool without any measurable change due to wear. When a check test under standard conditions indicated a noticeable change in forces or temperature, the tool was replaced by one that had been preconditioned to give mean standard values. By use of these precautions it is possible to obtain cutting data that are representative and which show most clearly the effect of the main variable of interest, which is work material in the present study.

In all turning experiments to be described the tool angles were as follows in accordance with the standard American Standards Association notation (17):

$$0,\ 10,\ 5,\ 5,\ 5,\ 0,\ 0.005.$$

Whenever a change in rake angle is mentioned, the side-rake angle is the one referred to.

Results of Tests. Results of tests using tools with different rake angles are shown in Fig. 9 for steels Nos. 5, 6, 7, and 8 cut at two cutting speeds (200 and 350 fpm). The energy per unit volume u, and the friction force F, are not good quantities to observe when studying the influence of rake angle, since an increase in rake angle is usually accompanied by a monatonic decrease in these quantities. The mean tool-face temperature is a better variable to observe in this case. For steels Nos. 5 and 7 that contain no lead, the best rake angle is seen to be 5 deg at 200 fpm but 15 deg at 350 fpm. The leaded steels are much less sensitive to changes in rake angle, as was pointed out in a previous publication (16). For leaded steels Nos. 6 and 8 there appears to be a weak optimum with regard to $\bar{\theta}_t$ at $\alpha = 5$ for a cutting speed of 200 fpm, but best results are obtained with a 15-deg tool at the higher cutting speed (350 fpm).

The observation that the optimum rake angle shifts to larger values as the cutting speed is increased is in agreement with general workshop practice. The influence of increased speed upon tool temperature is largely offset by the smaller cutting energy associated with a larger rake angle and the fact that at higher cutting speeds a greater proportion of the thermal energy leaves with the chip. The values of Fig. 9 clearly show that there is no justification for specifying a rake angle to closer than the nearest 5 deg. In most of the tests to follow a rake angle of 10 deg was used.

The rule, that the energy per unit volume u increases about 1 per cent for each degree decrease in rake angle, is seen to be in general agreement with the values in Fig. 9.

The two leaded steels Nos. 6 and 8 are seen to give lower values of u, F, and $\bar{\theta}_t$ in all cases than their nonleaded counterparts. The additional sulphur in steels Nos. 7 and 8 is seen to be less effective in decreasing u, F, and $\bar{\theta}_t$ at 350 fpm than at 200 fpm while the lead is seen to be most effective at the higher speed.

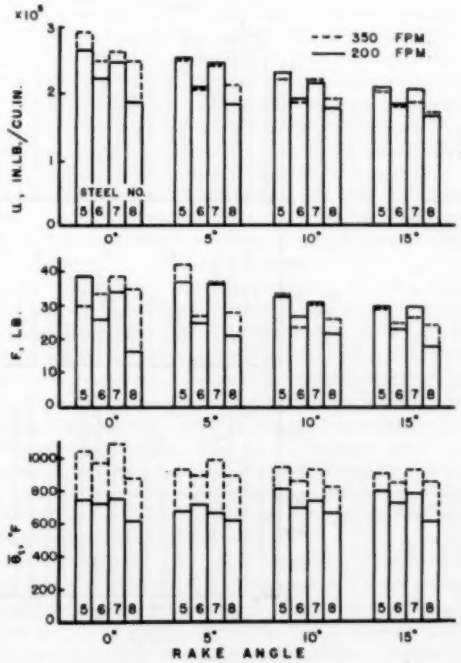

FIG. 9 CUTTING CHARACTERISTICS OF LEADED AND NONLEADED STEELS AT DIFFERENT RAKE ANGLES

(Tool material, T-15 HSS; feed, 0.0044 ipr; depth of cut, 0.05 in.; cutting fluid, cutting oil A; cutting speed, 200 and 350 fpm; work materials, steels Nos. 5, 6, 7, 8.)

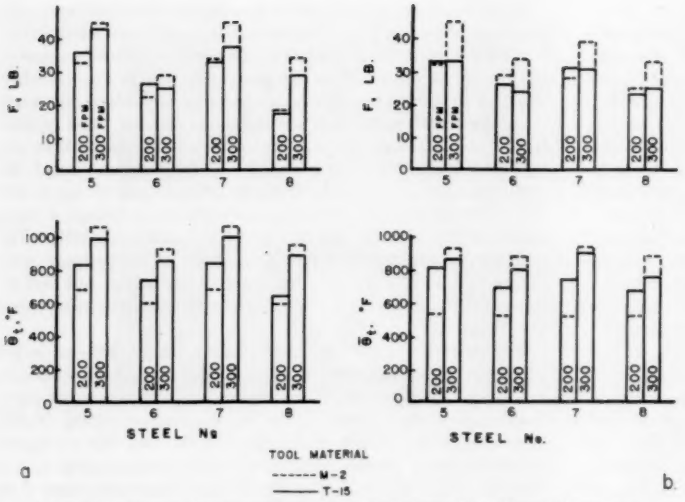

FIG. 10 CUTTING CHARACTERISTICS OF DIFFERENT HSS TOOL MATERIALS
(Tool materials, M-2 and T-15 HSS; feed, 0.0044 ipr; depth of cut, 0.05 in.; cutting fluids, [a] none, [b] cutting oil A; cutting speed, 200 and 300 fpm; work materials, steels Nos. 5, 6, 7, 8.)

A comparison of two HSS tool materials is given in Fig. 10. Here it is evident that while the M-2 steel gives better results with regard to friction force F, and tool temperature $\bar{\theta}_t$, at 200 fpm, the T-15 tool performs better at 300 fpm. While the reason for these results is not certain, it would appear that the lower temperatures observed with the M-2 tool at 200 fpm might be due to its greater thermal conductivity while its relatively poorer performance at 300 fpm might result from a tendency to soften (and hence to give higher friction) at elevated temperatures. The picture is little changed when a cutting oil is used. Inasmuch as less difference in results is obtained with changes in cutting speed with the T-15 material, this type of HSS was adopted for most of the remaining tests.

Feed Rate. The influence of a change in feed rate upon the cutting characteristics of leaded and nonleaded steels is shown in Fig. 11. Feed rate is seen to have a large influence upon the leaded steels, the greatest improvement from lead being evident at the highest feed rates (compare changes in u and F for different values of t). Values of F were so variable when cutting leaded steels at the lightest feed and highest speed using the cutting oil that these data are not shown in Fig. 11(*b*). The reason for this difficulty probably lies in the action of an oily fluid preventing lead from spreading over the surface of the chip. This action should be most pronounced at high speed where sufficient temperature to melt the lead is obtained and at light feed, which enables the oil to penetrate. The observation already made to the effect that lead becomes more beneficial with increased cutting speed can be verified in Fig. 11. From the friction-force data of Fig. 11 and data previously presented, it might be concluded that lead is most useful at high speeds and feeds, while sulphur is most useful at speeds below about 200

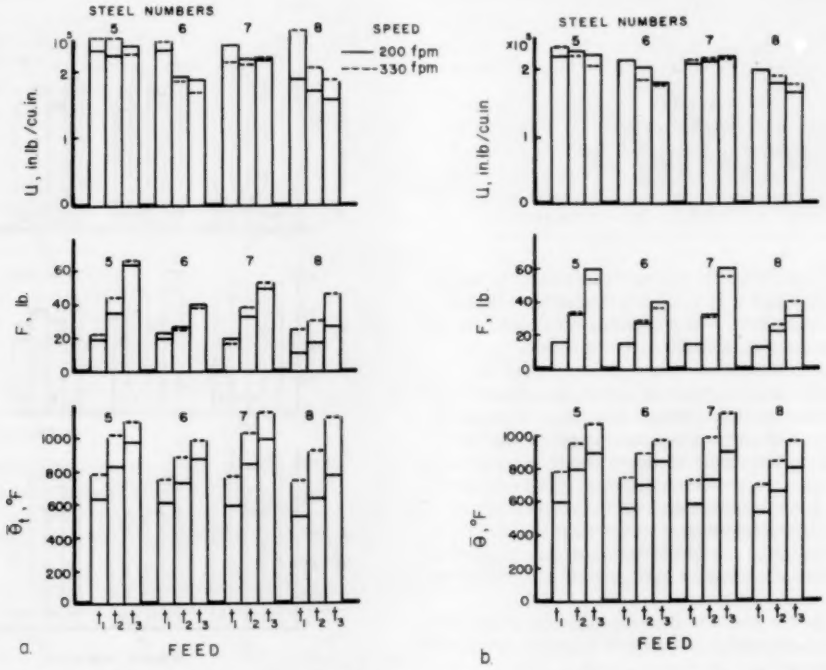

FIG. 11 VARIATION OF CUTTING CHARACTERISTICS OF LEADED AND NONLEADED STEELS WITH FEED RATE
(Tool material, T-15 HSS; depth of cut, 0.05 in.; rake angle, 10 deg; cutting fluid, [a] none, [b] cutting oil A.)
FEEDS
t_1 = 0.0023 ipr t_2 = 0.0044 ipr t_3 = 0.0080 ipr

fpm when using a 10-deg-rake-angle tool. Thus, while the additional sulphur in steels Nos. 7 and 8 appears to be of little value in lowering F, u, or $\bar{\theta}_t$ in Fig. 11, this would not be the case for speeds below 200 fpm.

A comparison of the data of Figs. 11(a) and 11(b) reveals that the improvement obtained from lead is far greater than that derived from the cutting fluid (see Table 3 also).

TABLE 3 COMPARISON OF TOOL-TEMPERATURE VALUES WHEN CUTTING WITH AND WITHOUT FREE-MACHINING LEAD AND WITH AND WITHOUT A CUTTING FLUID

(Depth of cut, 0.05 in.; feed, 0.008 ipr; cutting speed, 385 fpm; tool material, T-15 HSS; rake angle, 10 deg; cutting fluid, cutting oil A)

	No fluid, deg	With fluid, deg	Difference due to fluid, deg
Nonleaded steel 5.....	1100	1070	30
Leaded steel 6.....	980	970	10
Difference due to lead.....	120	100	..

Free-Machining Lead and Cutting Fluids. The relative performance of free-machining lead and cutting fluids is also shown in Fig. 12 for a different tool material. The influence of the cutting fluid upon the tool-friction force F is seen to be significant only at cutting speeds below about 150 fpm, while the influence of lead upon F is very important at all speeds. In this instance the oil-base fluid is seen to have a beneficial effect on F at low cutting speeds, whereas the water-base cutting fluid actually has a detrimental effect at low speeds. At all speeds the magnitude of the lowering of F due to lead is seen to be far greater than that achieved with the cutting fluid.

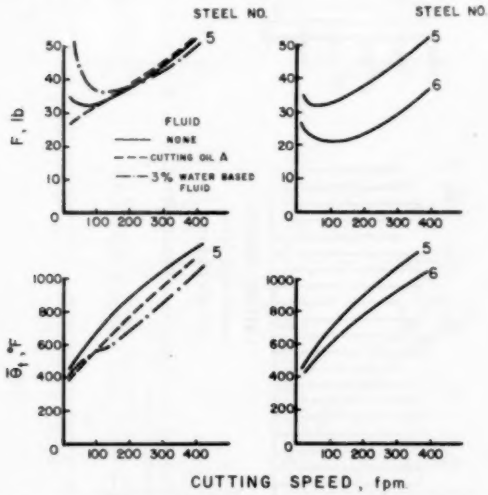

FIG. 12 COMPARISON OF PERFORMANCE OF FREE-MACHINING LEAD AND CUTTING FLUIDS

(Tool material, M-2 HSS; depth of cut, 0.05 in.; feed, 0.0044 ipr; rake angle, 10 deg; work materials, nonleaded steel No. 5 and leaded steel No. 6.)

While cutting fluids cease to have an influence on F in the vicinity of 150 fpm, they continue to influence $\bar{\theta}_t$ to higher speeds. From Fig. 12 it would appear that $\bar{\theta}_t$ would be decreased by use of the cutting oil to a speed of about 500 fpm while the water-base fluid might be effective in cooling the tool to a higher speed. On the other hand, there would appear to be no limit to the speed at which lead is effective in decreasing $\bar{\theta}_t$, since the temperature curves for steels Nos. 5 and 6 are diverging. At 400 fpm the dry cutting temperature for the leaded steel is about the same as the temperature for the nonleaded steel when a water-base fluid is used. As we shall see presently, the use of a water-base fluid that does not prevent lead from spreading can lower the temperature of the leaded steel a significant amount by cooling just as the lead lowers the temperature by decreasing F and, hence, by decreasing the amount of work done and the heat generated in cutting. The important observations to be made from Fig. 12 are:

1 That while cutting fluids cease to be effective in decreasing F at about 150 fpm, lead continues to lower F at all speeds.

2 Cutting fluids continue to play an important role in cooling the tool to speeds beyond where they cease to lubricate the tool face.

3 That a cutting fluid can have a detrimental effect in the case of free-machining steels containing lead or sulphur by interfering with the action of these free-machining additives.

It should be mentioned that the data of Fig. 12 are for M-2 HSS tools which have been seen to be more sensitive to changes in speed than T-15 HSS tools since this latter material has a flatter hardness versus temperature curve. When the results of Fig. 12 are repeated using T-15 HSS tools, the same general picture is obtained except the F and $\bar{\theta}_t$ values vary less rapidly with cutting speed.

Cutting results obtained using a large number of cutting oils and water-base fluids are given in Figs. 13 and 14. The following observations may be made from these data.

1 At the higher cutting speed (275 fpm) where lead tends to be most effective, the friction force F is greater with all cutting oils in the case of leaded steel No. 6 than when cutting dry, and hence the cutting temperatures for this steel are only slightly less with the cutting oils.

2 The friction force for leaded steel No. 6 is less when using water and certain water-base fluids (notably No. 6) than when cutting dry as are the corresponding cutting temperatures.

3 Observations 1 and 2 hold to a lesser extent for resulphurized steels Nos. 2 and 5 but only at the lower speed (100 fpm).

The foregoing observations are in agreement with results that have been presented already and may be explained readily in light of them. The oils have a detrimental effect on tool friction apparently since they tend to prevent the lead from spreading and hence acting as a lubricant. This effect is more pronounced at higher speeds where lead is normally most effective. The slight reduction in tool temperature that is obtained with cutting oils results from their cooling action being sufficient to slightly more than offset the poorer cutting performance reflected in the increased values of F obtained with the oils. These water-base materials that are most effective apparently do not interfere with the spreading of lead. Since water is as effective as the best commercial water-base materials at the higher speed, it does not appear that the high-speed performance of the better fluids is due to any lubricating action. However, water-base fluid No. 6 gives better results than water at 100 fpm, and this probably results from the ability of the commercial additive to lubricate the tool face at this speed. The much lower cutting temperatures obtained with the water-base fluids are due both to the effect of these fluids on F and their capacity for cooling. The oils are found to have a detrimental effect on F only at the lower speed for steels Nos. 2 and 5 since the sulphur in these steels is effective in lowering F only in this lower speed range. Hence the fact that it is kept from spreading is only important at the lower speed.

Lubrication Requirements. The foregoing cutting-fluid study reveals that the lubrication requirements for steels containing free-machining additives differ in an important way from those for other steels. In general, a cutting fluid or external lubricant is recognized as having two important functions. It should provide a low-shear-strength layer at the chip-tool interface and at the same time cause heat to be conducted from the cutting point more rapidly. When a cutting fluid is used in conjunction with an internal lubricant such as lead or sulphur, it is extremely important that the two be compatible. The lubricant must not interfere

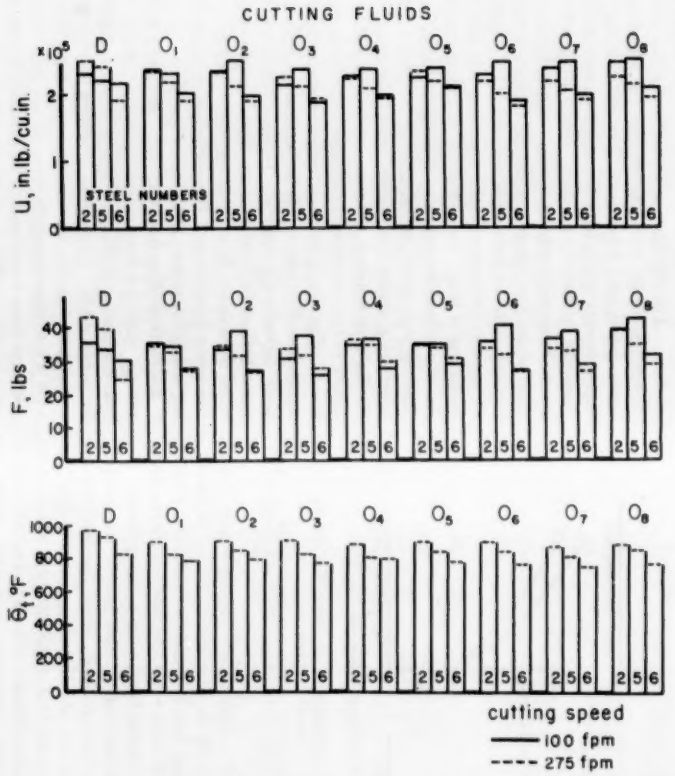

FIG. 13 CUTTING CHARACTERISTICS OF LEADED AND NONLEADED STEELS WITH OIL-BASE CUTTING FLUIDS

(Tool material, T-15 HSS; rake angle, 10 deg; feed, 0.0044 ipr; depth of cut, 0.05 in.; work materials, nonleaded, resulphurized, steels Nos. 2 and 5 and leaded steel No. 6.)

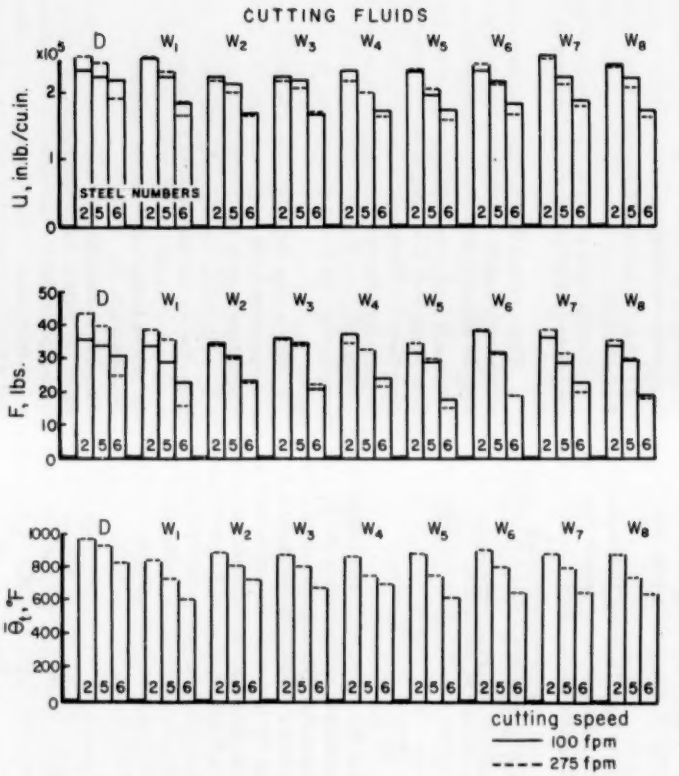

FIG. 14 CUTTING CHARACTERISTICS OF LEADED AND NONLEADED STEELS WITH WATER-BASE CUTTING FLUIDS

(Tool material, T-15 HSS; rake angle, 10 deg; feed, 0.0044 ipr; depth of cut, 0.05 in.; work materials, nonleaded, resulphurized steels Nos. 2 and 5 and leaded steel No. 6.)

with the action of the internal lubricant by making it more difficult for it to spread over the surface of the chip.

Tests performed upon steels Nos. 1 and 2 that differ only in that one is annealed while the other is cold-drawn to a reduction in area of 6.1 per cent failed to show any significant difference in F, u, or $\bar{\theta}_t$. This is not felt to represent the general case, for cold-drawing of even this small amount can improve the machining properties of a very soft steel.

Effect of Lead on Alloy Steels

In Fig. 2 physical properties for a leaded and nonleaded alloy steel (4140) are shown while high-speed chip photomicrographs for these steels are given in Fig. 7. The effect of lead is seen to be essentially the same for alloy steels as for resulphurized low-carbon steels. The addition of lead is found to have a negligible influence on the physical properties of the steel while the chip pictures reveal improved chip formation when lead is present in the steel. Fig. 15 shows representative cutting results for nonleaded 4140 steel No. 3 and its leaded counterpart (steel No. 4). In all cases the lead is seen to reduce the values of u, F, and $\bar{\theta}_t$. As previously noted for other steels, the effect of the lead is more pronounced at higher feed rates and at higher speeds.

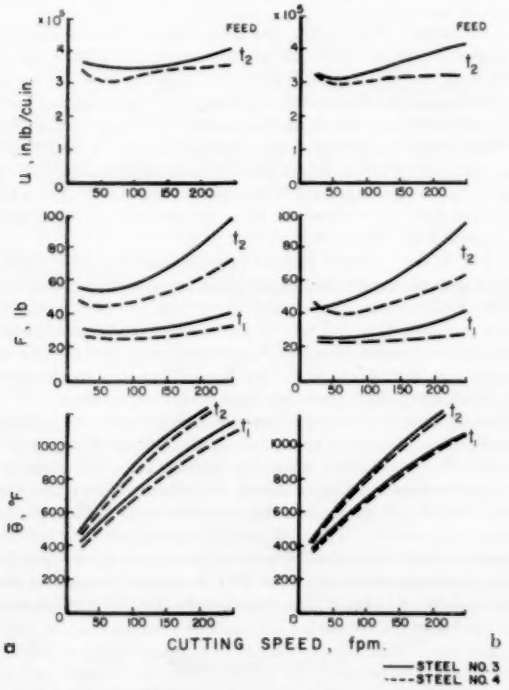

Fig. 15 Cutting Characteristics of Leaded and Nonleaded 4140 Steels

(Tool material, M-2 HSS; rake angle, 10 deg; depth of cut, 0.05 in.; feed, 0.0023 and 0.0044 ipr; cutting fluids, [a] none and [b] cutting oil A; feed, t_1 = 0.0023 ipr, t_2 = 0.0044 ipr.)

The effect of lead in 4140 steel on surface finish was particularly pronounced. This is to be expected from the large reduction in F associated with the use of lead. However, the decrease in temperature ($\bar{\theta}_t$) was not as great as might be expected from similar results on steels Nos. 5 and 6. This is probably due to the presence of a BUE on the tool when cutting the nonleaded 4140 steel. Whenever a BUE is present the measured temperature will be less than that actually existing at the tool point since the deposited chip metal will change the calibration of the chip-tool thermocouple in the direction of decreased sensitivity. Thus, it would appear that the decrease in cutting temperature that actually occurs when lead is present in the steel is largely masked by the tendency for the greater BUE in the case of the nonleaded steel to indicate a temperature that is too low. A large amount of BUE is evident in the photographs of Fig. 7 for the nonleaded steel but not for the leaded steel. The measured tool-temperature values ($\bar{\theta}_t$) provide a useful measure of tool performance only in the absence of large BUE and hence values of $\bar{\theta}_t$ must be used with some care.

Chip-Thickness Ratio. The chip-thickness-ratio values were found to be less for the leaded steel than for the nonleaded steel, despite the fact that the finish and friction were far more favorable when lead was present. From this it would appear that the chip-thickness ratio is useful as a criterion of cutting performance only under certain conditions. The chip-thickness ratio ceases to be a reliable index of cutting performance whenever the chip is badly broken or a large BUE is present. In Fig. 7 the nonleaded steel chips are seen to be far less continuous than the leaded-steel chips. The greater ductility of the leaded 4140 steel enables the chips to remain perfectly continuous until fully formed, whereas the nonleaded chips rupture periodically before they can undergo the strain called for by the large friction force acting between chip and tool. Also, the presence of a large BUE increases the effective rake angle which in turn increases the chip-length ratio even though cutting conditions are less favorable. The comparisons that were made between the chip-thickness-ratio values for cuts of Figs. 4 and 6 are meaningful since in these cases all chips are completely continuous and any BUE present is small.

Carbide Tools. A larger number of tests made using carbide tools were found to check the general picture that has been presented for HSS tools with one important exception. This has to do with the different friction characteristics of cemented carbide and HSS when each is caused to slide over steel. At low sliding speeds cemented carbide gives higher friction than HSS, but as the speed is increased the friction with carbide decreases more

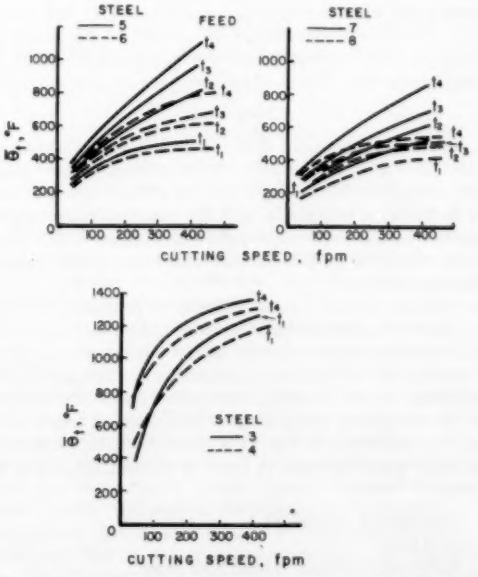

Fig. 16 Variation of Cutting Temperature With Cutting Speed

(Tool material, steel cutting type carbide for roughing; rake angle, 20 deg; cutting fluid, none; depth of cut, 0.05 in.; feed, t_1 = 0.0023 ipr, t_2 = 0.0044 ipr, t_3 = 0.0065 ipr, t_4 = 0.0116 ipr.)

rapidly than in the case of HSS. At speeds above about 100 fpm cemented-carbide friction becomes less than that obtained with HSS. This results in the cutting temperature being slightly higher with carbide tools at low cutting speeds, but significantly lower than for HSS at high speeds. Cutting temperatures are shown for three pairs of leaded and nonleaded steels cut at different speeds and feeds in Fig. 16. Here it is evident that the lead becomes more effective with increased feed or increased speed. The leaded-steel curves cross the nonleaded-steel curves for the 4140 steels at low speeds owing to the presence of a large BUE with the nonleaded 4140 at low speeds. As already mentioned, this is not to be interpreted as indicating larger temperatures for the leaded steel cut at low speed but rather as an indication that a BUE is falsifying the nonleaded-steel temperature values in this region. That this is so may be checked by noting that the values of F were actually considerably less for the nonleaded steel in the low-speed region.

The item of particular interest in Fig. 16 is the fact that steels Nos. 7 and 8 show considerably lower temperatures than steels Nos. 5 and 6, at speeds far above 200 fpm. Previously it was found with HSS tools that sulphur ceased to be effective in decreasing F, u, and $\bar{\theta}_t$ at about 200 fpm. For a 10-deg HSS the temperature corresponding to a speed of 200 fpm is found to be about 900 F. Since all temperatures in Fig. 16(b) are below this value despite the fact that speeds in excess of 400 fpm are considered, it would appear that time is not the item that limits the effectiveness of sulphur in lowering F, u, or $\bar{\theta}_t$ but rather temperature. It is now clear why sulphur appears to be more effective in decreasing F, u, or $\bar{\theta}_t$ at light feeds than at heavy feeds when the cutting speed is in the vicinity of 200 fpm for a HSS tool. Here the temperature falls below the critical value for low feeds but above for high values of feed.

An observation that follows from the foregoing picture is that sulphur should be expected to be most effective in providing good finish for alloy steels such as AISI 4140 and tool steels at low cutting speeds and feeds. At a feed of 0.0116 ipr, AISI 4140 steel is seen to reach the critical temperature (900 F at a speed of but 70 fpm when the carbide tool has a rake angle of 20 deg [see Fig. 16(c)]. Unlike sulphur, lead is not found to be temperature limited and a distinct advantage should result at all speeds from adding lead to alloy steels.

Tool Life

It should be emphasized that the foregoing conclusions relate to the quantities F, u, and $\bar{\theta}_t$. While these quantities directly reflect changes in finish to be expected, great care must be exercised in inferring changes in tool life based on such quantities. Values of F, u, and $\bar{\theta}_t$ correlate quite well when no BUE is present, but the presence of a BUE can lead to incorrect conclusions based on these quantities.

An example of this sort of difficulty is presented in Fig. 17. Here, the development of the wear land on the clearance surface of T-15 HSS tools is shown plotted against cutting time in minutes for steel No. 6. The cutting conditions are identical to those used in Figs. 13 and 14 except for cutting speed which was 300 fpm. By comparing the dash lines from Figs. 13 and 14 for the three fluid conditions of Fig. 17 for steel No. 6 it is evident that these fluids might be rated in order of decreasing u, F, or $\bar{\theta}_t$ as follows:

1 Commercial cutting oil A.
2 Dry tool.
3 Three per cent soluble fluid F in water.

The last two conditions are seen to be interchanged in the two lists. When values of surface roughness were observed they were found to be in accordance with the first order given previously,

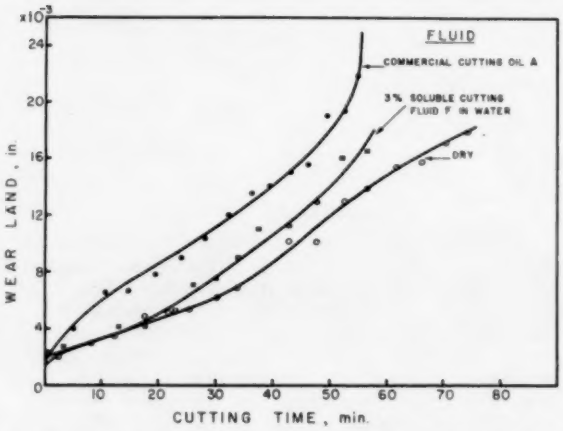

Fig. 17 Variation of Wear Land on Clearance Face of T-15 HSS Tools With Cutting Time

(Rake angle, 10 deg; feed, 0.0044 ipr; depth of cut, 0.05 in.; work material, leaded steel No. 6; cutting speed, 300 fpm; cutting fluid, as noted.)

the water-base fluid giving the best results. There was clear evidence of greater BUE for the tool cutting dry than for that used with the water-base fluid. The only explanation for this result that can be offered is that the larger BUE present on the dry tool protected this tool from wear and thus increased tool life.

The foregoing result also was experienced in an actual production test, where it was found that the tool life when cutting steel No. 6 with water-base fluid F was not improved over dry cutting as might have been expected from the decrease in F, u, and $\bar{\theta}_t$ evident in Figs. 13 and 14.

Thus, it is important to keep in mind that the conclusions of this paper relate only to the quantities measured (F, u, and $\bar{\theta}_t$). While surface finish has been found to improve when these quantities decrease, it is not safe to assume that an improvement in tool life also follows directly. What happens to tool life as a consequence of adding lead or sulphur to steel can only be ascertained by tool-life tests and this is a subject for future research.

The observation that an increased sulphur content in steel is beneficial in production operations carried out at all speeds is not necessarily inconsistent with the finding here that sulphur is effective in lowering F, u, or $\bar{\theta}_t$ only at cutting temperatures below about 900 F. Sulphur may still be effective to higher speeds in improving tool life. The fact that F (or surface finish) is not decreased by additions of sulphur for high cutting speeds is of little interest commercially since the BUE is normally insignificant at such speeds. At high cutting speeds only tool life is of interest in the workshop.

Acknowledgment

The authors are grateful to the LaSalle Steel Company of Chicago for a grant in support of the work reported. They are grateful to Messrs. T. A. Kelly, E. S. Nachtman, and E. A. Hoffman of that organization for their helpful suggestions. The specially prepared leaded and nonleaded steels used in this investigation were obtained by the LaSalle Steel Company through the courtesy of the Inland Steel Company. The high-speed photomicrographs were taken by Mr. John R. McNeil and Prof. Donald R. Walker using a flash tube kindly given them by Prof. Harold E. Edgerton of the Electrical Engineering Department at M.I.T. The aide of Mr. Marsbed Hablanian in certain of the experiments and in the preparation of the paper is also gratefully acknowledged.

BIBLIOGRAPHY

1 French Patents 839,239; 839,240; 839,241; March, 1939. U. S. Patents 2,172,758, 2,182,759 (1939); 2,215,734 (1940); 2,259,342 (1942).

2 "Character and Machine Performance of Lead Bearing Steels," by F. J. Robbins, *Iron Age*, vol. 142, November 17, 1938, p. 28.

3 "Properties of Some Free-Machining, Lead-Bearing Steels." by J. H. Nead, C. E. Sims, and O. E. Harder, *Metals and Alloys*, vol. 10, 1939, pp. 68 and 109; *Iron Age*, vol. 12, 1939, pp. 392 and 441.

4 "A Discussion of Leaded Steels," by F. J. Robbins and C. R. Caskey, Trans. ASM, vol. 27, 1939, p. 887.

5 "Metallwirtsch," by R. Hanel, *Bleistahl als Automatenstahl*, vol. 18, 1939, p. 789.

6 "Jernkontorets Annaler," by C. G. Carlsson, *Tekniska Meddelanden Blylegerat Automatstal*, vol. 123, 1939, p. 266.

7 "Bleihaltiger Automatenstahl," by G. Müller and P. Veit, *Stahl und Eisen*, vol. 60, 1940, p. 367.

8 "Revue de Metallurgie," by M. L. Guillet, *Memoires les Aciers au plomb*, vol. 37, 1940, p. 29.

9 Abstract of "Acciai al piombo," by M. G. Devoto, presented at RCI Convegno Naz Tecnici, *La Metallurgia Italiana*, vol. 34, April, 1942, p. 20.

10 "Leistungssteigerung bei Spanabhebender Bearbeitung durch Bleizustay zum Stahl," by H. Schrader, *Archiv für das Eisenhuttenwesen*, vol. 17, 1943, p. 65.

11 "Examination of Two Ingots of Free Cutting Steel, One Containing Lead and the Other Lead Free," by C. S. Graham, *Journal of the Iron and Steel Institute*, vol. 151, 1945, 273 pp.

12 "The Microscopical Examination of Samples of Lead Bearing and Lead Free Steels and Ingot Irons," by T. H. Schofield, *Journal of the Iron and Steel Institute*, vol. 151, 1945, 277 pp.

13 "Mode of Occurrence of Lead in Lead Bearing Steels and the Mechanism of the Exudation Test," by W. E. Bardgett and R. E. Lisner, *Journal of the Iron and Steel Institute*, vol. 151, 1945, 281 pp.

14 "Influence of Lead Additions on the Mechanical Properties and Machinability of Some Alloy Steels," by J. Woolman and A. Jacques, *Journal of the Iron and Steel Institute*, vol. 162, 1950, p. 257.

15 "Basic Reasons for Good Machinability of Free Machining Steels," by M. E. Merchant and N. Zlatin, Trans. ASM, vol. 41, 1949, pp. 647–677.

16 "Leaded Steel and the Real Area of Contact in Metal Cutting," by M. C. Shaw, P. A. Smith, N. H. Cook, and E. G. Loewen, published in this issue pp. 1165–1171.

17 Anon, American Standards Association Standard ASA B5,19 1946.

Discussion

F. W. Boulger.[6] This article was read with great interest particularly because the first leaded free-cutting steels were made and tested at Battelle in 1936. At that time no effort was made to investigate the mechanism by which lead improved machinability. The authors' careful study presents considerable evidence indicating that lead acts as an internal lubricant which lowers tool-chip interface temperatures.

Although they do not emphasize the point, the authors mention that sulphide inclusions also function as internal lubricants. Therefore, it is a little surprising to find that sulphur was less effective at high speeds. Perhaps the failure to find benefits from the higher sulphur contents of steels Nos. 6 and 8 compared to steels Nos. 5 and 7 was influenced by the order in which they were tested. Fig. 8 indicates that test cuts were made on both of the higher sulphur steels before the lower sulphur steels were machined. Sometimes, the performance of a specimen in a machining test is influenced by the effect of the preceding sample on a cutting tool. It is conceivable that the practice of cutting the higher sulphur steels first left some "lubricant" on the tool and improved the performance of the lower sulphur steels tested subsequently. We have encountered such effects of "heredity" in constant-pressure tests and in radioactive tool wear tests. For this reason, and as a matter of policy, it would be helpful if the authors would say whether they made more than two measurements in their tests and give estimates of the range in replicate measurements of "u," "F," t/t_c, and $\bar{\theta}_t$. Without this information it is difficult to evaluate the significance of the data.

Because the ductility and Charpy values of the leaded samples were particularly good, it would be desirable to know whether the compositions listed in Table 1 are for the bars tested or represent averages for entire heats.

The last sentence of the section on Lubrication Requirements is intriguing. Do the authors have any evidence that the effect of cold work on machining properties depends on the original hardness of the steel? It has been established reasonably well that certain amounts of cold work improve the machining properties of some materials. In the case of steels, one might expect the effect to vary with the amount of cold work, the composition of the steel, and the prior heat-treatment.

E. S. Nachtman.[7] The importance of metal removal methods in our economy cannot be over emphasized. Techniques for improving the quality of the machined product with respect to surface finish and dimensional accuracy as well as those for accelerating productivity of the metal removal process are of extreme importance. The discusser would like to comment on just a few points brought out in this paper.

The importance of a built-up edge in protecting the tool so as to give better tool life has long been recognized. However, the built-up edge results in an inferior surface finish. The addition of lead to steel makes possible excellent tool life at speeds where the built-up edge does not persist so that excellent surface finishes are obtainable. As has been pointed out, however, tool wear does not always occur on the tool edge; it may occur in different areas of the tool. Where wear is initiated depends upon a number of factors. Investigation of the factors responsible for wear location would be profitable to all of us concerned with the machining of steel.

A second important concept discussed in the paper is that dealing with the relationship between additions to steel which improve the cutting characteristics of the steel and externally applied cutting fluids. Further investigation of this relationship should prove interesting.

I believe that this paper will stimulate some new approaches directed toward improving the efficiency of metal removal processes.

Authors' Closure

As Mr. Boulger states, it appears that the chief role of the lead particles in a leaded steel is to act as an internal lubricant which decreases the tendency for the chip to adhere to the face of the tool. This is consistent with the observation that a thin layer of lead deposited on a steel surface significantly decreases the coefficient of sliding friction observed when a second steel specimen slides over the coated surface.

While the subject of this paper concerns lead rather than sulphur, the authors did mention the commonly held view that sulphur in the form of manganese sulphide also acts as an internal lubricant. However, since writing this paper, the authors have performed a simple friction experiment in which manganese sulphide was introduced as a lubricant between steel surfaces. It was found that the character of the manganese sulphide was not that of a lubricant, but instead caused a marked increase in the coefficient of friction over the value for dry surfaces. The authors should, therefore, like to take this opportunity to put forth the view that the role of sulphur in a free-machining steel is not that of a lubricant but just the reverse, tending to provide more points of stress concentration in the steel and promoting

[6] Chief, Ferrous Metallurgy Division, Battelle Memorial Institute, Columbus, Ohio. Mem. ASME.

[7] Research Director, Product Engineering Laboratory, LaSalle Steel Company, Chicago, Ill. Assoc. Mem. ASME.

rather than lessening the tendency for a built-up edge to form. This should not, however, be taken to mean that the presence of sulphur is detrimental to machining, for the tendency of an increased sulphur content according to the new view is to improve finish at low cutting speeds and to improve tool life at high cutting speeds. Details of this matter are beyond the scope of this paper and will be presented in a later paper with supporting data.

To answer Mr. Boulger's question concerning the properties of Table 1, they are averages for the heat of steel from which all bars were taken.

For each machining operation there appears to be an optimum workpiece hardness both with regard to surface finish and tool life. If the workpiece hardness is beyond the optimum then additional cold work will lead to poorer results and vice versa. In the case of very soft low-carbon steels it appears impossible to get the metal too hard from the standpoint of either surface finish or tool life.

We agree with Mr. Nachtman that a built-up edge can sometimes protect a tool from wear and extend tool life although this view is not shared by all workers in this field. It appears that the protection offered by the built-up edge is of most importance at intermediate cutting speeds where crater formation is usually not excessive.

Force Relationships in the Machining of Low-Carbon Steels of Different Sulphur Contents

By F. W. BOULGER,[1] H. E. HARTNER,[2] W. T. LANKFORD,[3] AND T. M. GARVEY[4]

The force relationships obtained in the machining of a series of low-carbon open-hearth steels containing various amounts of sulphur from 0.025 to 0.250 per cent were investigated in a constant-pressure lathe and in a conventional lathe. A wire-resistance, strain-gage dynamometer was used to measure the forces acting on a high-speed tool for various cutting conditions. In the constant-pressure test, sulphur additions increased the feed obtained with a given thrust load. The addition of sulphur reduced the forces acting on the tool for equivalent feeds in both test lathes. Theoretical calculations disclosed that the effectiveness of increased sulphur contents results from decreased friction between the chip and the tool and from an accompanying reduction in strain during chip formation. The decrease in friction and strain reduced the work required for removal of a unit volume of metal during machining. Shear stress was not a direct function of sulphur content, but generally decreased with feed. Results of conventional lathe tests generally corroborated those obtained in the constant-pressure lathe.

Introduction

A KNOWLEDGE of force relationships during metal cutting is essential for an understanding of the properties of a metal that are responsible for its performance in machining operations. Force determinations together with chip measurements provide the necessary data from which the mechanical quantities that affect machinability can be determined. When the controlling material properties are known, the problem of improving machinability can be approached more rationally than if purely empirical data must be relied upon.

In view of the beneficial effect of sulphide inclusions on machinability (1)[5] the effects of sulphur content were studied. Force relationships were investigated in a constant-pressure lathe as well as in a conventional lathe. The constant-pressure lathe has been used extensively for evaluating the machinability of low-carbon free-cutting steels (2 to 4). Machining in this lathe differs from normal machining processes in that the feed is not fixed, but is dependent upon the lateral force exerted on the tool as well as upon the resistance of the workpiece to tool penetration. The tests in the conventional lathe were conducted in order that force relationships could be determined for machining with predetermined feeds. It should be pointed out that one of the objectives of the present investigation was to obtain a clearer understanding of the factors influencing results in the constant-pressure lathe test.

Steels Tested

Mold additions of sulphur were made during teeming of a low-carbon open-hearth heat. The compositions of test bars from the series of steels obtained are shown in Table 1. Representative photomicrographs illustrating the inclusion characteristics of the steels are shown in Fig. 1. The photomicrographs show the increase in the number of manganese-sulphide inclusions with increasing sulphur content. Billets from the heat were hot-rolled to $^7/_8$-in-diam bars which were rough-machined to 0.86-in-diam rounds for testing.

TABLE 1 COMPOSITIONS OF $^7/_8$-IN-DIAM HOT-ROLLED BARS USED FOR EXPERIMENTS

Heat No.	Identification	Melting Process	Per Cent				
			C	Mn	P	S	Si
12J477	U-18	Open Hearth	0.15	0.79	0.009	0.025	0.005
"	U-19	"	0.14	0.79	0.008	0.092	0.003
"	U-20	"	0.13	0.78	0.008	0.190	0.001
"	U-21	"	0.14	0.78	0.007	0.250	0.001

Test bars were from middle billets rolled from successive ingots.

Experimental Procedure

A wire-resistance strain-gage dynamometer was used for measuring the vertical (cutting) and lateral (thrust) forces acting on the cutting tool in the experiments conducted on both the constant-pressure lathe and the conventional lathe. The dynamometer is similar to one that was developed by Loewen, Marshall, and Shaw (5). High-speed tools having the geometry shown in Fig. 2 were used for the tests. In all cases a $^1/_8$-in. depth of cut was taken.

Constant-pressure tests were made on the bars of each sulphur level at cutting speeds of 78 surface feet per minute (sfm) and 202 sfm with hanger weights of 3, 5, 8, and 12 lb. Tests also were made on these bars in the conventional lathe at a cutting speed of 79 sfm with feeds of 0.0022, 0.0039, and 0.008 inch per revolution (ipr). All tests were made without a cutting fluid.

An individual constant-pressure test comprised 1 in. of lateral tool travel, and at least three such tests were made for each cutting condition. The series of steels were tested as a group and the order of machining each steel was varied systematically in the three test groups. A similar procedure was followed for experiments conducted in the conventional lathe.

Chips formed during cutting were collected for microscopic examination and classification. Photomicrographs illustrating the types of chips obtained are presented in Fig. 3. (The chips

[1] Chief, Ferrous Metallurgy Division, Battelle Memorial Institute, Columbus, Ohio. Mem. ASME.

[2] Assistant Technologist, United States Steel Corporation, Pittsburgh, Pa.; formerly a Principal Metallurgist, Battelle Memorial Institute, Columbus, Ohio.

[3] Chief Research Engineer, Specialty Products, United States Steel Corporation, Pittsburgh, Pa. Mem. ASME.

[4] Chief Research Engineer, Carbon Bar and Semi-Finished, United States Steel Corporation, Pittsburgh, Pa.

[5] Numbers in parentheses refer to the Bibliography at the end of the paper.

Contributed by the Research Committee on Metal Processing and presented at the Semi-Annual Meeting, Cleveland, Ohio, June 17–21, 1956, of The American Society of Mechanical Engineers.

Note: Statements and opinions advanced in papers are to be understood as individual expressions of their authors and not those of the Society. Manuscript received at ASME Headquarters, October 28, 1955. Paper No. 56—SA-21.

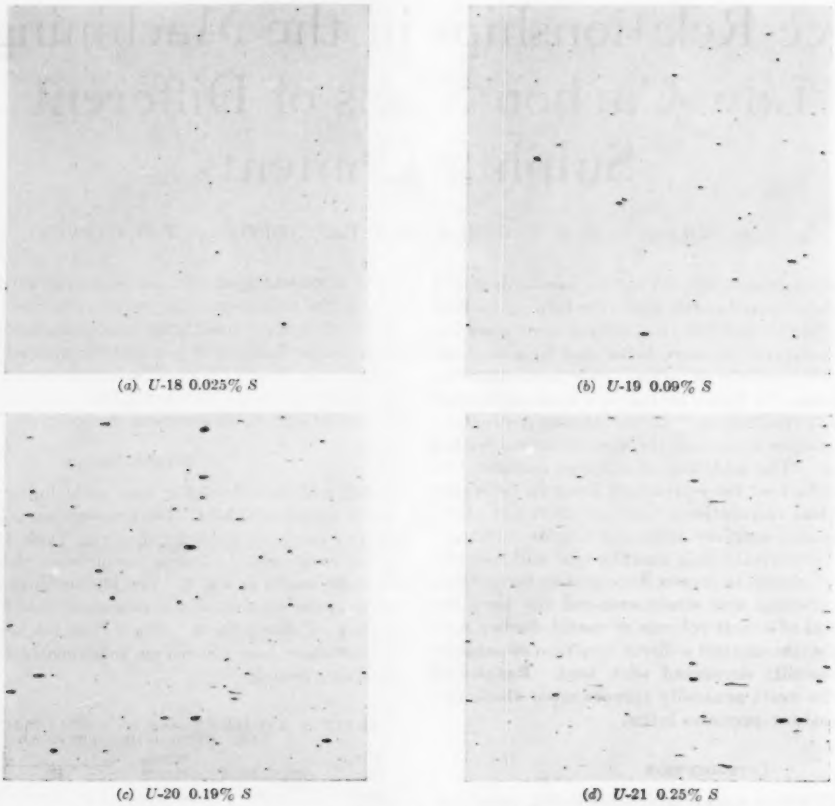

(a) *U*-18 0.025% *S* (b) *U*-19 0.09% *S*

(c) *U*-20 0.19% *S* (d) *U*-21 0.25% *S*

FIG. 1 TYPICAL SULPHIDE INCLUSIONS IN LONGITUDINAL SECTIONS OF SPECIMENS HAVING DIFFERENT SULPHUR CONTENTS. UNETCHED ×100

are from another low-carbon steel, but are typical of those obtained in this investigation.) Representative chips were straightened and at least 5 in. of chips were measured and weighed accurately in a balance. The average chip thickness was then calculated from the known density of the material.

The force measurements and chip thicknesses observed for the various steels and cutting conditions were used to calculate the mechanical quantities affecting machinability according to the theory of metal cutting developed by V. Piispanen (6) and independently by M. E. Merchant (7). Merchant's methods (7 to 9) are described elsewhere and consequently they will not be discussed in detail in this paper.

The analysis developed by Merchant for orthogonal cutting is based on machining conditions for which a continuous chip without a built-up edge is formed. Merchant found by experimentation, however, that if a built-up edge is small compared to the thickness of the chip only a minor error is introduced. Moreover, the analysis can be used to give approximate data even when a discontinuous chip is formed. Furthermore, as shown in Tables 2, 3, and 4, most of the chips obtained in this experiment were continuous or continuous with a slight built-up edge. In two tests some partially discontinuous chips were formed, Table 2. The machining conditions used for this project approximate orthogonal cutting (10).

Nomenclature. The following nomenclature is used in the representation of forces and other mechanical quantities in this work:

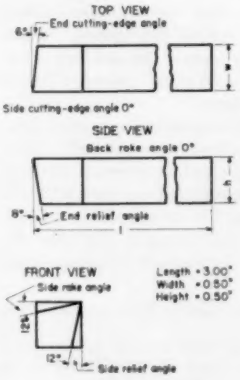

FIG. 2 SHAPE OF THE HIGH-SPEED-STEEL TOOLS USED IN ALL MACHINING TESTS

F = friction force between chip and tool

F_c = cutting force; force component acting in direction of motion of tool relative to workpiece

F_t = thrust force; force component acting in direction perpendicular to F_c

r_c = cutting ratio; ratio of thickness of "chip" material before removal to thickness of chip

S_s = mean shear stress on shear plane

W_f = work used in overcoming friction between chip and tool per unit volume of metal removed

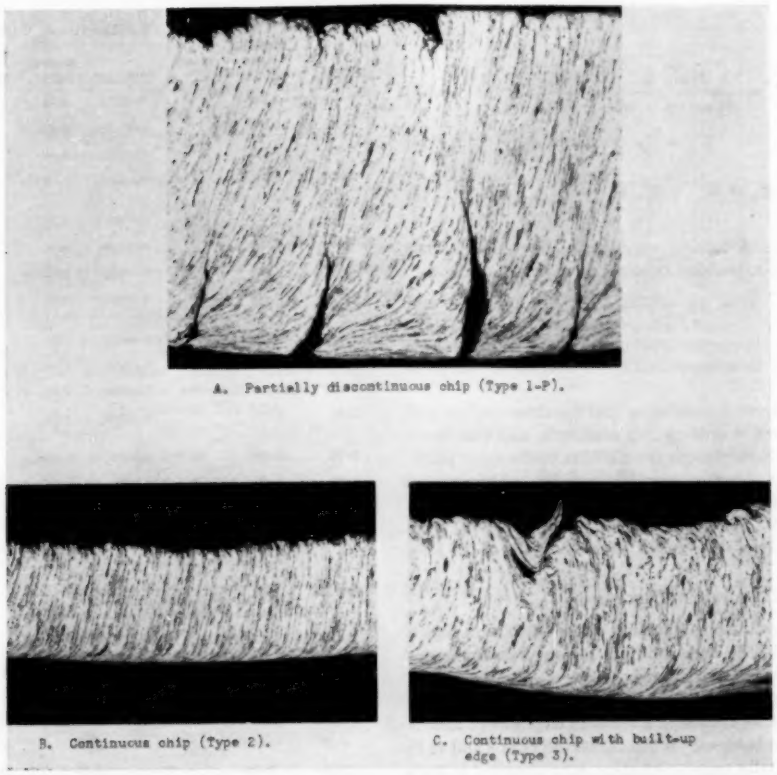

A. Partially discontinuous chip (Type 1-P).

B. Continuous chip (Type 2).

C. Continuous chip with built-up edge (Type 3).

FIG. 3 PHOTOMICROGRAPHS ILLUSTRATING THE TYPES OF CHIPS OBTAINED IN THE EXPERIMENTS. NITAL ETCH, ×100

W_s = work done in shearing of metal per unit volume of metal removed
W_c = total work of cutting per unit volume of metal removed
α = oblique rake angle of tool measured in plane perpendicular to its cutting edge = true rake angle for orthogonal cutting
e = shearing strain undergone by chip during process of formation
μ = dynamic coefficient of friction between sliding chip and tool face
τ = friction angle = arc tan μ
ϕ = shear angle; angle between shear plane and surface being generated measured in plane perpendicular to cutting edge of tool
A_0 = cross-sectional area of chip before removal from workpiece

The mathematical relationships developed by Merchant are as follows

$$\tan \phi = \frac{r_c \cos \alpha}{1 - r_c \sin \alpha} \quad \ldots\ldots [1]$$

$$e = \cot \phi + \tan (\phi - \alpha) \quad \ldots\ldots [2]$$

$$\mu = \frac{F_t + F_c \tan \alpha}{F_c - F_t \tan \alpha} \quad \ldots\ldots [3]$$

$$F = F_t \cos \alpha + F_c \sin \alpha \quad \ldots\ldots [4]$$

TABLE 2 HARDNESS AND MICROSCOPIC CLASSIFICATION OF CHIPS IN CONSTANT-PRESSURE TESTS AT 78 SFM

Material	Sulphur Content, per cent	Hanger Weight, lb.	Feed, ipr	Natural Strain	Average Knoop Hardness	Microscopic Classification*
U-18	0.025	3	0.00073	5.82	253	Type 2
U-19	0.092	"	0.00144	2.38	227	Type 2
U-20	0.190	"	0.00183	2.45	258	Type 2
U-21	0.250	"	0.00180	2.44	382	Type 2
U-18	0.025	5	0.00118	4.70	361	Type 2
U-19	0.092	"	0.00209	2.35	278	Type 3-0
U-20	0.190	"	0.00267	2.25	258	Type 3-0
U-21	0.250	"	0.00268	2.44	275	Type 3-0
U-18	0.025	8	0.00248	4.77	307	Type 3
U-19	0.092	"	0.00333	3.72	304	Types 1-P and 3
U-20	0.190	"	0.00426	3.43	273	Type 3
U-21	0.250	"	0.00414	3.30	296	Type 3
U-18	0.025	12	0.0045	3.00	296	Type 3
U-19	0.092	"	0.0054	3.03	276	Type 3
U-20	0.190	"	0.0059	2.98	286	Type 3 and traces of Type 1-P
U-21	0.250	"	0.0066	2.22	273	Type 3

* Type 1-P - Partially discontinuous
" 2 - Continuous without a built-up edge
" 3 - Continuous with a built-up edge
" 3-0 - Continuous with occasional built-up edge

$$S_s = \frac{F_c \sin\phi \cos\phi - F_t \sin^2\phi}{A_0} \quad [5]$$

$$W_f = \frac{F \sin\phi}{A_0 \cos(\phi - \alpha)} = \frac{Fr_c}{A_0} \quad [6]$$

$$W_s = S_s e \quad [7]$$

$$W_s = W_f + W_s = \frac{F_c}{A_0} \quad [8]$$

In addition to the foregoing quantities Merchant (9) has derived the following expression relating ϕ, τ, and α

$$C = 2\phi + \tau - \alpha \quad [9]$$

where C is the angle whose cotangent is the slope of the curve relating shear strength to compressive stress normal to the shear plane.

The equation is derived by assuming that the shear angle ϕ is so oriented that the work of cutting is a minimum, and that shear strength increases with increased normal stress on the shear plane. While it is known that fracture strength increases with increased normal pressure, a similar effect on shear strength has not been generally established. Shaw and his co-workers (11, 12) have questioned the validity of the concept expressed by C in the foregoing.

Results and Discussion

Chip Characteristics. At the cutting speed of 78 sfm and a hanger weight of 3 lb, the chips from all the steels in this series were continuous and did not show evidence of a built-up edge, Table 2. Increasing the thrust load by use of a 5-lb hanger weight resulted in the formation of a built-up edge except for the steel of lowest sulphur content. When thrust forces of 8 and 12 lb were used, some partially segmented chips were observed in tests at feeds of 0.0033 ipr and 0.0059 ipr. The formation of a built-up edge appeared to be a function of feed rather than of sulphur content at this cutting speed. The data indicate that at 78 sfm a feed of about 0.002 ipr is the limiting feed above which a built-up edge is formed in these steels in dry cutting. The Knoop hardnesses showed little tendency to increase with increased strain in the chips.

Tests conducted at 202 sfm also disclosed that continuous chips were obtained for the steels studied, Table 3. Again, increased feeds resulting from increased thrust forces resulted in the appearance of a built-up edge. At this higher cutting speed, built-up edges formed at lower feeds than at 78 sfm. This behavior is believed to be caused by an increase in friction at the tool-chip interface with the higher speed as will be discussed in a subsequent section. The hardnesses of chips formed at 202 sfm increased slightly with strain but were not much different, at equivalent strains, than those obtained at 78 sfm.

The chips formed at a cutting speed of 79 sfm in the conventional lathe were similar to those obtained in the constant-pressure test at equivalent feeds, Table 4. The hardness of these chips exhibited little tendency to increase with increased strain.

Analysis of Cutting Data. In the constant-pressure test the feed obtained is a function of the applied thrust load. Because of differences in cutting characteristics, different steels do not provide the same feed when cut with equivalent loads. Moreover, it has been shown by several investigators (13 to 15) that some of the mechanical quantities affecting metal cutting and machinability vary with feed for a given steel. For these reasons it is desirable to evaluate the measured and calculated properties in terms of feed in the constant-pressure test. Graphs were therefore prepared relating the mechanical properties to the feed produced by various thrust loads.

TABLE 3 HARDNESS AND MICROSCOPIC CLASSIFICATION OF CHIPS IN CONSTANT-PRESSURE TESTS AT 202 SFM

Material	Sulphur Content per cent	Hanger Weight lb.	Feed, ipr	Natural Strain	Average Knoop Hardness	Microscopic Classification*
U-18	0.025	3	0.00077	4.42	308	Type 2
U-19	0.092	"	0.00113	2.57	258	Type 2
U-20	0.190	"	0.00133	2.54	224	Type 2
U-21	0.250	"	0.00125	2.74	265	Type 2
U-18	0.025	5	0.00090	5.69	314	Type 3-0
U-19	0.092	"	0.00136	4.05	302	Type 3
U-20	0.190	"	0.00183	3.50	280	Type 3
U-21	0.250	"	0.00176	3.34	297	Type 3
U-18	0.025	8	0.00153	5.95	309	Types 2 and 3-0
U-19	0.092	"	0.00204	5.40	293	Type 3-0
U-20	0.190	"	0.00280	4.11	279	Type 3-0
U-21	0.250	"	0.00288	3.82	293	Type 3
U-18	0.025	12	0.0031	5.10	322	Types 2 and 3-0
U-19	0.092	"	0.0044	4.15	308	Types 2 and 3-0
U-20	0.190	"	0.0053	3.90	287	Type 3-0
U-21	0.250	"	0.0061	3.40	277	Type 3-0

* Type 2 - Continuous without a built-up edge
Type 3 - Continuous with a built-up edge
Type 3-0 - Continuous with occasional built-up edge

TABLE 4 HARDNESS AND MICROSCOPIC CLASSIFICATION OF CHIPS IN CONVENTIONAL-LATHE TESTS AT 79 SFM

Material	Sulphur Content, per cent	Feed, ipr	Natural Strain	Average Knoop Hardness	Microscopic Classification*
U-18	0.025	0.0022	3.86	308	Type 3
U-19	0.092	"	2.64	274	Type 3-0
U-20	0.190	"	2.29	326	Type 3
U-21	0.250	"	3.76	305	Type 3
U-18	0.025	0.0039	4.32	328	Type 3
U-19	0.092	"	2.42	287	Type 3
U-20	0.190	"	3.54	307	Type 3
U-21	0.250	"	3.40	284	Type 3
U-18	0.025	0.008	5.04	333	Type 2
U-19	0.092	"	3.54	288	Type 3
U-20	0.190	"	3.24	314	Type 3
U-21	0.250	"	3.12	289	Type 3

* Type 2 - Continuous without a built-up edge
Type 3 - Continuous with a built-up edge
Type 3-0 - Continuous with occasional built-up edge

The effect of increasing sulphur content on the feed obtained in the constant-pressure test for different thrust forces is shown in Fig. 4. As would be expected, increasing the sulphur content generally resulted in heavier feeds at both cutting speeds; the two steels containing the highest amounts of sulphur exhibited approximately equivalent feeds, except at the highest thrust force where the highest-sulphur steel exhibited the highest feed. Lower feeds were obtained at 202 sfm than at 78 sfm. The increase in feed with thrust force caused the cutting forces to increase. This effect is shown in Fig. 5. For a given thrust force the cutting force is less at 202 sfm than at 78 sfm. This effect is largely a result of the lower feeds obtained at 202 sfm.

Cutting force is shown as a function of feed in Figs. 6(a) and 6(b) for the two cutting speeds involved. The cutting force for

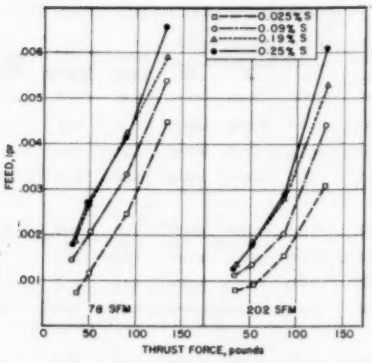

FIG. 4 EFFECT OF THRUST FORCE ON FEED IN THE CONSTANT-PRESSURE LATHE TEST AT 78 SFM AND 202 SFM

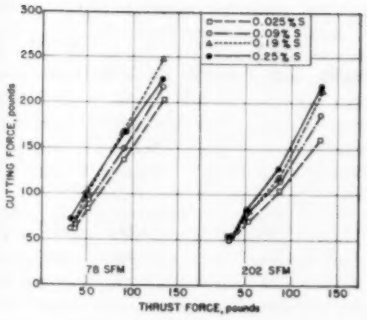

FIG. 5 RELATIONSHIP BETWEEN CUTTING FORCE AND THRUST FORCE IN CONSTANT-PRESSURE LATHE TEST AT 78 SFM AND 202 SFM

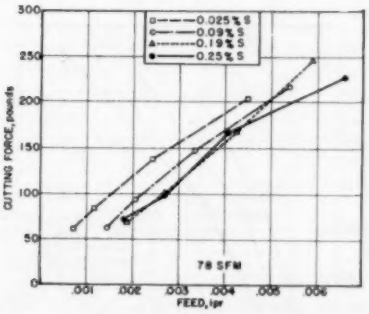

FIG. 6(a) RELATIONSHIP BETWEEN CUTTING FORCE AND FEED IN CONSTANT-PRESSURE LATHE TEST AT 78 SFM

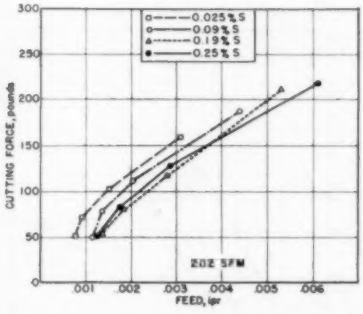

FIG. 6(b) RELATIONSHIP BETWEEN CUTTING FORCE AND FEED IN CONSTANT-PRESSURE LATHE TEST AT 202 SFM

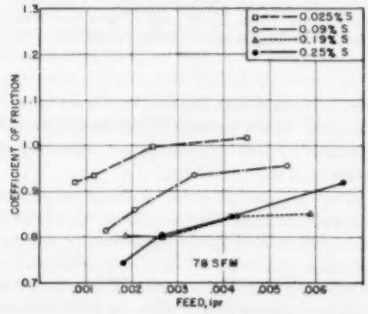

FIG. 7(a) RELATIONSHIP BETWEEN COEFFICIENT OF FRICTION AND FEED IN CONSTANT-PRESSURE LATHE TEST AT 78 SFM

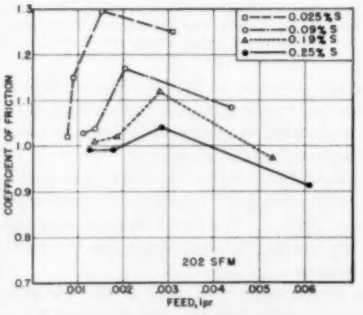

FIG. 7(b) RELATIONSHIP BETWEEN COEFFICIENT OF FRICTION AND FEED IN CONSTANT-PRESSURE LATHE TEST AT 202 SFM

a given feed decreased as the sulphur content was raised except that little difference existed between the cutting forces for the two steels containing 0.19 and 0.25 per cent sulphur, respectively. The results of tests conducted in the conventional lathe are shown in Table 5. These data also show that the cutting force generally decreased as the sulphur content was raised. For some unexplained reason, inconsistently low cutting forces were obtained on the steel which contained 0.09 per cent sulphur (U-19) at 0.0039 ipr. For equivalent cutting conditions, the thrust force also decreased as the sulphur content was raised in this test.

One of the most important factors that must be considered in interpreting metal-cutting phenomena is the friction at the tool-chip interface. In many instances the frictional characteristics are more subject to control than are the other variables associated with free-cutting metals. The coefficients of friction for the various steels are plotted as a function of feed in Figs. 7(*a*) and 7(*b*) for the two cutting speeds investigated. At both speeds, the coefficients decreased with increased sulphur content except that no consistent effect of sulphur was noted for the two steels that had the highest sulphur when tested at 78 sfm. The friction co-

TABLE 5 MECHANICAL QUANTITIES CALCULATED FOR CONVENTIONAL LATHE TESTS AT 79 SFM

Material	Feed, ipr	Cutting Ratio, rc	Shear Angle ϕ, degrees	Coefficient of Friction	Friction Force, lbs.	Shear Stress, psi	Work, in-lb./cu. in. of Metal Removed			Shear Strain	C, Degrees	Tool-Force, lbs.	
							Wf	We	Wc			Cutting	Thrust
U-18	0.0022	0.254	14.7	0.905	103.0	101500	95600	391500	487100	3.86	59.6	133	77
U-19	"	0.382	22.1	0.798	75.6	111000	106000	293500	399500	2.64	70.8	110	55
U-20	"	0.456	26.2	0.734	64.8	112700	108000	258000	366000	2.29	76.7	100	45
U-21	"	0.259	15.0	0.700	64.6	84850	61600	319000	380600	3.76	53.0	104	44
U-18	0.0039	0.226	13.1	0.922	191.6	94500	88300	406000	494300	4.32	56.9	244	144
U-19	"	0.423	24.4	0.870	129.7	98800	112000	239500	351500	2.42	77.8	172	96
U-20	"	0.276	16.0	0.766	133.2	93400	76000	331000	407000	3.54	55.5	198	94
U-21	"	0.290	16.8	0.797	130.7	96900	78500	329000	407500	3.40	58.7	196	92
U-18	0.008	0.194	11.2	1.051	375.7	71500	73900	360000	433900	5.04	56.8	427	293
U-19	"	0.279	16.1	0.948	293.7	78300	80300	277000	357300	3.54	63.7	364	223
U-20	"	0.305	17.6	0.869	269.5	84200	81200	273000	354200	3.24	64.2	339	199
U-21	"	0.317	18.4	0.852	252.3	83100	78900	259000	337900	3.12	65.2	343	185

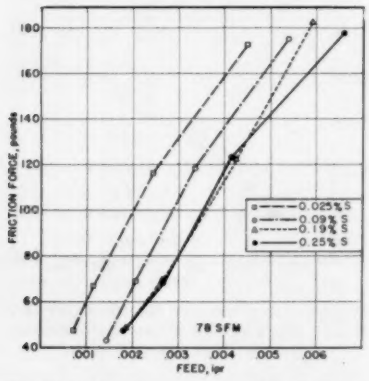

FIG. 8(a) RELATIONSHIP BETWEEN FRICTION FORCE ON TOOL AND FEED IN CONSTANT-PRESSURE LATHE TEST AT 78 SFM

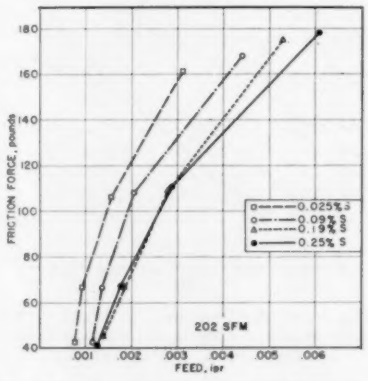

FIG. 8(b) RELATIONSHIP BETWEEN FRICTION FORCE ON THE TOOL AND FEED IN THE CONSTANT-PRESSURE LATHE TEST AT 202 SFM

efficients were higher at 202 sfm than at 78 sfm. The coefficient of friction increased with feed at 78 sfm. On the other hand, a maximum coefficient was observed at intermediate feeds for each steel when tests were conducted at 202 sfm.

The coefficients of friction calculated for the tests made in the conventional lathe at a cutting speed of 79 sfm also decreased with increased sulphur content, Table 5. As would be expected from the constant-pressure test results, the coefficients also increased with feed in this series of tests.

Tool performance as measured by tool wear or tool life generally may be more closely associated with the frictional force than with the coefficient of friction. The significance of the coefficient of friction for interpreting metal-cutting phenomena has not been established conclusively and its applicability to machinability evaluation has been questioned. It is often assumed that a low coefficient implies low tool temperature and long tool life. This is not necessarily true; the coefficient, which is the ratio of the frictional force to the normal force on the tool face, can decrease even when both forces increase.

Hahn (16) indicates that the concept of a coefficient of friction is not applicable to metal cutting because the actual contact area is about equal to the apparent contact area. Kronenberg (17) has shown that the use of a friction coefficient in metal-cutting research can be misleading. He points out, for example, that both force components can decrease and yet, if the normal force decreases faster than the friction force, the coefficient of friction increases. More recently Finnie and Shaw (18) have indicated that the coefficient of friction is not adequate to portray the friction process in metal cutting.

For the present series of steels containing various amounts of sulphur, increased sulphur contents up to 0.19 per cent progressively decreased the friction force for a given feed in the constant-pressure test at both 78 sfm and 202 sfm as shown in Figs. 8(a) and 8(b). Only at the heaviest feeds, however, did an increase in sulphur content to 0.25 per cent further decrease the friction force. At the higher speed the frictional force was greater, for an equivalent feed, than at the lower speed. The observation that the feeds obtained at 202 sfm are lower than those attained at 78 sfm apparently can be accounted for by the fact that higher frictional forces are developed at the higher cutting speed. As would be expected, the frictional force developed in the conventional lathe also tended to decrease with increased sulphur content.

In addition to the friction between the chip and tool, the shear stresses and strains developed in the material being machined are of paramount importance in the interpretation of force relationships, inasmuch as the formation of chips in any machining operation is fundamentally a process of plastic flow. The data shown graphically in Figs. 9(a) and 9(b) disclose that shear stress decreased with feed at both cutting speeds used until a feed of about

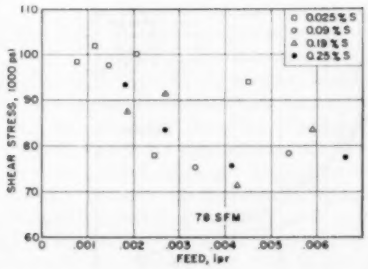

FIG. 9(a) RELATIONSHIP BETWEEN SHEAR STRESS AND FEED IN THE CONSTANT-PRESSURE LATHE TEST AT 78 SFM

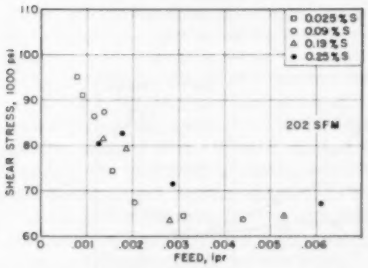

FIG. 9(b) RELATIONSHIP BETWEEN SHEAR STRESS AND FEED IN THE CONSTANT-PRESSURE LATHE TEST AT 202 SFM

0.003 ipr was reached. This type of relationship has been observed by other investigators and has been attributed to a size effect by Shaw, Smith, and Cook (19). The shear stress at 202 sfm was lower for a given feed than at 78 sfm. This change in shear stress with speed is opposite to that which would be expected from increasing the strain rate. Shear stress did not appear to be a function of sulphur content except for an indirect effect attributable to the increased feed obtained on specimens that contained high amounts of sulphur.

The conventional-lathe tests also showed that shear stress decreased, in general, as the feed was increased, Table 5. There appeared to be a tendency for the shear stress to increase slightly with increased sulphur content, but the data are not conclusive in this regard.

Since the work of cutting is greatly affected by the amount of chip deformation, it was very desirable to establish the relationship between sulphur content and shear strain. The natural strain occurring during chip formation is plotted as a function of feed in Figs. 10(*a*) and 10(*b*). At 78 sfm, and with small feeds, the nonresulphurized steel (0.025 per cent sulphur) underwent much greater deformation during chip formation than did the resulphurized steels. At this speed, but with heavier feeds, the shear strain for all the steels was about the same. There did not appear to be consistent significant differences in strain among any of the resulphurized specimens at 78 sfm. Shear strain was significantly lowered with increased sulphur content at 202 sfm. For a given feed, the amount of deformation was generally greater at 202 sfm than at 78 sfm. Shaw (20) has shown that if friction at the tool-chip interface is reduced by the use of a cutting fluid, the shear strain in the chips is also lowered. The increase in frictional characteristics as the cutting speed was increased may, therefore, at least partially account for the increased strain at the higher cutting speed.

There was a tendency for shear strain to increase as the coefficient of friction increased as would be predicted from Shaw's work (20) and from Merchant's equation, $C = 2\phi + \tau - \alpha$.

In the tests made in the conventional lathe, larger shear strains were obtained on the nonresulphurized (0.025 per cent sulphur) steel than on any of the resulphurized steels at the three feeds studied, Table 5. However, the resulphurized steels did not show a consistent effect of sulphur on strain.

In the usual methods of determining stress strain relationships in the plastic range, for example in the conventional tension test, stress always increases with strain for metals when tested at a temperature where work hardening occurs. On the other hand, metal-cutting tests have not normally indicated such a relationship between stress and strain. The present tests on the steels of different sulphur content in the constant-pressure lathe also indicate that shear stress does not increase with shear strain. The data from the conventional lathe showed a trend to decreasing shear stress with increased strain, Table 5.

With regard to the phenomenon just described, Backer, Marshall, and Shaw (21) have indicated that with low shear angles the region of shear is irregular and thick, whereas with larger shear angles (i.e., less strain) the shear region is sharper and more nearly a plane. They state it to be conceivable that the flow stress associated with a high shear angle will be greater than that with a low shear angle because the shear zone is smaller with the higher shear angle. This is designated as a shear-volume type of size effect to distinguish it from the size effect that is attributed to variations in feed.

The work expended in overcoming friction at the tool-chip interface in the constant-pressure test was not consistently affected

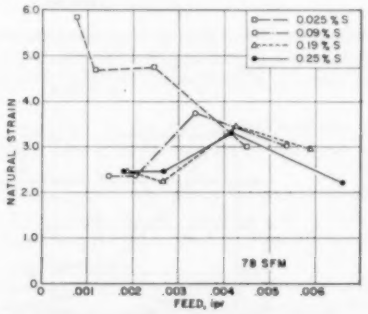

FIG. 10(a) RELATIONSHIP BETWEEN NATURAL STRAIN OCCURRING DURING CHIP FORMATION AND FEED IN CONSTANT-PRESSURE LATHE TEST AT 78 SFM

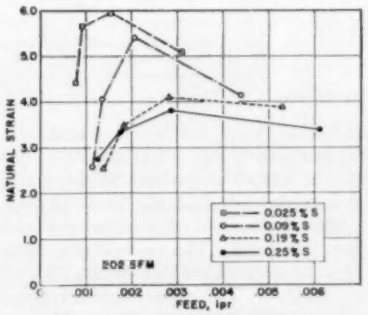

FIG. 10(b) RELATIONSHIP BETWEEN NATURAL STRAIN OCCURRING DURING CHIP FORMATION AND FEED IN CONSTANT-PRESSURE LATHE TEST AT 202 SFM

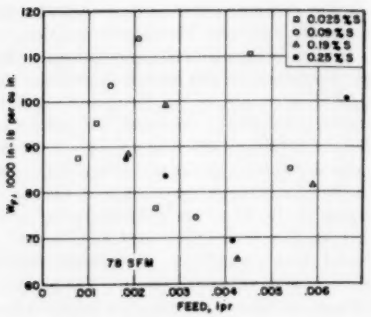

FIG. 11(a) RELATIONSHIP BETWEEN WORK REQUIRED TO OVERCOME TOOL-CHIP FRICTION (W_f) AND FEED IN CONSTANT-PRESSURE LATHE TEST AT 78 SFM

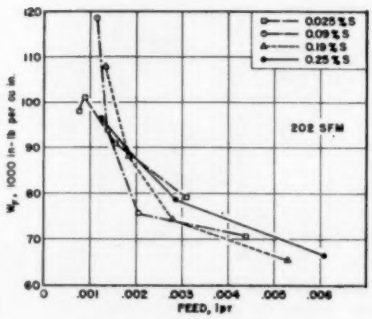

FIG. 11(b) RELATIONSHIP BETWEEN WORK REQUIRED TO OVERCOME TOOL-CHIP FRICTION (W_f) AND FEED IN CONSTANT-PRESSURE LATHE TEST AT 202 SFM

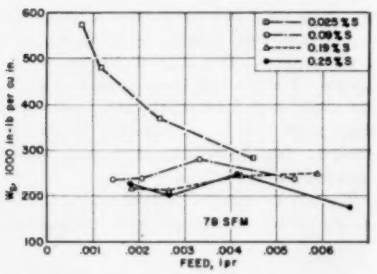

FIG. 12(a) RELATIONSHIP BETWEEN WORK REQUIRED FOR SHEARING CHIPS (W_s) AND FEED IN CONSTANT-PRESSURE LATHE TEST AT 78 SFM

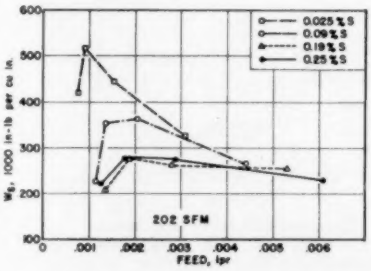

FIG. 12(b) RELATIONSHIP BETWEEN WORK REQUIRED FOR SHEARING CHIPS (W_s) AND FEED IN CONSTANT-PRESSURE LATHE TEST AT 202 SFM

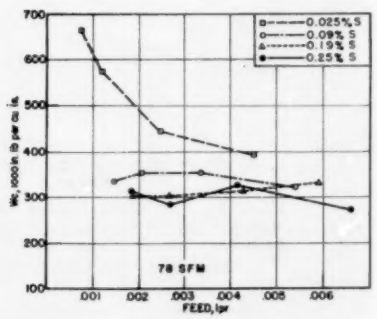

FIG. 13(a) RELATIONSHIP BETWEEN TOTAL WORK OF CUTTING (W_c) AND FEED IN CONSTANT-PRESSURE LATHE TEST AT 78 SFM

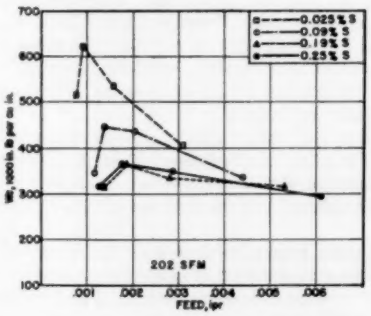

FIG. 13(b) RELATIONSHIP BETWEEN TOTAL WORK OF CUTTING (W_c) AND FEED IN CONSTANT-PRESSURE LATHE TEST AT 202 SFM

by changes in feed at 78 sfm, but decreased with feed of 202 sfm. These effects are shown in Figs. 11(*a*) and 11(*b*). There was no consistent effect of sulphur on the work of friction at equal feeds. Therefore, despite the fact that the frictional force decreased with added sulphur, the work required for overcoming friction did not follow this trend. The conventional lathe tests also showed no trend to lessened work of friction with increased sulphur content, Table 5. The reason for this appears to be that the effect of reduced frictional force is offset by the increased shear angle, i.e.

$$W_f = \frac{Fr_c}{A_0}$$

The other component of the total work of cutting is the work expended in shearing. At both 78 sfm and 202 sfm the work of shear was higher for the nonresulphurized steel at all feeds than for the other steels as shown in Figs. 12(*a* and *b*). This effect was most pronounced at low feeds. The work of shear decreased as the sulphur content was raised to 0.19 per cent, but increasing the sulphur content to 0.25 per cent did not consistently affect W_s further for this series of steels. The results obtained in the conventional lathe also showed that the highest work of shear was obtained on the nonresulphurized steel for the range of feeds investigated, Table 5. However, shear work was not uniformly

affected by the different sulphur contents of the resulphurized steels.

The work of shear is equal to the product of shear stress and shear strain. It was pointed out that shear stress is not a function of sulphur content. Therefore the effect of sulphur in reducing the work required to shear the chips is primarily due to its effect on chip strain. As pointed out earlier in this discussion, the reduction of strain is probably attributable to the decreased frictional characteristics at the tool-chip interface. It is of interest to note that, in machining these steels, the shear process necessitated the expenditure of much more work than that required to overcome the friction of the chips rubbing against the cutting tool. For example, at 202 sfm and a feed of 0.0018 ipr, about 275,000 in-lb per cu in. of metal removed were required to shear the chips of the steel containing 0.19 per cent sulphur whereas only 88,000 in-lb per cu in. of metal removed were required to overcome the friction between the chips and the cutting tool.

The total work expended in cutting is, of course, the sum of that used in shearing the chip and that consumed in overcoming the friction between the formed chip and the cutting tool. The total work used in machining this series is shown in Figs. 13(*a*) and 13(*b*). Primarily, because of the reduced amount of work required for shearing, the total work of cutting was lowest for the higher sulphur steels at both cutting speeds. As would be expected from the analysis of the data, there was no appreciable difference in total work between the steel containing 0.19 per cent sulphur and the steel containing 0.25 per cent sulphur.

The failure of many of the measured and calculated quantities to separate the two steels which had the highest sulphur contents is believed to be a result of differences in sulphide inclusion characteristics between these two steels. As shown in Fig. 1, specimens which contained 0.19 per cent sulphur had a greater proportion of globular sulphides than did those which contained 0.25 per cent sulphur. Previous investigations (1, 2, 3, 22) have shown that globular sulphides are preferable to thinner, elongated sulphides for improving machinability. The higher sulphur content, therefore, appears to have been offset by the somewhat less desirable inclusion characteristics.

The values of the quantity C, defined previously in Equation [9], were not constant in the constant-pressure lathe tests at 78 sfm, Table 6. At this cutting speed, C increased with feed when the lowest sulphur steel was machined, but did not change uniformly with feed for tests made on the resulphurized steels. At 202 sfm, however, C remained quite constant over the range of feeds investigated except that comparatively high values of C were obtained on the resulphurized steels at low feeds, Table 6. There was considerable variation in C when calculated from the data obtained in the conventional lathe, Table 5, except for the values obtained on the steel having the lowest sulphur content.

TABLE 6 RELATIONSHIP BETWEEN C AND FEED IN CONSTANT-PRESSURE TESTS

Steel	78 SFM Feed, ipr	C, degrees	Steel	202 SFM Feed, ipr	C, degrees
U-18	0.00073	49.8	U-18	0.00077	59.2
U-19	0.00144	77.0	U-19	0.00113	79.5
U-20	0.00183	74.7	U-20	0.00133	79.6
U-21	0.00180	72.7	U-21	0.00125	75.1
U-18	0.00118	55.0	U-18	0.00090	56.8
U-19	0.00209	79.2	U-19	0.00136	62.1
U-20	0.00267	80.0	U-20	0.00183	66.2
U-21	0.00268	75.0	U-21	0.00176	66.9
U-18	0.00248	56.5	U-18	0.00153	59.2
U-19	0.00333	61.6	U-19	0.00204	58.3
U-20	0.00426	61.3	U-20	0.00280	64.0
U-21	0.00414	62.5	U-21	0.00268	63.8
U-18	0.0045	71.5	U-18	0.0031	61.3
U-19	0.0054	69.3	U-19	0.0044	62.5
U-20	0.0059	66.9	U-20	0.0053	61.2
U-21	0.0066	84.6	U-21	0.0061	64.1

The results obtained in this investigation have shown that the constant-pressure test is quite sensitive to changes in friction between the chip and the cutting tool. This finding is in agreement with a theoretical discussion of the test presented by Merchant (10).

It should be pointed out that the relative importance of the various measured and calculated quantities with respect to tool wear and tool life is not presently known. It is evident, however, that for these steels having similar strength levels, the frictional characteristics at the chip-tool interface and the related values of shear strain in the chips are the primary factors associated with their machinability. The heat generated during machining is, of course, a function of the work expended. The work done in shearing and work used in overcoming friction, therefore, are among the factors that influence cutting-tool performance. In addition, tool abrasion also would be affected by the forces acting on the tool. These forces are dependent upon the properties of the workpiece under the cutting conditions.

Summary and Conclusions

The conclusions regarding the effectiveness of increased sulphur content in improving the machinability of a low-carbon, open-hearth steel can be summarized as follows:

1 The feed obtained on test bars in the constant-pressure lathe with a given thrust force is increased as the sulphur content is raised, largely because of reduced friction between the chip and the tool.

2 The reduction in friction at the chip-tool interface is normally accompanied by an increase in the shear angle with a consequent lowering of chip strain.

3 The reduced chip strain lowers the work required to form the chips and thereby reduces the total work of cutting.

4 Shear stress on the shear plane does not appear to be directly related to sulphur content.

In the constant-pressure test, tool-chip friction and the extent of chip deformation are greater at 202 sfm than at 78 sfm for the steels investigated.

Experiments in a conventional lathe are in good agreement with those conducted in the constant-pressure test.

Acknowledgments

This investigation was conducted as a co-operative research project supported by the United States Steel Corporation at Battelle Memorial Institute. The valuable contributions of many members of both organizations is hereby gratefully acknowledged.

Bibliography

1 "Basic Reasons for Good Machinability of Free-Machining Steels," by M. E. Merchant and N. Zlatin, Trans. ASM, vol. 41, 1949, pp. 647–671.

2 "Basic Reasons for Superiority of MX Explained," by F. W. Boulger, H. A. Moorhead, and T. M. Garvey, *Iron Age*, vol. 167, May 17, 1951, pp. 90–95.

3 "Correlation of Machinability With Inclusion Characteristics in Resulphurized Bessemer Steels," by L. H. Van Vlack, Trans. ASM, vol. 45, 1953, pp. 741–753.

4 "Constant-Pressure Lathe Test for Measuring the Machinability of Free-Cutting Steels," by F. W. Boulger, H. L. Shaw, and H. E. Johnson, Trans. ASME, vol. 71, 1949, pp. 431–438.

5 "Electric Strain Gage Tool Dynamometers," by E. G. Loewen, E. R. Marshall, and M. C. Shaw, Proceedings of the Society for Experimental Stress Analysis, vol. 8, no. 2, 1951, pp. 1–16.

6 "Theory of Formation of Metal Chips," by V. Piispanen, *Journal of Applied Physics*, vol. 19, no. 10, 1948, pp. 876–881.

7 "Basic Mechanics of the Metal-Cutting Process," by M. E. Merchant, *Journal of Applied Mechanics*, Trans. ASME, vol. 66, 1944, p. A-168.

8 "Mechanics of the Metal-Cutting Process I. Orthogonal Cutting and a Type 2 Chip," by M. E. Merchant, *Journal of Applied Physics*, vol. 16, no. 5, 1945, pp. 267–275.

9 "Mechanics of the Metal-Cutting Process II. Conditions in Orthogonal Cutting," by M. E. Merchant, *Journal of Applied Physics*, vol. 16, no. 6, 1945, pp. 318–324.

10 M. E. Merchant's discussion of reference (4).

11 "The Shear-Angle Relationship in Metal Cutting," by M. C. Shaw, N. H. Cook, and I. Finnie, Trans. ASME, vol. 75, 1953, pp. 273–283.

12 "The Shear Stress in Metal Cutting," by M. C. Shaw and I. Finnie, Trans. ASME, vol. 77, 1955, pp. 115–123.

13 "Principles of Metal Cutting and Machinability," Chapter in Tool Engineer's Handbook, published by McGraw-Hill Book Company, Inc., New York, N. Y., 1949, p. 313.

14 "Thermophysical Aspects of Metal Cutting," by B. T. Chao, K. J. Trigger, and L. B. Zylstra, Trans. ASME, vol. 74, 1952, pp. 1039–1049.

15 "New Methods of Analysis of Machining Processes," by M. E. Merchant and N. Zlatin, Proceedings of the Society for Experimental Stress Analysis, vol. 3, no. 2, 1946, pp. 4–27.

16 R. S. Hahn's discussion of "Cutting Temperatures and Metal-Cutting Phenomena," by B. T. Chao and K. J. Trigger, Trans. ASME, vol. 73, 1951, p. 788.

17 "Metal-Cutting Friction Coefficient Needs Reinterpretation," by M. Kronenberg, *The Tool Engineer*, vol. 31, no. 4, 1953, pp. 49–50.

18 "The Friction Process in Metal Cutting," by I. Finnie and M. C. Shaw, Trans. ASME, vol. 78, 1956, pp. 1649–1657.

19 "The Rotary Cutting Tool," by M. C. Shaw, P. A. Smith, and N. H. Cook, Trans. ASME, vol. 74, 1952, pp. 1065–1073.

20 "Cutting Fluid Theory," by M. C. Shaw, in Machining. Theory and Practice, published by American Society for Metals, Cleveland, Ohio, 1950, pp. 45–68.

21 "The Size Effect in Metal Cutting," by W. R. Backer, E. R. Marshall, and M. C. Shaw, Trans. ASME, vol. 74, 1952, pp. 61–71.

22 S. L. Case, U. S. Patent 2,485,358.

Discussion

E. S. NACHTMAN.[6] This paper raises an interesting question. Are manganese sulphides an effective chip-tool lubricant, or do they, in fact, act to decrease the strength of the material during its machining?

AUTHORS' CLOSURE

With reference to Mr. Nachtman's question, the data in Figs. 9(*a*) and 9(*b*) show that sulphur content did not affect the calculated shear stress for a given feed. Because the shear stress is equal to the shear strength of the steels for the testing conditions, it was concluded that increasing the number of manganese sulphide inclusions did not change the shear strength of the steels during machining. On the other hand, the data in Figs. 8(*a*) and 8(*b*) disclose that the friction force between the chip and the cutting tool was reduced as the sulphur content was increased from 0.025 to 0.19 per cent. We recognize that the mechanism by which "free-machining" additives affect the frictional characteristics at the tool-chip interface is not completely understood, and are of the opinion that the various aspects of tool-chip friction should receive further study.

---

[6] Manager, Product Engineering Laboratory, LaSalle Steel Company, Chicago, Ill. Assoc. Mem. ASME.

Leaded Steel and the Real Area of Contact in Metal Cutting

By M. C. SHAW,[1] P. A. SMITH,[2] N. H. COOK,[3] and E. G. LOEWEN[4]

The action of lead in free-machining steel is discussed and the thickness of the layer of lead responsible for the improved lubrication between chip and tool is found to be extremely thin. Measurements made on the same steel with and without lead present enable the real area of contact between chip and tool to be estimated and this is found to be between 1 and 2 per cent of the apparent area of contact. The cutting characteristics of steel containing lead are compared with those for steel without lead as well as those for pure lead. It is found that the presence of lead makes effective fluids such as carbon tetrachloride less sensitive to an increase in cutting speed.

Introduction

THE magnitude of the friction force F between chip and tool is determined primarily by the size, number, and strength of the minute welds that form along the area of contact (AC in Fig. 1) during sliding. As for all surfaces in sliding contact, we must distinguish between the real A_R and apparent A areas of contact. This is necessary because all surfaces appear rough when highly magnified. In Fig. 2, two representative surfaces in sliding contact are shown greatly magnified. The real area of contact corresponding to the apparent area extending from 1 to 6 would be the sum of areas 1–2, 3–4, and 5–6. For ordinary friction sliders the ratio of the apparent area of contact to the real area of contact (A/A_R) will usually be a large number of the order of 10^4. The fact that a cutting fluid can penetrate the space between chip and tool at low cutting speeds (below 100 fpm) and reduce the friction force by as much as 50 per cent attests the fact that even in metal cutting the real area of contact is a small fraction of the apparent area of contact. If this were not the case fluid could not find its way between these surfaces.

As the load between surfaces in contact is increased the real area will increase, the product of the deformation hardness of the metal H and the real area of contact always being just equal to the applied load W in accordance with the static equilibrium of forces. Thus

$$W = A_R H \quad [1]$$

Actually H will be a function of A_R due to the strain-hardening tendency exhibited by all metals. However, in the discussion to follow we need not be concerned with this refinement and H will be considered to be a constant of the material. For clean surfaces the friction force required to cause sliding will be the product of the mean shear stress τ required to break the junctions and the real area of contact A_R

$$F = A_R \tau \quad [2]$$

If a fraction of the real area of contact k is covered by a lubricating film of shear strength τ_L while the remaining fraction of the area $(1 - k)$ remains clean we will have

$$F = (1 - k)A_R \tau + kA_R \tau_L \quad [3]$$

In arriving at this expression it has been assumed that the friction force on the face of a tool results from the shear resistance of the many minute welds that form between high points on chip and tool. While tool friction is primarily of this origin, small components of friction may arise due to plowing of hard particles through softer material, a camlike action due to the interference of hard protuberances on the mating surfaces, an electrostatic reaction between oppositely charged areas on the surfaces, or a drag force resulting from the viscous shearing action in any small regions that happen to be separated by a thin fluid film. However, it is believed that all of these latter components are of secondary consequence in discussing tool friction.

Bowden and co-workers[5] have estimated the real area of contact associated with ordinary friction sliders by measuring the electrical conductivity of surfaces in sliding contact. However, this method is not well suited for estimating the real contact area of very heavily loaded surfaces such as those involved in metal cutting. In this paper the action of lead in steel is discussed and the results obtained are then applied to metal-cutting data to estimate the ratio of real to apparent areas of contact.

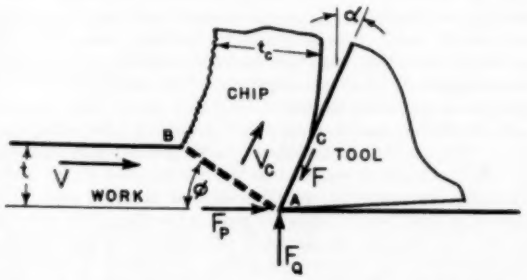

Fig. 1 Conditions at Point of Cutting Tool During Continuous Cutting, Width of Cut Along Cutting Edge = b

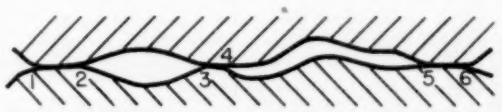

Fig. 2 Actual Surfaces in Contact at Very High Magnification

[1] Professor of Mechanical Engineering, Massachusetts Institute of Technology, Cambridge, Mass. Mem. ASME.

[2] Associate Professor of Mechanical Engineering, Massachusetts Institute of Technology, Cambridge, Mass. Mem. ASME.

[3] Assistant Professor of Mechanical Engineering, Massachusetts Institute of Technology, Cambridge, Mass.

[4] Staff Engineer, The Taft-Peirce Manufacturing Company, Woonsocket, R. I. Mem. ASME.

Contributed by the Research Committee on Metal Processing and presented at the Semi-Annual Meeting, Cleveland, Ohio, June 17–21, 1956, of The American Society of Mechanical Engineers.

Note: Statements and opinions advanced in papers are to be understood as individual expressions of their authors and not those of the Society. Manuscript received at ASME Headquarters, March 13, 1956. Paper No. 56—SA-37.

[5] "The Friction and Lubrication of Solids," by F. P. Bowden and D. Tabor, Oxford University Press, London, England, 1950.

Lead as a Free-Machine Additive

Lead has been used for a long time in free-machining brasses but for a relatively shorter time in free-machining steels. With steels it has been customary to use only a fraction of the amount of lead normally used in free-machining brasses (it is customary to add about $^1/_4$ per cent of lead to steel by weight or about 0.17 per cent by volume). One of the most successful uses of lead in steel has been in resulphurized open-hearth steels for automatic screw-machine applications. By use of sulphur and lead, low-carbon open-hearth steels can be made to machine more like free-machining brass than any other material available as screw stock. In addition to its use in screw-machine steels, lead has been found effective in improving the machinability of certain alloy steels.

To be effective lead must be very well dispersed throughout the steel. This may be accomplished by adding either pure lead shot or a lead containing material to the molten steel in the mold. Normally the individual particles of lead are very fine. The amount of lead usually added to steel is insufficient to alter the physical or chemical properties of the steel or its heat-treating characteristics significantly, including its ability to be case-hardened.

A leaded steel may be distinguished from a nonleaded steel by very simple spot test. A few drops of 5 per cent sodium hydroxide solution are allowed to remain on a freshly abraded piece of steel for 1 min and are then removed to a filter paper. When a few drops of 5 per cent sodium-sulphide solution are added to the spot on the filter paper a brown stain is formed if lead is present but no stain is found if lead is not present.

Elementary lead has several unusual properties that are of interest in connection with its role as a free-machining additive. These include:

1 A low melting point (621 F)

2 A low shear strength (about 5 per cent that for steel)

3 A high coefficient of thermal expansion, second only to that of zinc (16.3×10^{-6} in. per in. per deg F for lead as compared with 6.3×10^{-6} for steel)

4 A low surface tension in the molten state (465 dynes/cm compared with 452 for mercury)

5 A low viscosity in the molten state (1.7 centipoises at 700 F compared with 1 cp for water at room temperature).

In addition, lead is reported to be completely insoluble in iron and steel and the oxide of lead is insoluble in lead itself.

When lead is properly dispersed in steel as a free-machining additive it is present mainly as submacroscopic particles that are completely unalloyed. In constructing a picture of how the lead might appear in the steel we can first assume all particles to be the same size, uniformly dispersed, and spherical in shape. While it is not easy to photograph lead in steel this has been done by placing unetched metallographically polished specimen in a vacuum chamber and heating to 2100 F for 20 min.[6] In such studies Wragge found the size of the lead particles to be less than 0.0003 in. It would appear from his photomicrographs that a good average lead particle size (d) is 0.0001 in.

If the volume of lead per cubic inch of steel is v (v is usually about 0.00172 cu in. per cu in. corresponding to $^1/_4$ of 1 per cent of lead by weight) and there are n-particles per cubic inch then

$$v = n\left(\frac{\pi d^3}{6}\right) \quad [4]$$

The mean spacing of the lead particles in volume will be

$$r = \sqrt[3]{1/n} \quad [5]$$

[6] Discussion by W. B. Wragge, *Journal of the Iron and Steel Institute*, vol. 151, 1945, p. 297.

If a plane surface is produced on the steel the spacing of the lead particles on this surface will be greater than r since the particles of height d will be distributed randomly over depth r. The probability of particles on the surface having a spacing r will be $\sqrt{(d/r)}$ and hence the mean spacing of particles on the surface will be

$$x = \frac{r}{\sqrt{\left(\frac{d}{r}\right)}} \quad [6]$$

or from Equations [4] and [5]

$$x = \sqrt{\left(\frac{\pi}{6v}\right)}\, d \quad [7]$$

Statistically, the percentage of the plane area occupied by lead must be the same for all plane surfaces and hence independent of the size and shape of the lead particles. If we imagine the lead to consist of uniformly spaced parallel filaments running from the top to the bottom of a 1-in. cube of steel, the area of lead that will lie in the surface of a plane passing perpendicular to the filaments will be v sq in. where v is also the volume of lead per cubic inch of steel. Thus, the area of lead exposed on any plane surface will actually be v sq in. per sq in. of steel regardless of size, shape, or distribution of the lead particles.

Equation [7] may be checked by use of the foregoing observation. The mean area of a lead particle communicating with a plane surface will be

$$\bar{A} = \frac{\int_{-d/2}^{d/2} \frac{\pi d^2}{4}\, dy}{\int_{-d/2}^{d/2} dy} = \frac{\text{volume of sphere}}{\text{diameter of sphere}} = \frac{\pi d^2}{6} \quad [8]$$

The area of lead per square inch of steel v may then be computed by multiplying the number of lead particles communicating with 1 sq in. of steel surface $(1/x)^2$ by the mean area of a lead particle at the surface $\bar{A}$. Thus

$$v = \frac{\bar{A}}{x^2} = \frac{\pi d^2}{6x^2} \quad [9]$$

or

$$x = \sqrt{\left(\frac{\pi}{6v}\right)}\, d$$

which is seen to be identical with Equation [7], as it should be.

Before proceeding it might be well to consider some typical numerical values for the quantities already considered so that a representative picture of the size and distribution of lead in steel may be formed. If we take the volume concentration of lead to be 0.00172 cu in. per cu in. of steel ($^1/_4$ of 1 per cent of lead by weight and the mean diameter of the lead particles to be 0.0001 in., then from the foregoing considerations we have

Percentage area occupied by lead in any plane surface = 0.172 per cent

Mean spacing of lead particles in volume = 0.00067 in.

Mean spacing of lead particles on surface = 0.00174 in.

From the very small percentage of the area of a freshly cleaved surface occupied by lead (< 0.2 per cent) it is evident that the small amount of lead that is present in the surface must be smeared over the surface if it is to have a measurable effect on friction. Let us next consider the role the very large thermal expansion of lead might have in bringing the lead to the surface of the steel so that it might be spread. The mean particle of lead exposed to a free surface will be a hemisphere of diameter d as

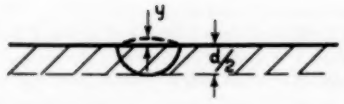

FIG. 3 THERMAL EXPANSION OF REPRESENTATIVE LEAD PARTICLE

shown in Fig. 3. If a layer of thickness $d/2$ is heated to the mean temperature of the surface of a chip which will be of the order of 1000 F, then the lead will hump up as shown as a result of the differential expansion between lead and steel ($16.3 \times 10^{-6} - 6.3 \times 10^{-6} = 10 \times 10^{-6}$ in. per in. per deg F). For a 1000 deg F temperature rise the elevation of the hump will be 0.01 in. per in. depth of lead at any point, or 1 per cent of the lead will lie in the hump above the surface of the steel. As will be seen later, 1 per cent of the lead present at a free surface is far too little to account for the observed action of lead, and we may conclude that the unusually high coefficient of thermal expansion of lead is not very important in its performance as a free-machining additive.

In the foregoing calculation the lead in the steel has been assumed to be stress-free. Actually, as the melt is cooled the steel will solidify first and the lead upon solidifying and cooling will attempt to shrink away from the steel and thus will be subjected to hydrostatic tension. When the load is subsequently released at a free surface, it should move inward from the surface, producing a depression at the center of the lead area. This effect however only tends to make the amount of lead appearing above the surface smaller than the 1 per cent estimate based on differential thermal expansion.

The only other mechanism that will make a greater percentage of the lead at the surface available to be spread is one in which the lead is squeezed out as the surface of the chip undergoes large plastic strains. At the temperature obtaining at the surface of a high-speed chip, the lead should be in a molten state and hence very fluid. Its low surface tension and low viscosity should play important parts in the spreading action that follows the squeezing action.

If all of the lead communicating with a free surface is squeezed out and caused to flow over the entire surface, the thickness of the resulting layer of lead will be very small. This thickness may be estimated in the following way:

The number of lead particles per square inch of surface area (n_a) will be from Equation [7]

$$n_a = \left(\frac{1}{x}\right)^2 = \frac{1}{d^2}\left(\frac{6v}{\pi}\right) \ldots\ldots [10]$$

The mean volume of a lead particle communicating with the surface will be $\pi d^3/12$ and hence the volume of lead available at each square inch of surface will be

$$v_a = \frac{\pi d^3}{12}(n_a) = \frac{vd}{2} \ldots\ldots [11]$$

If this lead should be spread over the 1 sq in. to which it is available, the height of the resulting layer $\bar{h}$ would be equal to v_a. If we now substitute the representative values from our previous example into this equation we find

$$\bar{h} = \frac{vd}{2} = \frac{(0.00172)(0.0001)}{2} = 8.6 \times 10^{-8} \text{ in.} \ldots [11a]$$

The important observation that may be made from the foregoing discussion is that lead in steel is characterized by a number of very small quantities. These involve first of all the total amount of lead present (0.25 per cent by weight), the size of the individual particles (<0.0001 in.), the mean spacing of the particles on the surface (about 0.002 in.), and finally the thickness of the lead layer if completely spread over the surface (a few atom layers of lead).

LOW-SPEED CUTTING TESTS

A number of low-speed (0.5 to 10 fpm) orthogonal cutting tests were made on a nonleaded steel (No. 5), the corresponding leaded steel (No. 6), and the pure lead. The steels used are described in Table 1. The reason for using such low cutting speeds lies in the improved reproducibility of data obtainable and the fact that ample time is provided for cutting fluids to act. Hence, cutting-fluid effects that are much smaller at higher cutting speeds may be more easily identified. Pure lead was included in order to appreciate better the friction and cutting characteristics of this component of a leaded steel.

The tool-face friction force F and specific energy ($u = F_p/bt$) are shown plotted for dry cutting under a wide range of conditions in Fig. 4. The friction force on the tool face, which may be determined readily as follows, is a sensitive measure of the lubrication

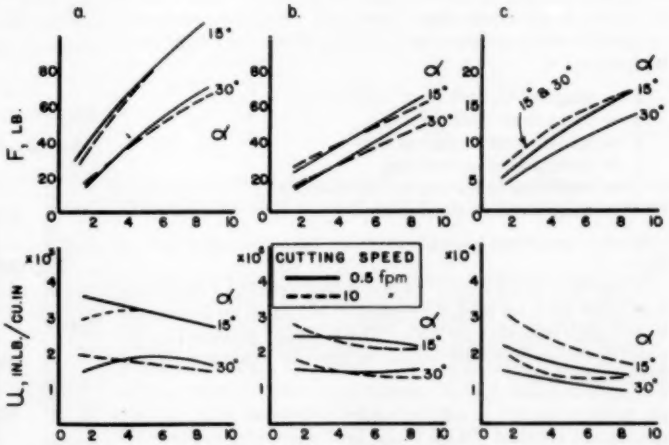

FIG. 4 VARIATION OF TOOL FACE FRICTION (F) AND TOTAL ENERGY PER UNIT VOLUME (u) WITH FEED RATE (t) FOR (a) NONLEADED RESULPHURIZED STEEL NO. 5; (b) LEADED RESULPHURIZED STEEL NO. 6; AND (c) PURE LEAD
(Tool material, 18-4-1, HSS; cutting fluid, none; depth of cut, 0.100 in.)

TABLE 1 DESCRIPTION OF STEELS INVESTIGATED

Steel No.	Description	Chemical composition w + % C	Mn	P	S	Pb	Cold work, per cent reduction	Brinell hardness No.	Tensile yield stress (0.2 per cent offset), psi	Ultimate tensile stress, psi	Per cent elongation	Per cent reduction of area	Charpy impact at 77F ft-lb
5	Low-carbon cold-drawn, resulphurized, OH steel without lead	0.09	0.97	0.049	0.288	0	6.1	109	59000	64500	18.8	56.0	12
6	Same as 5 with lead added	0.09	0.97	0.049	0.288	0.15/0.35	6.1	111	56900	64500	22.0	57.0	15

characteristics of a cutting fluid or free-machining additive (see Fig. 1 for explanation of notation)

$$F = F_p \sin \alpha + F_Q \cos \alpha \quad [12]$$

In Fig. 4, speed is seen to have less effect on F and u for the steels than pure lead. Since the recrystallization temperature of lead is about room temperature it is deformed when cut under hot working conditions where no strain-hardening is observed and where the material exhibits viscous-type characteristics, the shear stress being strongly influenced by the rate of strain. Steel on the other hand is normally cut under cold working conditions where flow occurs by a slip rather than by a viscous mechanism. When a material deforms by slip, strain-hardening is observed and shear stress is found to be largely independent of rate of strain. In the case of steel No. 6 we might expect to find a speed characteristic intermediate between that for steel No. 5 and that for pure lead. However, the energy involved in cutting lead is so small compared with that for steel (about 1 to 20) that the influence of steel will predominate and no significant influence of speed on F or u should then be expected for steel No. 6. This is seen to be the case in Fig. 4(*b*).

The friction force is seen to increase continuously with increasing feed t, for all materials, but at a decreasing rate. Similarly, the values of F are seen to be higher for smaller values of rake angle. This increase in F with increase in t or decrease in α is due to the fact that the normal force on the tool face will be greater when either t is increased or α is decreased. The decrease in specific energy u, with increase in t, is due to the size effect generally observed in metal-cutting tests.

The influence of rake angle upon F and u is seen to be less with the leaded steel (No. 6) than for the nonleaded steel (No. 5). From this it might be inferred that the presence of lead in steel will make choice of rake angle less critical. Some representative cutting-force data are given in Table 2 for steels 5 and 6 and pure lead, where

a = length of contact along tool face (AC in Fig. 1)
γ = mean shear strain in chip
F = friction force along tool face
N = normal force on tool face
f = coefficient of friction for tool face (F/N)
τ = shear stress on shear plane

and other quantities have already been defined or are shown in Fig. 1.

While the friction force F for lead is seen to be but a small fraction of the value for steel, the coefficient of friction for lead is seen to be higher than that for steel. This is readily explained by expressing the coefficient of friction in terms of Equations [1] and [2] as follows

$$f = \frac{F}{W} = \frac{A_R \tau}{A_R H} = \frac{\tau}{H} \quad [13]$$

Even though τ for lead is small, the value of H is likewise small and a rather high value of coefficient of friction f results. When, however, we have a thin layer of lead smeared over a harder material such as steel, the value of τ in Equation [13] will be that for lead while the value of H will be that for steel and a low value of f will result. Thus, steel No. 6 exhibits a lower value of f than does steel No. 5 owing to the presence of the thin layer of lead on the surface high spots. The lead layer causes a decrease of 19 per cent in f, of 34 per cent in F, and of 29 per cent in u_f. The reason the decrease in f is relatively less than the change in F is of course due to the fact that N will also decrease as F decreases.

The decrease in F when lead is present gives rise to an increase in the shear angle (ϕ) and hence a decrease in shear strain γ, just as in the case of a cutting fluid. The value of the shear stress on the shear plane τ is 9 per cent less for steel No. 6 than for steel No. 5. Since the presence of lead was observed to lower the flow stress of steel No. 6 by about 5 per cent from that for steel No. 5 in a tensile test, the decrease in shear stress due to the decrease in shear strain γ should therefore correspond to the remaining 4 per cent. In Table 2 the shear stress on the shear plane is found to be about $^1/_{20}$ that for steel when cutting pure lead.

The various energy changes resulting from the presence of lead may be summarized as follows for the foregoing example:

1 Lead causes a 34 per cent reduction in friction force F.

2 Owing to the increase in chip velocity that accompanies the increase in ϕ the decrease in u_f will be only 29 per cent.

3 The value of $u_s = \tau\gamma$ is decreased 20 per cent due to a decrease in both τ and γ when lead is present (τ is less by 9 per cent, γ by 12 per cent).

4 The decrease in u is 21 per cent, which is closer to the change in u_s than u_f since shear energy is a larger percentage of the total energy than is friction energy.

Real Area of Contact in Cutting

The values of Table 2 may be used to estimate the percentage of the real area of contact that has been covered by lead. Over a small range of normal stress we can assume to a good approximation that the real area of contact A_R will vary directly with the normal force on the tool face and inversely with the hardness of the steel. From true stress-true strain tensile tests (Fig. 5) we see that the values of flow stress (hardness) for steels Nos. 5 and 6 differ by but about 5 per cent. Thus we may write

$$\frac{A_{R5}}{A_{R6}} = \frac{N_5}{N_6}(0.95) = \frac{126}{102}\,0.95 = 1.17 \quad [14]$$

where A_{R5} is the real area for steel No. 5 and N_5 is the normal force

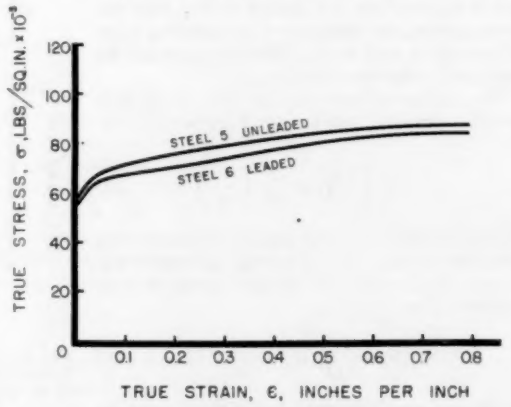

FIG. 5 TRUE STRESS-TRUE STRAIN TENSILE DATA FOR LEADED AND NONLEADED STEELS

(For descriptions of steels see Table 1. In all cases standard ASTM specimens were used, being 0.505 in. in diameter and of 2 in. gage length.)

TABLE 2 REPRESENTATIVE LOW-SPEED CUTTING DATA FOR A NONLEADED STEEL (5), LEADED STEEL (6), AND PURE LEAD

(Rake angle, α = 15 deg; feed, t = 0.005 in.; depth of cut, b = 0.1 in.; tool, 18-4-1 HSS; cutting fluid, none; cutting speed, 0.5 fpm.)

Material	F_P, lb	F_Q, lb	a, in.	ϕ, deg	γ	f, lb	n, lb	f	τ, psi	u_f, psi	u, psi
Steel 5	136	20	0.017	17.4	3.2	54.5	126	.43	74000	35000	272000
Steel 6	108	8	0.013	20.0	2.8	35.7	102	.35	67500	25000	216000
Pure lead	7.0	2.3	0.032	19.5	2.9	4.00	6.16	.65	3890	2700	13900

on the tool face for steel No. 5. This equation says that the real area for steel No. 5 will be 17 per cent greater than that for steel No. 6.

If k is the fraction of the real area that is covered by lead in the case of steel No. 6 we can write

$$F_6 = (1 - k)A_{R6}\tau_s + kA_{R6}\tau_L \quad [15]$$

where

F_6 = friction force for steel No. 6
τ_s = shear strength of the small steel junctions
τ_L = shear strength of the small lead junctions

From Equations [14] and [15]

$$F_6 = (1 - k)\frac{A_{R5}}{1.17}\tau_s + k\frac{A_{R5}}{1.17}\tau_L \quad [16]$$

Now, we must estimate τ_s/τ_L. Since the volume associated with the rupture of individual junctions is extremely small and hence the probability of finding a strength reducing imperfection will be correspondingly small we should expect the values of τ_s and τ_L to correspond closely to the theoretical values of strength of the metals in shear. The theoretical strength of a metal in shear is approximately $G/2\pi$, where G is the shear modulus of the metal. According to this point of view we would then have

$$\frac{\tau_S}{\tau_L} = \frac{G_S/2\pi}{G_L/2\pi} \cong \frac{2 \times 10^6}{0.1 \times 10^6} = 20 \quad [17]$$

It should be noted that even if the values of τ_s and τ_L did not correspond to the theoretical values, but were much less, the foregoing value for the ratio T_S/T_L would still hold. This may be seen by assuming the values of τ on the tool face to be equal to the values of τ on the shear plane. Then from Table 2 we find

$$\frac{\tau_S}{\tau_L} = \frac{74{,}000}{3890} = 19$$

Hence, we may assume τ_S/τ_L to be equal to 20, regardless of the magnitude of the size effect that is operative.

From Equations [16] and [17]

$$k = \frac{1 - \dfrac{1.17F_6}{A_{R5}\tau_S}}{0.95} \quad [18]$$

but

$$A_{R5}\tau_S = F_5 \quad [19]$$

and hence

$$k = \frac{1 - 1.17\dfrac{F_6}{F_5}}{0.95} \quad [20]$$

It should be noted that the derivation of this equation involves but two very reasonable assumptions, one for the ratio A_{R5}/A_{R6}, the other for the ratio τ_S/τ_L. Substituting values for F_5 and F_6 from Table 2, we find

$$k = \frac{1 - 1.17\dfrac{35.7}{54.5}}{0.95} = 0.246$$

Thus, for the example of Table 2 it would appear that about 25 per cent of the real area of contact is coated with lead.

The thickness of the layer of lead may be considered next. The amount of lead present for steel No. 6 of Table 2 was about 0.25 per cent by weight or 0.172 per cent by volume. As was shown earlier, the percentage of the area of any plane surface occupied by lead before spreading is equal to the percentage of lead by volume, which in this case is 0.172 per cent. If, after spreading, the area of lead is 24.6 per cent, the extension ratio of the area of lead corresponds to 24.6/0.172 = 143. The mean volume of a single lead particle at the surface will be $\pi d^3/12$, while the area of this particle after spreading will be 143 $\bar{A}$ which from Equation [8] becomes $143(\pi d^3/6)$. The mean thickness of the spread layer will then be

$$\bar{h} = \frac{\dfrac{\pi d^3}{12}}{143\dfrac{\pi d^2}{6}} = \frac{d}{286} \quad [21]$$

provided all of the lead available is spread. The value of $\bar{h}$ from Equation [21] is seen to be about four times that obtained from Equation [11a] as it should be inasmuch as only about $^1/_4$ the real area is covered with lead. If d is 10^{-4} in., as we have assumed previously, then $\bar{h}$ will be 0.35×10^{-6} in. Thus, the mean thickness of the layer of lead that is spread out on the high points of the surface of the chip is seen to be exceedingly small, being only some 25 atom layers in thickness.

TABLE 3 REAL AND APPARENT AREAS OF CONTACT

Material	A_R, sq in.	A, sq in.	A/A_R
Steel 5	27.2×10^{-6}	1700×10^{-6}	62.5
Steel 6	23.2×10^{-6}	1300×10^{-6}	56.0
Pure lead	40.0×10^{-6}	3200×10^{-6}	80.0

The real and apparent areas of contact between chip and tool are given in Table 3 for the three tests of Table 2. In computing A_R we have assumed the shear stresses at points of contact to correspond to the theoretical strengths of the metals ($G/2\pi = 2 \times 10^6$ psi for steel and 0.1×10^6 psi for lead). The values of A_R for lead and steel No. 5 were computed as follows

$$A_R = \frac{F}{G/2\pi} \quad [22]$$

while the values of A_R for steel No. 6 were obtained from Equation [14]. The apparent areas of contact were computed as follows

$$A = ab \quad [23]$$

The values of A/A_R are reasonable and what we might expect in metal cutting. In ordinary friction sliders, the ratio A/A_R is much larger (frequently as large as 10^4) than in metal cutting owing to the very much lighter normal stresses to which ordinary friction sliders are subjected. In order that it be possible for a cutting fluid to penetrate between chip and tool it is necessary that A/A_R be considerably greater than 1. If the value of A_R for steel No. 5 is recomputed based upon a tool-face shear stress equal to the shear stress on the shear plane (74,000 psi) then we obtain

$$A_{R5} = \frac{54.5}{74{,}000} = 737 \times 10^{-6} \text{ sq in.}$$

When this value is compared with the value of A for steel No. 5 we obtain $A/A_R = 2.3$. This value is considered to be too close to 1 to allow sufficient area for fluid penetration and it can be concluded that the shear strength (τ) at the points of actual contact must be considerably greater than the shear stress on the shear plane and probably close to $G/2\pi$.

Cutting Fluids

Resultant force values are shown plotted to scale in Fig. 6 for

a number of cuts with and without a fluid and for steels with and without lead. The well-known effect that a cutting fluid has is to cause a decrease in the resultant force and to rotate it upward into a position more nearly normal to the tool face. This action may be observed by comparing the positions of the resultant force vector for steel No. 5 in Figs. 6(*a*) and 6(*c*). The presence of lead in steel is observed to have the same effect on the resultant force as a fluid. This may be seen by comparing the resultant force vectors for steels Nos. 5 and 6 in Fig. 6(*a*). The reason that carbon tetrachloride ceases to be effective at increased speeds with steel No. 5 but not with steel No. 6 will be discussed later.

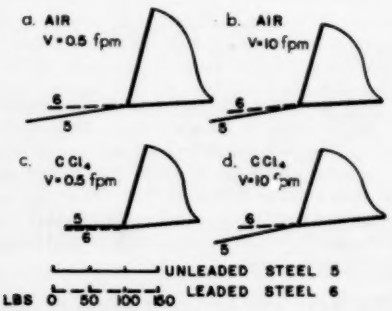

FIG. 6 CHANGES IN SIZE AND DIRECTION OF RESULTANT CUTTING FORCE DUE TO A CUTTING FLUID AND TO LEAD IN STEEL
(Tool material, 18-4-1 HSS; rake angle, 15 deg; feed, t = 0.005 in.; depth of cut, b = 0.100 in.; cutting speeds, 0.5 and 10 fpm as indicated.)

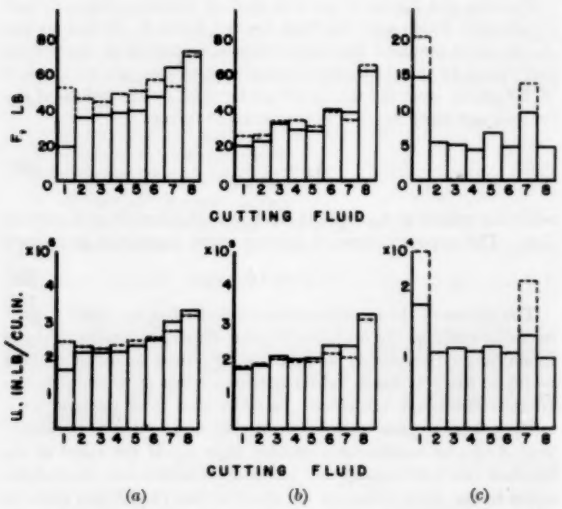

FIG. 7 VALUES OF TOOL FACE FRICTION (F) AND TOTAL ENERGY PER UNIT VOLUME (u) FOR DIFFERENT CUTTING FLUIDS WHEN CUTTING (*a*) NONLEADED RESULPHURIZED STEEL NO. 5; (*b*) LEADED RESULPHURIZED STEEL NO. 6; AND (*c*) PURE LEAD
(Tool material, 18-4-1 HSS; rake angle, 15 deg; feed, t = 0.005 in.; depth of cut, b = 0.100 in.; cutting speeds, 0.5 and 10 fpm as indicated.)

Description of Fluids

1—Carbon tetrachloride
2—Dodecyl mercaptan
3—0.1 per cent Aerosol OT in water (wetting agent)
4—3 per cent commercial cutting fluid (A) in water
5—Dodecyl chloride
6—Water
7—Air
8—Benzene

Cutting speed, fpm { ——— 0.5
..... 10

Results of a large number of low-speed tests using different cutting fluids are presented in Fig. 7. Here it is evident that in general the same fluid may exhibit a different relative effectiveness as well as a different sensitivity to cutting speed on one material than on another. In interpreting these data it is important to recognize that in order for a fluid to be effective it must first penetrate between chip and tool and then react or adsorb on the surface of the chip to form a low shear-strength film. Lead to be effective must be capable of being readily spread over the steel surface into a very thin film. There are two major influences of increased cutting speed which have opposing effects:

1 Less time for welds to form.
2 Less time for a cutting fluid to act.

Let us first consider the actions of the several fluids on steel No. 5. Carbon tetrachloride is seen to be very effective at low speed, but much less effective at the higher cutting speed. This is thought to be due to the relatively long time required for carbon tetrachloride to react with steel to form low shear-strength iron chloride. Benzene is found to be less effective than air owing to the fact that air is in fact a good cutting fluid and the benzene largely excludes air from the freshly cut surface. The slight improvement with increased speed in the case of benzene is to be expected since there is less time available for welds to form at the higher speed. Air is an extremely rapidly acting fluid and there is essentially no difference in the thickness of the film that is formed with cutting speed. Hence, as in the case of benzene, the shorter time available for welds to form in air is responsible for the improvement observed at the higher cutting speed.

When we study the variation in the values of F obtained with different fluids when cutting pure lead, Fig. 7(*c*), it is evident that carbon tetrachloride is unusually poor, air is also poor, and dodecyl chloride is somewhat poor. All other fluids, including benzene, are of approximately equal effectiveness. The lead chloride that is formed with carbon tetrachloride has a higher shear strength than the lead itself, and there appears to be some adverse chloride formation also in the case of dodecyl chloride. When lead is cut in the presence of air, the lead oxide that is formed is insoluble in the lead and undoubtedly will increase the shear-flow stress at the surface of the lead. All other materials, including benzene, are thought to be effective by excluding air from the tool point and thus preventing the formation of lead oxide.

The principal influence of lead in a leaded steel in decreasing F will be due to the decrease in the number of steel welds that must be sheared. The effect of fluids upon the shear strength of pure lead (as observed in Fig. 7) should not be expected to have an important influence upon the values of F for steel No. 6 for two reasons:

1 The shear strength of lead is small compared with steel.
2 The lead area to be sheared is usually smaller than the steel area to be sheared.

The most important influences of a fluid in the case of a leaded steel will be upon the lubrication of the steel areas that remain and upon the spreading characteristics of the lead. It is also not inconceivable that the presence of lead will alter the reaction rate of fluids with steel.

The results for the fluids on steel No. 6, Fig. 7(*b*), show that the presence of lead makes the steel less sensitive to changes in cutting speed. This is particularly noticeable in the case of carbon tetrachloride. This improvement in cutting-fluid performance when lead is present might be attributed to the following causes:

1 A catalytic or synergistic action of lead on the reaction between carbon tetrachloride and steel.
2 A decrease in the time required for fluid penetration be-

tween chip and tool due to the increase in A/A_g that results when lead is used.

It is not known which of these items is primarily responsible. It is of interest, however, to note that the materials that give distinctly better results on steel No. 6 than on steel No. 5 (i.e., carbon tetrachloride, air, and dodecyl chloride) are those which give the poorest results on pure lead. This would be explained if lead containing lead chloride or lead oxide on its surface would have a greater tendency to wet and spread over a surface of iron than would pure lead.

In every case the values of F and u in Figs. 5 and 7 are less for steel No. 6 than the corresponding values for steel No. 5. The presence of lead in steel is thus seen to be very effective when cutting in the low speed range from 0.5 to 10 fpm.

Acknowledgment

The authors are grateful to the LaSalle Steel Company of Chicago for a grant in support of the work reported. They are grateful to Messrs. T. A. Kelly, E. S. Nachtman, and E. A. Hoffman of that organization for their helpful suggestions. The specially prepared leaded and nonleaded steels used in this investigation were obtained by the LaSalle Steel Company through the courtesy of the Inland Steel Company. The aid of Mr. Marsbed Hablanian in certain of the experiments and in the preparation of the paper is also gratefully acknowledged.

Discussion

F. W. Boulger.[7] The authors are to be congratulated on this interesting and stimulating article. Their conclusions about the size, distribution, and effect of lead particles seem logical in view of the assumptions on which they were based. The assumptions probably appear reasonable to physicists and mechanical engineers even though they are based on very scanty published data. To a metallurgist, however, it appears that some of the assumptions should be reconsidered. Some of the reasons for this opinion can be enumerated briefly:

(1) Many of the lead particles found in steel are microscopic rather than submicroscopic in size. By newly developed techniques, the lead particles can be seen at magnifications as low as 250×.

(2) The method of Wragge quoted by the author is of doubtful accuracy for estimating the size of the lead particles. When using the procedure of Wragge, the metallographer looks at the holes formerly occupied by lead rather than at lead particles. Metallographers familiar with the difficulties of polishing specimens so that they are free of artifacts would recognize the limitations of this dubious practice.

(3) The authors assume that the lead particles are uniformly distributed, a point justifying some discussion. Since lead is practically insoluble in steel, it is concentrated in the liquid metal, probably as a dispersoid or vapor, during solidification. Presumably it condenses rather than precipitates with the last metal to freeze. Consequently a metallurgist expects lead to segregate as do sulphur, hydrogen, molybdenum, manganese, and other elements. It has been shown that much of the lead occurs in the same locations as sulphides. Alumina is an example of a nonmetallic compound which is not uniformly distributed in steel. The degree of uniformity of the lead distribution in steel would be expected to be influenced by ingot size, pouring temperature, and other factors.

(4) Finally, the authors point out that the proportion of plane area occupied by lead is statistically independent of the size and shape of the lead particles. They then proceed to show that the lead acts as an antiwelding agent. Do the authors believe that the size and shape of the lead particles have no effect on machining quality? That this is not true for sulphides in resulphurized steels has been shown by Boulger, Oswald, and Moorehead, and later in greater detail by Van Vlack. Furthermore, the available data on cast irons and on graphitic steels suggest that the size and shape of graphite particles also influence machining properties.

The possibility that the authors' assumptions suffer from these limitations is suggested for consideration because the factors influencing machinability are of interest to metallurgists as well as to physicists and mechanical engineers. Theories on metal cutting must take into account pertinent information from related fields if they are to be complete enough to be useful.

E. S. Nachtman.[8] It would be proper now to carry out an experimental determination of the distribution of lead in steel. It would be most interesting to investigate the relationship between lead distribution and the distribution of other inclusions in steel. The effect of sulphur and sulphides on the distribution of Pb would be most informative.

I believe that a paper such as this, with such a plausible theoretical solution of the lead distribution in steel, would be sadly incomplete if it does not trigger experimental investigation of some of the problems mentioned above.

Authors' Closure

The authors wish to thank Messrs. Boulger and Nachtman for their helpful comments. As a metallurgist, Mr. Boulger objects to Mr. Wragge's technique for making lead particles visible in steel on the grounds that holes are looked at rather than the lead particles themselves. When specimens containing holes in the surface are polished and then examined, the holes are apt to appear too large due to a rounding of the edges. However, Mr. Wragge carefully polishes his surfaces with the lead present. When such polished surfaces are examined under the microscope the lead particles cannot be distinguished nor can they be revealed by etching. The polished specimens are then treated in a vacuum so as to remove the lead from the surface and hence make the spaces originally occupied by lead visible. It is thought that this technique offers little chance for enlarging the lead cavities as might occur in a mechanical or electrolytic polishing operation on a surface containing empty holes. While better methods of making lead particles visible may exist, Mr. Wragge's technique appears to be the best that has been published and of which we have knowledge.

The authors acknowledge that simplifying assumptions have been made in their treatment but do not feel they need apologize for this since it is well known that in all engineering theory a model that is somewhat simpler than the actual system must be adopted in order to obtain a useful solution.

The authors agree with both Messrs. Boulger and Nachtman that lead distribution is a very important variable and hope that they will have the opportunity in the future to study this problem.

[7] Chief, Ferrous Metallurgy Division, Battelle Memorial Institute, Columbus, Ohio. Mem. ASME.

[8] Director of Research, Product Engineering Laboratory, LaSalle Steel Company, Chicago, Ill. Assoc. Mem. ASME.

Cutting-Fluid Evaluation

By H. W. HUSA,[1] WHITING, IND.

Transfer of radioactive material from a cutting tool to the chips produced in facing the end of a steel tube is used as a means of measuring tool-wear rate. The lathe is operated at commercial feeds and speeds. This technique permits accurate tool-wear evaluation with very short machining time and a consequent small consumption of stock. Protection of personnel against radiation requires simple precautions. Evaluation of a cutting oil may require consideration of the roughness of the cut surface or the cutting temperature in addition to the tool-wear rate. The properties of the material cut influence the type of tool wear experienced and may affect the choice of variables which must be considered in addition to tool-wear rate. Results for typical compound and mineral oils in the machining of both 1015 and 1045 steels are reported.

Introduction

CUTTING fluids improve machining operations through a complex cooling and lubricating mechanism which affects life of the cutting tool and the finish of the cut surface. Since the action of the fluid is complex, measurement of specific properties of the fluid does not provide an adequate representation of its effectiveness under machining conditions. Therefore the evaluation of a cutting fluid involves actual metal-cutting tests.

Metal-cutting research has provided a number of laboratory test methods which can be adapted to cutting-fluid evaluation. The more prominent of these are (1) measurement of tool-wear rate, (2) determination of chip-length ratio and coefficient of friction, (3) measurement of surface finish, and (4) determination of cutting temperature. Tool-wear rate has been determined by running to tool destruction under abnormally severe machining conditions, by microscopic measurement of tool-wear lands, and by use of radioactive-tracer techniques. Each test has advantages and limitations which must be considered in relation to the ultimate purpose of the test.

Machining to the point of tool destruction under severe conditions gives a rapid, direct measurement of tool life. However, extrapolation to the milder conditions of commercial practice is subject to considerable error. In particular, the changing effect of a cutting fluid with changing conditions makes extrapolation very questionable.

Microscopic measurement of tool-wear lands under normal cutting conditions has been shown to correlate satisfactorily with tool life in the case of carbide tools and with high-speed-steel tools under some circumstances. However, in many machining operations wear-land measurement is completely unreliable.

Measurement of total tool wear by sensitive radioactive-tracer techniques overcomes the objections of the two previous methods and also provides a high degree of accuracy. This procedure has been adopted as the best means of evaluating tool-wear rate.

Both chip-length ratio and coefficient of friction provide some understanding of chip formation and cutting mechanics. They are applicable only at slow speeds, however, and have little significance at commercial cutting conditions.

Surface finish of the cut stock is a measure of the quality of the machining operation. It is not satisfactory as the sole criterion of cutting-fluid effectiveness because of its sensitivity to properties of the stock, the speed and feed, and the tool geometry.

Temperature at the interface between the tool and the workpiece correlates roughly with tool-wear rate. Like surface finish it is sensitive to cutting conditions; hence it is an inadequate criterion alone.

Research on cutting-fluid evaluation at the Standard Oil Company utilizes the radioactive method of measuring tool-wear rate as the principal criterion. This is supplemented, in many cases, by the use of surface finish and temperature measurements to provide a more critical discrimination between fluids. The use of these several tests in combination avoids anomalous results which have been characteristic of previous cutting-oil studies.

Radioactive Measurement of Tool Wear

During machining, an unstable, irregular wedge-shaped layer of chip comprising the built-up edge is pressure welded to the face of the tool. Separation of chip from work occurs ahead of the tool and is accomplished by this built-up edge as illustrated in Fig. 1. In passing over the tool face the chip scours or scrapes the tool surface and in time forms a crater behind the edge. At the same time, the work, using fragments of the built-up edge as an abrasive, scours the flank of the tool. Which type of wear is predominant depends upon the actual conditions of operation.

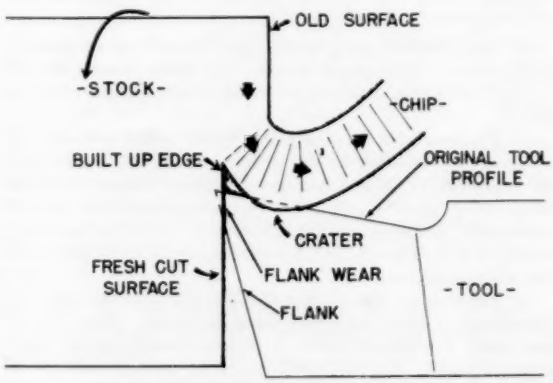

Fig. 1 Mechanisms of Metal Cutting and Tool Wear

The amount of tool material scraped off during the passage of one chip is too small to be detected accurately by any ordinary means, such as weighing. However, if the tool is radioactive, this wear may be measured by monitoring the radioactivity transferred to the cut metal chips. Merchant, Ernst, and Krabacker[2] found from their work with radioactive cutting tools that over

---

[1] Assistant Project Engineer, Standard Oil Company (Indiana), Assoc. Mem. ASME.

Contributed by the Research Committee on Metal Processing and presented at a meeting of the Chicago Section of The American Society of Mechanical Engineers on March 7, 1956.

Note: Statements and opinions advanced in papers are to be understood as individual expressions of their authors and not those of the Society. Manuscript received at ASME Headquarters, June 26, 1956.

[2] "Radioactive Cutting Tools for Rapid Tool-Life Testing," by M. E. Merchant, H. Ernst, and E. J. Krabacker, Trans. ASME, vol. 75, 1953, pp. 549–559.

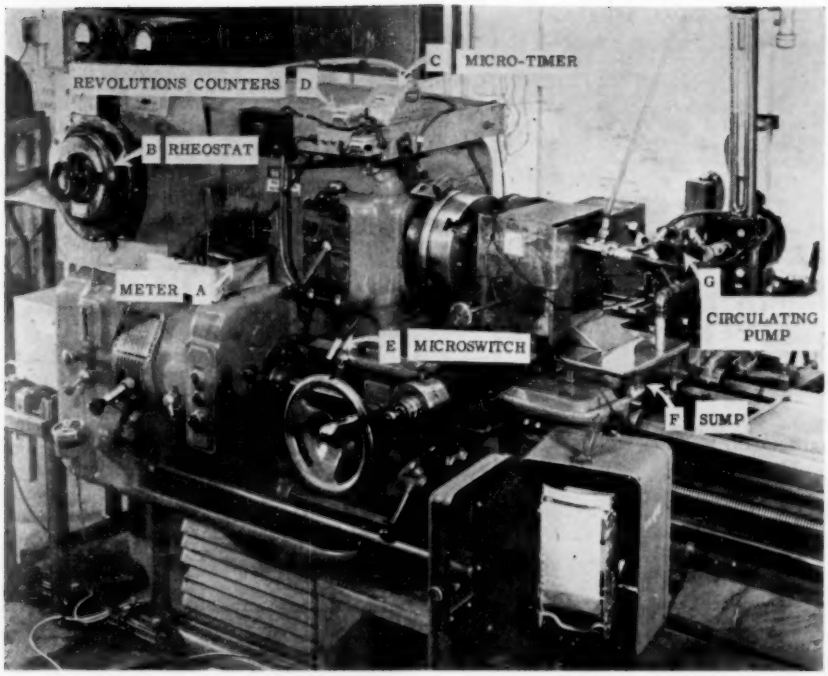

FIG. 2 EXPERIMENTAL SETUP

95 per cent of the tool-wear material adheres to the chip and the remainder is contained in the oil.

The radioactive method has the following advantages:

1 Very small amounts of wear may be determined accurately.
2 Metal-cutting tests may be conducted under conditions similar to those used in industry.
3 Stock is consumed in very small amounts with correspondingly small machining times.
4 Only two or three gallons of test oil are necessary for an oil evaluation.

Apparatus. The principal test equipment employed to determine wear includes the following:

1 A 16-in. × 54-in. lathe with a d-c motor drive.
2 Lead box shielding the radioactive tool.
3 A well-type geiger tube with a preset counter.

Fig. 2 shows the experimental setup. Cutting speed is indicated on meter A and is controlled by rheostat B. The average speed during cutting is calculated from data supplied by microtimer C and revolution counters D. The timer and counters are operated electrically by microswitch E which is adjusted to close at the start of the cut and open when cutting is completed.

The cutting oil under test is stored in $1^1/_2$-gal sump F attached to the carriage and is circulated by pump G at a rate of about 4 gpm.

Procedure. Orthogonal machining, as illustrated in Fig. 3, is conducted on the end of a $1^1/_2$-in-outside diameter × $^1/_4$-in-wall tube with a radioactive high-speed-steel tool at the selected and carefully controlled machining condition. Particulars of the cutting geometry, tool chemistry, and stock are listed in Table 1.

To insure rapid break-up of the chip into relatively uniform segments of a size that will pack in the well-type geiger counter both a chip breaker and filled slot in the workpiece are provided.

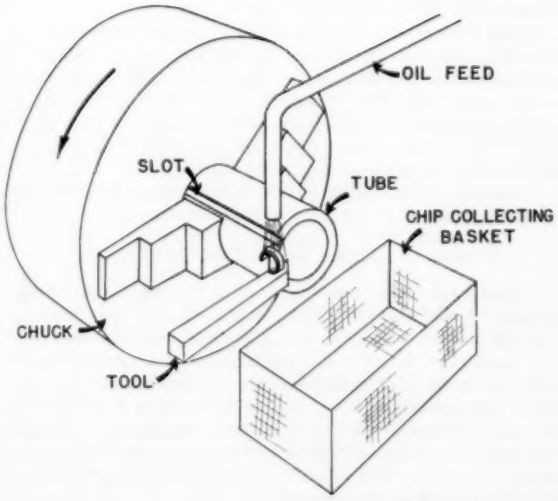

FIG. 3 ORTHOGONAL MACHINING ON END OF STEEL TUBE

When the slot passes over the tool, the chip is broken and each revolution of the stock produces one chip in the ideal case. Metal of the same or similar chemistry as that of the tube is used for slot fill.

A wire basket is inserted into the lead-shielded box after the first third of the run is completed and while the test is in progress. This divides the chip sample into two parts: The first part represents transitory conditions wherein the tool is coming up to temperature; the second part represents chips cut under constant-temperature conditions

TABLE 1 CUTTING-TOOL DATA AND CONDITIONS

(*A*) *High-Speed-Steel Tool*

1 Angles, deg
Back rake 0
Side rake 15
Side relief 6
Side cutting edge 0

2 Chemistry

C	Si	Mn	S	P	W
0.83	0.26	0.25	0.010	0.025	18.90

Cr	Va	Mo	Co	Fe
4.13	1.93	0.80	8.94	balance

3 Radioactive level
2 millicuries: Fig. 4
7 millicuries: Figs. 5, 6, 7

4 Weight: 2 grams

(*B*) *Stock*

1015 steel tubing; random lengths; 87 to 90 Rockwell B scale
1045 steel bar stock; hot rolled, shop drilled, and turned to tubing; 88 to 91 Rockwell B scale

(*C*) *Cutting Conditions*

Speed: 120 sfm except Fig. 7
Feed: as indicated
Depth of cut: 0.250 in.

Several measurements of counting rate of a chip sample are made in the well-type geiger counter. Background rates are measured between sample rates. Both are averaged and the difference is divided by the weight of the chip sample. The result is reported as the tool-wear rate in counts per second per gram of chips—cps/g. A sufficient number of counts is made to insure a counting error of less than 2 per cent as estimated from the confidence limits of the data.

Safety Precautions. Certain precautions are necessary to insure the safety of personnel. The cutting tool is adequately shielded on the lathe and proper storage facilities are provided for tools not in use. The operators are furnished with Keleket pocket dosimeters to check daily radiation dosage and are given blood tests twice a year. Other laboratory personnel are not permitted in the limited area about the lathe.

No special precautions are taken in handling an average chip sample because of the low level of radioactivity.

SURFACE ROUGHNESS AND CUTTING TEMPERATURE

Anomalies in the data have pointed up the need for additional criteria. Under certain cutting conditions very poor cutting oils will produce only a fraction of the tool wear obtained with very good oils. An oil evaluation based on the narrow limits of tool wear at one set of cutting conditions ignores benefits that may be derived through improved surface finish and is no measure of the capabilities of the oil over a variety of machining conditions. Measurements of surface roughness or temperature or both, in addition to tool wear for a series of cutting conditions, give the best basis for judging oil performance.

Apparatus and Procedure. In order to preserve a cut surface on the end of the tube which is typical of cutting conditions, the test is abruptly terminated by a rapid withdrawal of the tool. Surface roughness is measured with a standard profilometer.

Chip-tool temperatures are measured by the method of Shore[3] in which the interface between the chip and tool form the hot junction of a thermoelectric circuit. The dissimilar metals, of tool and workpiece, in contact during machining provide the thermoelectric indication. Temperature curves are traced on the photoelectric strip-chart recorder shown in the foreground of Fig. 2.

CUTTING-OIL EVALUATION

Oil evaluations are comparative in nature with a good commercial cutting fluid serving as the standad. Usually one or two unknown oils and the reference oil are run simultaneously for a number of cutting conditions. Test sequence is determined from a table of random numbers and analysis of the data is on the basis of a factorial design of experiment.

Accuracy of the data plotted in Figs. 4, 5, and 6 averaged about ±15 per cent as estimated from the pooled data (95 per cent confidence).

Analysis of Typical Data. Examples of the test data obtained are shown in Figs. 4, 5, 6, and 7.

Fig. 4 is a bar graph of wear-rate and surface-roughness data obtained on 1015 steel tubing with both mineral and compound oils. Crater wear was evident on the tool face but very little wear was observed on the tool flank. Under mild cutting conditions the apparent tool life for mineral oil was about $2^1/_2$ times that for compound oil. A change to moderate cutting conditions raised both wear rates but apparent tool life for mineral oil dropped to $^1/_4$ that for compound oil. Further testing showed the mineral oil to give lower wear rates only under mild conditions and only with a reasonably sharp tool.

Surface finishes produced when using compound oil were better under both sets of machining conditions and improved with the change from mild to moderate cutting conditions. Finishes produced when using mineral oil started rougher and deteriorated with the change to more severe operation.

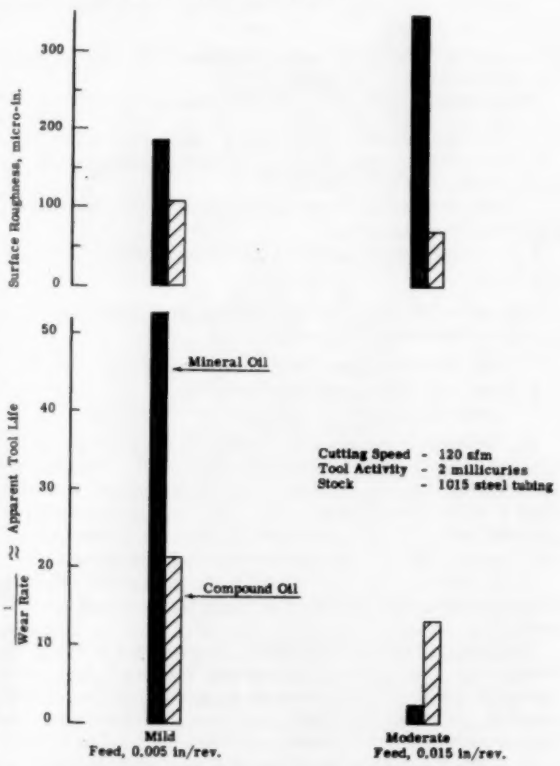

FIG. 4 PERFORMANCE COMPARISON, MINERAL VERSUS COMPOUND OIL

[3] By H. Shore, SM thesis, Massachusetts Institute of Technology, Cambridge, Mass., 1924.

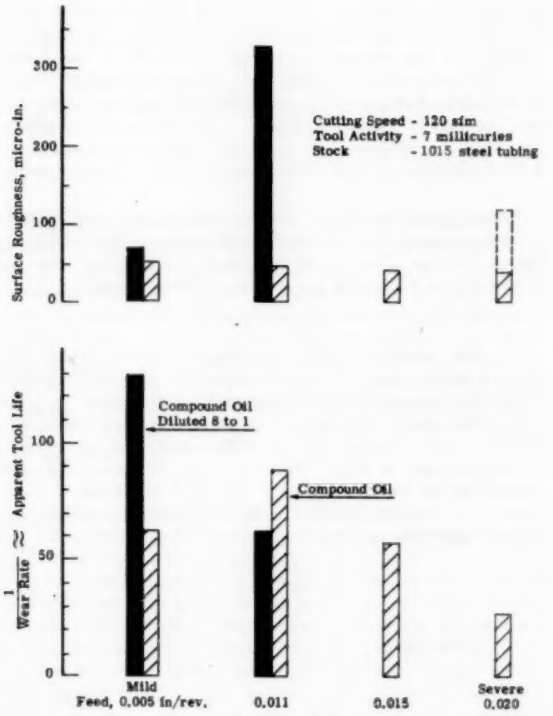

FIG. 5 ILLUSTRATION OF EFFECTS OF OIL DILUTION ON CUTTING PERFORMANCE

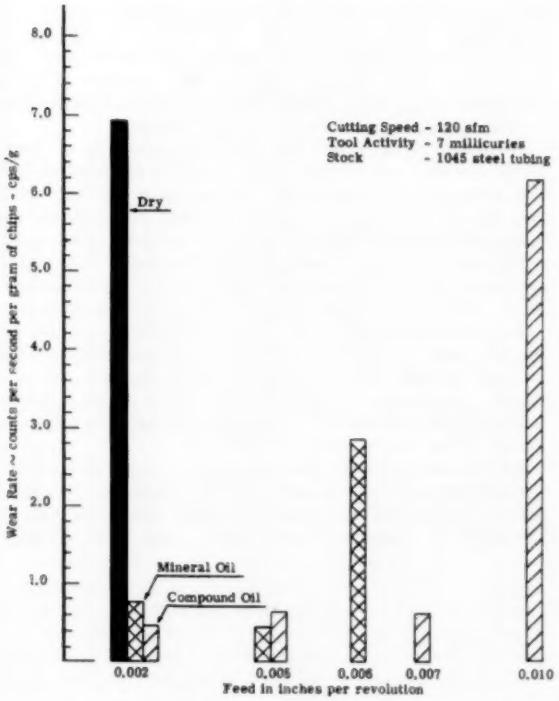

FIG. 6 EFFECT OF CUTTING FLUID ON TOOL-WEAR RATE

Compound oils achieve better cutting performance and smoother surface finishes through the formation of boundary lubricants. Extreme pressure (EP) agents, usually oil-soluble compounds containing chlorine or sulphur, react with the nascent metal surfaces to form an "easily sheared" surface layer. While ordinary boundary lubricants interpose some kind of thin film between rubbing surfaces, and thus protect the surfaces against attrition, EP agents by their very action, which is chemical, destroy the metal surface of both tool and work.

Tool wear, therefore, involves a balance between chemical attack, abrasion, and welding when the work is flooded with a compound oil. Under mild conditions, chemical attack might outweigh abrasion and welding and in this manner result in low tool-wear rates with mineral-oil floods. Under more severe conditions, welding of cut metal to the tool face governs and EP agents are essential. Beaubien and Cattaneo[4] also report instances where mineral oils give greater tool life than compound oils.

No satisfactory correlation of tool life and temperature for 1015 steel was obtained because of experimental difficulties.

Fig. 5 is a bar graph of data obtained on 1015 steel tubing with compound oil full strength and diluted 8 to 1 with base stock. The effect of dilution is very apparent.

Longer tool life was obtained with the diluted oil under mild cutting conditions but fell rapidly with a change to heavier duty. Machining at feeds beyond 0.011 in/revolution (ipr) with the diluted oil introduced the risk of seizure, as the cut metal piled up on the tool face and refused to form free flowing chips. No

[4] "A Study of the Role of the Cutting Fluid in Machining Operations," by S. J. Beaubien and A. G. Cattaneo, *Lubrication Engineering*, vol. 10, 1954, pp. 74–79.

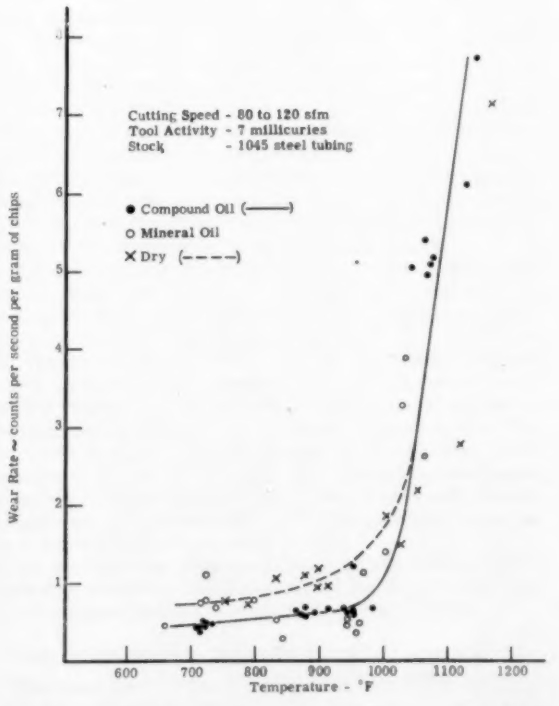

FIG. 7 CORRELATION OF TOOL-WEAR RATE AND CHIP-TOOL-INTERFACE TEMPERATURE

chip-flow difficulties were encountered with the full-strength compound oil.

Excellent surface finishes were obtained with the compound-oil flood until severe cutting conditions were encountered. The diluted-oil surface finishes were never as good and deteriorated with the change to more severe cutting conditions.

Data were obtained for 1045 steel with essentially the same physical setup used for 1015 steel. This was not the best cutting geometry for obtaining a good surface finish with 1045 steel, and all surface finishes were poor. A small improvement was noted with compound oil but this was masked by data scatter.

Fig. 6 is a bar graph of data obtained from metal-cutting tests conducted dry, with a mineral-oil flood and with a compound-oil flood. Both crater and flank wear were evident on the tool.

Dry cutting was possible only up to 0.002 ipr feed, and the tool life was prohibitively short. Mineral oil appears best at 0.005 ipr feed, but is inferior to compound oil at the other test conditions. No machining is practical at feeds in excess of 0.006–0.007 ipr with mineral oil. Compound oil performs well until severe cutting conditions are encountered.

All of the data from the 1045 series are plotted in Fig. 7. Temperature appears to be a good correlating criterion. No temperature below 650 F was obtained, possibly because this may be the minimum temperature in the shear plane where the chips separate from the stock. Below 800 F lower tool-wear rates were observed with compound oil than with mineral oil or dry cutting. In the temperature range about 900 F the lowest tool-wear rates were obtained with mineral-oil floods. Above 1050 F the curves appear to blend and tool-wear rate appears to be a function of temperature alone. The EP agents present in this particular compound oil apparently lose effectiveness above this temperature and the curve degenerates into a simple cooling curve.

Cutting temperatures produced when using compound oil were lower than when using mineral oil for the same cutting conditions. Presumably the reduction of friction at the chip-tool interface effected by the EP agents in compound oil is responsible.

Conclusions

(*a*) The radioactive-tool technique permits rapid and accurate measurement of instantaneous tool wear under cutting conditions comparable to industrial machining practice.

(*b*) No unique criterion of oil merit has been found, but tool-wear rate supplemented by surface-roughness or temperature data or both is a good index of oil performance. All three criteria should be considered at the start of an oil analysis. However, as the test proceeds it may be possible to subordinate one measure in the interests of economy.

An Effort to Use a Laboratory Test as an Index of Combustion Performance

By F. J. CEELY[1] and R. I. WHEATER,[2] NEW YORK, N. Y.

This paper discusses results of a study in progress to determine if the CRL[3] reactivity test can be applied as an index of combustion performance in pulverized fuel-fired steam generators. Before undertaking an extensive program of correlating laboratory data against actual combustion experience, it was necessary to conduct the study on a limited basis to establish whether or not the results would justify an extensive effort. The authors present some significant data accumulated during this study phase and conclude that further investigation is warranted on a larger scale.

Introduction

THERE are various properties of coal, and the solid derivatives of coal and petroleum, which are of foremost importance in each of the applications of these fuels. If we confine our remarks to the burning of pulverized fuels in suspension, then the most important properties are those comprising a general characteristic which may be called combustibility.

We sometimes conceive of combustibility as involving, first of all, the ignitibility of the fuel, and secondly, the nature and extent of the subsequent burn-out process. This simple analysis will suffice for the purposes of this paper. Both of these phases of combustibility are important and should be measured by any laboratory test (or tests) designed to predict behavior in large-scale equipment. In the United States, combustibility has been predicted almost exclusively from data provided by the standard proximate and ultimate analyses, together with a mass of accumulated experience. However, the necessity of designing equipment for fuels from new coking and charring processes and foreign coals of unknown behavior has emphasized the need for reliable laboratory-scale combustibility tests.

Considerable ingenuity has been expended in devising combustibility tests and an extensive literature exists on the subject (1, 2, 3).[4] Of the many tests described, few have been applied to the practical problem of prediction with which a design engineer is faced. There have been no published accounts, of which the authors are aware, of applications of any of the combustibility tests as design criteria in the important field of pulverized-fuel firing.

The authors' company has followed with interest many attempts to devise such methods and was particularly interested in the activities and reports of Subcommittee XVI of ASTM Committee D-5 on Coal and Coke. This subcommittee investigated the CRL reactivity test originally devised at the Coal Research Laboratory of the Carnegie Institute of Technology, by Sebastian and Mayers (4). Its investigation was reported to the ASTM annual meeting in 1941 and was summarized up to that date in an outstanding report by Sherman, Pilcher, and Ostborg published later that year (5). The subcommittee was generally optimistic with regard to the ability of this test to measure a temperature, called the "reactivity index," and the application of this index to practical predictions when additional correlation data became available.

It was evident that anyone desiring to use the test for design purposes would have to collect both reactivity data and combustion experience with a wide variety of fuels to determine if a reliable correlation were possible. One also would have to decide whether or not the test, which was conceived as an ignitibility test, yielded significant information regarding the burn-out phase of combustion, and modify or supplement the test if it did not.

A year ago, we initiated a program to resolve the problems as outlined. This interim report will give the results to date together with some indication of our future course of action.

Equipment Used for Correlation Study

We will not discuss the CRL test apparatus or method as this has been done adequately in the papers previously cited (4, 5, 6). It is important, however, to note that the CRL test in its present form, unlike other combustibility tests, seems to determine an independent property of the fuel (6). This property, known as the reactivity index, is a temperature at which the rate of oxidation of a sample attains a prescribed value under standard conditions. Specifically, the term reactivity index as used in this paper is known as T_{15} and is the temperature in degrees centrigrade corresponding to an adiabatic self-heating rate of 15 deg C per min. From this definition, it will be seen that the higher the reactivity index T_{15}, the less reactive, or less ignitible, is the fuel.

The combustion characteristics of the various fuels included in this study were determined by observing or testing steam generators when actually firing these fuels. For the anthracite fuels, we used the type of steam generator shown in Fig. 1. In this design, many carefully conceived provisions have been made to achieve good combustion of low-volatile fuels in a dry-bottom furnace. Pulverized fuel of high fineness is supplied to separating-type burners located in the two opposed arches. The burners vent a portion of the primary air, thus providing a rich mixture at the burner nozzles. After ignition is established, secondary air is admitted along the U-shaped flame path through air ports in the walls below the arches and a relatively large furnace is provided for ample residence time.

For the fuels other than the anthracites, we have used steam generators of various designs and taken into consideration those design factors which influence combustion characteristics.

Correlation of Combustibility With Reactivity Index

American experience has generally established the composition and amount of volatile matter in solid fuels as the major criteria for combustibility. Except in rare instances the composition of

---

[1] Head, Firing Equipment Section, Steam Department, Foster Wheeler Corporation. Mem. ASME.

[2] Staff Engineer, Steam Department, Foster Wheeler Corporation. Mem. ASME.

[3] Coal Research Laboratory of Carnegie Institute of Technology, Pittsburgh, Pa.

[4] Numbers in parentheses refer to the Bibliography at the end of the paper.

Contributed by the Fuels Division of The American Society of Mechanical Engineers and presented at the ASME-AIME Joint Fuels Conference, Washington, D. C., October 25–26, 1956.

Note: Statements and opinions advanced in papers are to be understood as individual expressions of their authors and not those of the Society. Manuscript received at ASME Headquarters, October 9, 1956. Paper No. 56—FU-6.

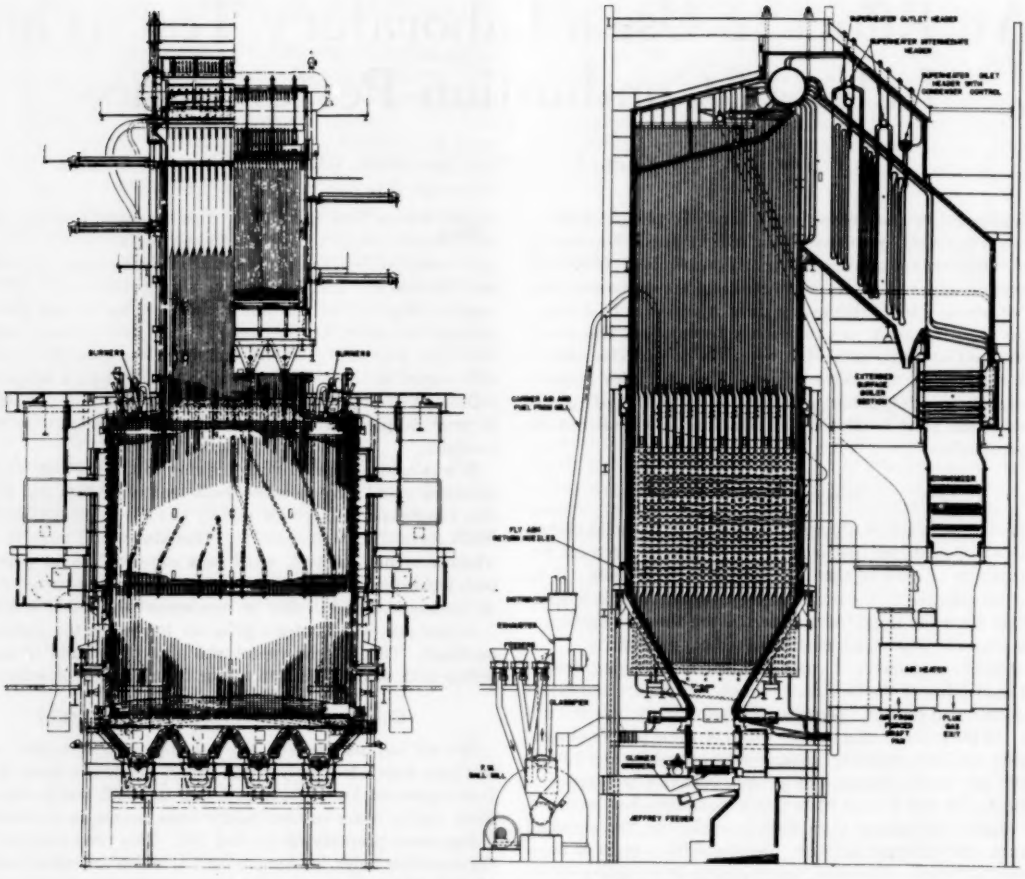

FIG. 1 A TYPICAL STEAM GENERATOR FOR ANTHRACITE FIRING

the volatile matter has been ignored because of its consistency. The most important applications of these criteria are, of course, in the design of equipment for those fuels, such as anthracites, and some cokes and chars, which are difficult to ignite and burn. Many successful units have been designed, and operating experience in this country confirms the close relationship between the volatile content and combustibility. Furthermore, work done by various investigators indicated that for all ranks of American coal, and for cokes having the same carbonization history, the reactivity index T_{18} was predictable with fair accuracy from the dry, ash-free volatile content alone. Formulas eventually were given in the literature for the calculation of T_{18} from volatile content (7, 8). This apparently established a general relation between T_{18} and combustibility.

However, our present study shows that the composition of the volatile matter cannot be neglected and that the combustibility of a fuel cannot be closely correlated with the amount of volatile matter alone. It also has revealed that the reactivity index cannot be calculated from volatile content alone with the degree of accuracy required to justify establishing a formula. An illustration of these points follows.

Many units of the type shown in Fig. 1 have been designed for Pennsylvania anthracites using volatile content alone as the major combustibility criterion since the composition of volatile matter in these fuels is quite consistent. Without exception, the performance of these units verified the correctness of the predictions. However, when virtually this same design was used for a French anthracite of approximately the same volatile content, predictions based upon the volatile content criterion were not valid since this fuel was clearly much more difficult to ignite and burn to completion than the Pennsylvania anthracite.

Laboratory test data for the fuels in question are shown on Table 1. It is most striking to note that the volatile content on a dry, ash-free basis is 11.4 per cent for the foreign fuel, and is only 8.55 per cent for the Pennsylvania anthracite. The measured reactivity indexes are 411 C and 310 C, respectively, showing the reactivity index is, as it should be, higher for the fuel which experience showed to be more difficult to ignite and burn. The comparison of measured and calculated values of T_{18} shows the formula from reference (8) to hold well for the Pennsylvania anthracite, but to diverge badly from the measured value for the French fuel.

There are several other points of interest in these data which should be considered briefly. The hydrogen content of the French anthracite is much lower, the ash content considerably higher, and the composition of the volatile matter quite different from that of the Pennsylvania anthracite. While the analysis of the volatile matter of the French fuel does not report the oxygen, carbon dioxide, and condensable vapor present, the inclusion of these constituents would only further reduce the hydrogen and

TABLE 1 FUEL ANALYSES AND RELATED DATA FOR TWO ANTHRACITE COALS

SAMPLE NO.		8		10	
SOURCE		FRANCE		PENNSYLVANIA	
PROXIMATE ANALYSIS:					
FIXED CARBON	%	62.73		78.22	
VOLATILE MATTER	%	8.08		7.31	
ASH	%	29.19		14.47	
VOLATILE CONTENT (DRY, ASH-FREE)	%	11.41		8.55	
ULTIMATE ANALYSIS:					
CARBON	%	64.97		78.68	
HYDROGEN	%	1.48		2.23	
OXYGEN	%	2.16		5.14	
NITROGEN	%	0.80		0.81	
SULFUR	%	1.80		0.67	
ASH	%	29.19		14.47	
HEATING VALUE (MEASURED)	BTU/LB	9804		12221	
HEATING VALUE (DULONG EQUATION)	BTU/LB	10265		12164	
REACTIVITY INDEX, T_{15} (MEASURED)	C	411		310	
REACTIVITY INDEX, T_{15} (EQ.7, REFERENCE 8)	C	273		301	
ANALYSIS OF VOLATILE MATTER		VOL.	WT.	VOL.	WT.
ILLUMINANTS	%	0.3	0.9	0.0	0.0
CO_2	%	—	—	2.0	15.3
O_2	%	—	—	1.1	6.1
H_2	%	55.3	8.4	83.9	29.4
N_2	%	10.3	22.1	2.0	9.8
CO	%	29.0	62.5	4.2	20.4
CH_4	%	5.1	6.3	6.8	19.0
GRINDABILITY — HARDGROVE		67		33	

methane reported. The condensable volatile matter present in the French coal is not found in Pennsylvania anthracites. Various checks on the heating value of the volatile matter of the French anthracite, aside from the foregoing data, have shown it to be in the order of 25 per cent of that of Pennsylvania anthracite. The heating values, as calculated by Dulong's formula, also are shown. It will be noted that the measured and calculated values of the Pennsylvania anthracite check closely, but the measured value is 4.5 per cent below the calculated value for the French coal. This fact has been noted on several other fuels which have high reactivity indexes.

In again considering only the correlation of volatile content with reactivity, we have found that the measured reactivity of many other fuels failed to agree with the formulas for coal and coke in the existing literature. Fig. 2 shows the comparison of the measured and calculated reactivity index T_{15} as a function of dry, ash-free volatile content for a number of coals of widely different rank and source, and for some chars and cokes. Referring to the two anthracites just discussed, it will be observed that the reactivity of the French fuel (Sample 8) is well above the curve, but that the American fuel (Sample 10) agrees well with the curve.

Other particularly interesting fuels whose reactivity is plotted in Fig. 2 are foreign anthracites (Samples 1 through 8), an American graphitic anthracite (Sample 13), fluid coke from the first commercial-scale fluid-coking unit (Samples 17, 18), a typical petroleum coke from a delayed-coking unit (Sample 19), and a low-temperature bituminous-coal char (Sample 20) More related data for these fuels may be found in the summary tabulation of Table 2. None of the anthracites is of meta-anthracite rank according to ASTM D388-38. However, many of those diverging most widely from the curve, for example, Samples 1, 2, 7, 8, and 13, occur in isolated lenses or pods and often exhibit a relatively soft structure and graphitic texture which one might associate with meta-anthracite. With regard to combustibility, all require special consideration for ignition and completion of combustion, and qualitatively substantiate the reactivity index as a criterion for predicting large-scale behavior. Those with the highest value of T_{15} are extremely difficult to burn.

Two samples of the fluid coke used in a series of large-scale burning tests (9) showed reactivity indexes of 348 C and 374 C. From the authors' observations during these tests, we consider these reactivity figures in accordance with the combustion characteristics noted.

The delayed petroleum coke (Sample 19) has a higher reactivity index than predicted for coke of the same volatile content derived from coal but approximately the same as coal of equal volatile content. Experience has shown that some supplemental fuel is required to maintain ignition of this fuel and achieve combustion characteristics equal to those of bituminous coal of the same reactivity when subjected to the same firing conditions.

The low-temperature bituminous-coal char (Sample 20) has a

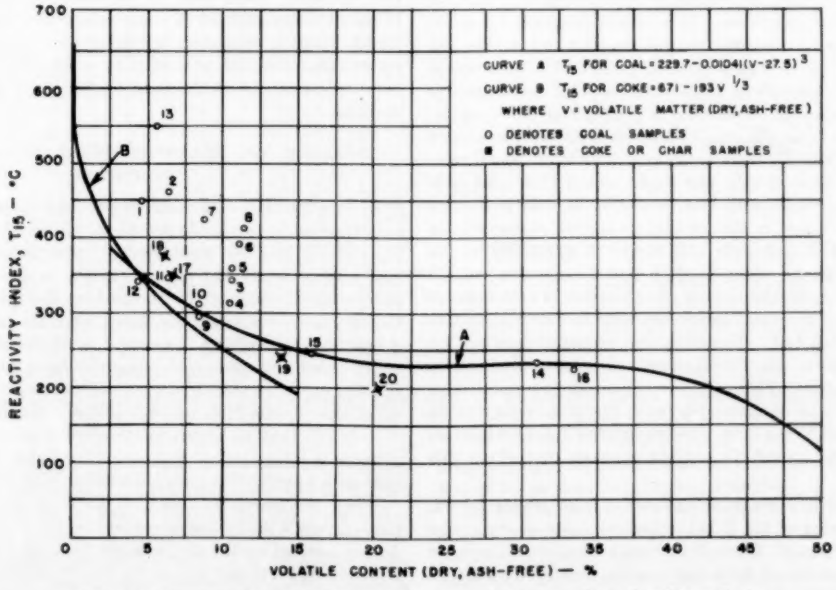

FIG. 2 REACTIVITY INDEX T_{15} VERSUS VOLATILE CONTENT; DRY ASH-FREE BASIS

TABLE 2 SUMMARY OF FUEL ANALYSES AND RELATED DATA

SAMPLE NUMBER	FUEL	SOURCE	PROXIMATE ANALYSIS (a) VOLATILE MATTER	FIXED CARBON	ASH	ULTIMATE ANALYSIS (a) C	H	O	N	S	ASH	HEATING VALUE (b) MEASURED	DULONG FORMULA	VOLATILE CONTENT (c)	GRINDABILITY HARDGROVE	REACTIVITY INDEX (d,e) OBSERVED	CALCULATED
1	ANTHRACITE	KOREA	4.10	81.47	14.43	78.92	1.22	4.00	0.25	1.18	14.43	11942	11972	4.79	214	448	352
2	ANTHRACITE	KOREA	4.17	59.73	36.10	59.08	1.22	2.97	0.40	0.23	36.10	8723	9212	6.53	48	480	326
3	ANTHRACITE	SPAIN	7.18	59.44	33.40	60.09	1.63	3.22	0.70	0.96	33.40	9207	9540	10.75	48	342	279
4	ANTHRACITE	SPAIN	7.44	63.05	29.51	63.67	2.31	2.32	0.87	1.32	29.51	10115	10567	10.55	48	312	280
5	ANTHRACITE	PORTUGAL	5.75	47.94	46.31	47.19	1.62	3.70	0.56	0.62	46.31	6930	7733	10.71	64	359	279
6	ANTHRACITE	PORTUGAL	5.83	46.01	48.16	45.33	1.20	3.99	0.56	0.77	48.16	6342	6893	11.25	91	390	274
7	ANTHRACITE	FRANCE	6.71	69.44	23.85	70.99	1.27	1.58	0.58	1.73	23.85	10681	11060	8.81	67	423	298
8	ANTHRACITE	FRANCE	8.08	62.73	29.19	64.97	1.48	2.16	0.60	1.60	29.19	9804	10265	11.41	67	411	273
9	ANTHRACITE	USA	7.05	74.91	18.04	74.32	2.45	3.67	0.91	0.61	18.04	11697	12069	8.60	42	299	301
10	ANTHRACITE	USA	7.31	78.22	14.47	76.68	2.23	5.14	0.81	0.67	14.47	12221	12184	8.55	33	310	301
11	ANTHRACITE	USA	5.34	77.30	17.36	76.77	1.93	2.63	0.77	0.54	17.36	11781	12373	6.46	51	346	328
12	ANTHRACITE	USA	4.00	83.11	12.89	81.86	1.90	1.85	0.79	0.69	12.89	12697	13223	4.59	56	341	355
13	ANTHRACITE	USA	3.80	62.20	34.00	62.80	0.40	2.20	0.10	0.50	34.00	8600	9228	5.76	22	551	369
14	BITUMINOUS	FRANCE	19.02	42.24	38.74	51.71	3.10	4.52	1.05	0.88	38.74	8939	9132	31.05	100	233	229
15	BITUMINOUS	HOLLAND	12.86	67.32	20.02	70.97	3.65	3.34	1.13	0.89	20.02	12144	12363	15.83	100	245	246
16	BITUMINOUS	USA	30.28	60.16	9.59	77.99	4.41	3.13	1.50	3.38	9.59	13990	13972	33.48	95	224	229
17	FLUID PET. COKE	USA	6.77	92.93	0.30	97.30	2.42	3.25	1.67	5.16	0.30	14128	14188	6.79	26	348	306 (f)
18	FLUID PET. COKE	USA	6.13	93.77	0.10	97.75	2.16	3.04	1.42	5.53	0.10	14310	14094	6.14	21	374	317 (f)
19	DELAYED PET. COKE	USA	14.02	85.56	0.42	88.33	3.38	2.52	1.18	4.17	0.42	15523	14917	14.07	127	241	208 (f)
20	LOW TEMP. CHAR	USA	18.50	72.37	9.13	76.02	3.48	7.47	1.60	2.35	9.13	13090	12709	20.35	148	198	233

(a) ANALYSES ON DRY BASIS
(b) HIGHER HEATING VALUE IN BTU PER POUND, DRY BASIS
(c) VOLATILE CONTENT ON DRY, ASH-FREE BASIS
(d) REACTIVITY INDEX T_{15} IN OXYGEN – °C
(e) CALCULATED VALUE OBTAINED FROM FORMULA 7 IN REFERENCE (8) EXCEPT SAMPLES 17–19
(f) SAMPLES 17–19 CALCULATED FROM FORMULA 8 IN REFERENCE (8)

reactivity index lower than coal of the same volatile content, and about equal to high-volatile Pennsylvania or West Virginia coals. Our experience with this char is limited to several short tests under conditions of low primary and secondary-air temperature, and pulverized-char fineness averaging 70 per cent through 200 mesh. Under these conditions, it was difficult to maintain ignition without supplemental fuel and the unburned combustible loss was high. When coals of the same reactivity as this char are fired under the same conditions in this equipment without supplemental fuel, the ignition is stable, and the unburned combustible loss is low.

From an ignitibility viewpoint, it would seem that the reactivity index of the low-temperature char and delayed petroleum coke is deceptively low, indicating an apparent ease of ignition not found in actual experience. It is equally plausible, however, to say that coals of the same volatile content as the coke and char ignite much more readily than their reactivity index would indicate. It is important to recall that the CRL test measures the rate of oxidation at the surface of a sample at low temperatures. Thus, in almost all cases, the sample is virtually unaltered by the test, and certainly there is no appreciable evolution of volatile matter. Because of this, one might expect that solid fuels which ignite in furnaces with little evolution of volatile matter and little or no change in surface area or surface characteristics would be correlated accurately with regard to ignitibility by the CRL test. If, on the other hand, a fuel does evolve volatile combustible matter or undergoes surface increase or activation at low temperatures, its actual ignitibility may be better than predicted by the CRL test. The CRL test probably does not account adequately for the "torch effect" of volatile combustible matter on ignitibility. This tentative conclusion is supported by the flat characteristic of the coal curve in Fig. 2 between volatile contents of 15 and 35 per cent, since experience indicates increasing ease of ignition as volatile content increases throughout this range.

Sample No. 13 is a graphitic anthracite from Rhode Island. The reactivity index of 551 C is the highest value of any of the raw-coal samples tested. There have been several attempts made in the past to burn Rhode Island anthracite, notably the tests reported in the ASME Transactions for 1924 (10). The present authors have consulted freely with one of the engineers responsible for carrying out the test program (11).

The tests clearly demonstrated that the Rhode Island anthracite could not be burned without supplemental fuel even in a furnace with refractory walls. Efforts to burn this fuel alone were unsuccessful even when tests were started using a mixture of this fuel and New River bituminous coal. Whenever, the bituminous-coal supply was depleted, the furnace began to cool and ignition was lost in all cases within 2 hr. It is evident from the available reports that the observed combustion characteristics of the Rhode Island anthracite are consistent with its high reactivity index.

In considering the burn-out phase, our study has indicated that the reactivity index can be correlated qualitatively with the burn-out characteristics of coals, cokes, and chars providing optimum ignition conditions are achieved. Additional data must be accumulated and evaluated to a common base before firm conclusions can be made as to usefulness of the index for predictions.

Correlation of Reactivity Index With Other Fuel Properties

A close correlation of reactivity index with one or more of the other fuel properties would provide a valuable check on determinations of T_{15}, and also would permit approximating T_{15} without a fuel sample where the other property is already known. Attempts have been made by the authors and others to find a relationship between reactivity index and almost all known fuel properties. Our efforts to establish a relationship between reactivity index and other fuel properties have indicated that some relation exists between hydrogen content and reactivity index on all of the various fuels tested. While it has been reported previously (8) that an approximate correlation exists between dry, ash-free volatile content and reactivity index, our study reveals that such a correlation does not exist on many of the fuels tested.

When the reactivity index of the fuels shown in Table 2 is plotted versus the hydrogen content on the dry basis, and the hydrogen content on the dry, ash-free basis on Figs. 3 and 4, some relationship is evident and curves may be drawn. It is interesting to note that the hydrogen content on the dry basis provides a

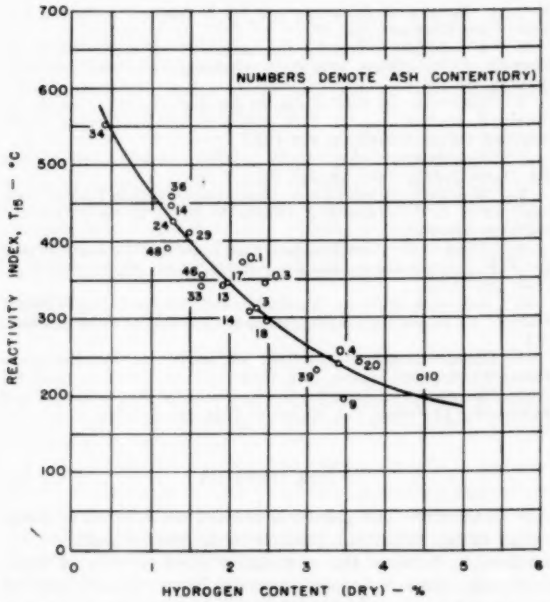

FIG. 3 REACTIVITY INDEX T_{15} VERSUS HYDROGEN CONTENT; DRY BASIS

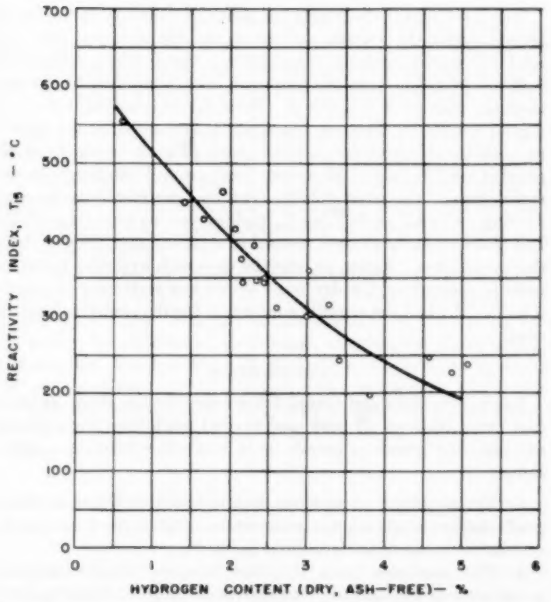

FIG. 4 REACTIVITY INDEX T_{15} VERSUS HYDROGEN CONTENT; DRY, ASH-FREE BASIS

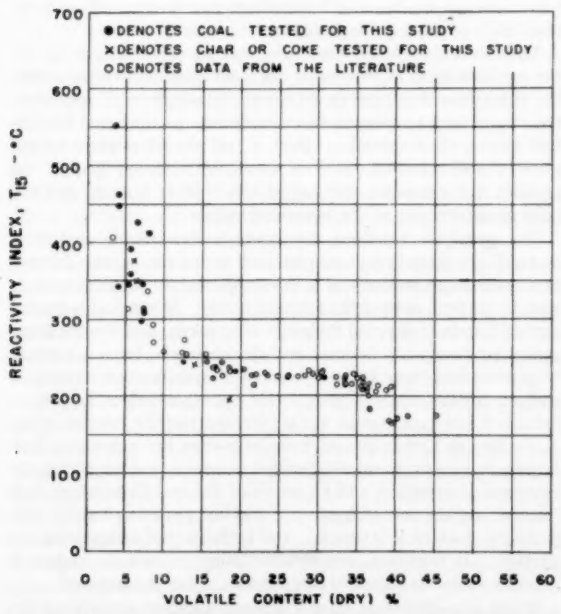

FIG. 5 REACTIVITY INDEX T_{15} VERSUS VOLATILE CONTENT; DRY BASIS

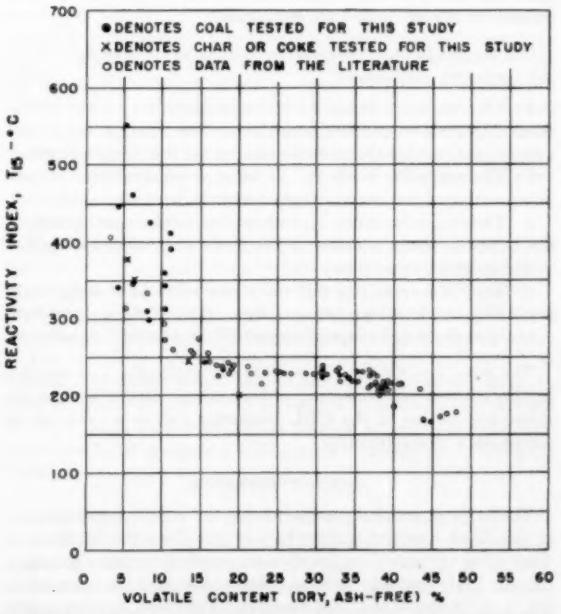

FIG. 6 REACTIVITY INDEX T_{15} VERSUS VOLATILE CONTENT; DRY, ASH-FREE BASIS

curve with less scattering of points than found when the dry, ash-free hydrogen content is used. The figures adjacent to the plotted points in Fig. 3 denote the ash content on the dry basis and it may be seen that samples of equal ash content are not consistently above or below the curve drawn. The maximum deviation of all reactivity data checked against this curve, including cokes and chars, is less than 45 deg C, thus showing that the hydrogen content on the dry basis may provide a usable approximation of T_{15} as more data become available.

Any conclusions relative to the apparent ash effect may be considered premature, since the role of ash in the reactivity test has not been definitely established as yet. Some speculations (12) have been made regarding the relative effect of ash acting as thermal ballast and as a catalyst.

In Figs. 5 and 6 the reactivity index of many fuels has been plotted versus the volatile content on the dry basis and the dry, ash-free volatile content, respectively. Since many additional data are available from the literature, they were used to supplement the data given in Table 2. These curves reveal that there is a good correlation between reactivity index and volatile content on both the dry and dry, ash-free basis of coals in the 15 to 35 per cent volatile range. However, in the low-volatile range, many anthracites of the same volatile content have reactivity indexes varying as much as 240 deg C, making correlations impossible. The chars and cokes tested seemed to correlate much better than the anthracites. Again, as was the case with hydrogen content, volatile content on the dry basis shows less scattering of points than found when the volatile content on the dry, ash-free basis is used.

Conclusions

Laboratory data and actual firing experience in steam generators using coals of all rank and several solid fuels from coking and charring processes permit us to make the following conclusions:

1 The volatile content alone does not provide either accurate predictions of combustion characteristics of all of the fuels tested, or reliable values of the reactivity index T_{15}.

2 The reactivity index T_{15} alone does not provide accurate predictions of the ignition characteristics of all of these fuels.

3 Additional performance data and firing experience are required on fuels having T_{15} values exceeding 350 C to establish the practical application of the reactivity index in predicting burn-out characteristics on large-scale equipment.

Our studies to date have also permitted us to make the following tentative conclusions:

1 The reactivity index T_{15} will only provide accurate predictions of ignition characteristics for those fuels which do not evolve appreciable combustible volatile matter at low temperatures.

2 The reactivity index T_{15} can be approximated with reasonable accuracy from the hydrogen content (dry basis) of the fuel.

3 The reactivity index T_{15} will provide accurate predictions of the burn-out characteristics of the fuels when they are ignited under optimum conditions.

4 The CRL reactivity test will prove valuable to designers in predicting combustion characteristics of anthracites, petroleum cokes, and chars as its capabilities and limitations are established.

The results of this study to date are gratifying and warrant further effort to resolve some problems encountered in the quantitative application of the CRL reactivity test as a criterion of combustion characteristics.

Acknowledgments

The authors gratefully acknowledge the generous co-operation of the Coal Research Laboratory of the Carnegie Institute of Technology in providing the data on reactivity indexes necessary for this investigation. Special thanks also must be extended to Dr. A. A. Orning of the Coal Research Laboratory for his valuable counsel.

BIBLIOGRAPHY

1 "Die Reaktionsfähigkeit des Koks," by R. Mezger and F. Piston, W. Knapp, Halle, Germany, 1927.

2 "The Solid Products of Carbonization of Coal," by the South Metropolitan Gas Company, London, England, 1934.

3 "Methods of Determining the Reactivity of Cokes," by M. A. Mayers, Contribution 36, Coal Research Laboratory, Carnegie Institute of Technology, Pittsburgh, Pa., March, 1936.

4 "Coke Reactivity: Determination by a Modified Ignition Point Method," by J. J. S. Sebastian and M. A. Mayers, *Industrial and Engineering Chemistry*, vol. 29, no. 10, 1937, pp. 1118–1124.

5 "A Laboratory Test for the Ignitibility of Coal," by R. A. Sherman, J. M. Pilcher, and H. N. Ostborg, ASTM Bulletin 112, 1941, pp. 23–34.

6 "Reactivity of Solid Fuels to Air and Oxygen," by A. A. Orning, S. Mallov, and M. Neff, *Industrial and Engineering Chemistry*, vol. 40, no. 3, 1948, pp. 429–432.

7 "Reactivity of Cokes," by H. L. Weisz and A. A. Orning, *Fuel*, vol. 31, no. 3, July, 1952, pp. 288–301.

8 "Reactivity of Solid Fuels—Influence of Oxygen Partial Pressure," by H. L. Weisz and A. A. Orning, *Fuel*, vol. 32, no. 4, October, 1953, pp. 435–440.

9 "Fluid Coke—New Fuel for Steam Industry," by F. H. Stracke and F. H. Schiffer, *Oil and Gas Journal*, vol. 54, no. 30, November 28, 1955, pp. 75–78.

10 "A Review of Recent Applications of Powdered Coal to Steam Boilers," by Henry Kreisinger, Trans. ASME, vol. 46, 1924, pp. 595–617.

11 Private communication from Martin Frisch, Vice-President, Foster Wheeler Corporation, New York, N. Y.

12 "Reactivity of Solid Fuels," by A. A. Orning, *Industrial and Engineering Chemistry*, vol. 36, no. 9, 1944, pp. 813–816.

Discussion

R. C. Corey.[5] This paper is a welcome contribution to a neglected, though important, phase of combustion technology: the relationship between the combustion characteristics of coals, cokes, and chars in a commercial-size boiler furnace, and the results of laboratory tests of the same fuels to determine their relative combustibility. The authors used the "reactivity index," which is based on a test developed in the Coal Research Laboratory, Carnegie Institute of Technology, as a measure of the combustibility of the solid fuels that were studied.

This writer contends that any test to determine, a priori, the combustibility of pulverized fuel must simulate to some degree the conditions that exist in a furnace, especially with respect to the rate of heat transfer to and through the particle, and the air-fuel mixing characteristics. Such a test should respond to the physical and chemical reactions associated with pyrolysis of the particle, the gas-phase burning of the volatile matter, and the solid-phase burning of the remaining carbon.

The pyrolytic reactions, from which the volatile matter is derived, are exceedingly complex and as yet not clearly defined. It is essential to understand that volatile matter does not exist as such in the fuel, as does the mineral matter. When coal is heated certain bonds in the coal molecule are broken, and the resulting molecular fragments interact and decompose to form a mixture of gaseous and tarry hydrocarbons, hydrogen, carbon monoxide, carbon dioxide, carbon, and water vapor, which is known as volatile matter. Although the mechanism and the kinetics of the formation and evolution of volatile matter are not clear, it is known that its chemical composition is determined largely by the chemical composition and structure of the fuel from which it is formed; by the rate of heating of the fuel particle; by the temperature at which it is formed; and by its rate of escape from the particle. In addition, the combustibility of volatile matter is determined by its chemical composition, other things equal.

These considerations raise a serious question concerning the value of the composition of the volatile matter as an index of combustibility in a furnace. Presumably, the volatile matter of both the French anthracite and the Pennsylvania anthracite was generated from a charge in a crucible, heated under specified conditions. If the volatile matter of each coal had been produced under other conditions, its composition might have been quite different.

---

[5] Chief, Division of Solid Fuels Technology, Region V, U. S. Bureau of Mines, Pittsburgh, Pa.

With regard to the burnout phase, much remains to be learned about the rate of combustion of nearly or completely devolatilized particles, especially with regard to the effects of: (*a*) the geometric and internal surface areas of such particles, (*b*) the amount and distribution of the ash, and (*c*) the heat-transfer characteristics of the particles.

There is clearly a need for more emphasis on fundamental studies of the physical and chemical reactions associated with the pyrolysis of coal particles; measurement of the rate of devolatilization of coal particles under controlled conditions would be a valuable step in this direction. Studies are needed also of the combustion kinetics of certain coals, cokes, and chars, to ascertain the reasons for unexpected combustion characteristics in furnaces.

The following questions may be asked the authors:

1 Under what conditions was the volatile matter produced for samples 8 and 10?

2 Have the anthracite samples that appeared to be graphitic been examined to determine if this structure existed, say, by means of x-ray diffraction?

3 Relative to the delayed coke, was the fluid coke easier to burn? What might be said about the combustion characteristics of delayed coke, relative to anthracite and bituminous coal?

4 Where comparisons were made of the combustion characteristics of foreign and Pennsylvania anthracites, were the heat-release rates, air-preheat temperatures, fuel-air ratios, and other significant operating variables comparable?

5 Other things equal, the combustible content of the fly ash from the various anthracites might provide a useful correlation factor. Are these data available?

6 Other than the need for supplementary fuel, and high carbon losses, associated with fuels that burned with relative difficulty, what other operating factors, especially those with quantitative significance, are available to compare performance? All clues of this kind are valuable in planning controlled, laboratory-scale experiments.

M. A. Mayers.[8] It has been interesting to learn that the subject of ignitibility of solid fuels is again arousing interest as a potentially significant characteristic.

It should be noted that the CRL method discussed in this and the companion paper[7] had a more limited objective than the measurement of ignitibility in the broad terms in which it was defined by Subcommittee XVI of ASTM Committee D-5. This limited objective was to measure the rate of the oxidizing reaction in a way that is characteristic of the coal material.

It was subsequently pointed out[8] that the effective ignition temperature in a fuel bed depended on the conditions existing within the bed. These conditions include mean particle size, rate of air flow, effective conductivity of the bed, and rate of fuel flow through the bed. For a particular set of conditions an attempt was made to estimate effective ignition temperatures from measurements of T_{15} and T_{75}. The estimates so arrived at were of the right order but there was no objective method available for determining whether they were, in fact, correct.

The large-scale ignitibility test reported by Nelson and Pilcher in Figs. 1 and 2 of their paper[7] may or may not correlate with the CRL method. Since the large-scale method does not compensate for the extraneous factors described in the previous paragraph, the relationship between reaction rate and rate of temperature rise upon which the CRL method is based is an approximation to the complete expressions for heat flow in fuel beds given in another paper.[9]

The CRL method eliminates the effect of thermal transport within the bed by establishing uniform temperature throughout the sample being tested and by limiting severely the rate of air or oxygen flow. When these quantities are not negligibly small, the simple relationship[7] between reaction rate and rate of temperature rise no longer holds.

Messrs. Ceely and Wheater call attention to differences in behavior under firing conditions of fuels having substantially the same values of T_{15}. Was any attempt made to correlate these differences with differences of E-value or with the difference in temperature between T_{15} and T_{75}? These quantities measure the rate of change of reaction rate with temperature and might be expected to point to differences under other operating conditions of fuels having the same value of T_{15} under CRL test conditions.

A. A. Orning.[10] The authors have shown that there are coals, in the low volatile-matter-content range, having reactive properties that cannot be predicted from their proximate analyses. Further experience may show that ultimate analyses and data on character of the volatile matter are adequate for prediction of reactive properties.

It appears that chars and cokes have combustion properties differing from those of coals with similar proximate analyses and reactivity indexes. The authors indicate that reactivity indexes correlate with burn-out characteristics "providing optimum ignition conditions are achieved." This optimum demands rapid heating of the fuel as it enters the combustion chamber, achieved by an intense flame held close to the burner mouth. Thermal changes in the solid residue, which must be burnt out, differ with rapid heating in the flame from those produced by slow heating in the carbonization process. These basic differences between coals and chars and cokes must be recognized in any broad correlation of combustion properties of solid fuels.

The CRL reactivity test has been recommended as a research tool in so far as reactive properties can be predicted with sufficient accuracy from proximate analyses. The present data show that this position must be modified. As applied to a wide range of low-volatile fuels, the proximate analysis is not adequate.

The reactivity test requires special equipment and skills. It cannot be justified unless the alternatives are equally difficult. Determination of ultimate analyses and qualitative examination of the volatile matter appear as possible alternatives. Correlations should be continued with special emphasis on low-volatile fuels.

R. A. Sherman.[11] To the writer, who was Chairman of Subcommittee XVI on Ignitibility of Coal and Coke of Committee D-5 of the ASTM during the several years of the life of the Subcommittee, the resurgence of interest in this subject is of considerable interest. Although the work done by the Subcommittee indicated that the CRL test so nicely developed by Mayers and his associates was one capable of giving reproducible results and

[8] Chief Mechanical Engineer, Burns and Roe, Inc., New York, N. Y. Mem. ASME.

[7] This discussion also pertains to "Ignitibility Testing as a Measure of the Burning Characteristics of Solid Fuels," by H. W. Nelson and J. M. Pilcher, ASME Paper No. 56—FU-2.

[8] "Some Factors Affecting Combustion in Fuel Beds," by M. A. Mayers, American Institute of Mining and Metallurgical Engineers Technical Publication No. 771, 1937.

[9] "Temperatures and Combustion Rates in Fuel Beds," by M. A. Mayers, Trans. ASME, vol. 59, 1937, pp. 279–285.

[10] Member of the Staff, Coal Research Laboratory, Carnegie Institute of Technology, Pittsburgh, Pa. Mem. ASME.

[11] Technical Director, Battelle Memorial Institute, Columbus, Ohio. Mem. ASME.

one of more than an empirical significance, yet the ability to interpret the results of the test in terms of the performance of a fuel in use led the Subcommittee to vote a recommendation for its dissolution some time before this was officially approved.

The paper by Nelson and Pilcher[7] is a good introduction to the symposium as it discusses the concept of ignitibility, the basis for the CRL test and its larger-scale counterpart as developed at Battelle, for the critical-air-blast method found so useful in Britain, and for the stoker-ignition test. It also presents such data on correlation as were available to the authors.

The Ceely-Wheater paper is particularly valuable because of the new data by the CRL method on a considerable variety of coals. These new data show that the volatile-matter content is not an accurate indication of the ignitibility. The data on the composition of the volatile matter of various coals is of interest but the ignitibility test is not a measure of the characteristics of the volatile matter but of the solid fuel before the volatile matter is formed and released.

The data given in the paper are, presumably, those obtained on −40 +60 mesh coal. Inasmuch as the interest of the authors was on the performance of the coal in pulverized form, the ignitibility of the coals in the sizes as pulverized for burning might be a better index of the relative expected performance. Certainly, the coals would have been pulverized to different degrees of fineness as indicated by experience.

That some degree of correlation between ignitibility and burn-out is anticipated by the authors is of interest. Inasmuch as the final burn-out is of a carbonized, highly heated residue, its degree of burn-out would not be expected to be affected by the initial ignitibility of the coal except in so far as this fixes the time available for combustion in the furnace. A delay in ignition will decrease the time available for combustion.

If this renewed interest in ignitibility is maintained with further data correlating the results of laboratory tests with performance in the furnace, it might well be profitable to reestablish the ASTM Subcommittee with fresh leadership and new blood.

Authors' Closure

The authors wish to extend their thanks to the discussers for the opinions and comments expressed on the subject matter of this paper. Some of the detailed questions cannot be answered at the present time since our study is not complete. It is expected however that work in progress may form the basis for replies to some of the unanswered questions.

Mr. Corey indicates that any test for combustibility must simulate to some degree the conditions of heat transfer and mixing that exist in a furnace. While the authors agree that such tests would probably provide useful measures of combustibility, it must be remembered that the major purpose of their study was to determine whether or not the CRL test, which is relatively simple, and is independent of burner and furnace types, can yield equally useful results. The many design and operating variables present in actual practice necessitate a test which measures a characteristic of the fuel itself independent of other influences.

Regarding Mr. Corey's comments on the pyrolysis of coal, the volatile matter for Samples 8 and 10 was evolved and measured under the same conditions. Our intent in introducing this data was merely to point out that some fuels of comparable volatile content, but with widely different reactivity indexes, also had marked differences in composition of the volatile matter.

The specific questions asked by Mr. Corey are answered as follows:

1 In general, the procedure followed was that published by the U. S. Steel Corporation in their, "Methods of Chemists for Sampling and Analysis of Coal, Coke, and By-Productions."

2 None of the apparently graphitic samples reported in this study have been examined by x-ray diffraction methods because of the difficulty of assigning quantitative significance to such results. Other experience of the authors with regard to x-ray diffraction procedures indicate that only rough differentiation is possible between samples of different graphitic content.

3 From our observations and data, we believe that the fluid petroleum coke is more difficult to ignite and burn than the delayed petroleum coke. The delayed coke is definitely more difficult to ignite and burn than bituminous coals and is easier to burn than anthracite.

4 In most cases the significant factors mentioned were comparable. In a few cases where these factors were not comparable we took the difference into consideration.

5 The combustible content of the flyash is available and has been used as far as possible to correlate burn-out characteristics with reactivity index. However, as pointed out in the paper the existing variations in those factors affecting burn-out make it extremely difficult to evaluate this data to a common base.

6 Other important operating factors such as range of stable burner operation, furnace exit-gas temperature, and permissible range of excess air may be used to compare performance when all other influencing variables are maintained constant.

Mr. Mayers has emphasized that the CRL test was originally devised to measure a low temperature oxidation rate in a way which is characteristic of the material itself. The purpose of the present study was to extend the significance of the CRL results, if possible, by determining if they correlate with actual burning characteristics.

An attempt was made to correlate E-values with firing behavior of fuels having substantially the same values of T_{18}. While such a correlation is not apparent at present, it is hoped that additional data will resolve this question.

Dr. Orning, who has done so much work with the CRL reactivity test, is certainly correct in his position that this test cannot be justified unless the alternatives are equally difficult. We are continuing our efforts to correlate the reactivity index with some more easily measured property of the fuel. Results on many samples tested since the presentation of this paper continue to indicate a reasonable correlation of T_{18} with hydrogen content (on the dry basis).

With reference to Mr. Sherman's comments, we understand that the reactivity test is not a measure of the characteristics of the volatile matter, but introduced the data showing composition of the volatile matter of Samples 8 and 10 only for the reasons outlined in the foregoing.

The reactivity indexes given in the paper were obtained using a −40 +60 mesh sample. For the purposes of this study, we did not want to introduce any variable, such as particle size, which by itself would affect the oxidation rate, since we were mainly interested in comparing fundamental characteristics of the fuels.

Turbulent Free-Convection, Heat-Transfer Rates in a Horizontal Pipe[1]

By J. P. FRASER[2] and D. J. OAKLEY,[3] SCHENECTADY, N. Y.

Heat-transfer rates are reported for turbulent free convection in a finite-length horizontal pipe containing sodium. Heat is added at one end and removed at the other. A generalized equation which correlates the data is proposed giving the ratio of heat transfer with turbulent convection to that on pure conduction in terms of the L/D ratio, Prandtl number, Grashof number, and Reynolds number. The solution is extended to inclined pipe with one or both ends open to plenums.

Nomenclature

The following nomenclature is used in the paper:

A = arbitrary constant
β = expansion coefficient, deg F^{-1}
C_p = specific heat, Btu/lb deg F
D = diameter, ft
ϵ_m = eddy coefficient of momentum, sq ft/hr
ϵ_h = eddy coefficient of heat, sq ft/hr
f = friction factor
g = gravitational acceleration, 4.17×10^8, ft/hr^2
θ = angle between pipe axis and horizontal
K = conductivity, Btu/hr ft deg F
L = length of pipe, ft
μ = viscosity, lb/ft hr
N = number of velocity heads loss
ΔP_t = thermal driving-pressure difference, psf
ΔP_r = resistance pressure drop, psf
Q = heat-transfer rate with turbulent convection, Btu/hr
Q_{cond} = heat-transfer rate with pure conduction, Btu/hr
ρ = density, pcf
T = temperature, deg F
τ = shear stress, psf
V = velocity, fph
x = axial distance, ft

Dimensionless Groupings

c = ratio of interface mixing length to diameter
Gr = Grashof number
L/D = ratio of length to diameter
Pr = Prandtl number
Q/Q_{cond} = ratio of forced free-convection heat-transfer rate to pure-conduction heat-transfer rate
Re = Reynolds number

Introduction

The present investigation was begun to determine the heat-transfer capabilities of the 8-in-ID horizontal piping leading from the SIR (sodium-cooled intermediate reactor) vessel through the shielding. Such information was needed either to estimate the required heat sink to freeze-seal the pipe for isolation purposes or the length of time required for a heat source external to the shield to thaw the reactor by heat transfer through the exit pipe. Heat-transfer measurements were taken for only one pipe configuration filled with sodium which duplicated the reactor exit-piping geometry.

Very few treatments of the unusual case of two streams of fluid moving in opposite directions within a common channel appear to exist in the literature. The laminar and turbulent velocity and temperature profiles in a heat-generating fluid for a long vertical parallel-sided cell having isothermal walls have been evaluated analytically (1).[4] The experimental investigation of heat transfer by free convection of a fluid in an isothermally heated vertical tube sealed at the lower end and open at the upper end to a cooled plenum has been reported (2). Findings were in close agreement with theoretical predictions of Lighthill (3).

The flow pattern reported herein has no axisymmetry in contrast with the previously referenced work. It is hoped that the generalized solutions will extend the usefulness of the test data; also that their derivation will suggest additional experimental work clarifying the mechanism and providing the basis for an improved general solution.

Experimental Work

Test Setup. The test section was a 10-ft-long piece of 8-in-diam pipe with a heating unit at one end and a cooling section at the other. The bends were introduced to mock up the reactor piping. A plan view of the configuration can be seen in Fig. 1. The heating section was 14 in. long consisting of five 3-kw calrod heaters wrapped around the pipe. The heat exchanger consisted of a concentric section of 10-in. pipe, sealed to the 8-in. test section with graphite packing. The water chamber was 24 in. long.

To insure complete filling of the horizontal-pipe test section, a 90-deg elbow and an 18-in. vertical section were welded to the horizontal section. At the heating section an expansion chamber was provided for the initial stages of thawing.

The entire test section was insulated (except the cooling-water jacket), with 4-in-thick mineral wool. To minimize heat losses to the stands a $^1/_2$-in-thick transite piece was placed between the pipe and stand.

Test instrumentation consisted of instruments to determine heat input, heat output, and temperature distribution within the sodium. Heat input was determined from voltage and current readings. Heat output was determined from water-flow rate and the temperature difference between inlet and outlet. Temperature distribution was measured with thermocouples placed at the bottom of wells extending 1 in. into the

[1] The Knolls Atomic Power Laboratory is operated by the General Electric Company for the Atomic Energy Commission. The work reported here was carried out under Contract No. W-31-109 Eng-52.

[2] Analytical Engineer, Heat Transfer and Fluid Flow, Knolls Atomic Power Laboratory, General Electric Company.

[3] Engineer, Heat Transfer, Knolls Atomic Power Laboratory, General Electric Company. Assoc. Mem. ASME.

Contributed by the Heat Transfer Division and presented at the Fall Meeting, Denver, Colo., September 10–12, 1956, of The American Society of Mechanical Engineers.

Note: Statements and opinions advanced in papers are to be understood as individual expressions of their authors and not those of the Society. Manuscript received at ASME Headquarters, May 9, 1956. Paper No. 56—F-6.

[4] Numbers in parentheses refer to the Bibliography at the end of the paper.

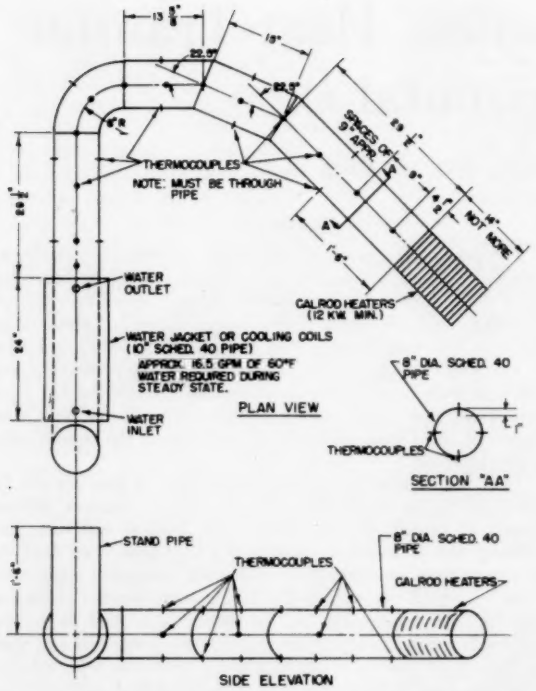

FIG. 1 TEST SECTION SHOWING METHODS OF HEAT ADDITION AND REMOVAL AND THERMOCOUPLE LOCATIONS

pipe, at top, bottom, and either side down the length of the test section. Fig. 1 shows the location of the thermocouples.

Test Procedure. The test section was preheated to about 350 F with heating-wire circuits and then filled with liquid sodium. The sodium level in the vertical standpipe was above the level in the horizontal pipe. The entire assembly was allowed to cool to approximately room temperature and then heat was applied by only the tubular heaters. When the thermocouples indicated the entire test section was molten, cooling water was passed through the water jacket and steady-state conditions established.

Test Results. Ten runs were made including the initial trial run. A summary of the test data is shown in Table 1. Fig. 2

TABLE 1 TEST DATA FOR HORIZONTAL PIPE

Run no.	Heat input Btu/hr $\times 10^{-4}$	Heat output Btu/hr $\times 10^{-4}$	Average temp, deg F	$(T_3 - T_2)_{avg}$, deg F	$(T_1 - T_2)_{avg}$, deg F
1	1.03	1.15	230	12.5	25.5
2	1.72	1.57	234	28	25.0
3	2.57	2.13	245	28.5	36.5
4	3.48	2.06	250	34.5	39.5
5	3.48	2.95	248	36.0	44.0
6	4.31	3.95	254	40.8	44.2
7	4.76	3.58	257	39.5	49.5
8	5.02	4.64	248	51.5	49.5
8A	5.02	4.64	261	49.5	45.5

shows measured heat-transfer rate as a function of the adjusted average temperature difference between streams. The heat transfer was observed to vary as the temperature difference raised to the three halves power as would be expected for turbulent free-convective heat transfer. Typical measured axial temperature distributions along the top and bottom of the pipe cross section are shown on Fig. 3.

The measured heat input, based on voltage and current readings, exceeded the measured heat output by 18 per cent on the

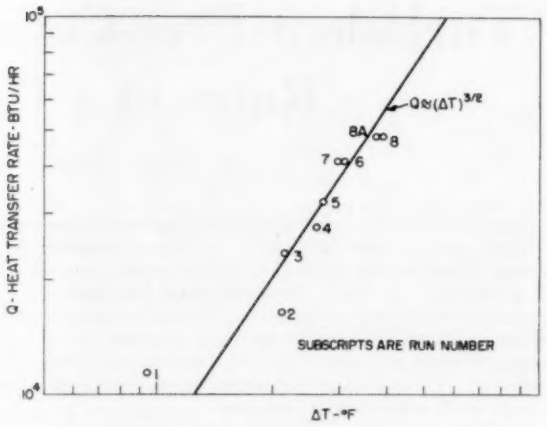

FIG. 2 MEASURED HEAT-TRANSFER RATES PLOTTED AGAINST AVERAGE ADJUSTED TEMPERATURE DIFFERENCE BETWEEN STREAMS

average. Because the heat outputs were based on low water-flow rates (small pressure drop) and small temperature differences, the heat-input measurements are considered more reliable.

ANALYTICAL PREDICTION OF HEAT-TRANSFER RATES

Since the flow and temperature patterns are not axisymmetric, the labor of a precise mathematical treatment appears unjustified if not impossible. Therefore the physical flow pattern will be reduced to a simple mathematical model retaining the principal features of the heat-transfer mechanism. The three geometries shown in Fig. 4 have been treated analytically, but the complete analysis will be developed for case (*a*) only.

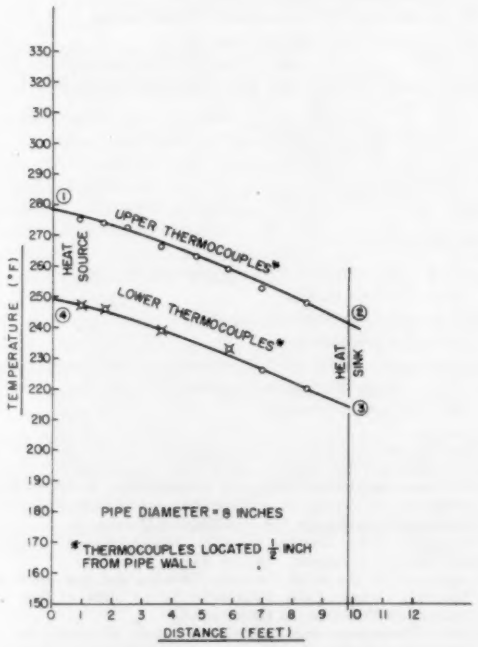

FIG. 3 TYPICAL TEMPERATURE DISTRIBUTION AROUND FREE-CONVECTION LOOP FOR A HEAT-TRANSFER RATE OF 23,500 BTU/HR

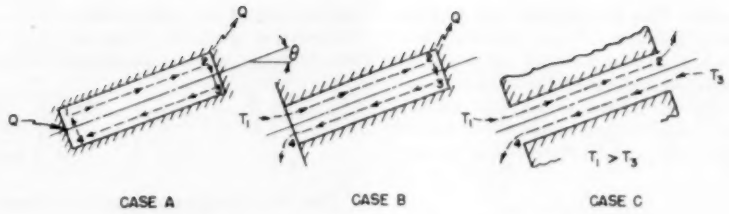

FIG. 4 GEOMETRIES FOR WHICH HEAT-TRANSFER-RATE EXPRESSIONS ARE DEVELOPED

The following assumptions are made:

1 The flow pattern is independent of axial position except near the ends.

2 The flow and temperature patterns are symmetrical about a horizontal diameter through the pipe center line.

3 The heat is added or removed over a small fraction of the pipe length.

4 The inner wall of the pipe is perfectly insulated.

5 The "centroids" of flow and temperature are ascribed to points 0.196 D above and below the pipe center line. The flow is said to be roughly equivalent to a flow of uniform velocity through a rectangle having a width of one diameter and a cross section half that of the pipe-flow cross section. The centroid is said to be at the center of this rectangle.

6 Velocity and temperature vary linearly between the upper and lower centroid locations.

7 The temperature distribution about the centroid path is a parallelogram, Fig. 3.

8 All fluid properties are constant and correspond to the average fluid temperature in the pipe except the density which is considered temperature-dependent when it contributes to the thermal driving head.

9 The ratio of the effective value of the mixing length at the interface to the pipe diameter is constant.

10 The flow resistance for each stream arises in two parts. The first results from wall shear over half the pipe periphery and may be computed on the basis that the effective hydraulic diameter of the semicircular flow section may be written in the conventional form

$$D_h = \frac{4 \text{ area}}{\text{perimeter}}$$

giving

$$D_h = \frac{4\left(\frac{\pi D^2}{8}\right)}{\frac{\pi D}{2} + D} = 0.611\ D \quad \ldots\ldots [1]$$

The friction factor is given by

$$f = \frac{0.184}{\mathrm{Re}^{0.2}} \quad \ldots\ldots [2]$$

The second part of the flow resistance is caused by eddy diffusion across the free surface interface between the two opposing streams. The turbulent shear at the interface is a function of eddy coefficient of momentum which is left as a function of the scale of mixing length to be determined from experiment.

11 Frictional resistance at the pipe periphery is not materially affected by substitution of a free-surface interface for a fixed boundary along a plane through the pipe center line.

12 The eddy coefficient of heat is equal to the eddy coefficient of momentum.

Thermal Driving Head. With the assumptions as background, the thermal driving pressure difference may be written

$$\Delta P_t = \rho\beta(0.392\ D \cos\theta)\left[\frac{(T_1 + T_4) - (T_2 + T_3)}{2}\right] + \rho\beta L \sin\theta\,(T_2 - T_3) \quad \ldots\ldots [3]$$

Flow Resistance. The resistance pressure drop is composed of three contributions. The first arises as a result of turning losses or losses through the heat exchangers and is expressed as

$$\Delta P_1 = N\frac{\rho V^2}{2g} \quad \ldots\ldots [4]$$

The second is the frictional pressure drop developed by wall friction. The applicable hydraulic diameter and friction factor are given under assumption (10) by Equations [1] and [2]. The second contribution is written

$$\Delta P_2 = \left(\frac{0.184}{\mathrm{Re}^{0.2}}\frac{\rho V^2}{2g}\frac{2L}{0.611D}\right)\left(\frac{\frac{\pi D^2}{2}}{\frac{\pi D}{2} + D}\right) \quad \ldots\ldots [5]$$

or

$$\Delta P_2 = \frac{0.368}{\mathrm{Re}^{0.2}}\frac{\rho V^2}{2g}\frac{L}{D} \quad \ldots\ldots [6]$$

The first term in parentheses of Equation [5] estimates the frictional pressure drop around the free-convection loop if there were a fixed boundary at the interface. The second term in parentheses reduces this pressure drop to that which may be charged to half the pipe periphery. It is reasoned that having a free interface does not greatly affect the shearing forces at the pipe wall.

The third is the contribution to pressure drop developed at the interface. This shear stress is a function of scale of turbulence at the interface. The average shear stress may be expressed (4)

$$\tau = \frac{\rho}{g}\epsilon_m\frac{dV}{dy} \doteq \frac{\rho}{g}\epsilon_m\frac{2V}{0.392D} = 5.10\,\epsilon_m\frac{\rho}{g}\frac{V}{D} \quad \ldots\ldots [7]$$

Based on the interface shear stress given by Equation [7], the resistance pressure drop developed at the interface may be written

$$\Delta P_3 = 52.0\frac{\epsilon_m}{V}\frac{L}{D^2}\frac{\rho V^2}{2g} \quad \ldots\ldots [8]$$

The total resistance pressure drop about the loop is given by the sum of the contributions represented by Equations [4], [6], and [8] or

$$\Delta P_r = \frac{\rho V^2}{2g}\left[N + \frac{0.368}{\mathrm{Re}^{0.2}}\frac{L}{D} + 52.0\frac{\epsilon_m}{V}\frac{L}{D^2}\right] \quad \ldots\ldots [9]$$

Transverse Heat Transfer. The temperatures which appear in the thermal driving head, Equation [3], are affected by transverse heat transfer owing to mass transport and conduction. In treating this heat transfer, the eddy coefficient of heat will be used with no mention of molecular conduction since turbulent diffusion is, for many fluids, the dominant mode of heat transfer. Setting up an energy balance on an axial increment of the upper stream, one obtains

$$0.392D^2\rho VC_p\,dT = -(A\rho C_p\epsilon_h)\frac{T_2 - T_3}{0.392D}\,Ddx \quad [10]$$

where A is an arbitrary undetermined constant. The effective conductivity is given by

$$K_{eff} = A\rho C_p\epsilon_h \quad [11]$$

Integration of Equation [10] over the pipe length gives

$$T_1 - T_2 = T_4 - T_3 = \frac{A\epsilon_h(T_2 - T_3)L}{0.1537\,VD^2} \quad [12]$$

Eddy Coefficient. Following Prandtl's mixing-length concept (4), the eddy coefficient of momentum may be written

$$\epsilon_m = l^2\frac{dV}{dy} \quad [13]$$

where l is the characteristic mixing length. The ratio of the effective characteristic mixing length at the interface to the pipe diameter has been assumed constant or

$$\frac{l}{D} = c = \text{const} \quad [14]$$

The velocity gradient at the interface is written

$$\left.\frac{dV}{dy}\right|_{\text{interface}} = \frac{2V}{0.392D} \quad [15]$$

Substituting mixing length and velocity gradient as given by Equations [14] and [15] in Equation [13]

$$\epsilon_m = \epsilon_h = 5.10\,c^2VD \quad [16]$$

since the eddy coefficients of momentum and heat have been assumed equal. The value of c^2 must be determined from test.

Axial Heat-Transfer Rate. The relationship between the axial and transverse temperature gradients is found by substituting the eddy coefficient of heat, Equation [16], in Equation [12] giving

$$\frac{T_1 - T_2}{T_2 - T_3} = 33.2\,Ac^2\frac{L}{D} \quad [17]$$

By equating the thermal driving pressure difference, Equation [3], to the total resistance pressure difference, Equation [9], substituting the eddy coefficient of momentum, Equation [16], and making use of the relationship between axial and transverse temperature gradients, Equation [17], flow velocity may be related to the temperature difference across the heat sink

$$\frac{V^2}{gD} = 2\beta\frac{L}{D}(T_2 - T_3)\left[\frac{\sin\theta + 13.0\,Ac^2\cos\theta}{N + \frac{L}{D}\left(\frac{0.368}{\text{Re}^{0.2}} + 265c^2\right)}\right] \quad [18]$$

The rate of heat transfer may be written

$$Q = \frac{\pi}{8}D^2\rho C_p(T_2 - T_3)V \quad [19]$$

The axial heat-transfer rate may be calculated on a pure conduction basis as

$$Q_{\text{cond}} = \frac{\pi D^2}{4}K\frac{T_2 - T_3}{L} \quad [20]$$

for comparison. The ratio of the heat transfer with turbulent convection to that which would be calculated on a conduction basis, a Nusselt number, is found by dividing Equation [19] by Equation [20] and substituting solution of Equation [18] for velocity into quotient, yielding

$$\frac{Q}{Q_{\text{cond}}} = 0.706\,\text{PrGr}^{1/4}(L/D)^{1/4}\left[\frac{\sin\theta + 13.0Ac^2\cos\theta}{N + \frac{L}{D}\left(\frac{0.368}{\text{Re}^{0.2}} + 265c^2\right)}\right]^{1/4} \quad [21]$$

where

$$\text{Gr} = \frac{g\beta D^3(T_2 - T_3)\rho^2}{\mu^2} \quad [22]$$

The temperature difference across the heat sink has been chosen as the reference temperature difference rather arbitrarily.

Re-Examination of Assumption That Flow Pattern Is Independent of Axial Position (reference Fig. 5.) It is recognized that constant-velocity flow cannot exist in two directions in a common horizontal channel. Therefore flow distribution will be calculated approximately so that the differences between actual flow and the flow assumed in the analysis may be appreciated.

To do this, the pressure differential across an axial increment of each stream will be expressed in terms of frictional drop and velocity change. (The role of buoyancy forces will be omitted as secondary away from the ends.) Then the pressure differentials for the two stream increments will be equated under the assumption that the axial pressure gradient does not vary across the section.

It will be assumed that pipe-wall frictional resistance may be neglected in comparison with the turbulent shear resistance at the interface. The interface shear stress given by Equation [7] will be assumed independent of axial position when written in

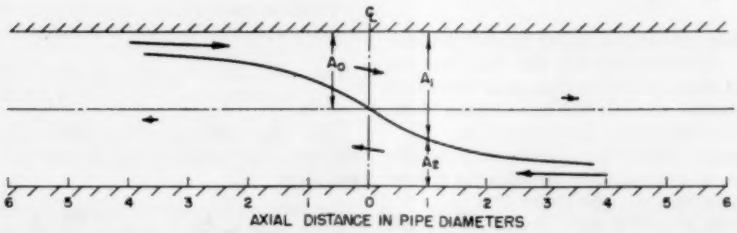

FIG. 5 ESTIMATED FLOW PATTERN IN HORIZONTAL PIPE BASED ON EQUATION [33]

TABLE 2 EVALUATION OF CONSTANTS FROM TABLE 1 TEST DATA

Run no.	Avg. heat-transfer rate, Btu/hr × 10^{-6}	Adjusted[a] $(T_2 - T_3)_{avg}$, deg F	$(T_1 - T_3)_{avg}$, deg F	Ac^2 (Eq. [17]) × 10^{-3}	Velocity (Eq. [19]), ft/hr	Reynolds number	N (assumed)	c^2 (Eq. [18]) × 10^{-4}	K_{eff} (Eq. [11]) Btu/hr deg F ft
3	2.35	21.4	36.5	4.37	334	5400	5	10.4	93.4
4	2.77	25.9	39.5	3.90	325	5770	5	14.2	81.2
5	3.22	27.0	44.0	4.16	363	5880	5	11.0	96.5
6	4.13	30.6	44.2	3.69	412	6760	5	5.45	97.3
7	4.17	29.6	49.5	4.28	430	7150	5	6.01	118
8	4.83	38.6	49.5	3.29	397	6520	5	9.78	83.7
8A	4.83	37.1	45.5	3.13	400	6750	5	8.16	80.2

[a] Adjusted $(T_2 - T_3)_{avg} = 0.75\ (T_2 - T_3)_{test\ avg}$ (see Fig. 6).

terms of velocity and eddy coefficient of momentum based on Equations [18] and [7] giving

$$\tau_{interface} = 5.10\ \epsilon_m \frac{\rho}{g} \frac{V_0}{D} \quad [23]$$

where

$$\epsilon_m = 5.10\ c^2 V_0 D \quad [24]$$

Then the differential pressure changes due to interface shear become

$$\delta P_1 = -26.0\ c^2 \frac{\rho}{g} V_0^2 D \frac{dx}{A_1} \quad [25]$$

for the upper-stream increment and

$$\delta P_2 = 26.0\ c^2 \frac{\rho}{g} V_0^2 D \frac{dx}{A_2} \quad [26]$$

for the lower-stream increment. Flow cross section is designated by A.

The pressure increments due to axial momentum changes are

$$\delta P_1 = \frac{\rho V_1^2}{g} \frac{dA_1}{A_1} \quad [27]$$

and

$$\delta P_2 = \frac{\rho V_2^2}{g} \frac{dA_2}{A_2} \quad [28]$$

The total axial pressure differentials for the hot and cold streams are found by adding Equations [25], [27], [26], and [28], respectively, giving

$$dP_1 = -26.0\ c^2 \frac{\rho}{g} V_0^2 D \frac{dx}{A_1} + \frac{\rho V_1^2}{g} \frac{dA_1}{A_1} \quad [29]$$

and

$$dP_2 = 26.0\ c^2 \frac{\rho}{g} V_0^2 D \frac{dx}{A_2} + \frac{\rho V_2^2}{g} \frac{dA_2}{A_2} \quad [30]$$

By equating [29] and [30] and recognizing that

$$dA_1 = -dA_2 \quad [31]$$

and

$$V_1 A_1 = V_2 A_2 \quad [32]$$

one obtains, after some manipulation

$$\frac{dA_1}{D_3} = 26.0\ c^2 \left(\frac{A_1}{A_0}\right)^2 \frac{1 + \frac{A_1}{A_2}}{1 + \left(\frac{A_1}{A_2}\right)^2} \frac{dx}{D} \quad [33]$$

Fig. 5 is based on Equation [33] using a value of the constant c^2 determined from test data. The calculated flow distribution suggests that eddy diffusivity should be treated as a function of axial position; also that the value of c^2 recommended from test data should be dependent upon the length-to-diameter ratio.

Evaluation of Constants Using Table 1 Test Data

The three constants—Ac^2, c^2, and K_{eff}—have been calculated according to the sequence shown in Table 2. The average of measured heat input and removal rates has been used. Runs 1 and 2 have been omitted because of the scatter shown in Fig. 2. Fluid properties of the sodium used in calculations (5), corresponding to a 250 F temperature, were

$\rho = 57.6$ pcf

$C_p = 0.327$ Btu/lb deg F

$K = 49.0$ Btu/hr ft deg F

$\beta = 1.416 \times 10^{-4}$ deg F^{-1}

$\nu = 2.48 \times 10^{-5}$ sq ft/hr

The measured temperature difference between the two streams has been reduced by a factor of 0.75 according to the assumed vertical temperature distribution of Fig. 6. This curve is highly

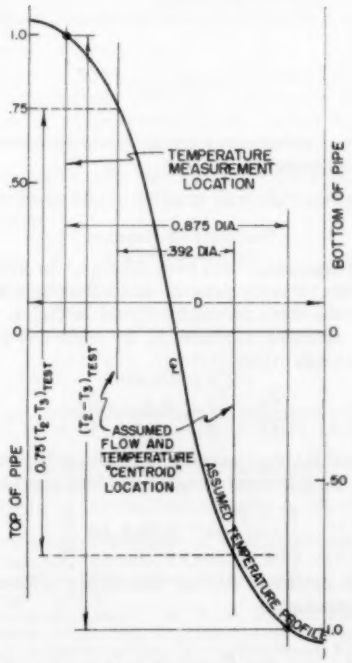

Fig. 6 Assumed Relationship Between Measured Transverse Temperature Difference and That Employed in Analysis

arbitrary; it is included to illustrate the difficulty of defining an effective temperature difference.

Since the range of the Reynolds number covered in the test runs was so small and the test-data scatter so great, values of Ac^2, c^2, and K_{eff} have been averaged for the seven test runs of Table 2 to give

$$Ac^2 = 3.83 \times 10^{-3}$$

$$c^2 = 9.28 \times 10^{-4}$$

$$K_{eff} = 92.9 \text{ Btu/hr ft deg F}$$

The effective conductivity (Equation [11]) used in the analysis assumed that the ratio of molecular conductance to conductance by eddy diffusion is small. Based on test results, this ratio is calculated, using a velocity of 400 fph, as

$$\frac{K}{\rho C_p \epsilon_h} = \frac{49}{23.7} = 2.07$$

The analysis of Martinelli of heat transfer in molten metals (6) would give a predicted ratio of about 6.1 based on flow in one direction. Since the opposed flows reported herein may be expected to increase the scale of turbulence, the ratios of 2.07 and 6.1 do not appear to be inconsistent.

If the conductivity were retained in Equation [11], it becomes

$$K_{eff} = A(K + \rho C_p \epsilon_h) = 92.9$$

Substituting the previous values of K and $\rho C_p \epsilon_h$

$$A = 1.28$$

This value is close to a value of unity which would be expected with a perfect mathematical model.

If the fluid involved has a very low thermal conductivity, so that

$$\frac{\rho C_p \epsilon_h}{K} \gg 1$$

and the scale of turbulence is assumed to be that measured with sodium, the recommended value is

$$Ac^2 = 1.28\,(9.28 \times 10^{-4}) = 1.19 \times 10^{-3}$$

Summary of Results

Analytical expressions have been developed for turbulent free-convection, heat-transfer rates in an inclined pipe having zero net flow for the three geometries shown in Fig. 4. The axial temperature difference is related to the transverse temperature difference for Cases (a) and (b) by

$$\frac{T_1 - T_2}{T_2 - T_3} = 33.2\, Ac^2 \frac{L}{D} \quad \ldots\ldots [17]$$

while, for Case (c), the temperature difference between plenums is related to the transverse temperature difference by

$$\frac{T_1 - T_3}{T_2 - T_3} = 1 + 33.2\, Ac^2 \frac{L}{D} \quad \ldots\ldots [34]$$

Velocity is related to driving temperature difference by the following expressions:

Case (a)

$$\frac{V^2}{gD} = 2\beta \frac{L}{D} (T_2 - T_3) \left[\frac{\sin\theta + 13.0\, Ac^2 \cos\theta}{N + \frac{L}{D}\left(\frac{0.368}{\mathrm{Re}^{0.2}} + 265c^2\right)} \right] \quad \ldots\ldots [18]$$

Case (b)

$$\frac{v^2}{gD} = 2\beta \frac{L}{D} (T_2 - T_3) \left[\frac{\sin\theta + 13.0 Ac^2 \cos\theta + \frac{0.196 \cos\theta}{L/D}}{N + \frac{L}{D}\left(\frac{0.368}{\mathrm{Re}^{0.2}} + 265c^2\right)} \right] \quad \ldots\ldots [35]$$

Case (c)

$$\frac{V^2}{gD} = 2\beta \frac{L}{D} (T_1 - T_3) \left[\frac{\frac{\sin\theta}{1 + 33.2\, Ac^2 L/D} + \frac{0.392 \cos\theta}{L/D}}{N + L/D\left(\frac{0.368}{\mathrm{Re}^{0.2}} + 265c^2\right)} \right] \quad \ldots\ldots [36]$$

Reynolds number for all three cases is defined by

$$\mathrm{Re} = \frac{0.611\, DV\rho}{\mu} \quad \ldots\ldots [37]$$

The rate of heat transfer to the heat sink for Cases (a) and (b) and to the upper plenum for Case (c) is given by

$$Q = \frac{\pi}{8} D^2 \rho c_p V (T_2 - T_3) \quad \ldots\ldots [19]$$

Appropriate values of the constants Ac^2 and c^2 for sodium are

$$Ac^2 = 3.83 \times 10^{-3}$$

and

$$c^2 = 9.28 \times 10^{-4}$$

based on heat-transfer measurements in a horizontal 8-in-ID pipe closed at both ends (Case a) which was 14.7 diameters in length and contained sodium at 250 F. Measurements covered a Reynolds-number range from 4000 to 7000.

For liquids having a low conductivity, so that eddy diffusion controls heat transfer, the values

$$Ac^2 = 1.19 \times 10^{-3}$$

and

$$c^2 = 9.28 \times 10^{-4}$$

appear appropriate based on the same test data.

The solutions may be written in the form of a Nusselt number, the ratio of the heat-transfer rate to that calculated on the basis of pure axial conduction.

For Case (a)

$$\frac{Q}{Q_{cond}} = 0.706\, \mathrm{PrGr}^{1/3} \left(\frac{L}{D}\right)^{1/3} \left[\frac{\sin\theta + 13.0 Ac^2 \cos\theta}{N + \frac{L}{D}\left(\frac{0.368}{\mathrm{Re}^{0.2}} + 265\, c^2\right)} \right]^{1/2} \quad \ldots\ldots [21]$$

For Case (b)

$$\frac{Q}{Q_{cond}} = 0.706\, \mathrm{PrGr}^{1/3} \left(\frac{L}{D}\right)^{1/3} \left[\frac{\sin\theta + 13.0\, Ac^2 \cos\theta + \frac{0.196 \cos\theta}{L/D}}{N + \frac{L}{D}\left(\frac{0.368}{\mathrm{Re}^{0.2}} + 265\, c^2\right)} \right]^{1/2} \quad \ldots\ldots [38]$$

For Case (c)

$$\frac{Q}{Q_{cond}} = 0.706 \frac{\mathrm{PrGr}^{1/3}\left(\frac{L}{D}\right)^{3/7}}{1 + 33.2Ac_2L/D} \left[\frac{\frac{\sin\theta}{1 + 33.2\,Ac^2L/D} + \frac{0.392\cos\theta}{L/D}}{N + \frac{L}{D}\left(\frac{0.368}{\mathrm{Re}^{0.2}} + 265\,c^2\right)}\right]^{1/2} \quad \ldots\ldots [39]$$

For Cases (a) and (b)

$$Q_{cond} = \frac{\pi}{4} D^2K \frac{T_2 - T_3}{L} \quad \ldots\ldots [20]$$

and

$$\mathrm{Gr} = \frac{g\beta D^3(T_2 - T_3)\rho^2}{\mu^2} \quad \ldots\ldots [22]$$

For Case (c)

$$Q_{cond} = \frac{\pi}{4} D^2K \frac{(T_1 - T_3)}{L} \quad \ldots\ldots [40]$$

and

$$\mathrm{Gr} = \frac{g\beta D^3(T_1 - T_4)\rho^2}{\mu^2} \quad \ldots\ldots [41]$$

Example of Application of Results

Problem. Two plenums are connected by a 20-ft pipe of 1 ft ID inclined at 30 deg to the horizontal. The plenums and pipe contain water at 500 F and 2000 psia. The water temperature in the lower plenum is 5 deg F higher than the temperature in the upper plenum. What is the rate at which heat is added to the upper plenum?

Solution. The physical properties of water at 500 F and 2000 psia are taken as

$$\beta = 1.04 \times 10^{-3} \text{ deg F}^{-1}$$

$$\rho = 49.6 \text{ pcf}$$

$$\mu = 0.260 \text{ lb/ft hr}$$

$$K = 0.356 \text{ Btu/hr ft deg F}$$

$$C_p = 1.153 \text{ Btu/lb deg F}$$

Equations [34] and [36] are needed for solutions. Values for the constants Ac^2 and c^2 appropriate for water are

$$Ac^2 = 1.19 \times 10^{-3} \quad \text{and} \quad c^2 = 9.28 \times 10^{-4}$$

Substituting in Equation [34]

$$\frac{(T_2 - T_3)}{(T_1 - T_3)} = \frac{1}{1 + 33.2(1.19 \times 10^{-3})\,(20)} = 0.56$$

or

$$(T_2 - T_3) = 0.56\,(T_1 - T_3) = 2.80 \text{ F}$$

Assume that entrance and exit-velocity head losses make up three velocity heads. Assume $\mathrm{Re}^{0.2} = 11.5$. Making substitutions in Equation [36]

$$V^2 = 2g(1.04 \times 10^{-3})\,(20)\,(5) \left[\frac{0.5}{1 + 33.2(1.19 \times 10^{-3})\,(20)} + \frac{0.392(0.866)}{20}\right] \Big/ \left[3 + 20\left[\frac{0.368}{11.5} + 265\,(9.28 \times 10^{-4})\right]\right]$$

or

$$V = 1730 \text{ fph} = 0.481 \text{ fps}$$

Reynolds number may now be calculated (Equation [37]) as

$$\mathrm{Re} = \frac{0.611\,VD\rho}{\mu} = \frac{0.611(1730)(1)(49.6)}{0.260} = 202{,}000$$

or

$$\mathrm{Re}^{0.2} = 11.5$$

as assumed.

The rate of heat transfer to the upper plenum is given by Equation [19] as

$$Q = \frac{\pi}{8}(1)^2\,(1730)\,(49.6)\,(1.153)\,(2.80) = 108{,}700 \text{ Btu/hr}$$

Conclusions

A vigorous, single, turbulent, free-convection loop may be set up in a horizontal large-diameter pipe containing liquid sodium by adding heat at one closed end and removing it at the other closed end. The rate of heat transfer, which varies approximately as the diameter raised to the five-halves power, may be much greater than expected. The ratio of the measured rate of heat transfer compared to that calculated on the basis of axial conduction was of the order of 600 for the test data reported.

First estimates of the magnitudes of turbulent, free-convection, heat-transfer rates within a horizontal or inclined pipe having no net flow may be calculated based on the analysis and test data reported.

The resistance to flow at the interface appears to be of the order of five times greater than the frictional resistance to flow at the pipe periphery.

The correlations presented have little experimental support. Additional experimental and analytical efforts are needed to clarify such matters as:

(a) Actual velocity and temperature profiles across the pipe cross section.

(b) Criterion for turbulent flow.

(c) Possibility of mixed flow—part laminar and part turbulent.

(d) Effect of buoyancy forces on interface scale of turbulence.

(e) Manner in which solution would change if actual flow-distribution variation along pipe length were factored in.

The same general approach should be extended to laminar flow, and to laminar and turbulent flow with some small superimposed net flow.

Acknowledgment

The authors wish to express their appreciation and thanks to Mr. Frank C. Steiner for setting up and conducting the experiment.

BIBLIOGRAPHY

1 "Thermal Convection in a Long Cell Containing a Heat Generating Fluid," by W. Murgatroyd, AERE ED/R 1559, November, 1954.

2 "Free Convection in an Open Thermosyphon With Special Reference to Turbulent Flow," by B. W. Martin, Proceedings of the Royal Society of London, England, series A, vol. 230, 1955, pp. 502–530.

3 "Theoretical Considerations on Free Convection in Tubes," by M. J. Lighthill, *Quarterly Journal of Mechanics and Applied Mathematics*, vol. 6, 1953, Oxford University Press, Amen House, London, England, E.C. 4.

4 "Aerodynamic Theory," by W. F. Durand, Julius Springer, Berlin, Germany, vol. 3, 1935, Divisions F-I, pp. 127–135.

5 "Liquid Metals Handbook," U. S. Government Printing Office, Washington, D. C., second edition, June, 1952, p. 53.

6 "Heat Transfer to Molten Metals," by R. C. Martinelli, Trans. ASME, vol. 69, 1947, pp. 947–959.

Mollier Diagrams for Water Near Bubble Point

By ANDRÉ VAN HAUTE[1] AND B. H. SAGE,[1] PASADENA, CALIF.

In many problems of engineering interest a knowledge of the thermodynamic properties of water in the heterogeneous region near bubble point is of value. A series of Mollier diagrams for water at states from bubble point to a quality of 0.05 was prepared and similar diagrams relating to the behavior of the condensed liquid were included. The Mollier diagram was employed because of its utility in connection with graphical operations of a thermodynamic nature pertaining to the flow of homogeneous and heterogeneous fluids near bubble point. An example of the application of the diagrams to the solution of the simple problem of flow in short tubes was included.

Nomenclature

The following nomenclature is used in the paper:

H = specific enthalpy, Btu/lb
H = residual entropy, Btu/lb (see Equation [5])
j = friction associated with a differential change in state, Btu/lb
n = quality, weight fraction gas
P = pressure, psi
S = specific entropy, Btu/(lb) (deg R)
T = thermodynamic temperature, deg R
V = specific volume, cu ft/lb
α = coefficient (see Equation [3])

Introduction

The thermodynamic properties of water have been investigated adequately for many conditions of engineering interest. Keenan and Keyes[3] presented a satisfactory tabulation of the properties of water in the gaseous and liquid regions which supplements the earlier compilations of Marks and Davis.[4] The data are particularly useful because they include a detailed tabulation of properties of the saturated gas, known also as dew-point gas, and the saturated liquid, known as bubble-point liquid, at low temperatures. Such information is directly applicable in problems relating to cavitation,[4] and the performance of ejectors, injectors, and air-conditioning equipment involving the flow of water as a heterogeneous fluid at relatively low quality.

There appears to be little reason to dwell upon the accuracy of the data pertaining to the thermodynamic behavior of the dew-point gas and the bubble-point liquid because they have been carefully reviewed by Keenan and Keyes.[2] However, in the liquid region at pressures above vapor pressure the data are not presented in detail. Often it is convenient to evaluate changes in enthalpy and entropy associated with changes in state in the homogeneous-liquid region in much the same fashion as is done in the homogeneous-gas region.

To establish with precision the effect of temperature and pressure upon the properties of the liquid phase, the formulations proposed by Keenan and Keyes[2] were employed to evaluate the small, isothermal changes in enthalpy and entropy with pressure in that region. Isothermal changes in enthalpy were established from

$$\left(\frac{\partial H}{\partial P}\right)_T = V - T\left(\frac{\partial V}{\partial T}\right)_P \quad [1]$$

Changes in entropy were determined in the following way

$$\left(\frac{\partial S}{\partial P}\right)_T = -\left(\frac{\partial V}{\partial T}\right)_P \quad [2]$$

Isobaric changes in volume with temperature were determined from the formulations of Keenan and Keyes,[2] supplemented by residual graphical operations. The enthalpy and entropy of the saturated liquid and gas were taken directly from tabulations available.[2] Agreement of the calculated isothermal changes in enthalpy and entropy with those obtained earlier[2] was realized. Such agreement is only an indication of the precision of the two sets of calculations since the same data[2] were used in both cases. The enthalpy and entropy were computed for pressures up to 2000 psi.

The primary purpose of the present discussion was to present thermodynamic data in a form suitable for the graphical solution of problems involving the flow of heterogeneous and homogeneous fluids near bubble point. In problems involving homogeneous or heterogeneous flow under adiabatic conditions it is convenient to define the path of the flow process by the following differential expression

$$TdS = \pm \alpha dH = j \quad [3]$$

The term j represents the friction associated with the flow process. For many situations involving relatively short tubes, the quantity α is a more convenient quantity to correlate by the methods of fluid mechanics with flow conditions than is friction.[5] The value of α varies widely, depending upon the nature of the process. For example, the heterogeneous flow of water through a diffuser sometimes yields values of α as high as 0.25 whereas the convergent flow of a homogeneous liquid may give a value of α as low as 0.02. It is beyond the scope of this discussion to consider means of predicting the magnitude of the friction associated with a specified flow process. In many instances the flow process is of such a nature that the value of α varies markedly along the

---

[1] Department of Chemical Engineering, California Institute of Technology.

[3] "Thermodynamic Properties of Steam," by J. H. Keenan and F. G. Keyes, John Wiley & Sons, Inc., New York, N. Y., 1936.

[4] "Tables and Diagrams of the Thermal Properties of Saturated and Superheated Steam," by L. S. Marks and H. N. Davis, Longmans Green and Company, New York, N. Y., 1929.

[4] "Fluid Mechanics, With Engineering Applications," by R. L. Daugherty and A. C. Ingersoll, McGraw-Hill Book Company, Inc., New York, N. Y., fifth edition, 1954.

Contributed by the Heat Transfer Division and presented at the Fall Meeting, Denver, Colo., September 10–12, 1956, of The American Society of Mechanical Engineers.

Note: Statements and opinions advanced in papers are to be understood as individual expressions of their authors and not those of the Society. Manuscript received at ASME Headquarters, February 29, 1956. ASME Paper No. 56—F-9.

[5] "On the Extent and Action of the Heating Surface for Steam Boilers," by O. Reynolds, Proceedings of the Manchester Literary and Philosophical Society, vol. 14, 1874, p. 7.

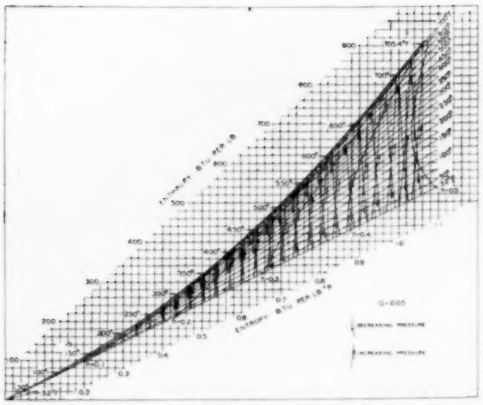

FIG. 1 MOLLIER DIAGRAM WITH LINES OF CONSTANT α

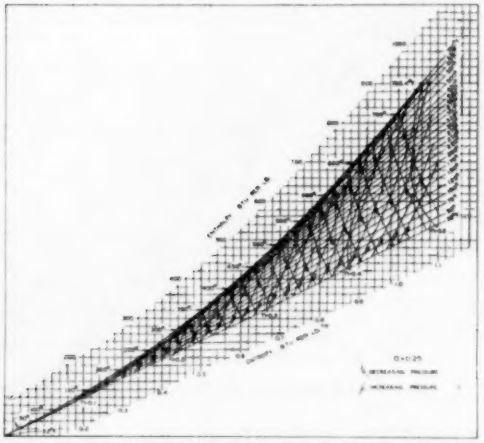

FIG. 2 MOLLIER DIAGRAM WITH LINES OF CONSTANT α

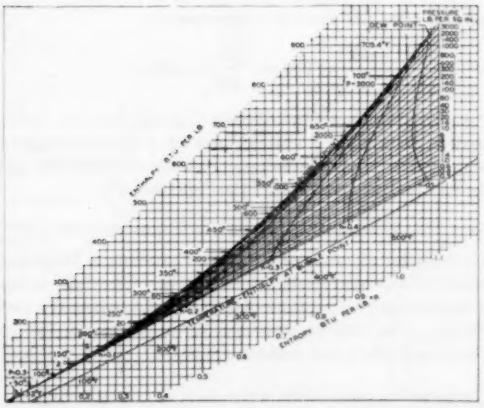

FIG. 3 MOLLIER DIAGRAM FOR WATER IN THE HETEROGENEOUS REGION FOR QUALITIES BETWEEN 0.1 AND 0.5

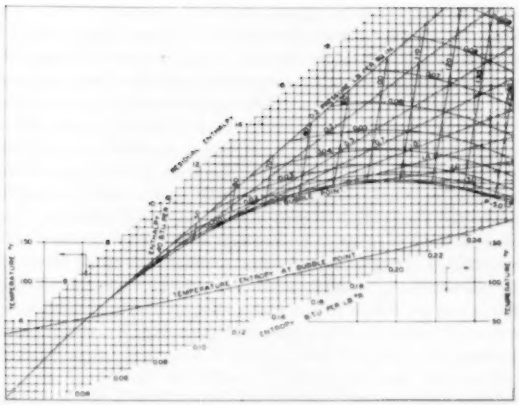

FIG. 4 MOLLIER DIAGRAM FOR WATER IN THE HETEROGENEOUS REGION FOR QUALITIES BETWEEN 0.01 AND 0.09

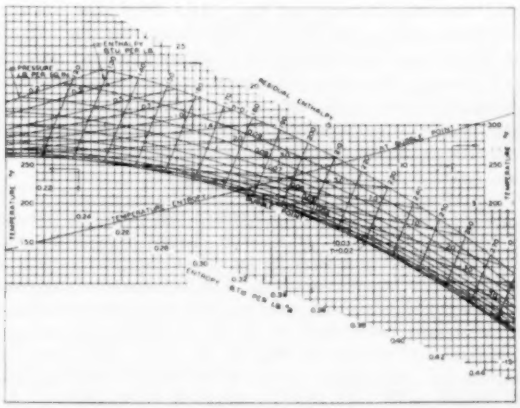

FIG. 5 MOLLIER DIAGRAM FOR WATER IN THE HETEROGENEOUS REGION FOR QUALITIES BETWEEN 0.02 AND 0.1

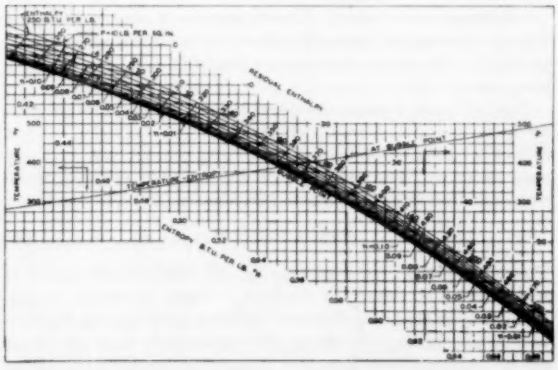

FIG. 6 MOLLIER DIAGRAM FOR WATER IN THE HETEROGENEOUS REGION FOR QUALITIES BETWEEN 0.01 AND 0.10

path. In such cases the process should be treated in two or more steps. It should be emphasized that the use of Equation [3] to describe the path of the process involves a number of limitations. Among these limitations consideration of the flow process as one-dimensional and inclusion of all forms of entropy gain in a single term are perhaps the most important. However, when the exchanges between internal and kinetic energy are large, the path of the process may be described by Equation [3] with an accuracy adequate for many purposes even though the coefficient α has been established with poor accuracy by empirical methods.

It is desired to present Mollier diagrams for water upon which flow problems may be solved when a knowledge of the friction or of α is available. Equation [3] may be rewritten in the following form

$$\frac{dH}{dS} = \pm \frac{T}{\alpha} \quad \ldots\ldots\ldots\ldots\ldots\ldots [4]$$

In this instance, each member of the equation represents the slope of a line describing the path of a process upon a Mollier diagram and thus makes the latter form of presentation particularly useful in the solution of flow problems. Figs. 1 and 2 present such diagrams for water in the heterogeneous region upon which a series of lines of constant value of α have been placed. The values of α used were chosen arbitrarily for illustrative purposes. As would be expected, Fig. 1 shows that when α is equal to 0.05 the paths are much more nearly isentropic than those in Fig. 2 with a value of 0.25 for α. Arrows are shown upon the paths because the entropy increases regardless of whether the enthalpy increases or decreases during the process. The number of curves shown in the heterogeneous region has been limited in order to avoid undue complexity of these illustrative diagrams.

Mollier Diagrams

Mollier diagrams in the heterogeneous region are characterized by a linear isothermal or isobaric change in enthalpy with entropy and with but small change in enthalpy with pressure or temperature at constant entropy. For this reason it is necessary to employ relatively large scales to yield the desired precision of representation, particularly at low temperatures and pressures. This fact is illustrated in Fig. 3. It is an enthalpy-entropy diagram for qualities only as low as 0.1 since at lower qualities the isobars are too close together for proper representation. Isobars and lines of constant quality were included on this diagram. A single line directly relating the temperature to the enthalpy at bubble point was shown for reference purposes. From a knowledge of either a temperature or a pressure it is possible to establish the enthalpy and entropy at bubble point. No difficulty results from linear interpolation between the isobars in the heterogeneous region. The appropriate values of the slope dH/dS expressed in degrees Rankine may be obtained from Equation [4]. The slope is a single-valued function of α and the temperature.

Figs. 4, 5, and 6 present residual Mollier diagrams for progressively increasing temperatures in the heterogeneous region. Upon each diagram lines of constant pressure, quality, and enthalpy were included. The residual enthalpy reported as the ordinate was evaluated from the following expression

$$\mathbf{H} = 600S - H \quad \ldots\ldots\ldots\ldots\ldots\ldots [5]$$

The relationship of the entropy of the bubble-point liquid to temperature is shown in addition. These diagrams overlap sufficiently so that in many cases the same state may be found on two of the figures. It should be emphasized that the slopes dH/dS obtained from Equation [4] are not directly applicable to paths on these residual diagrams. It is necessary to construct a path to the accuracy desired by a suitable step-wise process if the path is not isentropic. This can be done readily with a set of parallel rules, and the following expression

$$\frac{d\mathbf{H}}{dS} = 600 - \frac{dH}{dS} = 600 \pm \frac{T}{\alpha} \quad \ldots\ldots\ldots\ldots [6]$$

Figs. 7 and 8[8] are residual Mollier diagrams for water in the condensed-liquid regions showing lines of constant temperature, pressure, volume, and enthalpy. In these diagrams the residual enthalpy also was established from Equation [5].

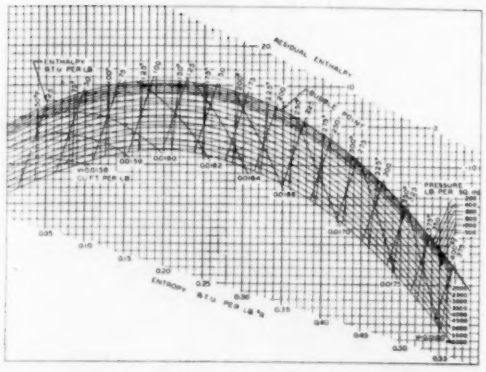

Fig. 7 Mollier Diagram for Water in Condensed-Liquid Region at Temperatures Between 32 and 400 F

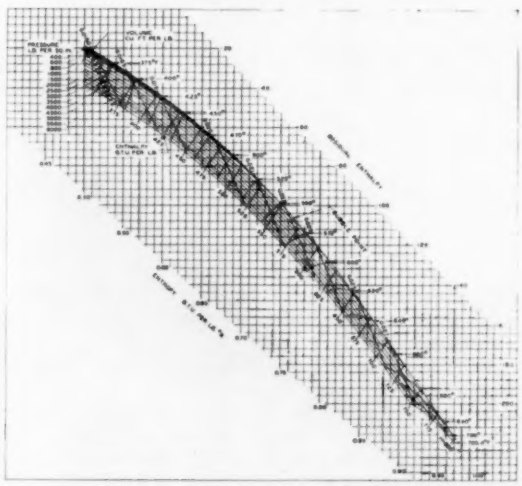

Fig. 8 Mollier Diagram for Water in Condensed-Liquid Region at Temperatures Between 375 and 705 F

Illustrative Use of Diagrams

A schematic diagram of a diffuser handling a heterogeneous mixture of water is presented in Fig. 9. The fluid enters the diffusing section at a pressure of 6 psi and discharges at a pressure of 600 psi. The conditions assumed at the entrance to the diffuser at D are set forth in one column of Table 1. A value of α of 0.15

[8] Large-scale copies of Figs. 4 to 8, inclusive, may be obtained from the authors for the cost of reproduction. These diagrams are arranged to facilitate the graphical solution of flow problems directly upon the charts supplied.

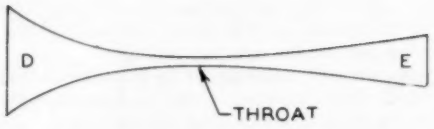

FIG. 9 SCHEMATIC DIAGRAM OF DIFFUSER

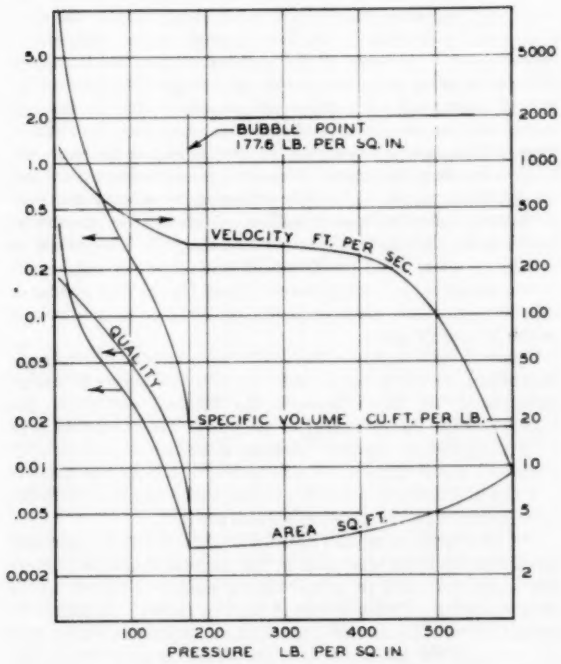

FIG. 10 PATH OF FLOW PROCESS IN DIFFUSER

TABLE 1 INLET, BUBBLE-POINT, AND OUTLET CONDITIONS FOR A DIFFUSER

Quantity	Inlet[a]	Bubble point	Outlet[a]
Temperature, deg F	170.06	372.0	373.2
Pressure, psia	6	177.6	600
Velocity, fps	1311	300	10
Weight rate of flow, lb/sec	50	50	50
Cross-sectional area, sq ft	0.414	0.00305	0.091
Quality	0.175	0	0
Coefficient α	0.15		0.05
Enthalpy, Btu/lb			
Liquid	137.96		
Gas	1134.2		
Heterogeneous	312.3	344.8	346.6
Entropy, Btu/(lb)(deg R)			
Liquid	0.2472		
Gas	1.8292		
Heterogeneous	0.5240	0.5310	0.5311
Specific volume, cu ft/lb			
Liquid	0.01645	0.01827	0.1822
Gas	61.98		
Heterogeneous	10.86		

[a] Values predicted on $\alpha = 0.15$ in heterogeneous and 0.05 in homogeneous-liquid region.

was assumed to apply in the heterogeneous region and of 0.05 in the homogeneous region within the diffuser. It was assumed that the average velocity of the liquid and gas phases was identical in computing kinetic energy. From the information submitted in Figs. 5 and 6, the path of the process assuming local equilibrium was estimated from the initial state to bubble point, as shown in Fig. 10. The conditions at bubble point are recorded in Table 1. The remaining part of the diffusion process was followed upon Fig. 7, which applied to the condensed liquid region. The latter part of the path is also shown in Fig. 10 and exit conditions are set forth in Table 1. The curves shown in Fig. 10 were computed by the step-wise solution of Equation [4] utilizing the information submitted in Figs. 6 and 7 to establish the actual path of the process. For persons interested in the details of this example, the states at a number of points along the path are presented in Table 2. These calculations illustrate the utility of graphical representation of thermodynamic data for low qualities upon a Mollier diagram.

ACKNOWLEDGMENT

Paul L. Armstrong and Elizabeth McLaughlin assisted with the calculations and W. N. Lacey reviewed the mansucript.

Discussion

K. M. TREADWELL[7] AND R. E. BRUCKNER.[8] The authors are to be complimented for their work in making available to engineers Mollier charts in the low-quality region, which is becoming of increasing importance not only in commercial air conditioning but also in certain phases of nuclear-power plant development.

At the Westinghouse Research Laboratories, when it was found that existing steam charts did not extend below qualities of 50 per cent, it was decided to construct a large-scale chart showing the properties of wet steam down to 0 quality. This work was embodied in Research Report 60-8-05-24-R21, entitled "Properties of Wet Steam at Low Pressures," by T. C. Tsu and D. T. Beecher. Preliminary studies of different ways of plotting such a chart compared:

1 Entropy versus pressure.
2 Entropy versus enthalpy (Mollier chart), as in the present paper.
3 Pressure versus entropy.
4 Entropy versus volume.

Mollier chart was considered undesirable because "near the saturated liquid region, all the lines of constant pressure converge toward a point and are quite congested." Further study of other methods of plotting resulted in the choice of Method 1 "entropy versus pressure" with lines of constant entropy and constant quality. This gives a chart as open and readable as the familiar Mollier chart of the high-quality region.

Again referring to the paper, the heavy-print **H** in the

[7] Atomic Power Division, Westinghouse Electric Corporation, Pittsburgh, Pa. Assoc. Mem. ASME.

[8] Research Engineer, Atomic Power Division, Westinghouse Electric Corporation, Pittsburgh, Pa. Mem. ASME.

TABLE 2 PATH OF FLOW PROCESS IN DIFFUSER

	Pressure, psi						
	6[a]	40	60	100	177.6	400	600[a]
Entropy, Btu/(lb) (deg R)	0.5240	0.5290	0.5298	0.5503	0.5310	0.5310	0.5311
Enthalpy, Btu/lb	312.3	335.6	339.2	342.8	344.8	345.4	346.6
Quality (fraction vapor)	0.175	0.107	0.084	0.050	0	0	0
Coefficient[a] α, dimensionless	0.15	0.15	0.15	0.15	0.05	0.05	0.05
Specific volume, cu ft/lb	10.86	1.137	0.621	0.237	0.01826	0.01824	0.01822
Velocity, fps ±5 fps	1310	740	610	435	300	245	10
Area, sq ft	0.414	0.0767	0.051	0.0272	0.00305	0.00372	0.0911
Radius, ft	0.362	0.156	0.127	0.093	0.0306	0.0344	0.170
Weight rate of flow,[a] lb/sec	50	50	50	50	50	50	50

[a] Established conditions.

nomenclature should, of course, read "residual enthalpy" not "residual entropy." Equation [3] is not the usual form of the differential equation for compressible flow. It would appear to be true for a constant-pressure process for which Vdp would be 0—unless the authors intend that the new term "alpha" should include the Vdp quantity. This point should be clarified.

Analysis of Table 2 shows that the total energy (enthalpy plus kinetic energy) remains constant at 346.6 Btu/lb throughout flow. However, the total pressure (static pressure plus dynamic pressure) varies widely, even in the homogeneous all-water part of the flow beyond the bubble point. Here the static pressure rises from 177.6 to 600 psi. The total pressure is 708 at the 177.6 static psi point, 755 at the 400 static psi point, and 601 at the 600 static psi point E. It is possible that these large random variations in total pressure result from the aforementioned converging of the lines of constant pressure in the Mollier diagram of Fig. 7 on which this part of the flow in Table 2 was based. If so, this would indicate further the desirability of presenting the data in the form of an enthalpy-pressure chart.

G. L. West, Jr.[9] The authors have supplied curves which should meet one of the comments on a paper by M. W. Benjamin and J. G. Miller.[10] It is possible by choosing α easily to avoid making the common assumption of an isentropic-flow process. By choosing several α's, the effect of the flow process can be estimated in order to find a range of uncertainty. Although it is outside the scope of this paper some criteria for the determination of α would be a beneficial addition. It is true, however, that with large flows and high pressure drops the exact value of the friction factor does not have a large effect; therefore, the exact determination of α is not important.

The authors assume that the velocity of the gaseous and liquid phases is the same. This assumption appears to be justified for most engineering calculations. However, this question previously has been raised and should be resolved. Even though the exact determination of the friction factor is not important for high flows and pressure drops, the thermodynamic process is important. The use of the equilibrium states for the foregoing condition is open to question. Since the present paper contains no experimental work, it is not being suggested that these data should have been included, but that future work should consider the flow mechanisms.

The paper is a worthy addition to the literature on the properties of water. There have been numerous times when the writer could have made good use of these diagrams.

[9] Newport News Shipbuilding and Dry Dock Company, Newport News, Va.

[10] "The Flow of a Flashing Mixture of Water and Steam Through Pipes," by J. G. Miller and M. W. Benjamin, Trans. ASME, vol. 64, 1942, pp. 657–669.

Authors' Closure

The authors agree with Messrs. Treadwell and Bruckner that an enthalpy-pressure diagram will satisfactorily display the thermodynamic properties in the heterogeneous region adjacent to bubble point. However, in the authors' opinion the enthalpy-entropy diagram possesses certain advantages for the description of nearly adiabatic frictional processes. It was for this reason that these residual diagrams were prepared. The limitations of Equation [3] as stated by Treadwell and Bruckner are valid in treating the system from a macroscopic standpoint but the approach can be materially extended by microscopic considerations following the principles of irreversible thermodynamics as set forth by de Groot[11] and Denbigh.[12] The variations in total pressure cited by Treadwell and Bruckner may result from a somewhat arbitrary choice of path for the flow process in this diffuser, rather than from the convergence of the isobars on the Mollier diagram.

Equation [3] appears applicable to any one-dimensional, macroscopic flow process wherein the only exchanges in energy encountered are those between the internal energy of the system and the kinetic energy of the flow. The expression is in no way limited to constant pressure processes as indicated by Treadwell and Bruckner. The term VdP mentioned by them is included in this evaluation of the energy exchanges along with the other derivative of the pressure-volume product.

The assumption of equal velocities for the liquid and gas phases mentioned by West was made in the example employed, otherwise some deviation from the kinetic energy indicated would result from the differing speeds of the two phases. In regard to deviations from equilibrium, the authors' experience shows that subcooling of the gas phase does not persist for more than a few microseconds in flows normally experienced in nozzles. Somewhat greater deviations may be realized in the evaporation of liquid into the gas phase.

[11] "Thermodynamics of Irreversible Processes," by S. R. de Groot, Interscience Publishers, Inc., New York, N. Y., 1952.

[12] "The Thermodynamics of the Steady State," by K. G. Denbigh, John Wiley and Sons, Inc., New York, N. Y., 1951.

Determination of Thermal Conductivities of Metals by Measuring Transient Temperatures in Semi-Infinite Solids

By S. T. HSU,[1] DAYTON, OHIO

The temperature on the flat side of a semi-infinite solid is suddenly raised to a certain value. Then at two stations inside the solid, the temperature variations with time are recorded by means of thermocouples, a string galvanometer, and synchronized photographic equipment. Both the thermal conductivity and specific heat can be determined in the same experiment. The time for measurement is only 30 sec. The result is estimated to be accurate to within 2 per cent for certain metals.

Introduction

VARIOUS methods (1–18)[2] have been devised in the past for measuring the thermal conductivities of metals at ordinary or higher temperatures. Fundamentally they can be classified into two categories; namely, the steady methods and the transient methods. The former usually determine the conductivities while the latter give the diffusivities. The steady methods often involve the measurement of heat quantity which results in a real problem on the elimination of heat loss. The time required for testing is also rather long. In transient methods, the changing temperatures instead of heat quantity are measured. But for the several methods developed in recent years, the testing specimens are mostly in the form of long rods or wire, which are not always available in certain metals. Furthermore, they usually require much longer time for the measurement.

It has been a difficult task to maintain a constant temperature at the end of a rod or wire, or on one side of a plate for the duration of the test. This problem is solved in this method by bringing two plates together so that the temperature at the contact plane remains constant during the testing period.

Temperature Changes Inside Semi-Infinite Solids

Let us consider a semi-infinite solid which has a plane $x = 0$ on the left and extends in all other directions to infinity. If the solid is initially kept at a uniform temperature of θ deg C and the temperature at the plane $x = 0$ is suddenly raised to ϑ_0 and maintained there throughout the period of measurement, then the temperature ϑ inside the solid at various distances x from the plane $x = 0$ will change with time according to the following equation

$$\frac{\vartheta - \vartheta_0}{\theta - \vartheta_0} = G(z) = G\left(\frac{x}{\sqrt{(4at)}}\right) \quad \ldots\ldots [1]$$

where

G = Gauss error integral $\dfrac{2}{\sqrt{\pi}} \displaystyle\int_0^{\frac{x}{\sqrt{(4at)}}} e^{-P^2} dP$

t = time in hours

a = thermal diffusivity = $\dfrac{\lambda}{\gamma c}$, m²/h

with

λ = thermal conductivity, Kcal/mh C

γ = density, Kg/m³

c = specific heat, Kcal/Kg C

Were it possible to maintain the temperature ϑ_0 for a certain length of time in practical experiments, the value a could be determined by measuring ϑ and the corresponding time at a certain station x distance from the plane $x = 0$. Attempts made in the past to secure this constant temperature were not very successful. This is the first time that an answer has been found by the use of two semi-infinite plates simultaneously as shown in Fig. 1.

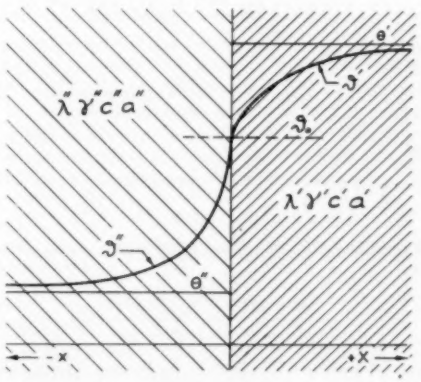

FIG. 1

Assume that the plate at left has an initial uniform temperature of θ' and that at right θ''. If they are suddenly brought into perfect contact with each other, then the temperature at the plane $x = 0$ will stay at, say, ϑ_0 constantly, so long as the plates are insulated.

Under these conditions

$$\lambda' \left(\frac{\partial \vartheta'}{\partial x}\right)_{x=0} = \lambda'' \left(\frac{\partial \vartheta''}{\partial x}\right)_{x=0} \quad \ldots\ldots [2]$$

and for $x \geq 0$

$$\frac{\vartheta' - \vartheta_0}{\theta' - \vartheta_0} = G\left(\frac{x}{\sqrt{(4a't)}}\right) \quad \ldots\ldots [3]$$

---

[1] Chairman, Mechanical Engineering Department, University of Dayton.

[2] Numbers in parentheses refer to the Bibliography at the end of the paper.

Contributed by the Heat Transfer Division and presented at the Fall Meeting, Denver, Colo., September 10–12, 1956, of THE AMERICAN SOCIETY OF MECHANICAL ENGINEERS.

 Manuscript received at ASME Headquarters, June 19, 1956. Paper No. 56—F-11.

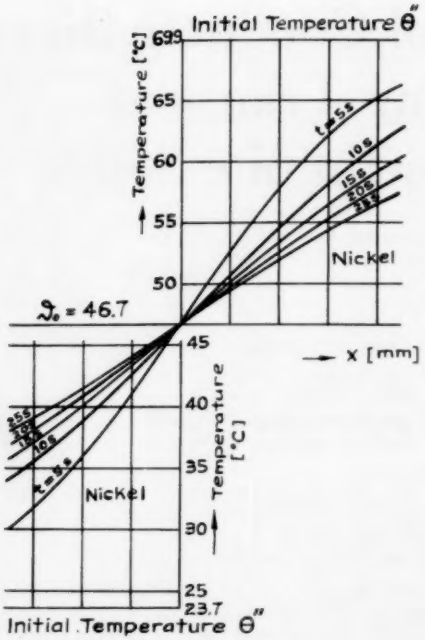

FIG. 2

for $x \leq 0$

$$\frac{\vartheta'' - \vartheta_0}{\theta'' - \vartheta_0} = G\left(\frac{x}{\sqrt{(4a''t)}}\right) \quad [4]$$

therefore

$$\lambda'\left(\frac{\partial\vartheta'}{\partial x}\right)_{x=0} = \frac{\sqrt{(\lambda'\gamma'c')}}{\sqrt{(\pi t)}}(\theta' - \vartheta_0) \quad [5]$$

Likewise

$$\lambda''\left(\frac{\partial\vartheta''}{\partial x}\right)_{x=0} = -\frac{\sqrt{(\lambda''\gamma''c'')}}{\sqrt{(\pi t)}}(\theta'' - \vartheta_0) \quad [6]$$

When Equations [5] and [6] are substituted in Equation [2], the result is

$$\frac{\theta' - \vartheta_0}{\vartheta_0 - \theta''} = \frac{\sqrt{(\lambda''\gamma''c'')}}{\sqrt{(\lambda'\gamma'c')}} \quad [7]$$

The term $\sqrt{(\lambda\gamma c)} = b$ is called the coefficient of heat penetration. This is based on the assumption that ϑ_0 remains constant during the process of heat transfer.

In case the two semi-infinite plates are made of the same material, the temperature at the contact plane will then be equal to the arithmetic mean of the initial temperatures of the two plates. If the temperature at a distance x from the contact plane is measured at a certain instant, a' can be determined with known values of x, t, θ', ϑ' and ϑ_0. The values γ' and c' are usually known or can be determined easily by simple experiments. Therefore λ' can be computed. This plate of known properties is then to be used as a standard specimen for testing unknown metals.

When the standard specimen and a metal plate of unknown properties are brought together into contact, the temperature ϑ_0 at the contact plane will assume the value as indicated in Equation [7]. With the data from experiment, the temperature ϑ_0 is determined by the graphical method. Starting from the moment when the contact begins, if the temperatures are measured in both testing specimens at various predetermined distances from the contact plane at various time intervals, the data can be plotted in curves as shown in Fig. 2. Theoretically, all these curves should meet in one point at the contact plane with perfect contact. So the point of intersection of all these curves will indicate on the temperature scale the contact temperature ϑ_0, which will lead to the determination of λ through Equation [7] if γ and c are known.

Otherwise Equation [7] will give the value $b = \sqrt{(\lambda\gamma c)}$. At the same time, every point on the curves of Fig. 2 indicates a value of temperature ϑ and the corresponding values of x and t. With known values of θ and ϑ_0, the thermal diffusivity a can then be determined. Since $a = \lambda/\gamma c$, it is evident that the product of $ab^2 = \lambda^2$ and the ratio of $b/\sqrt{a} = \gamma C$. As γ can be measured rather easily, the specific heat C can therefore be calculated. In consequence, this method can be used for measuring not only λ but also C of a metal.

Duration and Accuracy

Since this method is based upon the principle of a semi-infinite solid, it would seem impossible to have a huge test specimen made. But if the time of measurement is limited to a very short duration, the temperature wave penetrates into the solid only a small depth so that the metal affected by the temperature variation will have a thickness of at most a few inches. It is important however, that heat be confined to flow in one direction. As shown in the arrangement of Fig. 4, a nickel plate of 70 mm thickness will act just the same as a semi-infinite solid if the time of measurement is kept so short that the value of $L/\sqrt{(4at)}$ does not go below 1.77.

It can be seen later that the accuracy of this method depends upon the accuracy of the simultaneous measurements made on temperature, time, and distance. Since the Gauss function does not change appreciably for value of $z > 1$, it is important to adjust the measurement so that the values of z will be relatively smaller than 1.

Heat-Transfer Resistance at the Contact Plane

It has been assumed so far that the contact between the two semi-infinite bodies is perfect. In case a very thin layer of air, liquid, or other substance exists between the two surfaces, the solution of this problem would certainly be more complicated.

In the equation

$$\frac{\partial\vartheta}{\partial t} = a\frac{\partial^2\vartheta}{\partial x^2} \quad [8]$$

the initial condition is

$$x \geq 0, \quad t < 0: \ \vartheta = \theta = \text{constant}$$

For the simple case when the two semi-infinite plates are made of the same material, the temperature distribution on both sides naturally will still be symmetric as before. The boundary condition is

$$x = 0, \quad t \geq 0: \ -\lambda\frac{\partial\vartheta}{\partial x} + h(\vartheta - \vartheta_0) = 0$$

where h is the coefficient of heat transfer at the contact plane. Assume that h is constant throughout the period of measurement, then (19)

$$\frac{\vartheta - \vartheta_0}{\theta - \vartheta_0} = G\left(\frac{x}{\sqrt{(4at)}}\right) + e^{hx + h^2at}\left[1 - G\left(\frac{x}{\sqrt{(4at)}} + h\sqrt{(at)}\right)\right] \quad [9]$$

In order to reduce this equation to a simpler form, let

$$z = \frac{x}{\sqrt{(4at)}}, \quad y = h\sqrt{(at)}, \quad \text{and} \quad q = y + z$$

Then

$$hx + h^2at = -z^2 + (z + y)^2 = -z^2 + q^2$$

and Equation [9] becomes

$$\frac{\vartheta - \vartheta_0}{\theta - \vartheta_0} = G(z) + e^{-z^2}e^{q^2}\,[1 - G(q)] \ldots\ldots\ [10]$$

Tables (20) are available for the factors $G(z)$, e^{-z^2}, and e^{q^2}.

For every value of

$$\frac{\vartheta - \vartheta_0}{\theta - \vartheta_0}$$

a series of values q and z or a and h may be assumed and found so that the function $a = f(h)$ can be plotted and the intersection of such curves will give the required values of a and h. In actual cases, h is not constant and the curves will not intersect at one point. As a result, the solution is not definite. Furthermore, when the two plates are made of different materials, Equation [9] becomes so complicated that the method will be of very little practical value. This necessitates the elimination of this resistance at the contact plane during the measuring period. Then the contact can be assumed to be perfect in the evaluation of experimental results. After a series of experiments, this objective was finally achieved by the application of a thin layer of grease mixed with graphite powder on both sides and a considerable amount of pressure from a hand-operated arbor press to force the two surfaces together. The pressure was approximately 500 psi.

Description of Measuring and Recording Apparatus

The temperature variations inside the specimen were transformed by means of thermocouples into microvoltage fluctuations which produced various degrees of deflections on the fine golden string of a string-galvanometer. The thermocouples were made of copper and constantan wires of 0.3 mm diam and installed in the holes of 1 mm diam. Quartz tubes of 0.9 mm OD were used for insulation. The holes, drilled radially from and perpendicular to the center line of the cylinder, extended from the center line of the cylinder to the outside surface. They were spaced at 90 deg from each other.

The shadow of the string created by a beam of light from a strong arc lamp was cast on the sensitive photographic paper of a rotating-drum camera. The arrangement is shown diagrammatically in Fig. 3. The two coils of the galvanometer have a combined resistance of 1.8 ohm. The golden string has a diameter of 0.010 mm and a resistance of 31 ohms. The light beam from the arc lamp, cooled by the water-filled lens, passed through the condenser lens and struck the golden string. From there it traveled through the objective lens, a round hole, a narrow opening, and finally fell on the sensitive paper when the camera shutter was opened. Since the temperature changed with time, the deflection of the string and hence the position of its shadow on the photographic paper changed accordingly. As the paper drum rotated at a certain previously set speed, the enlarged curve of deflection in millimeters against time in seconds was recorded automatically.

The specimens were insulated as shown in Fig. 4. An electric oven was used for heating one specimen and a refrigerator for cooling the other. The thermocouple leads were left outside the oven and refrigerator so that the temperatures inside the specimens could be checked for their uniformity before the measurement was made. It is not desirable to have temperature gradient inside the testing specimens.

Since the holes for the thermocouples are 1 mm diam and 25 mm deep, the cross-sectional area of the hole is 25 mm². The specimen has a cross-sectional area of 1960 mm². Therefore the thermocouple hole occupies about 1.27 per cent of the total cross-sectional area of the specimen. Some perturbance of heat flow doubtlessly occurs near the thermocouples, but the error can be neglected.

Computations and Results

The photograph from the rotating-drum camera shows nine parallel calibration lines. The space between two lines indicates 0.2 millivolt. The dotted straight line below the last calibration line is a measure of time. Each space and dash corresponds to 1 sec. The picture shows two bands of curves. The upper band of four curves represents the temperature variations at four stations inside one nickel specimen (later on used as standard speci-

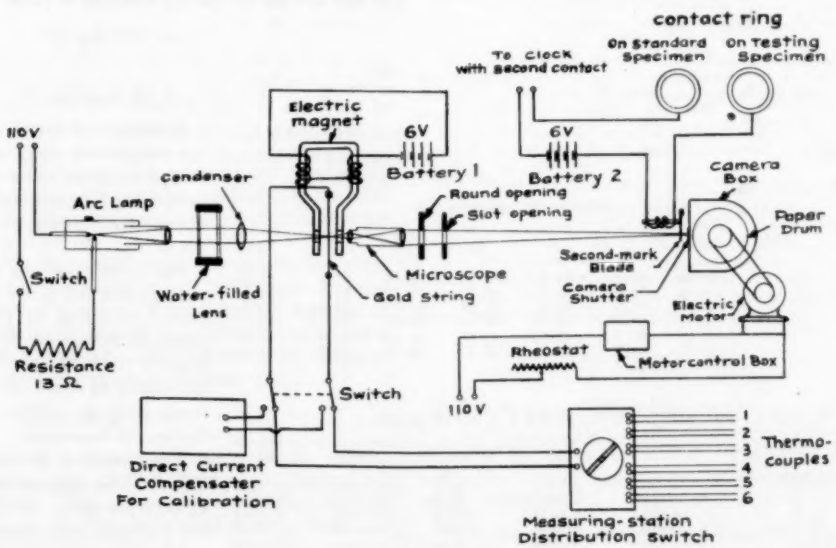

Fig. 3

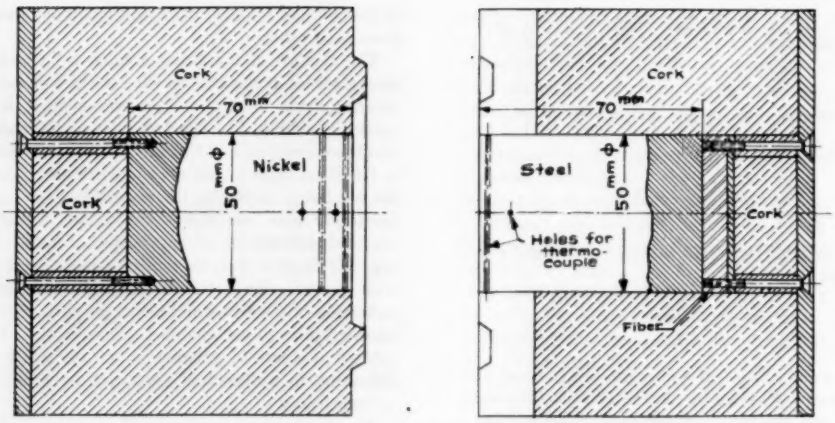

FIG. 4

men) and the lower band of two curves represents the temperature variations at two stations inside the other nickel specimen (the testing specimen). Here

$$\theta' = 69.9 \text{ C}$$

$$\theta'' = 23.7 \text{ C}$$

The various distances from the temperature curves to the zero calibration line can now be measured. The computed values of the corresponding temperatures are shown in Table 1. When these values are plotted, the intersection of the curves gives the temperature at the contact plane as illustrated in Fig. 2

$$\vartheta_0 = 46.7 \text{ C}$$

which proves to be very close to the arithmetic mean of θ' and θ''. Now the temperature difference $(\vartheta - \vartheta_0)$ can be calculated.

With the differences between the initial temperatures and the temperature at contact surface

$$\theta' - \vartheta_0 = 69.9 - 46.7 = 23.2 \text{ C}$$

and

$$\theta'' - \vartheta_0 = 23.7 - 46.7 = -23.0 \text{ C}$$

the temperature ratios

$$\frac{\vartheta' - \vartheta_0}{\theta' - \vartheta_0} \text{ and } \frac{\vartheta_0 - \vartheta''}{\vartheta_0 - \theta''}$$

can be determined.

TABLE 1 TEMPERATURES IN DEGREES C

		Time, sec					
	x in mm	0	5	10	15	20	25
Standard specimen	14.95	69.9	64.6	60.85	58.65	57.3	56.15
	8.92	69.9	59.0	55.65	54.2	53.2	52.5
	5.01	69.9	53.9	51.85	50.95	50.45	50.0
	2.09	69.9	49.85	48.9	48.45	48.25	48.1
Testing specimen	−2.69	23.7	42.75	43.8	44.45	44.7	44.95
	−9.96	23.7	33.7	37.1	38.65	39.7	40.4

TABLE 2 THERMAL DIFFUSIVITY $a = \frac{x}{4lz^2}$ IN M²/H

	a in m²/h	Time, sec					
	x in mm	0	5	10	15	20	25
Standard specimen	14.95		0.0554	0.0554	0.0550	0.0544	0.0563
	8.92		0.0549	0.0562	0.0549	0.0557	0.0566
	5.01		0.0568	0.0570	0.0560	0.0545	0.0560
	2.09		0.0537	0.0555	0.0586	0.0559	0.0577
Testing specimen	−2.69		0.0557	0.0519	0.0575	0.0545	0.0572
	−9.96		0.0576	0.0593	0.0578	0.0586	0.0581

According to Equation [1]

$$\frac{\vartheta - \vartheta_0}{\theta - \vartheta_0} = G(z) \quad \text{with} \quad z = \frac{x}{\sqrt{(4at)}}$$

the values z can be found with the aid of Gauss error integral tables. Then the required values of a can be solved (see Table 2).

The mean value of a for the standard specimen (20 points) is

$$a' = 0.0558 \text{ m}^2/\text{h}$$

in the temperature range 46.7 to 69.9 C, and for the testing specimen (10 points)

$$a'' = 0.0568 \text{ m}^2/\text{h}$$

in the temperature range 23.7 to 46.7 C.

The mean value of all the 30 points is

$$a = 0.0561 \text{ m}^2/\text{h}$$

The error from the mean value for the standard specimen is 0.5 per cent and for the testing specimen is 1.2 per cent. With

$$\gamma = 8870 \text{ Kg/m}^3$$

and

$$C = 0.109 \text{ Kcal/Kg C}$$

the coefficient of heat conductivity is $\lambda' = 53.9$ Kcal/mh C for the standard specimen, in the temperature range 46.7 to 69.9 C; $\lambda'' = 54.9$ Kcal/mh C for the testing specimen, in the temperature range 23.7 to 46.7 C; and their mean value $\lambda = 54.2$ Kcal/mh C.

The nickel used was commercial nickel with guaranteed purity of at least 99 per cent. According to Table 3 the value would be very close to 54.2 if the purity happens to be 99.1 per cent. It would be interesting to check the result with that from a steady method as used by the Bureau of Standards.

A specimen of stainless steel also was tested. The composition was as follows: C, 0.18 per cent; Cr, 13.5 per cent; Ni, 0.7 per cent. The same nickel standard specimen was used

TABLE 3 HEAT CONDUCTIVITY OF NICKEL (λ)

Purity of nickel, per cent	Conductivity in Kcal/mh C	Temp, deg C	Reference
99.9	78.0	20	Koch (22)
99.5	61.5	20	Hogan, Sawyer (18)
99.2	59.0	20	Koch (22)
99.0	50.4	18	Landolt and Boernstein (21)

$$\theta' = 64.0 \text{ C}$$

$$\theta'' = 26.95 \text{ C}$$

$$\vartheta_0 = 50.4 \text{ C}$$

According to Equation [7]

$$\frac{\sqrt{(\lambda''\gamma''C'')}}{\sqrt{(\lambda'\gamma'C')}} = \frac{\theta' - \vartheta_0}{\vartheta_0 - \theta''} = \frac{13.60}{23.45} = 0.580$$

$$= (0.580)^2 = 17{,}600 \text{ K cal}^2/\text{m}^4\text{h C}^2$$

with

$$a = \frac{\lambda''}{\gamma''C''} = 0.0227 \text{ m}^2/\text{h}$$

$$\lambda'' = 20.0 \text{ Kcal/mh C}$$

in the temperature range 26.95 to 50.4 C, and

$$\gamma''C'' = 880 \text{ Kcal/m}^3 \text{ C}$$

As measured

$$\gamma'' = 7690 \text{ Kg/m}^3$$

Therefore

$$C = 0.114 \text{ Kcal/Kg C}$$

According to Koch, a similar grade of steel has the following properties at 20 C:

10 per cent Cr: $= 7760$ Kg/m^3, $C = 0.11$ Kcal/Kg C, $= 27$ Kcal/mh C

20 per cent Cr: $= 7670$ Kg/m^3, $C = 0.11$ Kcal/Kg C, $= 20$ Kcal/mh C

The value of specific heat is very close to the result of the test. While the testing temperature was about 30 deg higher than 20 C, the conductivity could vary with temperature. It also could be influenced by the different contents of Si and Mn in the steel.

As definite data on the metals used in these experiments are not available at present, it is not easy to figure out the accuracy of this method. However, with some improvements in the technique of handling the specimens, an accuracy within about 2 per cent probably can be achieved.

All experiments were performed within the temperature range of 20 to 80 C. The specimens were brought into contact at room temperature. However, if special mechanisms are designed to handle the specimens, the experiments can be carried out inside a controlled-temperature chamber. This will permit the measurement of thermal conductivity at any temperature range.

Acknowledgments

The author wishes to acknowledge most gratefully the invaluable suggestions of Prof. G. Eichelberg, Swiss Federal Institute of Technology. The assistance rendered by Mr. P. Hollenstein in making the specimens and helping with the measurements is also greatly appreciated.

Bibliography

1 "An Experimental Enquiry Into the Laws of the Conduction of Heat in Bars and Into the Conducting Power of Wrought Iron," by J. D. Forbes, Transactions of the Royal Society of Edinburgh, Scotland, vol. 23, 1862, pp. 133–146; vol. 24, 1865, pp. 73–85.

2 "The Absolute Thermal Conductivity of Nickel," by T. C. Baillie, Transactions of the Royal Society of Edinburgh, Scotland, vol. 39, 1897–1898, pp. 361–382.

3 "The Thermal and the Electrical Conductivity of a Copper Crystal at Various Temperatures," by W. G. Kannuluik and T. H. Laby, Proceedings of the Royal Society of London, England, series A, vol. 121, 1928, pp. 640–653.

4 "A Radial Heat-Flow Apparatus for the Determination of Thermal Conductivity," by A. C. Burr, *Canadian Journal of Technology*, vol. 29, 1951, pp. 451–457.

5 "Die Vermeidung eines Schutzringes bei der Messung der Wärmeleitfähigkeit plattenförmiger Körper," by E. Schmidt, *Abhandlungen der Braunschweigischen Wissenschaftlichen Gesellschaft*, vol. 4, 1952, pp. 176–180.

6 "Über den stationaeren Temperaturzustand eines elektrisch geheizten Leiters," by F. Kohlrausch, *Annalen der Physik*, vol. 4, F. 1, 1900, pp. 132–158.

7 "Neue Methode das Wärmeleitungsvermoegen der Körper zu bestimmen," by A. J. Angstrom, *Annalen der Physik*, vol. 114, 1861, p. 513; vol. 123, 1864, p. 628.

8 "Vergleichende Untersuchungen über die Methode von Angstrom und Neumann zur Bestimmung der Wärmeleitung der Körper," by K. L. Hagström, *Öfversigt af Kongl. Vetenskaps Akademiens Förhandlingar*, Stockholm, Sweden, vol. 48,1891, pp. 45, 289, and 381.

9 "Expériences sur la conductibilité calorifique des solides," by F. Neumann, *Annales Chimie de Physique*, Paris, France, vol. 66, 1862, pp. 183–187.

10 "A Method of Measuring Heat Conductivities," by R. W. King, *Physical Review*, vol. 6, 1915, pp. 437–445.

11 "An Improved Method for the Determination of Thermal Diffusivities," by Ch. Starr, *Review of Scientific Instruments*, vol. 8, 1937, pp. 61–64.

12 "Über eine Methode zur Bestimmung der Wärmeleitung fester Körper," by F. A. Schultze, *Annalen der Physik* N. F., vol. 66, 1898, pp. 207–223.

13 "Wärmeleitungsfähigkeit des Kupfers, aus dem stationaeren und variabeln Temperaturzustand bestimmt, und Wärmefluss in einer durch Kuehlwasser bespuelten Endflaeche eines Wärmeleiters," by W. Schaufelberger, *Annalen der Physik* 4, F. 7, 1902, pp. 589–630.

14 "A Precision Method for Determining the Thermal Diffusivity of Solids," by R. H. Frazier, *Physical Review*, vol. 39, 1932, pp. 515–524.

15 "The Theory of Moving Sources of Heat and Its Application to Metal Treatment," by D. Rosenthal, Trans. ASME, vol. 68, 1946, pp. 849–866.

16 "A New Method of Determining Thermal Diffusivity of Solids at Various Temperatures," by A. Ambrosio and D. Rosenthal, Trans. ASME, vol. 73, 1951, pp. 971–974.

17 "Thermal Conductivity of Homogeneous Materials—Determination by an Unsteady-State Method," by K. O Beatty, Jr , A. A. Armstrong, and E. M. Schoenborn, *Industrial and Engineering Chemistry*, vol. 42, 1950, pp. 1527–1532.

18 "The Thermal Conductivity of Metals at High Temperature," by C. L. Hogan and R. B. Sawyer, *Journal of Applied Physics*, vol. 23, 1952, pp. 177–190.

19 "Tafeln hoeherer Funktionen," by Jahnke-Emde, Teubner, Leipzig, Germany, 1948.

20 "Conduction of Heat in Solids," by H. S. Carslaw and J. C. Jaeger, Clarendon Press, Oxford, England, 1948.

21 "Physikalisch-chemische Tabellen," by Landolt and Boernstein, Julius Springer, Berlin, Germany, 5. Aufl., 1935.

22 "Grundlagen des Wärmeaustausches (Stoffwerte)," by B. Koch, Beucke & S. (Dissen), 1950.

Discussion

P. J. Schneider.[3] The author is to be congratulated on adding still another technique to the long list of known schemes for measuring the thermal conductivity of solid materials. The new technique of maintaining a uniform and constant surface temperature is indeed novel.

[3] Department of Mechanical Engineering, University of Minnesota, Minneapolis, Minn.

As in many other innovations, however, the new approach might appear simply to trade one set of problems for another. One question which might arise in this connection is: "Why trade the steady method for a more difficult transient method if thermal conductivities rather than thermal diffusivities are of interest?" The transient method used here is difficult because it must satisfy a difficult initial and surface condition[4]; namely, an instantaneous rise in surface temperature. Even if high contact conductances are achieved in the present method, this condition can only be approximated at best. If it is not well satisfied, then the complete temperature history in the two solids is affected. Although Fig. 2[5] indicates (by extrapolation) that steady contact temperatures were achieved, no information is given with regard to the 5-sec transient preceding the first instantaneous temperature profile illustrated. A question also arises as to whether measurements at only two depths in the test specimen are sufficient to establish this instantaneous temperature profile.

The actual contact conductance between the specimens is known to be sensitive to such things as surface roughness, joint pressure, hardness of the softer material, and the properties of any entrapped fluid. Unfortunately it also depends on the mean contact temperature and conductivities of the two materials, both unknown. On the other hand an exact solution can be obtained which includes the effect of this interface resistance, and a separate experiment could be undertaken to evaluate it. The question naturally would arise (in regard to the final experiment) that if the contact resistance is strongly dependent on the contact pressure, how close to instantaneous can one apply the required pressure by means of a hand arbor?

Another question arises in connection with the testing procedure; since thermocouples were not installed to measure the contact temperature, one could not be absolutely certain that initial temperature gradients were zero. Further, if an initial temperature gradient did exist, it would be greatest in this region between the surface and first thermocouple. It also might be worth while to install thermocouples at several radii for the first measuring station to see if both initial and subsequent radial temperature gradients are zero. If one assumes a uniform surface temperature on an insulated circular rod, then no radial temperature gradients can exist. However, if one specifies a uniform heat input over the contact face, then radial temperature gradients can exist. Under the latter condition, the assumption of one-dimensional flow no longer holds.

There is, presently, an urgent need for conductivity data at elevated temperatures, and one naturally asks if the present method can be adapted to this need. Particular reference is made here to the problem of oxidation of the contact faces at higher temperatures.

It is hoped that the author's ambitious program of investigation will be continued in an effort not only to explore the full potentiality of his new technique, but to obtain sufficient data to compare with thermal conductivities obtained independently by other methods.

J. R. Woolf.[6] It appears that the author has practically eliminated the contact resistance so that the thermal diffusivity of metals may be determined from the classical solution of the transient-temperature distribution in the semi-infinite solid. His results will be appreciated by all who have attempted to make similar measurements and also by those who feel the need for more and better thermophysical data on the materials which engineers encounter frequently.

The method of reducing the contact resistance to an acceptable value seems to have been successful. It would be desirable, as the author notes, to compare results of exact duplicate alloys with values established by the methods previously considered the most accurate. The great variation of thermal conductivity with alloy composition makes comparison of data rather difficult and often meaningless.

While reading this paper, one question kept occurring: "Is the interface temperature necessarily independent of time for any experimental run?" Obviously it is for the case of both bodies being of the same material and having like properties γ, C, and λ. From consideration of the first law of thermodynamics, however, one finds that the final temperatures at thermal equilibrium are, for geometrically identical bodies, given by the following

$$\gamma' C' (\vartheta_0 - \theta') = \gamma'' C'' (\theta'' - \vartheta_0)$$

Solving for ϑ_0, the interface temperature which, of course, would be the temperature of both bodies throughout

$$\vartheta_0 = \frac{\theta' + \dfrac{\gamma'' C''}{\gamma' C'} \theta''}{1 + \dfrac{\gamma'' C''}{\gamma' C'}}$$

In the author's case of measuring the diffusivity of a steel, using the nickel as a standard, the following values were used or determined

$\vartheta_0 = 50.4$ C = initial interface temperature

Nickel		Steel
$\theta' = 64.0$	deg C	$\theta'' = 26.95$
$C' = .109$	Kcal/kg C	$C'' = 0.114$
$\gamma' = 8870$	kg/m^3	$\gamma'' = 7690$
$\lambda' = 54.2$	Kcal/mh C	$\lambda'' = 20.0$

The equilibrium interface temperature is calculated as

$$\vartheta_0 = \frac{64.0 + \dfrac{0.109(8870)}{0.114(7690)} (26.95)}{1 + \dfrac{0.109(8870)}{0.114(7690)}} = 44.28 \text{ C}$$

The difference between the initial interface temperature and the equilibrium interface temperature is 16.6 per cent of the difference between the original temperatures of the two bodies. However, further consideration reveals that the initial interface temperature will hold until the temperature of the ends of the bodies changes from the original temperature. Therefore, the author's calculations are valid since the specimen size and time of observations were prescribed by this same condition. It was felt that this point should be mentioned as a caution in conducting further experiments along this line.

Frequently the end of such a project as the author has undertaken is the proof of the accuracy of the apparatus. Let us hope that, in this case, he will be able to use his apparatus for a useful purpose—the production of data on the conductivity and diffusivity of solids, particularly metals at moderately high temperatures. There is a need for these data and he has the ability and the interest to obtain them for us.

Author's Closure

All the comments and remarks appearing in the discussion are greatly appreciated. While Dr. Schneider pointed out that the initial condition following Equation [8] is incomplete, the only item which was left out is

[4] The initial condition following Equation [8] of the paper is incomplete.

[5] This figure lacks an abscissa scale.

[6] Professor of Mechanical Engineering, A. and M. College of Texas, College Station, Texas. Mem. ASME.

$$\vartheta = \vartheta_0 \text{ at } x = 0$$

which is actually independent of time. The abscissa scale of Fig. 2 is equal to 4 mm per space.

Theoretically, a steady method would appear more simple than the transient method for the determination of thermal conductivities rather than thermal diffusivities. Yet the problem of eliminating the heat loss and reducing the time of measurement has not been successfully solved. Here again the steady method involves usually the measurement of heat quantity which is well known to be very difficult. By cutting down the measuring time to a few seconds, the transient method offers many advantages. A close examination of the arrangement will show that the initial condition is well satisfied to give the results accurately enough for engineering purposes.

If it is necessary, the temperature profile within the first 5-second transient period can also be plotted in the figure. To establish accurate instantaneous temperature profile, it is not sufficient to have measurements at only two depths in the test specimen. However, the important thing in this case is not the instantaneous temperature profile but the intersection of all the temperature curves. So far the portions of the curves near the contact plane assume fairly straight shapes; measurements at two depths are quite adequate. The drawback of having too many thermocouples inside the specimen is that the heat flow-pattern will be greatly distorted.

It is obvious that the contact resistance cannot be completely eliminated. To apply contact pressure together with a thin coat of graphite will reduce this resistance to a value low enough to yield accurate results. In order to achieve an instantaneous application of the required pressure, a special arrangement of certain mechanical devices would be desirable. The author used two contact indicators in conjunction with the hand press so that the measurement of zero time can be fairly accurate.

For the purpose of determining whether an initial temperature gradient did exist inside the specimen, a separate test was made by inserting six thermocouples along the axis of a specimen and measuring the temperature at various depths with a rotary switch. The temperature was found to be uniform throughout the length of the axis of the specimen. With the insulations as shown in Fig. 4, it is doubtless that the flow of heat is one-dimensional at least around the area near the axis.

This method can certainly be used for conductivity data at elevated temperature. In this case the author suggests that the specimen be heated together with another protective plate of same material. They should be clamped together during the heating process so as to avoid the oxidation of the specimen's surface. Of course automatic mechanism must be designed for handling the specimen.

Professor Woolf indicated that for geometrically identical bodies the final temperatures at thermal equilibrium are given by the relation

$$r'c'(\vartheta_0 - \theta') = r''c''(\theta'' - \vartheta_0)$$

This is true only when ϑ_0 is the final uniform equilibrium temperature of the bodies. However, in this case, within a certain definite time interval, the heat wave travels farther in one body than in the other. Consequently, this equation can no longer be applied. This is in agreement with Professor Woolf's statement that the initial interface temperature will hold until the temperature of the ends of the bodies changes from the original temperature. In fact, the measurement of temperatures has to be completed before the heat wave reaches the end of the specimen, or the value of $L/(4at)^{1/2}$ must be > 1.77.

ADVANCES IN NUCLEAR ENGINEERING

HOT LABORATORY OPERATION AND MAINTENANCE

In August, the rich fund of information brought into the 1957 NUCLEAR CONGRESS will be published in three volumes titled:

By arrangement with the publishers, you can purchase this 3-volume set from the ASME at a special pre-publication price of $35 provided your order is received by August 15th. Price after that date will be $45.

The two volumes covering Advances in Nuclear Engineering contain the 125 papers with available discussion from the 2nd Nuclear Engineering and Science Conference of the Congress.

The sixty-two of these contributions which are in Volume I are concerned with:

manufacture, production, recovery, and economics of nuclear fuels . . . spent fuel processing . . . plant containment concepts and design . . . plant components . . . waste disposal . . . protection and safety measures . . . radiation processing.

The other seventy-three articles, assigned to Volume II, deal with:

reaction design . . . reactor core design . . . operation and maintenance of reactors . . . metallurgy . . . heat transfer and heat evolution . . . educational uses of reactors . . . standardization planning in the nuclear field.

The third volume's sixty-one papers pertain to:

equipment for hot chemical, physical, mechanical, and metallurgical operations . . . hot cell installations . . . hot laboratory facilities . . . operation and administration . . . specialized hot operations.

A resume of the international outlook for atomic power, and the highlights of the 1956 meeting of the American Nuclear Society are also given.

THE 1957 NUCLEAR CONGRESS

was held in Philadelphia, Pa. last March to afford engineers and scientists in the fields of nuclear science, engineering, and management an opportunity to exchange knowledge, information, and ideas on the peaceful application of atomic energy.

Over 450 participated in discussions which explored the problems and developments of 34 specific areas of nuclear technology.

The Congress was sponsored by the following organizations with the Engineers Joint Council co-ordinating their efforts.

Amer Chem Soc • Amer Geol Inst • Amer Inst Chem Engrs • Amer Inst Elec Engrs • Amer Inst Indus Engrs • Amer Inst Mining Engrs • Amer Inst Physics • Amer Nuclear Soc • Amer Public Health Assn • Amer Rocket Soc • Amer Soc Civil Engrs • Amer Soc Engrg Educ • Amer Soc Heating and Air Conditioning Engrs • Amer Soc Mech Engrs • Amer Soc Metals • Amer Soc Testing Materials • Amer Water Works Assn • Engrg Inst of Canada • Federation of Sewage & Industrial Wastes Assns • Health Physics Soc • Hot Laboratories Committee • Inst of Aero Sciences • Inst of Radio Engrs • Nat'l Indus Conference Board • Soc Automotive Engrs • Soc Naval Arch & Marine Engrs.

In brief, this 3-volume set transmits to you a wealth of NEW information for opening new avenues for the peaceful use of atomic development. So don't wait — use this handy coupon Now to reserve YOUR set.

From the ASME, members of sponsoring organizations may purchase the two volumes containing Selected Papers From the 1st Nuclear Congress held December 1955 for $28, which is 20% less than charged the general public.

Volume I covers most of the field of "reactor safeguards;" reviews reactor materials, their properties, behavior, and uses; treats reactor design, components and techniques; deals with the processes of heat generation, heat transfer and fluid dynamics.

Volume II is concerned with waste disposal and radiation hazards, dissolution of solid fuel elements, the chemistry and engineering of the aqueous processing of fuel and blanket materials, pyrochemical methods, methods involving fluoride volatility differences, experimental low-power assemblies, reactor physics, instrumentation and control.

Date _____

AMER. SOC. MECH. ENGRS.
29 W. 39th St., New York 18

(Please Check)

Reserve for me
☐ The 3 volumes of the 1957 Nuclear Congress Proceedings entitled Advances in Nuclear Engineering and Hot Laboratory Operation and Maintenance at the special pre-publication price of $35.* Bill will be rendered when books are mailed.

Mail immediately
☐ The 2 volumes containing Selected Papers from the 1st Nuclear Congress. Price, $28. Payment to be made upon receipt of bill.

Name _____

Address _____

City _____ Zone _____ State _____

*Effective to August 15, 1957.